Title
Design and Synthesis of "Clickable" Azido-Lipid/Glycolipid Probes

Permalink
https://escholarship.org/uc/item/4xs1r10k

Author
Hsu, Jonathan

Publication Date
2021

Peer reviewed|Thesis/dissertation

Design and Synthesis of "Clickable" Azido-Lipid/Glycolipid Probes

By

JONATHAN HSU
THESIS

Submitted in partial satisfaction of the requirements for the degree of

MASTER OF SCIENCE

in

Pharmaceutical Chemistry

in the

OFFICE OF GRADUATE STUDIES

of the

UNIVERSITY OF CALIFORNIA

DAVIS

Approved:

_____
Dr. Jacquelyn Gervay-Hague, Chair

_____
Dr. Xi Chen

_____
Dr. Suvarn S. Kulkarni

Committee in Charge

2021

Table of Contents

Abstract

Cholesterol, a major lipid component of animal plasma membranes (PM) and a small component in some plants, has been associated with the development of various diseases and infections, like Alzheimer's disease (AD), Parkinson's diseases (PD), *H. pylori* infection, etc., through an imbalance in cholesterol homeostasis or cholesterol modification. In addition to the bioactivity of lipids like cholesterol, glycolipids (glycosylceramides and sterol glycosides) have been reported to influence the release of T-helper 1 (T_H1) and T-helper 2 (T_H2) cytokines in mammals. Also, cholesterol has been reported to undergo a sugar exchange with glucosyl ceramides. In previous studies, cholesterol analogues with intrinsic or extrinsic fluorescent groups were used as probes to monitor biodistribution of cholesterol and the sugar exchange with glucosyl ceramides. However, problems arose with these cholesterol probes from disrupting plasma membranes to difficult extraction for metabolite characterization. Recently, a dehydroepiandrosterone (DHEA) probe with a primary alkoxyl-azido group mimicked cholesterol well while providing efficient extraction via copper(I)-catalyzed azide/alkyne cycloaddition (CuAAC) with 4-*N*-methylamino-1,8-napthalimidopropyne (**MAN**) for metabolite characterization and minimal disruption of plasma membranes. Currently, there are no azido-glycolipid probes available to monitor the metabolism of glycolipids during T_H1 and T_H2 cytokine release in addition to the sugar exchange with ceramides. In this project, two secondary C_{17} azido-DHEA (**5** and **8**) probes were prepared and six azido-glycolipid (**14**, **15**, **16**, **17**, **22**, and **24**) probes were proposed to study the metabolism of lipids and glycolipids in various environments. Chapter 1 will focus on the bioactivity of sterols/sterol glycosides and previous sterol probes. Chapter 2 will discuss the total synthesis of the two secondary C_{17} azido-DHEA probes (**5** and **8**). Chapter 3 will cover the NMR characterization of various DHEA derivatives while Chapter 4 will describe previous glycosylceramide derivatives, the bioactivity of glycosylceramides, and the future synthesis of six azido-glycolipid probes (**14**, **15**, **16**, **17**, **22**, and **24**).

List of Figures

xvi

xvii

List of Schemes

List of Tables

Chapter 1

Sterol/sterol glycoside bioactivity and probe synthesis

Section 1.1: Sterols/Sterol Glycosides

In the human body, there are biological macromolecules: carbohydrates, nucleic acids, proteins, and lipids (B. Jirgensons, 1996). Previous studies and the current project are focused primarily on the bioactivity or distribution of sterols/sterol glycosides.
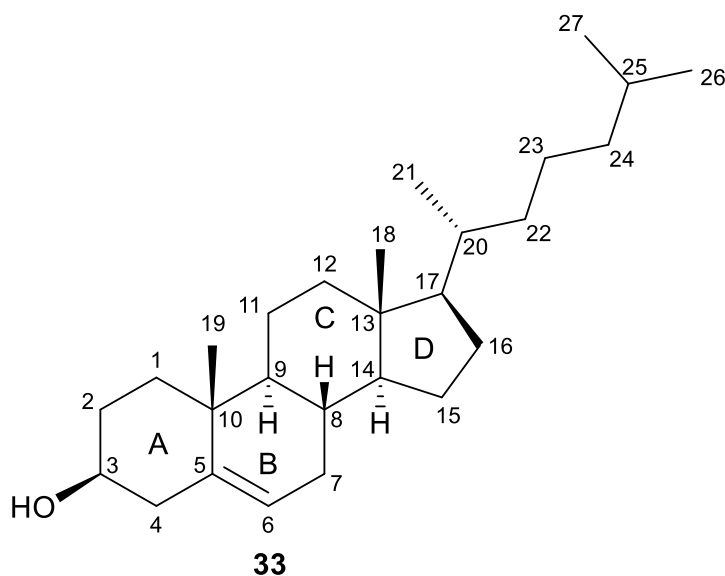
Figure 1.1 Cholesterol (33)

Cholesterol (**33**) is described as a major lipid component of animal plasma membranes (PM) and a small component in plants (Solanko et al., 2015). Within cell plasma membranes made of saturated and unsaturated phospho- or sphingolipids at a high sterol mole fraction, cholesterol (**33**) was shown to induce phase coexistence between liquid ordered (lo) and liquid disordered (ld) in a d_{62}-dipalmitoyl-PC-cholesterol multi-bilayer system using deuterium nuclear magnetic resonance (NMR), calorimetry, and electron paramagnetic resonance (EPR) (Solanko et al., 2015; Hjort Ipsen et al., 1987). Lo refers to the liquid-crystalline phase at high cholesterol concentrations while ld refers to the liquid-crystalline phase at low cholesterol concentrations (Hjort Ipsen et al., 1987). Even though cholesterol (**33**) is primarily synthesized in the endoplasmic reticulum, the majority (60%) is located in PMs while the remaining is spread among the endoplasmic reticulum, mitochondria, Golgi apparatus, and other organelles through vesicular or

non-vesicular pathways (Solanko et al., 2015; Králová et al., 2018). Cholesterol (**33**) is composed of four fused rings with an alkyl chain connected to C_{17} in the D ring. In addition, there is a hydroxyl group attached in a β orientation to C_3 of the A ring. There is also a double bond between C_5 and C_6 in the B ring (see Figure 1.1). Cholesterol's major PM functions include controlling membrane structural integrity and fluidity and regulating the activity of various membrane proteins (Králová et al., 2018). Additionally, cholesterol (**33**) reduces the transport of neutral solutes, hydrogen ions, and sodium ions across the plasma membrane (Králová et al., 2018). In addition to plasma membrane function, cholesterol (**33**) plays an important role in various signaling pathways, like Hedgehog (Hh) signaling (Králová et al., 2018; Jao et al., 2015). In particular, cholesterol (**33**) forms an ester linkage to the Hh ligand (see Figure 1.8) and activates the seven-spanner membrane protein Smoothened (Smo), thus aiding signal transduction (Jao et al., 2015). Cholesterol (**33**) also serves as a precursor for various steroid hormones and vitamins (Králová et al., 2018; Jao et al., 2015).

Although cholesterol (**33**) is a fundamental lipid component of the body, it has been associated with the development of various diseases or defects. A small portion of these diseases are caused by an imbalance in cholesterol homeostasis. Typically, cholesterol homeostasis is controlled by various mechanisms: cellular uptake, storage, synthesis or efflux (Králová et al., 2018). In addition, it was stated that excess cholesterol is converted to cholesterol esters via acyl-coenzyme A acyl transferase (ACAT) and later stored as liquid droplets (Solanko et al., 2015). Having unrestrained cholesterol concentration or deregulated cholesterol movement can lead to atherosclerosis, Niemann-Pick's disease type C (NPC), Alzheimer's disease (AD), Parkinson's diseases (PD), and possibly Huntington's disease (HD) (Solanko et al., 2015; Králová et al., 2018).
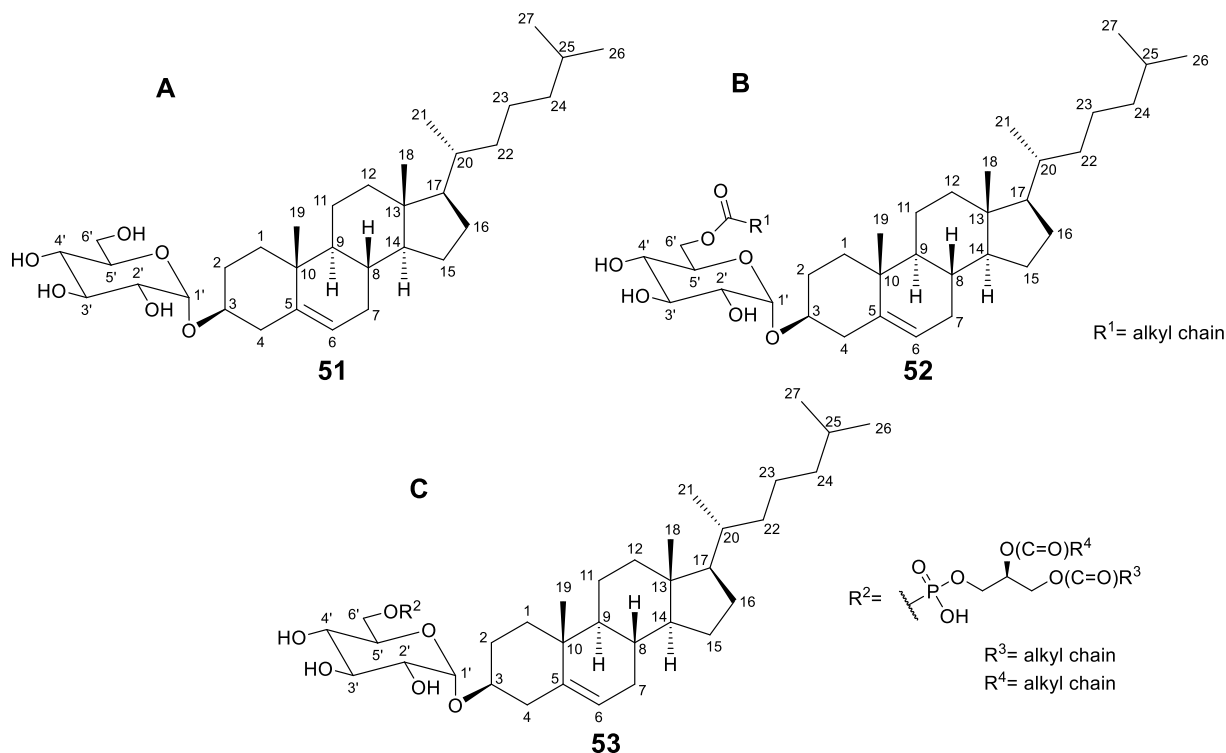
Figure 1.2 Cholesterol derivatives. (A) Cholesteryl-α-D-glucopyranoside (CG, 51), (B) Cholesteryl-6'-O-acyl-α-D-glucopyranoside (CAG, 52), (C) Cholesteryl-6'-O-phosphatidyl-α-D-glucopyranoside (CPG, 53)

Cholesterol (**33**) also plays an important role in pathogenic diseases. For example, *Helicobacter pylori* (*H. pylori*) was shown to cause chronic gastritis, gastric carcinoma, gastric mucosa-associated lymphoid tissue lymphoma, or cancer-related demises (Jan et al., 2016; Jan et al., 2020). Specifically, *H. pylori* uptakes cholesterol (**33**) from its host and modifies the cholesterol via α-glucosylation (Jan et al., 2016; Jan et al., 2020). The cholesterol glucoside derivatives formed during *H. pylori* infection consist of cholesteryl-α-D-glucopyranoside (CG, **51**) (see Figure 1.2A), cholesteryl-6'-O-acyl-α-D-glucopyranoside (CAG, **52**) (see Figure 1.2B), and cholesteryl-6'-O- phosphatidyl-α-D-glucopyranoside (CPG, **53**) (see Figure 1.2C) (Jan et al., 2016). CPGs (**53**) were shown to have no direct role in promoting *H. pylori* pathogenesis, so further discussion will be focused on CGs (**51**) and CAGs (**52**) (Jan et al., 2016; Jan et al., 2020). CGs (**51**) are synthesized by a bacterial glucosyltransferase encoded by *hp0421*, attaching an α-linked glucose moiety to the 3-hydroxyl group of cholesterol (**33**) (Jan et al., 2016; Jan et al.,

2020). CAGs (**52**) are synthesized by cholesteryl-α-D-glucopyranoside-6'-acyltransferase (CGAT) encoded by *hp0499*, adding a fatty acid chain to the 6'-hydroxyl group of CGs (**51**) (Jan et al., 2020). CGAT is primarily located in the outer membrane of *H. pylori* and later distributed by outer membrane vesicles (OMVs) to the host cell to produce CAGs (**52**) (Jan et al., 2020). Specifically, it was concluded that α-CGs (**51**) prevent phagocytosis by macrophages (Grille et al., 2010; Wunder et al., 2006). In contrast, Wunder et al. reported that cholesteryl-β-D-glucopyranoside (**62**) promotes phagocytosis of *H. pylori* by macrophages (Wunder et al., 2006). This difference in bioactivity between the two cholesterol glucoside anomers could explain *H. pylori's* primary synthesis of α-CGs (**51**) when infecting its host. In addition, CAGs (**52**) were shown to enhance lipid raft formation in host cells, cytotoxin-associated gene A (CagA) translocation, and subsequent tyrosine phosphorylation to promote *H. pylori* pathogenicity (Jan et al., 2016; Jan et al., 2020).

It should be noted that CGs (**51**) are specific examples of a larger class of compounds generally referred to as sterol glycosides (SGs). Likewise, CAGs (**52**) represent specific members of a larger collection of compounds called acylated sterol glycosides (ASGs). In contrast to CG (**51**) and CAG (**52**), the vast majority of SG and ASG exhibit a β-linkage between the sugar and sterol. The distribution of SGs and ASGs among mammals is not clearly defined and more research is needed. However, a large proportion of SG and ASG have been defined within various plants. For instance, the ratio of ASG to SG in different fresh (tomato, banana, spinach, etc.) and dry (cashew, peanut, red beans, etc.) food samples ranged from 0.4-3.6 (Nyström et al., 2012). The sterol scaffold of these sterol glycosides/derivatives contained common plant sterols including sitosterol, campesterol, stigmasterol, stanols, and other various sterols (Nyström et al., 2012). These glycosylated sterols contributed 5-60% of the total sterol content among different plant samples (Nyström et al., 2012). Continuing, phytosterol glycosides/derivatives have been shown to promote a positive outcome on mammals. Lin et al. demonstrated the effect of ASG on

the reduction of cholesterol within mice intestines by ~45% in a three-day experiment. It was discerned that the cleavage of the acyl group from the 6' hydroxyl group of ASG led to the reduction in cholesterol absorption (Lin et al., 2011). In addition, it was stated that sitosteryl-β-glucoside increases the concentration of IFNγ and IL-2 (T_H1 cytokines) in mice and humans (Grille et al., 2010; Bouic et al., 1996; Lee et al., 2007). These results indicate the effect of sitosteryl-β-glucoside in creating a dominant T_H1 response, vide infra.

To study the bioactivity and/or biodistribution of cholesterol (**33**), sterol probes have been synthesized and used for cellular monitoring. Two main features of these sterol probes thus far include 1) Optimal fluorescence, 2) Minimal changes to structure and bioactive properties of cholesterol (**33**) (Solanko et al., 2015; Králová et al., 2018). In addition to minimal changes to structure and bioactive properties of cholesterol (**33**), biased partitioning into the lo phase would be beneficial for sterol probes. Among previous studies, there are three major classes of sterol probes: intrinsic, extrinsic, and click chemistry probes. In terms of studying the bioactivity and/or biodistribution of sterol glycosides, there is a lack of sterol glycoside probes available for use thus signaling the need to synthesize these probes.

Section 1.2: Previous Sterol Probes
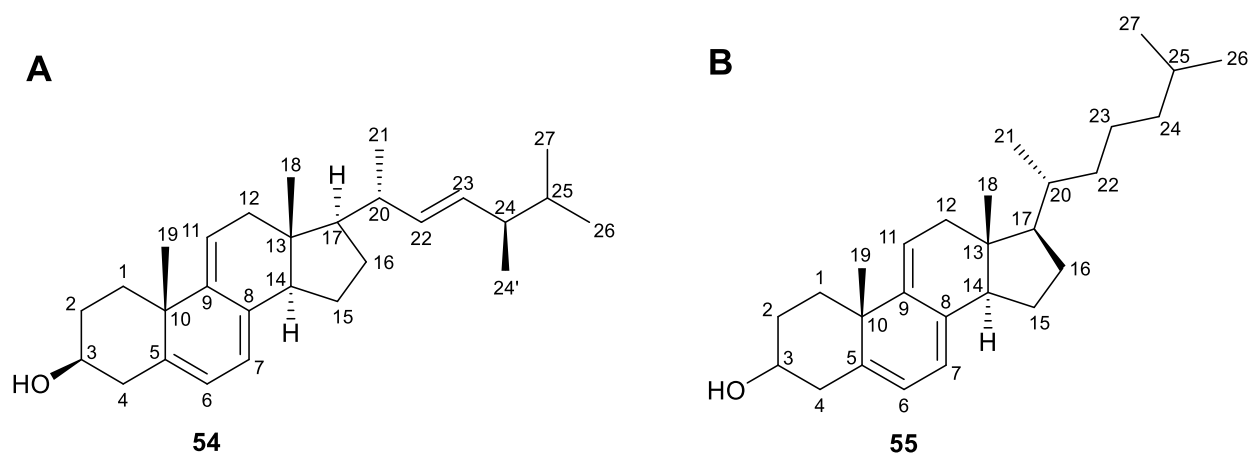
Figure 1.3 Intrinsic probes. (A) Dehydroergosterol (DHE, 54), (B) Cholestatrienol (CTL, 55)

Intrinsic probes contain several conjugated bonds within the four-ring system. Examples of intrinsic probes include dehydroergosterol (DHE, **54**) and cholestatrienol (CTL, **55**) (see Figure 1.3A-B). DHE (**54**) is an analogue of ergosterol with the addition of a double bond ($\Delta^{9,11}$) in the C ring. In regard to its mimicry of cholesterol (**33**), DHE (**54**) was concluded to have lower affinity for several cholesterol metabolizing proteins, such as SCAP/SREBP2, compared to cholesterol (**33**) (Solanko et al., 2015). However, Solanko et al. summarized DHE (**54**) mimicking cholesterol in plasma membranes somewhat well at moderate concentrations up to 10 mol% i.e., 10% of lipid molecules. In addition, DHE (**54**) was concluded to portion into the lo phase compared to the ld phase just like cholesterol (Solanko et al., 2015). It was stated that partitioning preference for lo or ld of fluorescent cholesterol analogues, like DHE (**54**), was measured by fluorescence microscopy of giant unilamellar vesicles (GUVs) (Solanko et al., 2015). Lo and ld assignment of GUVs were determined by area fraction, connectivity, and partitioning of fluorophores with known partitioning behavior (Baumgart et al., 2007). These factors helped determine the partitioning preference for various fluorescent cholesterol probes shown below. Although DHE (**54**) maintains moderate structural similarity to cholesterol (**33**), it was reported to have a low extinction coefficient ($\varepsilon \approx 11,000$ M-1 cm-1) and quantum yield ($\Phi_f = 0.04$ in ethanol) resulting in low fluorescence signaling (Solanko et al., 2015; Králová et al., 2018).

Cholestatrienol (CTL, **55**) is a close analogue of cholesterol (**33**), adding two double bonds ($\Delta^{7,8}$ and $\Delta^{9,11}$) in the B and C ring, while still maintaining the aliphatic side chain. Primary induction of the lo phase in addition to low fluorescence properties were concluded to be similar between DHE (**54**) and CTL (**55**) (Solanko et al., 2015; Králová et al., 2018). However, CTL (**55**) was summarized to have a linear relationship between ordering capability of fatty acyl chains and its concentration in the lipid bilayer similar to that of cholesterol (Solanko et al., 2015). Also, cholesterol (**33**) and CTL (**55**) both contain an eight carbon aliphatic side chain. CTL (**55**)

derivatives, like 25-hydroxy-CTL, were concluded to mimic the bioactive properties of its counterpart, 25-hydroxycholesterol (Solanko et al., 2015).
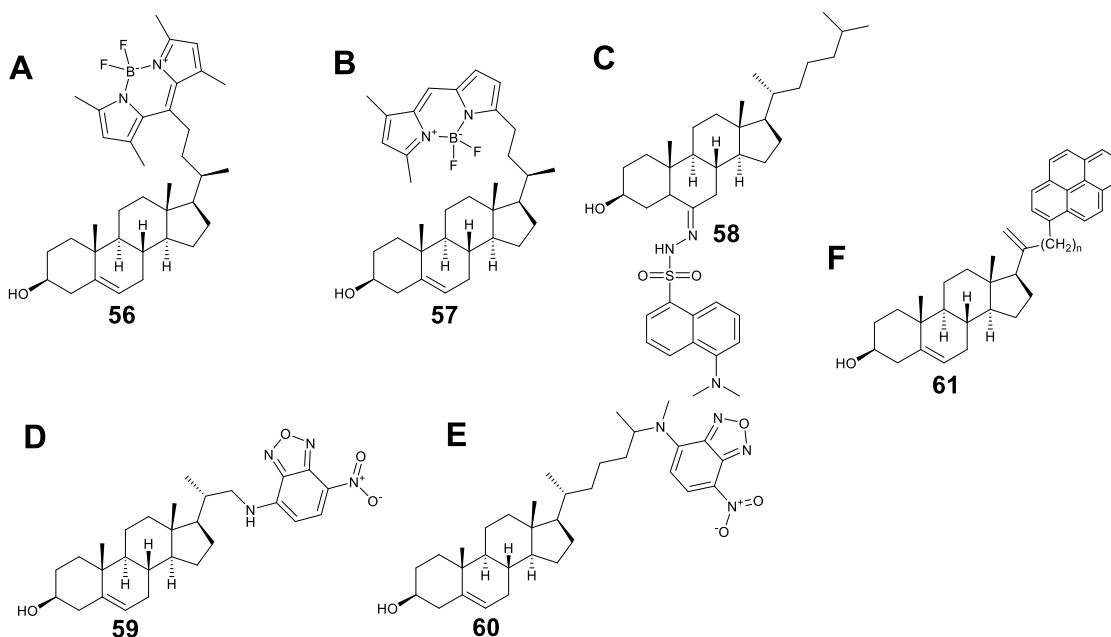
Figure 1.4 Extrinsic Probes. (A) BODIPY-cholesterol (B-Chol, 56). (B) BODIPY-P-cholesterol (B-P-Chol, 57). (C) Dansyl-cholestanol (Dchol, 58). (D) 22-NBD-cholesterol (59). (E) 25-NBD-cholesterol (60). (F) Pyrene-cholesterol (Pyr-met-Chol, 61)

Extrinsic probes have a fluorescence label directly attached to the backbone of the sterol. Examples of extrinsic probes reported in earlier studies include BODIPY-cholesterol (B-Chol, **56**), BODIPY-P-cholesterol (B-P-Chol, **57**), Dansyl-cholestanol (Dchol, **58**), 22-NBD-cholesterol (**59**), 25-NBD-cholesterol (**60**), and Pyrene-cholesterol (Pyr-met-Chol, **61**) (see Figure 1.4A-F). Both B-Chol (**56**) and B-P-Chol (**57**) were stated to participate primarily in the lo phase (Solanko et al., 2015). It was shown that B-P-Chol (**57**) was able to diffuse twice as fast through the membrane compared to B-Chol (**56**), thus emphasizing the importance of configuration between the sterol backbone and the fluorescence label. The two BODIPY-cholesterol derivatives were concluded to have 600-fold greater fluorescence intensity compared to DHE (**54**) and CTL (**55**) (Solanko et al., 2015). However, B-Chol (**56**) showed no ability to order fatty acid chains in lipid bilayers as stated by Solanko et al. (Solanko et al., 2015). Condensing the lipid bilayer is a crucial role of

cholesterol (**33**), thus dampening the reliability of BODIPY-cholesterol probes for metabolic or imaging studies.

The next extrinsic probe, Dansyl-cholestanol (Dchol, **58**), contains a dansyl group on C_6 while removing the double bond between C_5 and C_6. Dchol (**58**) was concluded to have been esterified to the same extent as cholesterol (**33**) in CT43 cells (Solanko et al., 2015). It was also reported to have a high quantum yield which results in a strong fluorescence signal. However, it was stated that the dansyl group extends out from the sterol backbone which likely results in the disturbance of lipid membrane rigidity induced by cholesterol (Solanko et al., 2015). Dchol (**58**) was also shown to have high preference for the ld phase in model membranes and photobleaching tendency. All the pros and cons of Dchol (**58**) make its use as a metabolic probe for cholesterol questionable.

Continuing with extrinsic probes, 22-NBD-cholesterol (**59**), and 25-NBD-cholesterol (**60**), both derivatives have a 7-nitrobenz-2-oxa-1,3-diazole (NBD) group attached to C_{22} or C_{25} of cholesterol (**33**). Both NBD-cholesterol derivatives were indicated to show shorter mean half-times (10–120 seconds) compared to cholesterol (**33**), DHE (**54**), or CTL (**55**) (45 -60 min) through cell membranes (Solanko et al., 2015). 25-NBD-cholesterol (**60**) was determined to solely monitor the physical properties of cell membranes in cholesterol (**33**) depleted cells (Solanko et al., 2015). Between the two NBD-cholesterol derivatives, 25-NBD-cholesterol (**60**) was reported to mimic cholesterol (**33**) better and therefore was used in a sterol glucosyltransferase (SGTase) assay with glucosyl ceramides (Akiyama et al., 2011; Akiyama et al., 2013).
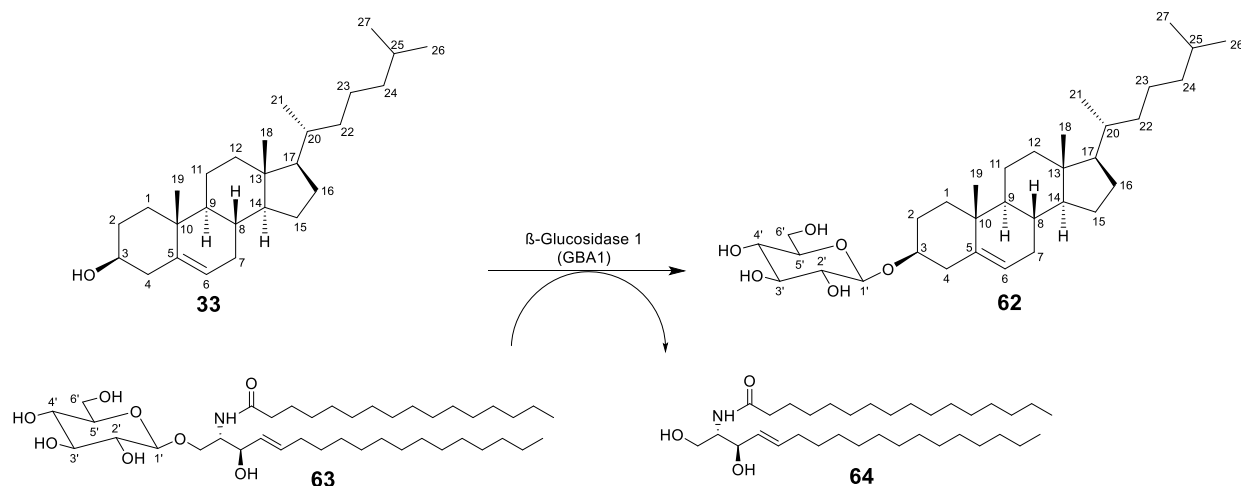
Figure 1.5 Cholesterol transglycosylation with ceramides in mammals

It was previously proposed that formation of cholesterol glucosides in mammals was aided by the transfer of glucose from ceramides to cholesterol (see Figure 1.5) (Akiyama et al., 2013). In the SGTase assay, 25-NBD-cholesterol (**60**) was reacted with glucosyl ceramides (**63**) using various glucocerebrosidase (GCase, GlcCer-degrading glycosidase) in mammalian cells *in vitro* (Akiyama et al., 2013). Among the GCases used, β-glucosidase 1 (GBA1, lysosomal acid GCase) had the highest SGTase activity, showing its function as the mammalian SGTase (Akiyama et al., 2013). The 25-NBD-cholesterol (**60**) probes were extracted and characterized by mass spectrometry (MS). The results showed that glucose was transferred from the glucosyl ceramide (**63**) to form β-cholesterol glucoside (**62**) and ceramide (**64**), thereby presenting a plausible mechanism for steryl glycoside formation in mammals (Akiyama et al., 2013). Although 25-NBD-cholesterol (**60**) shows potential as a cholesterol probe, 25-NBD cholesterol (**60**) did not present distinct staining in plasma membranes. The results concluded miss-targeted staining to mitochondria (Solanko et al., 2015). Both analogues were asserted to have moderate fluorescence, high partition to the ld phase, incapability to condense lipid membranes, and photobleaching tendencies (Solanko et al., 2015). These negative properties associated with NBD cholesterol derivatives make them dubious as probes for cholesterol (**33**).

Pyrene-cholesterol (Pyr-met-Chol, **61**) or 21-methylpyrenyl-cholesterol contains a pyrene group attached to C_{20} of cholesterol (**33**). It was shown to incorporate into cell membranes like cholesterol (Solanko et al., 2015). Although experiments discussing the partition of Pyr-met-Chol (**61**) into the ld or lo phase are not known, it could be deduced that the pyrene group would interfere with cholesterol induced membrane condensation due to its bulky nature and result in a prominent ld phase (Solanko et al., 2015). In addition, Pyr-met-Chol (**61**) was stated to have strong intracellular fluorescence which disagrees with cholesterol's dominant presence in plasma membranes (Solanko et al., 2015). In regard to metabolism, Pyr-met-Chol (**61**) was concluded to forgo esterification in contrast to cholesterol and other extrinsic probes (Solanko et al., 2015). All in all, it seems the reliability of all these extrinsic probes are uncertain and further research is needed.
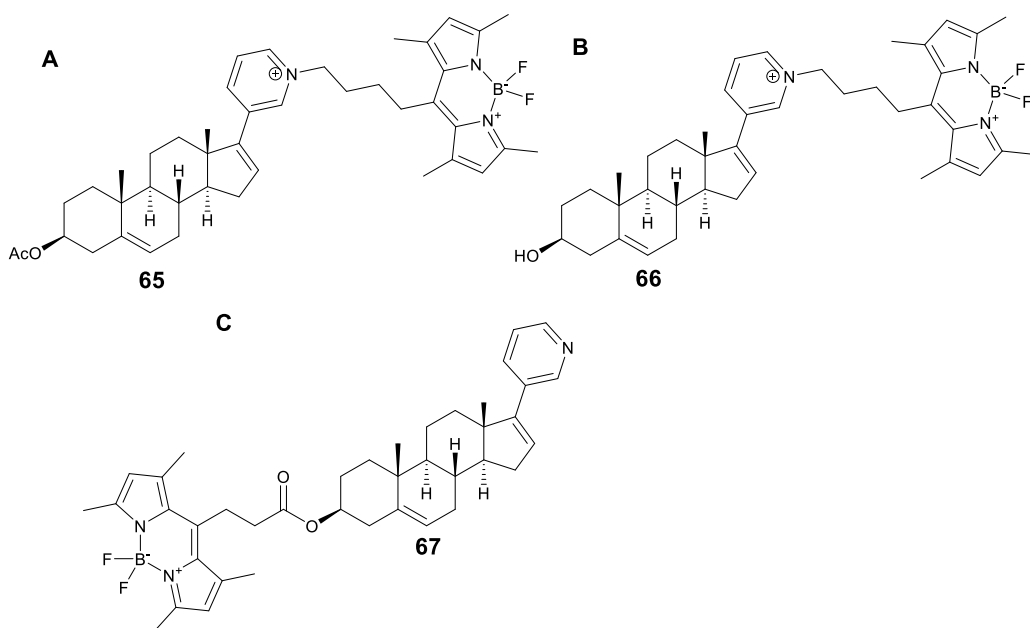
Figure 1.6 Heterocyclic extrinsic probes. (A) FP-5 (65), (B) FP-7 (66), (C) FP-2 (67)

Recently reported by Králová et al., heterocyclic extrinsic sterol probes were synthesized to explore their potential as possible cholesterol analogues (see Figure 1.6). Herein, two sterol backbones were derivatized with a pyridine ring directly attached to either C_{17} or the A ring (between C_3 and C_4). Next, a fluorophore, such as coumarin, pyrene, BODIPY, or a derivative of

BODIPY, was added indirectly to the 3 or 17 position of both heterocyclic sterol backbones (Králová et al., 2018). Fourteen heterocyclic probes were screened for cellular uptake efficiency. Among the fourteen heterocyclic probes, fluorophores attached indirectly to the 3-position, like FP-2 (**67**) (see Figure 1.6C) displayed none to low cellular uptake and low fluorescence intensity, emphasizing the importance of fluorophore attachment. Two probes showed significant uptake: FP-5 (**65**) and FP-7 (**66**) (see Figure 1.6A-B). Both of these probes were shown to have faster cellular uptake compared to B-Chol (**56**), a common extrinsic probe (Králová et al., 2018). However, B-Chol (**56**) was able to attain comparable fluorescence intensity at a slower rate. Between FP-5 (**65**) and FP-7 (**66**), FP-5 (**65**) seems to be a better candidate for mimicking cholesterol as FP-5 (**65**) displayed strong uptake in PM while FP-7 (**66**) showed none (Králová et al., 2018). Although FP-5 (**65**) showed similar cellular distribution to cholesterol, Králová et al. reported ~40% of FP-5 (**65**) was converted to FP-7 (**66**) via hydrolysis within 24 h, thus highlighting FP-5's (**65**) *in vivo* lability and casting doubt on its ability as a cholesterol (**33**) probe.
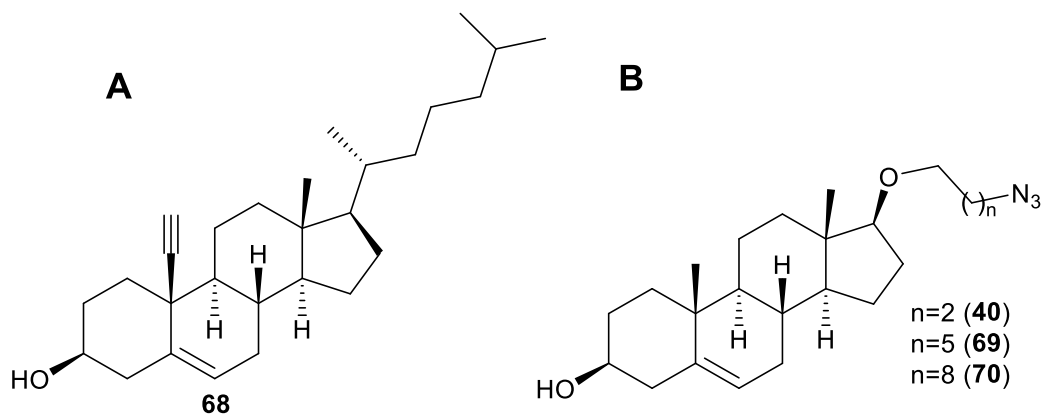
Figure 1.7 Click chemistry probes. (A) 19-ethynylcholesterol (eChol, 68), (B) C$_{17}$-alkoxyl N$_3$ (40, 69-70)

Click chemistry probes are sterol probes that have either an azide or alkyne group attached directly to the backbone. The "click" reaction occurs when the azide/alkyne sterol reacts with a fluorophore reagent containing the counter alkyne/azide group via a copper(I)-catalyzed azide-alkyne cycloaddition (CuAAC) (Jao et al., 2015; Jan et al., 2016; Jan et al., 2020). The

conjugate formed is a 1,2,3-triazole like product. Recently, two click chemistry sterol probes, 19-ethynylcholesterol (eChol, **68**) and C_{17}-alkoxyl N_3 **(40, 69-70)**, were able to mimic cholesterol (**33**), minimize interference *in vivo*, and/or be extracted from cells for metabolite characterization after biological interactions.

EChol (**68**) (see Figure 1.7A) is a cholesterol analogue in which the methyl group of C_{19} was replaced with an ethynyl group. Reasons for adding the ethynyl group to the 19-position included synthetic accessibility, steric accessibility, and close mimicry of the cholesterol backbone (Jao et al., 2015). Jao et al. tested the ability of eChol (**68**) in proliferation of cholesterol in M19 CHO cells, which have a defect in cholesterol biosynthesis (Jao et al., 2015). It was observed that both eChol (**68**) and cholesterol (**33**) were able to induce cholesterol proliferation in the auxotrophic cells. As cholesterol (**33**) was previously described to be a key component in Hh signaling, eChol (**68**) was substituted in lieu of cholesterol to see if the Hh signaling pathway would still function properly and determine the extent of eChol's (**68**) mimicry of cholesterol (**33**).
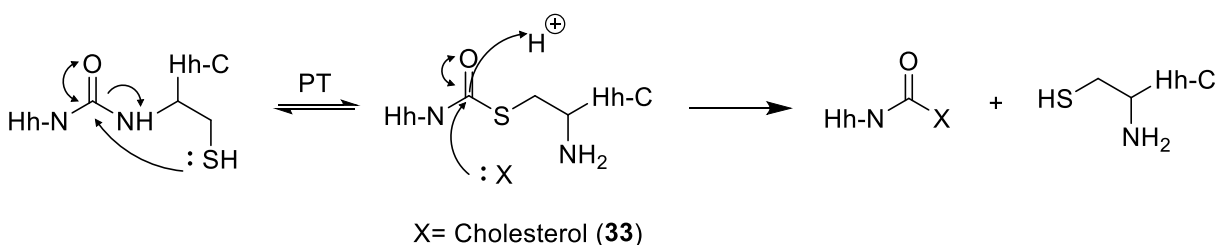
X= Cholesterol (**33**)

Figure 1.8 Cholesterol modification of Hh ligand

The Hh signaling pathway is initiated by the thiol side chain of Cys[258] attacking the carbonyl of Gly[257], forming a thioester (see Figure 1.8) (Porter et al., 1996). The reactive intermediate then undergoes nucleophilic attack by cholesterol (**33**) via the 3-hydroxyl group, resulting in a cholesterol *N*-terminal fragment and a *C*-terminal fragment (see Figure 1.8) (Porter et al., 1996). The cleavage by cholesterol (**33**) was crucial for proper Hh signaling. When substituted for eChol (**68**), an eChol *N*-terminal fragment was detected by CuAAC, further supporting eChol's potential of imitating cholesterol. Cholesterol (**33**) was also previously shown to play a role in the

recruitment of Smo to the cilium, a crucial component of Hh signal transduction (Jao et al., 2015). Jao et al. reported that both cholesterol (**33**) and eChol (**68**) were able to recruit Smo in sterol-depleted cells. In terms of imaging cholesterol cellular distribution, eChol (**68**) displayed moderate to strong fluorescence intensity when "clicked" with an azide fluorophore and its cellular distribution was similar to cholesterol. However, eChol (**68**) levels were reported to be the highest in mitochondria compared to the ER and PM (Jao et al., 2015). The observed distribution of eChol (**68**) seems to contradict cholesterol's expected distribution, being primarily located in the PM. These contradictions throw eChol's (**68**) ability as a cholesterol probe into question, thus showing that changes in the sterol backbone may lead to variations in distribution.

Alternative approaches to developing metabolic sterol probes include the C_{17}-alkoxyl N_3 analogues (**40**, **69-70**) (see Figure 1.7B). Three derivatives (see Table 1.1) were synthesized and evaluated with n=2 (**40**), 5 (**69**), or 8 (**70**). Previously reported, *H. pylori* is auxotrophic for cholesterol and absorbs it from the host cell. From there, cholesterol (**33**) is converted to CG (**51**) and CAG (**52**) via the glucosyltransferase encoded by *hp0421* and CGAT, respectively (Jan et al., 2016; Jan et al., 2020). These cholesterol derivatives help innervate *H. pylori's* pathogenicity. The C_{17}-alkoxyl N_3 analogues (**40**, **69-70**) was used to study the latter phenomenon and characterize the various CAGs (**52**). Like 25-NBD cholesterol (**60**), the C_{17}-alkoxyl N_3 probes (**40**, **69-70**) were extracted and characterized for metabolic changes by not only MS, but also NMR.

Table 1.1 Kinetic parameters of cholesterol and its derivatives in the catalysis of glucosyltransferase encoded by *hp0421* (Jan et al., 2016)

Compound	k_{cat} (min^{-1})	K_m (µM)	k_{cat}/ K_m (µM^{-1} min^{-1})	Normalized catalytic efficiency (%)
Cholesterol (**33**)	3.58 ± 0.37	66.33 ± 15.99	0.0539 ± 0.0141	100.0
40	6.13 ± 0.46	134.80 ± 19.65	0.0455 ± 0.0074	84.3
69	6.82 ± 0.41	193.10 ± 20.25	0.0353 ± 0.0043	65.5
70	10.41 ± 2.65	324.70 ± 88.90	0.0321 ± 0.0105	59.5
22-NBD-Cholesterol (**59**)	n.d.	n.d.	n.d.	n.d.

	n.d.	n.d.	n.d.	n.d.
25-NBD-Cholesterol (**60**)				
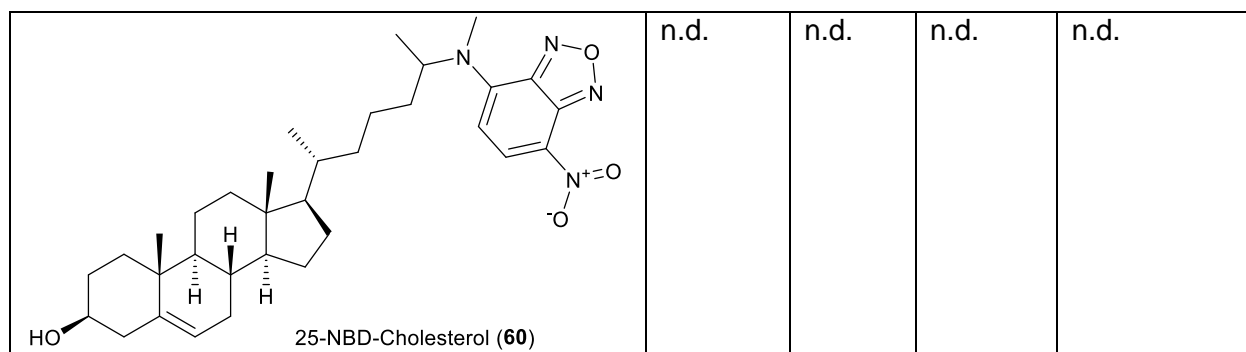
The glucosyltransferase encoded by *hp0421* was overexpressed and mixed with the three analogues of C_{17}-alkoxyl N_3 (**40**, **69-70**). The catalytic efficiency (k_{cat}/K_m) values for the three azide analogues (**40**, **69-70**) ranged from 59-84% that of cholesterol (**33**) with the analogue of the shortest alkyl chain (n=2, **40**) showing the highest catalytic efficiency (see Table 1.0) (Jan et al., 2016). In addtion, the catalytic efficiency was considerably higher for the three C_{17}-alkoxyl N_3 analogues (**40**, **69-70**) compared to the two NBD-cholesterol derivatives, 22-NBD-Cholesterol (**59**) (see Figure 1.4D) and 25-NBD-Cholesterol (**60**) (see Figure 1.4E). Although the C_{17}-alkoxyl N_3 analogues (**40**, **69-70**) show potential as cholesterol probes, their catalytic efficiency were lower than cholesterol (**33**) which indicates that the alkyl side chain at C_{17} is crucial for glycosylation (Jan et al., 2016).

The C_{17}-alkoxyl N_3 glycosides were then catalyzed by CGAT to form C_{17}-alkoxyl N_3 acylated glycosides, further showing the efficiency of these probes in mimicking cholesterol. The C_{17}-alkoxyl N_3 metabolites were able to be extracted via CuAAC and it was observed that the acyl chains attached to 6'-OH and phosphatidyl groups were composed of human fatty acid chains (Jan et al., 2016). In imaging studies, C_{17}-alkoxyl N_3 derivatives were shown to induce lipid raft formation in host cells, CagA translocation, and subsequent tyrosine phosphorylation similar to that of cholesterol with strong fluorescence intensity (Jan et al., 2016; Jan et al., 2020). It was previously reported that integrins α5 and β1 were recruited to lipid rafts to aid in *H. pylori* attachment (Jan et al., 2020). To verify the latter statement, the azide probes were observed to recruit integrins α5 and β1 in addition to Lewis[b] and sialyl Lewis[x] antigens to the lipid rafts, proving

their assistance in bacterial adhesion (Jan et al., 2020). The recruitment of these adhesion molecules was verified via coexistence of fluorescence with C_{17}-alkoxyl N_3. All in all, C_{17}-alkoxyl N_3 probes (**40**, **69-70**) seem viable for future metabolism studies, like the current study.

Section 1.3: Current Project Sterol/Sterol Glycoside Probes
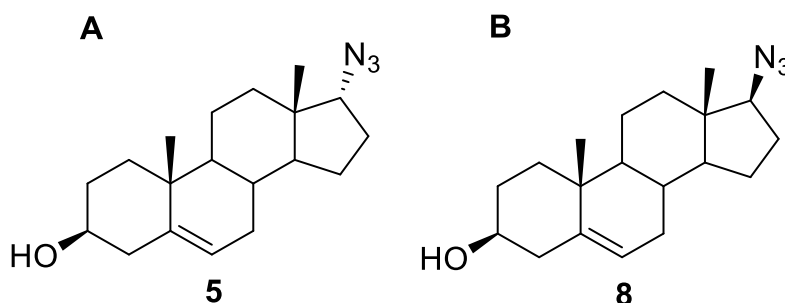
Figure 1.9 DHEA C_{17} N_3 probes. (A) [17R]-DHEA C_{17} N_3 (5), (B) [17S]-DHEA C_{17} N_3 (8)

From comparing the pros and cons of the three types of sterol probes, the "click" sterol probes were deemed to be the most successful class and therefore, two previously synthesized "click" sterol probes were chosen (see Figure 1.9A-B). The DHEA C_{17} N_3 probes, [17S]-DHEA C_{17} N_3 (**8**) and [17R]-DHEA C_{17} N_3 (**5**), were previously synthesized as precursors for the development of male contraceptives and inhibitors of 17α-hydroxylase-$C_{17,20}$-lyase enzyme (P450$_{17α}$), an enzyme that participates in prostate cancer (Blanco et al., 2014), (Kiss et al., 2018). For this project, one of the main goals for these probes is to observe how well the probes mimic cholesterol's structure and bioactivity. In terms of bioactivity, the probes could potentially be subjected to previous assays done by Jao et al. to see if the DHEA C_{17} N_3 probes (**5** and **8**) would stimulate cholesterol proliferation in M19 CHO cells, which are auxotrophic for cholesterol biosynthesis. As previously described by Jan et al., *H. pylori* required cholesterol from the mammalian host in order to transfer its pathogenetic factor to the host cells for infection. C_{17}-alkoxyl N_3 probes (**40**, **69-70**) were substituted in for cholesterol and they were successful in promoting *H. pylori* infection, thus indicating their efficient mimicry of cholesterol. In addition, the C_{17}-alkoxyl N_3 probes (**40**, **69-70**) were extracted via CuAAC for metabolite characterization by

NMR and mass spectrometry. Although the C_{17}-alkoxyl N_3 probes (**40**, **69-70**) proved to be successful in mimicking cholesterol (**33**) and CuAAC extraction, the DHEA C_{17} N_3 probes (**5** and **8**) were chosen for this project as these probes replace the alkyl side chain at C_{17} with a secondary azido group, which distinguishes **5** and **8** as diastereomers and gives generalized sterol probes that can be used in various metabolic studies. In addition, the types of metabolites extracted with **5/8** via CuAAC will be characterized and compared to previous literature findings. Also, the metabolites will help determine if being diastereomers affects the types of metabolites extracted. Therefore, the DHEA C_{17} N_3 probes (**5** and **8**) will be subjected to the same experimental procedure reported by Jan et al. to measure the extent of *H. pylori* infection and compare the results with previous data utilizing C_{17}-alkoxyl N_3 probes (**40**, **69-70**), thus determining how well DHEA C_{17} N_3 probes (**5** and **8**) mimic cholesterol. Next, the DHEA C_{17} N_3 probes (**5** and **8**) will be subjected to a *H. pylori*/AGS bioassay and extracted via CuAAC for metabolite characterization that will be compared to previous C_{17}-alkoxyl N_3 probes' (**40**, **69-70**) metabolites. In addition, the DHEA C_{17} N_3 probes (**5** and **8**) will be subjected to three bioassays/environments: *Camellia sinensis*, Invariant natural killer T (iNKT)/Dendritic Cell (DC), and *H. pylori*/AGS to observe the metabolism of sterols from extraction via CuAAC. The details regarding the previous and current synthesis of the DHEA C_{17} N_3 probes (**5** and **8**) will be discussed in Chapter 2.
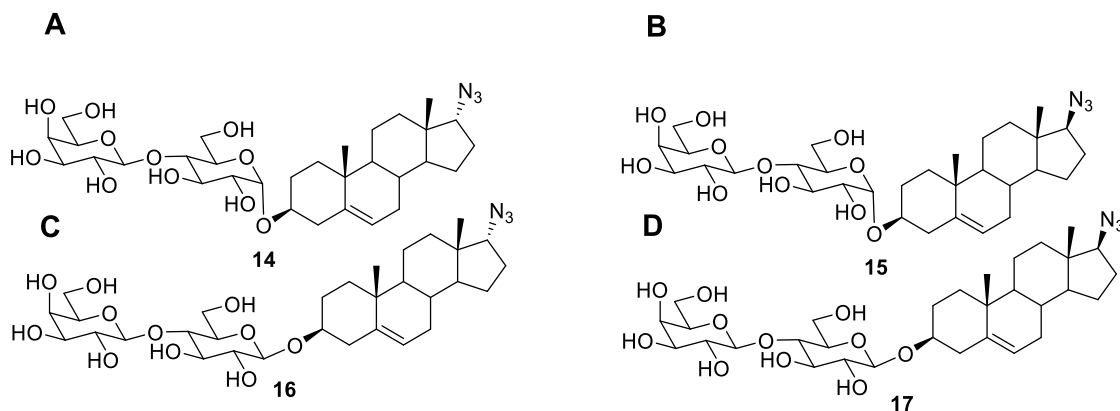
Figure 1.10 DHEA C_{17} N_3 lactosyl Probes. (A) α-lactosyl-[17R]-DHEA C_{17} N_3 (14), (B) α-lactosyl-[17S]-DHEA C_{17} N_3 (15), (C) β-lactosyl-[17R]-DHEA C_{17} N_3 (16), (D) β-lactosyl-[17S]-DHEA C_{17} N_3 (17)

In order to study the medicinal properties of sterol glycosides, four azido sterol glycoside probes were proposed. The purpose of the DHEA C_{17} N_3 lactosyl probes: α-lactosyl-[17R]-DHEA C_{17} N_3 (**14**), α-lactosyl-[17S]-DHEA C_{17} N_3 (**15**), β-lactosyl-[17R]-DHEA C_{17} N_3 (**16**), and β-lactosyl-[17S]-DHEA C_{17} N_3 (**17**) is to study the effect of sterol glycosides on CD1d binding and T_H1/T_H2 cytokine release (see Figure 1.10A-D). It was concluded that the effect of sterol glycosides on T cells is currently partly understood (Grille et al., 2010). Details, like T_H1/T_H2 cytokine release, metabolic changes to sterol glycosides, or the mechanism of sterol glycoside activation of T cells, are uncertain. Grille et al. previously summarized that the effect of cholesterol-α-glucoside (**51**) or cholesterol-β-glucoside (**62**) on T cell activation needs to be explored. Also, there seems to be few studies reporting on the effect of sterol glycosides on CD1d binding. Therefore, the DHEA C_{17} N_3 lactosyl probes (**14-17**) can be used to measure potential T_H1/T_H2 cytokine release, observe any metabolic changes to the probe, and quantify CD1d binding. In addition, these DHEA C_{17} N_3 lactosyl probes (**14-17**) will be used to observe the exchange of the lactose group with ceramide probes which will be discussed below in more detail. The synthesis of the DHEA azide backbone will be described in Chapter 2. The α/β attachment of the lactose moiety to the sterol backbone will be conducted using methods previously described (Davis et al., 2015). The specific details regarding the synthesis of the DHEA C_{17} N_3 lactosyl probes (**14-17**) will be described in Chapter 4.

Section 1.4: References

Akiyama, H., Kobayashi, S., Hirabayashi, Y., & Murakami-Murofushi, K. (2013). Cholesterol glucosylation is catalyzed by transglucosylation reaction of β-glucosidase 1. *Biochemical and Biophysical Research Communications*, *441*(4), 838–843. https://doi.org/10.1016/j.bbrc.2013.10.145

Akiyama, H., Sasaki, N., Hanazawa, S., Gotoh, M., Kobayashi, S., Hirabayashi, Y., & Murakami-Murofushi, K. (2011). Novel sterol glucosyltransferase in the animal tissue and cultured cells:

Evidence that glucosylceramide as glucose donor. *Biochimica et Biophysica Acta - Molecular and Cell Biology of Lipids*, *1811*(5), 314–322. https://doi.org/10.1016/j.bbalip.2011.02.005

B. Jirgensons. (1996). Natural organic macromolecules. *Rep. Prog. Phys.*, *59*, 867–933. https://doi.org/10.1088/0034-4885/77/5/056502

Baumgart, T., Hunt, G., Farkas, E. R., Webb, W. W., & Feigenson, G. W. (2007). Fluorescence probe partitioning between Lo/Ld phases in lipid membranes. *Biochimica et Biophysica Acta - Biomembranes*, *1768*(9), 2182–2194. https://doi.org/10.1016/j.bbamem.2007.05.012

Blanco G., Georg G. I., Syeda S. S., inventors. Regents of the University of Minnesota, The University of Kansas, assignees. Contraceptive Agents. US 2014/0005132. 2014 January 02

Bouic, P. J. D., Etsebeth, S., Liebenberg, R. W., Albrecht, C. F., Pegel, K., & Van Jaarsveld, P. P. (1996). Beta-sitosterol and beta-sitosterol glucoside stimulate human peripheral blood lymphocyte proliferation: Implications for their use as an immunomodulatory vitamin combination. *International Journal of Immunopharmacology*, *18*(12), 693–700. https://doi.org/10.1016/S0192-0561(97)85551-8

Davis, R. A., Fettinger, J. C., & Gervay-Hague, J. (2015). Synthesis of cholesteryl-α-d-lactoside via generation and trapping of a stable β-lactosyl iodide. *Tetrahedron Letters*, *56*(23), 3690–3694. https://doi.org/10.1016/j.tetlet.2015.05.012

Grille, S., Zaslawski, A., Thiele, S., Plat, J., & Warnecke, D. (2010). The functions of steryl glycosides come to those who wait: Recent advances in plants, fungi, bacteria and animals. *Progress in Lipid Research*, *49*(3), 262–288. https://doi.org/10.1016/j.plipres.2010.02.001

Hjort Ipsen, J., Karlström, G., Mourtisen, O. G., Wennerström, H., & Zuckermann, M. J. (1987). Phase equilibria in the phosphatidylcholine-cholesterol system. *BBA - Biomembranes*,

905(1), 162–172. https://doi.org/10.1016/0005-2736(87)90020-4

Jan, H.-M., Chen, Y.-C., Yang, T.-C., Ong, L.-L., Chang, C.-C., Muthusamy, S., Abera, A. B., Wu, M.-S., Gervay-Hague, J., Mong, K.-K. T., & Lin, C.-H. (2020). Cholesteryl α-D-glucoside 6-acyltransferase enhances the adhesion of *Helicobacter pylori* to gastric epithelium. *Communications Biology*, *3*(1), 1–13. https://doi.org/10.1038/s42003-020-0855-y

Jan, H. M., Chen, Y. C., Shih, Y. Y., Huang, Y. C., Tu, Z., Ingle, A. B., Liu, S. W., Wu, M. S., Gervay-Hague, J., Mong, K. K. T., Chen, Y. R., & Lin, C. H. (2016). Metabolic labelling of cholesteryl glucosides in: *Helicobacter pylori* reveals how the uptake of human lipids enhances bacterial virulence. *Chemical Science*, *7*(9), 6208–6216. https://doi.org/10.1039/c6sc00889e

Jao, C. Y., Nedelcu, D., Lopez, L. V., Samarakoon, T. N., Welti, R., & Salic, A. (2015). Bioorthogonal probes for imaging sterols in cells. *ChemBioChem*, *16*(4), 611–617. https://doi.org/110.1016/j.bbi.2017.04.008

Kiss, A., Herman, B. E., Görbe, T., Mernyák, E., Molnár, B., Wölfling, J., Szécsi, M., & Schneider, G. (2018). Synthesis of novel 17-triazolyl-androst-5-en-3-ol epimers via Cu(I)-catalyzed azide-alkyne cycloaddition and their inhibitory effect on 17α-hydroxylase/C17,20-lyase. *Steroids*, *135*(February), 79–91. https://doi.org/10.1016/j.steroids.2018.03.006

Králová, J., Jurášek, M., Krčová, L., Dolenský, B., Novotný, I., Dušek, M., Rottnerová, Z., Kahle, M., Drašar, P., Bartůněk, P., & Král, V. (2018). Heterocyclic sterol probes for live monitoring of sterol trafficking and lysosomal storage disorders. *Scientific Reports*, *8*(1), 1–11. https://doi.org/10.1038/s41598-018-32776-6

Lee, J. H., Lee, J. Y., Park, J. H., Jung, H. S., Kim, J. S., Kang, S. S., Kim, Y. S., & Han, Y. (2007). Immunoregulatory activity by daucosterol, a β-sitosterol glycoside, induces protective Th1

immune response against disseminated Candidiasis in mice. *Vaccine*, *25*(19), 3834–3840. https://doi.org/10.1016/j.vaccine.2007.01.108

Lin, X., Ma, L., Moreau, R. A., & Ostlund, R. E. (2011). Glycosidic bond cleavage is not required for phytosteryl glycoside-induced reduction of cholesterol absorption in mice. *Lipids*, *46*(8), 701–708. https://doi.org/10.1007/s11745-011-3560-2

Nyström, L., Schär, A., & Lampi, A. M. (2012). Steryl glycosides and acylated steryl glycosides in plant foods reflect unique sterol patterns. *European Journal of Lipid Science and Technology*, *114*(6), 656–669. https://doi.org/10.1002/ejlt.201200033

Porter, J. A., Young, K. E., & Beachy, P. A. (1996). *Cholesterol Modification of Hedgehog Signaling Proteins in Animal Development Author (s): Jeffrey A . Porter , Keith E . Young and Philip A . Beachy Published by : American Association for the Advancement of Science Stable URL : https://www.jstor.org/st*. 274(5285), 255–259.

Solanko, K. A., Modzel, M., Solanko, L. M., & Wüstner, D. (2015). Fluorescent sterols and cholesteryl esters as probes for intracellular cholesterol transport. *Lipid Insights*, *2015*, 95–114. https://doi.org/10.4137/Lpi.s31617

Wunder, C., Churin, Y., Winau, F., Warnecke, D., Vieth, M., Lindner, B., Mollenkopf, H., Heinz, E., & Meyer, T. F. (2006). Cholesterol glucosylation promotes immune evasion by Helicobacter pylori. *Nature Medicine*, *12*(9), 1030–1038. https://doi.org/10.1038/nm1480

Chapter 2

Synthesis of "clickable" azido-sterol probes

Section 2.1: Synthesis of DHEA C_{17} N_3 Probes (**5** and **8**)

In order to study the role and distribution of lipids, like cholesterol, in various biological phenomenon, several functionalized sterol probes were synthesized to provide *in vivo* and *in vitro* monitoring. Recently, sterol probes with azido groups (*O*-17 alkoxy probes) were able to not only provide real time monitoring, but also allow characterization of metabolic changes on the probe (Jan et al., 2016). Therefore, "click" sterol probes have the potential to unlock the mysterious role and metabolism of lipids, like sterols, in different biological settings, which leads to the utilization of the DHEA C_{17} N_3 probes (**5** and **8**) for the current project (see Scheme 2.1). The latter probes (**5** and **8**) were chosen based on their generalized design (secondary -N_3 group and loss of alkyl side chain at C_{17}) to study the metabolism of sterols in plants, mammals, and microbes. Both **5** and **8** will be synthesized to determine if they efficiently "click" with 4-*N*-methylamino-1,8-napthalimidopropyne (**MAN**), which is a requirement before it can be determined if being different diastereomers will affect the types of metabolites extracted via CuAAC. The previous design and synthesis of the DHEA C_{17} N_3 probes (**5** and **8**) were reported by Kiss et al. and Blanco et al., but the exact procedure has been modified (vide infra). In addition, achieving complete NMR characterization of each synthetic intermediate to identify diagnostic peaks characteristic of each intermediate was a second goal of this project which will be described in detail in Chapter 3.
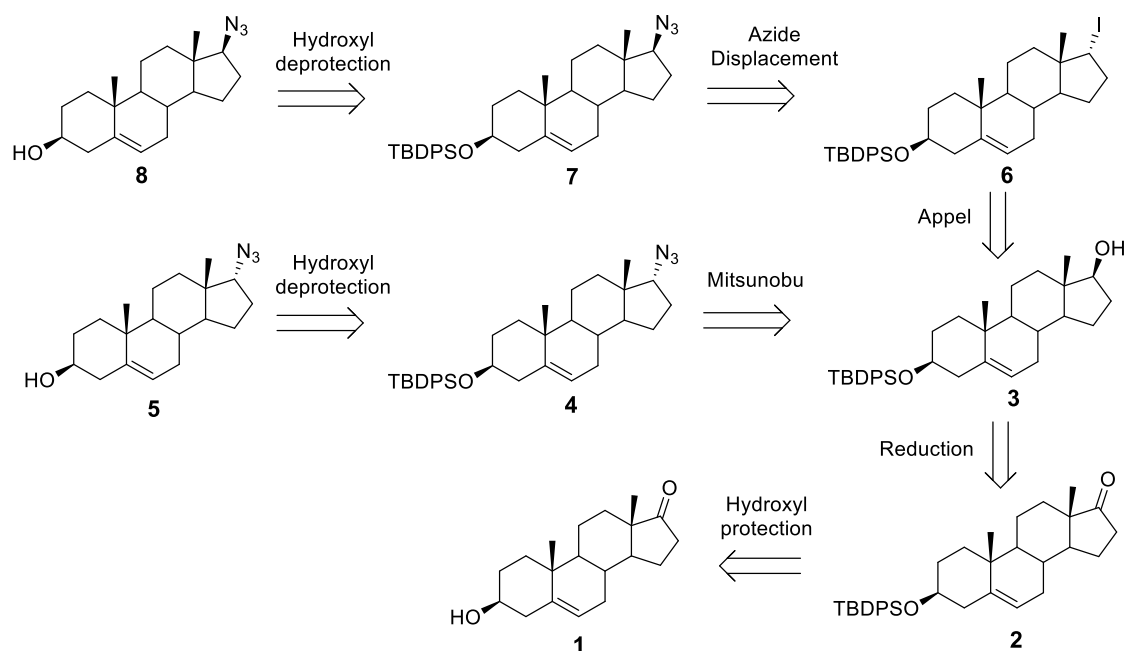
Scheme 2.1 Retrosynthesis of DHEA C$_{17}$ N$_3$ Probes

From the retrosynthesis (see Scheme 2.1), a *tert*-butyldiphenylsilyl (TBDPS) protecting group is attached to the hydroxyl group on C$_3$ of **8** and **5** to make **7** and **4**, respectively as described by Jan et al. (Jan et al., 2016). Next, **7** undergoes functional group interconversion (FGI) from -N$_3$ to -I to form **6** as described by Kiss et al. (Kiss et al., 2018). Continuing, both **6** and **4** are converted to **3** through FGI to -OH as described by Kiss et al. and Blanco et al., respectively (Blanco et al., 2014) (Kiss et al., 2018). Compound **3** is then transformed into **2** through FGI to -C=O as described by Jan et al. (Jan et al., 2016). Finally, a disconnection of the TBDPS group occurs at C$_3$ of **2** thus leading to the commercially available starting material, dehydroepiandrosterone (DHEA, **1**) as described by Jan et al. (Jan et al., 2016).
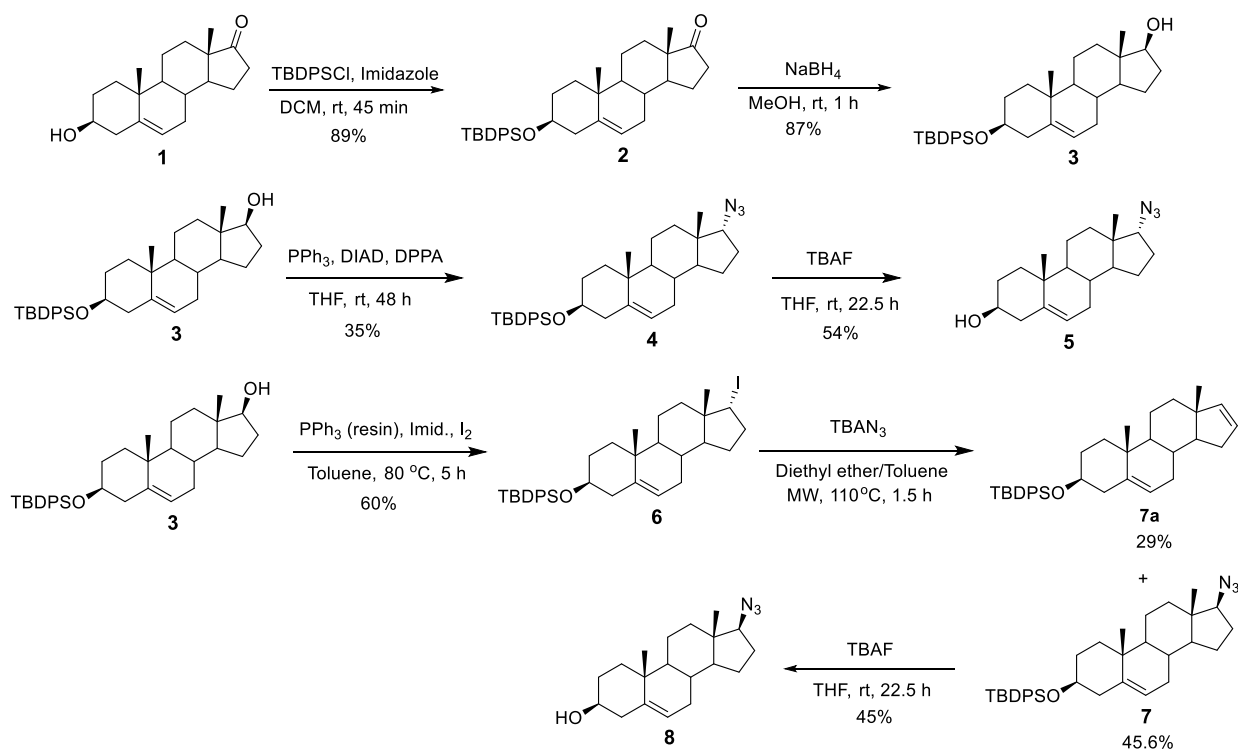
Scheme 2.2 DHEA C$_{17}$ N$_3$ Probes Synthetic Scheme

The synthetic scheme began with **1** being protected at 3-OH with a TBDPS group to give

2 (see Scheme 2.2). Previously reported by Jan et al., 2.5 eq. of imidazole and TBDPSCl was

mixed with **1** in anhydrous DMF (0.12 M) to form **2** (see Scheme 2.3A). The reaction took place

at 50 °C for 18 h resulting in a 98% yield (Jan et al., 2016). In a different approach, 2.0 eq. of

imidazole and 1.1 eq. TBDPSCl was mixed with **1** in DCM (0.14 M) to form **2** (see Scheme 2.3B).

The reaction took place at rt for 5 h resulting in a 98% yield (Blanco et al., 2014).
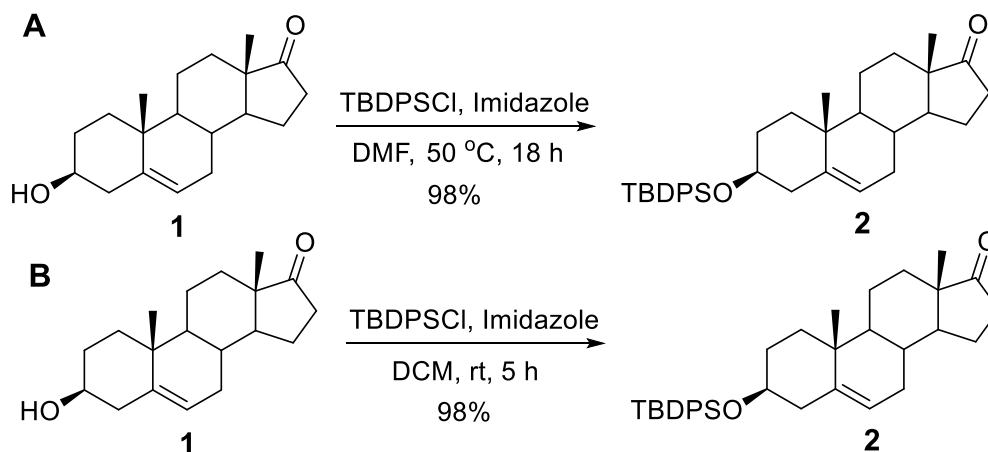
Scheme 2.3 Hydroxyl Protection Step. (A) Jan et al. TBDPS Protection Step, (B) Blanco et al. TBDPS Protection Step

For the current study, a modified version of the Jan procedure designed by a member of the Gervay-Hague research group, Matthew Orellana, was used. First, the solvent was changed from DMF to DCM, as DMF was difficult to remove during work-up procedures. Second, 1.1 eq. of TBDPSCl and 4 eq. imidazole were employed. Third, the solvent was changed to DCM and the concentration of the reaction was increased (0.36 vs. 0.12). The reaction was conducted at rt under argon and was complete after 45 min. Although the yield was lower than reported (89% vs. 98%), the reaction time was shortened dramatically from 18 h to 45 min and DCM was easily removed during work-up procedures.
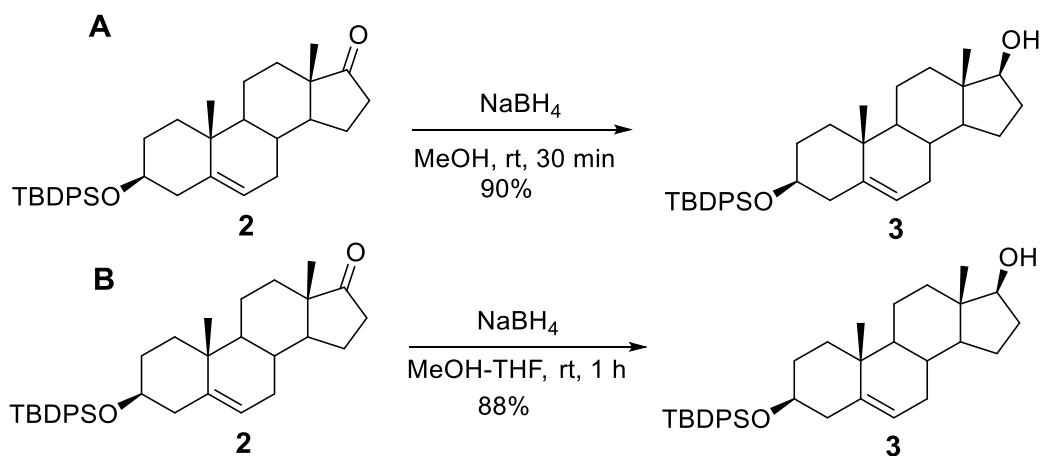
Scheme 2.4 Reduction Step. (A) Jan et al. Reduction Step, (B) Blanco et al. Reduction Step

For the next step, the carbonyl group at C_{17} of **2** was reduced to a hydroxyl group with [17S] stereochemistry to give **3** using $NaBH_4$ (see Scheme 2.2). Compound **3** was previously synthesized by Jan et al. using 1.5 eq. of $NaBH_4$ with **2** dissolved in anhydrous methanol (0.07 M). The reaction took place at rt for 30 min resulting in a 90% yield (see Scheme 2.4A) (Jan et al., 2016). In an alternative approach, compound **3** was synthesized utilizing 3 eq. of $NaBH_4$ dissolved in a 1:1 MeOH-THF solution (0.11 M) (Blanco et al., 2014). The reaction was completed with an 88% yield in 1 h, which is 2x longer compared to Jan et al (see Scheme 2.4B). Therefore, the current study used the exact same procedure reported in Jan et al. with slight modification; 2 vs. 1.5 eq. of $NaBH_4$ was used and the concentration of MeOH was increased from 0.07 to 0.1 M in the hopes of decreasing reaction time. The reaction was completed in 1 h at rt with an 87% yield. The observed yield was similar to that of the reported yield (87% vs. 90%) indicating the modification had minimal effect.
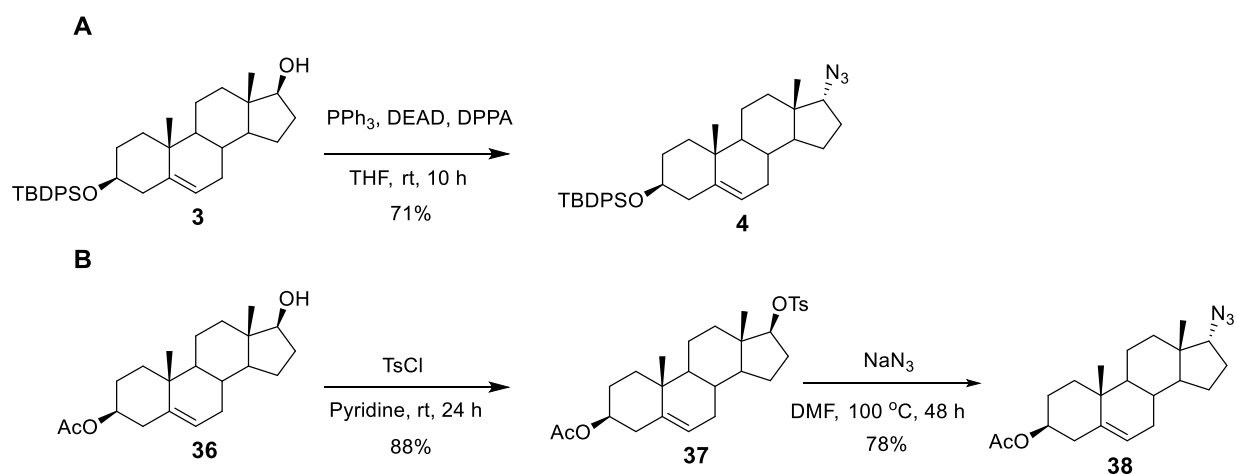
Scheme 2.5 Mitsunobu Rxn Step. (A) Blanco et al. Mitsunobu Rxn Step, (B) Kiss et al. Azide Displacement Step

Once forming **3**, it was subjected to a Mitsunobu reaction substituting the -OH group with a $-N_3$ group of opposite stereochemistry [17S]→[17R] to give **4** (see Scheme 2.2). As noted above, this and other similar compounds were synthesized previously by Kiss et al. and Blanco et al. In the procedure conducted by Kiss et al., **36** dissolved in pyridine (0.33 M) was treated with

1.5 eq. of TsCl (see Scheme 2.5B). The reaction took place at rt for 24 h resulting in a 88 % yield

of **37** (Kiss et al., 2018). Next, **37** was treated 4 eq. of NaN_3 in DMF (0.13M). The reaction took

place at 100 °C for 48 h resulting in a 78% yield of **38** (Kiss et al., 2018). In an alternative approach,

1.3 eq. of PPh_3, 1.5 eq. of DEAD, and 1.5 eq. of DPPA was dissolved in anhydrous THF (0.08 M)

with **3** (Blanco et al., 2014). The reaction took place at rt for 10 h resulting in a 71% yield of **4** (see

Scheme 2.5A). For the current study, a slightly modified Blanco et al. experimental procedure was

utilized. The azodicarboxylate was changed from DEAD to DIAD as DIAD is stable at rt while

DEAD is not. In addition, the concentration of the reaction was increased from 0.08 to 0.1 M. The

reaction was conducted at rt in the dark under argon, but never went to full completion resulting

in a 35% yield based on recovered starting material (BORSM). Although a low yield was attained,

the modified procedure was kept due to safety and toxicity concerns regarding DEAD.
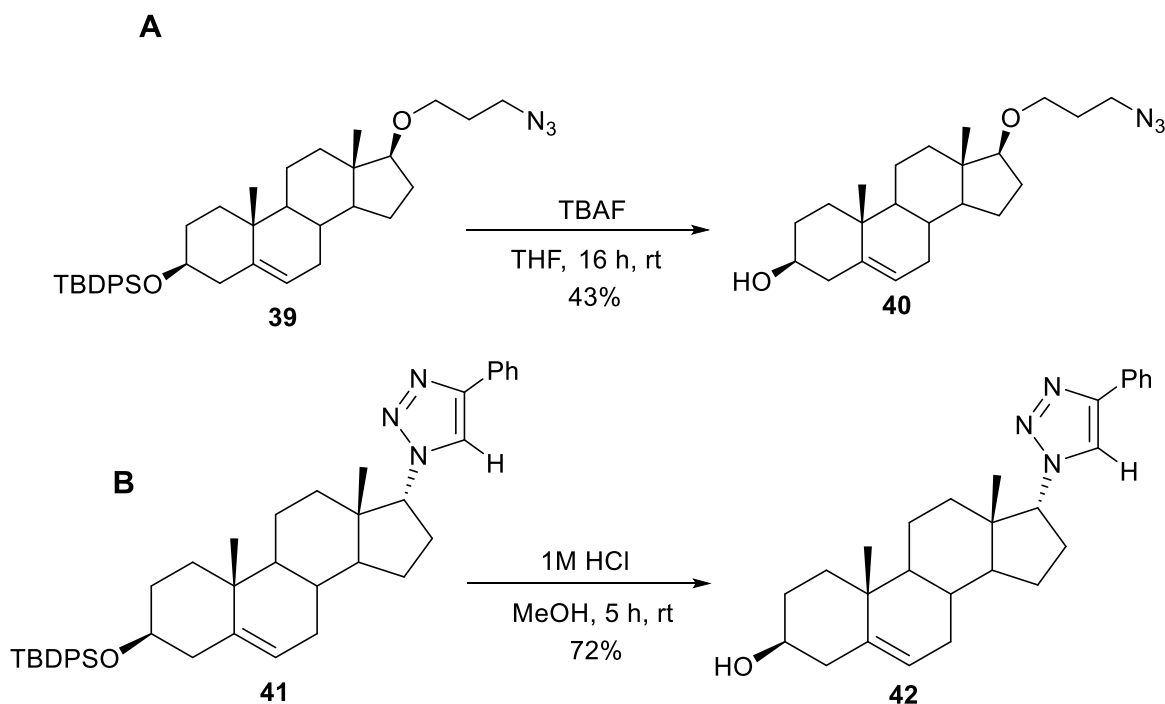
Scheme 2.6 Hydroxyl Deprotection Step. (A) Jan et al. TBDPS Deprotection Step, (B) Blanco et al. TBDPS Deprotection Step

With **4**, the TBDPS group was then removed with TBAF to give **5** (see Scheme 2.2). As

reported by Jan et al., **39** dissolved in anhydrous THF (0.05 M) was treated with 10 eq. of TBAF

(1 M solution in THF) (see Scheme 2.6A). The reaction was conducted at rt and reached

completion in 16 h with a 43% yield of **40** (Jan et al., 2016). In a different approach, **41** was

dissolved in 1M HCl in MeOH (0.076 M) (see Scheme 2.6B). The reaction was conducted at rt

and reached completion in 5 h with a 72% yield of **42** (Blanco et al., 2014). For the current study,

the procedure conducted by Jan et al. was used under neat conditions (no solvent). However, the

reaction time was increased from 16 h to 22.5 h, but the yield increased from 43% to 54%.
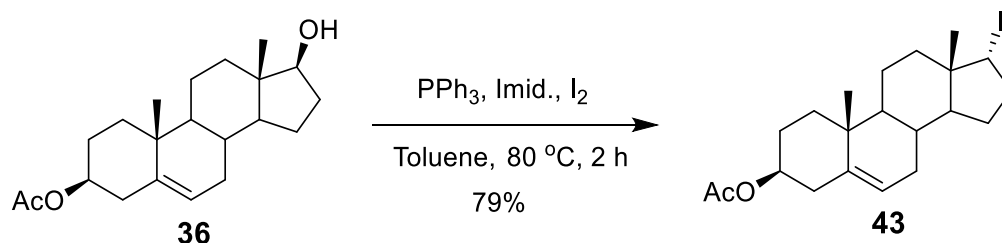
Scheme 2.7 Kiss et al. Appel Rxn Step

To make the other diastereomer probe, **8**, previous procedures from Kiss et al. and Jan et

al. were utilized. Starting from **3**, the -OH group was substituted with an iodide group of opposite

stereochemistry [17S]→[17R] in an appel reaction to give **6** (see Scheme 2.2). As described by

Kiss et al., **36** dissolved in toluene (0.06 M)was treated with 4 eq. of PPh_3, imidazole, and I_2 to

substitute and invert the -OH group into an iodo group (see Scheme 2.7). The reaction was

conducted at 80 °C and reached completion in 2 h with a 79% yield of **43** (Kiss et al., 2018). For

the current project, instead of PPh_3, a PPh_3 resin was used which led to easier purification. In

addition, the concentration of toluene was changed from 0.06 to 0.04 M. With all these

modifications however, the reaction time was increased from 2 to 5 h and a 60% yield was

observed.
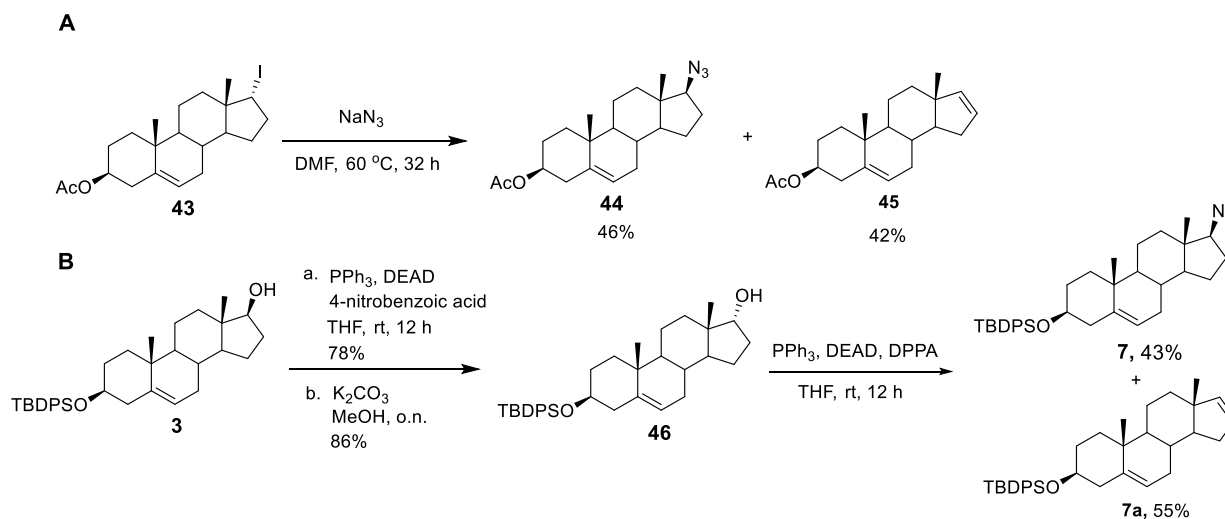
Scheme 2.8 Azide Displacement Step. (A) Kiss et al. Azide Displacement Step, (B) Blanco et al. Mitsunobu Rxn Step

Continuing with **6**, it was subjected to a S_N2 reaction substituting the iodide group with a -N_3 group of opposite stereochemistry [17R]→[17S] to give **7** (see Scheme 2.2). This and other similar compounds were synthesized previously by Kiss et al. and Blanco et al. In the procedure conducted by Kiss et al., **43** was treated with 7.5 eq. NaN_3 in DMF at 60 °C to form **44** with a 46% yield in 32 h and **45** in a 42% yield (see Scheme 2.8A) (Kiss et al., 2018). In an alternative approach, 2 eq. of PPh_3, 2.2 eq. of DEAD, and 2.4 eq. of 4-nitrobenzoic acid was dissolved in THF (0.49 M) with **3**, substituting the -OH group with a 4-nitrobenzoate group of [17R] configuration (Blanco et al., 2014). The reaction took place at rt for 12 h resulting in a 78% yield (see Scheme 2.8B step a). With the 4-nitrobenzoate derivative of **3**, the derivative was dissolved in THF (0.15 M) and MeOH (0.46 M). Next, 2 eq. powdered K_2CO_3 was added to solution and stirred overnight at rt resulting in a 86% yield of **46** (see Scheme 2.8B step b) (Blanco et al., 2014). Compound **46** dissolved in anhydrous THF (0.07 M) was treated with 1.3 eq. of PPh_3, 1.5 eq. of DEAD, and 1.7 eq. of DPPA (Blanco et al., 2014). The reaction took place at rt for 12 h resulting in a 43% yield of **7** and 55% yield of **7a**. For the current project, a modified Kiss et al. procedure was employed. First, $TBAN_3$ instead of NaN_3 was selected to be the azide donor due to safety concerns (Wang et al., 2019). Second, the solvent system was switched from DMF to diethyl

ether/toluene. Third, the reaction was converted from batch to microwave conditions (Hansen & Jensen, 2009). The reaction was conducted at 110 °C under Ar with microwave irradiation and a 45% yield of **7** was observed in addition to a 29% yield of **7a**. Although the yield was slightly lower (45 vs 46), the reaction time was decreased dramatically from 32 h to 1.5 h.
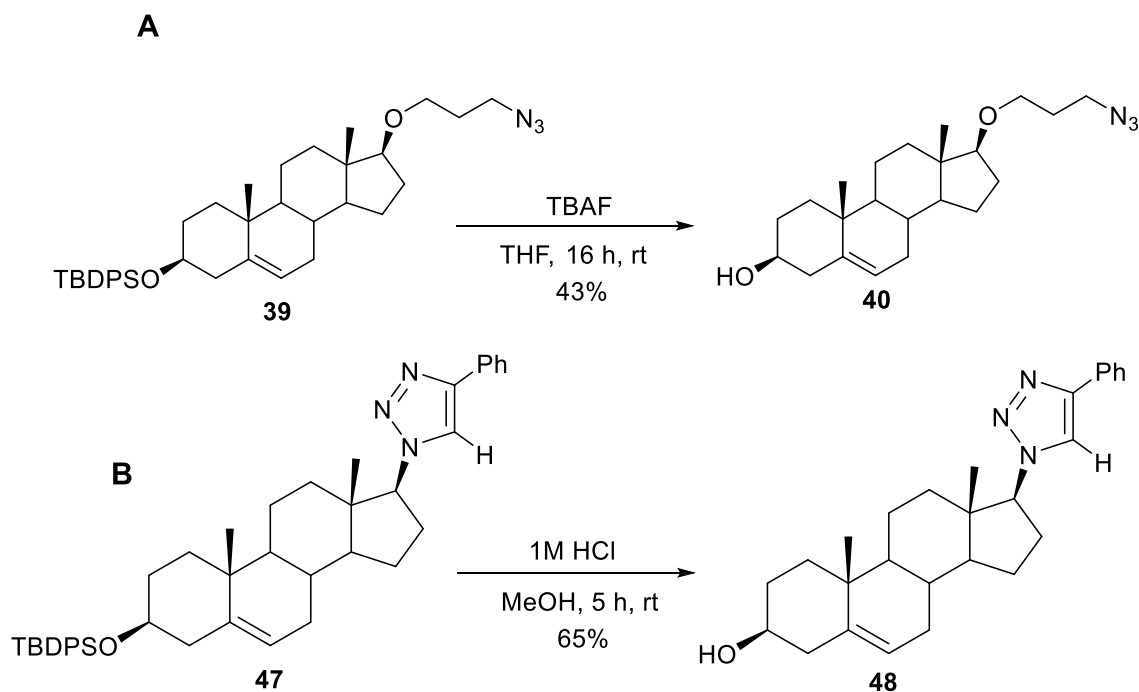
Scheme 2.9 Hydroxyl Deprotection Step. (A) Jan et al. TBDPS Deprotection Step, (B) Blanco et al. TBDPS Deprotection Step

With **7**, the TBDPS group was then removed with TBAF to give **8** (see Scheme 2.2). As reported by Jan et al., **39** dissolved in anhydrous THF (0.05 M) was treated with 10 eq. of TBAF (1 M solution in THF). The reaction was conducted at rt and reached completion in 16 h with a 43% yield of **40** (see Scheme 2.9A) (Jan et al., 2016). In an alternative approach, **47** was dissolved in 1M HCl in MeOH (0.076 M). The reaction was conducted at rt and reached completion in 5 h with a 65% yield of **48** (see Scheme 2.9B) (Blanco et al., 2014). For the current study, the procedure conducted by Jan et al. was used under neat conditions (no solvent present). However, the reaction time was increased from 16 h to 22.5 h, but the yield slightly increased from 43% to 45%.
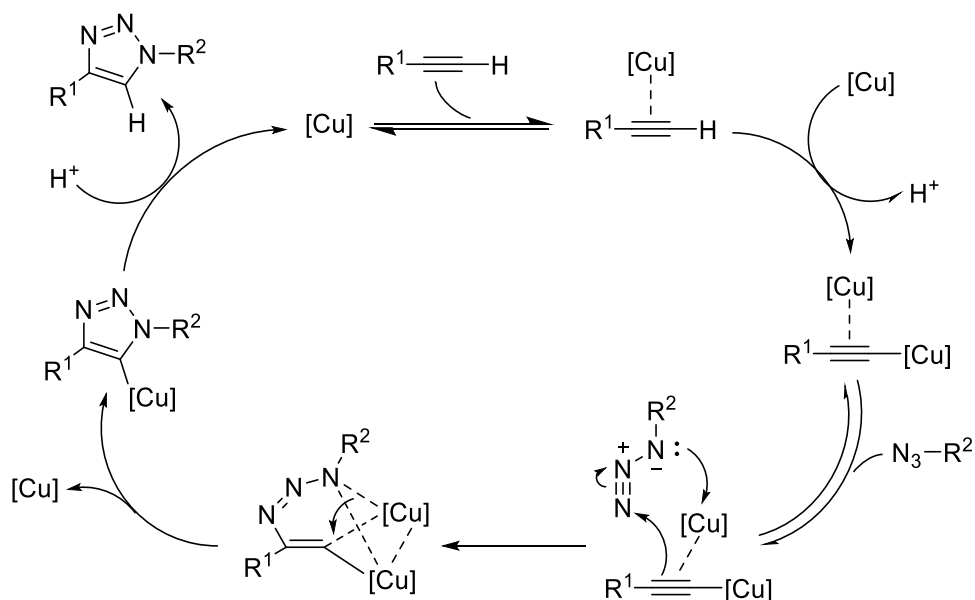
Figure 2.1 Worrell et al. Proposed CuAAC Mechanism

      Copper(I)-catalyzed azide-alkyne cycloaddition or CuAAC is a reaction in which an azide

and terminal alkyne conjugate together to form a 1,4-disubstituted-1,2,3-triazole. In the above

CuAAC mechanism proposed by Worrell et al. (see Figure 2.1), a copper(I) ion first interacts with

the terminal alkyne via cation-pi interactions while another copper(I) ion displaces the proton on

the terminal carbon of the alkyne (Worrell et al., 2013). With the copper coupled alkyne

intermediate, the β-carbon of the alkyne attacks N-3 of the azide, forming the first covalent C-N

bond, while the lone pairs on N-1 of the azide forms a reversible interaction with one of the

copper(I) atoms (Worrell et al., 2013). As the azide-alkyne complex stabilizes, the second

covalent C-N bond forms during ring closure and the copper(I) ion catalyst is regenerated, thus

producing the 1,4-disubstituted-1,2,3-triazole (see Figure 2.1).
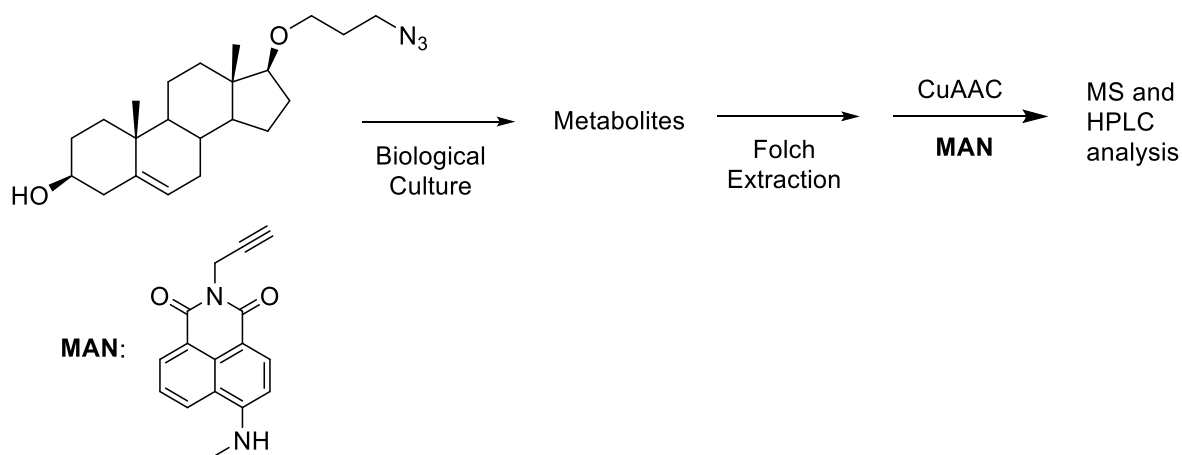
Figure 2.2 Jan et al. Metabolite Extraction Process

For this project, CuAAC will be used to extract metabolites of **5** and **8** after subjection to biological assays via conjugation to a fluorescent alkyne (**MAN**) using a strategy previously developed by Jan et al. (see Figure 2.2). The synthesis of **MAN** was performed by a graduate student in the Gervay-Hague research group, Matthew Orellana, using a procedure described by Jan et al. (not shown). Upon extraction, the metabolites of **5** and **8** conjugated to **MAN** will be characterized via NMR and mass spectrometry to discern the metabolism of sterols in various biological environments, like mammalian, microbial, and plant cultures. Currently, there are two CuAAC reactions developed by Kiss et al. and Blanco et al. for **5/8** and **4/7**, respectively.
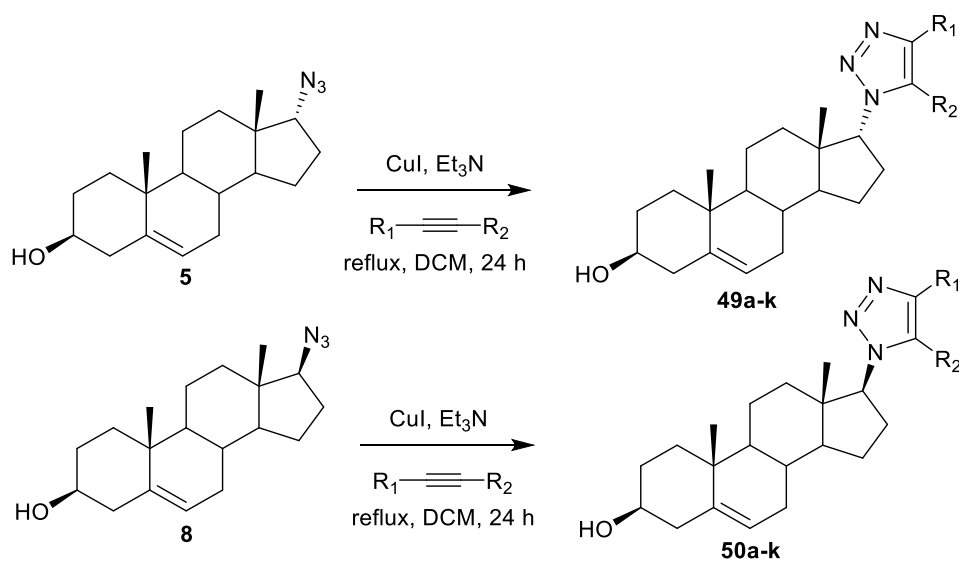
Scheme 2.10 Kiss et al. Click Procedure with 5 and 8

Kiss et al. described a click procedure in which **5** and **8** were reacted with 2 eq. of alkyne, 0.1 eq. of CuI, and 2 eq. of Et$_3$N in DCM (0.05 M) and refluxed for 24 h (see Scheme 2.10) (Kiss et al., 2018). Starting with **5**, variable yields were observed for **49a-k** (see Table 2.1). For terminal alkynes with an aromatic or heteroaromatic group (entries 1-3, 7), a 38-64% yield was seen while terminal alkynes with aliphatic groups (entries 4-6) observed a 45-96% yield. However, terminal alkynes with an ethoxybenzene or ethyl benzoate group (entries 8-11), a 62-88% yield was identified (Kiss et al., 2018). Conclusively, the terminal alkynes with an ethoxybenzene or ethyl benzoate group for R$_1$ displayed the highest average yields. From averaging out the yields for entries 1-11, an average 66% yield was calculated.

Table 2.1 Kiss et al. Procedure % Yield of 49a-k
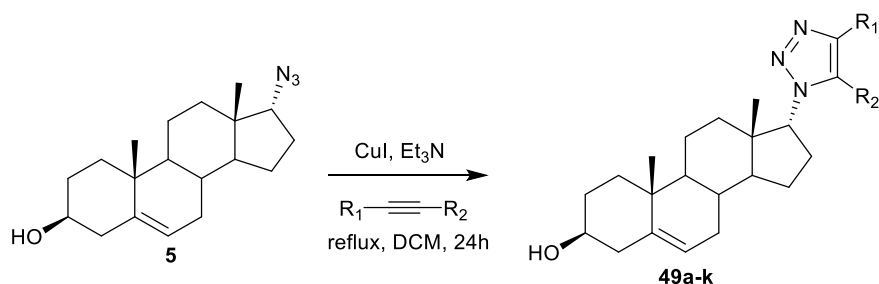
Entry	Compound #	R$_1$	R$_2$	Yield
1	**49a**		H	56%
2	**49b**	—CH$_3$	H	45%
3	**49c**	—OCH$_3$	H	38%
4	**49d**		H	96%
5	**49e**		H	45%
6	**49f**		H	71%
7	**49g**	N	H	64%
8	**49h**	—CH$_2$—O	H	76%
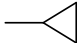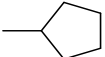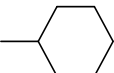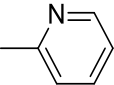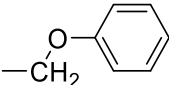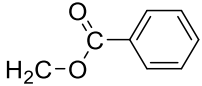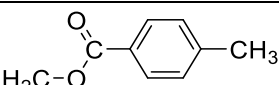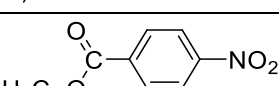
9	**49i**		H	81%
10	**49j**		H	88%
11	**49k**		H	62%

Continuing with **8**, variable yields were observed for **50a-k** (see Table 2.2). For terminal alkynes with an aromatic or heteroaromatic group (entries 1-3, 7), a 67-79% yield was seen while terminal alkynes with aliphatic groups (entries 4-6) observed a 45-71% yield. However, terminal alkynes with an ethoxybenzene or ethyl benzoate group (entries 8-11), a 48-79% yield was identified (Kiss et al., 2018). Conclusively, the terminal alkynes with an aromatic or heteroaromatic group for R_1 displayed the highest average yields which is opposite as seen with **5**. From averaging the yield for entries 1-11, a total average yield of 65% was calculated. By comparing the total average yields of **5** and **8**, it seems stereochemistry of the secondary azido group plays a role in CuAAC as **5** has a slightly higher yield than **8**.

Table 2.2 Kiss et al. Procedure % Yield for 50a-k
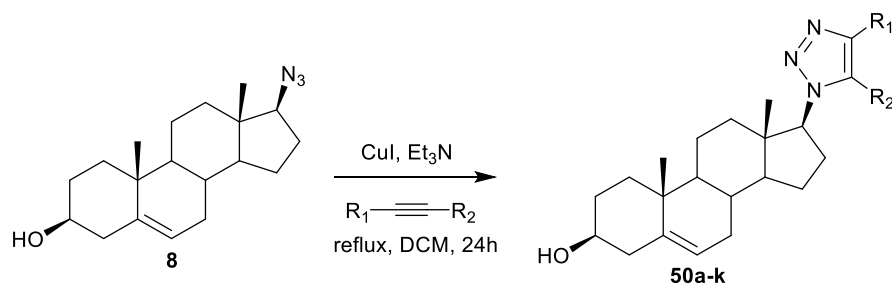
Entry	Compound #	R_1	R_2	Yield
1	**50a**		H	68%
2	**50b**		H	77%
3	**50c**		H	67%

4	**50d**		H	45%
5	**50e**		H	71%
6	**50f**		H	59%
7	**50g**		H	79%
8	**50h**		H	79%
9	**50i**		H	48%
10	**50j**		H	51%
11	**50k**		H	72%
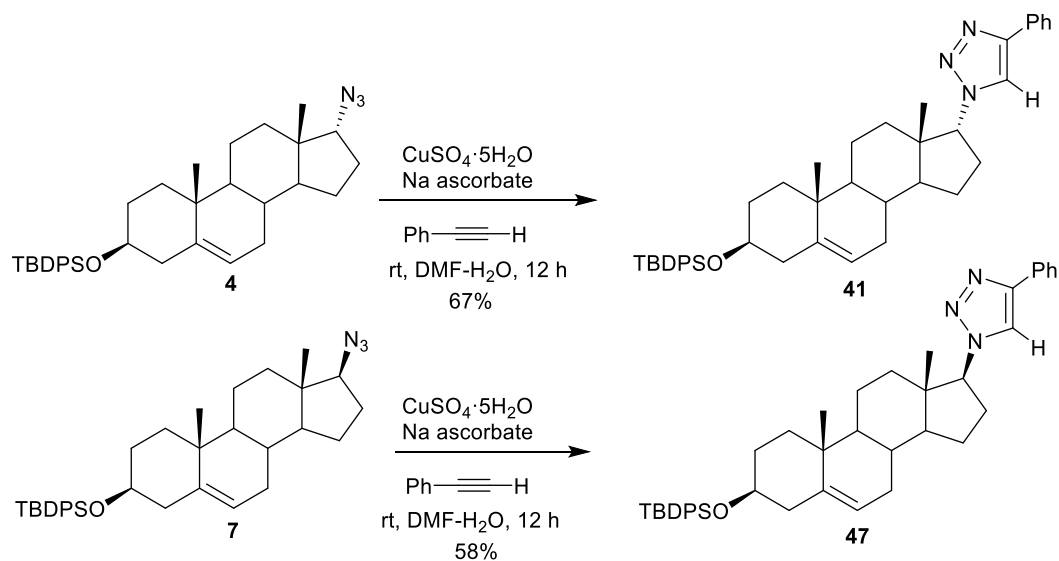
Scheme 2.11 Blanco et al. Click Procedure with 4 and 7

In addition to the Kiss et al. procedure, Blanco et al. described an alternative click

procedure in which **4** and **7** were reacted with 2 eq. of phenylacetylene, 0.2 eq. of $CuSO_4 \cdot 5H_2O$,

and 0.4 eq. of Na ascorbate in DMF-H_2O (0.14 M) and reacted for 12 h to achieve 67% of **41** and

58% yield of **47** (see Scheme 2.11) (Blanco et al., 2014). From the observing the yields for **4** and **7**, it seems the stereochemistry of the secondary azido group at C_{17} plays an important role in facilitating CuAAC, like seen in the Kiss et al. procedure. In general, the [17R] azide gives high yields.

Section 2.3: CuAAC between **5** and **MAN**
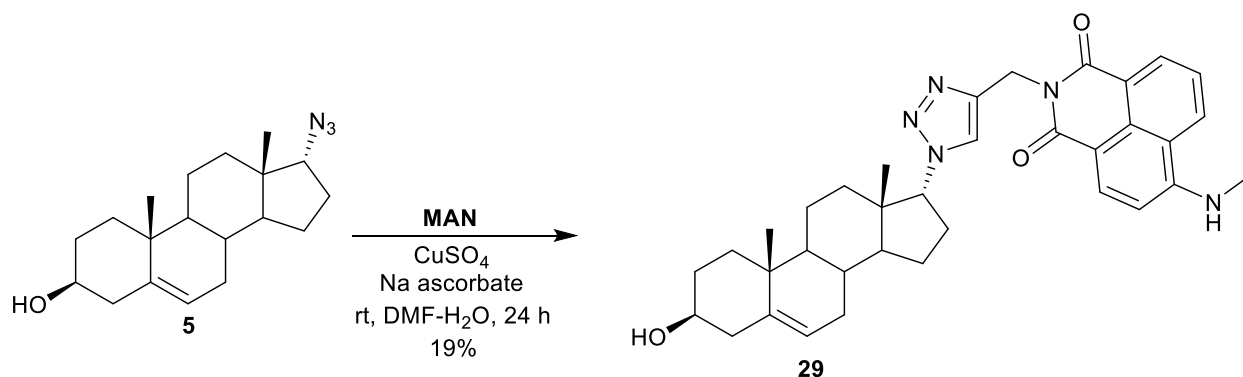
Scheme 2.12 Blanco et al. Click Procedure between 5 and MAN

For this project, the Blanco et al. click procedure was repeated with modified parameters as it closely resembles the Jan et al. procedure, which will be described below. Compound **5** was chosen first to react with **MAN** to form **29** as the azido group on C_{17} was in the [R] configuration while the methyl group on C_{18} is in the [S] configuration for **5**; however, the azido group on C_{17} and the methyl group on C_{18} for **8** are both in the [S] configuration, thus presenting a possible steric hinderance issue for CuAAC between **8** and **MAN**. With **5**, the azido probe was reacted with 2 eq. of **MAN**, 0.2 eq. of $CuSO_4$, and 0.4 eq. of Na ascorbate in DMF-H_2O (0.06 M) and reacted for 24 h to achieve an isolated 19% yield of **29** (see Scheme 2.12) that was identified by NMR and HRMS in the positive ion mode.
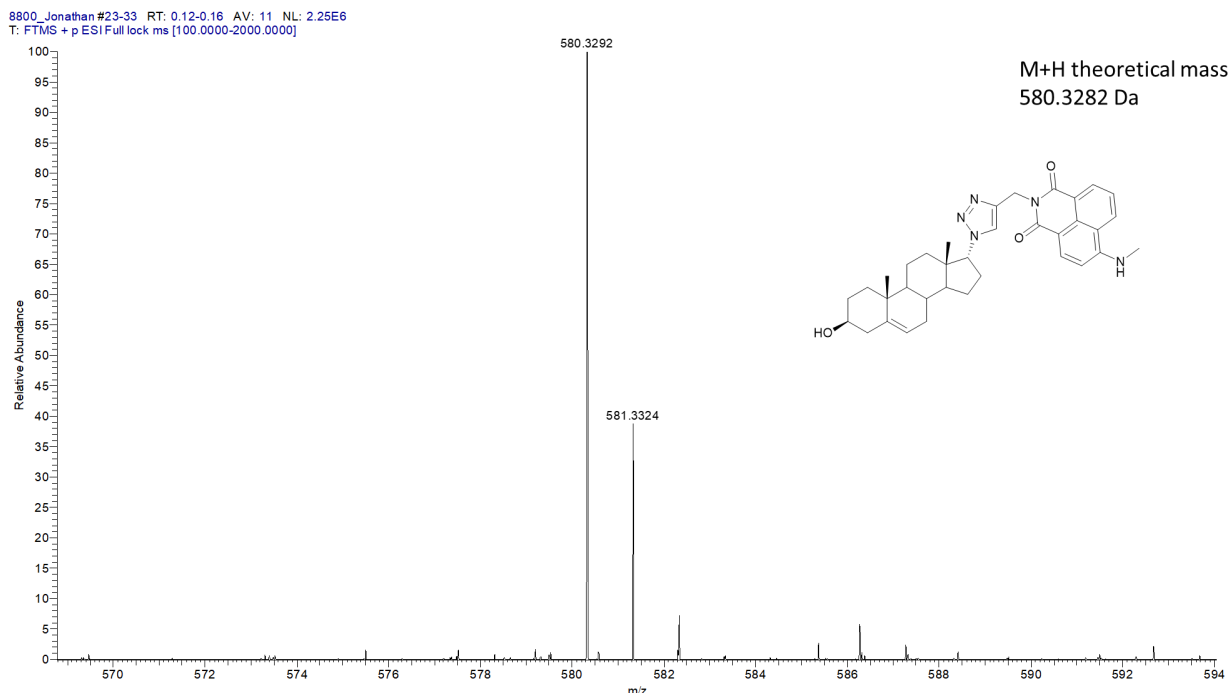
Figure 2.3 HRMS Spectrum of 29 (Blanco et al. CuAAC Reaction)

The [M+H] for **29** was calcd. for $C_{35}H_{41}N_5O_3^+$, 580.3282; found, 580.3292 (see Figure 2.3).

The HRMS data for **29** is acceptable as the difference between the expected (580.3282) and

observed mass (580.3292) is 0.001. Comparing the yield of **29** with the yield of **51**, the yield of **29**

is dramatically lower, which indicates a ligand such as TBTA may be required to improve % yield.
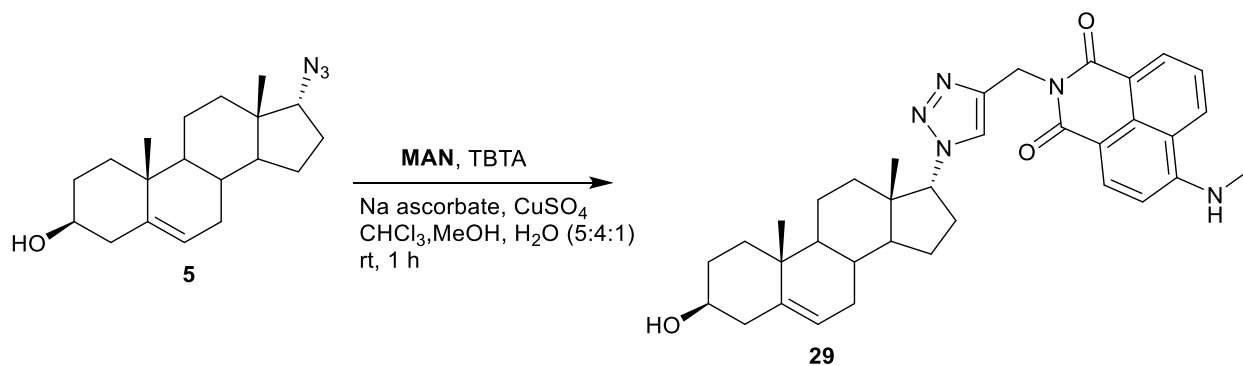
Scheme 2.13 Jan et al. Click Procedure between 5 with MAN

Although the modified Blanco et al. procedure (see Scheme 2.12) showed some promise

as a potential "click" procedure, the Jan et al. procedure was repeated as they utilized **MAN** for

its studies and obtained "clicked" product in a short time frame. As explained by Jan et al., the

azido probe was reacted with 0.25 mM **MAN** (5 eq.), 1.25 mM tris(benzyltriazolylmethyl)amine (TBTA) (25 eq.), 12.5 mM sodium ascorbate (250 eq.), and 0.25 mM copper sulfate (5 eq.) for 1 h at rt in chloroform/methanol/water (5:4:1, v/v/v) at a very dilute concentration (50 µM) (see Scheme 2.13) (Jan et al., 2016). The "clicked" product was then identified by mass spectrometry, but a yield was not reported.
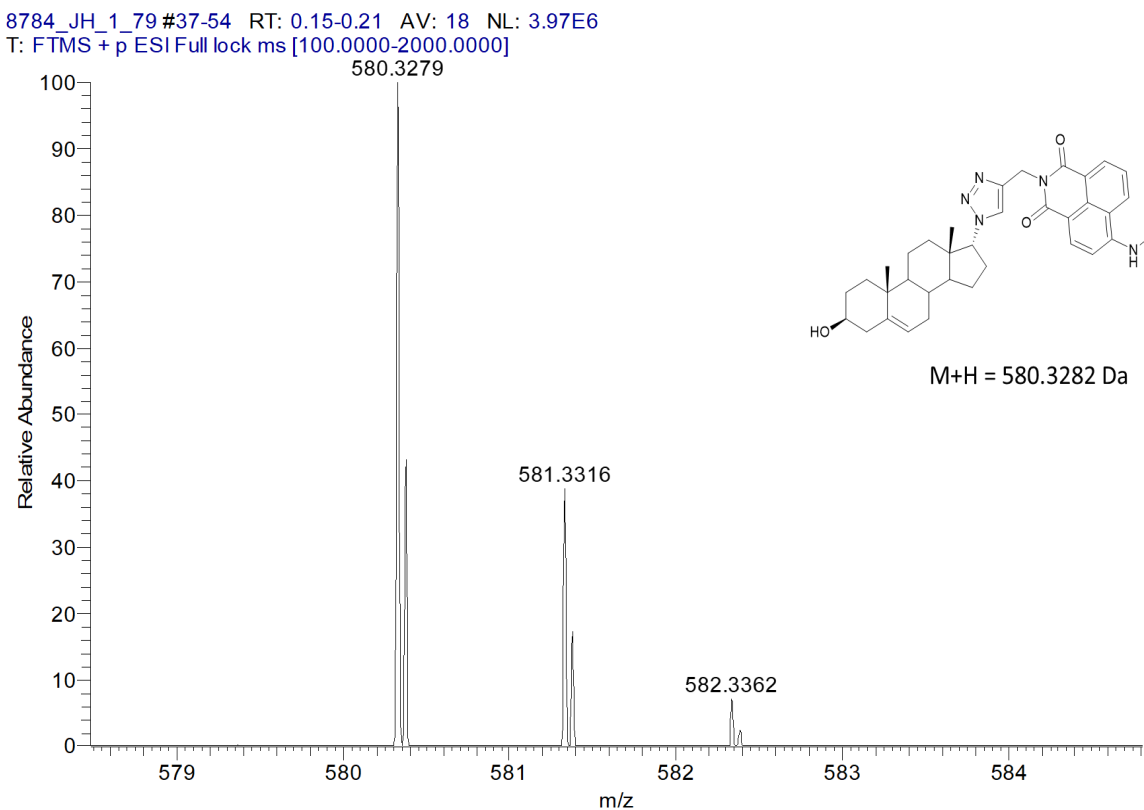
Figure 2.4 HRMS Spectrum of 29 (Jan et al. CuAAC Reaction)

For this project, the clicked product, **29**, between **5** and **MAN** can be detected after 1 h of reacting by high resolution mass spectrometry (HRMS) in the positive ion mode at the femtomolar concentration due to **MAN**'s increased sensitivity. In Figure 2.4, the [M+H] for **29** was calcd. for $C_{35}H_{41}N_5O_3^+$, 580.3282; found, 580.3279 which is acceptable as the difference between the expected and observed mass is 0.0003.
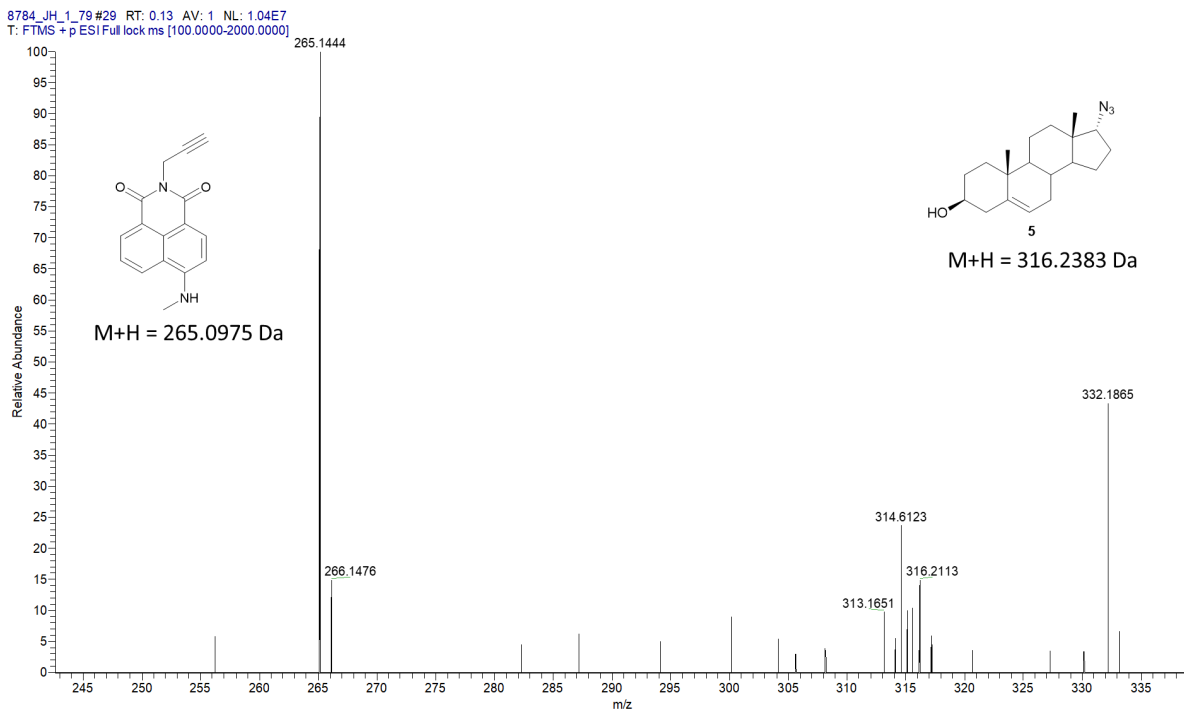
Figure 2.5 HRMS Spectrum of 5 and MAN (Jan et al. CuAAC Reaction)

In Figure 2.5, the [M+H] for **5** was calcd. for $C_{19}H_{29}N_3O^+$, 316.2383; found, 316.2113 and the [M+H] for **MAN** was calcd. for $C_{16}H_{12}N_2O_2^+$, 265.0975; found, 265.1444. Based on the intensive mass peak for **MAN** and the less intensive mass peak for **5**, this indicates that a portion of **5** did not "click" with **MAN** and quantitative yield was not achieved (see Figure 2.5). The difference between the expected and observed masses for **MAN** and **5** were less than or equal to 0.04 which is an acceptable difference. However, the relative abundance of **29**, **5**, and **MAN** could not be determined via HRMS due to a difference in ionization energies. In addition, **29** was not detected by NMR, thus indicating a very low yield.
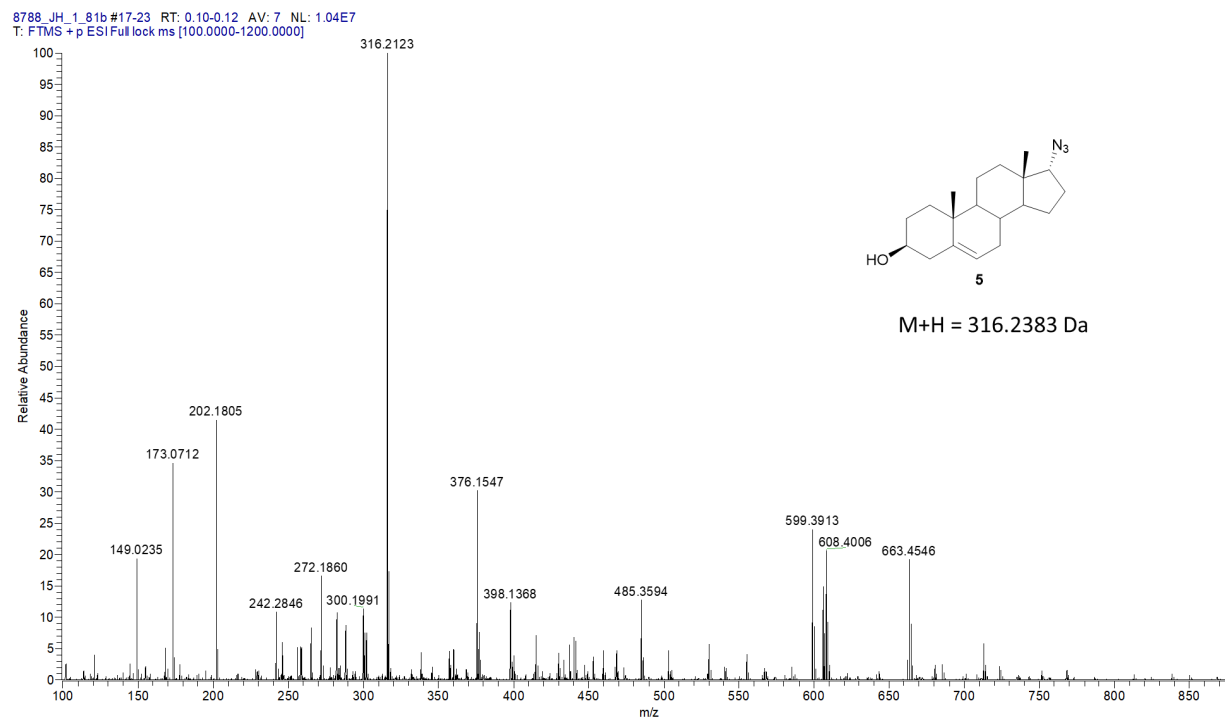
Figure 2.6 HRMS Spectrum of 5 (Jan et al. CuAAC Reaction w/o TBTA)

       The presence of TBTA was crucial for the Jan et al. CuAAC reaction between **5** and **MAN** to yield **29** as its role is to protect the Cu^+ ion catalyst in solution. The CuAAC reaction between **5** and **MAN** shown in Scheme 2.13 was repeated with the same parameters described above in the absence of TBTA but left to react overnight. In Figure 2.6, the [M+H] for **5** was calcd. for $C_{19}H_{29}N_3O^+$, 316.2383; found, 316.2123.

       In Figure 2.7, the [M+H] for **29** was calcd. for $C_{35}H_{41}N_5O_3^+$, 580.3282; found, 580.3286. Both observed mass peaks had a difference less than 0.04 in respect to their calculated mass which is acceptable. Based on the intensive mass peak for **5** and the less intensive mass peak for **29**, it was concluded that a majority of **5** was left unreacted while a minute trace of **29** was detected thereby reiterating the importance of TBTA in the CuAAC reaction (see Figure 2.6). Although **29** was detected by HRMS, **29** was not detected by NMR, thus indicating a low yield. Even in the presence of TBTA, the presence of **29** could not be identified by NMR indicating a different CuAAC method may be necessary.
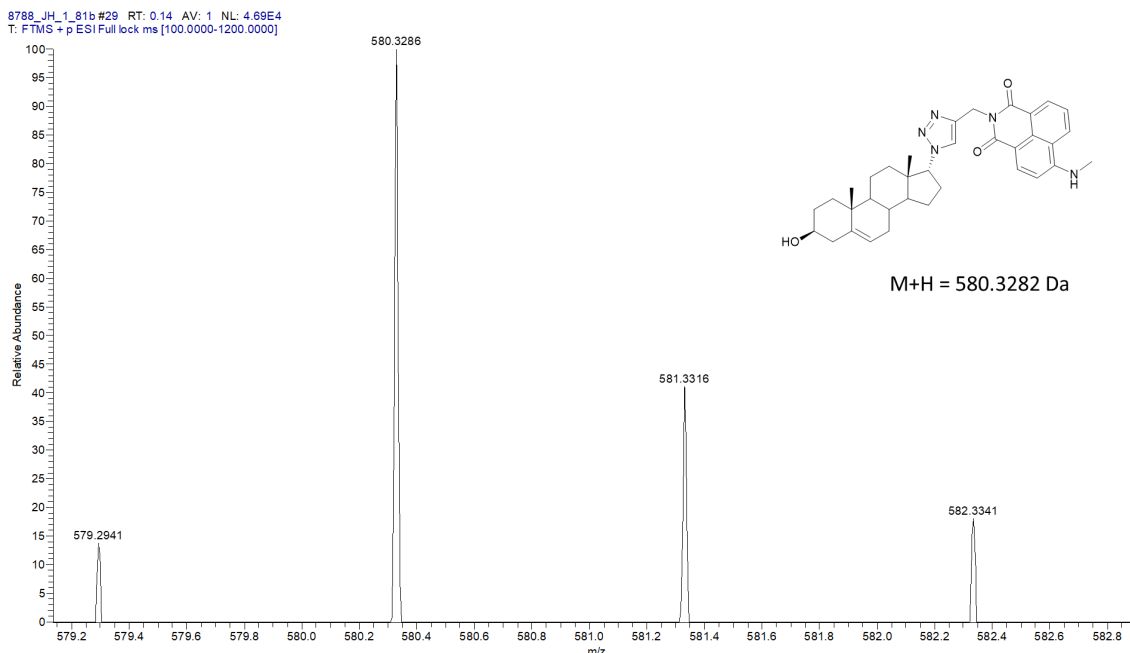
Figure 2.7 HRMS Spectrum of 29 (Jan et al. CuAAC Reaction w/o TBTA)

From comparing the results obtained reacting **5** and **MAN** with either the modified Blanco et al. or Jan et al. procedure, it seems the modified Blanco et al. procedure showed the most potential for this project as **29** was detected by both NMR and HRMS. However, a low 19% yield after purification was achieved for **29** only after reacting overnight and quantitative yield was not attained. Therefore, a possible modification to improve yield and lower reaction time may be the addition of TBTA (Jan et al. procedure) which will be applied in the future. Upon optimization of the modified Blanco et al. click procedure between **5** and **MAN**, the procedure will be conducted between **8** and **MAN** and the yield of **30** (see Figure 2.8) will be compared to that of **29**.
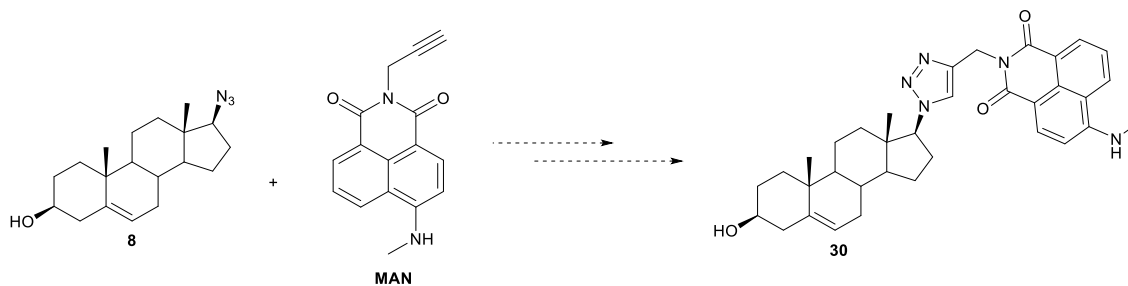
Figure 2.8 CuAAC Product between 8 and MAN (30)

Thin Layer Chromatography. All TLC experiments were run on silica gel-coated glass-backed plates (Millipore). TLC plates were cut into 2x5cm pieces.

TLC Stains: CAM stain was prepared using ceric ammonium sulfate (0.5 g), ammonium molybdate tetrahydrate (12 g), concentrated sulfuric acid (15 mL), and deionized water (235 mL).

Nuclear Magnetic Resonance (NMR) Experiments. NMR experiments were performed at 293 K on an 800 MHz Bruker Avance III NMR spectrometer equipped with a cryogenic probe, 600 MHz Varian VNMRS spectrometer, or 400 MHz Bruker Nanobay AVIIIHD spectrometer. NMR samples of 300-500 µL were contained in 5 mm outside diameter Wilmad tubes. All NMR experiments were completed in $CDCl_3$. Complete assignments are listed, and the methods used for achieving full assignment are reported in Sections 3.2-3.11. Special thanks to Matthew Orellana, a graduate student in the Gervay-Hague research group, for providing ^{1}H, ^{13}C, COSY, HSQC, HMBC, and NOESY spectra fid for compounds **1**, **3**, **4**, and **5**.

Specific Rotation Experiments. Specific rotation was measured at 589 nm (sodium D-line) at 26°C with the Ruldolph Autopol IV Polarimeter. Specific rotation was reported as $[\alpha]_D^{26}$ (*c*=concentration in $g \cdot mL^{-1}$, solvent).

High Resolution Mass Spectrometry (HRMS) Experiments. HRMS analysis was performed on a Thermo Q-Exactive HF (High-field Orbitrap) spectrometer. The mass spectrometer was operated in the positive electrospray ion mode. Special thanks to Will Jewel of the UC Davis Campus Mass Spectrometry Facilities (CMSF) for running these HRMS experiments and providing HRMS spectra.

<u>Preparation of **2**: (3S,10R,13S)-3-((tert-butyldiphenylsilyl)oxy)-10,13-dimethyl-1,2,3,4,7,8,9,10,11,12,13,14,15,16-tetradecahydro-17H-cyclopenta[a]phenanthren-17-one</u>
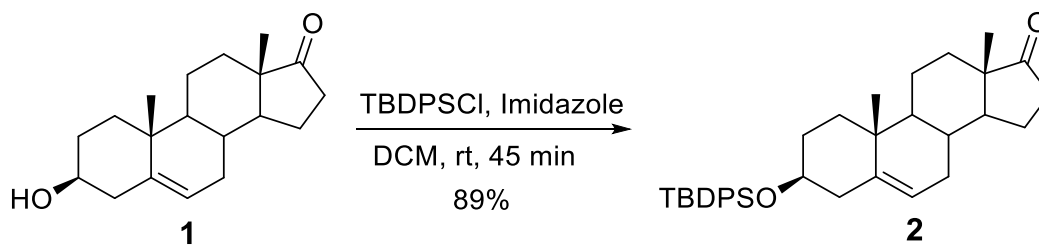
In a dry 25 mL round bottom flask, commercially available DHEA (**1**) (403 mg, 1.4 mmol) and imidazole (386 mg, 5.6 mmol) was added. The reaction vessel was then purged of air and supplemented with argon gas. Next, 4.0 mL (0.35 M) of DCM was added via syringe needle and stirred with a stir bar at rt until all the solids dissolved. Once the solids dissolved, the solution was cooled via ice bath to 0 °C for approximately 15 min. TBDPSCl (400 µL, 1.54 mmol) was added dropwise via syringe needle over 2 min. The solution was then brought to rt and stirred for 45 min. The reaction was cooled to 0 °C via ice bath and then quenched with sat. aqueous NH_4Cl and stirred for 10-20 min. The solvent was removed *in vacuo* and the solids were dissolved in ethyl acetate. The resulting solution was washed with DI H_2O and brine sequentially. The organic layer was then dried over $MgSO_4$ and concentrated in vacuo to give crude extract. The crude was then purified via recrystallization with cold MeOH to yield **2** (657 mg, 89%) as a white solid. TLC (ethyl acetate/hexanes = 20/80, v/v): Rf = 0.79; ^1H NMR (400 MHz, chloroform-*d*) δ 7.70 – 7.65 (m, 4H, Ar-H), 7.45 – 7.33 (m, 6H, Ar-H), 5.17 – 5.14 (m, 1H, H_6), 3.60 – 3.48 (m, 1H, H_3), 2.48 – 2.39 (m, 1H, H_{16}), 2.35 (ddd, *J* = 13.6, 10.9, 2.7 Hz, 1H, H_4), 2.16 (ddd, *J* = 13.3, 5.0, 2.2 Hz, 1H, $H_{4'}$), 2.12 – 1.99 (m, 2H, H_7, $H_{16'}$), 1.95 – 1.87 (m, 1H, H_{15}), 1.81 (ddd, *J* = 12.8, 4.2, 2.7 Hz, 1H, H_{12}), 1.75 – 1.65 (m, 2H, H_1, H_2), 1.64 – 1.56 (m, 3H, $H_{2'}$, H_8, H_{11}), 1.55 – 1.38 (m, 3H, $H_{7'}$, $H_{11'}$, $H_{15'}$), 1.22 (ddd, *J* = 13.0, 7.6, 3.1 Hz, 2H, $H_{12'}$, H_{14}), 1.06 (s, 9H, *t*-Bu), 1.01 (s, 3H, H_{19}), 0.90 (ddd, *J* = 4.0, 3.2 Hz, 2H, $H_{1'}$, H_9), 0.86 (s, 3H, H_{18}); ^{13}C NMR (100 MHz, chloroform-*d*) δ 221.23 (C_{17}), 141.55 (C_5), 135.77 (Ar-C), 134.79 (Ar-C), 129.49 (Ar-C), 127.48 (Ar-C), 120.40 (C_6), 73.09 (C_3), 51.78

(C_{14}), 50.18 (C_9), 47.55 (C_{13}), 42.46 (C_4), 37.16 (C_1), 36.64 (C_{10}), 35.85 (C_{16}), 31.82 (C_2), 31.48

(C_{12}), 31.44 (C_8), 30.78 (C_7), 27.02 (t-Bu), 21.88 (C_{15}), 20.32 (C_{11}), 19.46 (C_{19}), 19.15 (t-Bu), 13.54

(C_1). The NMR data matched previously published NMR results (Jan et al., 2016).

Preparation of **3**: (3S,10R,13S,17S)-3-((tert-butyldiphenylsilyl)oxy)-10,13-dimethyl-2,3,4,7,8,9,10,11,12,13,14,15,16,17-tetradecahydro-1H-cyclopenta[a]phenanthren-17-ol
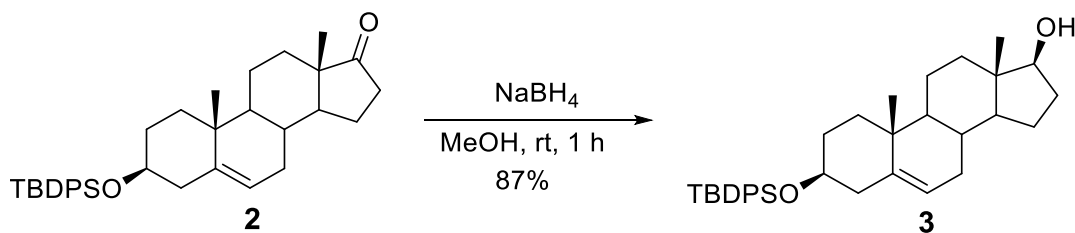
In a dry 25 mL round bottom flask, **2** (527 mg, 1 mmol) was added to 10 mL (0.1 M) of

anhydrous MeOH and stirred until all the solids dissolved. The solution was then cooled to 0 °C

via ice bath. Next, $NaBH_4$ (76 mg, 2 mmol) was added to the solution while stirring. The reaction

was stirred for 1 h at rt. The solution was then quenched with DI H_2O at 0 °C with vigorous stirring.

The resulting solution was then dried *in vacuo* to give a dry solid that was then dissolved in ethyl

acetate. The organics were washed with DI H_2O and brine sequentially, dried over $MgSO_4$, and

concentrated *in vacuo* to give a crude oil. The crude was purified by recrystallization with hot

MeOH to yield **3** (459 mg, 87%) as a white solid. TLC (ethyl acetate/hexanes = 20/80, v/v): Rf =

0.50; ^{1}H NMR (400 MHz, chloroform-d) δ 7.71 – 7.65 (m, 4H, Ar-H), 7.44 – 7.34 (m, 6H, Ar-H),

5.17 – 5.08 (m, 1H, H_6), 3.61 (t, *J* = 8.5 Hz, 1H, H_{17}), 3.57 – 3.50 (m, 1H, H_3), 2.34 (t, *J* = 12.3 Hz,

1H, H_4), 2.19 – 2.11 (m, 1H, $H_{4'}$), 2.10 – 1.99 (m, 1H, H_{16}), 1.96 – 1.87 (m, 1H, H_7), 1.83 – 1.77

(m, 1H, H_{12}), 1.75 – 1.64 (m, 2H, H_1, H_2), 1.63 – 1.49 (m, 3H, $H_{2'}$, H_{11}, H_{15}), 1.49 – 1.38 (m, 4H,

$H_{7'}$, H_8, $H_{11'}$, $H_{16'}$), 1.31 – 1.19 (m, 1H, $H_{15'}$), 1.07 (s, 9H, t-Bu), 1.04 – 1.02 (m, 1H, $H_{12'}$), 1.00 (s,

3H, H_{19}), 0.94 – 0.78 (m, 3H, $H_{1'}$, H_9, H_{14}), 0.74 (s, 3H, H_{18}); ^{13}C NMR (100 MHz, chloroform-d) δ

141.40 (C_5), 135.78 (d, *J* = 1.7 Hz, Ar-C), 134.81 (d, *J* = 2.3 Hz, Ar-C), 129.44 (d, *J* = 2.3 Hz, Ar-

C), 127.46 (d, *J* = 2.4 Hz, Ar-C), 120.82 (C_6), 81.91 (C_{17}), 73.19 (C_3), 51.34 (C_{14}), 50.18 (C_9),

42.71 (C_{13}), 42.49 (C_4), 37.25 (C_1), 36.58 (C_{10}, C_{12}), 31.93 (C_8), 31.87 (C_2), 31.48 (C_7), 30.52 (C_{16}), 27.01 (*t*-Bu), 23.43 (C_{15}), 20.62 (C_{11}), 19.47 (C_{19}), 19.15 (*t*-Bu), 10.94 (C_{18}). The NMR data matched previously published NMR results (Jan et al., 2016).

Preparation of **4**: (((3S,10R,13S,17R)-17-azido-10,13-dimethyl-2,3,4,7,8,9,10,11,12,13,14,15,16,17-tetradecahydro-1H-cyclopenta[a]phenanthren-3-yl)oxy)(tert-butyl)diphenylsilane
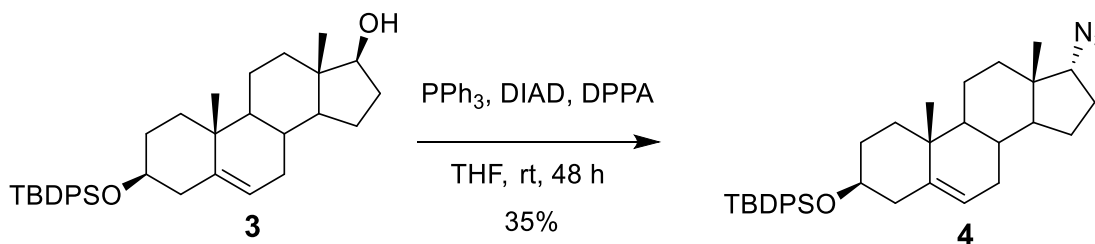
In an oven dried 100 mL round bottom flask, PPh_3 (315 mg, 1.2 mmol) was dissolved in 5 mL (0.20 M) anhydrous THF. The reaction vessel was purged of air and supplemented with argon gas. DIAD (275 µL, 1.4 mmol) was added to the solution and stirred for 10 min in the dark. Compound **3** (530 mg, 1 mmol) dissolved in 5 mL (0.20 M) anhydrous THF was added to solution and stirred for 10 min. DPPA (300 µL, 1.4 mmol) was added dropwise and stirred at rt for 48 h. The reaction was diluted with ethyl acetate and quenched with 1M HCl. The resulting solution was washed with 1M HCl and brine, dried with Na_2SO_4, and concentrated *in vacuo* to give a yellow oil. The yellow oil was purified by MPLC with an ethyl acetate/hexanes solvent system (see Figure S2.6) to yield **4** (48 mg, 35% BORSM) as a viscous oil. TLC (ethyl acetate/hexanes = 10/90, v/v): Rf = 0.60; ^{1}H NMR (400 MHz, chloroform-*d*) δ 7.75 – 7.65 (m, 4H, Ar-H), 7.47 – 7.34 (m, 6H, Ar-H), 5.17 – 5.09 (m, 1H, H_6), 3.60 – 3.52 (m, 1H, H_3), 3.50 (d, *J* = 6.7 Hz, 1H, H_{17}), 2.34 (t, *J* = 12.3 Hz, 1H, H_4), 2.19 – 2.09 (m, 2H, $H_{4'}$, H_{16}), 1.98 – 1.90 (m, 1H, H_7), 1.78 – 1.63 (m, 4H, H_1, H_2, H_{15}, $H_{16'}$), 1.62 – 1.51 (m, 5H, $H_{2'}$, $H_{7'}$, H_{11}, H_{12}, $H_{12'}$), 1.50 – 1.34 (m, 2H, H_8, $H_{11'}$), 1.29 – 1.14 (m, 2H, H_{14}, $H_{15'}$), 1.07 (s, 9H, *t*-Bu), 0.99 (s, 3H, H_{19}), 0.93 – 0.82 (m, 2H, $H_{1'}$, H_9), 0.74 (s, 3H, H_{18}); ^{13}C NMR (100 MHz, chloroform-*d*) δ 141.22 (C_5), 135.80 (Ar-C), 134.81 (Ar-C), 129.48 (Ar-C), 127.49

47

(Ar-C), 120.88 (C_6), 73.17 (C_3), 71.48 (C_{17}), 49.85 (C_{14}), 49.71 (C_9), 45.71 (C_{13}), 42.47 (C_4), 37.24 (C_1), 36.56 (C_{10}), 32.47 (C_{12}), 32.14 (C_7), 32.05 (C_8), 31.87 (C_2), 28.70 (C_{16}), 27.03 (*t*-Bu), 24.81 (C_{15}), 20.57 (C_{11}), 19.46 (C_{19}), 19.16 (*t*-Bu), 17.43 (C_{18}). The NMR data matched previously published NMR results (Blanco et al., 2014).

Preparation of **5**: (3S,10R,13S,17R)-17-azido-10,13-dimethyl-2,3,4,7,8,9,10,11,12,13,14,15,16,17-tetradecahydro-1H-cyclopenta[a]phenanthren-3-ol

In a dry 10 mL round bottom flask, **4** (187 mg, 0.34 mmol) was added and purged with Ar. TBAF (1M in THF, 3.4 mL, 3.4 mmol) was added dropwise and stirred at rt for 22.5 h. The reaction was quenched with saturated aqueous NH_4Cl and stirred for 10 min. The solvent was removed *in vacuo* to afford a dry residue that was diluted with ethyl acetate. The resulting solution was washed with DI H_2O and brine, dried with $MgSO_4$, and concentrated *in vacuo* to give crude oil. The crude mixture was purified via MPLC with an ethyl acetate/hexanes solvent system (see Figure S2.7) to yield **5** (58 mg, 54%) as a white solid. TLC (ethyl acetate/hexanes = 10/90, v/v): Rf = 0.19; ^{1}H NMR (400 MHz, chloroform-*d*) δ 5.37 – 5.32 (m, 1H, H_6), 3.52 (d, *J* = 6.4 Hz, 2H, H_3, H_{17}), 2.34 – 2.21 (m, 2H, H_4, $H_{4'}$), 2.21 – 2.10 (m, 1H, H_{16}), 2.06 – 1.95 (m, 1H, H_7), 1.89 – 1.81 (m, 2H, H_1, H_2), 1.80 – 1.73 (m, 1H, H_{15}), 1.72 – 1.55 (m, 5H, $H_{7'}$, H_{11}, H_{12}, $H_{12'}$, $H_{16'}$), 1.52 – 1.39 (m, 3H, $H_{2'}$, H_8, $H_{11'}$), 1.30 – 1.17 (m, 2H, H_{14}, $H_{15'}$), 1.14 – 1.04 (m, 1H, $H_{1'}$), 1.00 (s, 3H, H_{19}), 0.99 – 0.93 (m, 1H, H_9), 0.75 (s, 3H, H_{18}); ^{13}C NMR (100 MHz, chloroform-*d*) δ 140.69 (C_5), 121.45 (C_6), 71.69 (C_3), 71.45 (C_{17}), 49.86 (C_{14}), 49.76 (C_9), 45.72 (C_{13}), 42.23 (C_4), 37.26 (C_1), 36.55 (C_{10}), 32.47 (C_{12}), 32.14 (C_7), 32.06 (C_8), 31.61 (C_2), 28.71 (C_{16}), 24.81 (C_{15}), 20.62 (C_{11}),

19.46 (C_{19}), 17.44 (C_{18}). [M+H] calcd. for $C_{19}H_{29}N_3O^+$, 316.2383; found, 316.2123. The NMR data matched previously published NMR results (Blanco et al., 2014), (Kiss et al., 2018).

Preparation of **6**: tert-butyl(((3S,10R,13S,17R)-17-iodo-10,13-dimethyl-2,3,4,7,8,9,10,11,12,13,14,15,16,17-tetradecahydro-1H-cyclopenta[a]phenanthren-3-yl)oxy)diphenylsilane

In a dry 25 mL round bottom flask, **3** (106 mg, 0.2 mmol), imidazole (54 mg, 0.8 mmol), and PPh_3 on resin (1 mmol/g resin, 800 mg, 0.8 mmol) was added to 5 mL (0.04 M) toluene. The reaction flask was heated to 80 °C via oil bath and I_2 (203 mg, 0.8 mmol) was added in portions in the dark and stirred for 5 h. The reaction was quenched with Na_2SO_3 and stirred for 1 h. The resin was removed via filtration and the solution was diluted with ethyl acetate. The resulting solution was washed with Na_2SO_3 and brine, dried with Na_2SO_4, and concentrated *in vacuo* to give a white oil. The oil was purified by MPLC with a dichloromethane/hexanes solvent system (see Figure S2.8) to yield **6** (73 mg, 60%) as a white solid. TLC (ethyl acetate/hexanes = 20/80, v/v): Rf = 0.75; ^{1}H NMR (600 MHz, chloroform-*d*) δ 7.70 – 7.65 (m, 5H, Ar-H), 7.39 – 7.29 (m, 5H, Ar-H), 5.15 – 5.12 (m, 1H, H_6), 4.34 (dd, *J* = 7.2, 1.2 Hz, 1H, H_{17}), 3.58 – 3.48 (m, 1H, H_3), 2.77 (ddd, *J* = 12.4, 9.1, 5.5 Hz, 1H, H_{16}), 2.40 (ddd, *J* = 16.0, 9.2, 6.2 Hz, 1H, $H_{16'}$), 2.34 (tt, *J* = 10.9, 2.9 Hz, 1H, H_4), 2.14 (ddd, *J* = 13.3, 4.9, 2.2 Hz, 1H, $H_{4'}$), 1.95 (ddt, *J* = 18.1, 6.0, 3.1 Hz, 1H, H_7), 1.89 – 1.81 (m, 1H, H_{15}), 1.71 (ddd, *J* = 16.6, 10.6, 2.9 Hz, 2H, H_1, H_2), 1.64 – 1.43 (m, 5H, $H_{2'}$, $H_{7'}$, H_{11}, H_{12}, H_{14}), 1.42 – 1.34 (m, 2H, H_8, $H_{12'}$), 1.33 – 1.24 (m, 2H, $H_{11'}$, $H_{15'}$), 1.07 (s, 9H, *t*-Bu), 0.99 (s, 3H, H_{19}), 0.93 – 0.85 (m, 2H, $H_{1'}$, H_9), 0.81 (s, 3H, H_{18}); ^{13}C NMR (100 MHz, chloroform-*d*) δ 141.18 (C_5), 135.79 (Ar-C), 134.76 (Ar-C), 129.51 (Ar-C), 127.52 (Ar-C), 120.89 (C_6), 73.19

(C$_3$), 49.43 (C$_9$, C$_{14}$), 48.12 (C$_{17}$), 45.18 (C$_{13}$), 42.46 (C$_4$), 40.66 (C$_{12}$), 37.22 (C$_1$), 36.82 (C$_{16}$), 36.49 (C$_{10}$), 32.54 (C$_8$), 31.95 (C$_7$), 31.87 (C$_2$), 27.04 (*t*-Bu), 25.18 (C$_{15}$), 21.79 (C$_{11}$), 19.57 (C$_{19}$), 19.18 (*t*-Bu), 15.47 (C$_{18}$). The NMR data matched previously published NMR results (Kiss et al., 2018).

Preparation of **7** and **7a**: (((3S,10R,13S,17S)-17-azido-10,13-dimethyl-2,3,4,7,8,9,10,11,12,13,14,15,16,17-tetradecahydro-1H-cyclopenta[a]phenanthren-3-yl)oxy)(tert-butyl)diphenylsilane and tert-butyl(((3S,10R,13R)-10,13-dimethyl-2,3,4,7,8,9,10,11,12,13,14,15-dodecahydro-1H-cyclopenta[a]phenanthren-3-yl)oxy)diphenylsilane
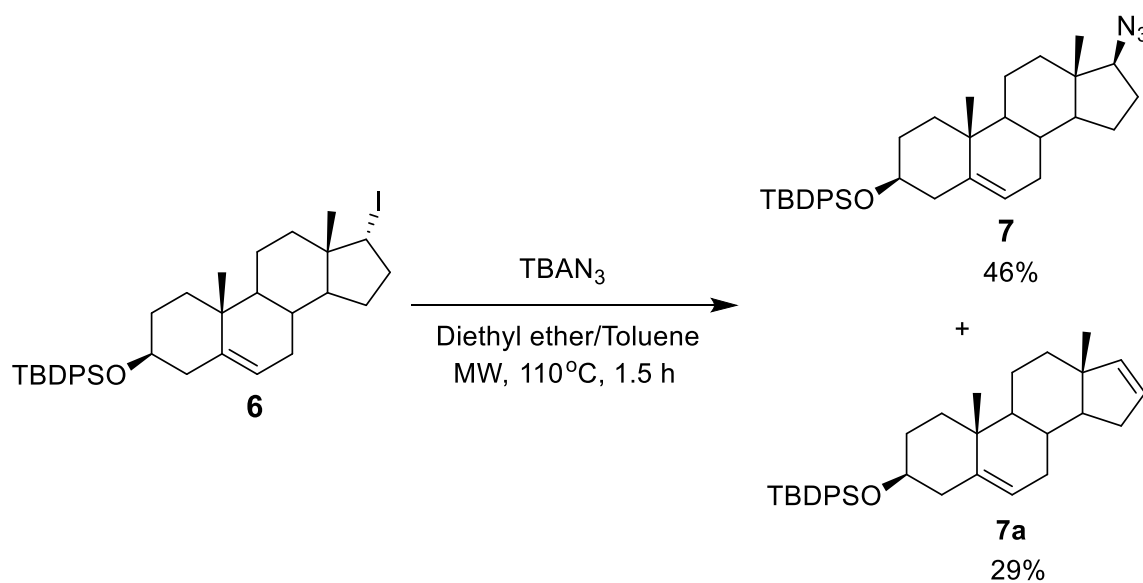
In a dry microwave vial, **6** (19 mg, 0.03 mmol) was purged with Ar, and dissolved in 0.8 mL (0.04 M) anhydrous diethyl ether. TBAN$_3$ (164 mg, 0.6 mmol) dissolved in 4 mL (0.01 M) anhydrous toluene was added to the vial and microwaved at 110 °C for 1.5 h with a 5 min pause every 15 min interval of microwave radiation. The solution was filtered and then diluted with ethyl acetate. The resulting solution was washed with DI H$_2$O and brine, dried with Na$_2$SO$_4$, and concentrated *in vacuo* to give a yellowish oil. The oil was purified by MPLC with an ethyl acetate/hexanes solvent system (see Figure S2.9) to yield **7** (7.5 mg, 46%) as a white solid and

7a (4 mg, 29%) as a viscous oil. (**7**) TLC (ethyl acetate/hexanes = 10/90, v/v): Rf = 0.19; ^{1}H NMR (800 MHz, chloroform-*d*) δ 7.69 – 7.65 (m, 4H, Ar-H), 7.43 – 7.39 (m, 2H, Ar-H), 7.38 – 7.34 (m, 4H, Ar-H), 5.11 (dt, *J* = 5.3, 1.9 Hz, 1H, H$_6$), 3.56 – 3.49 (m, 1H, H$_3$), 3.28 (t, *J* = 9.0 Hz, 1H, H$_{17}$), 2.33 (ddd, *J* = 13.6, 4.9, 2.4 Hz, 1H, H$_4$), 2.13 (ddd, *J* = 13.4, 4.9, 2.3 Hz, 1H, H$_{4'}$), 2.05 – 1.98 (m, 1H, H$_{16}$), 1.90 (ddt, *J* = 12.0, 6.7, 3.2 Hz, 1H, H$_7$), 1.85 (ddd, *J* = 12.5, 4.3, 2.8 Hz, 1H, H$_{12}$), 1.72 – 1.65 (m, 2H, H$_1$, H$_2$), 1.65 – 1.56 (m, 3H, H$_{2'}$, H$_{15}$, H$_{16'}$), 1.51 (dtd, *J* = 13.8, 4.4, 2.9 Hz, 1H, H$_{11}$), 1.45 – 1.37 (m, 3H, H$_{7'}$, H$_8$, H$_{11'}$), 1.29 – 1.22 (m, 1H, H$_{15'}$), 1.09 (td, *J* = 13.0, 4.4 Hz, 1H, H$_{12'}$), 1.05 (s, 9H, *t*-Bu), 0.99 (s, 3H, H$_{19}$), 0.96 – 0.92 (m, 1H, H$_{14}$), 0.90 – 0.80 (m, 2H, H$_{1'}$, H$_9$), 0.74 (s, 3H, H$_{18}$); ^{13}C NMR (200 MHz, chloroform-*d*) δ 141.41 (C$_5$), 135.78 (d, *J* = 3.0 Hz, Ar-C), 134.78 (d, *J* = 2.5 Hz, Ar-C), 129.46 (d, *J* = 3.6 Hz, Ar-C), 127.47 (d, *J* = 4.4 Hz, Ar-C), 120.64 (C$_6$), 73.14 (C$_3$), 71.23 (C$_{17}$), 52.41 (C$_{14}$), 49.99 (C$_9$), 44.21 (C$_{13}$), 42.45 (C$_4$), 37.21 (C$_1$), 37.07 (C$_{12}$), 36.55 (C$_{10}$), 31.95 (C$_8$), 31.82 (C$_2$), 31.50 (C$_7$), 27.00 (*t*-Bu), 26.91 (C$_{16}$), 23.61 (C$_{15}$), 20.57 (C$_{11}$), 19.45 (C$_{19}$), 19.15 (*t*-Bu), 12.11 (C$_{18}$). (**7a**) TLC (ethyl acetate/hexanes = 20/80, v/v): Rf = 0.80; ^{1}H NMR (800 MHz, chloroform-*d*) δ 7.68 (ddt, *J* = 7.3, 5.9, 1.4 Hz, 4H, Ar-H), 7.43 – 7.39 (m, 2H, Ar-H), 7.36 (tdd, *J* = 8.0, 4.9, 1.3 Hz, 4H, Ar-H), 5.82 (ddd, *J* = 5.7, 2.5, 1.1 Hz, 1H, H$_{17}$), 5.69 (ddd, *J* = 5.8, 3.1, 1.5 Hz, 1H, H$_{16}$), 5.14 (dt, *J* = 5.4, 2.1 Hz, 1H, H$_6$), 3.56 – 3.51 (m, 1H, H$_3$), 2.34 (tq, *J* = 11.3, 2.9 Hz, 1H, H$_4$), 2.14 (ddd, *J* = 13.3, 4.8, 2.3 Hz, 1H, H$_{4'}$), 2.08 (dddd, *J* = 15.2, 6.7, 3.1, 1.1 Hz, 1H, H$_{15}$), 1.94 (dtd, *J* = 17.3, 5.2, 2.8 Hz, 1H, H$_7$), 1.91 – 1.87 (m, 1H, H$_{15'}$), 1.73 (dt, *J* = 12.3, 3.8 Hz, 1H, H$_{12}$), 1.71 – 1.66 (m, 2H, H$_1$, H$_2$), 1.63 – 1.54 (m, 2H, H$_{2'}$, H$_8$), 1.54 – 1.49 (m, 3H, H$_{7'}$, H$_{11}$, H$_{11'}$), 1.36 – 1.31 (m, 1H, H$_{12'}$), 1.27 – 1.24 (m, 1H, H$_{14}$), 1.06 (s, 9H, *t*-Bu), 1.02 (s, 3H, H$_{19}$), 0.94 – 0.88 (m, 1H, H$_9$), 0.86 (td, *J* = 14.3, 13.7, 4.0 Hz, 1H, H$_{1'}$), 0.76 (s, 3H, H$_{18}$); ^{13}C NMR (200 MHz, chloroform-*d*) δ 143.86 (C$_{17}$), 141.58 (C$_5$), 135.79 (d, *J* = 3.0 Hz, Ar-C), 134.82 (d, *J* = 5.9 Hz, Ar-C), 129.45 (d, *J* = 5.1 Hz, Ar-C), 129.35 (C$_{16}$), 127.47 (d, *J* = 5.7 Hz, Ar-C), 120.98 (C$_6$), 73.23 (C$_3$), 56.21 (C$_{14}$), 50.86 (C$_9$), 45.37 (C$_{13}$), 42.54 (C$_4$), 37.16 (C$_1$), 36.80 (C$_{10}$), 35.86 (C$_{12}$), 32.08 (C$_{15}$), 31.89 (C$_2$), 31.72 (C$_7$), 30.41 (C$_8$), 27.02 (*t*-Bu), 20.81 (C$_{11}$), 19.37 (C$_{19}$), 19.16 (*t*-Bu),

16.84 (C_{18}). The NMR data matched previously published NMR results (Blanco et al., 2014), (Kiss et al., 2018).

<u>Preparation of **8**: (3S,10R,13S,17S)-17-azido-10,13-dimethyl-2,3,4,7,8,9,10,11,12,13,14,15,16,17-tetradecahydro-1H-cyclopenta[a]phenanthren-3-ol</u>
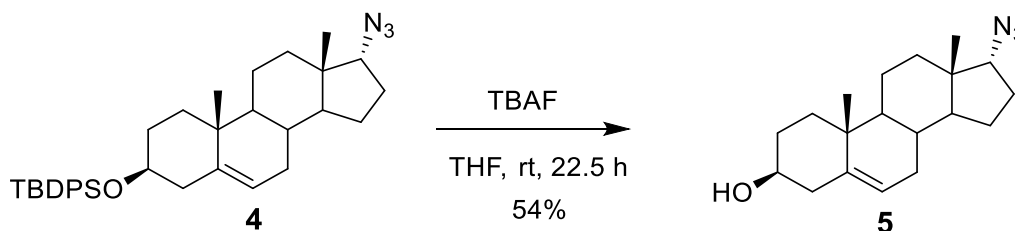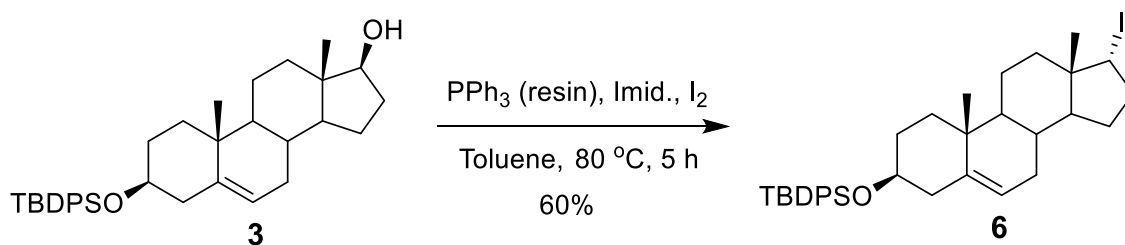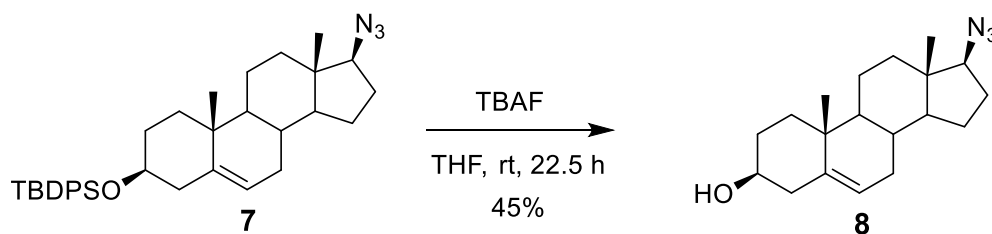

In a dry 5 mL round bottom flask, **7** (7 mg, 0.013 mmol) was added and purged with Ar. TBAF (1M in THF, 0.13 mL, 0.13 mmol) was added dropwise and stirred at rt for 22.5 h. The reaction was quenched with saturated aqueous NH_4Cl and stirred for 10 min. The solvent was removed *in vacuo* to afford a dry residue that was diluted with ethyl acetate. The resulting solution was washed with DI H_2O and brine, dried with $MgSO_4$, and concentrated *in vacuo* to give crude extract. The crude was purified via MPLC with an ethyl acetate/hexanes solvent system (see Figure S2.10) to yield **8** (2 mg, 45%) as a white solid. TLC (ethyl acetate/hexanes = 10/90, v/v): Rf = 0.10; ^{1}H NMR (800 MHz, chloroform-*d*) δ 5.35 (dt, *J* = 4.8, 2.0 Hz, 1H, H_6), 3.57 − 3.49 (m, 1H, H_3), 3.32 (t, *J* = 9.0 Hz, 1H, H_{17}), 2.30 (ddd, *J* = 13.0, 5.0, 2.4 Hz, 1H, H_4), 2.26 − 2.21 (m, 1H, $H_{4'}$), 2.04 (dtd, *J* = 13.7, 9.4, 6.0 Hz, 1H, H_{16}), 2.01 − 1.97 (m, 1H, H_7), 1.92 − 1.89 (m, 1H, H_{12}), 1.87 − 1.82 (m, 2H, H_1, H_2), 1.70 − 1.65 (m, 1H, H_{15}), 1.65 − 1.57 (m, 2H, H_{11}, $H_{16'}$), 1.54 − 1.42 (m, 4H, $H_{2'}$, $H_{7'}$, H_8, $H_{11'}$), 1.31 − 1.27 (m, 1H, $H_{15'}$), 1.16 (td, *J* = 12.9, 4.2 Hz, 1H, $H_{12'}$), 1.08 (td, *J* = 14.5, 13.8, 4.1 Hz, 1H, $H_{1'}$), 1.02 (s, 3H, H_{19}), 1.01 − 0.99 (m, 1H, H_{14}), 0.95 (ddd, *J* = 12.5, 10.7, 4.8 Hz, 1H, H_9), 0.77 (s, 3H, H_{18}); ^{13}C NMR (200 MHz, chloroform-*d*) δ 140.89 (C_5), 121.23 (C_6), 71.71 (C_3), 71.24 (C_{17}), 52.43 (C_{14}), 50.07 (C_9), 44.23 (C_{13}), 42.25 (C_4), 37.27 (C_1), 37.09 (C_{12}), 36.58 (C_{10}), 32.00 (C_8), 31.63 (C_2), 31.53 (C_7), 26.93 (C_{16}), 23.64 (C_{15}), 20.64 (C_{11}), 19.44 (C_{19}),

12.15 (C$_{18}$). The NMR data matched previously published NMR results (Blanco et al., 2014), (Kiss et al., 2018).

Preparation of **29**: 2-((1-((3S,10R,13S,17R)-3-hydroxy-10,13-dimethyl-2,3,4,7,8,9,10,11,12,13,14,15,16,17-tetradecahydro-1H-cyclopenta[a]phenanthren-17-yl)-1H-1,2,3-triazol-4-yl)methyl)-6-(methylamino)-1H-benzo[de]isoquinoline-1,3(2H)-dione
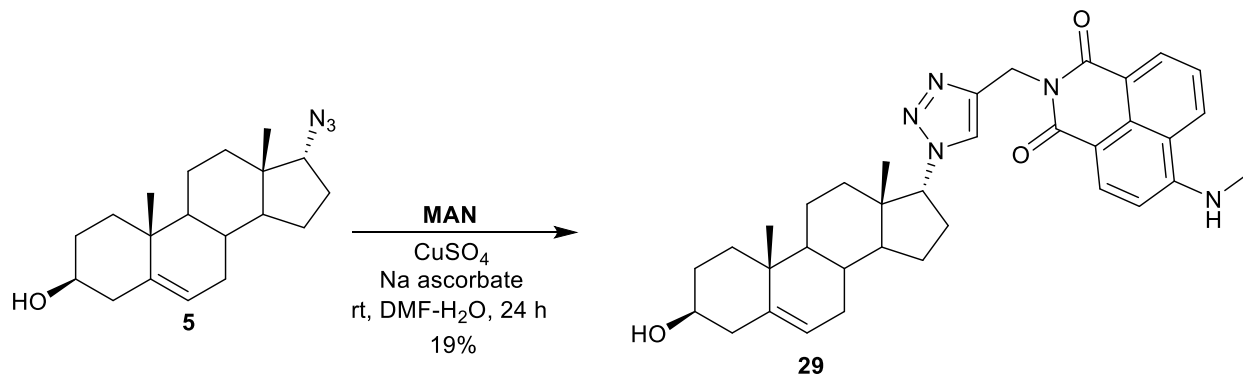
In a dry 5 mL round bottom flask, **5** (10 mg, 0.03 mmol) and **MAN** (16.6 mg, 0.06 mmol) were added and dissolved in 0.56 mL (0.06 M) anhydrous DMF. Sodium ascorbate (0.05 M in DI H$_2$O, 0.26 mL, 0.01 mmol) was added dropwise and stirred at rt for 2 min. Next, copper sulfate (0.03 M in DI H$_2$O, 0.22 mL, 0.01 mmol) was added and the reaction was stirred at rt for 24 h. The solvent was then removed *in vacuo* to afford a dry residue that was first washed with ethyl acetate and then chloroform to afford two crude mixtures. The crude mixture from the chloroform extraction was purified via MPLC first with an ethyl acetate/hexanes solvent system (see Figure S2.11) and then a methanol/dichloromethane solvent system (see Figure S2.12) to yield **29** (3.5 mg, 19%) as a yellow solid. TLC (methanol/dichloromethane = 10/90, v/v): Rf = 0.54; [α]$_D^{26}$ = −20.5 (*c* = 0.0004, CHCl$_3$); ^{1}H NMR (800 MHz, chloroform-*d*) δ 8.46 (dd, *J* = 7.3, 1.0 Hz, 1H, Ar-H), 8.43 (d, *J* = 8.4 Hz, 1H, Ar-H), 7.98 (d, *J* = 8.3 Hz, 1H, Ar-H), 7.55 (s, 1H, Triazole), 7.45 (dd, *J* = 8.3, 7.3 Hz, 1H, Ar-H), 6.64 (d, *J* = 8.4 Hz, 1H, Ar-H), 5.77 (s, 1H, N*H*-CH$_3$), 5.48 (d, *J* = 4.4 Hz, 2H, N-C*H$_2$*), 5.35 – 5.33 (m, 1H, H$_6$), 4.55 (dd, *J* = 8.7, 1.9 Hz, 1H, H$_{17}$), 3.52 – 3.47 (m, 1H, H$_3$), 3.11 (d, *J* = 4.6 Hz, 3H, NH-C*H$_3$*), 2.48 – 2.42 (m, 1H, H$_{16}$), 2.28 (ddd, *J* = 13.1, 5.0, 2.4 Hz,

1H, H$_4$), 2.26 – 2.19 (m, 2H, H$_{4'}$, H$_{16'}$), 2.06 – 2.03 (m, 2H, H$_7$, H$_{15}$), 1.79 (d, J = 12.3 Hz, 1H, H$_2$), 1.74 (dt, J = 13.4, 3.6 Hz, 1H, H$_1$), 1.70 – 1.66 (m, 1H, H$_{7'}$), 1.56 – 1.47 (m, 2H, H$_8$, H$_{14}$), 1.48 – 1.29 (m, 5H, H$_{2'}$, H$_{11}$, H$_{11'}$, H$_{12}$, H$_{15'}$), 0.98 (s, 4H, H$_1$, H$_{19}$), 0.92 (s, 3H, H$_{18}$), 0.84 – 0.81 (m, 1H, H$_9$), 0.29 – 0.23 (m, 1H, H$_{12'}$); ^{13}C NMR (200 MHz, chloroform-d) δ 164.40 (C=O), 163.82 (C=O), 150.64 (Ar-C), 143.50 (Triazole), 140.61 (C$_5$), 134.73 (Ar-C), 131.20 (Ar-C), 129.69 (Ar-C), 126.12 (Ar-C), 124.57 (Ar-C), 123.30 (Triazole), 122.76 (Ar-C), 121.40 (C$_6$), 120.14 (Ar-C), 109.89 (Ar-C), 103.87 (Ar-C), 71.67 (C$_3$), 70.18 (C$_{17}$), 50.04 (C$_{14}$), 49.32 (C$_9$), 46.04 (C$_{13}$), 42.20 (C$_4$), 37.10 (C$_1$), 36.47 (C$_{10}$), 35.08 (N-CH$_2$), 32.34 (C$_{12}$), 32.19 (C$_8$), 31.95 (C$_7$), 31.58 (C$_2$), 30.44 (NH-CH$_3$), 28.66 (C$_{16}$), 25.33 (C$_{15}$), 20.39 (C$_{11}$), 19.39 (C$_{19}$), 18.39 (C$_{18}$). HRMS (m/z): [M+H] calcd. for C$_{35}$H$_{41}$N$_5$O$_3^+$, 580.3282; found, 580.3292.

Figure S2.1 HRMS Spectrum of 29 (Jan et al. Crude Click Reaction)

M+H = 580.3282 Da

8784_JH_1_79 #37-54   RT: 0.15-0.21   AV: 18   NL: 3.97E6
T: FTMS + p ESI Full lock ms [100.0000-2000.0000]
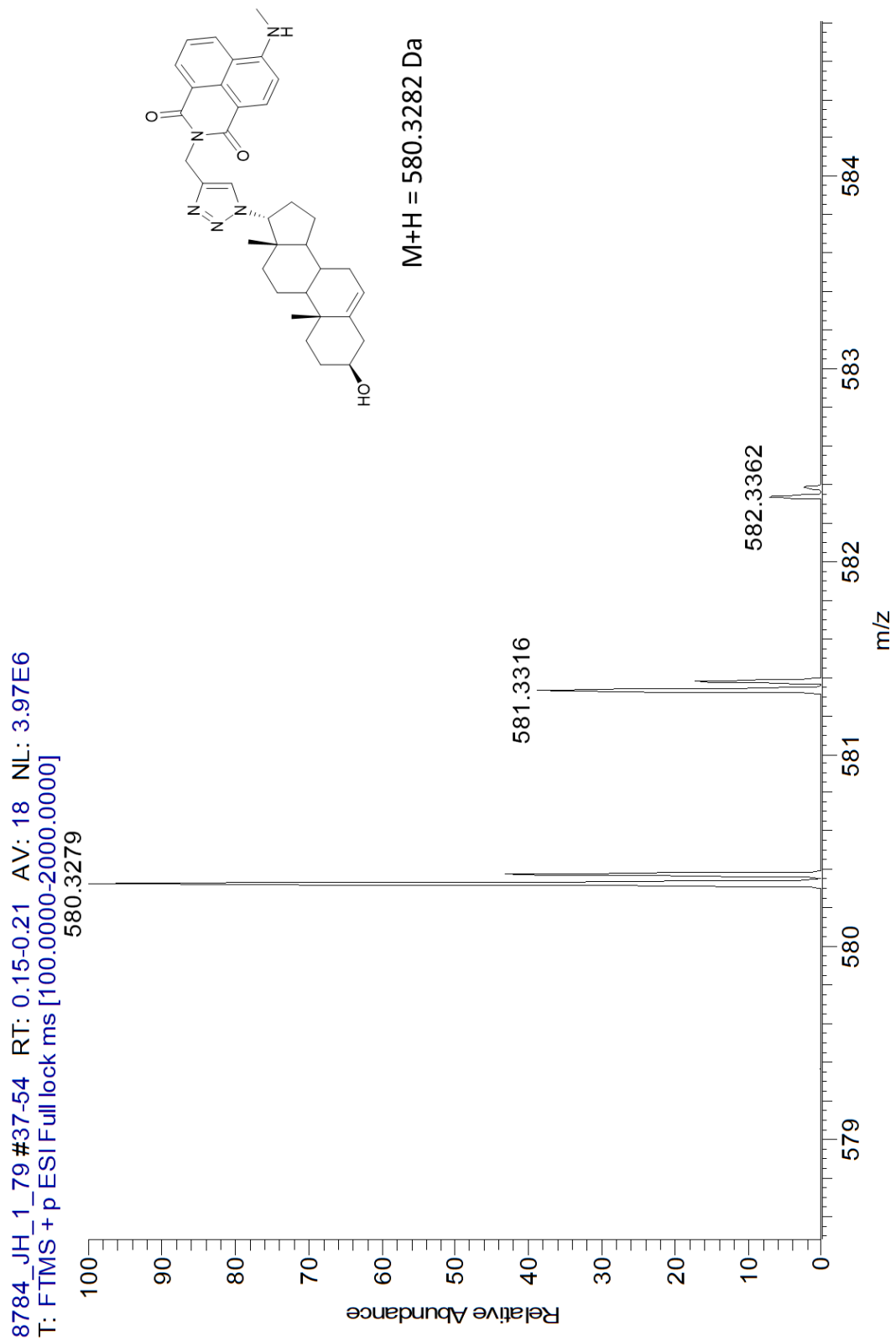
Figure S2.2 HRMS Spectrum of 5 and MAN (Jan et al. Crude Click Reaction)
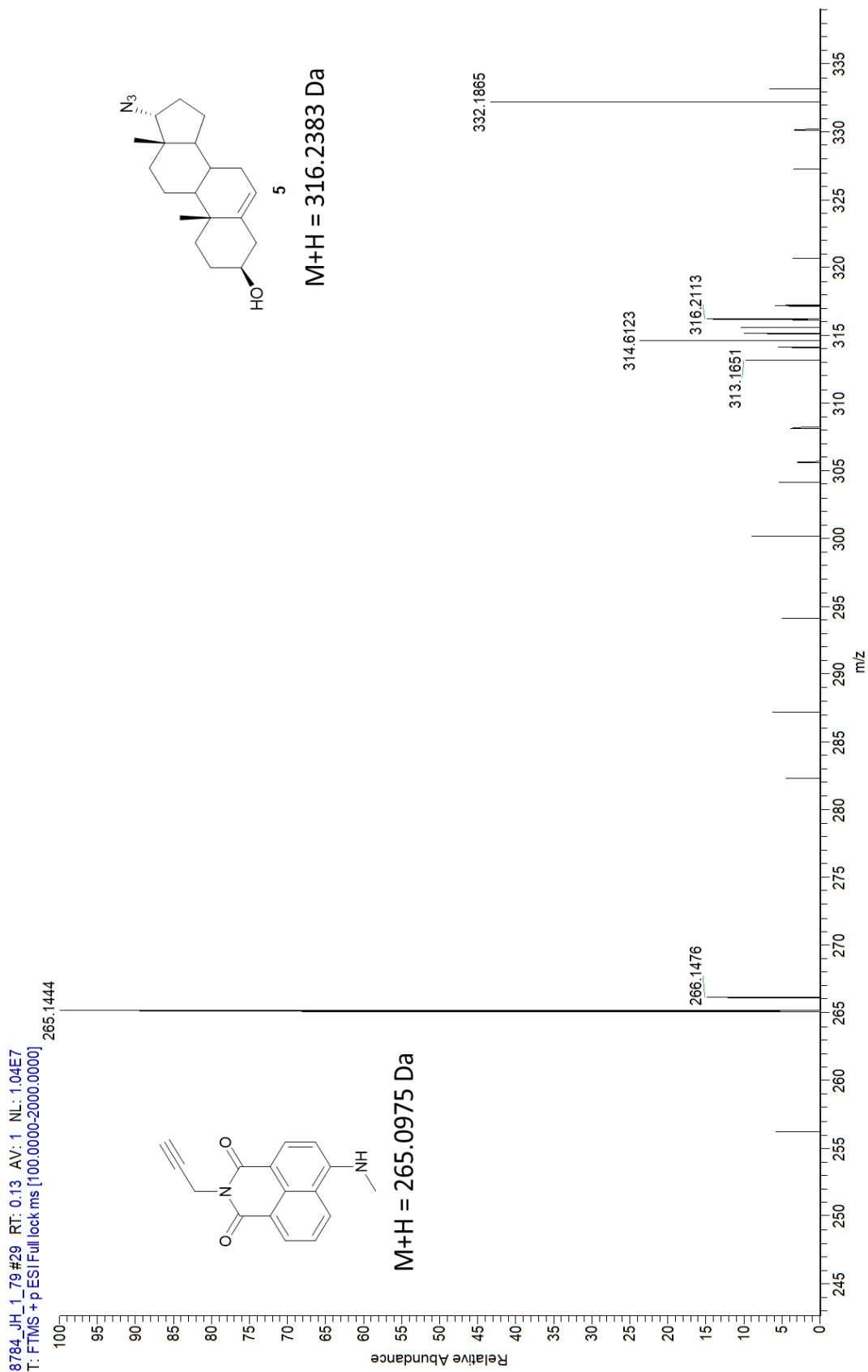
Figure S2.3 HRMS Spectrum of 5 (Jan et al. Crude Click Reaction w/o TBTA)

M+H = 316.2383 Da

5
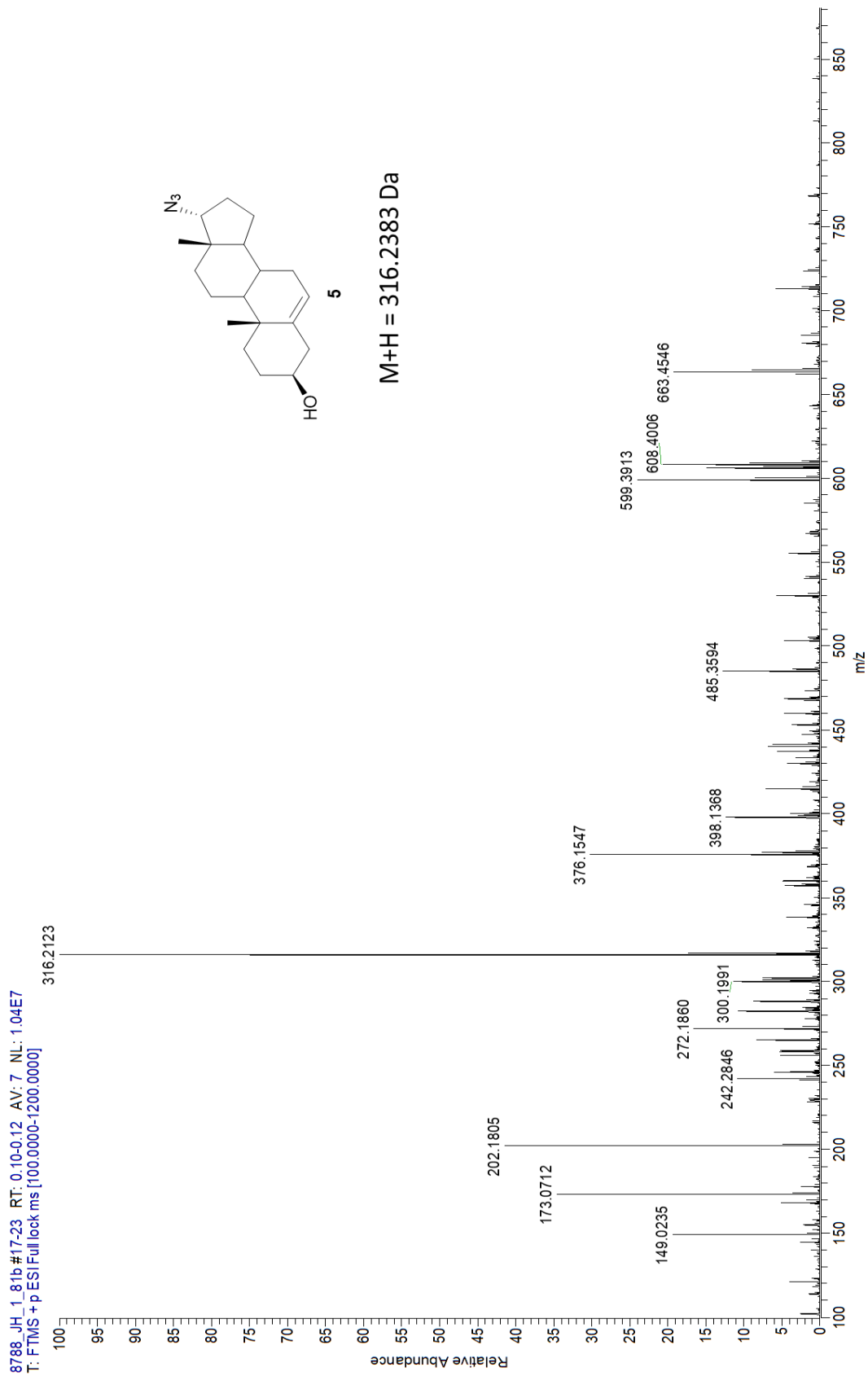
Figure S2.4 HRMS Spectrum of 29 (Jan et al. Crude Click Reaction w/o TBTA)

M+H = 580.3282 Da
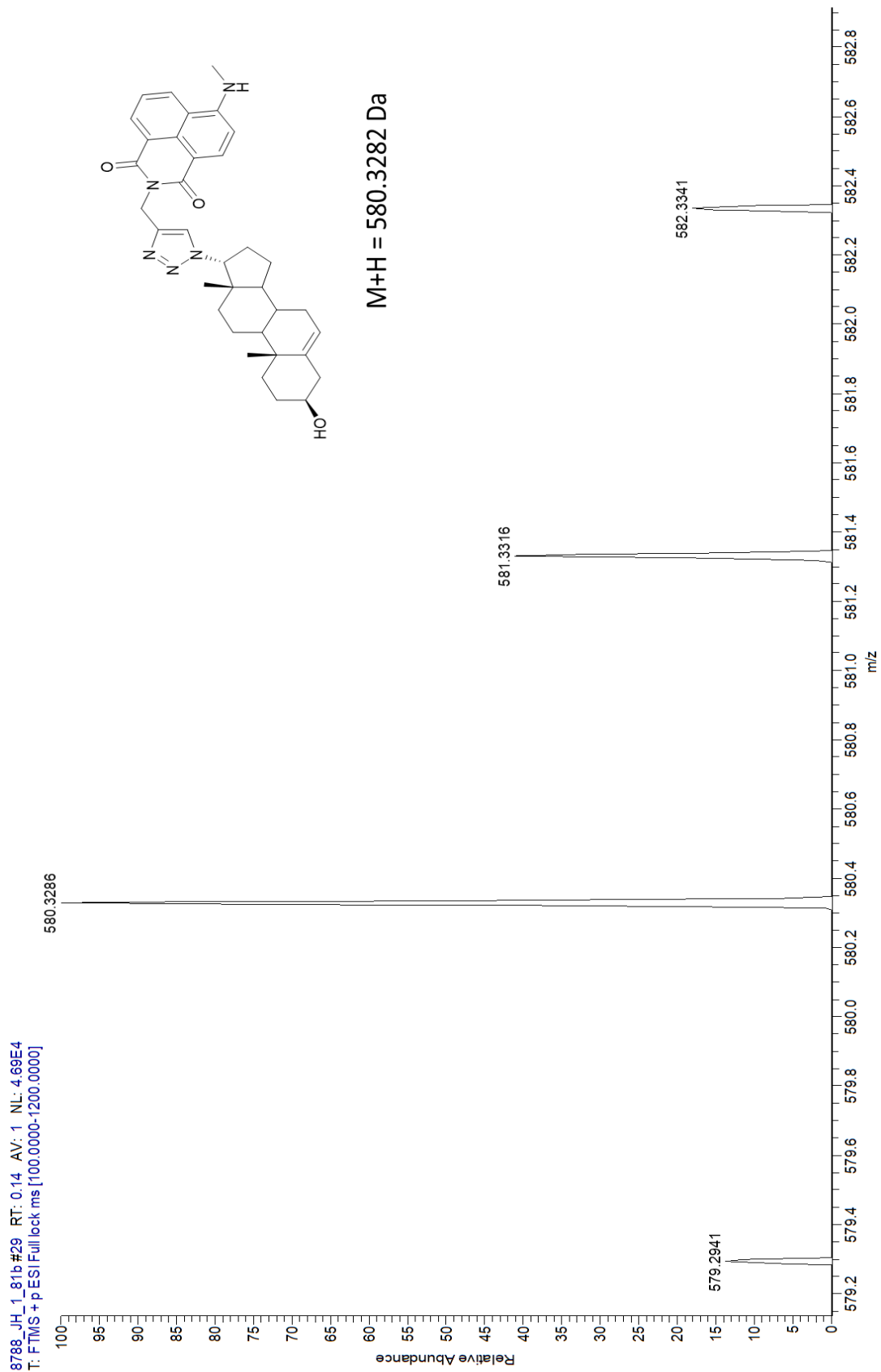
Figure S2.5 HRMS Spectrum of 29 (Blanco et al. Click Reaction)

M+H theoretical mass
580.3282 Da

8800_Jonathan #23-33   RT: 0.12-0.16   AV: 11   NL: 2.25E6
T: FTMS + p ESI Full lock ms [100.0000-2000.0000]

580.3292

581.3324

Flash

-For dry loading, a 1 part crude mixture to 2 part silica (1:2) was used

-Compound **4** came out at fraction 5

	CV	Solvents	% 2nd
1	0.0	AB	5
2	10.0	AB	5
3	7.8	AB	5
4	7.8	AB	0
5	0.8	AB	0

Gradient Table

1 - 201F

Figure S2.6 MPLC Purification of 4

Flash

BUCHI

Column: Generic Silica 12g
Flow Rate: 28 mL/min
Equilibration: 4.0 CV
Run Length: 36.8 CV
Mode: Flash Dry

Solvent A: Hexane
Solvent B: Ethyl acetate
Solvent C: Empty
Solvent D: Empty
Slope Detection: Off

UV Threshold: 0.05 AU
UV Sensitivity: Low
UV1 λ: 254 nm (M)
UV2 λ: 265 nm (M)
UV3 λ: 280 nm (M)
UV4 λ: 320 nm (M)
UV scan start λ: 254 nm (M)
UV scan end λ: 400 nm (M)

ELSD Threshold: 20 mV
ELSD Sensitivity: Low
Collection: Collect All
Per-Vial Volume: 8 mL
Non-Peak Volume: 8 mL
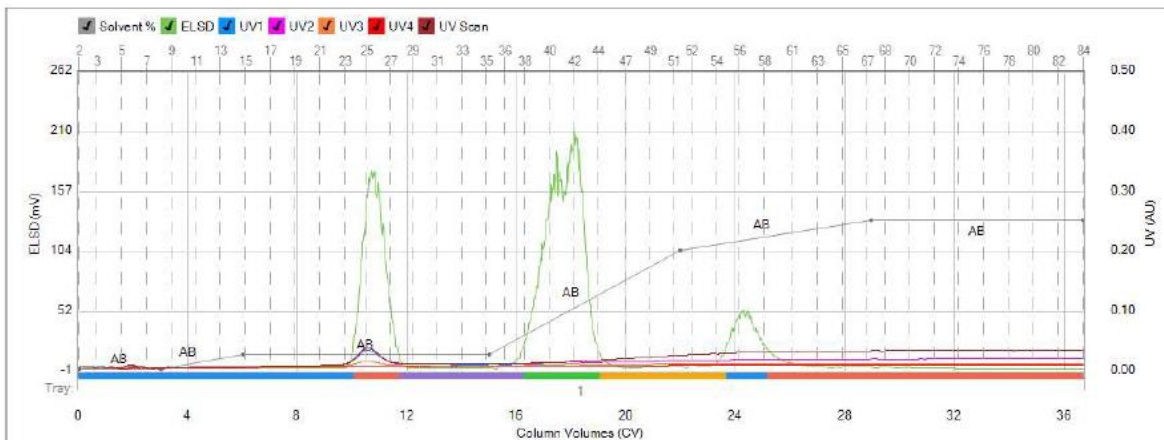
1 - 201F
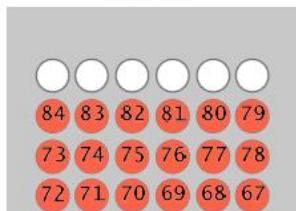
-For dry loading, a 1 part crude mixture to 1 part silica (1:1) was used

-Compound **5** came out between fractions 36-46

Gradient Table

	CV	Solvents	% 2nd
1	0.0	AB	0
2	3.0	AB	0
3	3.0	AB	5
4	9.0	AB	5
5	7.0	AB	40
6	7.0	AB	50
7	7.8	AB	50

Figure S2.7 MPLC Purification of 5

Flash

BÜCHI

Column: Generic Silica 12g
Flow Rate: 28 mL/min
Equilibration: 6.0 CV
Run Length: 4.7 CV
Mode: Flash Dry

Solvent A: Hexane
Solvent B: Dichloromethane
Solvent C: Empty
Solvent D: Empty
Slope Detection: Off

UV Threshold: 0.05 AU
UV Sensitivity: Low
UV1 λ: 254 nm (M)
UV2 λ: 265 nm (M)
UV3 λ: 280 nm (M)
UV4 λ: 320 nm (M)
UV scan start λ: 254 nm (M)
UV scan end λ: 400 nm (M)

ELSD Threshold: 20 mV
ELSD Sensitivity: Low
Collection: Collect All
Per-Vial Volume: 8 mL
Non-Peak Volume: 8 mL
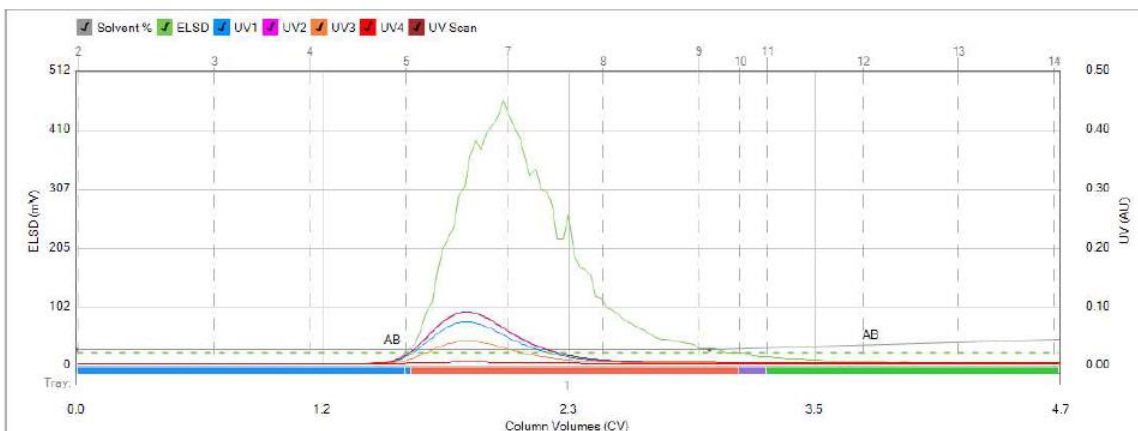
1 - 7340

-For dry loading, a 1 part crude mixture to 3 part silica (1:3) was used

-Compound **6** came out between fractions 5-11

Gradient Table			
	CV	Solvents	% 2nd
1	0.0	AB	5
2	3.0	AB	5
3	7.0	AB	20

Figure S2.8 MPLC Purification of 6

Figure S2.9 MPLC Purification of 7 and 7a

The figure contains:

Flash — Method Name: / Run Name: JH/JH-1-87 dryload #1 / Run Date: 2021-02-23 14:20 — BÜCHI

Column: FP ID HP Si 12g
Flow Rate: 30 mL/min
Equilibration: 4.0 CV
Run Length: 27.0 CV
Mode: Flash Dry

Solvent A: Hexane
Solvent B: Ethyl acetate
Solvent C: Empty
Solvent D: Empty
Slope Detection: Off

UV Threshold: 0.05 AU
UV Sensitivity: Low
UV1 λ: 254 nm (M)
UV2 λ: 265 nm (M)
UV3 λ: 280 nm (M)
UV4 λ: 320 nm (M)
UV scan start λ: 254 nm (M)
UV scan end λ: 400 nm (M)

ELSD Threshold: 20 mV
ELSD Sensitivity: Low
Collection: Collect All
Per-Vial Volume: 8 mL
Non-Peak Volume: 8 mL
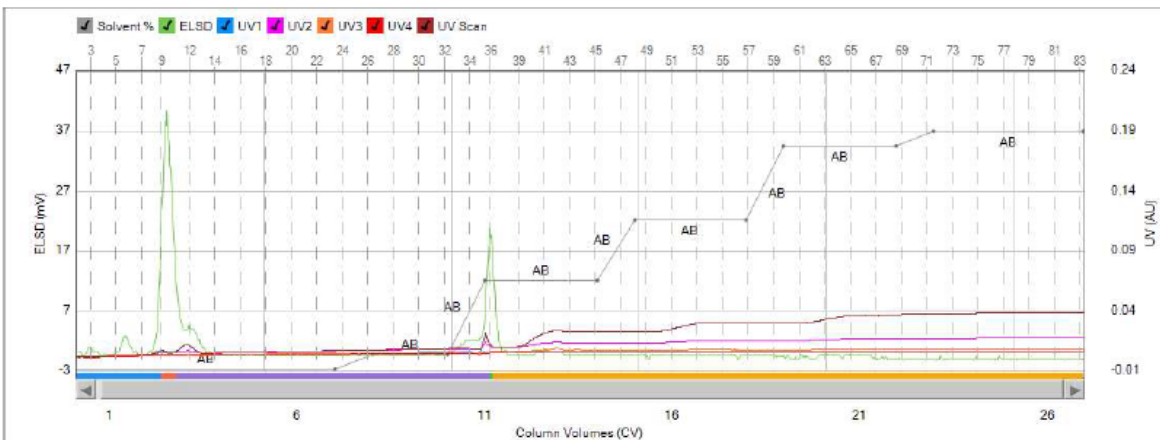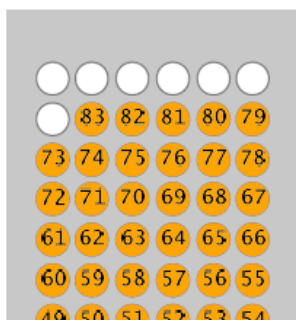
-For dry loading, a 1 part crude mixture to 1 part silica (1:1) was used

-Compound **7** came out between fractions 32-38 and compound **7a** came out between fractions 7-9

	CV	Solvents	% 2nd
1	0.0	AB	0
2	7.0	AB	0
3	1.0	AB	5
4	2.0	AB	5
5	1.0	AB	30
6	3.0	AB	30
7	1.0	AB	50
8	3.0	AB	50
9	1.0	AB	75
10	3.0	AB	75
11	1.0	AB	80

Gradient Table

1 - 201F

63

Flash

Method Name:
Run Name: JH/JH-1-65 dryload #1
Run Date: 2020-10-14 15:00

BUCHI

Column: Generic Silica 12g
Flow Rate: 28 mL/min
Equilibration: 4.0 CV
Run Length: 23.0 CV
Mode: Flash Dry

Solvent A: Hexane
Solvent B: Ethyl acetate
Solvent C: Empty
Solvent D: Empty
Slope Detection: Off

UV Threshold: 0.05 AU
UV Sensitivity: Low
UV1 λ: 254 nm (M)
UV2 λ: 265 nm (M)
UV3 λ: 280 nm (M)
UV4 λ: 320 nm (M)
UV scan start λ: 254 nm (M)
UV scan end λ: 400 nm (M)

ELSD Threshold: 20 mV
ELSD Sensitivity: Low
Collection: Collect All
Per-Vial Volume: 8 mL
Non-Peak Volume: 8 mL
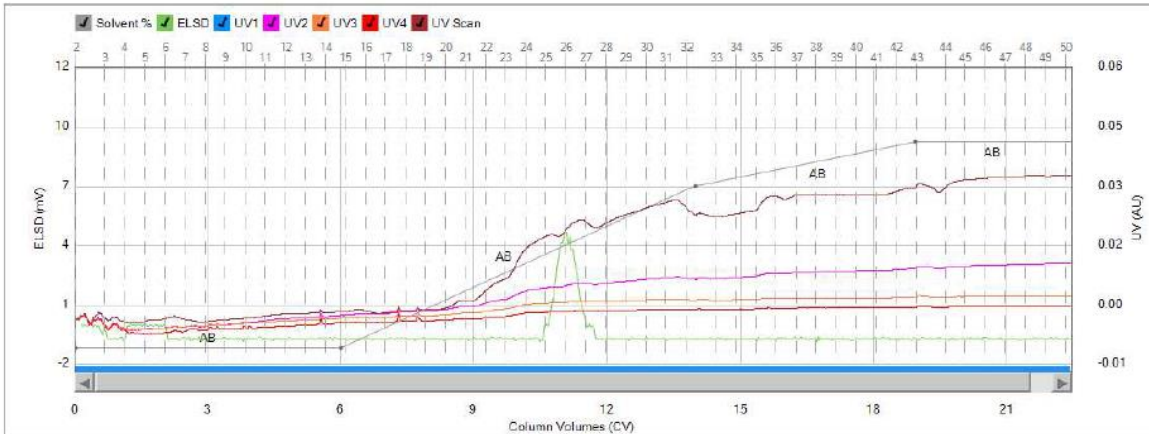
1 - 201F
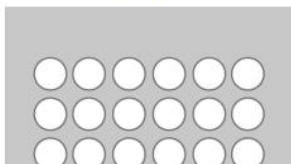
-For dry loading, a 1 part crude mixture to 3 part silica (1:3) was used

-Compound **8** came out between fractions 25-27

Gradient Table

	CV	Solvents	% 2nd
1	0.0	AB	5
2	6.0	AB	5
3	8.0	AB	60
4	5.0	AB	75
5	4.0	AB	75

Figure S2.10 MPLC Purification of 8

Flash

BUCHI

Column: FP ID HP Si 12g
Flow Rate: 30 mL/min
Equilibration: 4.0 CV
Run Length: 21.0 CV
Mode: Flash Dry

Solvent A: Hexane
Solvent B: Ethyl acetate
Solvent C: Empty
Solvent D: Empty
Slope Detection: Off

UV Threshold: 0.05 AU
UV Sensitivity: Low
UV1 λ: 254 nm (M)
UV2 λ: 265 nm (M)
UV3 λ: 280 nm (M)
UV4 λ: 320 nm (M)
UV scan start λ: 254 nm (M)
UV scan end λ: 400 nm (M)

ELSD Threshold: 20 mV
ELSD Sensitivity: Low
Collection: Collect All
Per-Vial Volume: 8 mL
Non-Peak Volume: 8 mL
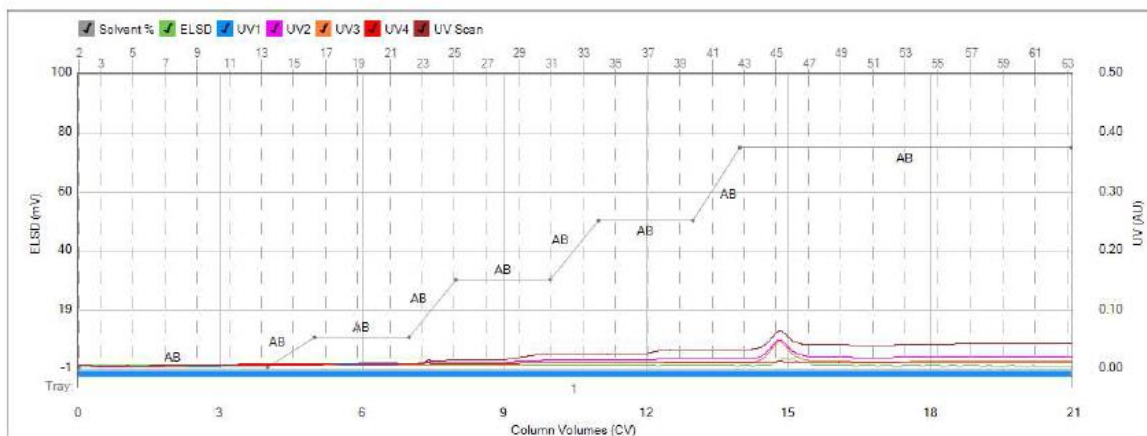
1 - 201F
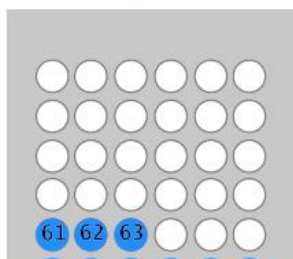
-For dry loading, a 1 part crude mixture to 3 part silica (1:3) was used

-**MAN** came out between fractions 45-46

Gradient Table

	CV	Solvents	% 2nd
1	0.0	AB	0
2	4.0	AB	0
3	1.0	AB	10
4	2.0	AB	10
5	1.0	AB	30
6	2.0	AB	30
7	1.0	AB	50
8	2.0	AB	50
9	1.0	AB	75

Figure S2.11 MPLC Purification of 29 (Removal of MAN)

Flash

Method Name:
Run Name: JH/JH-1-91 dryload #1 recovery
Run Date: 2021-03-24 15:28

BÜCHI

Column: FP ID HP Si 12g
Flow Rate: 30 mL/min
Equilibration: 0.0 CV
Run Length: 20.0 CV
Mode: Flash Dry

Solvent A: Dichloromethane
Solvent B: Methanol
Solvent C: Empty
Solvent D: Empty
Slope Detection: Off

UV Threshold: 0.05 AU
UV Sensitivity: Low
UV1 λ: 254 nm (M)
UV2 λ: 265 nm (M)
UV3 λ: 280 nm (M)
UV4 λ: 320 nm (M)
UV scan start λ: 254 nm (M)
UV scan end λ: 400 nm (M)

ELSD Threshold: 20 mV
ELSD Sensitivity: Low
Collection: Collect All
Per-Vial Volume: 8 mL
Non-Peak Volume: 8 mL
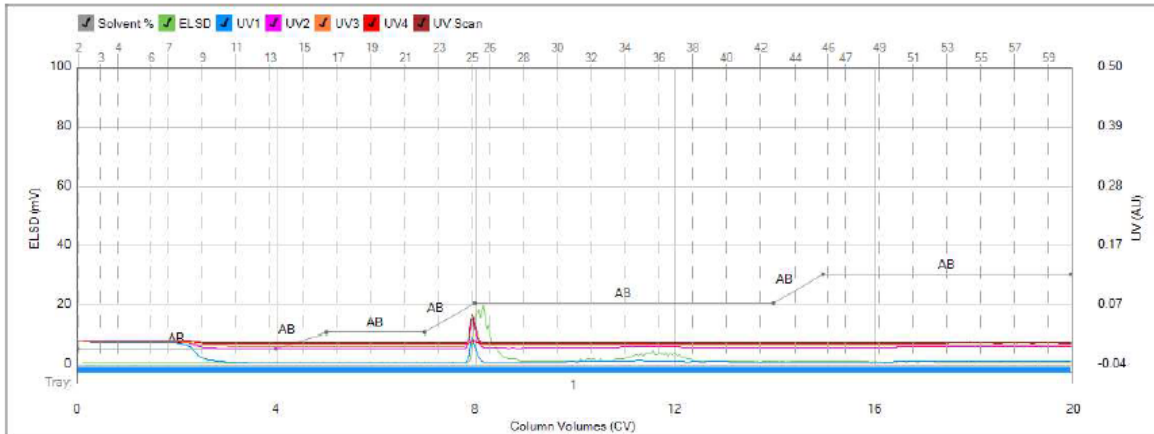
1 - 7340
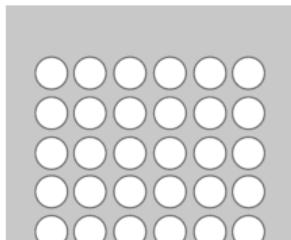
-For dry loading, a 1 part crude mixture to 3 part silica (1:3) was used

-Compound **29** came out between fractions 25-27

Gradient Table

	CV	Solvents	% 2nd
1	0.0	AB	5
2	4.0	AB	5
3	1.0	AB	10
4	2.0	AB	10
5	1.0	AB	20
6	6.0	AB	20
7	1.0	AB	30
8	5.0	AB	30

Figure S2.12 MPLC Purification of 29

Section 2.6: References

Blanco G., Georg G. I., Syeda S. S., inventors. Regents of the University of Minnesota, The University of Kansas, assignees. Contraceptive Agents. US 2014/0005132. 2014 January 02

Hansen, S. G., & Jensen, H. H. (2009). Microwave irradiation as an effective means of synthesizing uninfstituted N-linked 1,2,3-triazoles from vinyl acetate and azides. *Synlett*, *20*, 3275–3278. https://doi.org/10.1055/s-0029-1218366

Jan, H. M., Chen, Y. C., Shih, Y. Y., Huang, Y. C., Tu, Z., Ingle, A. B., Liu, S. W., Wu, M. S., Gervay-Hague, J., Mong, K. K. T., Chen, Y. R., & Lin, C. H. (2016). Metabolic labelling of cholesteryl glucosides in: *Helicobacter pylori* reveals how the uptake of human lipids enhances bacterial virulence. *Chemical Science*, *7*(9), 6208–6216. https://doi.org/10.1039/c6sc00889e

Kiss, A., Herman, B. E., Görbe, T., Mernyák, E., Molnár, B., Wölfling, J., Szécsi, M., & Schneider, G. (2018). Synthesis of novel 17-triazolyl-androst-5-en-3-ol epimers via Cu(I)-catalyzed azide-alkyne cycloaddition and their inhibitory effect on 17α-hydroxylase/C17,20-lyase. *Steroids*, *135*(February), 79–91. https://doi.org/10.1016/j.steroids.2018.03.006

Wang, C. G., Chong, A. M. L., Lu, Y., Liu, X., & Goto, A. (2019). Metal-Free fast azidation by using tetrabutylammonium azide: effective synthesis of alkyl azides and well-defined azido-end polymethacrylates. *Chemistry - A European Journal*, *25*(56), 13025–13029. https://doi.org/10.1002/chem.201903188

Worrell, B. T., Malik, J. A., & V. V. Fokin. (2013). Direct Evidence of a Dinuclear Copper Intermediate in Cu(I)-Catalyzed Azide-Alkyne Cycloadditions. *Science*, *340*(I), 457–460.

Chapter 3

NMR Characterization of DHEA derivatives
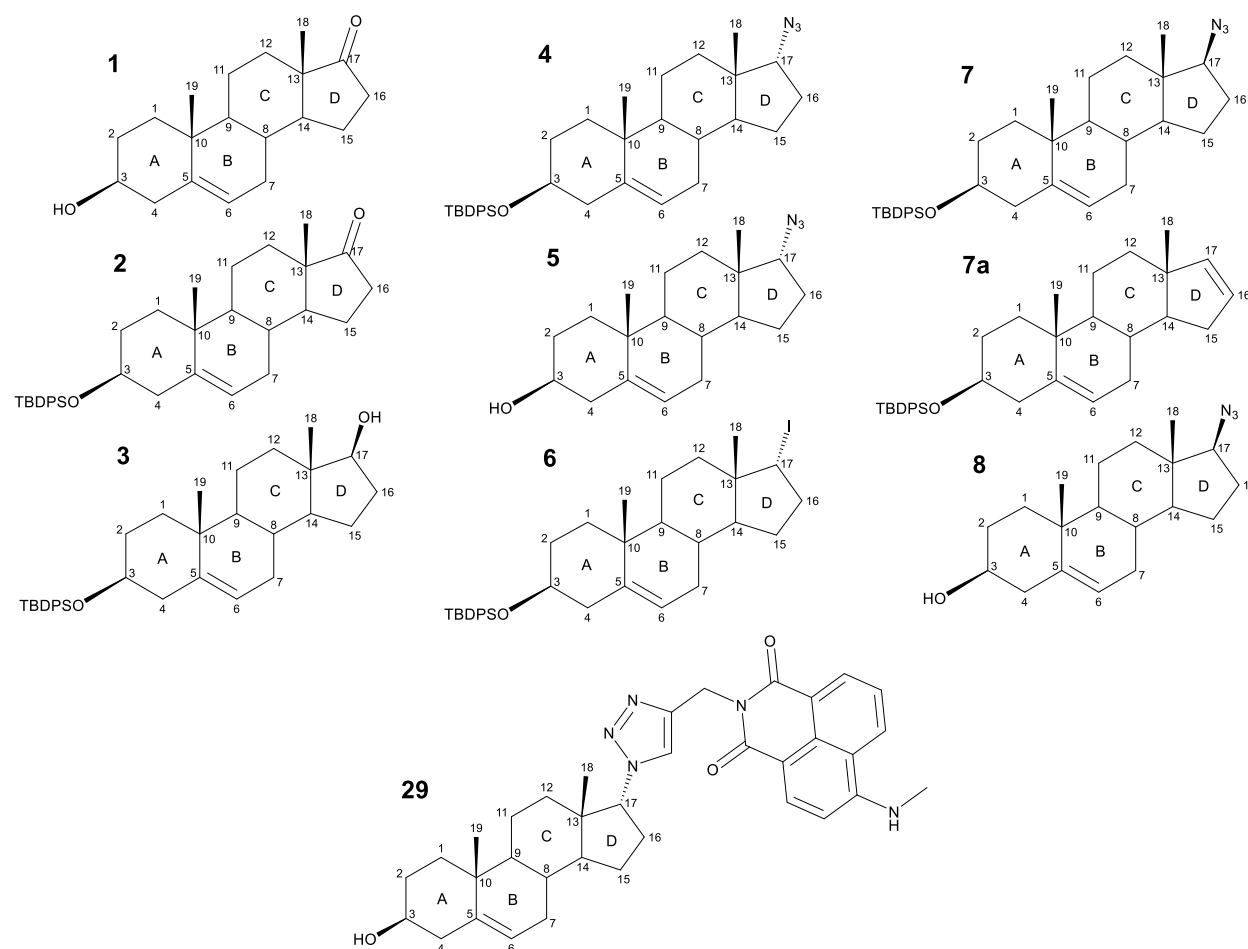
Figure 3.1 Compounds 1-8 and 29 A-D Rings Numbering/Identification

The synthesis of **2-8** has been described in previous literature: (Blanco et al., 2014), (Kiss et al., 2018), and (Jan et al., 2016). Full ^{1}H characterization of DHEA (**1**) by NMR has been accomplished (Wishart et al., 2009). However, minor characterization of **2-8** via NMR has been accomplished. In particular, the easily distinguishable protons (H$_3$, H$_6$, H$_{17}$, H$_{18}$, H$_{19}$) were assigned for **2-8**, but their corresponding carbons (C$_3$, C$_6$, C$_{17}$, C$_{18}$, C$_{19}$) were only explicitly assigned for **5** and **8**. Numbering and identification of the A-D rings for **1-8** and **29** are shown above (see Figure 3.1). These proton NMR assignments were primarily used for compound identification. Meanwhile, the methylene protons (H$_{1-1'}$, H$_{2-2'}$, H$_{4-4'}$, H$_{7-7'}$, H$_{11-11'}$, H$_{12-12'}$, H$_{15-15'}$, and H$_{16-16'}$), methine protons (H$_8$, H$_9$, H$_{14}$), methylene carbons (C$_1$, C$_2$, C$_4$, C$_7$, C$_{11}$, C$_{12}$, C$_{15}$, C$_{16}$),

methine carbons (C_8, C_9, C_{14}), and quaternary carbons (C_5, C_{10}, C_{13}) were not assigned for **2-8**. For this project, every proton ($H_{1-1'}$-H_{19}) and carbon (C_1-C_{19}) for **1-8** and **29** were assigned via 1D and 2D NMR spectra independently. Each individual methylene proton in the A-C ring ($H_{1-1'}$, $H_{2-2'}$, $H_{4-4'}$, $H_{7-7'}$, $H_{11-11'}$, $H_{12-12'}$) was assigned as axial or equatorial based on chemical shift as equatorial protons appear more downfield compared to axial protons on the same carbon atom in cyclohexane rings due to hyperconjugation. The methylene protons in the D ring ($H_{15-15'}$ and $H_{16-16'}$) could not be discriminated as they reside in a cyclopentane ring. The methine and methyl protons in the A-C ring (H_3, H_8, H_9, H_{14}, H_{18}, and H_{19}) were assigned as axial based on the known absolute configuration of DHEA (**1**). From characterization of **1-8**, it was discovered that the chemical shift of a few key protons ($H_{4-4'}$, H_6, H_{14}, $H_{16-16'}$, H_{17}) and carbons (C_3, C_{12}, C_{16}, C_{17}, and C_{18}) can be used to track the progress from **1** to **8**. In addition, trends in ^1H chemical shifts for the C-D ring could be used to track the "click" reaction from **5** to **29**.
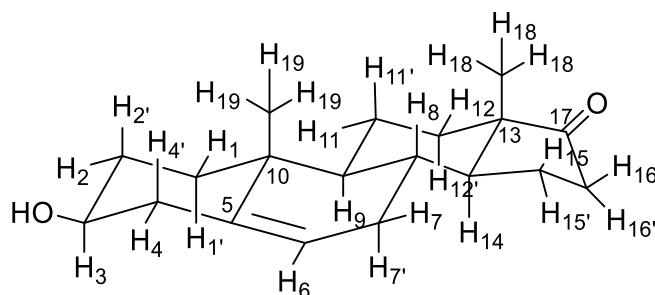
Figure 3.2A Chair Conformation for 1
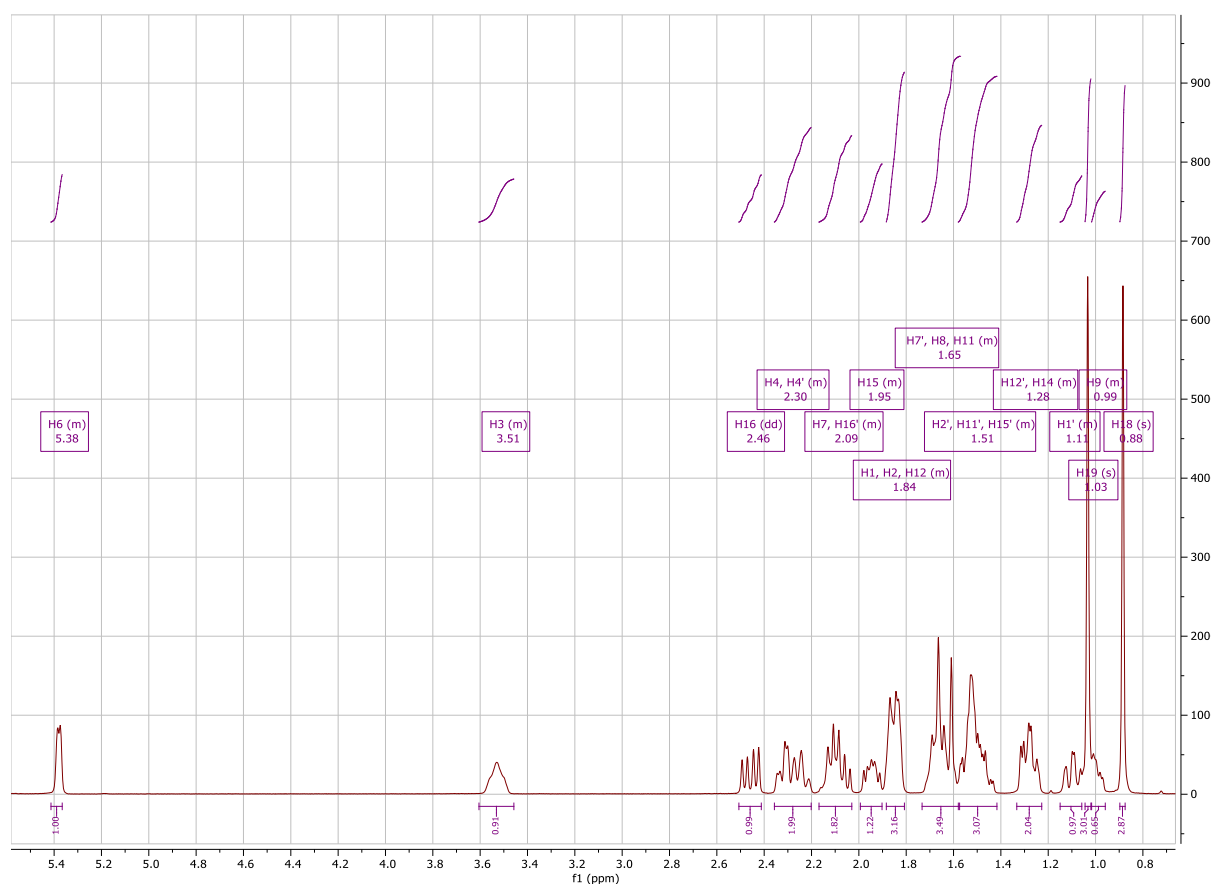
Figure 3.2B ^{1}H Spectrum of DHEA (1)

Although full ^{1}H characterization of DHEA (**1**) has been accomplished (Wishart et al., 2009), Section 3.2 will make independent ^{1}H assignments for DHEA (**1**) and compare to previous results while also making independent ^{13}C assignments. Initially, δ_H 5.38 and δ_H 3.51 were identified as H_6 and H_3 respectively based upon chemical shift and splitting (see Figure 3.2B).

71

The methyl protons on C_{18} and C_{19} could be identified at either δ_H 1.03 or δ_H 0.88 (see Figure 3.2B).
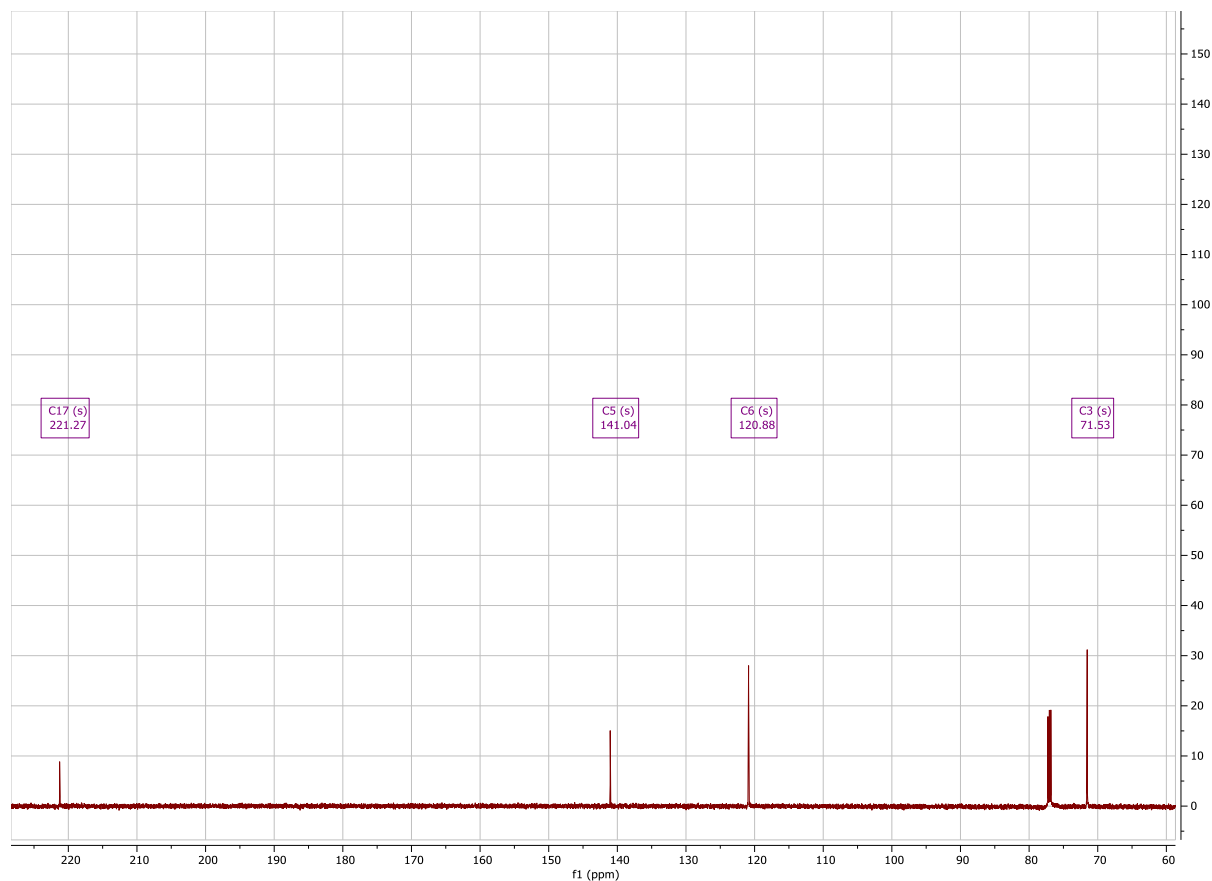
Figure 3.2C ^{13}C Spectrum of DHEA (1)

δ_C 221.27 and δ_C 71.53 were identified as C_{17} and C_3 respectively based on chemical shift (see Figure 3.2C). δ_C 141.04 and δ_C 120.88 were identified as C_5 and C_6 respectively based on chemical shift and peak height (see Figure 3.2C).
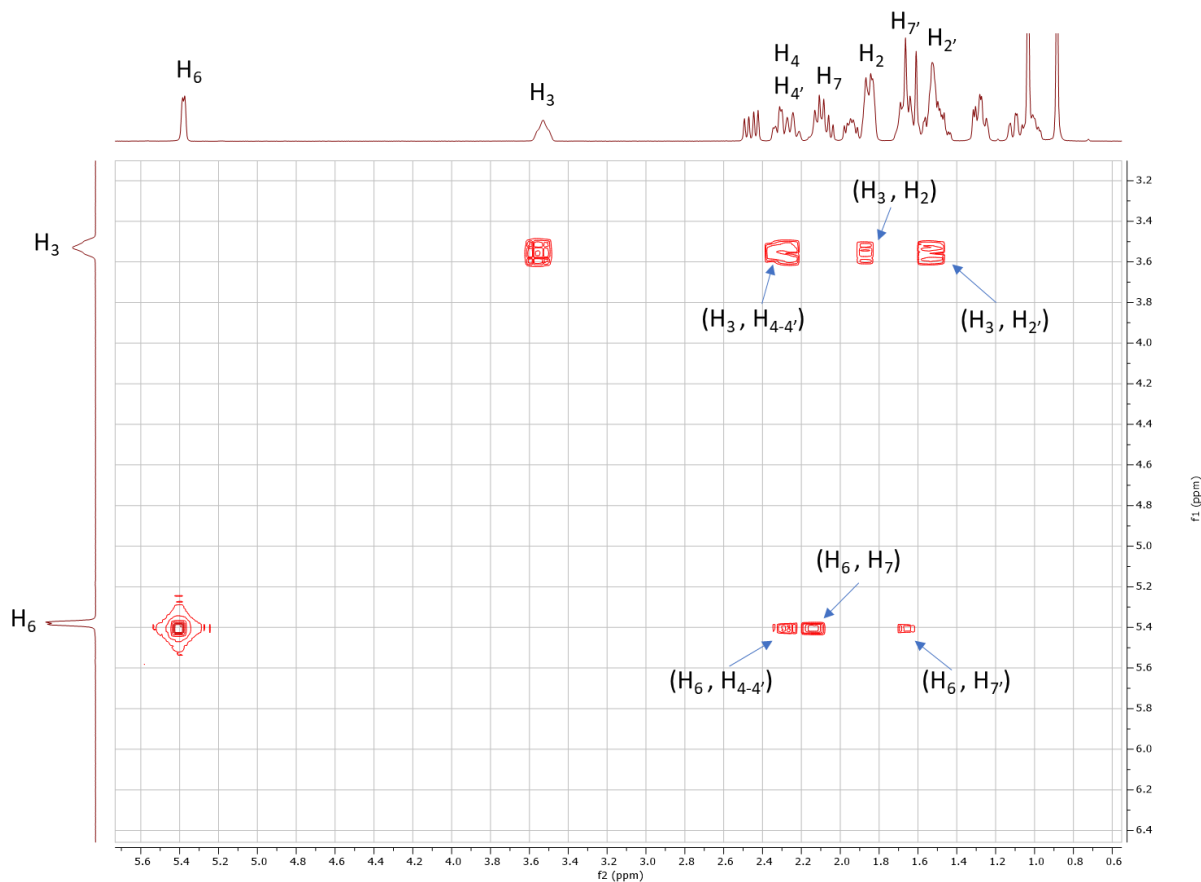
Figure 3.3 Initial ¹H-¹H COSY Correlations for DHEA (1)

Diastereotopic protons, δ_H 2.30 (H$_4$) and δ_H 2.30 (H$_{4'}$), from the A ring were identified from COSY correlations with H$_3$ (δ_H 3.51) and H$_6$ (δ_H 5.38) (see Figure 3.3). Methylene protons, δ_H 1.84 (H$_2$) and δ_H 1.51 (H$_{2'}$), were discerned from COSY correlations with H$_3$ (δ_H 3.51) (see Figure 3.3). In addition, diastereotopic protons δ_H 2.09 (H$_7$) and δ_H 1.65 (H$_{7'}$) in the B ring were identified from COSY correlations with H$_6$ (δ_H 5.38) (see Figure 3.3). In the D ring, diastereotopic proton, H$_{16}$ (δ_H 2.46, dd) was discerned based on splitting and chemical shift (see Figure 3.2B).
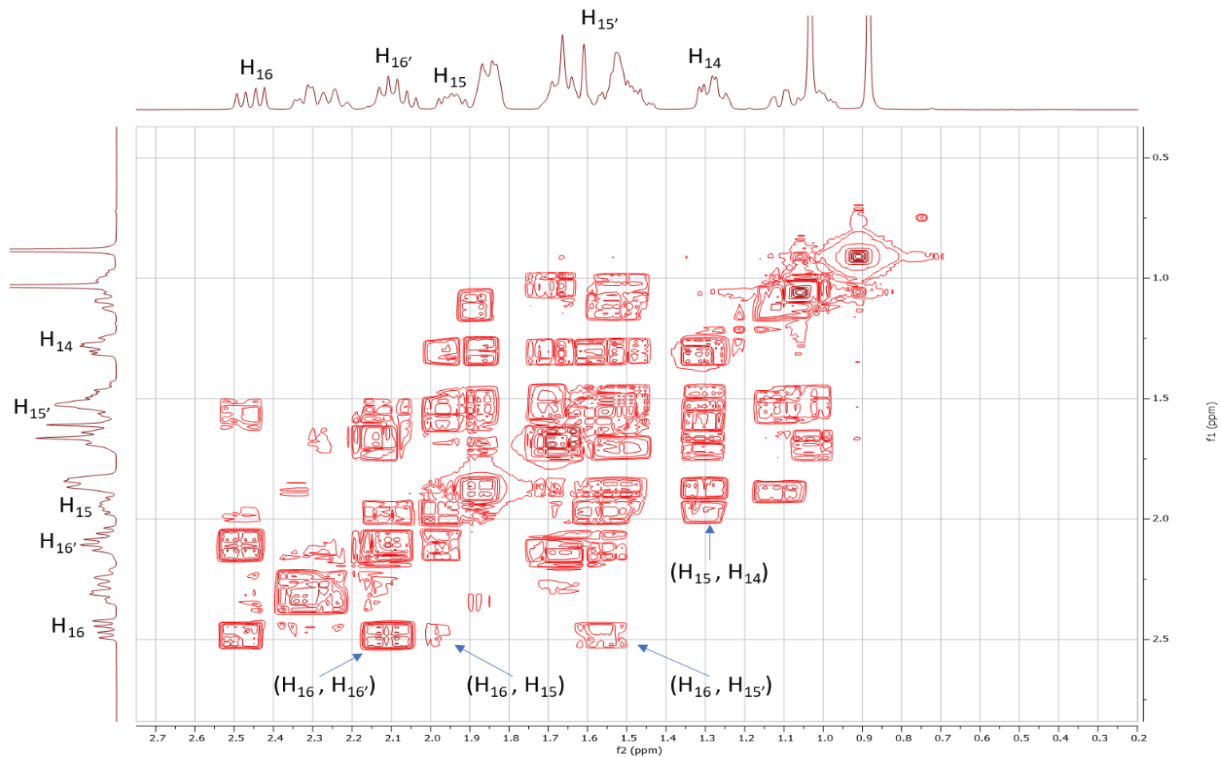
Figure 3.4A ^{1}H-^{1}H COSY Correlations in D ring for DHEA (1)
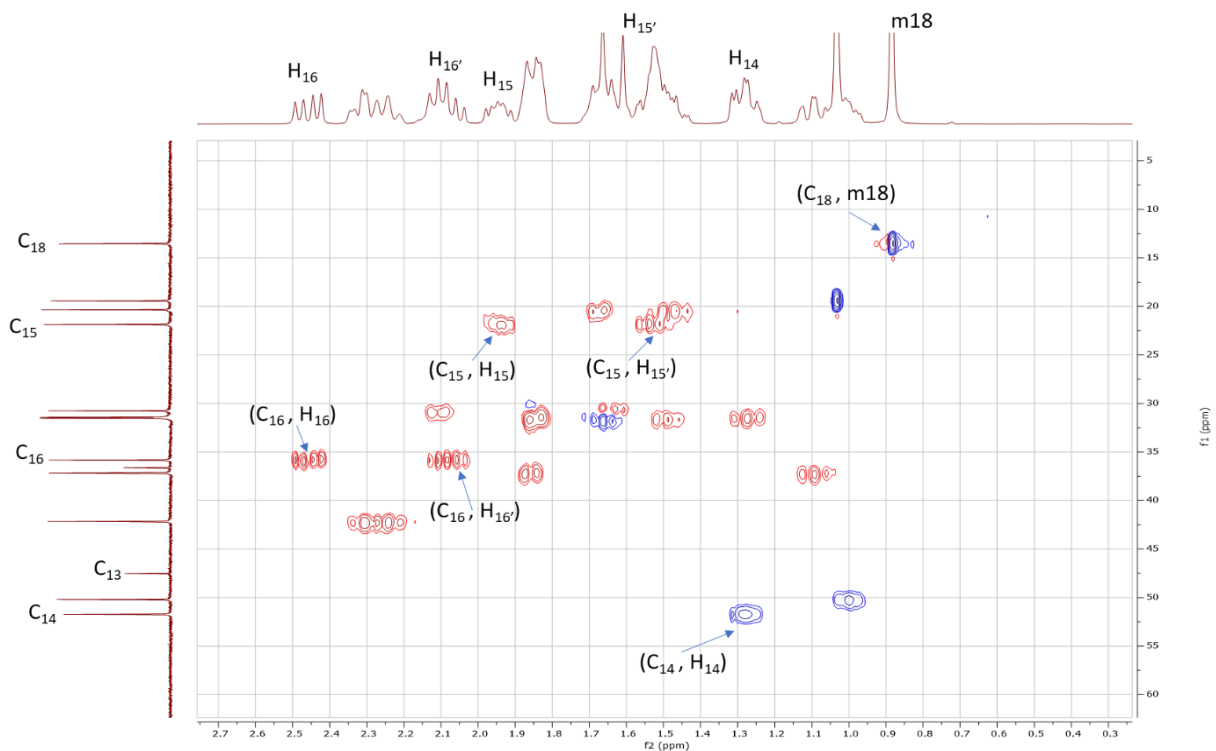
Figure 3.4B ^{1}H-^{13}C HSQC Correlations in D ring for DHEA (1)
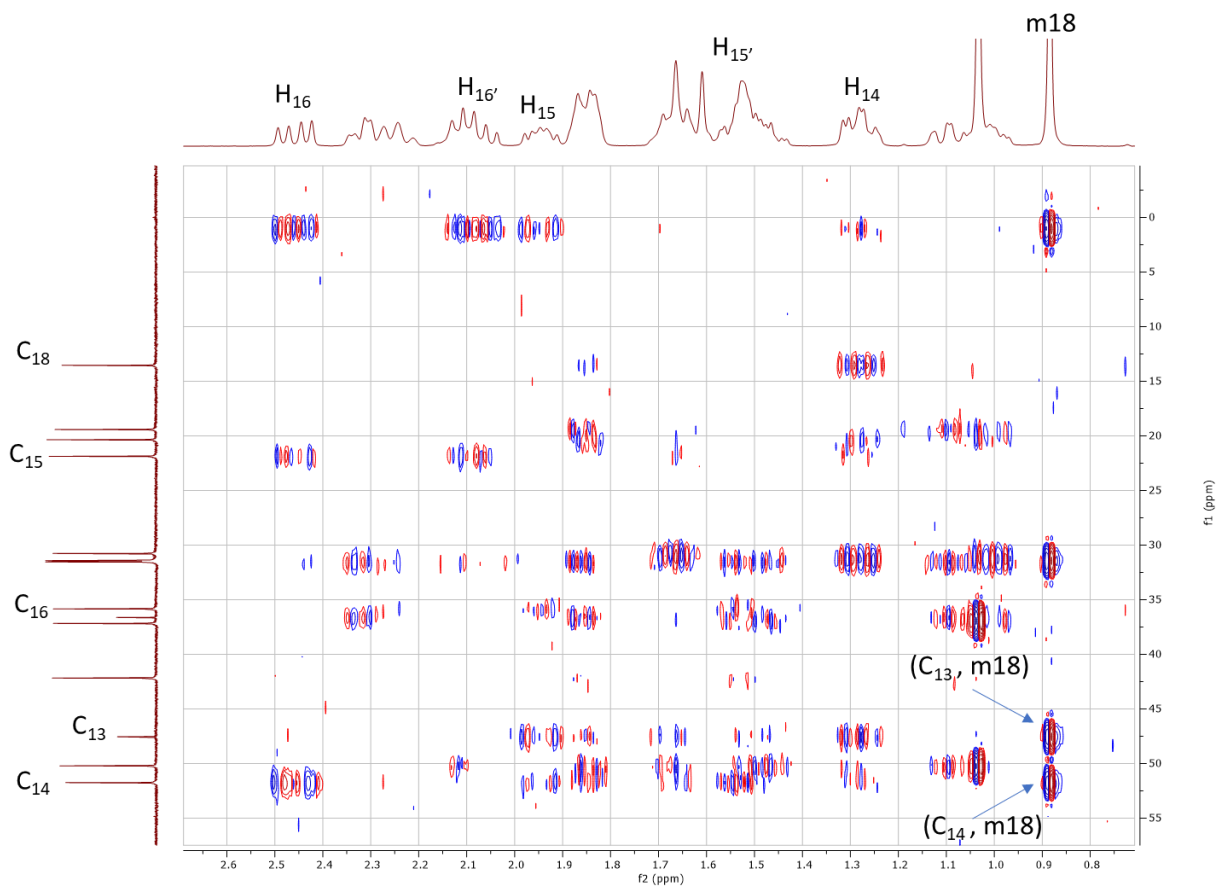
Figure 3.4C ^{1}H-^{13}C HMBC Correlations in D ring for DHEA (1)

Starting with the D ring, methylene proton, δ_H 2.09 (H$_{16'}$), was correlated by HSQC to δ_C 35.86 (C$_{16}$) and by COSY to δ_H 2.46 (H$_{16}$) (see Figure 3.4A and 3.4B). Next, diastereotopic protons, δ_H 1.95 (H$_{15}$) and δ_H 1.51 (H$_{15'}$), showed a HSQC correlation to δ_C 21.90 (C$_{15}$) and COSY correlation to H$_{16}$ (δ_H 2.46) (see Figure 3.4A and 3.4B). Methine proton, δ_H 1.28 (H$_{14}$), displayed HSQC correlation to δ_C 51.79 (C$_{14}$) and COSY correlation to H$_{15}$ (δ_H 1.95) (see Figure 3.4A and 3.4B). Methyl protons on C$_{18}$, m18 (δ_H 0.88), were discerned from HMBC correlation to C$_{14}$ (δ_C 51.79) (see Figure 3.4C). Continuing with m18, δ_C 13.56 (C$_{18}$) was identified from HSQC correlation to m18 (δ_H 0.88) (see Figure 3.4B). Therefore, the methyl protons on C$_{19}$, m19 could be identified at δ_H 1.03 based on integration and splitting (see Figure 3.2B). Quaternary carbon, δ_C 47.54 (C$_{13}$), was discerned from HMBC correlation to m18 (δ_H 0.88) and no observable HSQC correlation (see Figure 3.4B and 3.4C).

75

Figure 3.5A ^{1}H-^{13}C HSQC Correlations in B ring for DHEA (1)

Figure 3.5B ^{1}H-^{13}C HSQC Correlations in B ring for DHEA (1) (C_5-C_6)
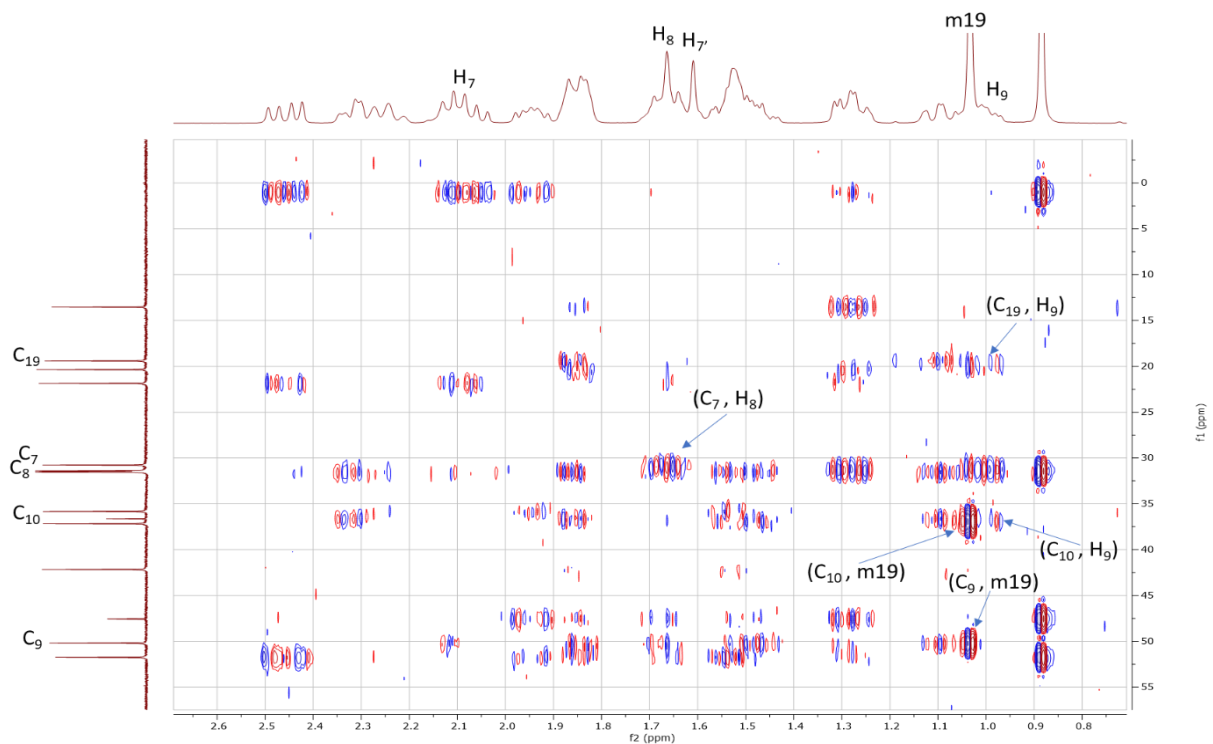
Figure 3.5C ^{1}H-^{13}C HMBC Correlations in B ring for DHEA (1)
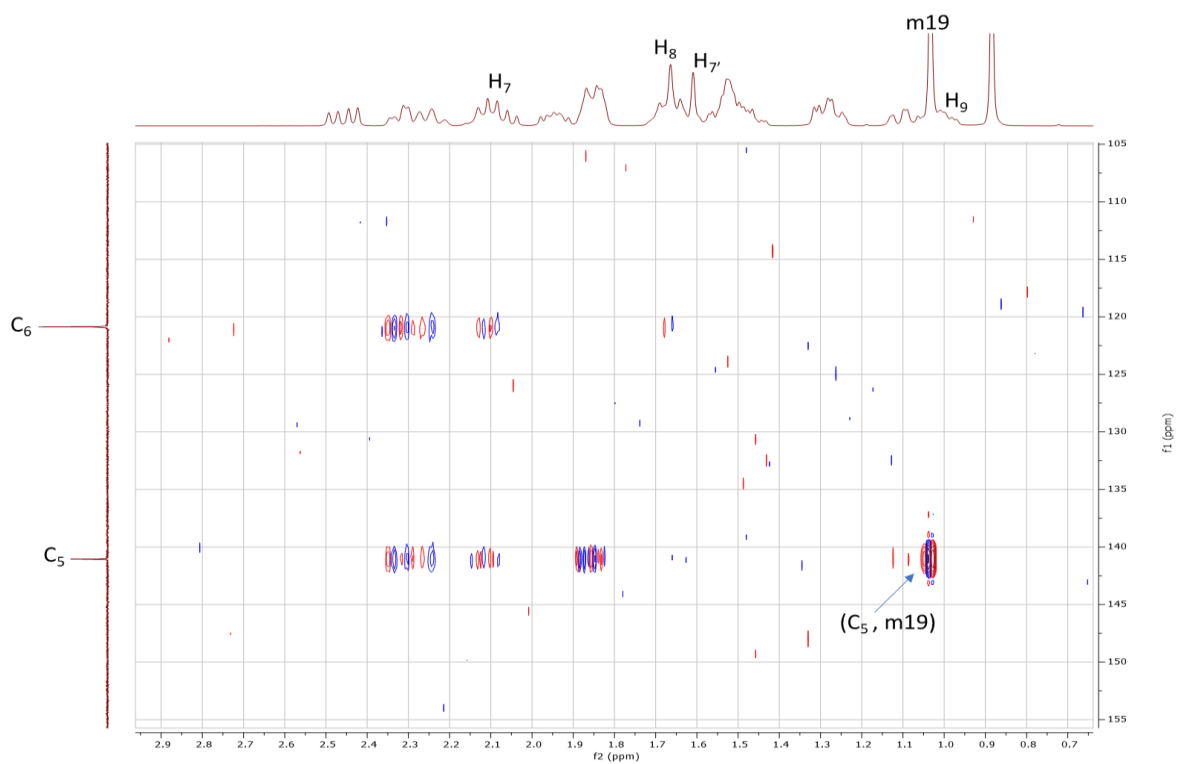
Figure 3.5D ^{1}H-^{13}C HMBC Correlations in B ring for DHEA (1) (C$_5$-C$_6$)

Next with the B ring, methyl protons, m19 (δ_H 1.03) exhibited HSQC correlation to δ_C 19.44 (C_{19}) (see Figure 3.5A). δ_C 141.04 (C_5) was determined on the basis of no HSQC correlation, chemical shift, and HMBC correlation to m19 (δ_H 1.03) (see Figure 3.5B and 3.5D). Vinyl carbon, C_6 (δ_C 120.95) was correlated by HSQC to δ_H 5.38 (H_6) (see Figure 3.5B). Methylene protons, δ_H 2.09 (H_7) and δ_H 1.65 ($H_{7'}$), exhibited HSQC correlation to δ_C 30.80 (C_7) (see Figure 3.5A). Methine proton, H_8, was discerned at δ_H 1.65 based on HMBC correlation to C_7 (δ_C 30.80) (see Figure 3.5C). C_8 (δ_C 31.61) was correlated by HSQC to δ_H 1.65 (H_8) (see Figure 3.5A). The remaining methine proton, H_9 (δ_H 0.99), displayed correlation by HSQC to δ_C 50.26 (C_9) and by HMBC to δ_C 19.44 (C_{19}) (see Figure 3.5A and 3.5C). Quaternary carbon, C_{10} (δ_C 36.66), was assigned based upon HMBC correlation to m19 (δ_H 1.03) along with H_9 (δ_H 0.99) and no correlation in HSQC (see Figure 3.5A and 3.5C).
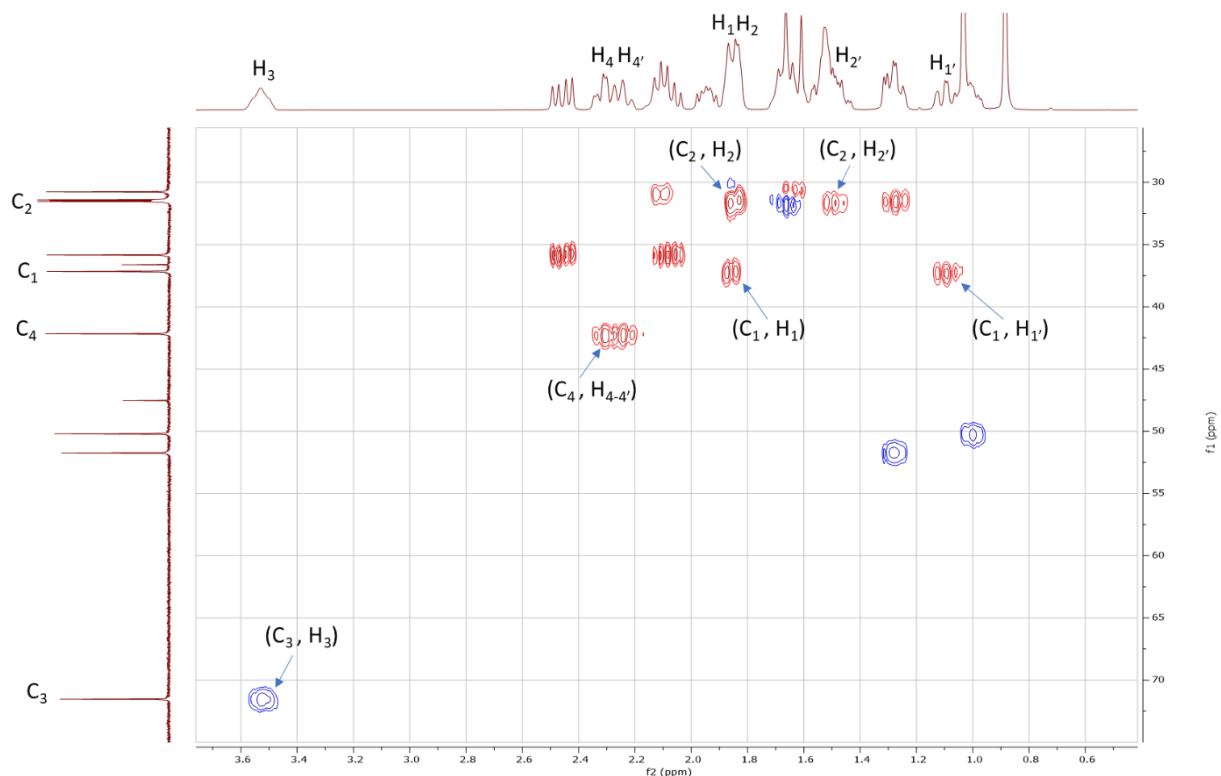
Figure 3.6A ^{1}H-^{13}C HSQC Correlations in A ring for DHEA (1)
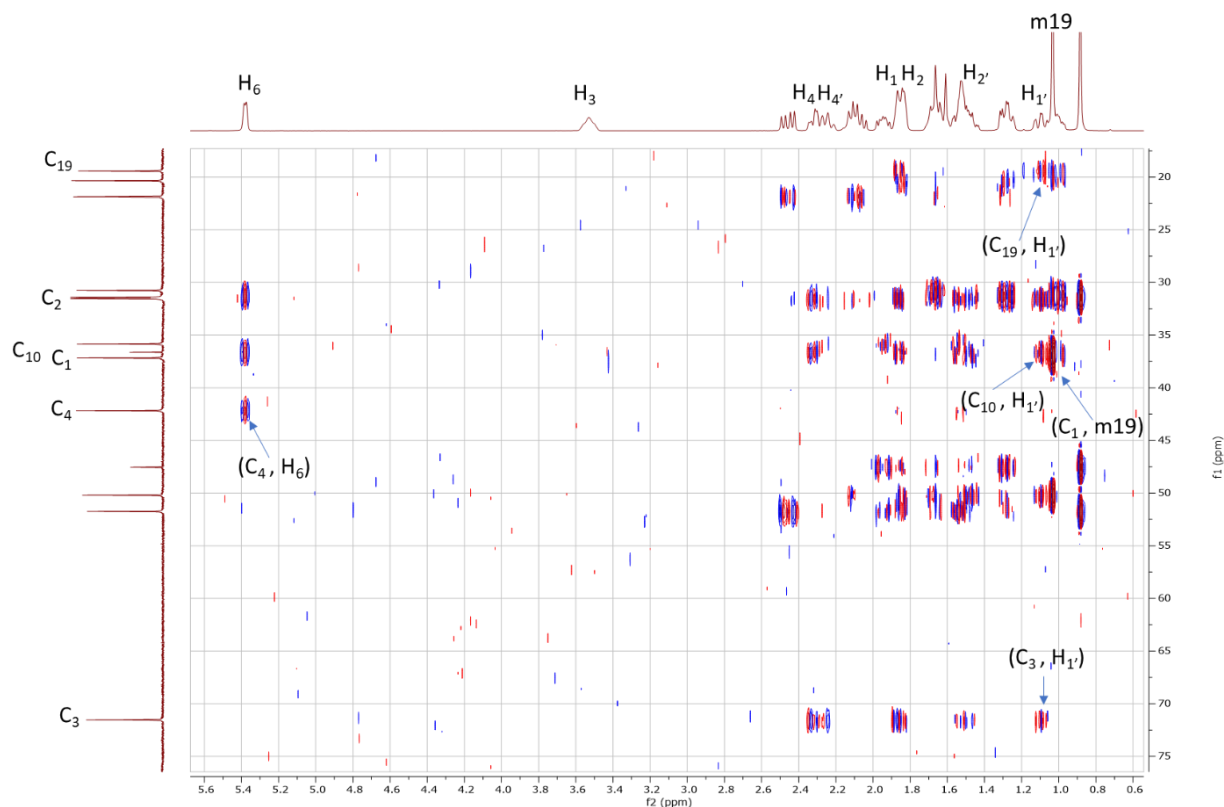
Figure 3.6B ^{1}H-^{13}C HMBC Correlations in A ring for DHEA (1)

Continuing with the A ring, δ_H 3.53 (H$_3$) exhibited HSQC correlation to δ_C 71.62 (C$_3$) (see

Figure 3.6A). Methylene protons, δ_H 2.30 (H$_4$) and δ_H 2.30 (H$_{4'}$), displayed HSQC correlation to δ_C

42.23 (C$_4$), which shows HMBC correlation to H$_6$ (δ_H 5.38) (see Figure 3.6A and 3.6B).

Diastereotopic protons, δ_H 1.84 (H$_2$) and δ_H 1.51 (H$_{2'}$), displayed HSQC correlation to δ_C 31.52 (C$_2$)

(see Figure 3.6A). δ_C 37.25 (C$_1$) was discerned from HMBC correlation to m19 (δ_H 1.03) (see

Figure 3.6B). δ_C 37.20 (C$_1$) exhibited HSQC correlation δ_H 1.84 (H$_1$) and δ_H 1.11 (H$_{1'}$) (see Figure

3.6A). Methylene proton, δ_H 1.11 (H$_{1'}$), displayed HMBC correlation to δ_C 36.66 (C$_{10}$), δ_C 71.62

(C$_3$), and δ_C 19.44 (C$_{19}$) (see Figure 3.6A and 3.6B).
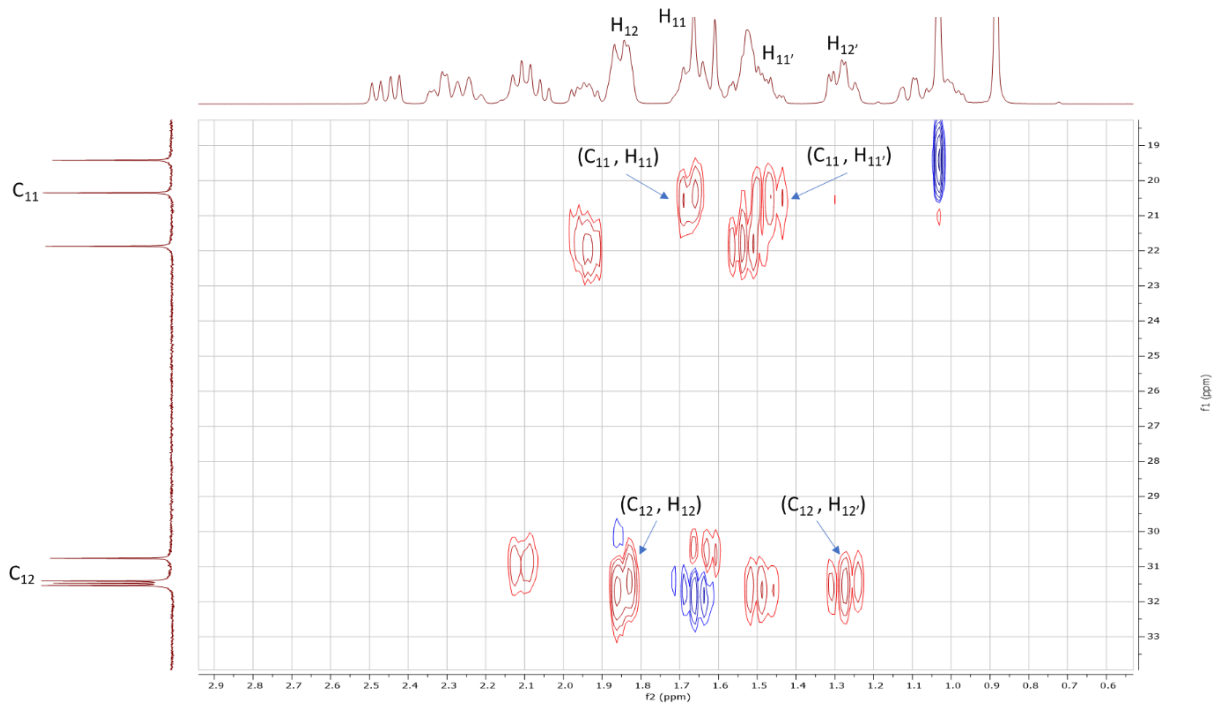
Figure 3.7A ¹H-¹³C HSQC Correlations in C ring for DHEA (1)

Figure 3.7B ¹H-¹³C HMBC Correlations in C ring for DHEA (1)

Concluding with the C ring, δ_C 31.46 (C_{12}) displayed HSQC correlation to δ_H 1.28 ($H_{12'}$) and

δ_H 1.84 (H_{12}), which also showed HMBC correlation to C_{14} (δ_C 51.79) and C_{18} (δ_C 13.56) (see

80

Figure 3.7A and 3.7B). The remaining peak, δ_C 20.39 (C_{11}) displayed HSQC correlations to δ_H 1.65 (H_{11}) and δ_H 1.51 ($H_{11'}$) which also showed HMBC correlation to C_9 (δ_C 50.26) (see Figure 3.7A and 3.7B). Thus, full ^1H and ^{13}C assignment of DHEA (**1**) has been completed. In addition, the ^1H assignment for $H_{1-1'}$-H_{19} matched previous reported data (Wishart et al., 2009).

Section 3.3: DHEA PG (**2**)
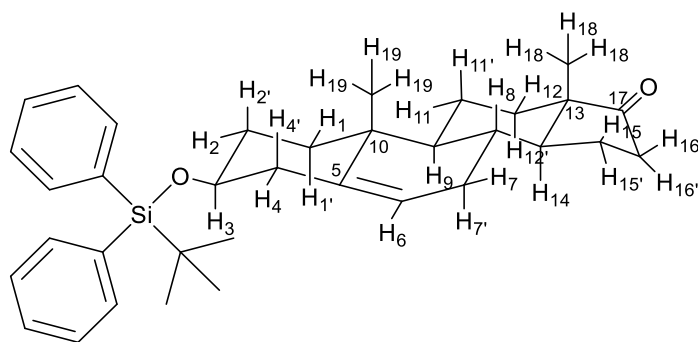
Figure 3.8A Chair Conformation for 2

Figure 3.8B ^1H Spectrum of DHEA PG (2)

Aromatic protons of the TBDPS group were identified at δ_H 7.38 and δ_H 7.68 based upon chemical shift (see Figure 3.8B). δ_H 5.15 and δ_H 3.54 were identified as H_6 and H_3 respectively based upon chemical shift and splitting (see Figure 3.8B). The methyl protons on C_{18} and C_{19} could be identified at either δ_H 1.01 or δ_H 0.86 (see Figure 3.8B). The latter assignments for H_3, H_6, H_{18}, and H_{19} matched previous ^{1}H assignments (Blanco et al., 2014), (Jan et al., 2016).
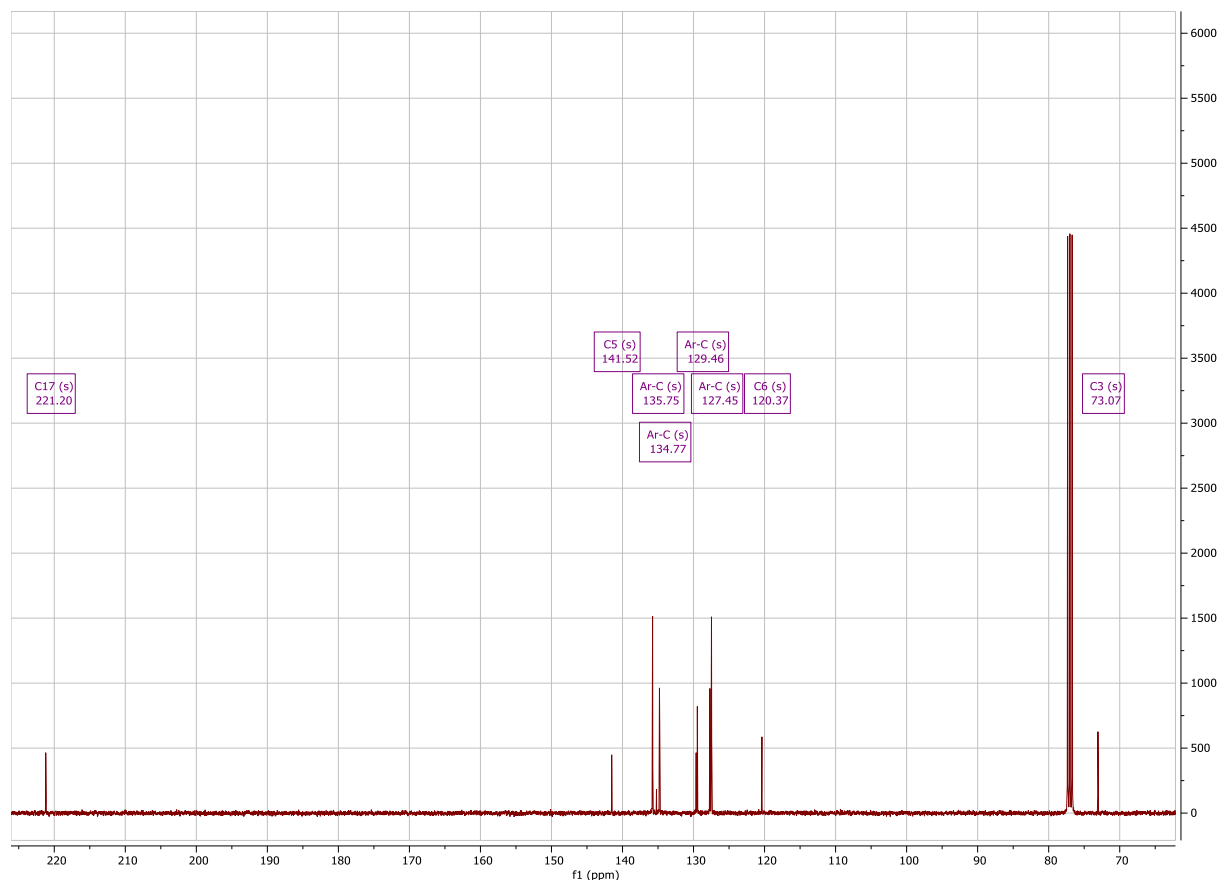
Figure 3.8C [13]C Spectrum of DHEA PG (2)

δ_C 221.20 and δ_C 73.07 were identified as C_{17} and C_3 respectively based on chemical shift (see Figure 3.8C). δ_C 141.52 and δ_C 120.37 were identified as C_5 and C_6 respectively based on chemical shift and peak height (see Figure 3.8C). In addition, the presence of the aromatic carbons of the TBDPS group were detected based on the appearance of additional carbon peaks between δ_C 120-140 (see Figure 3.8C).
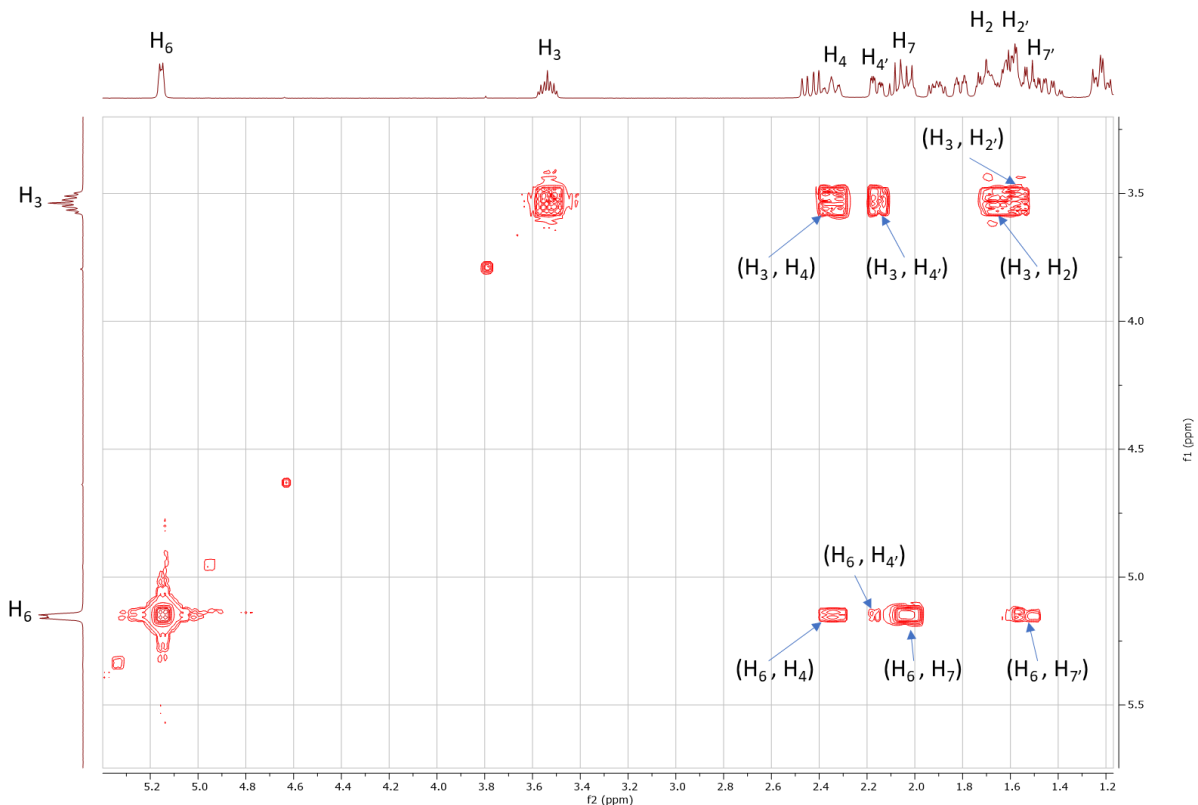
Figure 3.9 Initial ^{1}H-^{1}H COSY Correlations for DHEA PG (2)

Diastereotopic protons, δ_H 2.35 (H$_4$) and δ_H 2.16 (H$_{4'}$), from the A ring were identified from COSY correlations with H$_3$ (δ_H 3.54) and H$_6$ (δ_H 5.15) (see Figure 3.9). Methylene protons, δ_H 1.71 (H$_2$) and δ_H 1.60 (H$_{2'}$), were discerned from COSY correlations with H$_3$ (δ_H 3.54) (see Figure 3.9). In addition, diastereotopic protons δ_H 2.05 (H$_7$) and δ_H 1.47 (H$_{7'}$) in the B ring were identified from COSY correlations with H$_6$ (δ_H 5.15) (see Figure 3.9). In the D ring, diastereotopic proton, H$_{16}$ (δ_H 2.44, m) was discerned based on splitting and chemical shift (see Figure 3.8B).
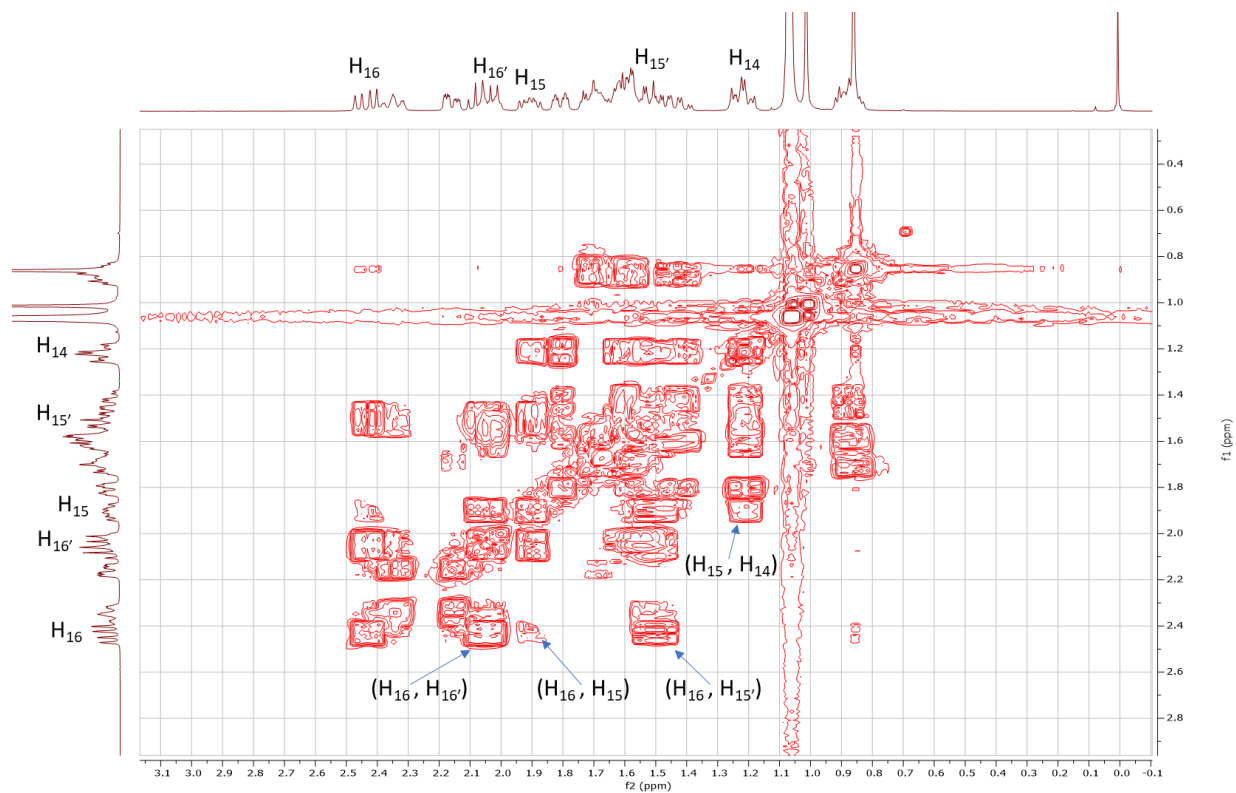
Figure 3.10A ^{1}H-^{1}H COSY Correlations in D ring for DHEA PG (2)
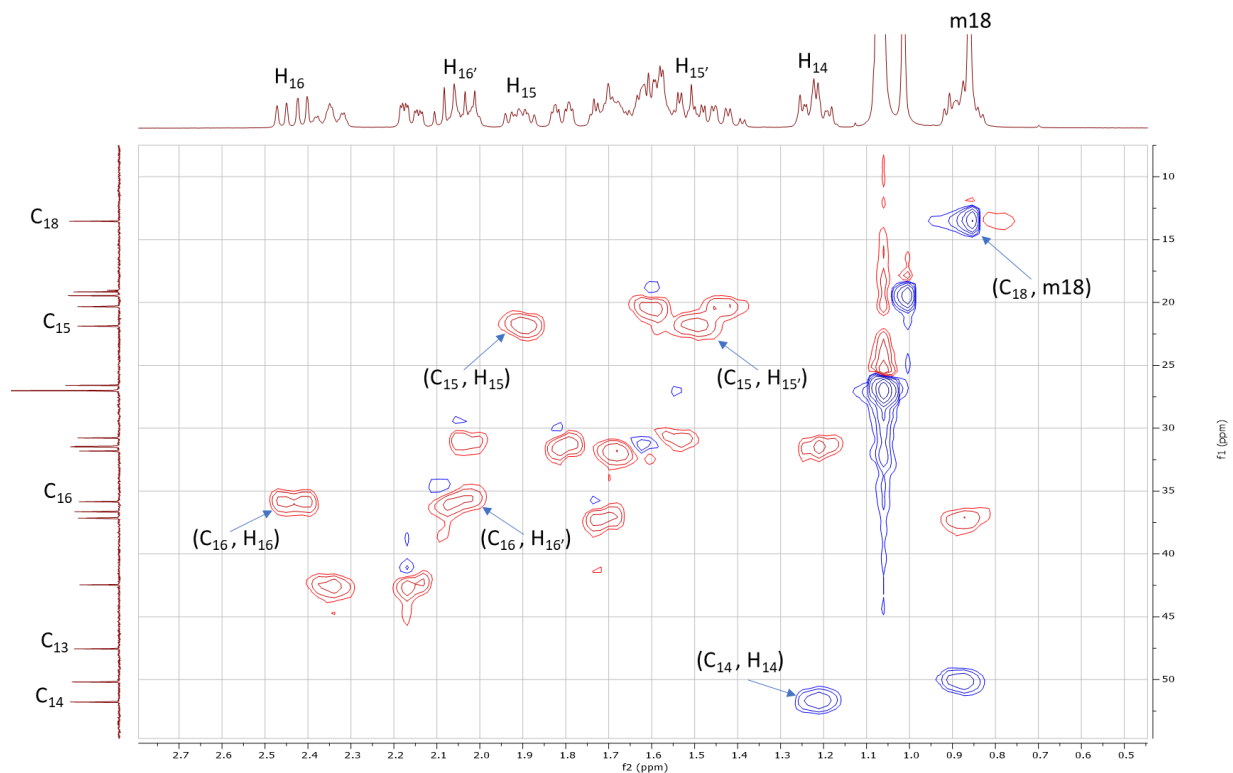
Figure 3.10B ^{1}H-^{13}C HSQC Correlations in D ring for DHEA PG (2)
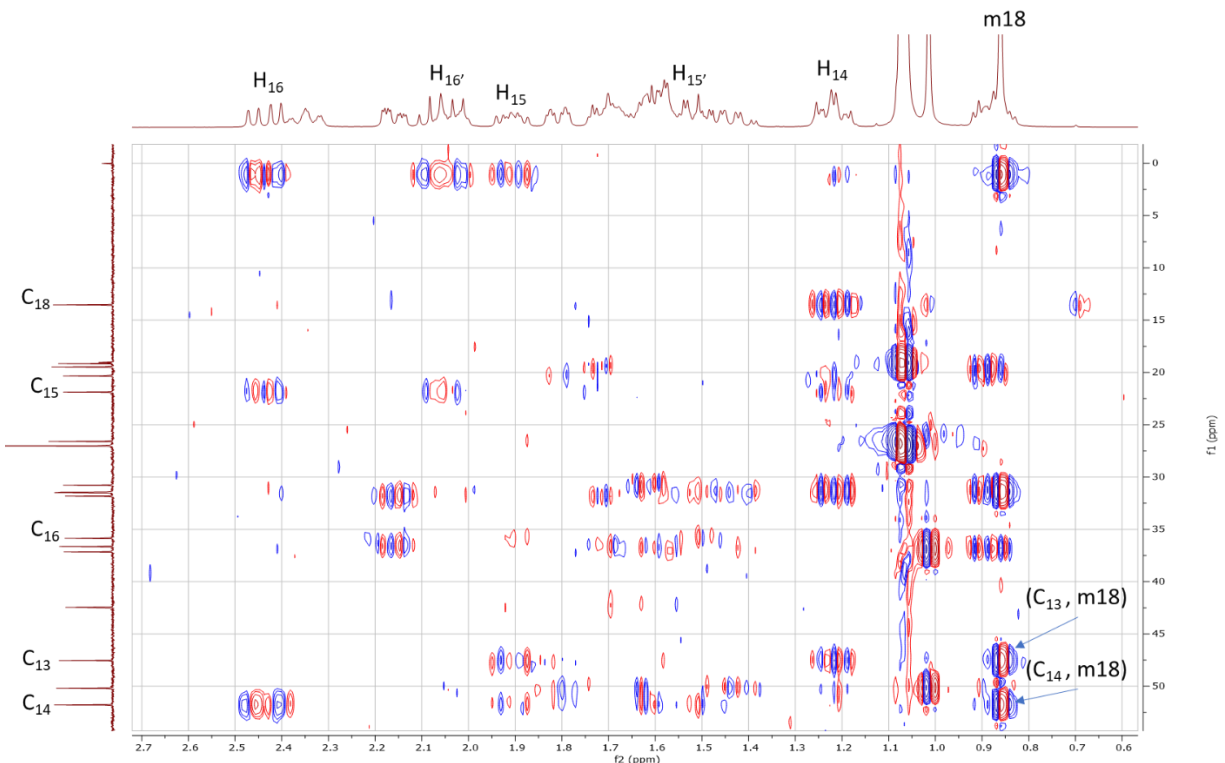
Figure 3.10C ^{1}H-^{13}C HMBC Correlations in D ring for DHEA PG (2)

Starting with the D ring, methylene proton, δ_H 2.05 (H$_{16'}$), was correlated by HSQC to δ_C 35.85 (C$_{16}$) and by COSY to δ_H 2.44 (H$_{16}$) (see Figure 3.10A and 3.10B). Next, diastereotopic protons, δ_H 1.90 (H$_{15}$) and δ_H 1.47 (H$_{15'}$), showed a HSQC correlation to δ_C 21.88 (C$_{15}$) and COSY correlation to H$_{16}$ (δ_H 2.44) (see Figure 3.10A and 3.10B). Methine proton, δ_H 1.22 (H$_{14}$), displayed HSQC correlation to δ_C 51.78 (C$_{14}$) and COSY correlation to H$_{15}$ (δ_H 1.90) (see Figure 3.10A and 3.10B). Methyl protons on C$_{18}$, m18 (δ_H 0.86), were discerned from HMBC correlation to C$_{14}$ (δ_C 51.78) (see Figure 3.10C). Continuing with m18, δ_C 13.54 (C$_{18}$) was identified from HSQC correlation to m18 (see Figure 3.10B). Therefore, the methyl protons on C$_{19}$, m19 could be identified at δ_H 1.01 based on integration and splitting (see Figure 3.8A). Quaternary carbon, δ_C 47.55 (C$_{13}$), was discerned from HMBC correlation to m18 (δ_H 0.86) and no observable HSQC correlation (see Figure 3.10B and 3.10C).
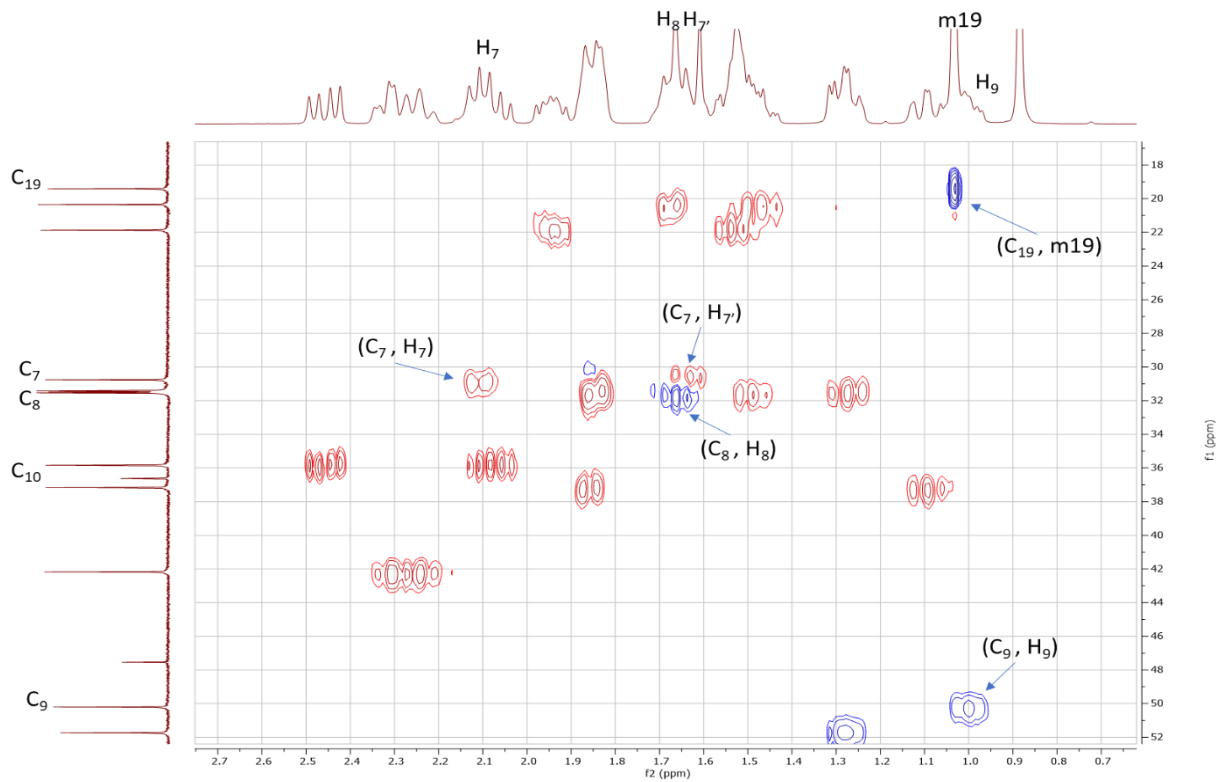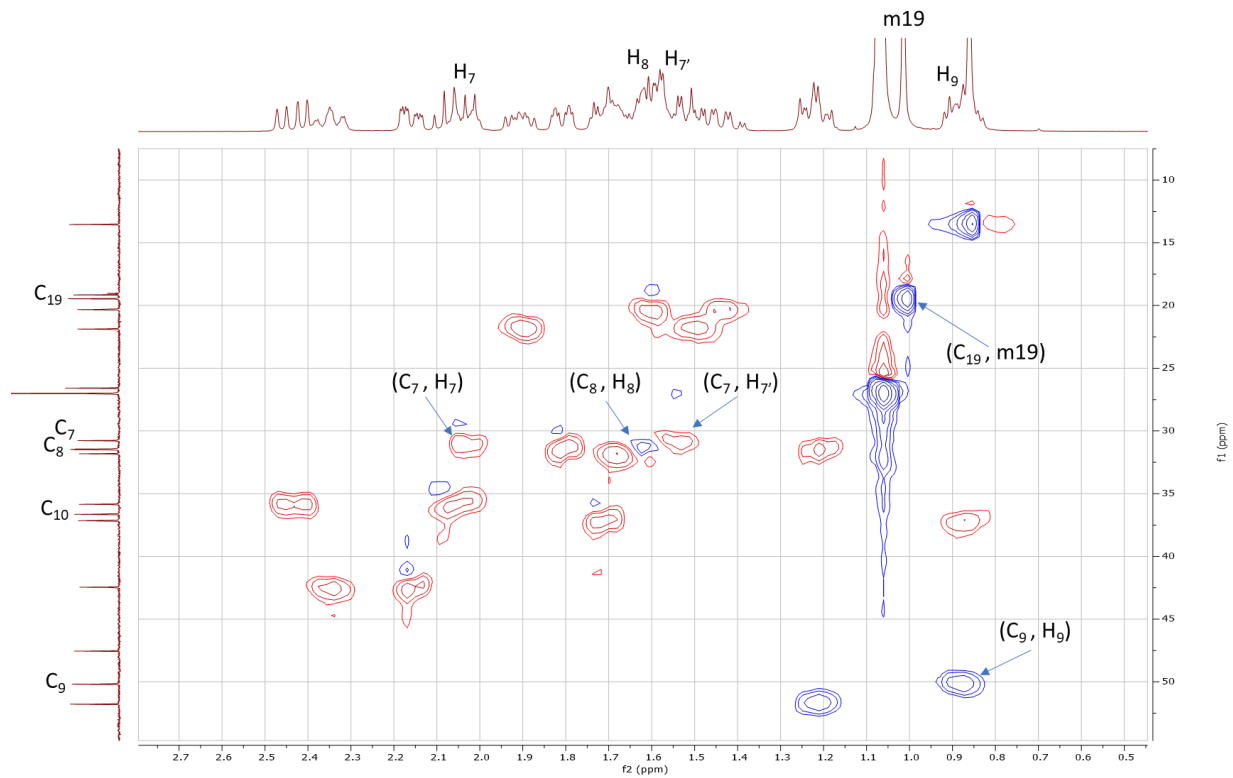
Figure 3.11A ^{1}H-^{13}C HSQC Correlations in B ring for DHEA PG (2)

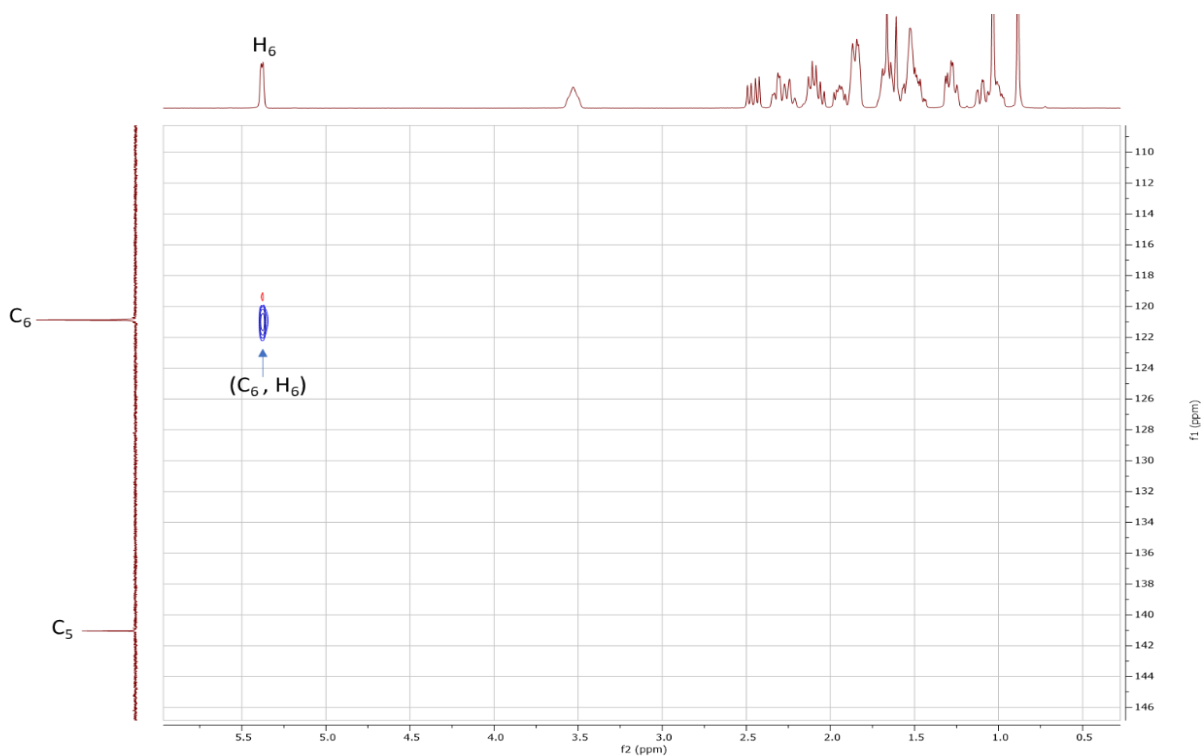**Figure 3.11B** ^{1}H-^{13}C HSQC Correlations in B ring for DHEA PG (2) (C_5-C_6)
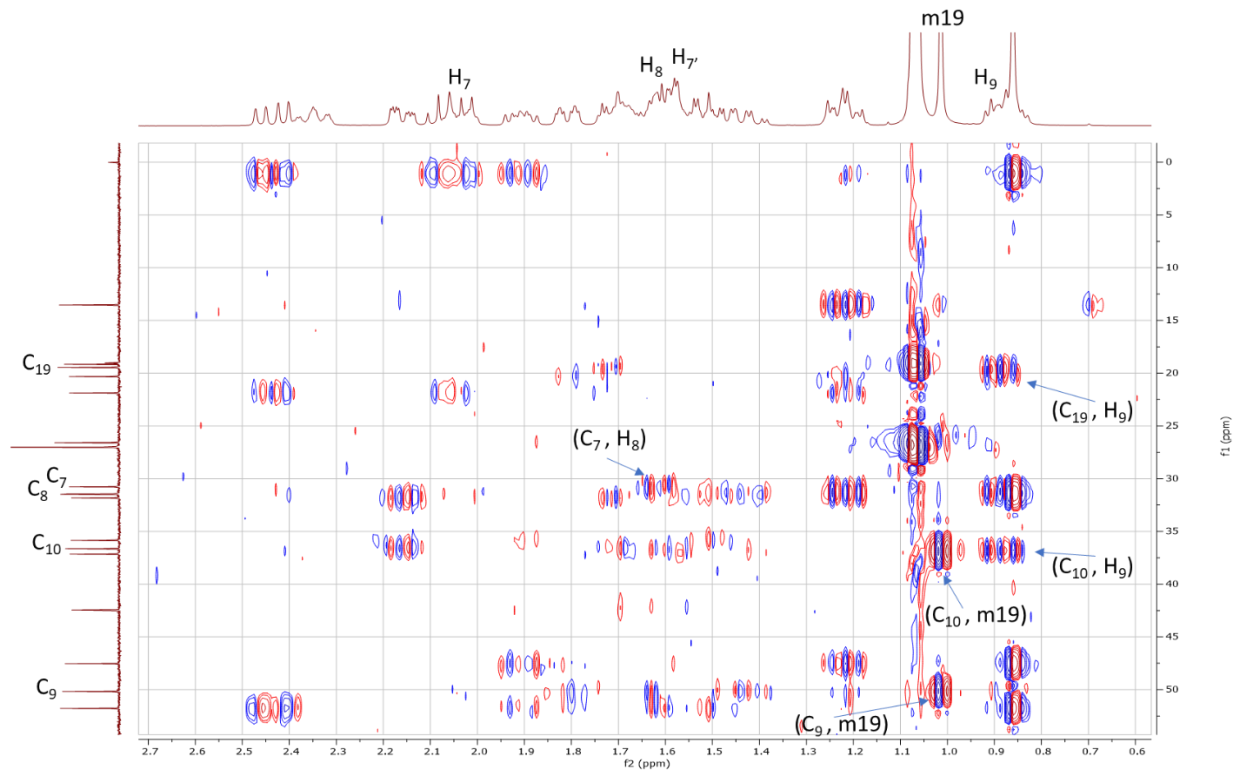
Figure 3.11C ^{1}H-^{13}C HMBC Correlations in B ring for DHEA PG (2)
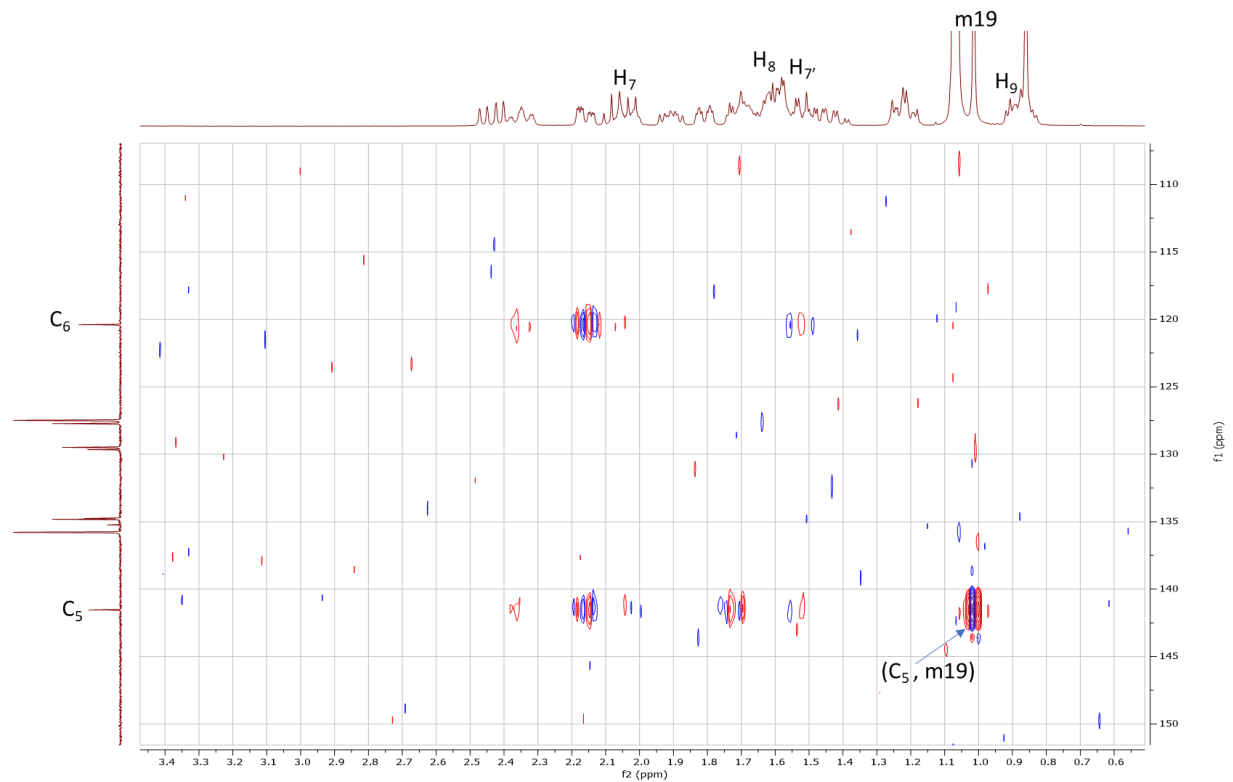
Figure 3.11D ^{1}H-^{13}C HMBC Correlations in B ring for DHEA PG (2) (C$_5$-C$_6$)

Next with the B ring, methyl protons, m19 (δ_H 1.01) exhibited HSQC correlation to δ_C 19.46 (C_{19}) (see Figure 3.11A). δ_C 141.55 (C_5) was determined on the basis of no HSQC correlation, chemical shift, and HMBC correlation to m19 (δ_H 1.01) (see Figure 3.11B and 3.11D). Vinyl carbon, C_6 (δ_C 120.40) was correlated by HSQC to δ_H 5.15 (H_6) (see Figure 3.11B). Methylene protons, δ_H 2.05 (H_7) and δ_H 1.47 ($H_{7'}$), exhibited HSQC correlation to δ_C 30.80 (C_7) (see Figure 3.11A). Methine proton, H_8, was discerned at δ_H 1.60 based on HMBC correlation to C_7 (δ_C 30.80) (see Figure 3.11C). C_8 (δ_C 31.44) was correlated by HSQC to δ_H 1.60 (H_8) (see Figure 3.11A). The remaining methine proton, H_9 (δ_H 0.90), displayed correlation by HSQC to δ_C 50.18 (C_9) and by HMBC to δ_C 19.46 (C_{19}) (see Figure 3.11A and 3.11C). Quaternary carbon, C_{10} (δ_C 36.64), was assigned based upon HMBC correlation to m19 (δ_H 1.01) along with H_9 (δ_H 0.90) and no correlation in HSQC (see Figure 3.11A and 3.11C).
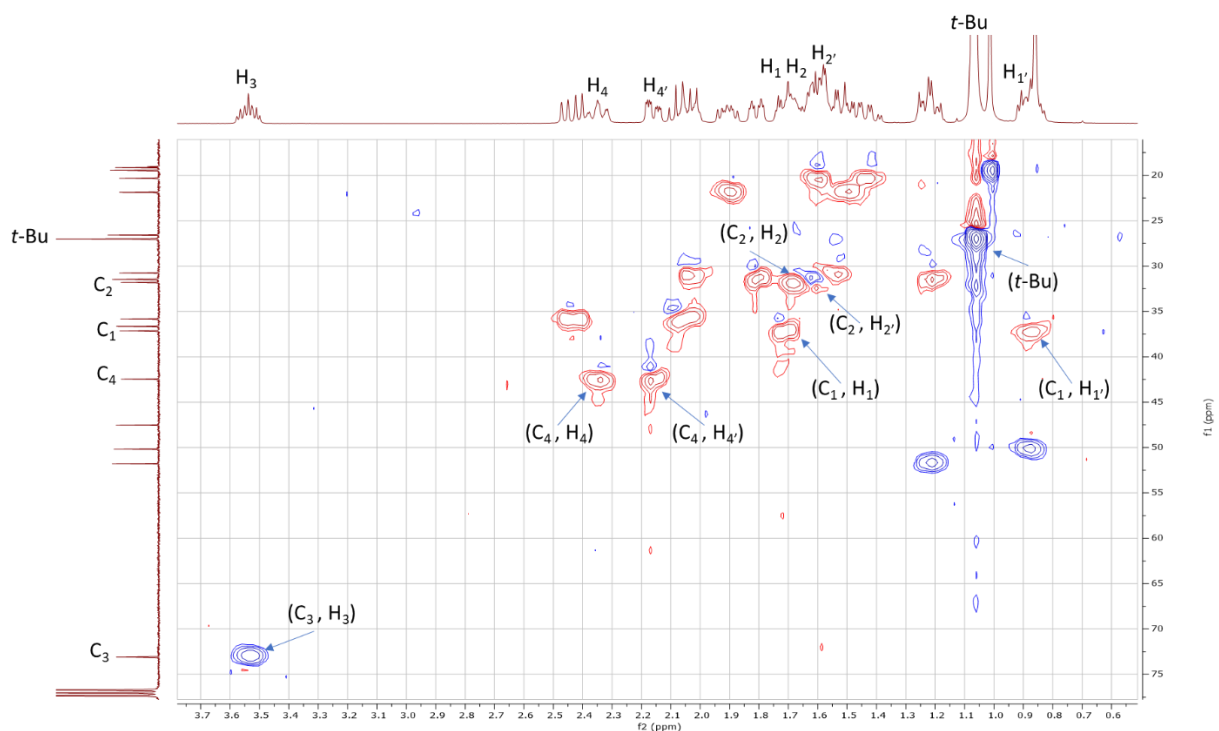
Figure 3.12A ^{1}H-^{13}C HSQC Correlations in A ring for DHEA PG (2)
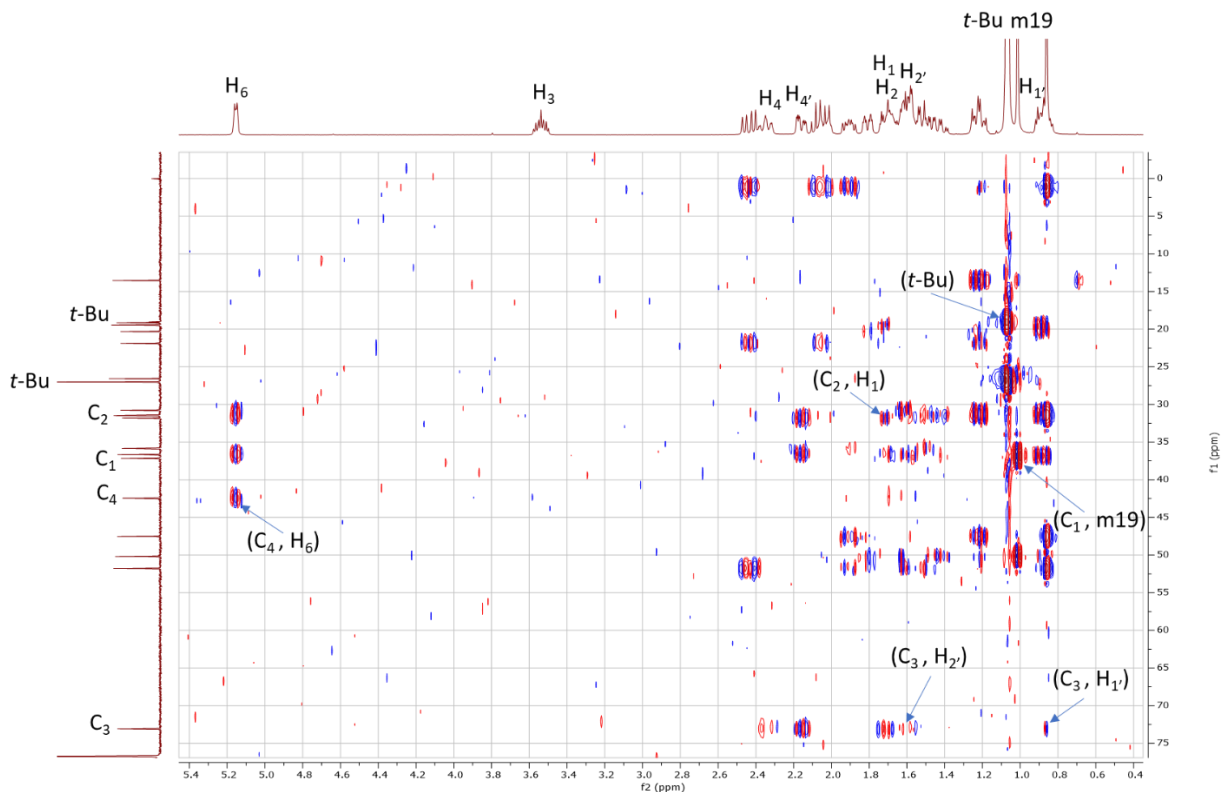
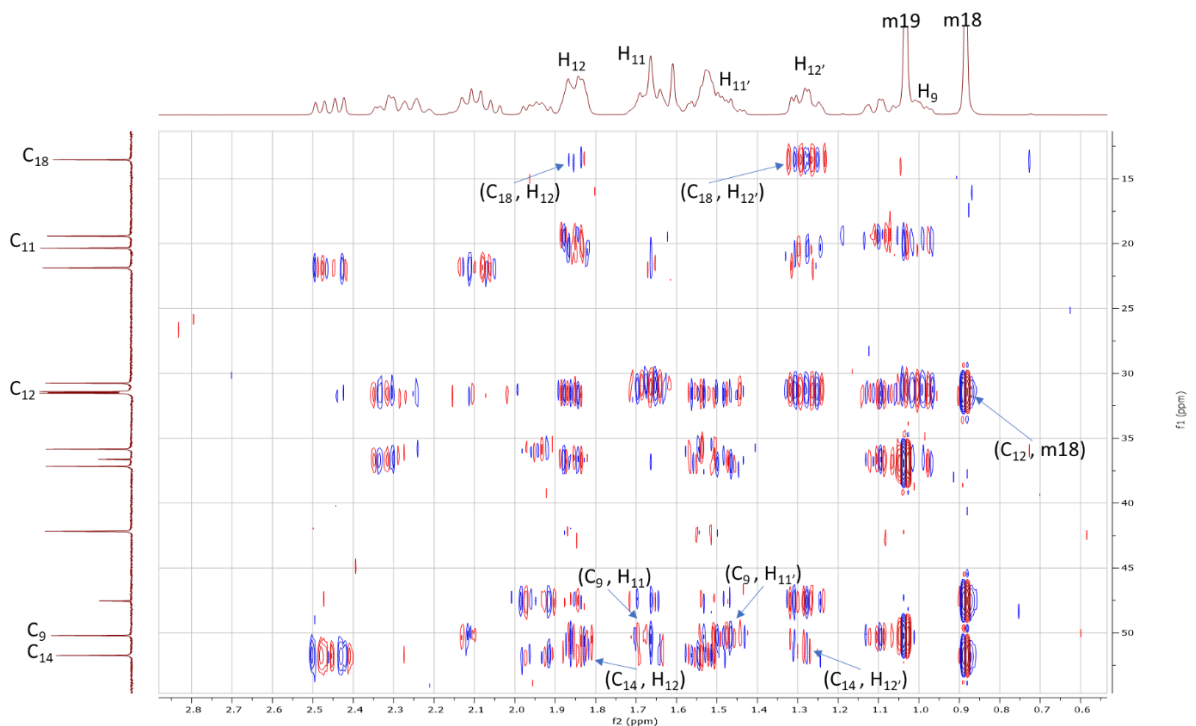**Figure 3.12B ^{1}H-^{13}C HMBC Correlations in A ring for DHEA PG (2)**

Continuing with the A ring, δ_H 3.54 (H$_3$) exhibited HSQC correlation to δ_C 73.07 (C$_3$) (see

Figure 3.12A). Methylene protons, δ_H 2.35 (H$_4$) and δ_H 2.16 (H$_{4'}$), displayed HSQC correlation to

δ_C 42.46 (C$_4$), which shows HMBC correlation to H$_6$ (δ_H 5.15) (see Figure 3.12A and 3.12B).

Diastereotopic protons, δ_H 1.71 (H$_2$) and δ_H 1.60 (H$_{2'}$), displayed HSQC correlation to δ_C 31.82 (C$_2$)

while 1.60 (H$_{2'}$) displayed HMBC correlation to C$_3$ (δ_C 73.07) (see Figure 3.12A and 3.12B). δ_C

37.16 (C$_1$) was discerned from HMBC correlation to m19 (δ_H 1.01) (see Figure 3.12B). Methylene

proton, δ_H 1.71 (H$_1$), displayed HMBC correlation to δ_C 31.82 (C$_2$) while methylene proton, δ_H 0.90

(H$_{1'}$), displayed HMBC correlation to δ_C 73.09 (C$_3$) (see Figure 3.12B). δ_C 37.16 (C$_1$) exhibited

HSQC correlation δ_H 1.71 (H$_1$) and δ_H 0.90 (H$_{1'}$) (see Figure 3.12A). The *tert*-butyl (*t*-Bu) protons

of TBDPS were recognized based as the δ_H 1.07 singlet, which integrated to nine (see Figure

3.8B). In addition, δ_C 27.01 (*t*-Bu) displayed HSQC correlation to δ_H 1.07 (*t*-Bu) (see Figure 3.12A).

δ_C 19.15 (*t*-Bu) displayed HMBC correlation to δ_H 1.07 (*t*-Bu) (see Figure 3.12B).
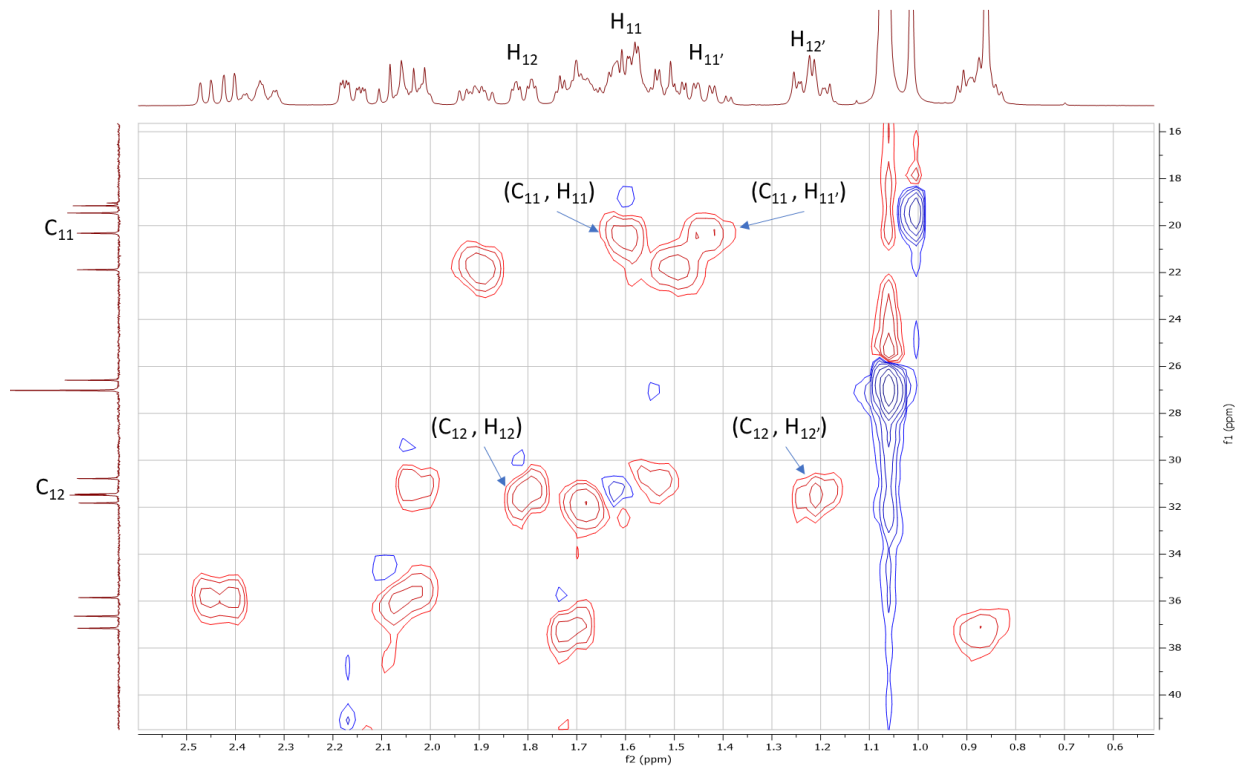
Figure 3.13A ^{1}H-^{13}C HSQC Correlations in C ring for DHEA PG (2)
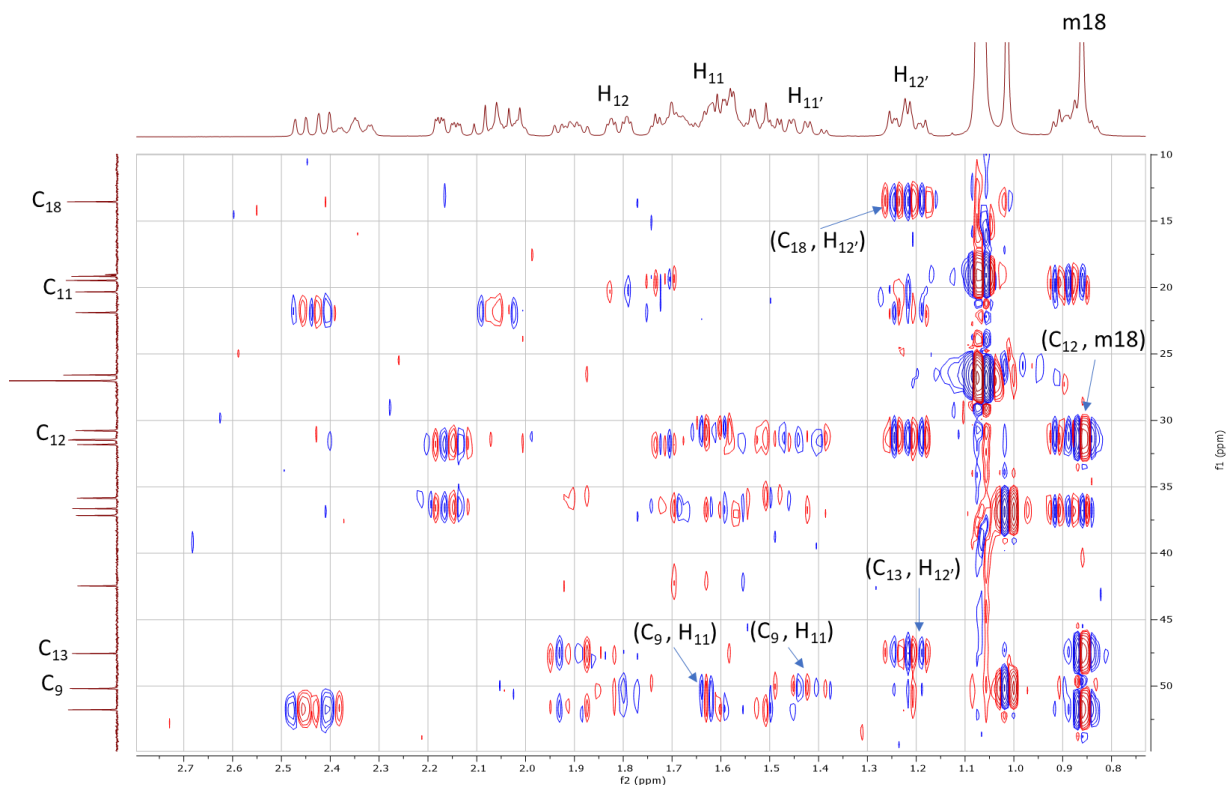
Figure 3.13B ^{1}H-^{13}C HMBC Correlations in C ring for DHEA PG (2)

Concluding with the C ring, δ_C 31.46 (C_{12}) displayed HSQC correlation to δ_H 1.81 (H_{12}) and δ_H 1.22 ($H_{12'}$), which also shows HMBC correlation to C_{13} (δ_C 47.55) and C_{18} (δ_C 13.54) (see Figure 3.13A and 3.13B). The final methylene protons, δ_H 1.60 (H_{11}) and δ_H 1.47 ($H_{11'}$) were discerned from HSQC correlations to δ_C 20.32 (C_{11}) and HMBC correlation to C_9 (δ_C 50.18) (see Figure 3.13A and 3.13B). Thus, full proton and carbon assignment of DHEA PG (**2**) has been completed.
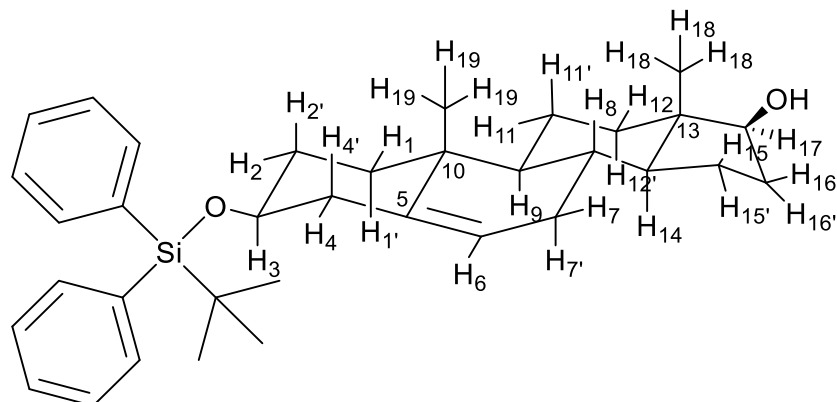
Figure 3.14A Chair Conformation for 3
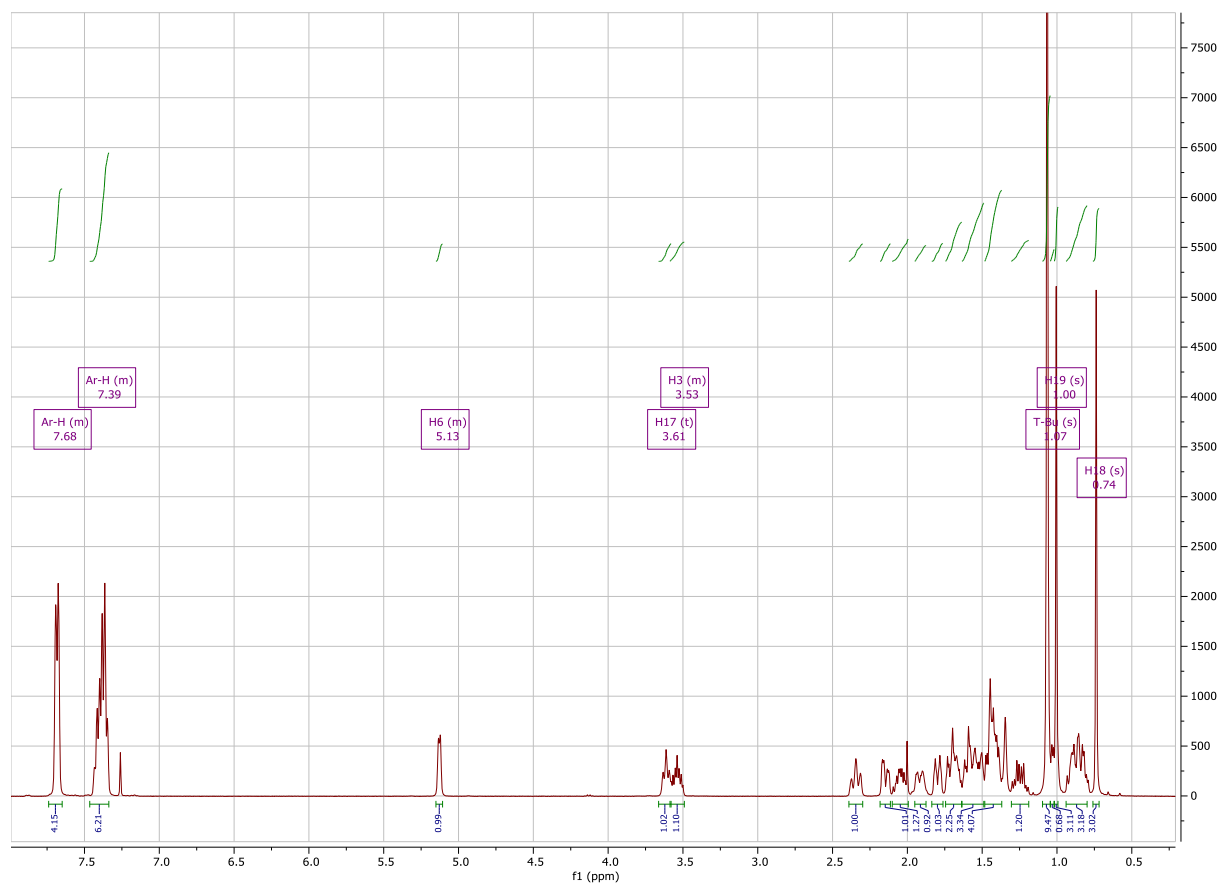
Figure 3.14B ^{1}H Spectrum of DHEA C$_{17}$ OH PG (3)

Aromatic protons of the TBDPS group were identified at δ_H 7.39 and δ_H 7.68 based upon chemical shift (see Figure 3.14B). δ_H 5.13, δ_H 3.61, and δ_H 3.53 were identified as H$_6$, H$_{17}$, and

H_3 respectively based upon chemical shift and splitting (see Figure 3.14B). The methyl protons on C_{18} and C_{19} could be identified at either δ_H 1.00 or δ_H 0.74 (see Figure 3.14B). The latter assignments for H_3, H_6, H_{17}, H_{18}, and H_{19} matched previous ^{1}H assignments (Blanco et al., 2014), (Jan et al., 2016).
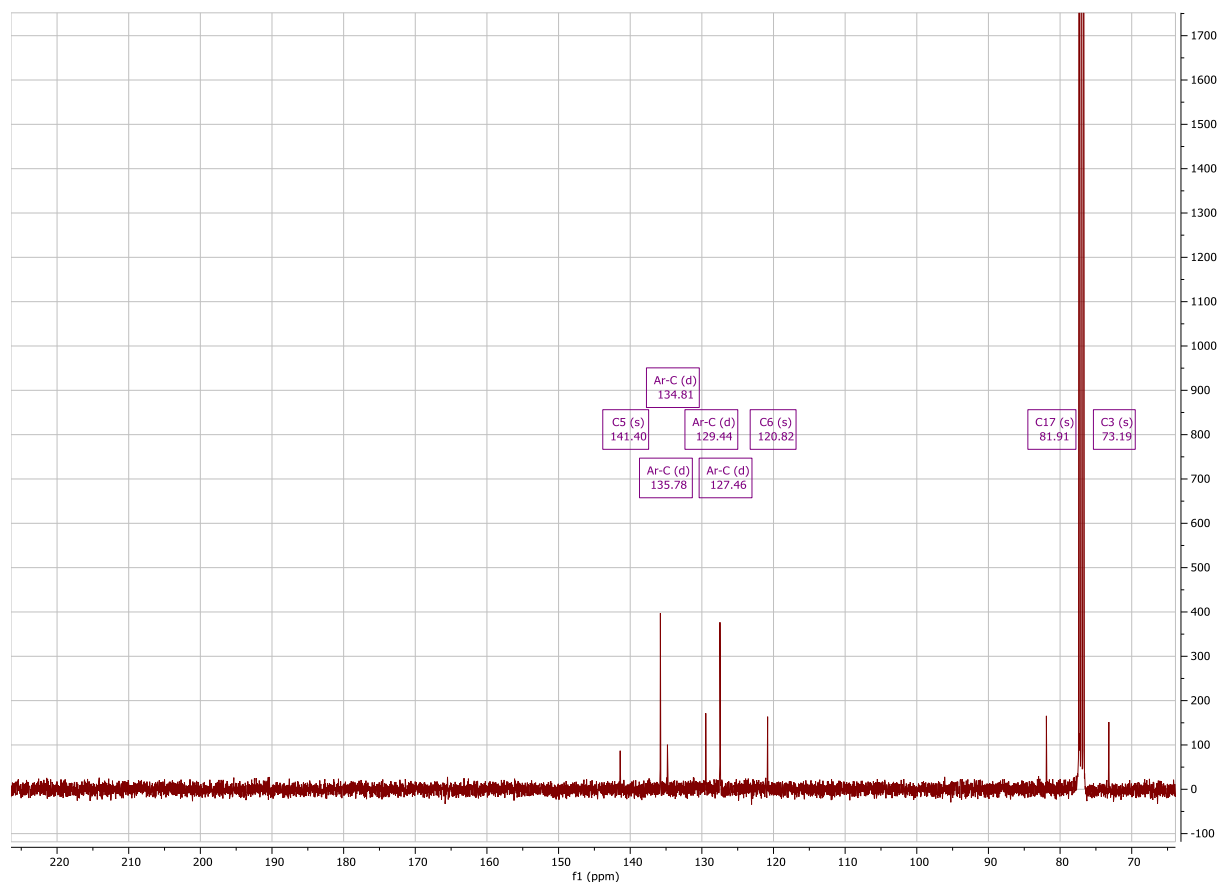
Figure 3.14C [13]C Spectrum of DHEA C_{17} OH PG (3)

The loss of δ_C 221.20 (C_{17}, **2**) and gain of δ_C 81.91 (C_{17}, **3**) indicates the reduction of the carbonyl peak to a hydroxyl group based on DHEA PG (**2**) (see Figure 3.14C). δ_C 141.40, δ_C 120.82, and δ_C 73.19 were identified as C_5, C_6, and C_3 respectively based on chemical shift and previous characterization of $C_5/C_6/C_3$ for DHEA PG (**2**) (see Figure 3.14C). In addition, the presence of the aromatic carbons of the TBDPS group were detected based on the previous appearance of carbon peaks between δ_C 120-140 (see Figure 3.14C).
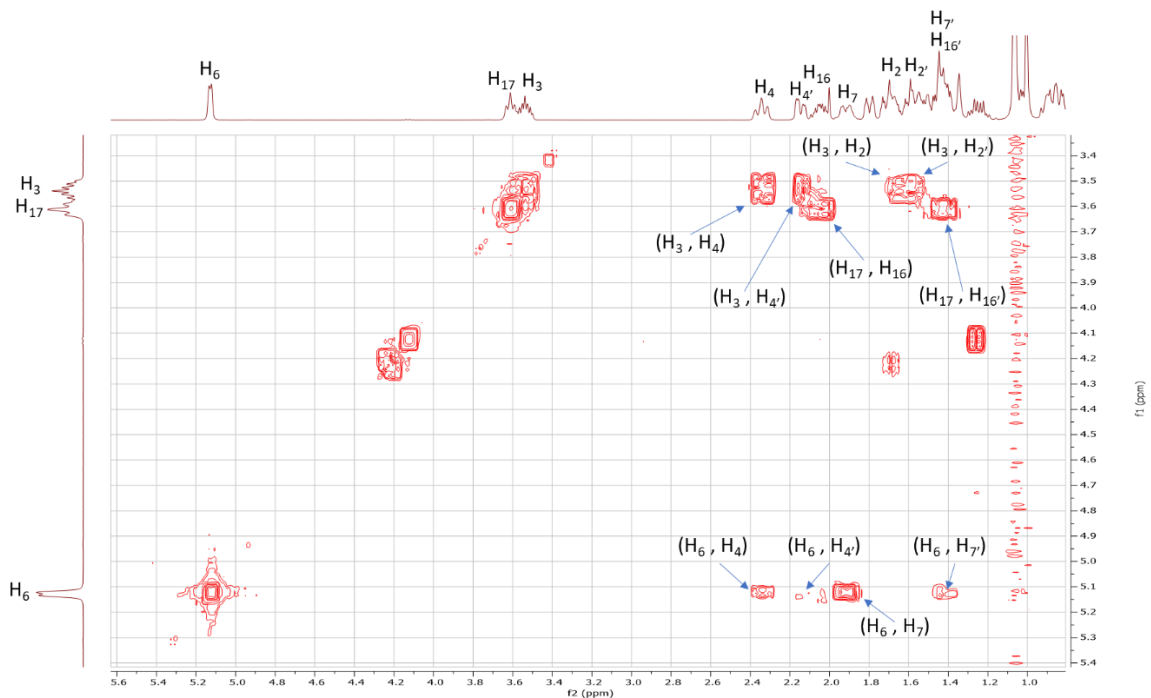
Figure 3.15 Initial ^{1}H-^{1}H COSY Correlations for DHEA C$_{17}$ OH PG (3)

Diastereotopic protons, δ_H 2.34 (H$_4$) and δ_H 2.15 (H$_{4'}$), from the A ring were identified from COSY correlations with H$_3$ (δ_H 3.53) and H$_6$ (δ_H 5.13) (see Figure 3.15). Methylene protons, δ_H 1.70 (H$_2$) and δ_H 1.55 (H$_{2'}$), were discerned from COSY correlations with H$_3$ (δ_H 3.53) (see Figure 3.15). In addition, diastereotopic protons δ_H 1.92 (H$_7$) and δ_H 1.43 (H$_{7'}$) in the B ring were identified from COSY correlations with H$_6$ (δ_H 5.13) (see Figure 3.15). In the D ring, diastereotopic protons δ_H 2.03 (H$_{16}$) and δ_H 1.43 (H$_{16'}$) were discerned from COSY correlations with H$_{17}$ (δ_H 3.61) (see Figure 3.15).
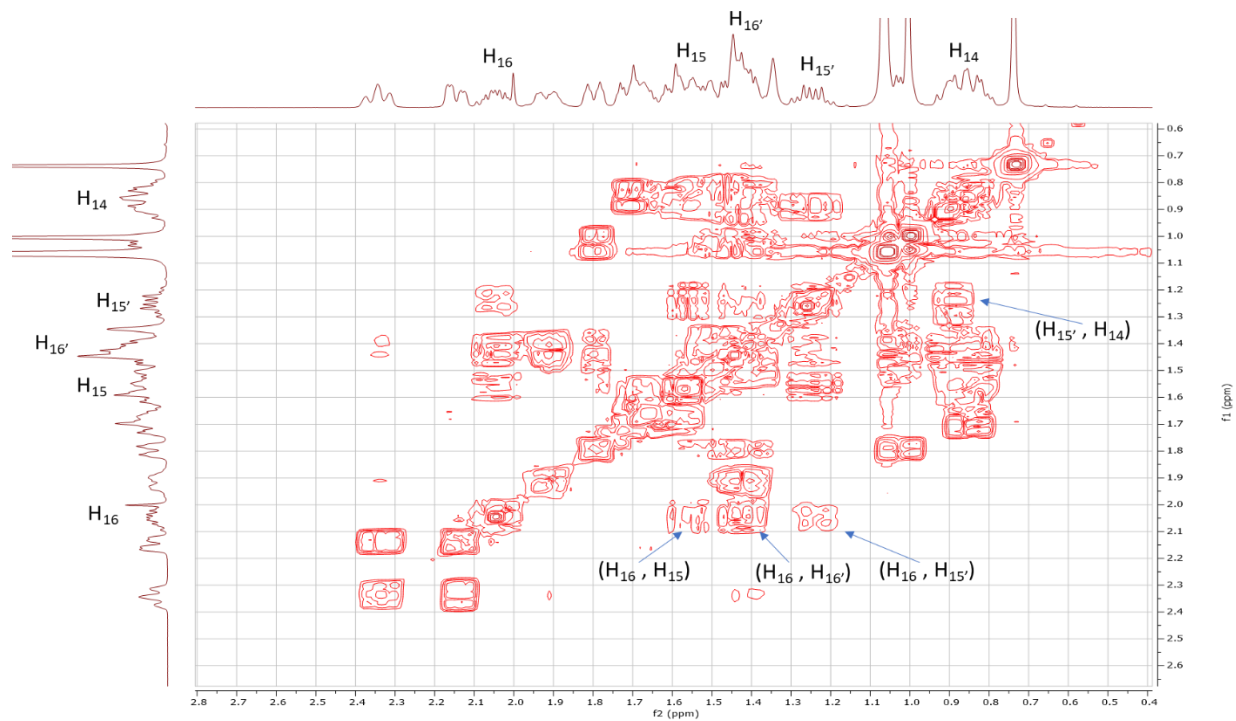
Figure 3.16A ^{1}H-^{1}H COSY Correlations in D ring for DHEA C$_{17}$ OH PG (3)
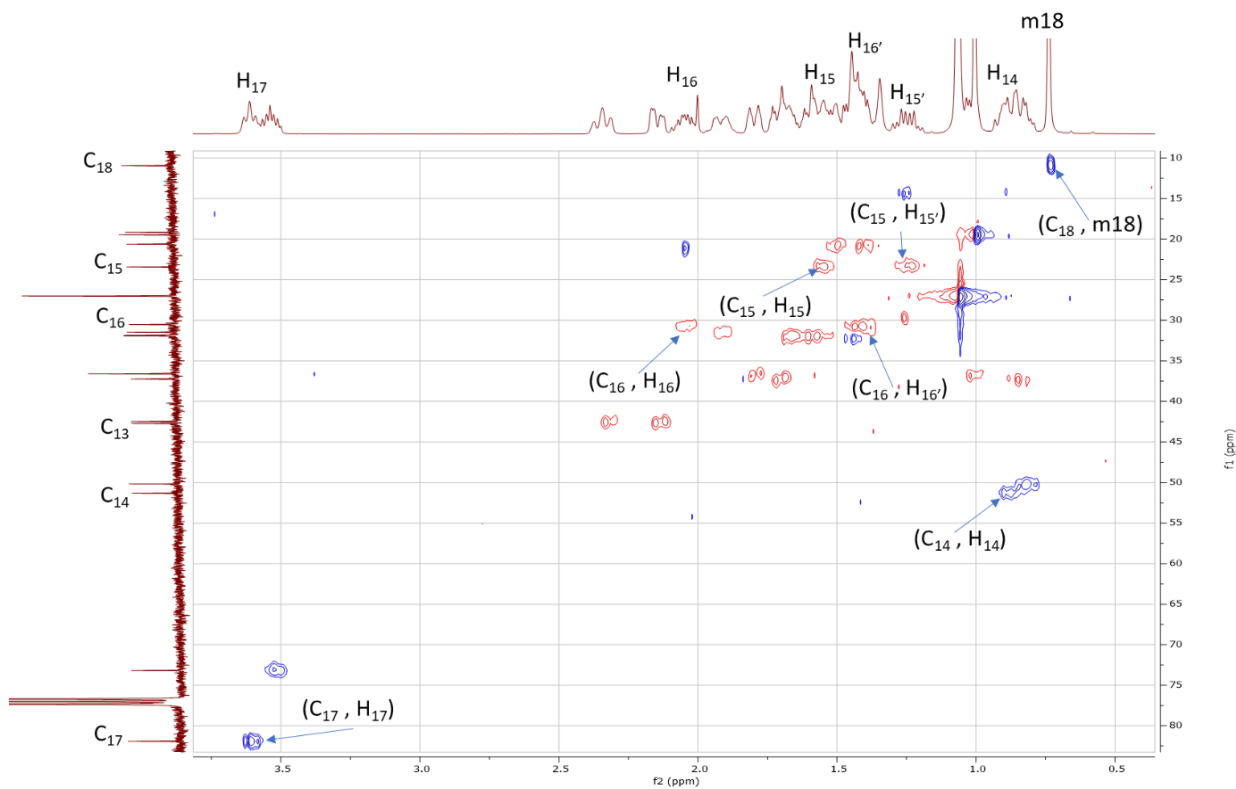
Figure 3.16B ^{1}H-^{13}C HSQC Correlations in D ring for DHEA C$_{17}$ OH PG (3)
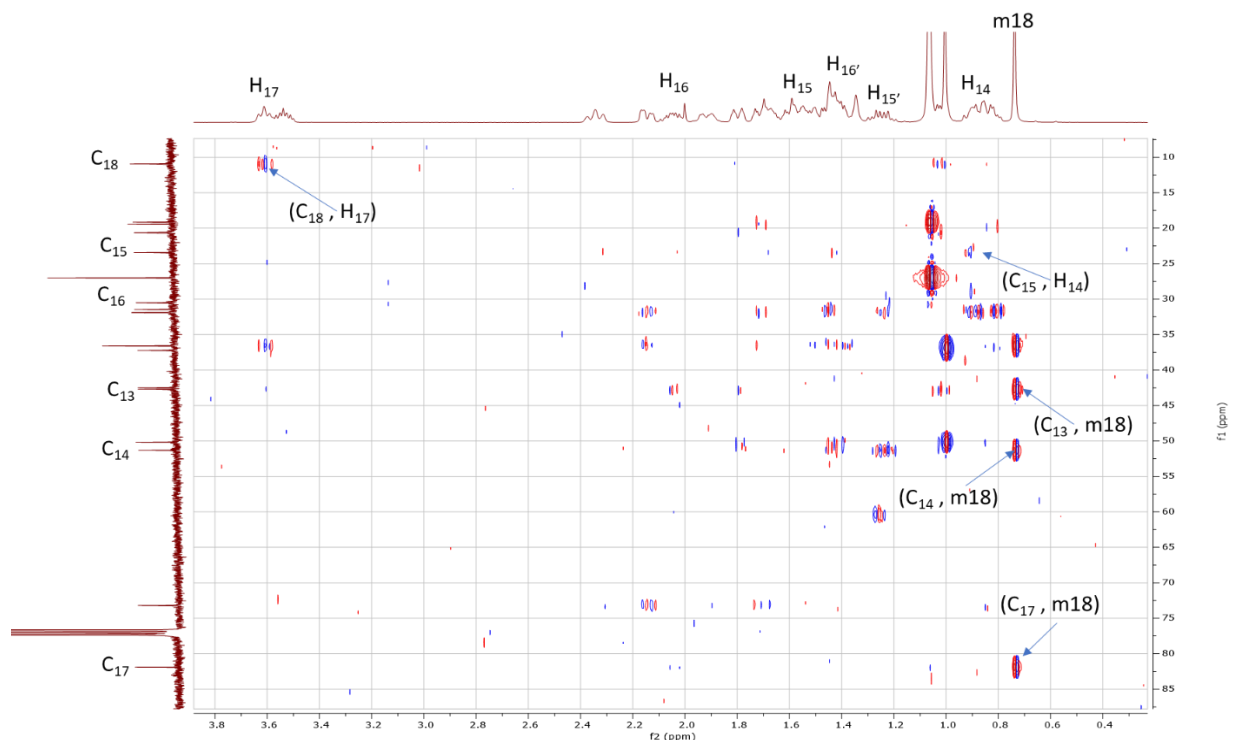
Figure 3.16C ^{1}H-^{13}C HMBC Correlations in D ring for DHEA C$_{17}$ OH PG (3)

Starting with the D ring, δ_C 81.91 was identified as C$_{17}$ from the HSQC correlation with δ_H 3.61 (H$_{17}$) and HMBC correlations to m18 (δ_H 0.74), the methyl protons on C$_{18}$ (see Figure 3.16B and 3.16C). Methylene protons, δ_H 2.03 (H$_{16}$) and δ_H 1.43 (H$_{16'}$), were correlated by HSQC to δ_C 30.52 (C$_{16}$) (see Figure 3.16B). With COSY correlations with H$_{16}$ (δ_H 2.03), diastereotopic protons H$_{15}$ (δ_H 1.55) and H$_{15'}$ (δ_H 1.25) were identified (see Figure 3.16A). In regard to H$_{15'}$ (δ_H 1.25), methine proton, H$_{14}$ (δ_H 0.94), was distinguished by COSY correlation (see Figure 3.16A). Next, diastereotopic protons, δ_H 1.55 (H$_{15}$) and δ_H 1.25 (H$_{15'}$), showed a HSQC correlation to δ_C 23.43 (C$_{15}$) (see Figure 3.16B). Methine proton, δ_H 0.94 (H$_{14}$), discerned a HSQC correlation to δ_C 51.34 (C$_{14}$) and a HMBC correlation to C$_{15}$ (δ_C 23.43) (see Figure 3.16B and 3.16C). Methyl protons on C$_{18}$, m18 (δ_H 0.74), were discerned from HMBC correlation to C$_{14}$ (δ_C 51.34) (see Figure 3.16C). Continuing with m18, δ_C 10.94 (C$_{18}$) was identified from HSQC correlation to m18 and HMBC correlation to δ_H 3.61 (H$_{17}$) (see Figure 3.16B and 3.16C). Therefore, the methyl protons on C$_{19}$, m19, could be identified at δ_H 1.00 based on integration and splitting (see Figure 3.14B).

Quaternary carbon, δ_C 42.71 (C_{13}), was discerned from HMBC correlation to m18 (δ_H 0.74) and no observable HSQC correlation (see Figure 3.16B and 3.16C).

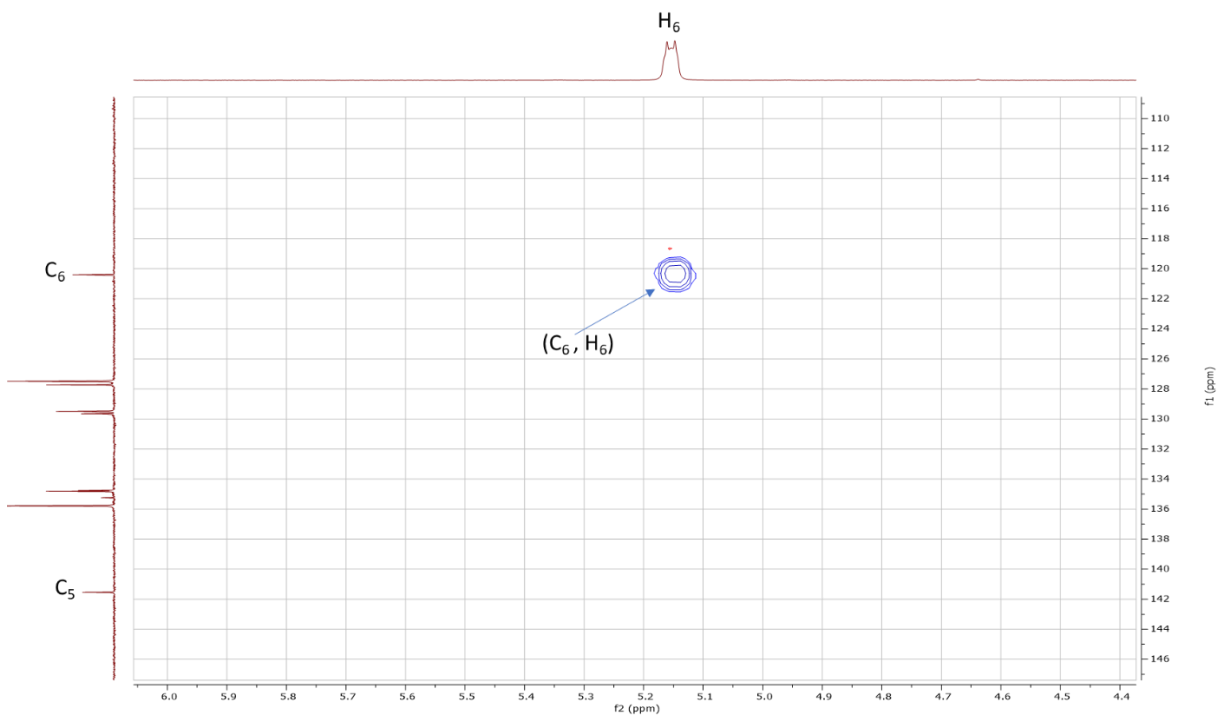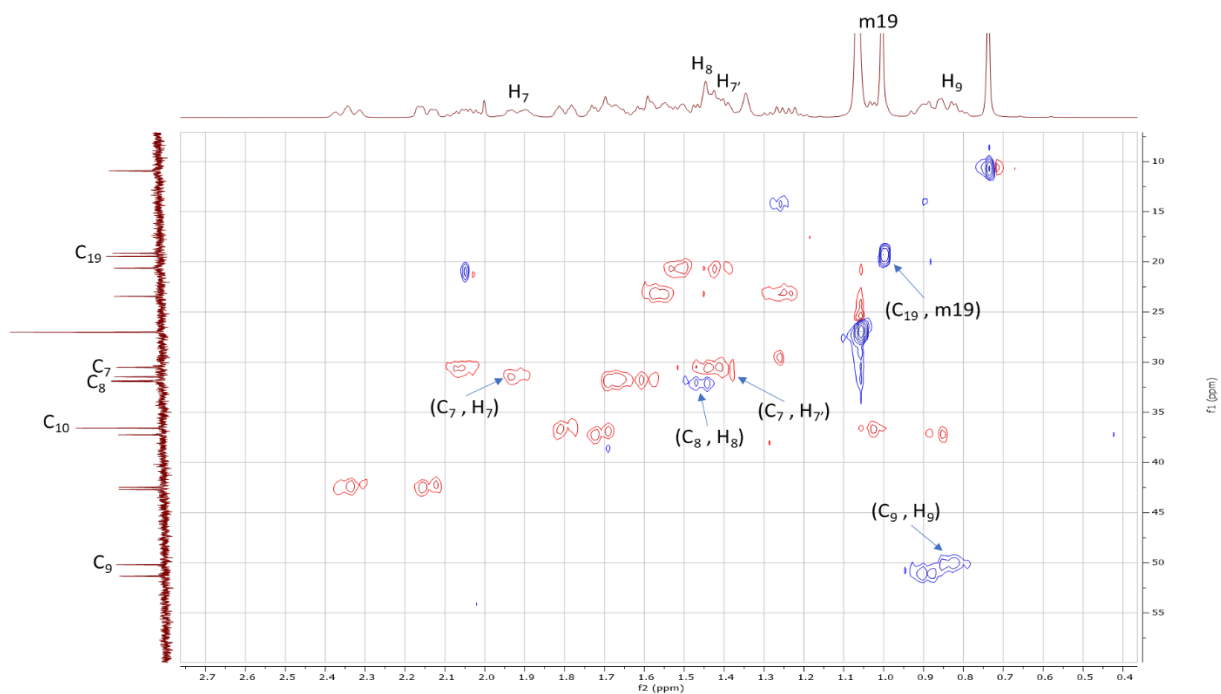**Figure 3.17A ^{1}H-^{13}C HSQC Correlations in B ring for DHEA C_{17} OH PG (3)**

Figure 3.17B ^{1}H-^{13}C HSQC Correlations in B ring for DHEA C_{17} OH PG (3) (C_5-C_6)

Figure 3.17C ^1H-^{13}C HMBC Correlations in B ring for DHEA C_{17} OH PG (3)
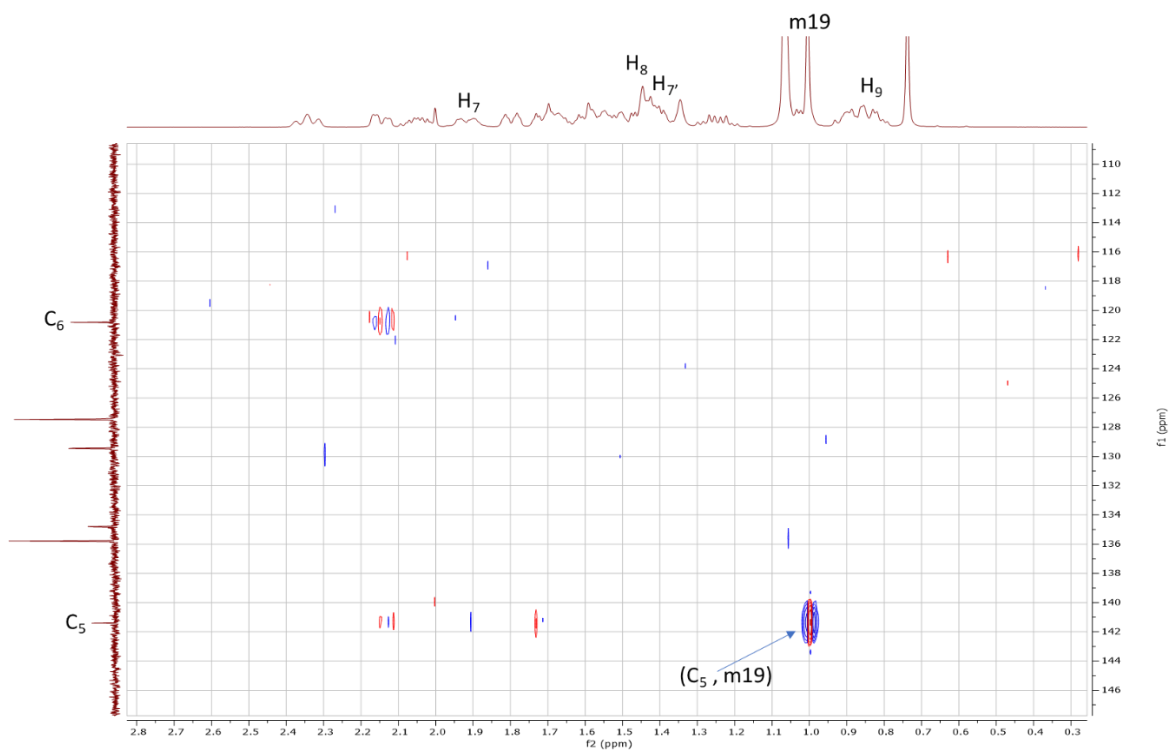
Figure 3.17D ^1H-^{13}C HMBC Correlations in B ring for DHEA C_{17} OH PG (3) (C_5-C_6)

Next with the B ring, methyl protons, m19 (δ_H 1.00) exhibited HSQC correlation to δ_C 19.47 (C_{19}) (see Figure 3.17A). δ_C 141.40 (C_5) was determined on the basis of no HSQC correlation, chemical shift, and HMBC correlation to m19 (δ_H 1.00) (see Figure 3.17B and 3.17D). Vinyl carbon, C_6 (δ_C 120.82) was correlated by HSQC to δ_H 5.13 (H_6) (see Figure 3.17B). Methylene protons, δ_H 1.92 (H_7) and δ_H 1.43 ($H_{7'}$), exhibited HSQC correlation to δ_C 31.48 (C_7) (see Figure 3.17A). Methine proton, H_8, was discerned at δ_H 1.43 based on HMBC correlation to C_7 (δ_C 31.48) (see Figure 3.17C). C_8 (δ_C 31.92) was correlated by HSQC to δ_H 1.43 (H_8) (see Figure 3.17A). C_9 (δ_C 50.18) displayed HMBC correlation to m19 (δ_H 1.00) (see Figure 3.17C). The remaining methine proton, H_9 (δ_H 0.84), displayed correlation by HSQC to δ_C 50.18 (C_9) (see Figure 3.17A). With δ_C 36.58 displaying double intensity in peak height, it was inferred two unique carbons are present (see Figure 3.17A). Quaternary carbon, C_{10} (δ_C 36.58), was assigned based upon previous C_{10} assignment for DHEA PG (**2**) and HMBC correlation to m19 (δ_H 1.00) along with H_6 (δ_H 5.13) (see Figure 3.17C and 3.18B). With respect to δ_C 36.58, a methylene carbon is also present from HSQC correlations to two protons (see Figure 3.17A).
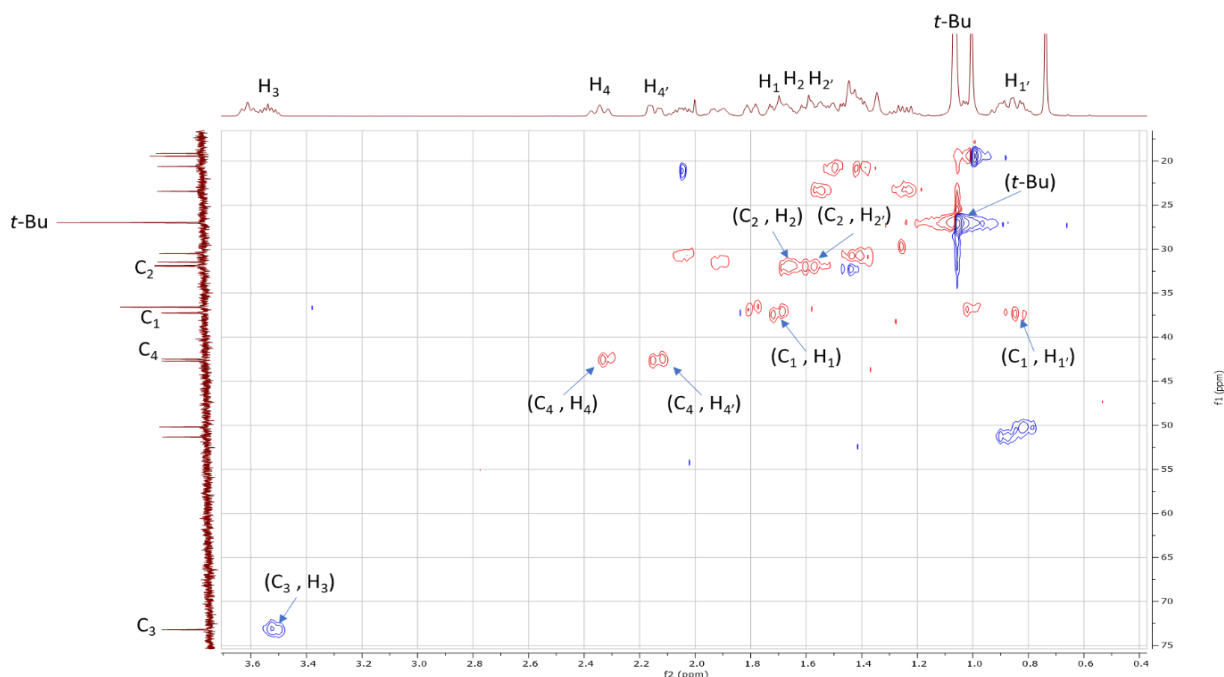
Figure 3.18A ^{1}H-^{13}C HSQC Correlations in A ring for DHEA C_{17} OH PG (3)
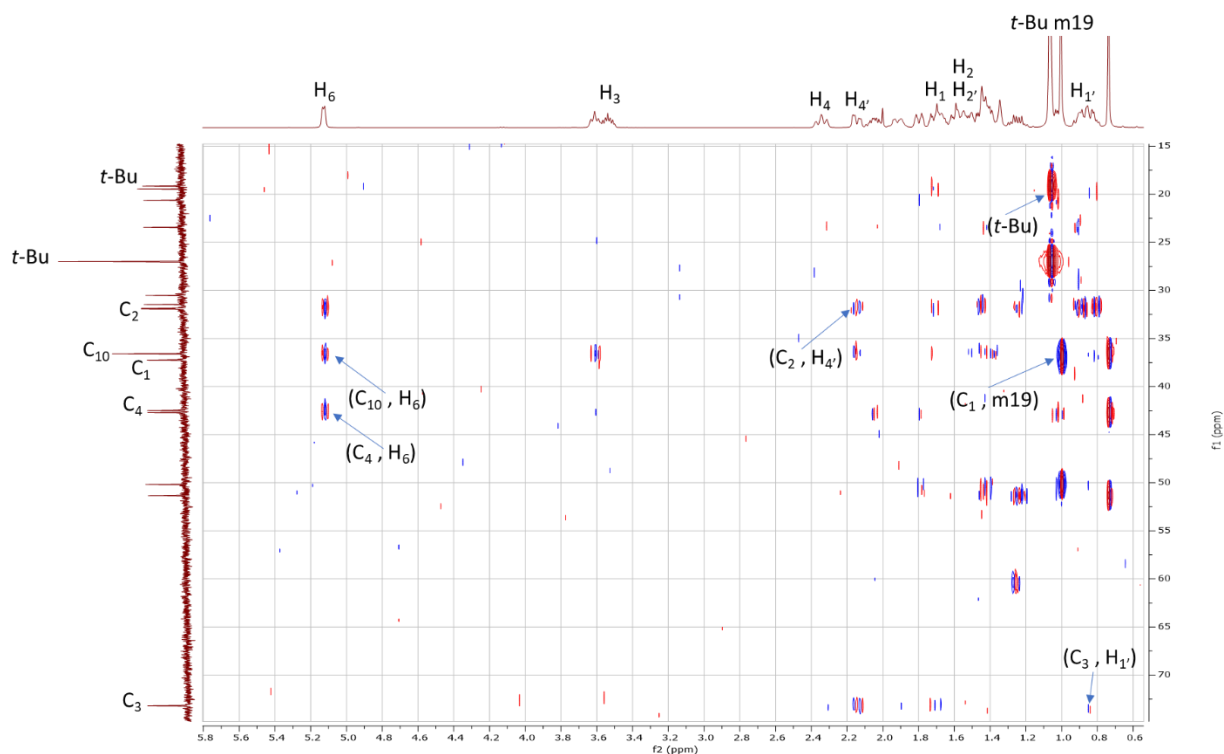
Figure 3.18B ^{1}H-^{13}C HMBC Correlations in A ring for DHEA C$_{17}$ OH PG (3)

Continuing with the A ring, δ_H 3.53 (H$_3$) exhibited HSQC correlation to δ_C 73.19 (C$_3$) (see

Figure 3.18A). Methylene protons, δ_H 2.34 (H$_4$) and δ_H 2.15 (H$_{4'}$), displayed HSQC correlation to

δ_C 42.49 (C$_4$), which shows HMBC correlation to H$_6$ (δ_H 5.13) (see Figure 3.18A and 3.18B).

Diastereotopic protons, δ_H 1.70 (H$_2$) and δ_H 1.55 (H$_{2'}$), displayed HSQC correlation to δ_C 31.87

(C$_2$), which showed HMBC correlation to H$_{4'}$ (δ_H 2.15) (see Figure 3.18A and 3.18B). δ_C 37.25 (C$_1$)

was discerned from HMBC correlation to m19 (δ_H 1.00) (see Figure 3.18B). From there, methylene

protons, δ_H 1.70 (H$_1$) and δ_H 0.87 (H$_{1'}$) displayed HSQC correlation to δ_C 37.25 (C$_1$) and HMBC

correlation to δ_C 73.19 (C$_3$) (see Figure 3.18A and 3.18B). The *tert*-butyl (*t*-Bu) protons of TBDPS

were recognized based as the δ_H 1.06 singlet, which integrated to nine (see Figure 3.14B). In

addition, δ_C 27.01 (*t*-Bu) displayed HSQC correlation to δ_H 1.06 (*t*-Bu) (see Figure 3.18A). δ_C 19.17

(*t*-Bu) displayed HMBC correlation to δ_H 1.06 (*t*-Bu) (see Figure 3.18B).

Figure 3.19A ^{1}H-^{13}C HSQC Correlations in C ring for DHEA C_{17} OH PG (3)
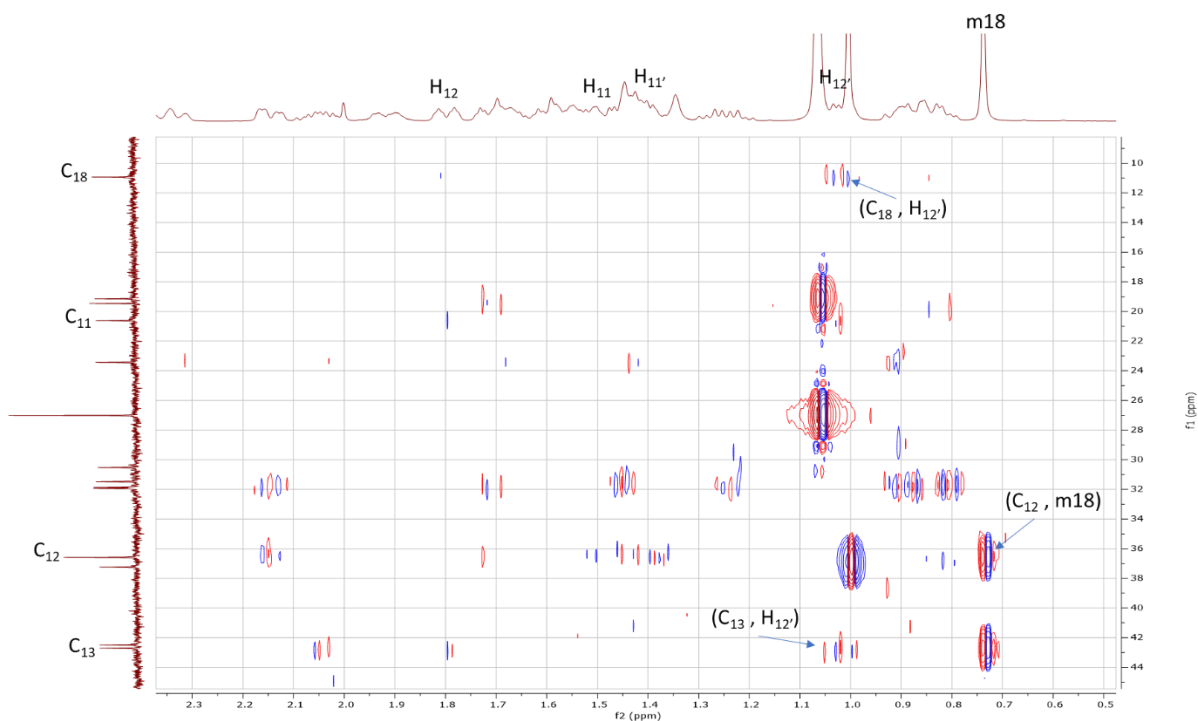
Figure 3.19B ^{1}H-^{13}C HMBC Correlations in C ring for DHEA C_{17} OH PG (3)

Concluding with the C ring, δ_C 36.58 (C_{12}) displayed HMBC correlations to m18 (δ_H 0.74) (see Figure 3.19B). δ_H 1.80 (H_{12}) and δ_H 1.03 ($H_{12'}$) were discerned from HSQC correlations to δ_C

36.58 (C_{12}) and HMBC correlations to C_{13} (δ_C 42.71) and C_{18} (δ_C 10.94) (see Figure 3.19A and 3.19B). The remaining δ_C 20.62 (C_{11}) displayed HSQC correlation to δ_H 1.55 (H_{11}) and δ_H 1.43 ($H_{11'}$) (see Figure 3.19A), thus completing full assignment of DHEA C17 OH PG (**3**).
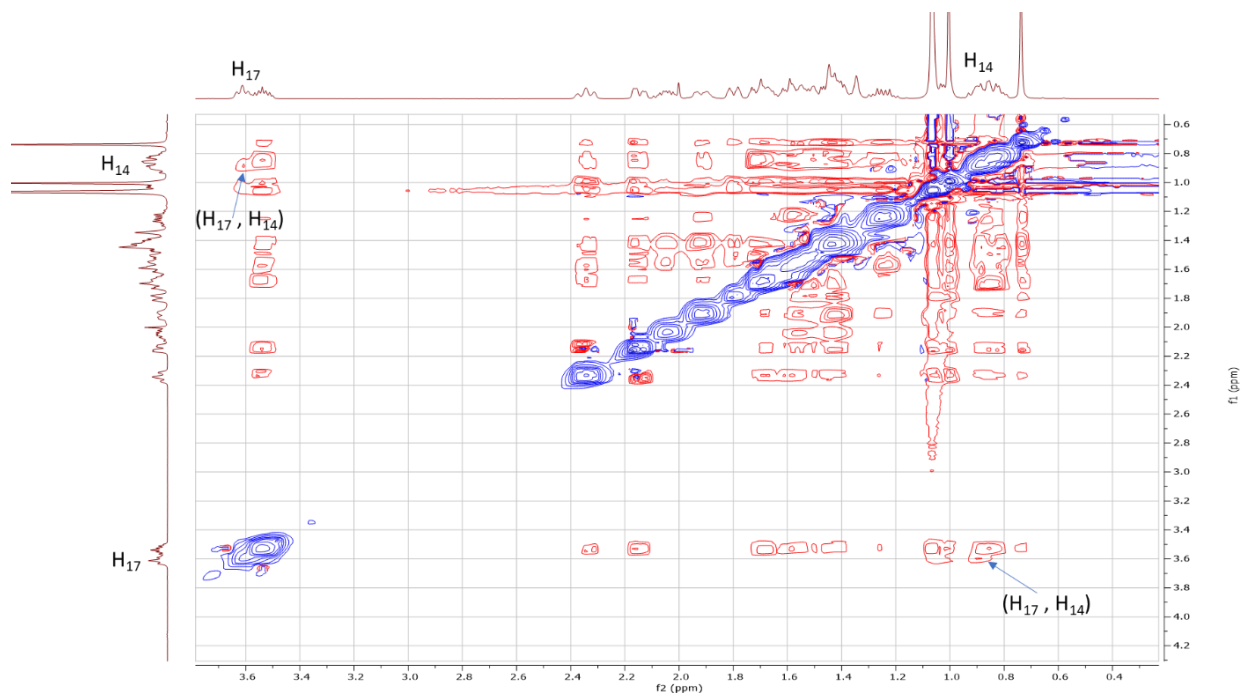
Figure 3.20 ^{1}H-^{1}H NOESY Correlations for DHEA C_{17} OH PG (3)

The stereochemistry of the hydroxyl group at C_{17} is "S" based on NOESY correlation between δ_H 3.61 (H_{17}) and δ_H 0.94 (H_{14}) (see Figure 3.20).
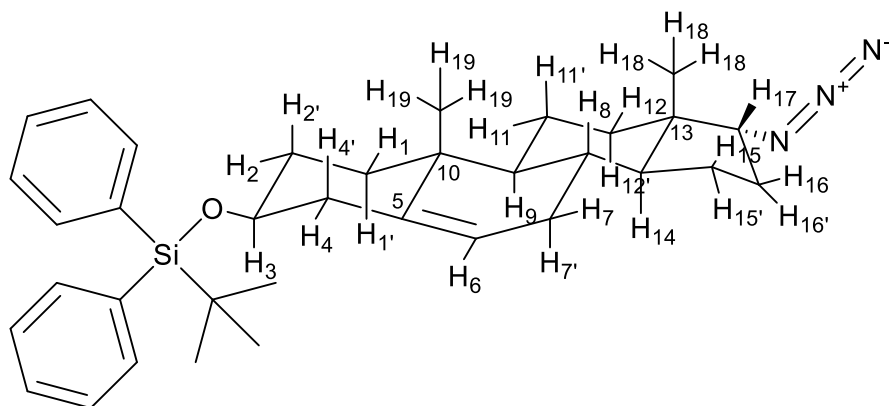
Figure 3.21A Chair Conformation for 4
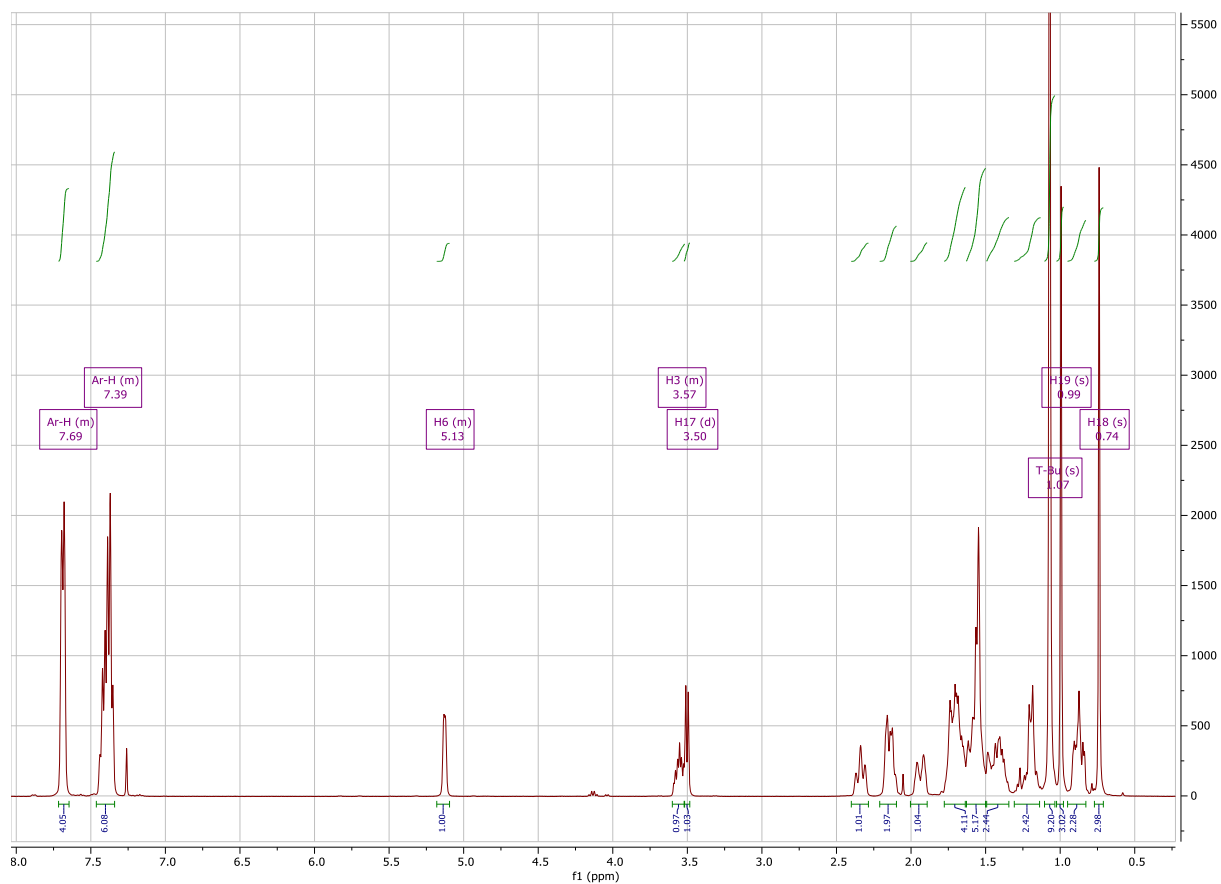
Figure 3.21B ^{1}H Spectrum of DHEA C$_{17}$-(R)-N$_3$ PG (4)

Aromatic protons of the TBDPS group were identified at δ$_H$ 7.39 and δ$_H$ 7.69 based upon chemical shift (see Figure 3.21B). δ$_H$ 5.13, δ$_H$ 3.50, and δ$_H$ 3.57 were identified as H$_6$, H$_{17}$, and

H$_3$ respectively based upon chemical shift and splitting (see Figure 3.21B). The methyl protons on C$_{18}$ and C$_{19}$ could be identified at either δ$_H$ 0.99 or δ$_H$ 0.74 (see Figure 3.21B). The latter assignments for H$_3$, H$_6$, H$_{17}$, H$_{18}$, and H$_{19}$ matched previous ^{1}H assignments (Blanco et al., 2014), (Kiss et al., 2018).
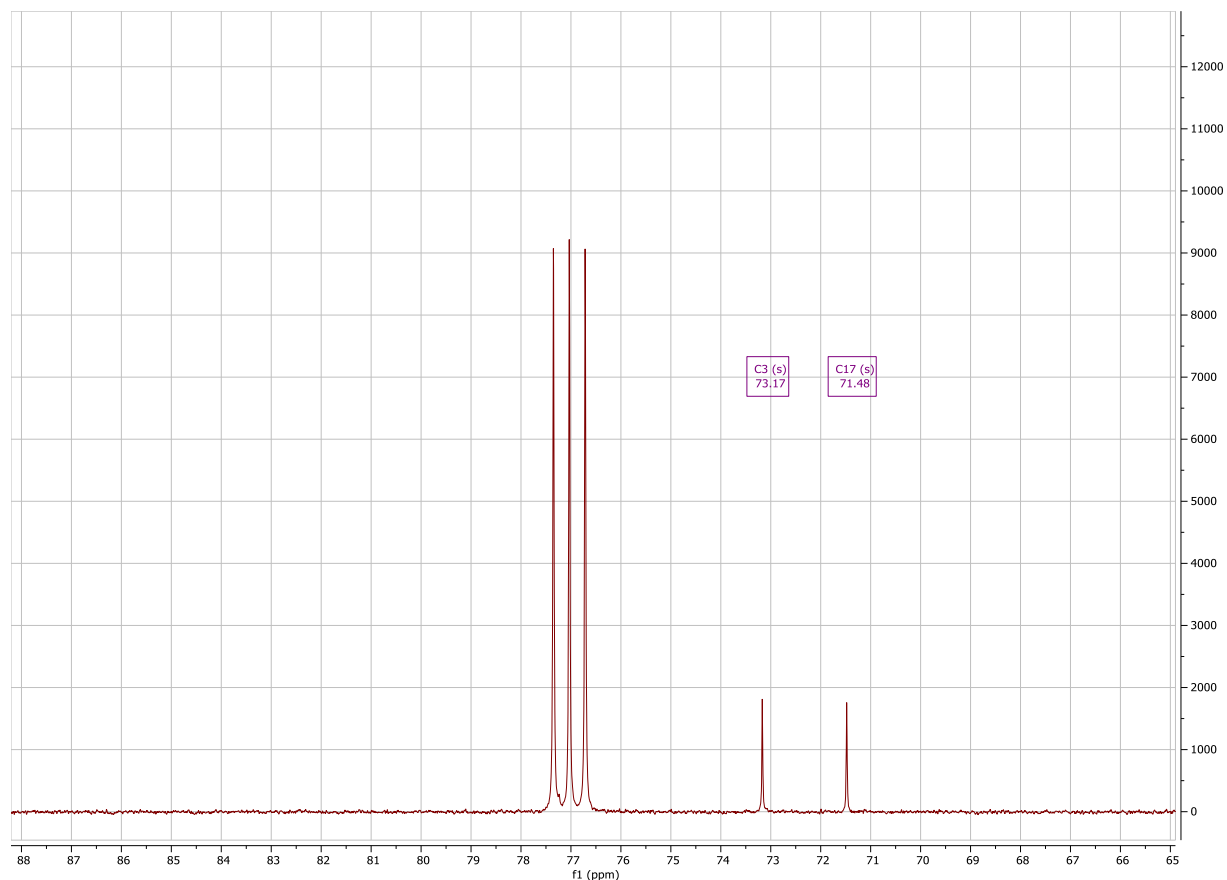
Figure 3.21C ^{13}C Spectrum of DHEA C$_{17}$-(R)-N$_3$ PG (4)

The loss of δ$_C$ 81.91 (C$_{17}$, **3**) and gain of δ$_C$ 71.48 (C$_{17}$, **4**) indicates the substitution of the hydroxyl group from a Mitsunobu reaction to an azide group based on DHEA C$_{17}$ OH PG (**3**) (see Figure 3.21C). δ$_C$ 73.17 was identified as C$_3$ based on chemical shift and previous characterization of C$_3$ for DHEA C$_{17}$ OH PG (**3**) (see Figure 3.21C).
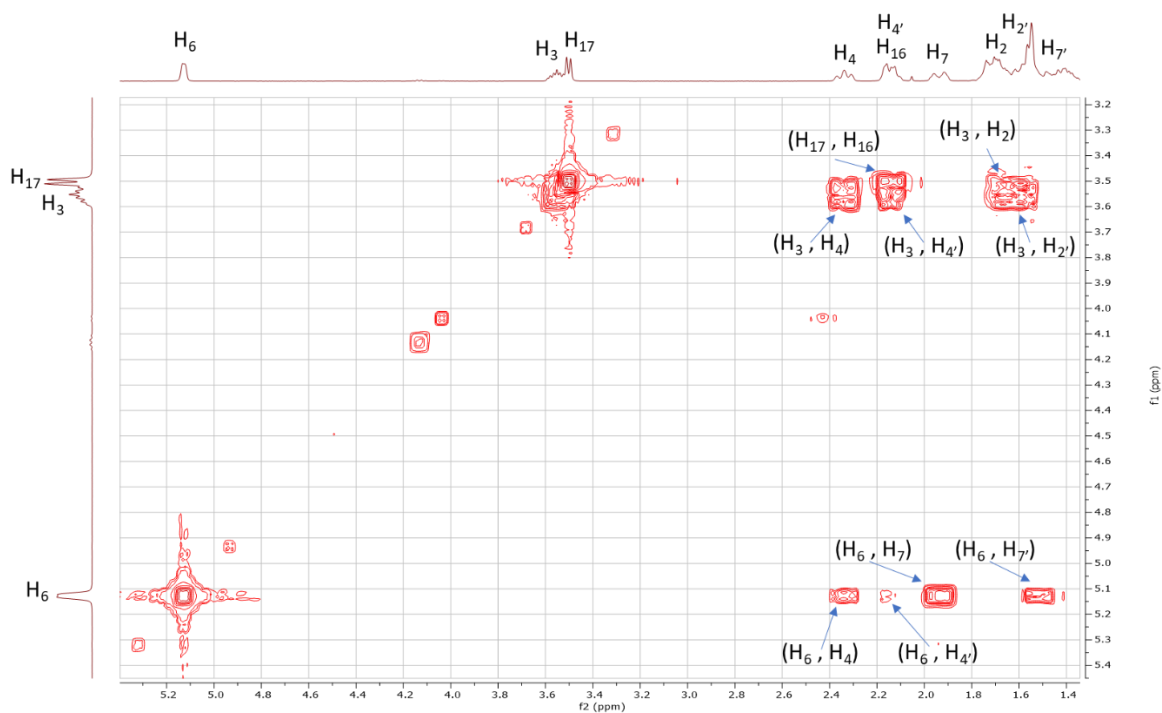
Figure 3.22 Initial ^1H-^1H COSY Correlations for DHEA C_{17}-(R)-N_3 PG (4)

Diastereotopic protons, δ_H 2.34 (H_4) and δ_H 2.15 ($H_{4'}$), from the A ring were identified from COSY correlations with H_3 (δ_H 3.57) and H_6 (δ_H 5.13) (see Figure 3.22). Methylene protons, δ_H 1.70 (H_2) and δ_H 1.56 ($H_{2'}$), were discerned from COSY correlations with H_3 (δ_H 3.57) (see Figure 3.22). In addition, diastereotopic protons δ_H 1.95 (H_7) and δ_H 1.56 ($H_{7'}$) in the B ring were identified from COSY correlations with H_6 (δ_H 5.13) (see Figure 3.22). In the D ring, one of the diastereotopic protons δ_H 2.15 (H_{16}) was discerned from COSY correlations with H_{17} (δ_H 3.50) (see Figure 3.22).
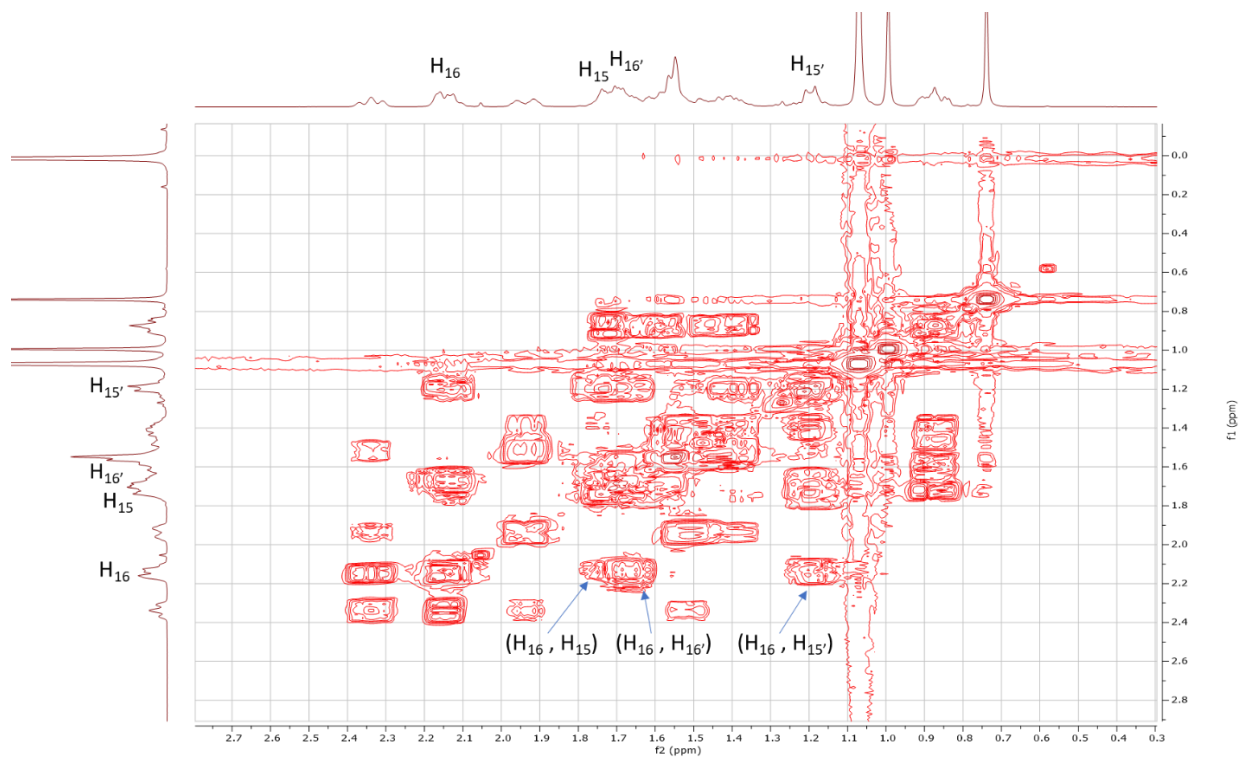
Figure 3.23A ^{1}H-^{1}H COSY Correlations in D ring for DHEA C$_{17}$-(R)-N$_3$ PG (4)
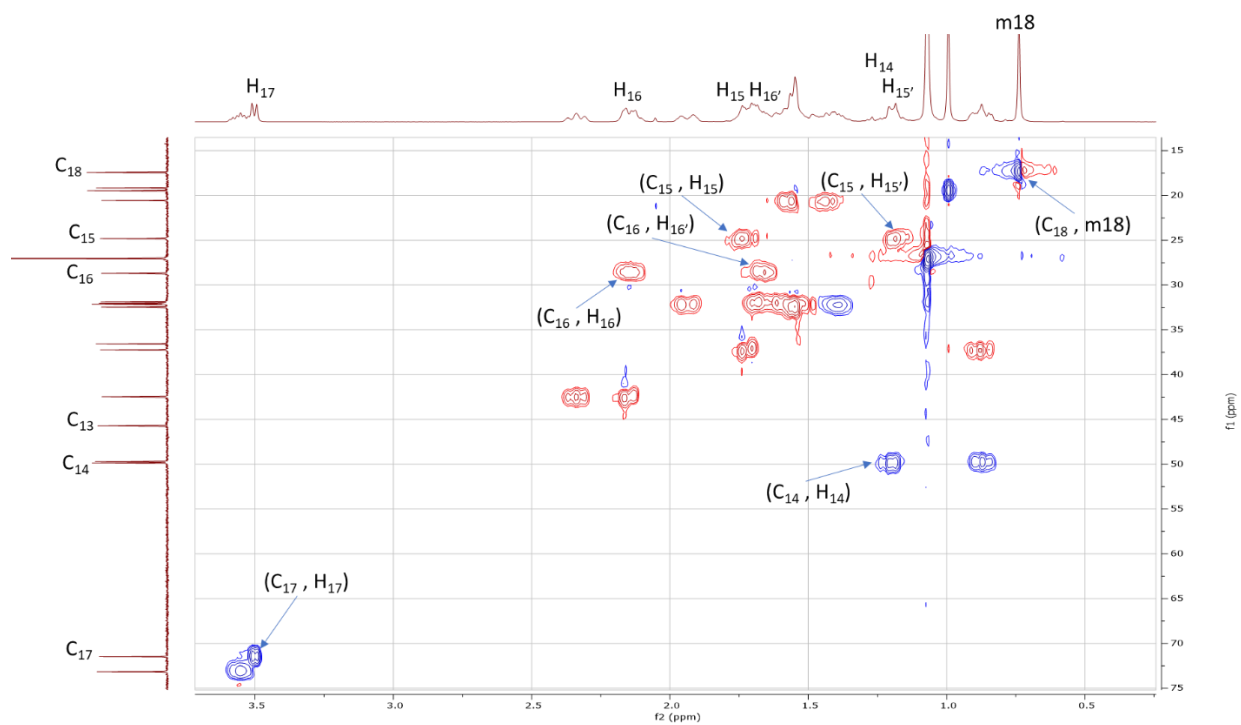
Figure 3.23B ^{1}H-^{13}C HSQC Correlations in D ring for DHEA C$_{17}$-(R)-N$_3$ PG (4)
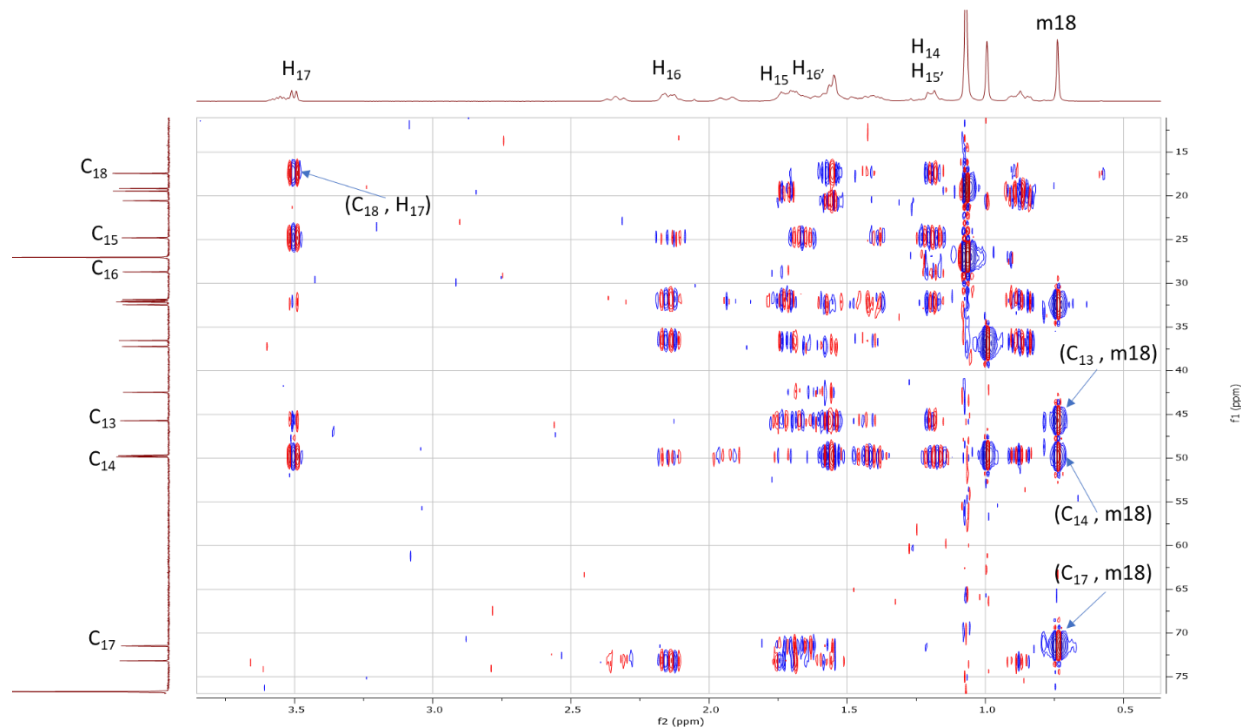
Figure 3.23C ^{1}H-^{13}C HMBC Correlations in D ring for DHEA C$_{17}$-(R)-N$_3$ PG (4)

Starting with the D ring, δ_C 71.48 was identified as C$_{17}$ from the HSQC correlation with δ_H 3.50 (H$_{17}$) and HMBC correlations to m18 (δ_H 0.74), the methyl protons on C$_{18}$ (see Figure 3.23B and 3.23C). One of the methylene protons, δ_H 2.15 (H$_{16}$), was correlated by HSQC to δ_C 28.70 (C$_{16}$) (see Figure 3.23B). From there, δ_H 1.70 (H$_{16'}$) was identified by HSQC correlation to δ_C 28.70 (C$_{16}$) and COSY correlation to δ_H 2.15 (H$_{16}$) (see Figure 3.23A and 3.23B). Next, diastereotopic proton, δ_H 1.21 (H$_{15'}$), was discerned from COSY correlation to H$_{16}$ (δ_H 2.15) (see Figure 3.23A). Next, δ_H 1.21 (H$_{15'}$) showed HSQC correlation to δ_C 24.81 (C$_{15}$) (see Figure 3.23B). H$_{15}$ (δ_H 1.73) was then identified by HSQC correlation to C$_{15}$ (δ_C 24.81) and COSY correlation to δ_H 2.15 (H$_{16}$) (see Figure 3.23A and 3.23B). C$_{14}$ (δ_C 49.85) was identified by HMBC correlation to m18 (δ_H 0.74) (see Figure 3.23C). H$_{14}$ (δ_H 1.21) was distinguished based on HSQC correlation to C$_{14}$ (δ_C 49.85) (see Figure 3.23B). Continuing with m18, δ_C 17.43 (C$_{18}$) was identified from HSQC correlation to m18 and HMBC correlation to δ_H 3.50 (H$_{17}$) (see Figure 3.23B and 3.23C). Therefore, the methyl protons on C$_{19}$, m19, could be identified at δ_H 0.99 based on integration and splitting (see Figure

107

3.21B). Quaternary carbon, δ_C 45.71 (C_{13}), was discerned from HMBC correlation to m18 (δ_H 0.74) and no observable HSQC correlation (see Figure 3.23B and 3.23C).

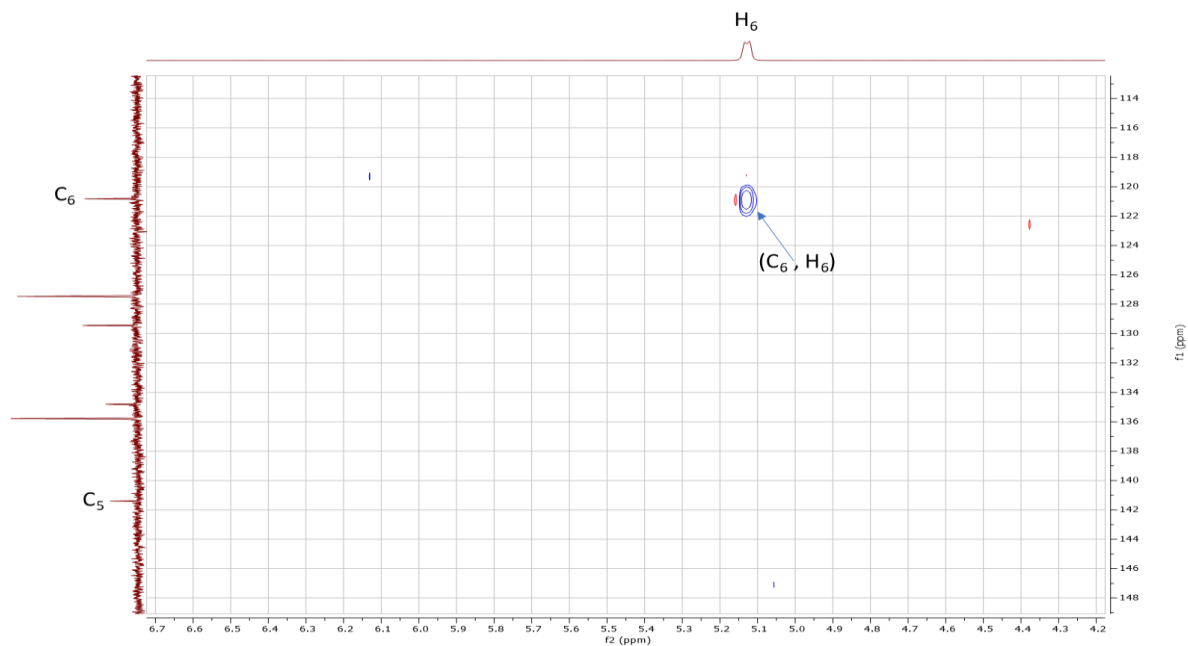**Figure 3.24A ^{1}H-^{13}C HSQC Correlations in B ring for DHEA C_{17}-(R)-N$_3$ PG (4)**

Figure 3.24B ^{1}H-^{13}C HSQC Correlations in B ring for DHEA C_{17}-(R)-N$_3$ PG (4) (C_5-C_6)

Figure 3.24C ^{1}H-^{13}C HMBC Correlations in B ring for DHEA C$_{17}$-(R)-N$_3$ PG (4)
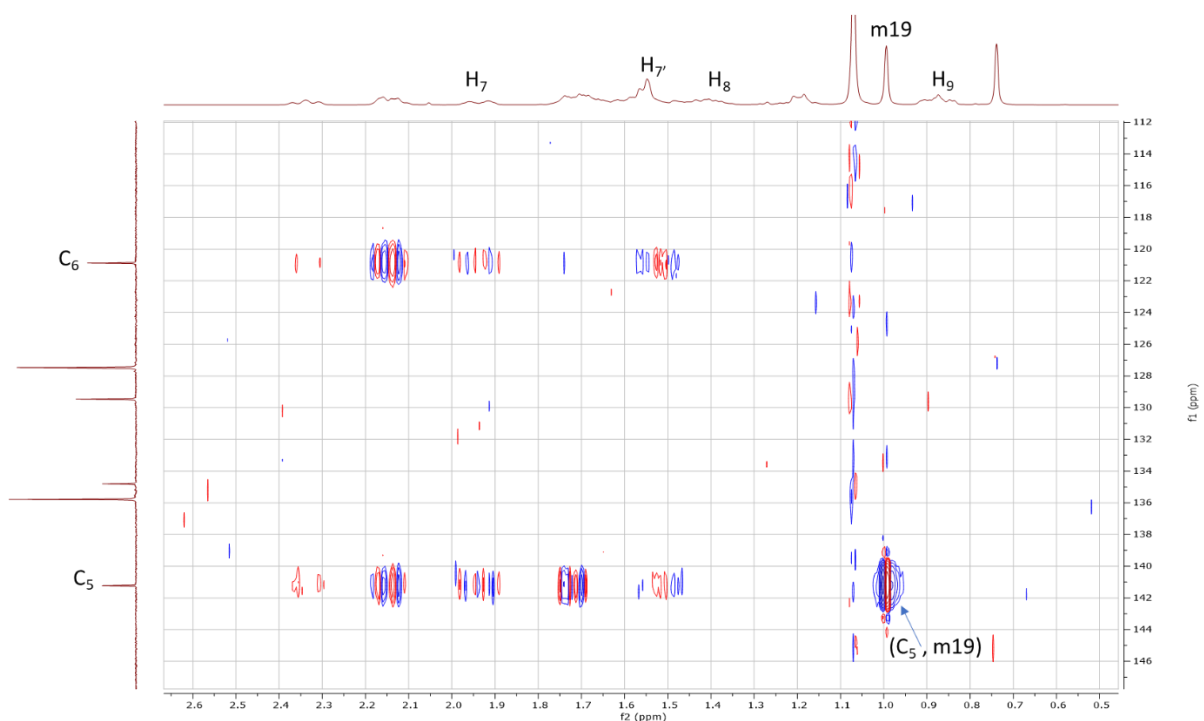
Figure 3.24D ^{1}H-^{13}C HMBC Correlations in B ring for DHEA C$_{17}$-(R)-N$_3$ PG (4) (C$_5$-C$_6$)

Next with the B ring, methyl protons, m19 (δ_H 0.99) exhibited HSQC correlation to δ_C 19.46 (C$_{19}$) (see Figure 3.24A). δ_C 141.22 (C$_5$) was determined on the basis of no HSQC correlation,

chemical shift, and HMBC correlation to m19 (δ_H 0.99) (see Figure 3.24B and 3.24D). Vinyl carbon, C_6 (δ_C 120.88) was correlated by HSQC to δ_H 5.13 (H_6) (see Figure 3.24B). Methylene protons, δ_H 1.95 (H_7) and δ_H 1.56 ($H_{7'}$), exhibited HSQC correlation to δ_C 32.14 (C_7) (see Figure 3.24A). C_8 (δ_C 32.05) was correlated by HMBC to δ_H 1.56 ($H_{7'}$) (see Figure 3.24C). Methine proton, H_8, was discerned at δ_H 1.42 based on HMBC correlation to C_{15} (δ_C 24.81) and HSQC correlation to C_8 (δ_C 32.05) (see Figure 3.24A and 3.24C). The remaining methine proton, H_9 (δ_H 0.87), displayed correlation by HSQC to δ_C 49.71 (C_9) and by HMBC to δ_C 19.46 (C_{19}) (see Figure 3.24A and 3.24C). Quaternary carbon, C_{10} (δ_C 36.56), was assigned based on HMBC correlation to H_6 (δ_H 5.13) along with m19 (δ_H 0.99) and no HSQC correlation (see Figure 3.24B and 3.24C).
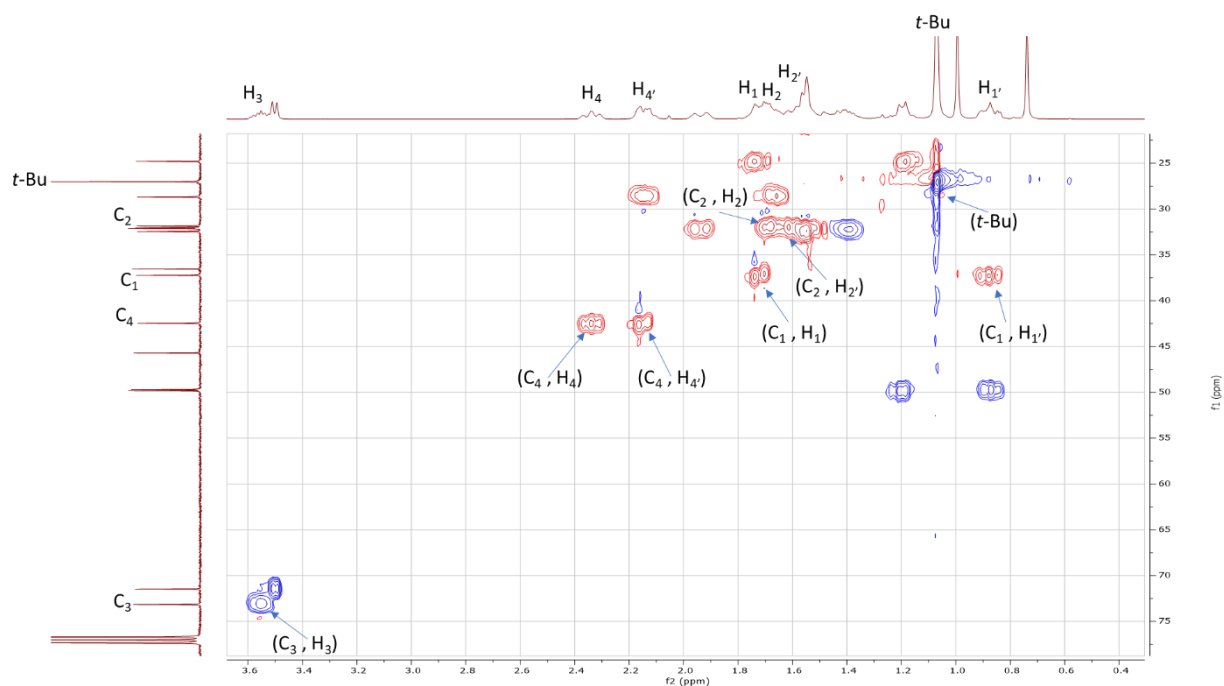
Figure 3.25A ^{1}H-^{13}C HSQC Correlations in A ring for DHEA C_{17}-(R)-N_3 PG (4)
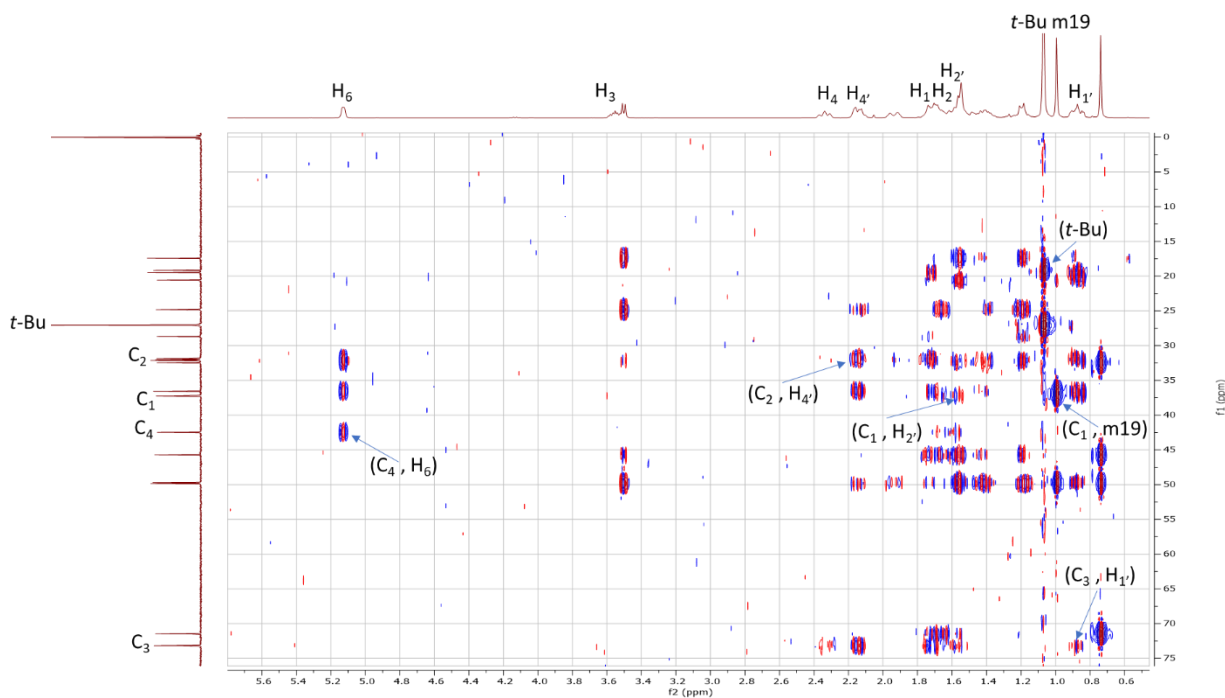
Figure 3.25B ^{1}H-^{13}C HMBC Correlations in A ring for DHEA C$_{17}$-(R)-N$_3$ PG (4)

Continuing with the A ring, δ_H 3.57 (H$_3$) exhibited HSQC correlation to δ_C 73.17 (C$_3$) (see Figure 3.25A). Methylene protons, δ_H 2.34 (H$_4$) and δ_H 2.15 (H$_{4'}$), displayed HSQC correlation to δ_C 42.47 (C$_4$), which shows HMBC correlation to H$_6$ (δ_H 5.13) (see Figure 3.25A and 3.25B). Diastereotopic protons, δ_H 1.70 (H$_2$) and δ_H 1.56 (H$_{2'}$), displayed HSQC correlation to δ_C 31.87 (C$_2$), which showed HMBC correlation to H$_{4'}$ (δ_H 2.15) (see Figure 3.25A and 3.25B). δ_C 37.24 (C$_1$) was discerned from HMBC correlation to m19 (δ_H 0.99) and H$_{2'}$ (δ_H 1.56) (see Figure 3.25B). From there, methylene protons, δ_H 1.70 (H$_1$) and δ_H 0.87 (H$_{1'}$) displayed HSQC correlation to δ_C 37.24 (C$_1$) and HMBC correlation to δ_C 73.17 (C$_3$) (see Figure 3.25A 3.25B). The *tert*-butyl (*t*-Bu) protons of TBDPS were recognized based as the δ_H 1.07 singlet, which integrated to nine (see Figure 3.21B). In addition, δ_C 27.03 (*t*-Bu) displayed HSQC correlation to δ_H 1.07 (*t*-Bu) (see Figure 3.25A). δ_C 19.16 (*t*-Bu) displayed HMBC correlation to δ_H 1.07 (*t*-Bu) (see Figure 3.25B).
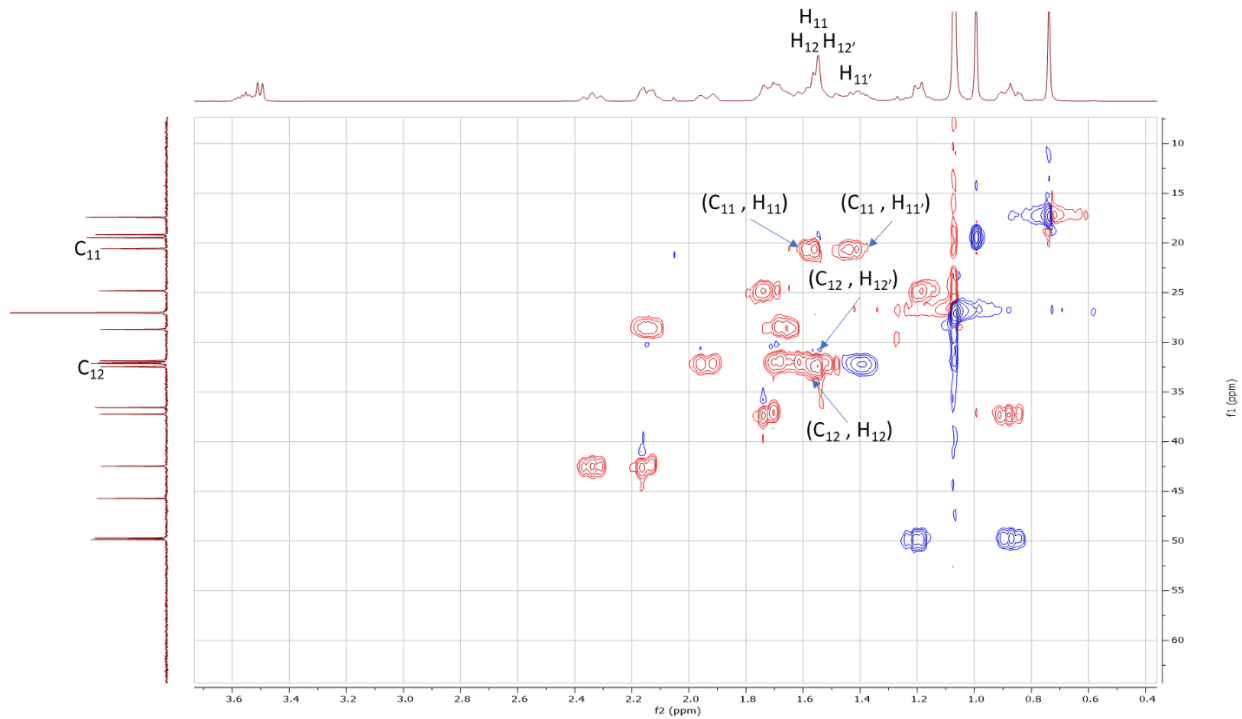
Figure 3.26A ^{1}H-^{13}C HSQC Correlations in C ring for DHEA C$_{17}$-(R)-N$_3$ PG (4)
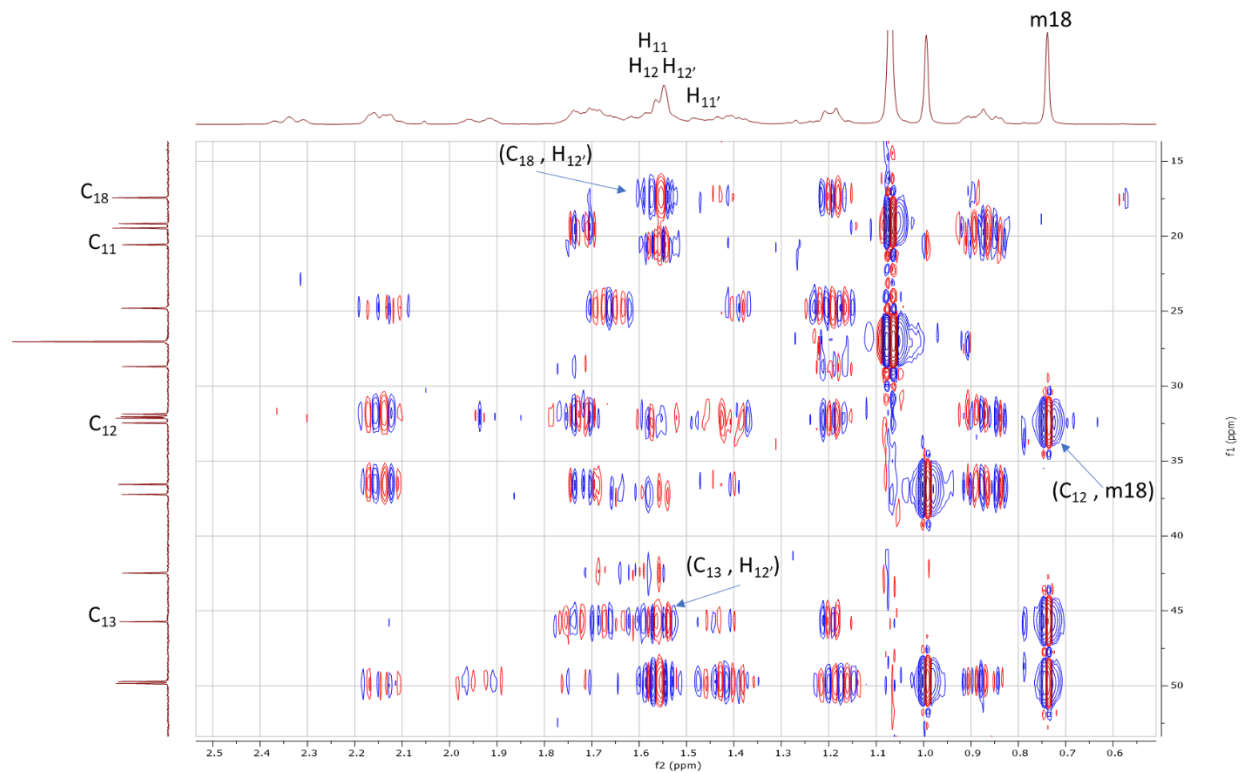
Figure 3.26B ^{1}H-^{13}C HMBC Correlations in C ring for DHEA C$_{17}$-(R)-N$_3$ PG (4)

Concluding with the C ring, δ_C 32.47 (C_{12}) displayed HMBC correlations to m18 (δ_H 0.74) (see Figure 3.26B). δ_H 1.56 (H_{12}) and δ_H 1.56 ($H_{12'}$) were discerned from HSQC correlations to δ_C 32.47 (C_{12}) and HMBC correlations to C_{13} (δ_C 45.71) and C_{18} (δ_C 17.43) (see Figure 3.26A and 3.26B). The remaining δ_C 20.57 (C_{11}) displayed HSQC correlation to δ_H 1.56 (H_{11}) and δ_H 1.42 ($H_{11'}$) (see Figure 3.26A), thus completing full assignment of DHEA C_{17}-(R)-N_3 PG (**4**).
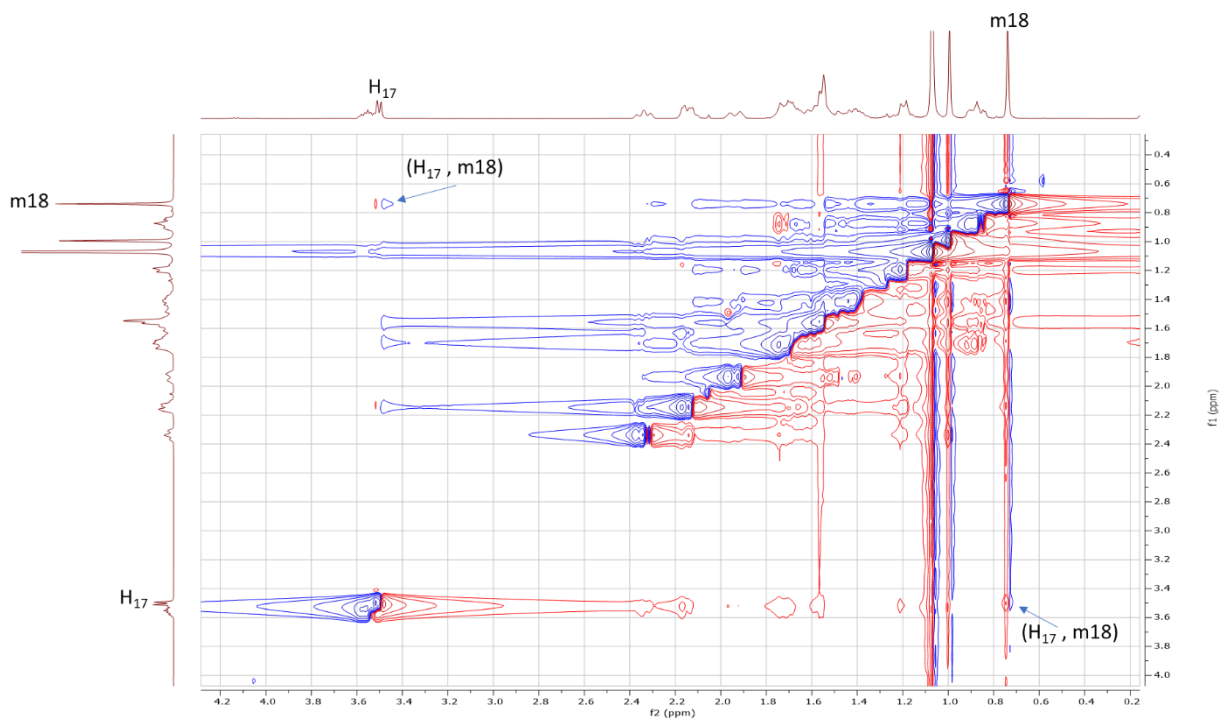
Figure 3.27 ^{1}H-^{1}H NOESY Correlations for DHEA C_{17}-(R)-N_3 PG (4)

The stereochemistry of the azide group at C_{17} is "R" based on NOESY correlation between δ_H 3.50 (H_{17}) and δ_H 0.74 (m18) (see Figure 3.27).
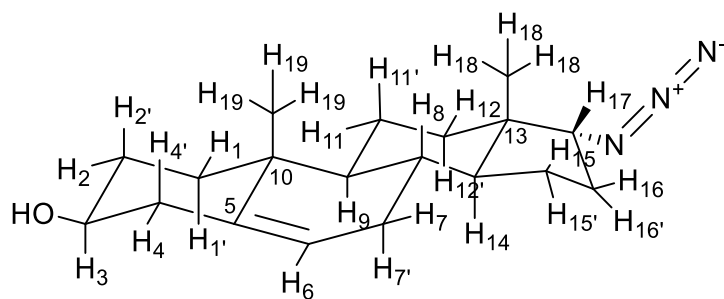
Figure 3.28A Chair Conformation for 5
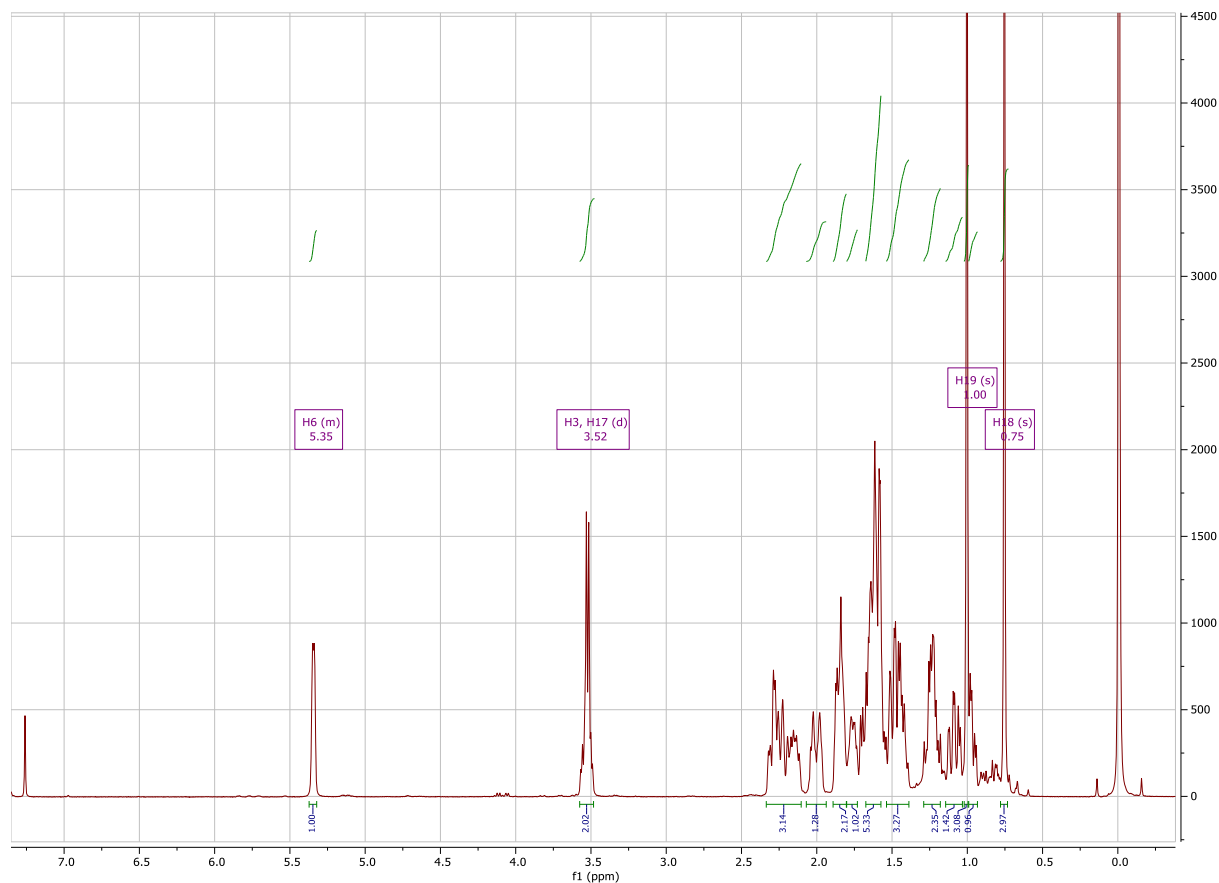
Figure 3.28B ^{1}H Spectrum of DHEA C_{17}-(R)-N_3 probe (5)

There is no presence of the TBDPS protecting group as nothing appeared from δ_H 6.5-8 (see Figure 3.28B). δ_H 5.35, δ_H 3.52, and δ_H 3.52 were identified as H_6, H_{17}, and H_3 respectively based upon chemical shift and splitting (see Figure 3.28B). The methyl protons on C_{18} and C_{19}

could be identified at either δ_H 1.00 or δ_H 0.75 (see Figure 3.28B). The latter assignments for H_3, H_6, H_{17}, H_{18}, and H_{19} matched previous ^{1}H assignments (Blanco et al., 2014), (Kiss et al., 2018).
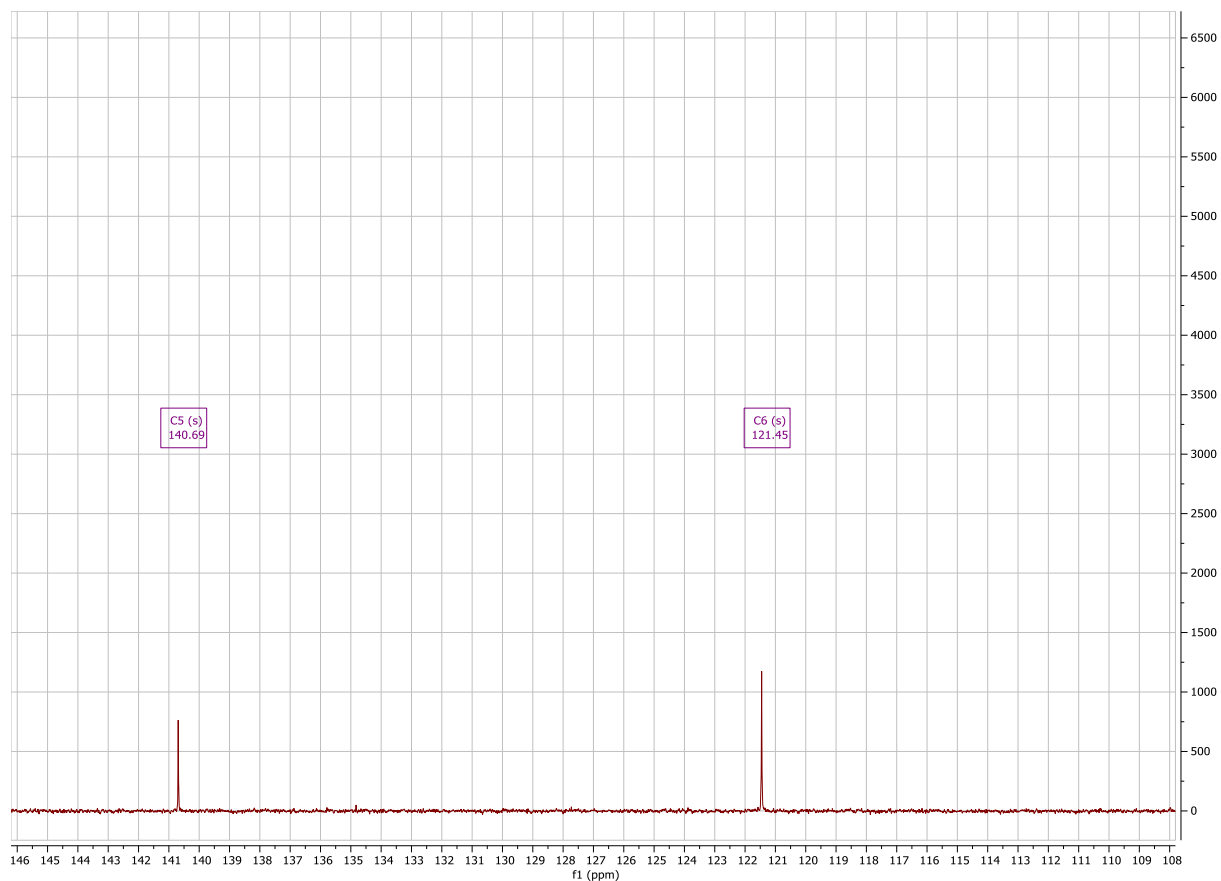
Figure 3.28C ^{13}C Spectrum of DHEA C_{17}-(R)-N_3 probe (5)

The loss of the TBDPS protecting group was shown by the reduction of peaks between δ_C 120-140 (see Figure 3.28C). In addition, δ_C 121.45 and δ_C 140.69 were identified as C_6 and C_5 based on chemical shift and peak height (see Figure 3.28C).
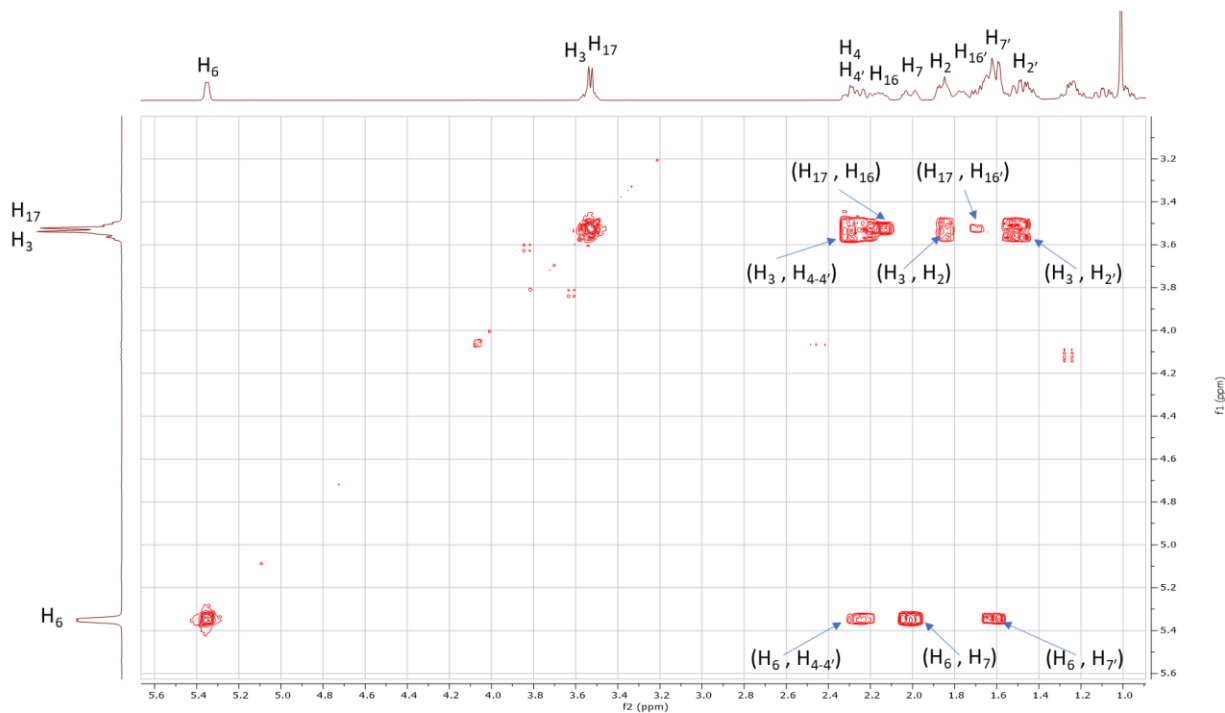
Figure 3.29 Initial ^{1}H-^{1}H COSY Correlations for DHEA C$_{17}$-(R)-N$_3$ probe (5)

Diastereotopic protons, δ_H 2.28 (H$_4$) and δ_H 2.28 (H$_{4'}$), from the A ring were identified from COSY correlations with H$_3$ (δ_H 3.52) and H$_6$ (δ_H 5.35) (see Figure 3.29). Methylene protons, δ_H 1.85 (H$_2$) and δ_H 1.45 (H$_{2'}$), were discerned from COSY correlations with H$_3$ (δ_H 3.52) (see Figure 3.29). In addition, diastereotopic protons δ_H 2.00 (H$_7$) and δ_H 1.62 (H$_{7'}$) in the B ring were identified from COSY correlations with H$_6$ (δ_H 5.35) (see Figure 3.29). In the D ring, diastereotopic protons δ_H 2.16 (H$_{16}$) and δ_H 1.62 (H$_{16'}$) were discerned from COSY correlations with H$_{17}$ (δ_H 3.52) (see Figure 3.29).
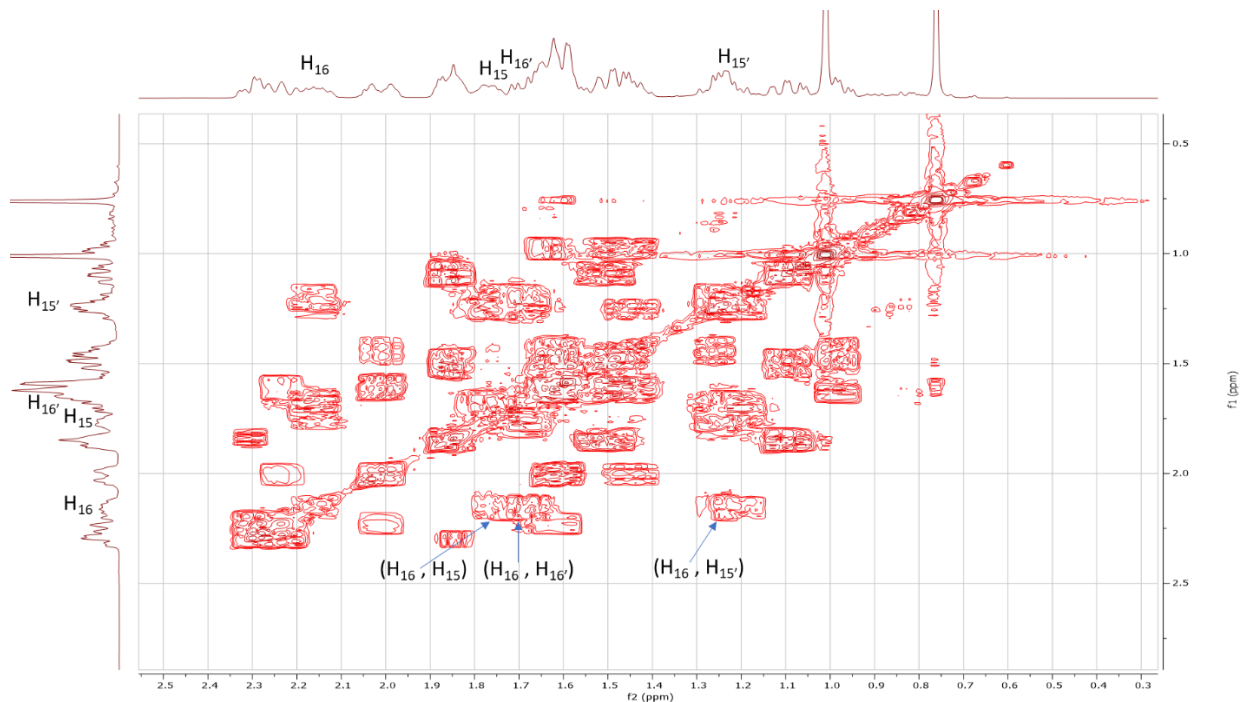
Figure 3.30A ^{1}H-^{1}H COSY Correlations in D ring for DHEA C$_{17}$-(R)-N$_3$ probe (5)
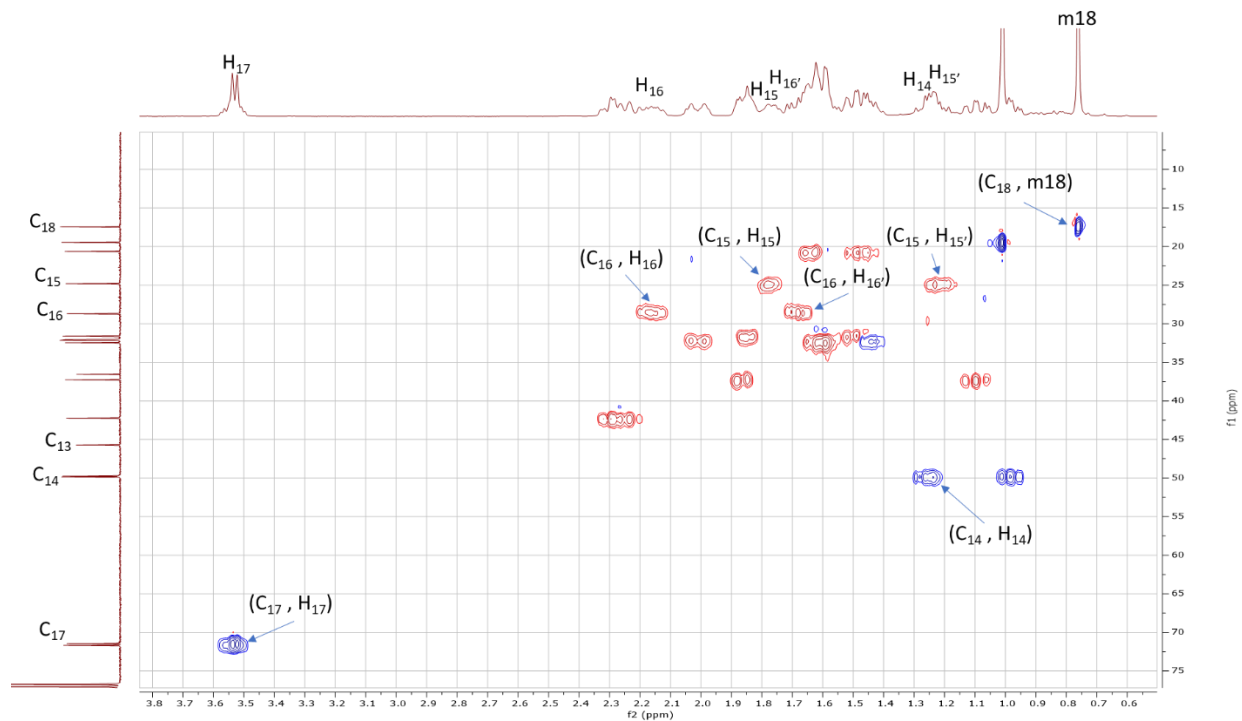
Figure 3.30B ^{1}H-^{13}C HSQC Correlations in D ring for DHEA C$_{17}$-(R)-N$_3$ probe (5)

117
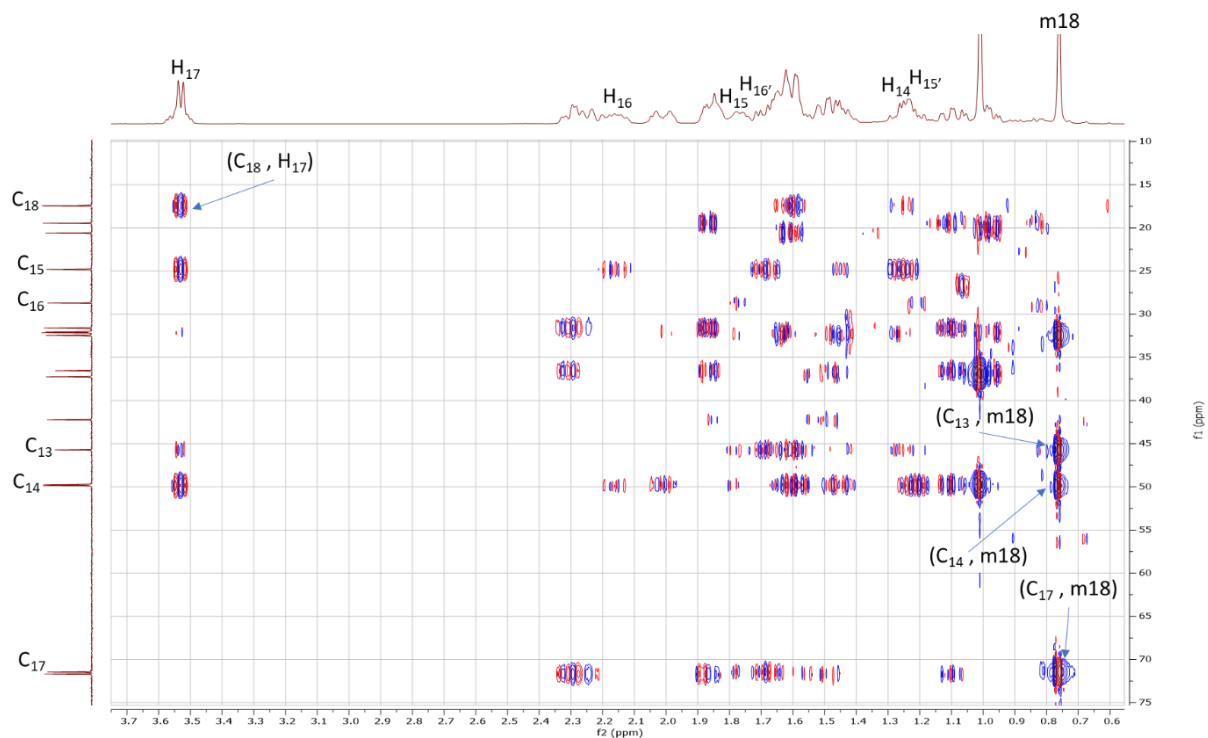
Figure 3.30C ^{1}H-^{13}C HMBC Correlations in D ring for DHEA C$_{17}$-(R)-N$_3$ probe (5)

Starting with the D ring, δ_C 71.45 was identified as C$_{17}$ from the HSQC correlation with δ_H 3.52 (H$_{17}$) and HMBC correlations to m18 (δ_H 0.75), the methyl protons on C$_{18}$ (see Figure 3.30B and 3.30C). Methylene protons, δ_H 2.16 (H$_{16}$) and δ_H 1.62 (H$_{16'}$), was correlated by HSQC to δ_C 28.71 (C$_{16}$) (see Figure 3.30B). Next, diastereotopic protons, δ_H 1.23 (H$_{15'}$) and δ_H 1.76 (H$_{15}$), was discerned from COSY correlation to H$_{16}$ (δ_H 2.16) (see Figure 3.30A). From HSQC correlation, δ_H 1.23 (H$_{15'}$) and δ_H 1.76 (H$_{15}$), showed HSQC correlation to δ_C 24.81 (C$_{15}$) (see Figure 3.30B). C$_{14}$ (δ_C 49.86) was identified by HMBC correlation to m18 (δ_H 0.75) (see Figure 3.30C). H$_{14}$ (δ_H 1.23) was distinguished based from HSQC correlation to C$_{14}$ (δ_C 49.86) (see Figure 3.30B). Methyl protons, m18 (δ_H 0.75), were discerned from HMBC correlation to C$_{17}$ (δ_C 71.45) (see Figure 3.30C). Continuing with m18, δ_C 17.44 (C$_{18}$) was identified from HSQC correlation to m18 and HMBC correlation to δ_H 3.52 (H$_{17}$) (see Figure 3.30B and 3.30C). Therefore, the methyl protons on C$_{19}$, m19, could be identified at δ_H 1.00 based on integration and splitting (see Figure 3.28B).

Quaternary carbon, δ_C 45.72 (C_{13}), was discerned from HMBC correlation to m18 (δ_H 0.75) and no observable HSQC correlation (see Figure 3.30B and 3.30C).
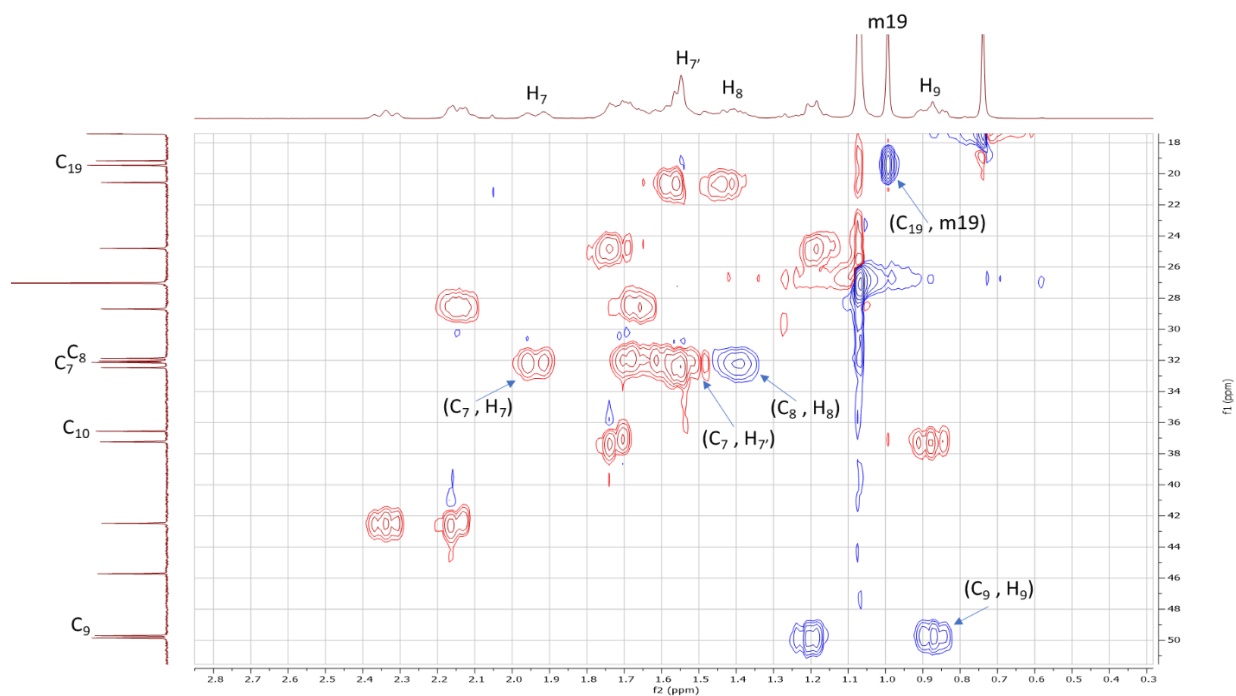

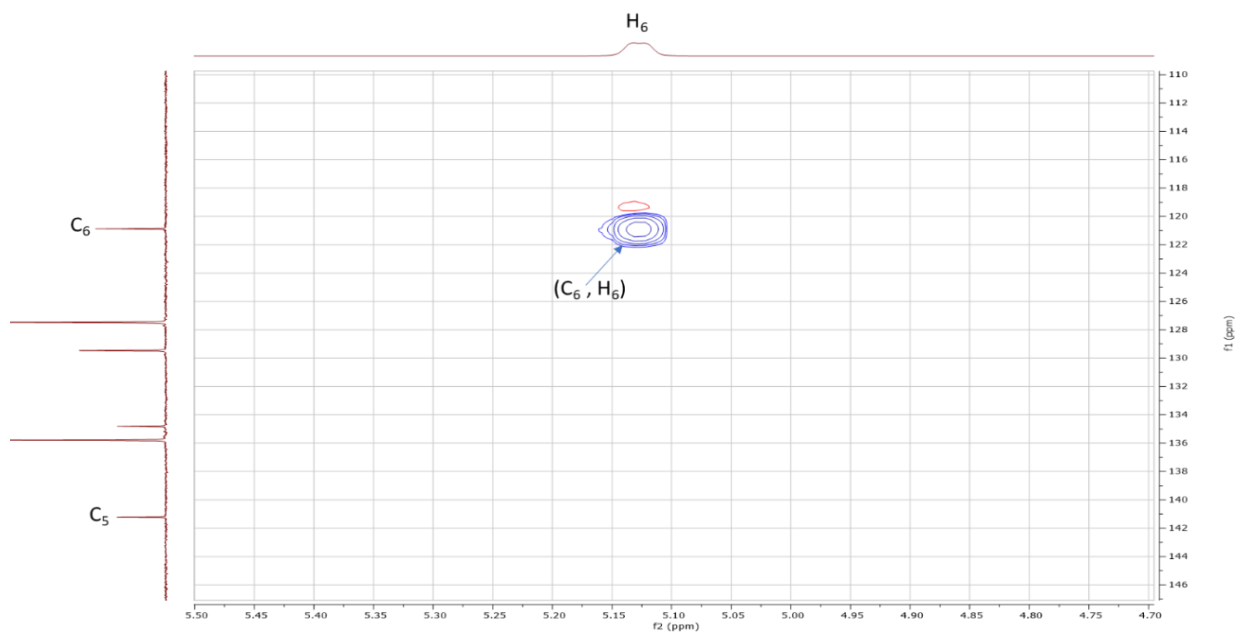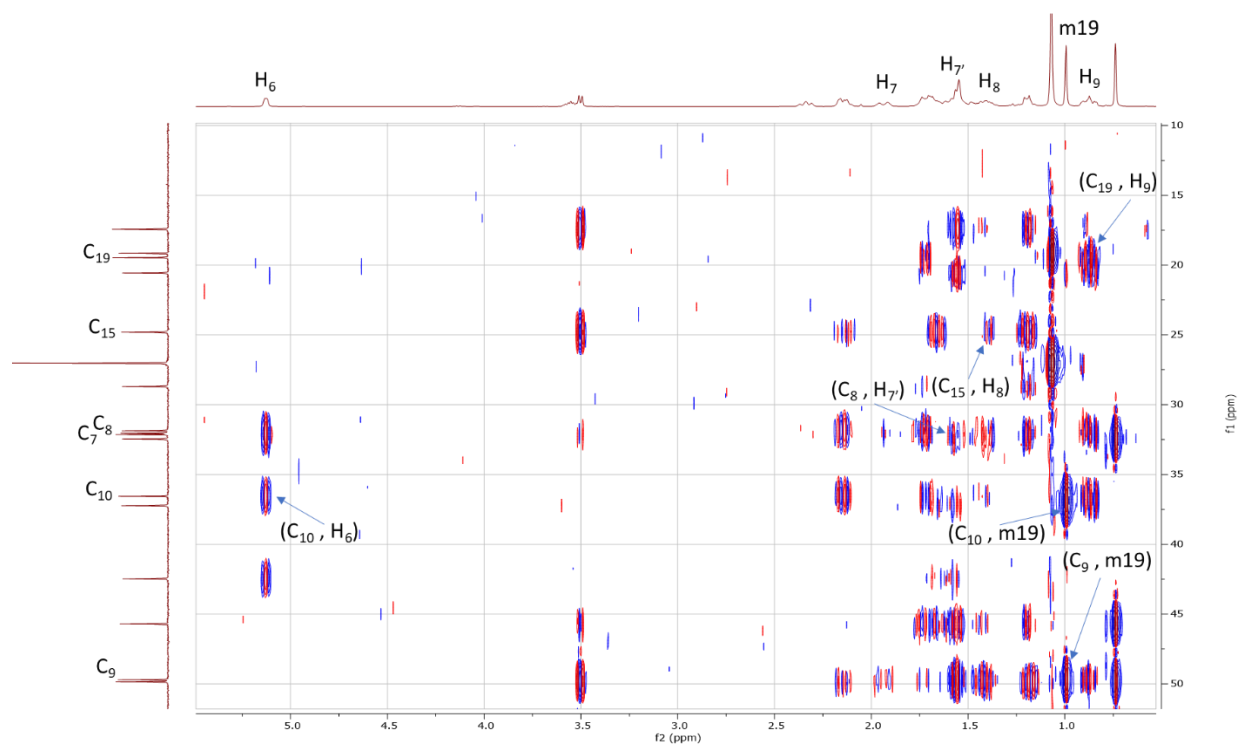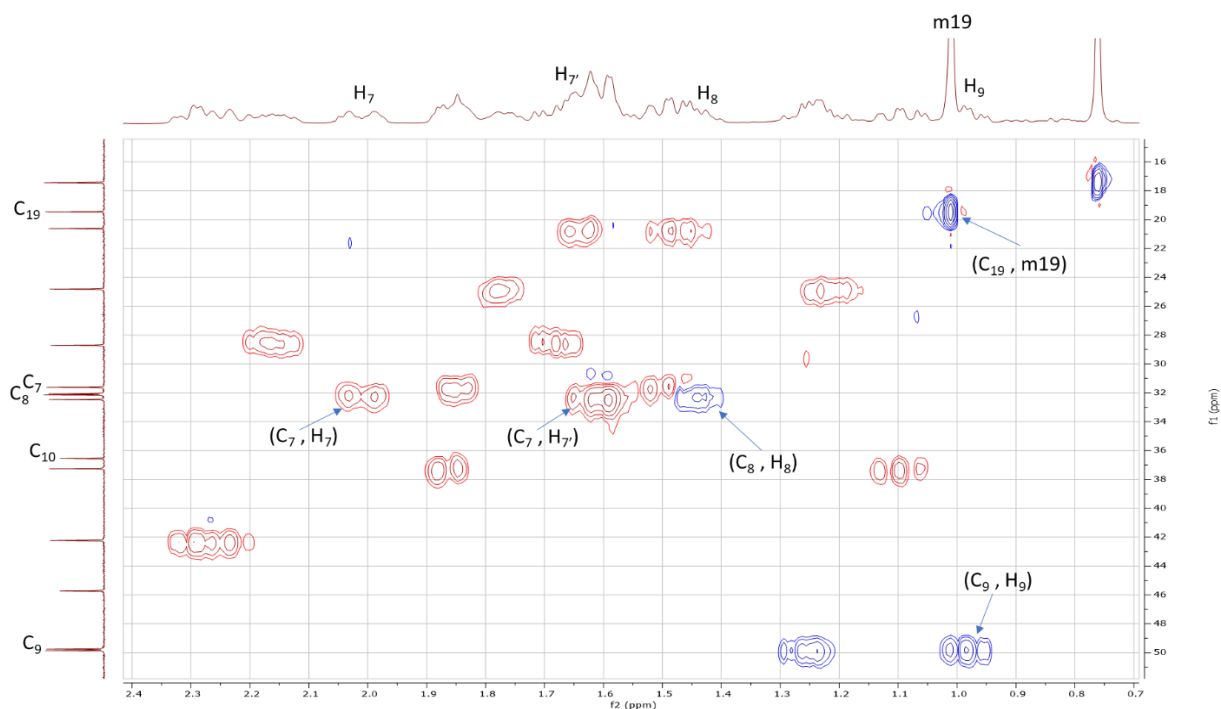**Figure 3.31A ^{1}H-^{13}C HSQC Correlations in B ring for DHEA C_{17}-(R)-N$_3$ probe (5)**
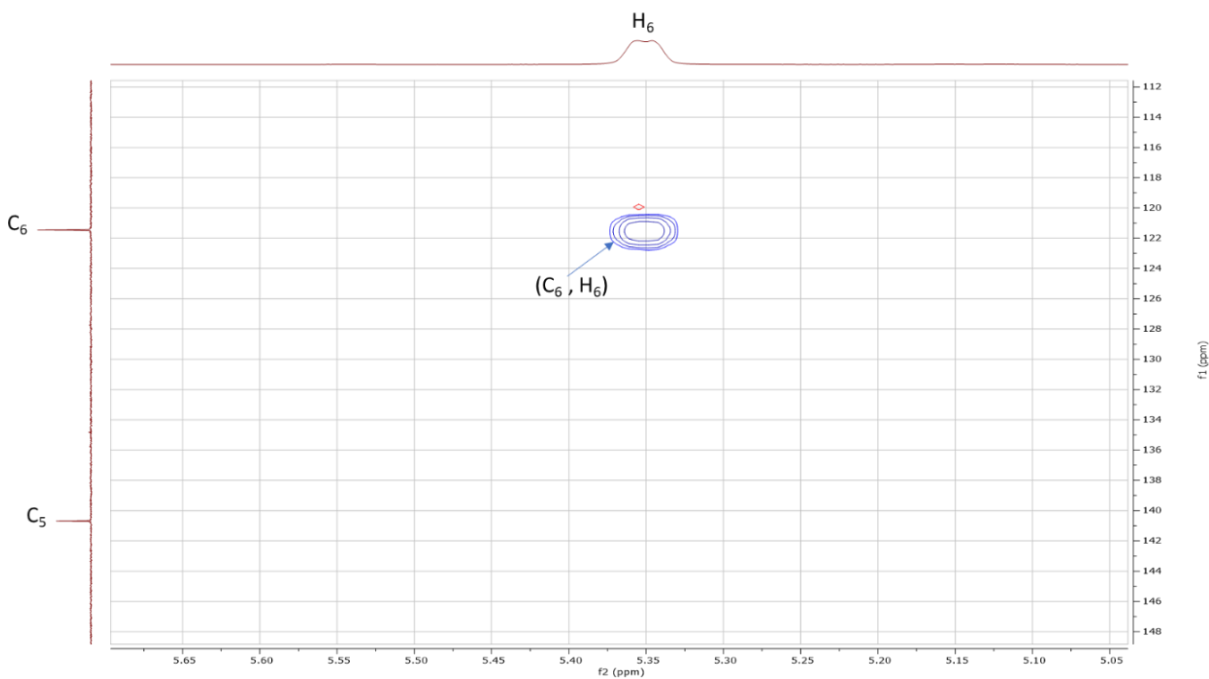
Figure 3.31B ^{1}H-^{13}C HSQC Correlations in B ring for DHEA C_{17}-(R)-N$_3$ probe (5) (C_5-C_6)
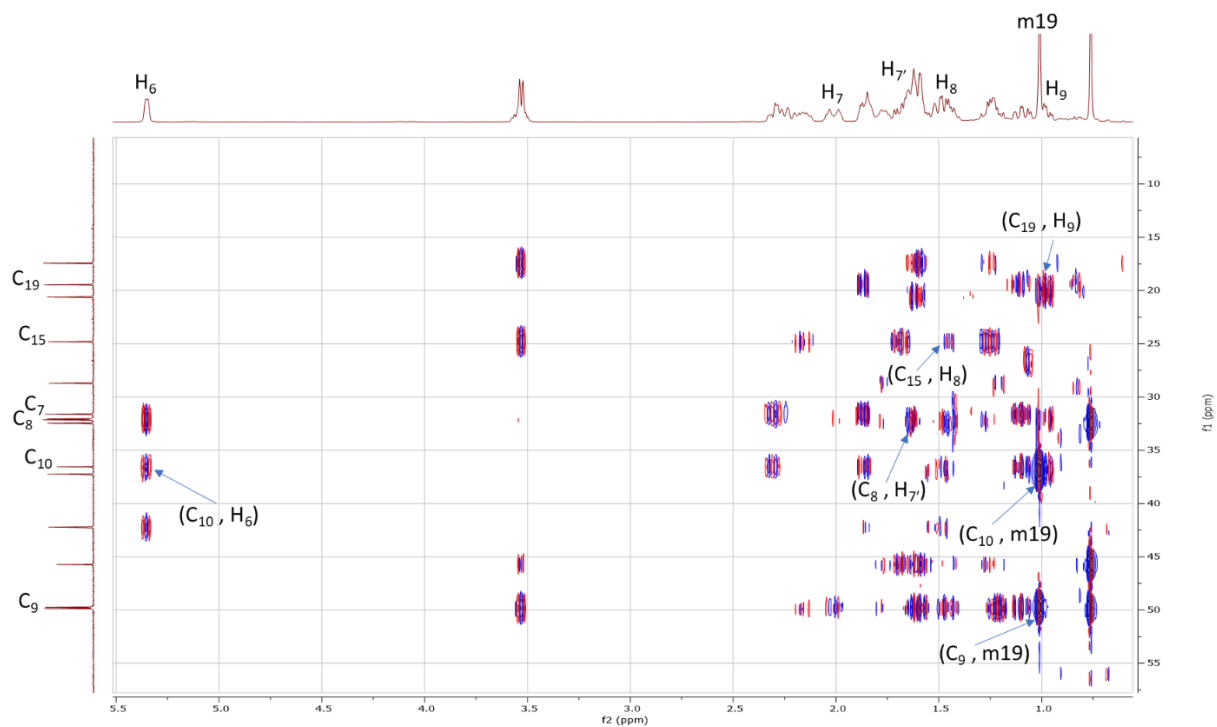
Figure 3.31C ^1H-^{13}C HMBC Correlations in B ring for DHEA C_{17}-(R)-N_3 probe (5)
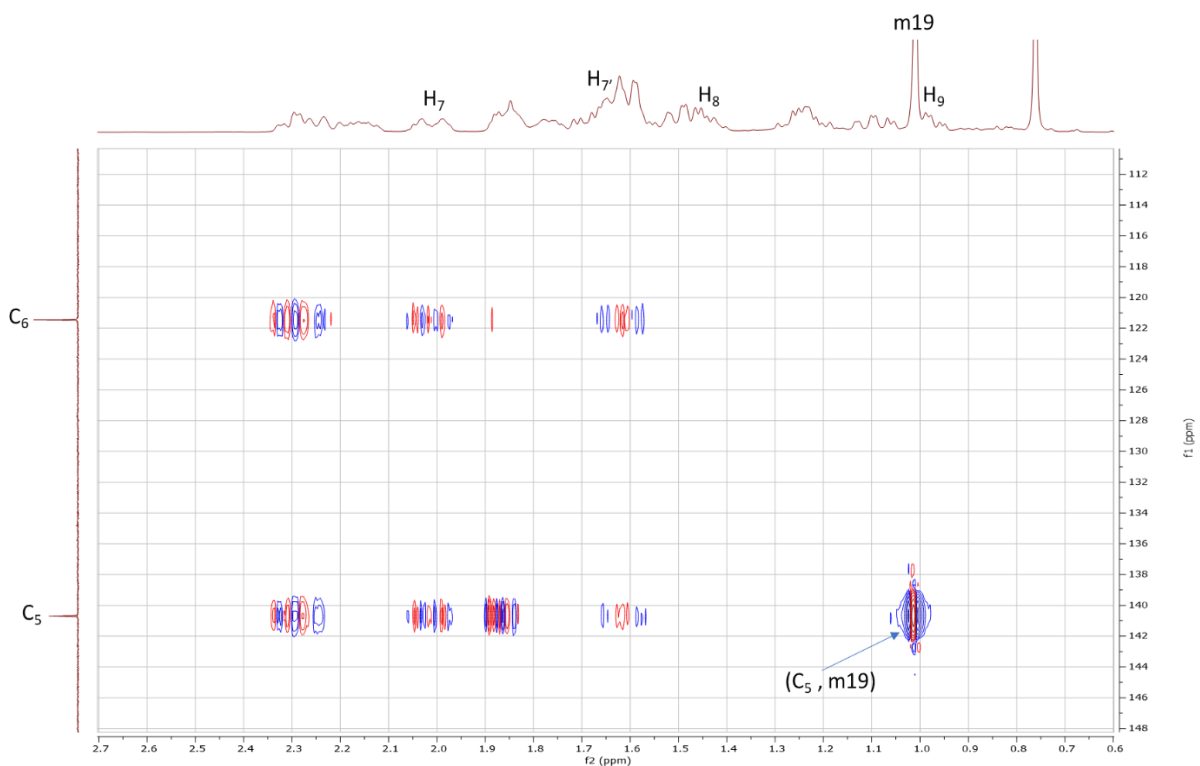
Figure 3.31D ^1H-^{13}C HMBC Correlations in B ring for DHEA C_{17}-(R)-N_3 probe (5) (C_5-C_6)

Next with the B ring, methyl protons, m19 (δ_H 1.00) exhibited HSQC correlation to δ_C 19.46 (C_{19}) (see Figure 3.31A). δ_C 140.69 (C_5) was determined on the basis of no HSQC correlation, chemical shift, and HMBC correlation to m19 (δ_H 1.00) (see Figure 3.31B and 3.31D). Vinyl carbon, C_6 (δ_C 121.45) was correlated by HSQC to δ_H 5.35 (H_6) (see Figure 3.31B). Methylene protons, δ_H 2.00 (H_7) and δ_H 1.62 ($H_{7'}$), exhibited HSQC correlation to δ_C 32.14 (C_7) (see Figure 3.31A). C_8 (δ_C 32.04) was correlated by HMBC to δ_H 1.62 ($H_{7'}$) (see Figure 3.31C). Methine proton, H_8, was discerned at δ_H 1.45 based on HMBC correlation to C_{15} (δ_C 24.81) and HSQC correlation to C_8 (δ_C 32.04) (see Figure 3.31A and 3.31C). The remaining methine proton, H_9 (δ_H 0.96), displayed correlation by HSQC to δ_C 49.76 (C_9) and by HMBC to δ_C 19.46 (C_{19}) (see Figure 3.31A and 3.31C). Quaternary carbon, C_{10} (δ_C 36.55), was assigned based on HMBC correlation to H_6 (δ_H 5.35) along with m19 (δ_H 1.00) and no HSQC correlation (see Figure 3.31A and 3.31C).
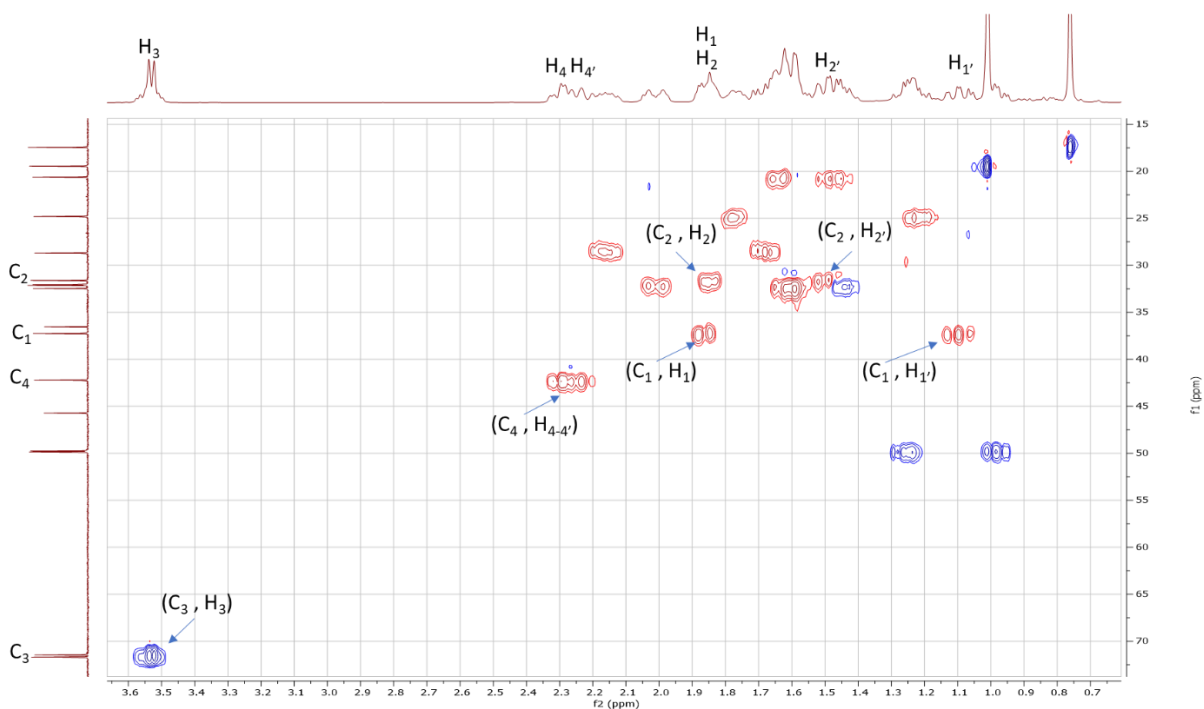
Figure 3.32A ^{1}H-^{13}C HSQC Correlations in A ring for DHEA C_{17}-(R)-N$_3$ probe (5)
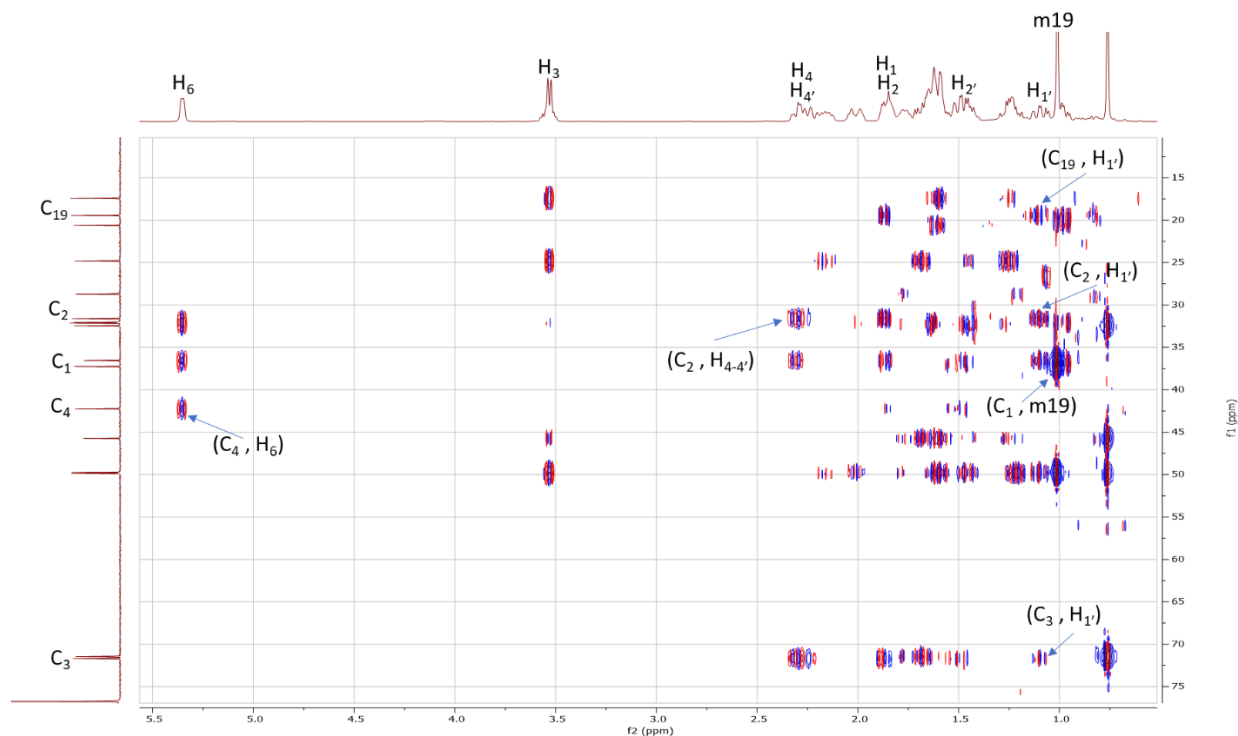
Figure 3.32B ^{1}H-^{13}C HMBC Correlations in A ring for DHEA C$_{17}$-(R)-N$_3$ probe (5)

Continuing with the A ring, δ_H 3.52 (H$_3$) exhibited HSQC correlation to δ_C 71.69 (C$_3$) (see

Figure 3.32A). Methylene protons, δ_H 2.28 (H$_4$) and δ_H 2.28 (H$_{4'}$), displayed HSQC correlation to

δ_C 42.23 (C$_4$), which shows HMBC correlation to H$_6$ (δ_H 5.35) (see Figure 3.32A and 3.32B).

Diastereotopic protons, δ_H 1.85 (H$_2$) and δ_H 1.45 (H$_{2'}$), displayed HSQC correlation to δ_C 31.61

(C$_2$), which showed HMBC correlation to H$_{4'}$ (δ_H 2.28) and H$_4$ (δ_H 2.28) (see Figure 3.32A and

3.32B). δ_C 37.26 (C$_1$) was discerned from HMBC correlation to m19 (δ_H 1.00) (see Figure 3.32B).

From there, methylene protons, δ_H 1.85 (H$_1$) and δ_H 1.09 (H$_{1'}$) displayed HSQC correlation to δ_C

37.26 (C$_1$) along HMBC correlation to δ_C 31.61 (C$_2$), δ_C 71.69 (C$_3$), and δ_C 19.46 (C$_{19}$) (see Figure

3.32A and 3.32B).
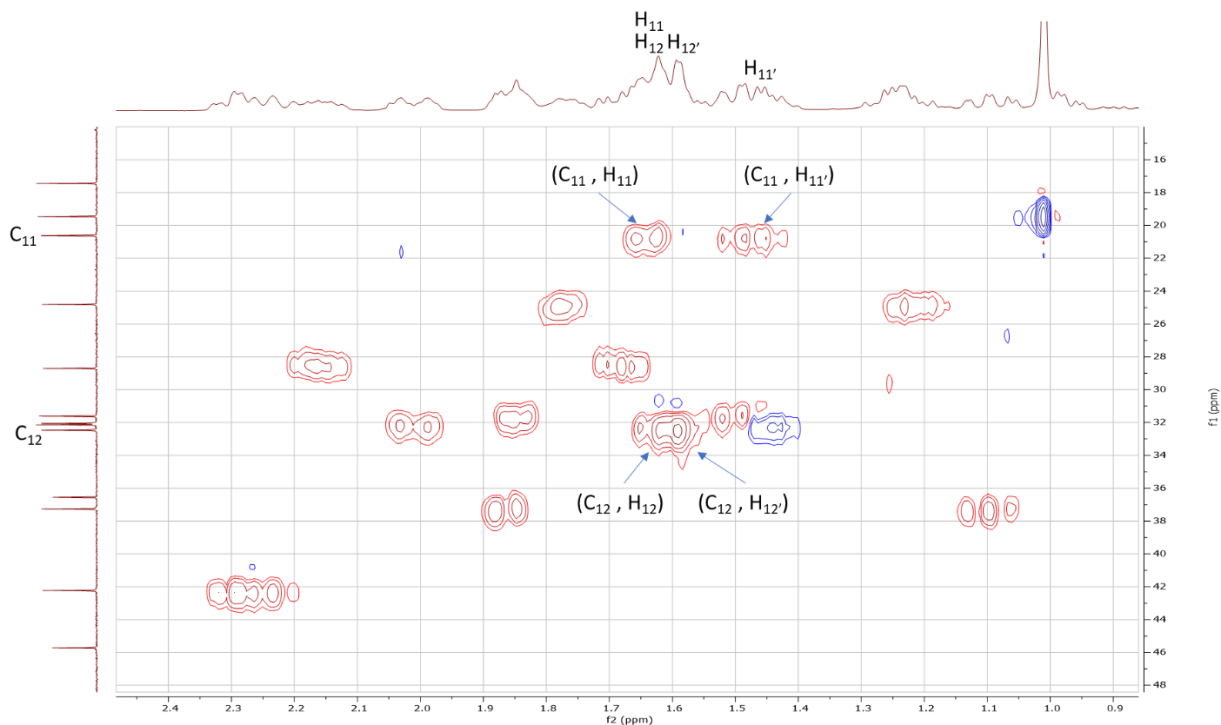
Figure 3.33A ^{1}H-^{13}C HSQC Correlations in C ring for DHEA C_{17}-(R)-N_3 probe (5)
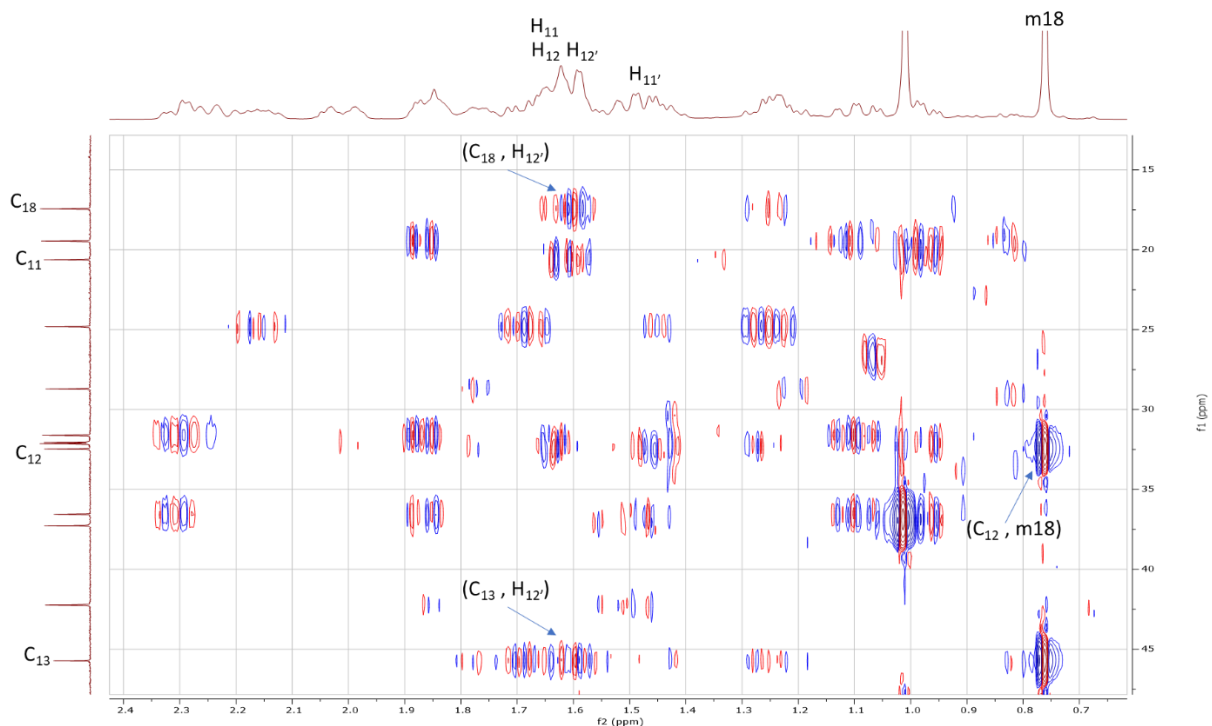
Figure 3.33B ^{1}H-^{13}C HMBC Correlations in C ring for DHEA C_{17}-(R)-N_3 probe (5)

Concluding with the C ring, δ_C 32.47 (C_{12}) displayed HMBC correlations to m18 (δ_H 0.75) (see Figure 3.33B). δ_H 1.62 (H_{12}) and δ_H 1.62 ($H_{12'}$) were discerned from HSQC correlations to δ_C

32.47 (C_{12}) and HMBC correlations to C_{13} (δ_C 45.72) and C_{18} (δ_C 17.44) (see Figure 3.33A and 3.33B). The remaining δ_C 20.62 (C_{11}) displayed HSQC correlation to δ_H 1.62 (H_{11}) and δ_H 1.45 ($H_{11'}$) (see Figure 3.33A), thus completing full assignment of DHEA C_{17}-(R)-N_3 probe (**5**).
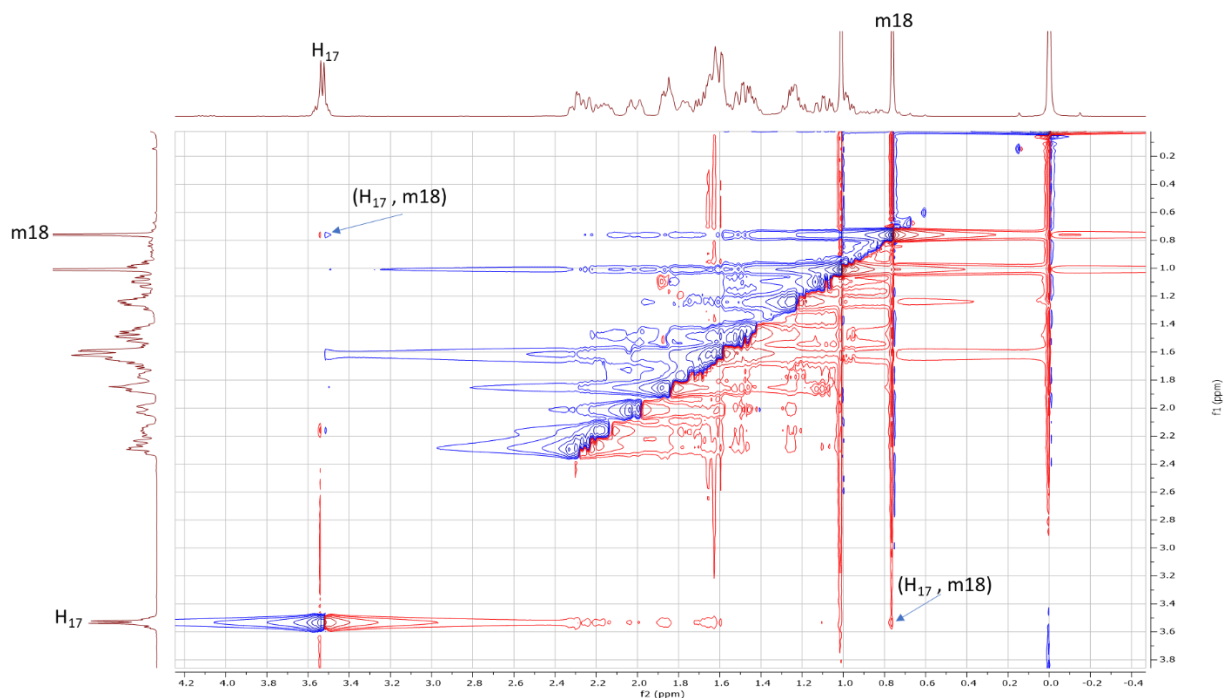
Figure 3.34 ^{1}H-^{1}H NOESY Correlations for DHEA C_{17}-(R)-N_3 probe (5)

The stereochemistry of the azide group at C_{17} is "R" based on NOESY correlation between δ_H 3.52 (H_{17}) and δ_H 0.75 (m18) (see Figure 3.34).
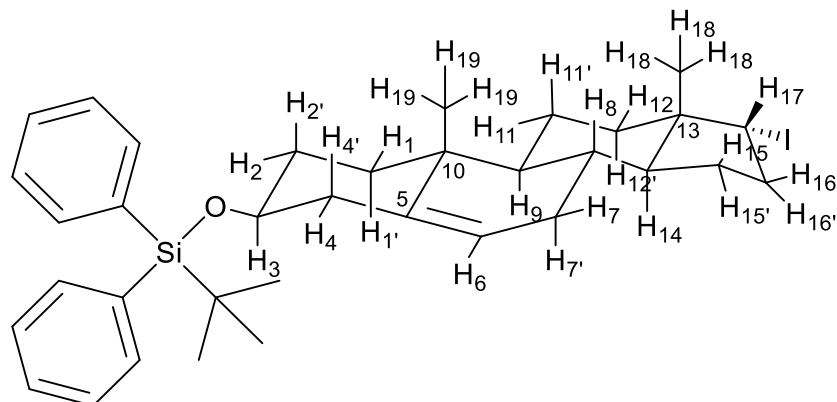
Figure 3.35A Chair Conformation for 6
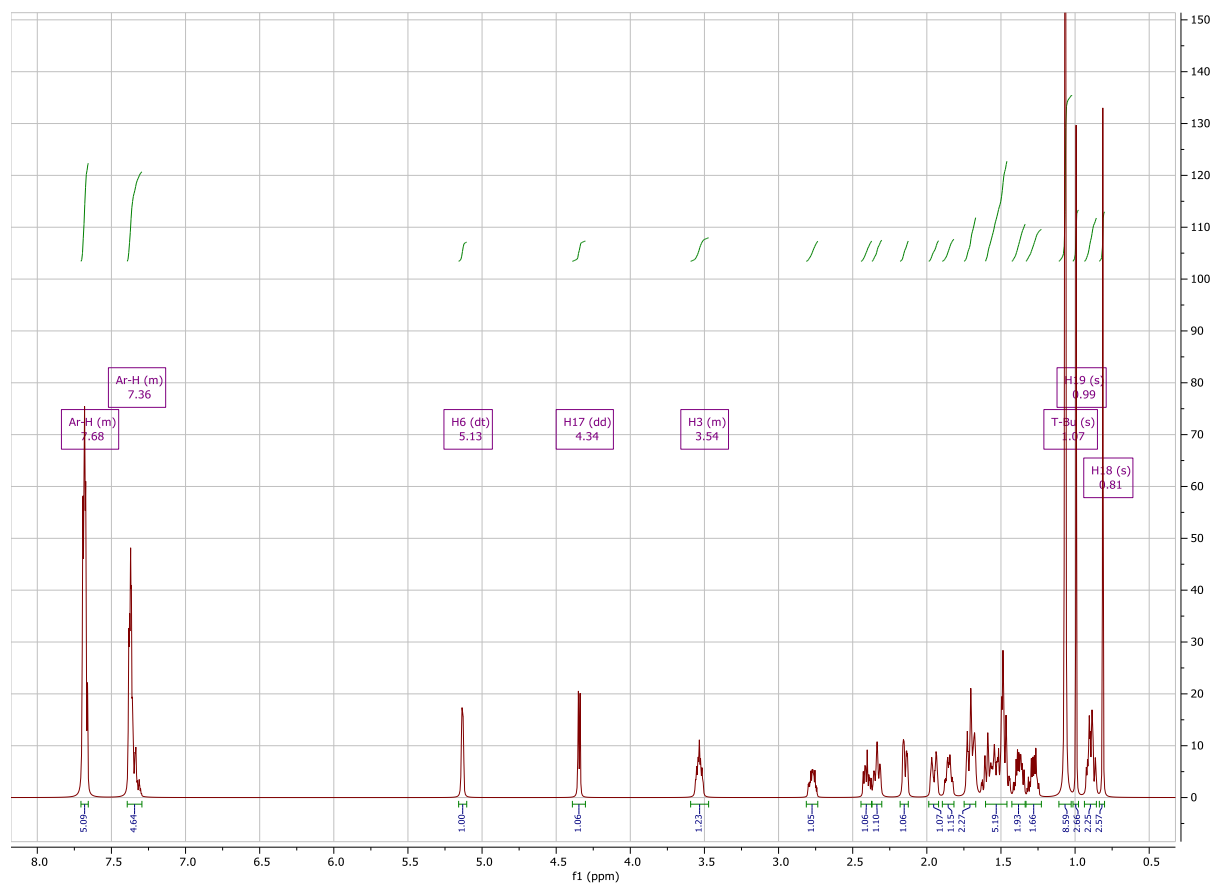
Figure 3.35B ^{1}H Spectrum of DHEA C$_{17}$ Iodide PG (6)

Aromatic protons of the TBDPS group were distinguished at δ$_H$ 7.68 and δ$_H$ 7.36 (see

Figure 3.35B). δ$_H$ 5.13, δ$_H$ 4.34, and δ$_H$ 3.54 were identified as H$_6$, H$_{17}$, and H$_3$ respectively based

on chemical shift and splitting (see Figure 3.35B). δ_H 0.99 and δ_H 0.81 were discerned as the methyl protons on C_{18} or C_{19} based on integration and splitting (see Figure 3.35B). The latter assignments for H_3, H_6, H_{17}, H_{18}, and H_{19} matched previous ^{1}H assignments (Blanco et al., 2014), (Kiss et al., 2018), and (Jan et al., 2016).
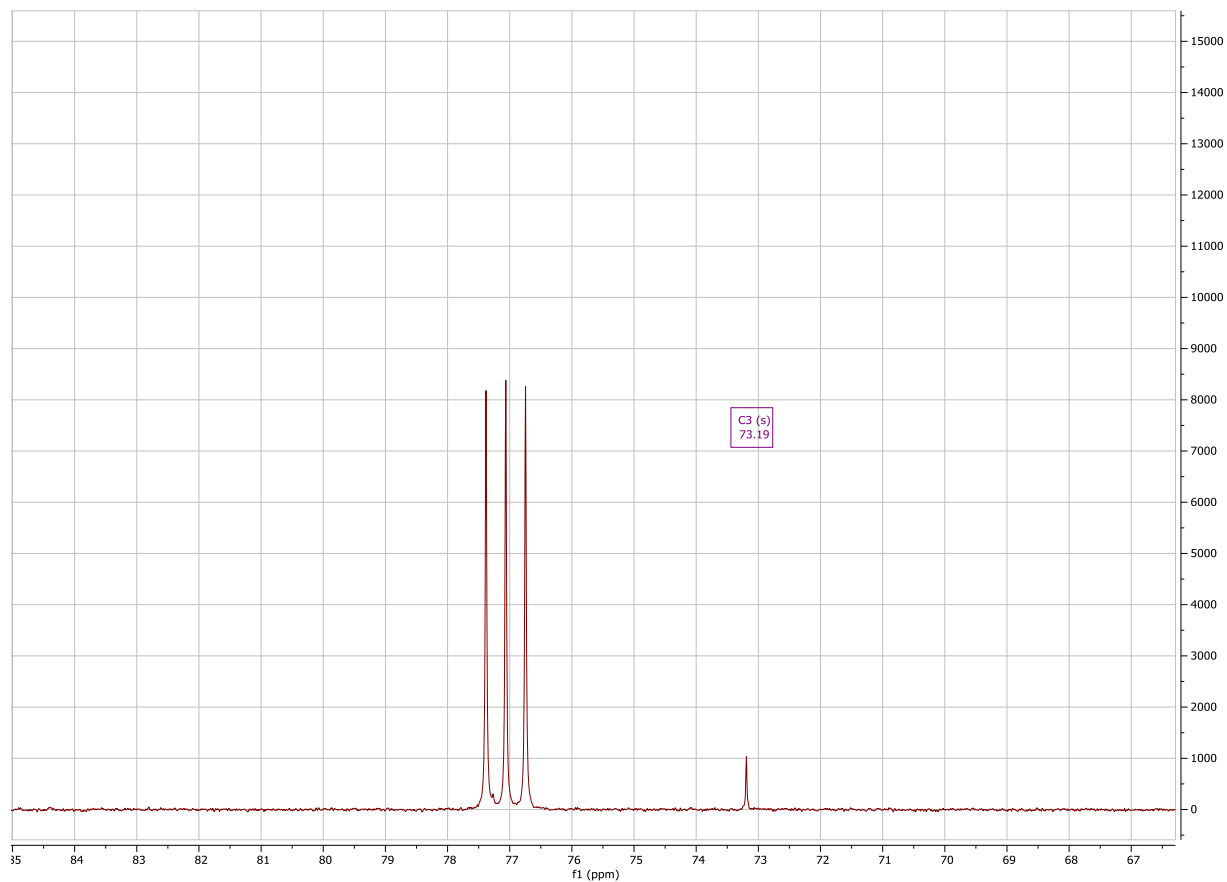
Figure 3.35C [13]C Spectrum of DHEA C_{17} Iodide PG (6)

The substitution of the hydroxyl group to an iodide group through an Appel reaction was potentially observed by the loss of δ_C 81.91 (C_{17}, **3**) based on DHEA C_{17} OH PG (**3**) (see Figure 3.35C). δ_C 73.19 was identified as C_3 based on chemical shift and previous characterization of C_3 for DHEA C_{17} OH PG (**3**) (see Figure 3.35C).
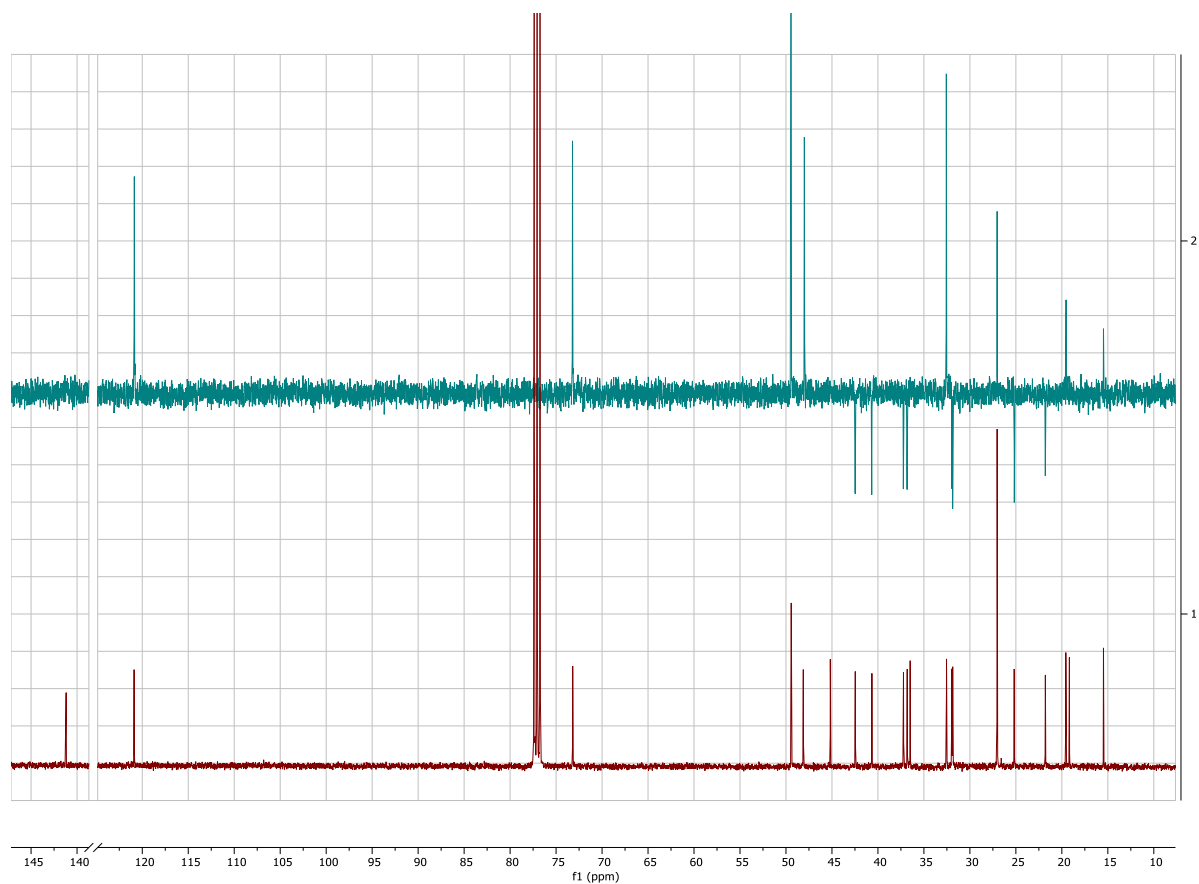
Figure 3.35D DEPT-135 Spectrum of DHEA C$_{17}$ Iodide PG (6)

δ_C 120.89, δ_C 73.19, δ_C 49.43, δ_C 48.12, δ_C 32.54, δ_C 27.04, δ_C 19.57, and δ_C 15.47 were identified to be either -CH or -CH$_3$ groups (see Figure 3.35D). δ_C 42.46, δ_C 40.66, δ_C 37.22, δ_C 36.82, δ_C 31.95, δ_C 31.87, δ_C 25.18, and δ_C 21.79 were discerned to be -CH$_2$ groups (see Figure 3.35D). δ_C 141.18, δ_C 45.18, δ_C 36.49, and δ_C 19.18 were distinguished as quaternary carbons (see Figure 3.35D).
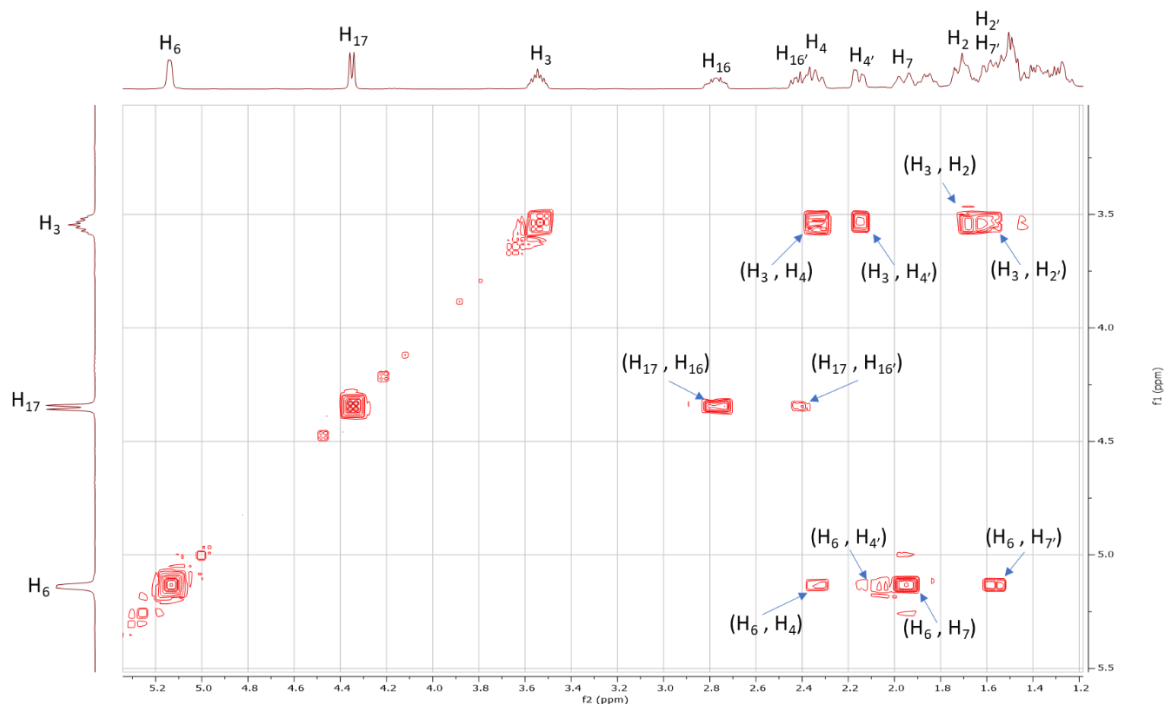
Figure 3.36 Initial ¹H-¹H COSY Correlations for DHEA C₁₇ Iodide PG (6)

Diastereotopic protons, δ_H 2.34 (H₄) and δ_H 2.14 (H₄'), from the A ring were identified from COSY correlations with H₃ (δ_H 3.54) and H₆ (δ_H 5.13) (see Figure 3.36). Methylene protons, δ_H 1.71 (H₂) and δ_H 1.53 (H₂'), were discerned from COSY correlations with H₃ (δ_H 3.54) (see Figure 3.36). In addition, diastereotopic protons δ_H 1.95 (H₇) and δ_H 1.53 (H₇') in the B ring were identified from COSY correlations with H₆ (δ_H 5.13) (see Figure 3.36). In the D ring, diastereotopic protons δ_H 2.77 (H₁₆) and δ_H 2.40 (H₁₆') were discerned from COSY correlations with H₁₇ (δ_H 4.34) (see Figure 3.36).
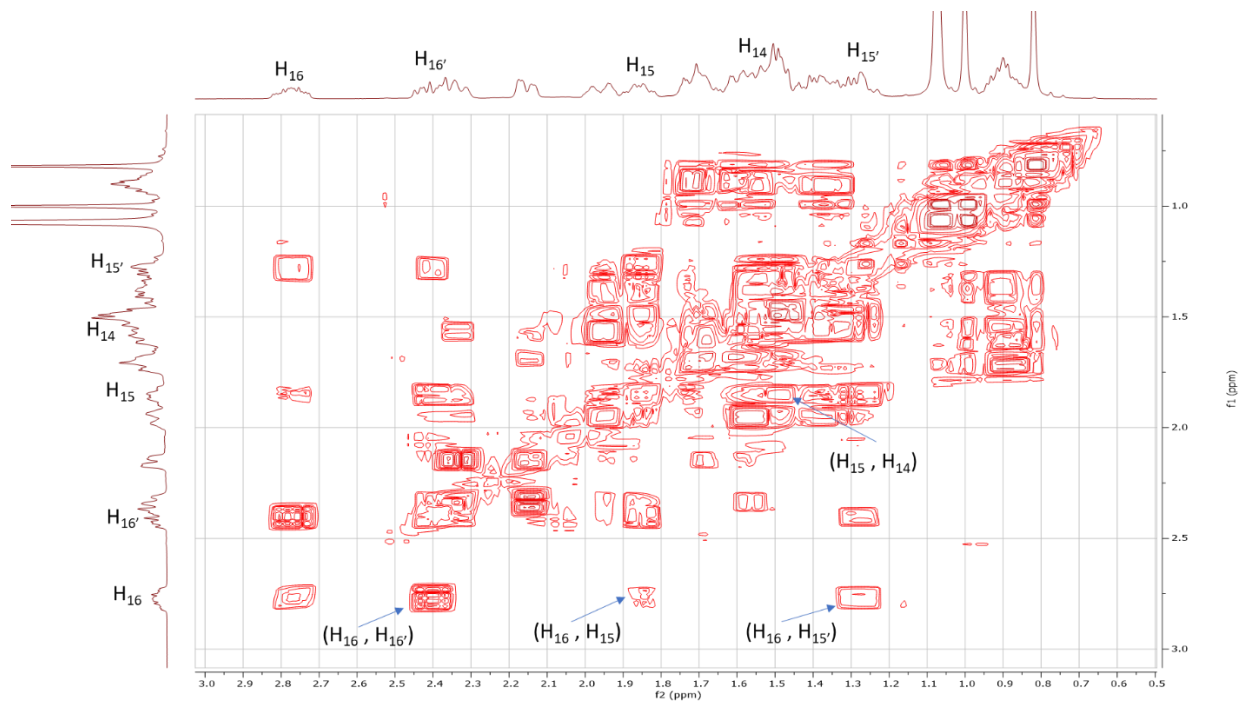
Figure 3.37A ^{1}H-^{1}H COSY Correlations in D ring for DHEA C$_{17}$ Iodide PG (6)
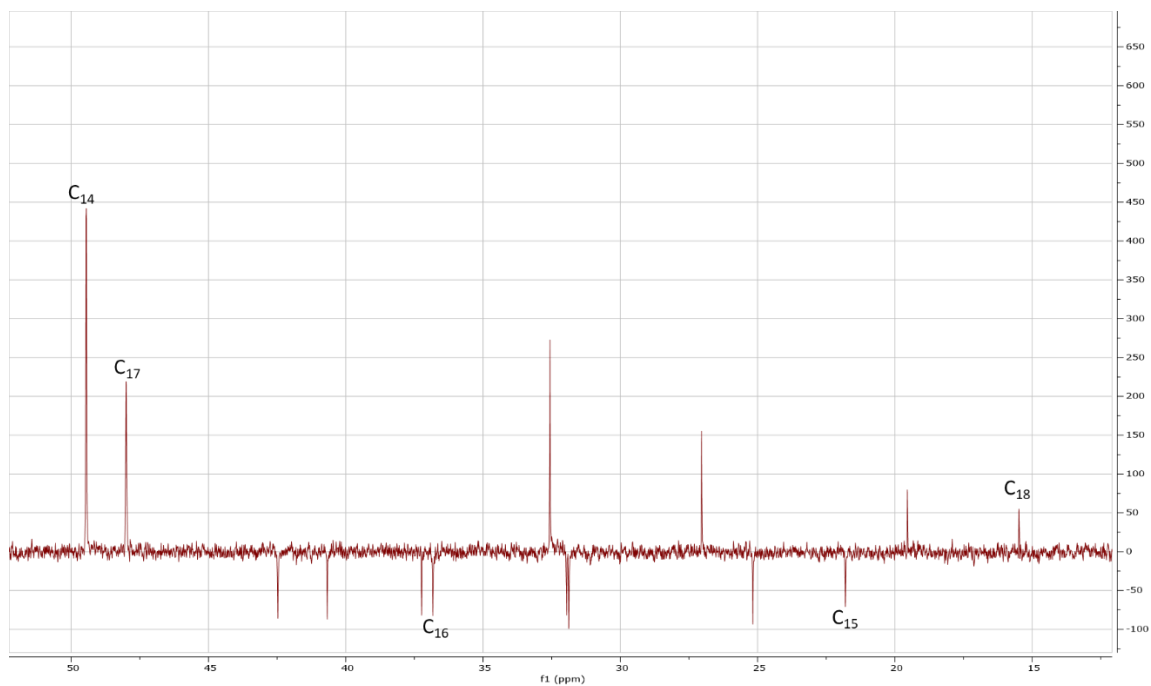
Figure 3.37B DEPT-135 Correlations in D ring for DHEA C$_{17}$ Iodide PG (6)
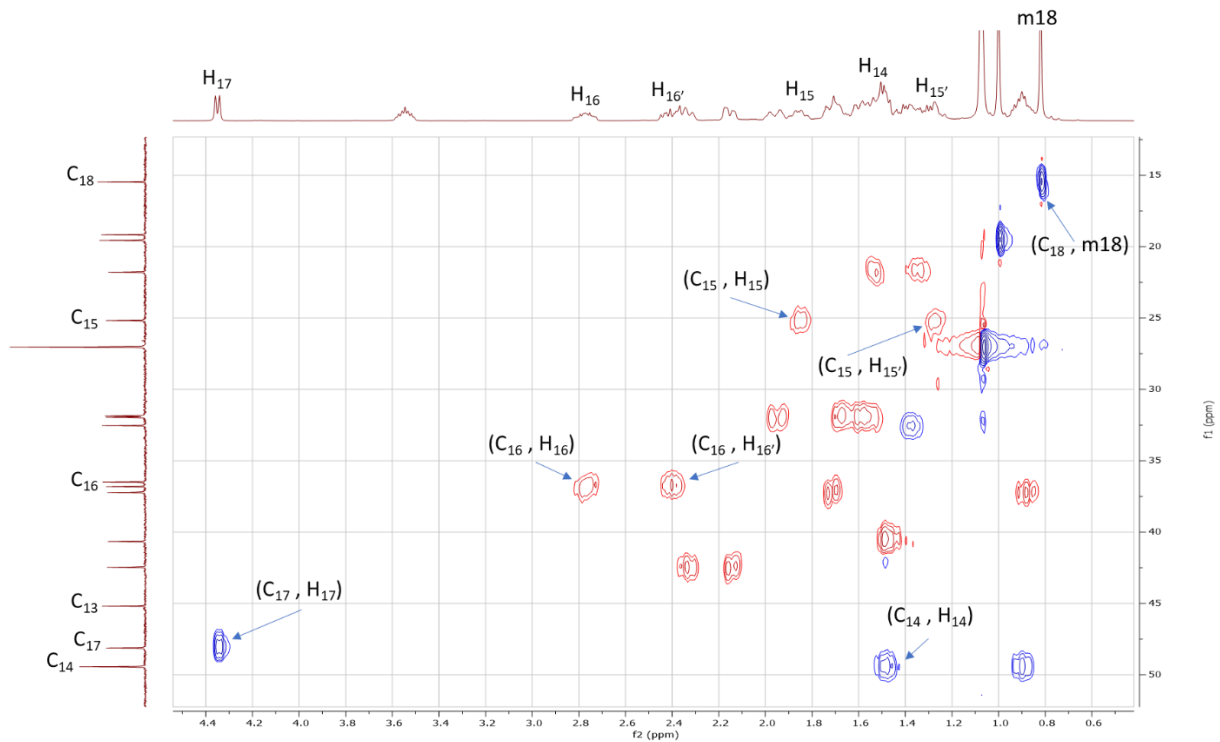
Figure 3.37C ^{1}H-^{13}C HSQC Correlations in D ring for DHEA C$_{17}$ Iodide PG (6)
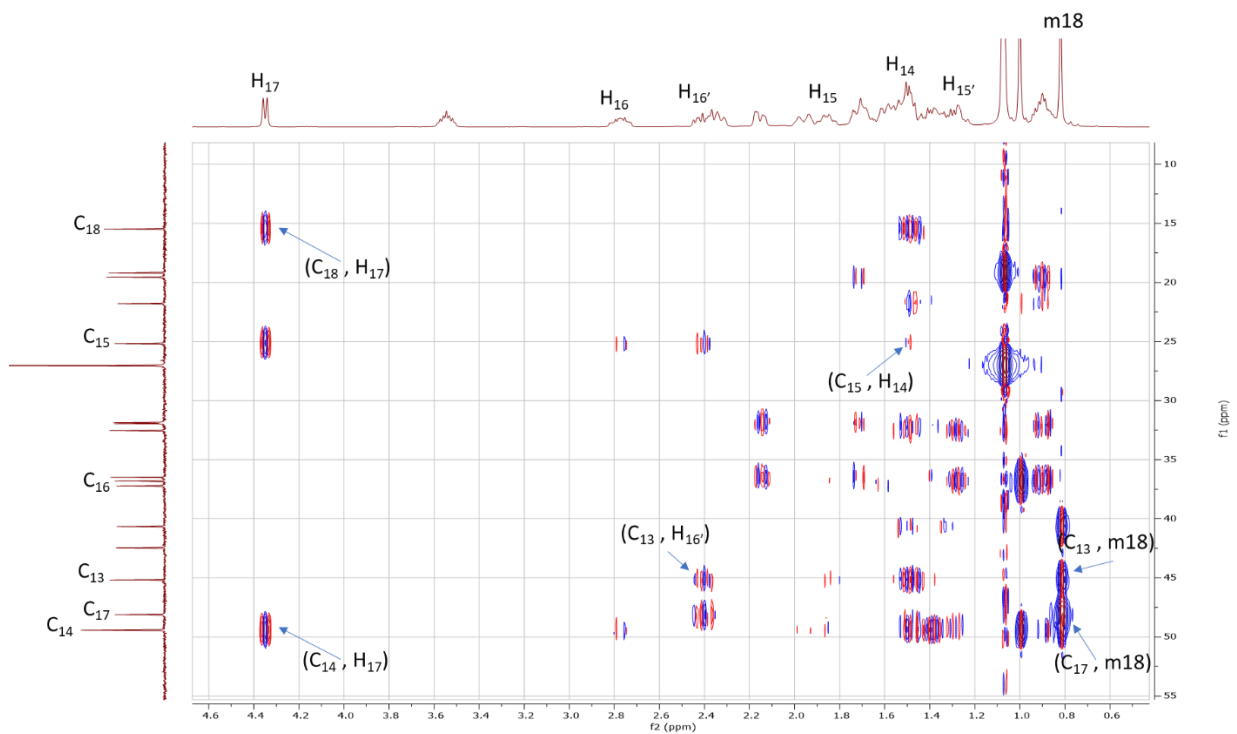
Figure 3.37D ^{1}H-^{13}C HMBC Correlations in D ring for DHEA C$_{17}$ Iodide PG (6)

Starting with the D ring, δ_C 48.12 was identified as C_{17} from the HSQC correlation to δ_H 4.34 (H_{17}) and HMBC correlations to m18 (δ_H 0.81) (see Figure 3.37C and 3.37D). H_{17} (δ_H 4.34) also displayed HMBC correlation to C_{14} (δ_C 49.43) (see Figure 3.37D). Methylene protons, δ_H 2.77 (H_{16}) and δ_H 2.40 ($H_{16'}$), were correlated by HSQC to δ_C 36.82 (C_{16}) (see Figure 3.37C). With COSY correlations with H_{16} (δ_H 2.77), diastereotopic protons H_{15} (δ_H 1.85) and $H_{15'}$ (δ_H 1.28) were identified (see Figure 3.37A). In regard to H_{15} (δ_H 1.85), methine proton, H_{14} (δ_H 1.53), was distinguished by COSY correlation (see Figure 3.37A). Next, diastereotopic protons, δ_H 1.85 (H_{15}) and δ_H 1.28 ($H_{15'}$), showed a HSQC correlation to δ_C 25.18 (C_{15}) (see Figure 3.37C). H_{14} (δ_H 1.53) displayed a HSQC correlation to δ_C 49.43 (C_{14}), HMBC correlation to C_{15} (δ_C 25.18), and DEPT-135 -CH correlation (see Figure 3.37B, 3.37C, and 3.37D). Quaternary carbon, δ_C 45.18 (C_{13}), was discerned from HMBC correlation to $H_{16'}$ (δ_H 2.40) along with m18 (δ_H 0.81) and no observable HSQC correlation (see Figure 3.37C and 3.37D). Continuing with m18, δ_C 15.47 (C_{18}) was identified from HSQC correlation to m18 and HMBC correlation to δ_H 4.34 (H_{17}) (see Figure 3.37C and 3.37D). Therefore, the methyl protons on C_{19}, m19, could be identified at δ_H 0.99 based on integration and splitting (see Figure 3.35B).
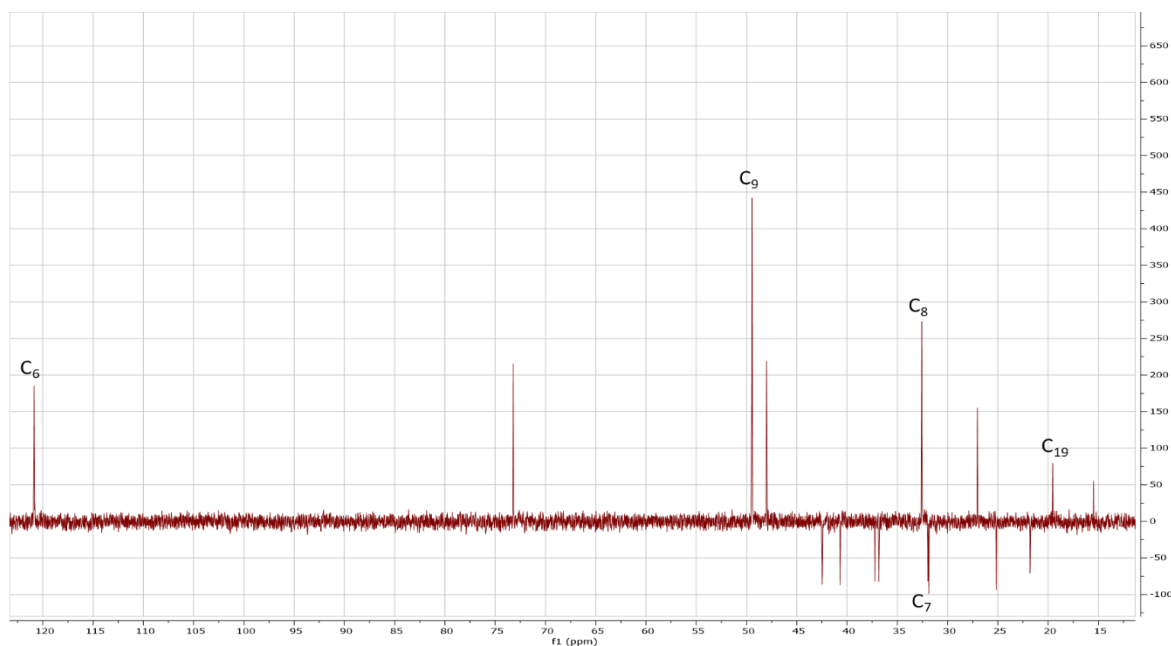
Figure 3.38A DEPT-135 Correlations in B ring for DHEA C_{17} Iodide PG (6)
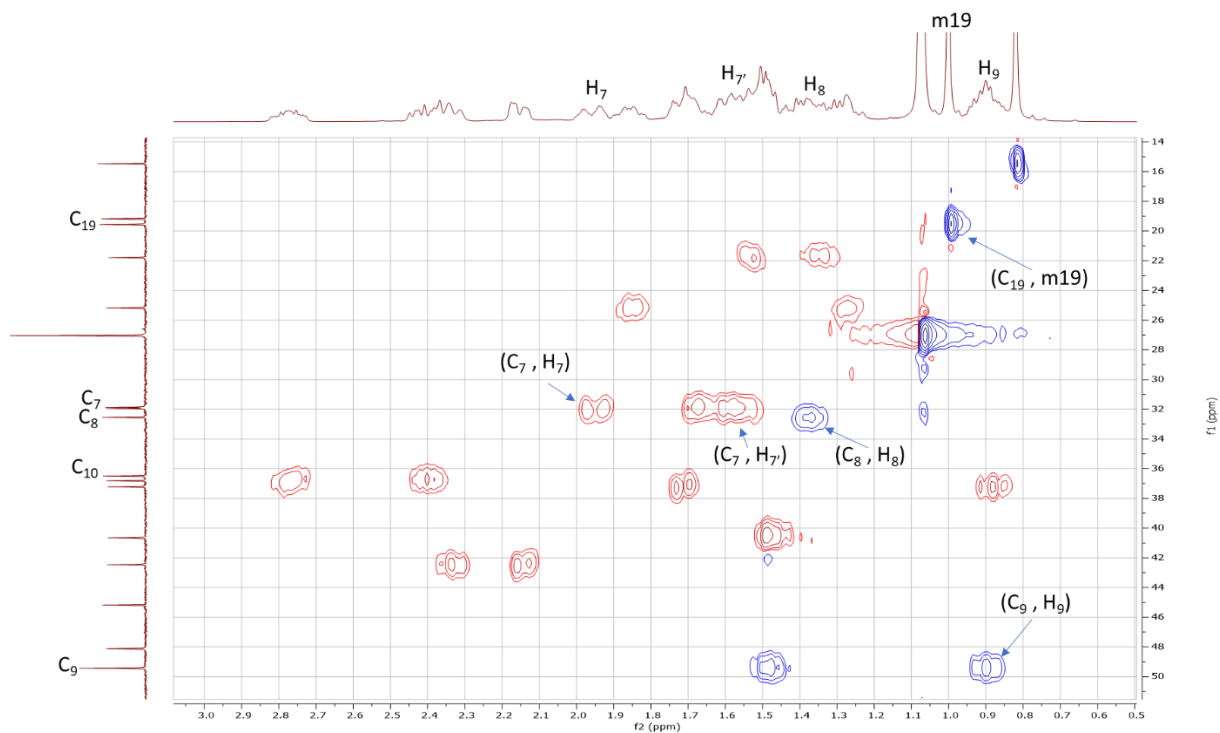
Figure 3.38B ^{1}H-^{13}C HSQC Correlations in B ring for DHEA C$_{17}$ Iodide PG (6)
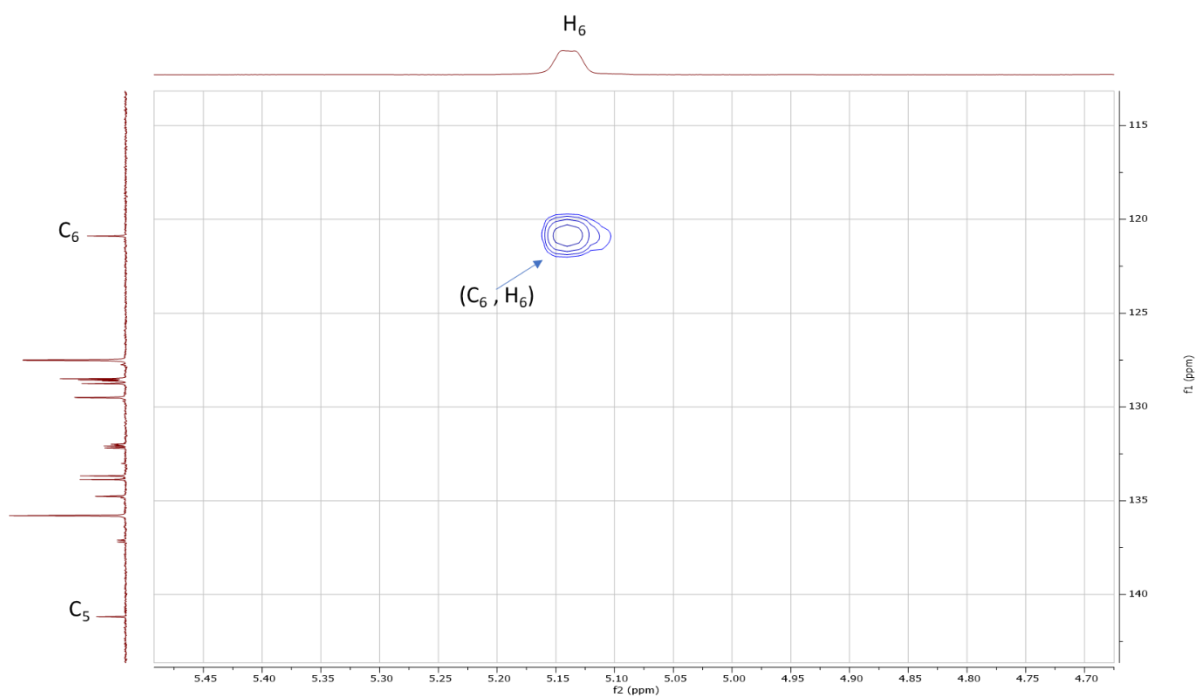
Figure 3.38C ^{1}H-^{13}C HSQC Correlations in B ring for DHEA C$_{17}$ Iodide PG (6) (C$_5$-C$_6$)
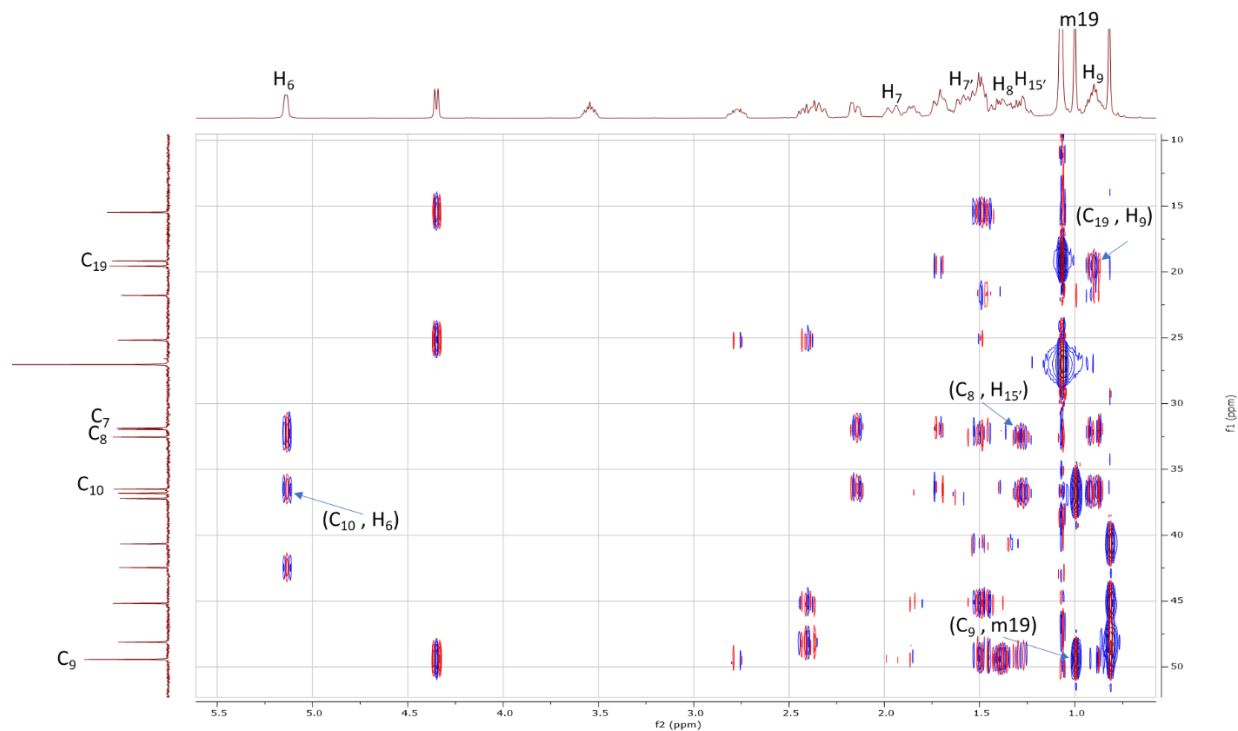
Figure 3.38D ^{1}H-^{13}C HMBC Correlations in B ring for DHEA C$_{17}$ Iodide PG (6)

Figure 3.38E ^{1}H-^{13}C HMBC Correlations in B ring for DHEA C$_{17}$ Iodide PG (6) (C$_5$-C$_6$)

Next with the B ring, methyl protons, m19 (δ_H 0.99) exhibited HSQC correlation to δ_C 19.57 (C$_{19}$) (see Figure 3.38B). δ_C 141.18 (C$_5$) was determined on the basis of no HSQC correlation,

chemical shift, HMBC correlation to m19 (δ_H 0.99), and no DEPT-135 correlation (see Figure 3.38A, 3.38C and 3.38E). Vinyl carbon, C_6 (δ_C 120.89) was correlated by HSQC to δ_H 5.13 (H_6) (see Figure 3.38C). Methylene protons, δ_H 1.95 (H_7) and δ_H 1.53 ($H_{7'}$), exhibited HSQC correlation to δ_C 31.95 (C_7) (see Figure 3.38B). C_8 (δ_C 32.54) was correlated by HMBC to $H_{15'}$ (δ_H 1.28) and DEPT-135 -CH correlation (see Figure 3.38A and 3.38D). H_8 (δ_H 1.38) was correlated by HSQC to δ_C 32.54 (C_8) (see Figure 3.38B). Based on DEPT-135 and HSQC spectra, δ_C 49.43 contained two methine carbons (see Figure 3.38A and 3.38B). Therefore, the remaining methine proton, H_9 (δ_H 0.89), was correlated by HSQC to δ_C 49.43 (C_9), HMBC to δ_C 19.57 (C_{19}), and DEPT-135 -CH correlation (see Figure 3.38A, 3.38B, and 3.38D). Quaternary carbon, C_{10} (δ_C 36.49), was identified by HMBC correlation to H_6 (δ_H 5.13), no HSQC correlation, and no DEPT-135 correlation (see Figure 3.38A, 3.38B, and 3.38D).
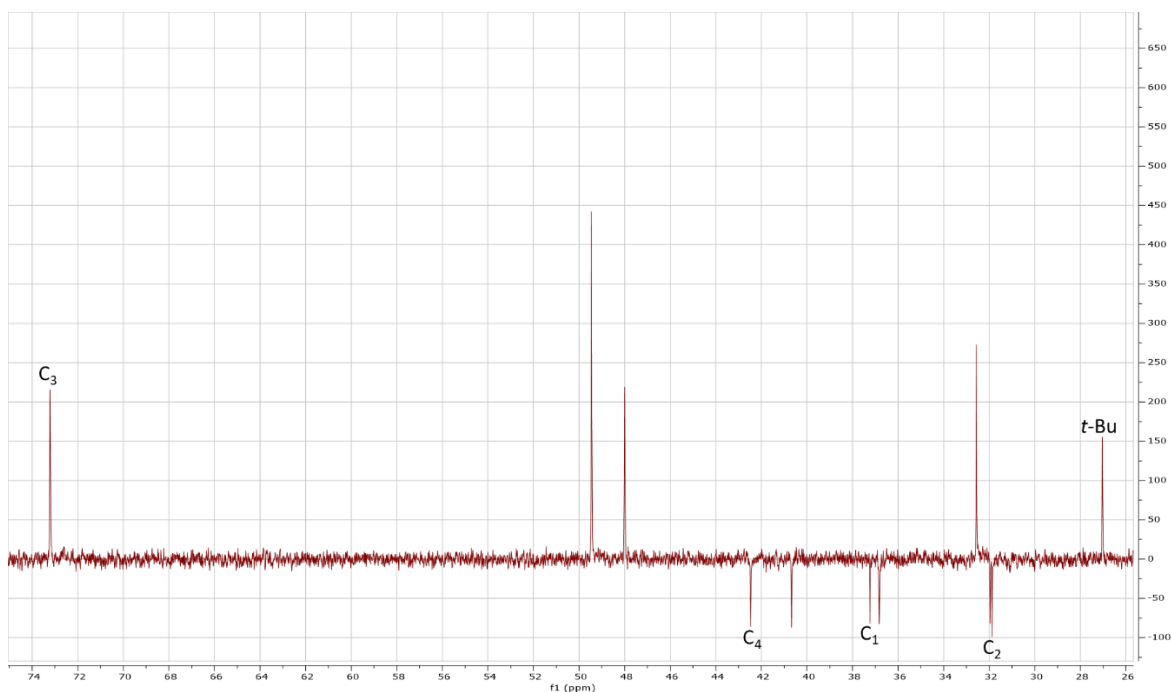
Figure 3.39A DEPT-135 Correlations in A ring for DHEA C_{17} Iodide PG (6)
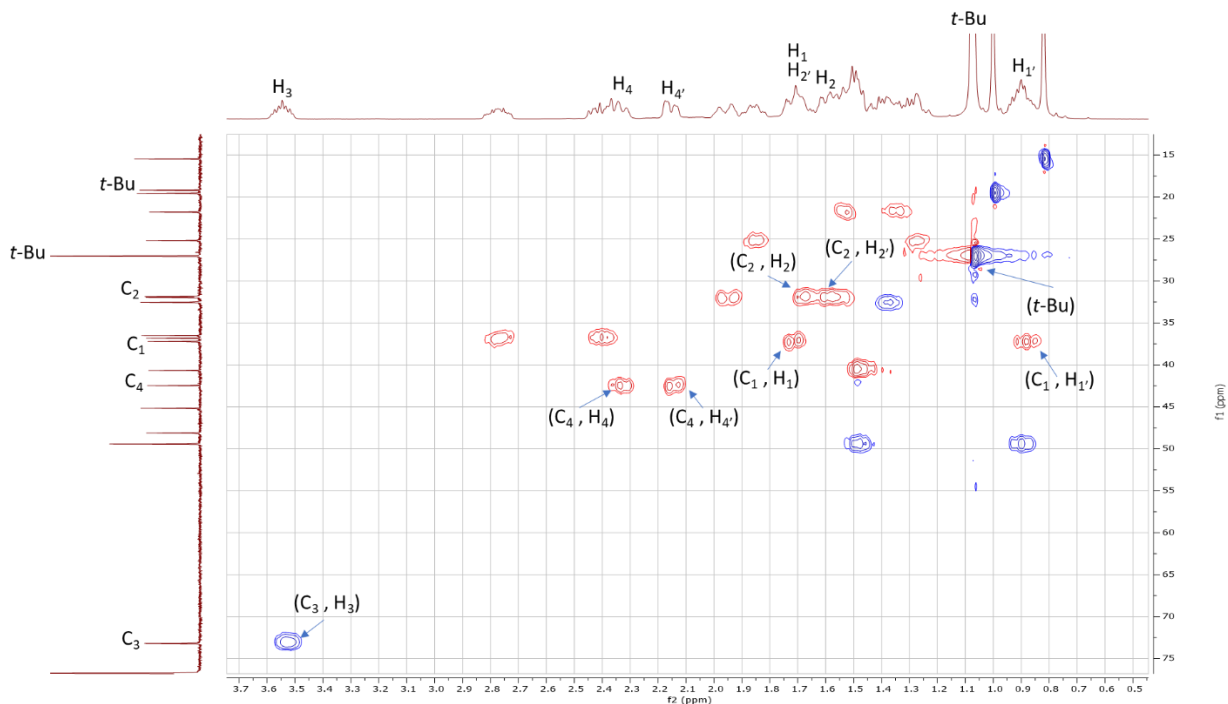
Figure 3.39B ^1H-^{13}C HSQC Correlations in A ring for DHEA C_{17} Iodide PG (6)
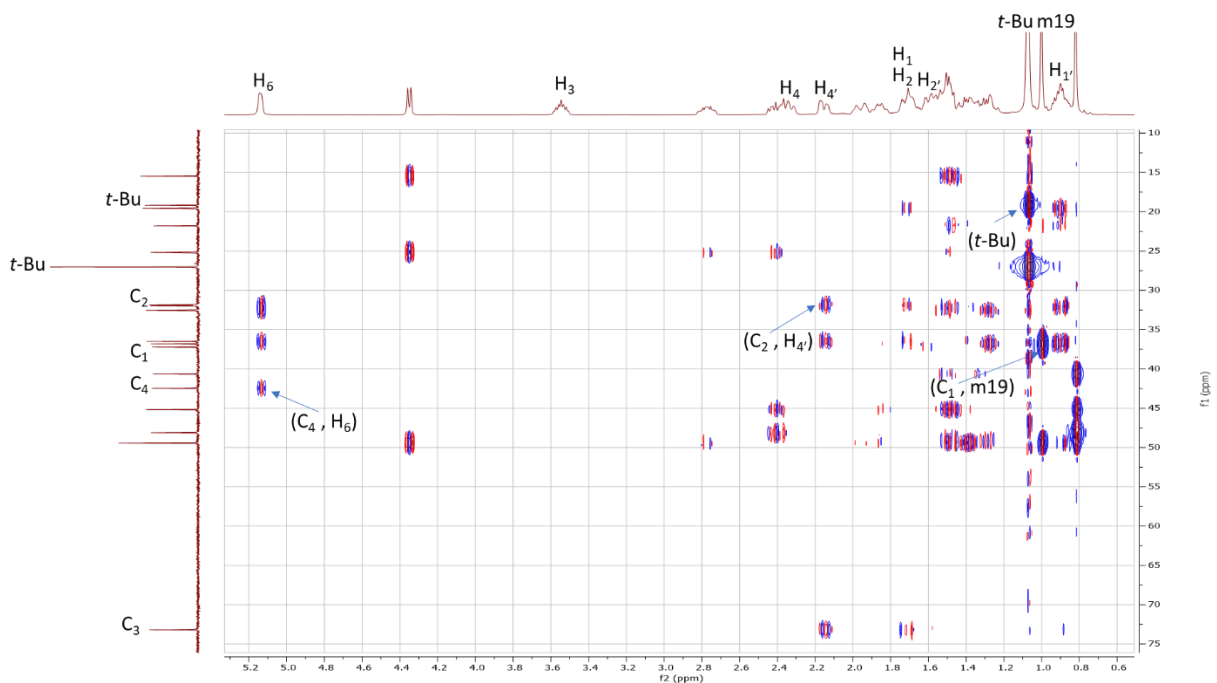
Figure 3.39C ^1H-^{13}C HMBC Correlations in A ring for DHEA C_{17} Iodide PG (6)

Continuing with the A ring, δ_H 3.54 (H_3) exhibited HSQC correlation to δ_C 73.19 (C_3) (see Figure 3.39B). Methylene protons, δ_H 2.34 (H_4) and δ_H 2.14 ($H_{4'}$), displayed HSQC correlation to δ_C 42.46 (C_4), which shows HMBC correlation to H_6 (δ_H 5.13) (see Figure 3.39B and 3.39C).

135

Diastereotopic protons, δ_H 1.71 (H$_2$) and δ_H 1.53 (H$_{2'}$), displayed HSQC correlation to δ_C 31.87 (C$_2$), which showed HMBC correlation of H$_{4'}$ (δ_H 2.14) (see Figure 3.39B and 3.39C). δ_C 37.22 (C$_1$) was discerned from HMBC correlation to m19 (δ_H 0.99) (see Figure 3.39C). From there, methylene protons, δ_H 1.71 (H$_1$) and δ_H 0.89 (H$_{1'}$) displayed HSQC correlation to δ_C 37.22 (C$_1$) (see Figure 3.39B). The *tert*-butyl (*t*-Bu) protons of TBDPS were recognized as the δ_H 1.07 singlet, which integrated to nine (see Figure 3.35B). In addition, δ_C 27.04 (*t*-Bu) displayed HSQC correlation to δ_H 1.07 (*t*-Bu) (see Figure 3.39B). δ_C 19.15 (*t*-Bu) displayed HMBC correlation to δ_H 1.07 (*t*-Bu) and no DEPT-135 correlation (see Figure 3.39A and 3.39C).
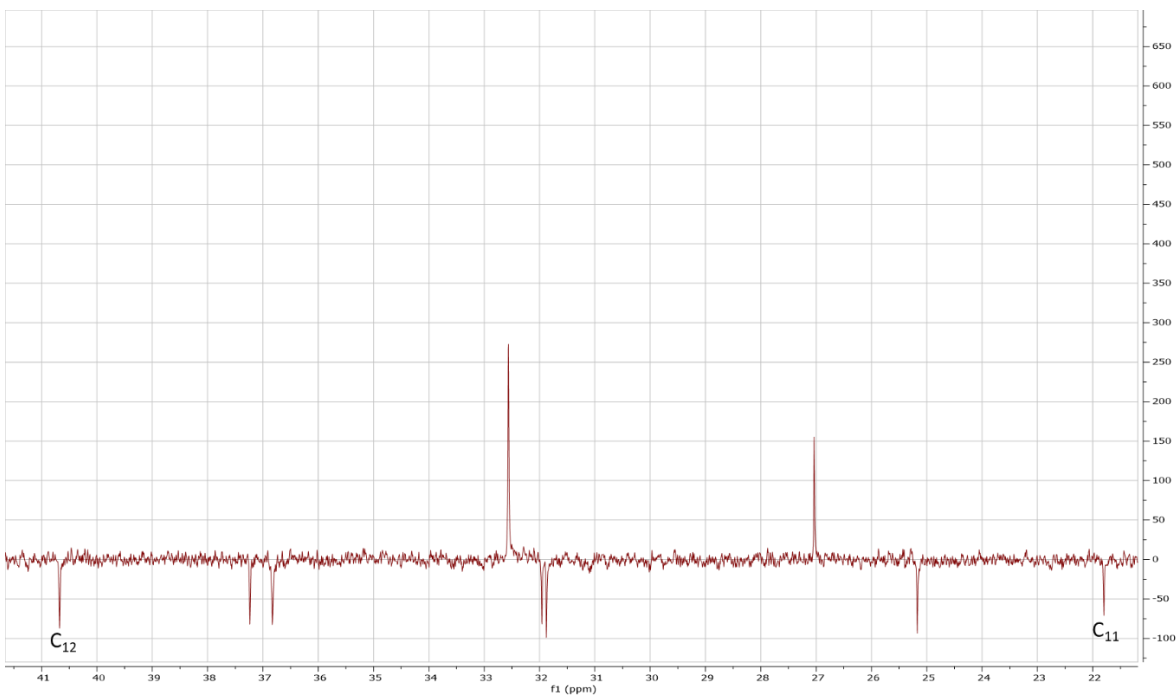
Figure 3.40A DEPT-135 Correlations in C ring for DHEA C$_{17}$ Iodide PG (6)
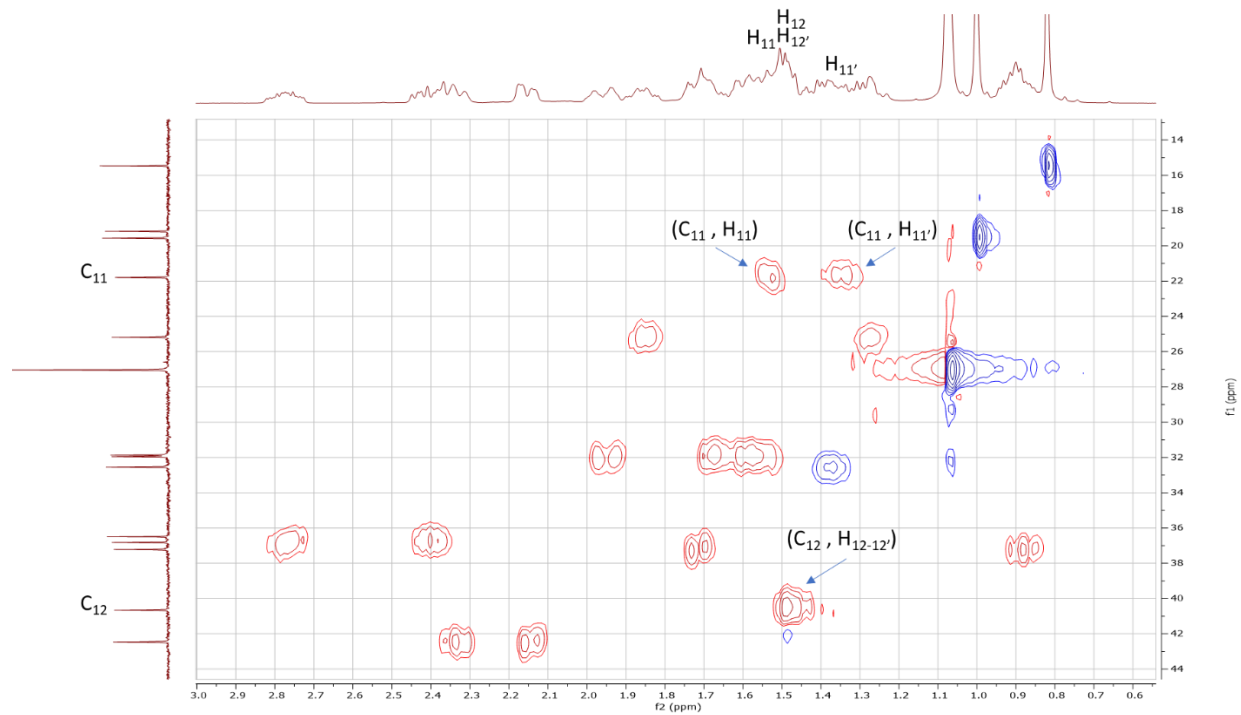
Figure 3.40B ^{1}H-^{13}C HSQC Correlations in C ring for DHEA C_{17} Iodide PG (6)
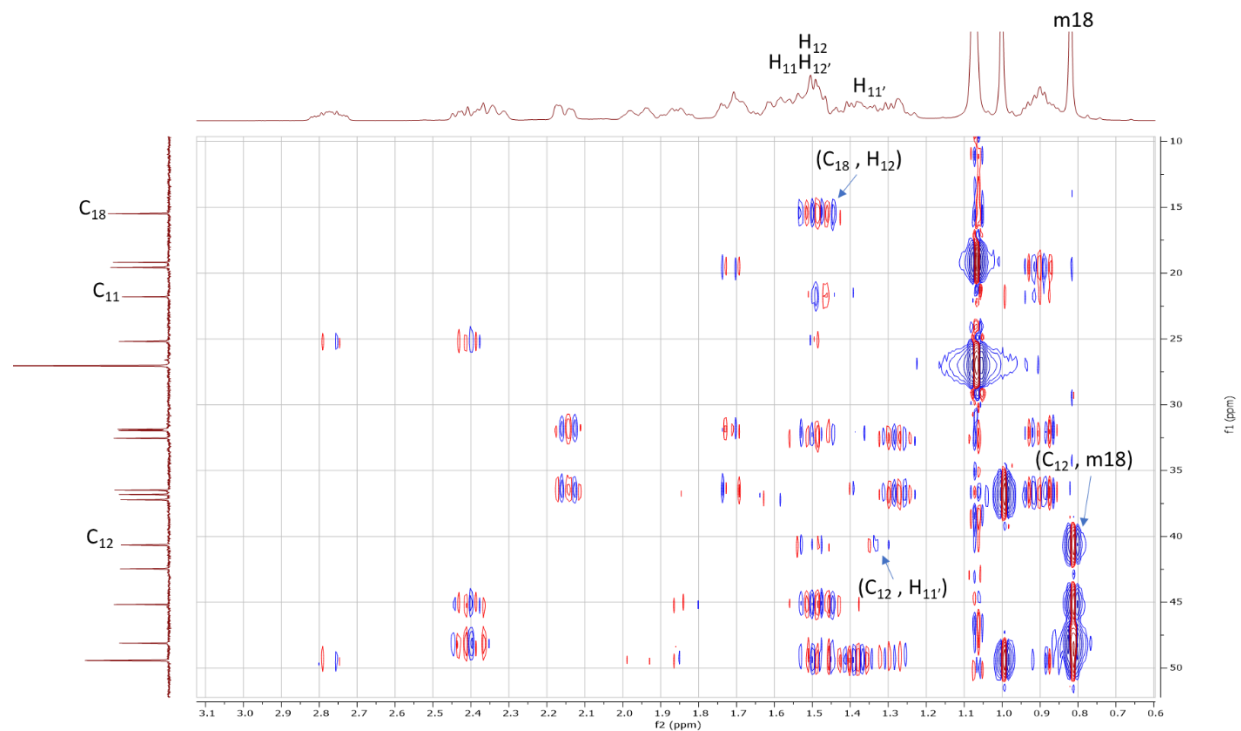
Figure 3.40C ^{1}H-^{13}C HMBC Correlations in C ring for DHEA C_{17} Iodide PG (6)

Concluding with the C ring, δ_C 40.66 (C_{12}) displayed moderate to strong HMBC correlations to m18 (δ_H 0.81) and $H_{11'}$ (δ_H 1.28) (see Figure 3.40C). δ_H 1.53 (H_{12}) and δ_H 1.38 ($H_{12'}$) were

discerned from HSQC correlations to δ_C 36.58 (C_{12}), HMBC correlation to C_{18} (15.47) and DEPT-135 -CH_2 correlation (see Figure 3.40A, 3.40B, and 3.40C). The remaining δ_C 21.79 (C_{11}) displayed HSQC correlation to δ_H 1.53 (H_{11}) and δ_H 1.28 ($H_{11'}$) (see Figure 3.40B), thus completing full assignment of DHEA C_{17} Iodide PG (**6**).
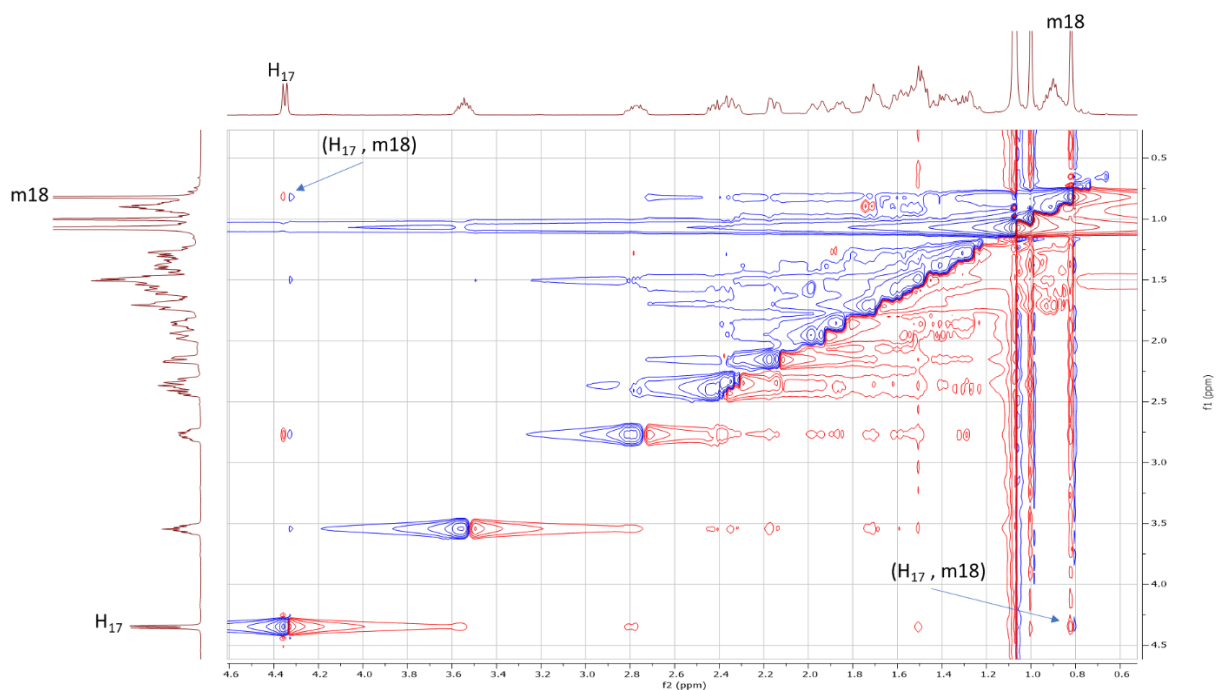
Figure 3.41 ^{1}H-^{1}H NOESY Correlations for DHEA C_{17} Iodide PG (6)

The stereochemistry of the iodide group at C_{17} is "R" based on NOESY correlation between δ_H 4.34 (H_{17}) and δ_H 0.81 (m18) (see Figure 3.41).
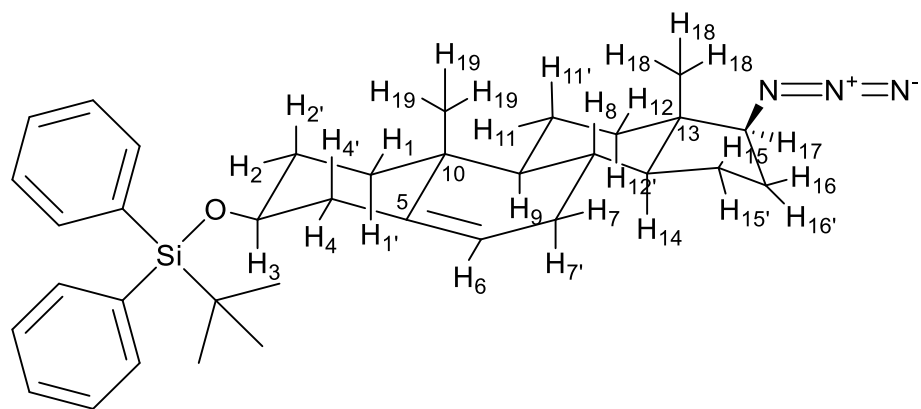
Figure 3.42A Chair Conformation for 7
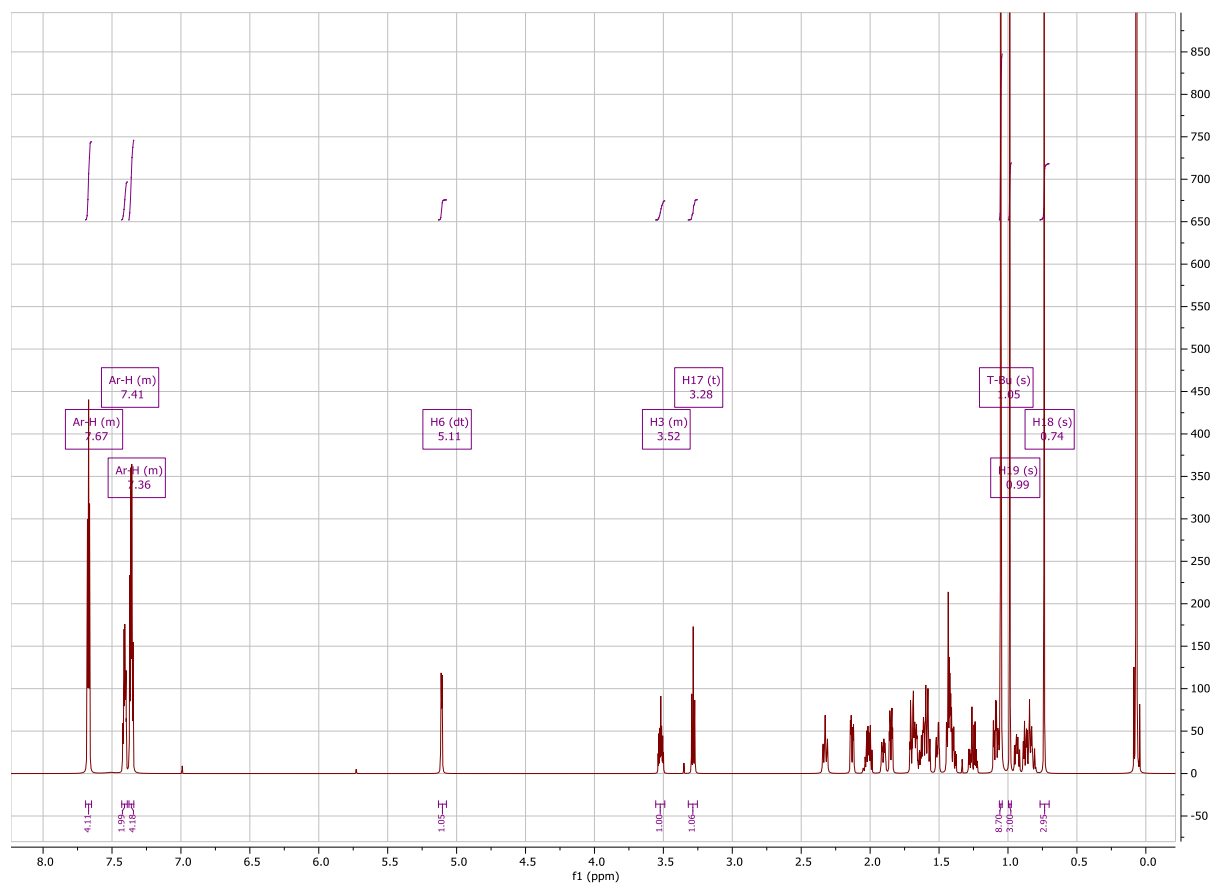
Figure 3.42B ^{1}H Spectrum of DHEA C$_{17}$-(S)-N$_3$ PG (7)

Aromatic protons of the TBDPS group were identified at δ$_H$ 7.36, δ$_H$ 7.41, and δ$_H$ 7.67 based upon chemical shift (see Figure 3.42B). δ$_H$ 5.11, δ$_H$ 3.28, and δ$_H$ 3.52 were identified as H$_6$, H$_{17}$, and H$_3$ respectively based upon chemical shift and splitting (see Figure 3.42B). The

methyl protons on C_{18} and C_{19} could be identified at either δ_H 0.99 or δ_H 0.74 (see Figure 3.42B).

The latter assignments for H_3, H_6, H_{17}, H_{18}, and H_{19} matched previous ^{1}H assignments (Blanco et al., 2014), (Kiss et al., 2018).
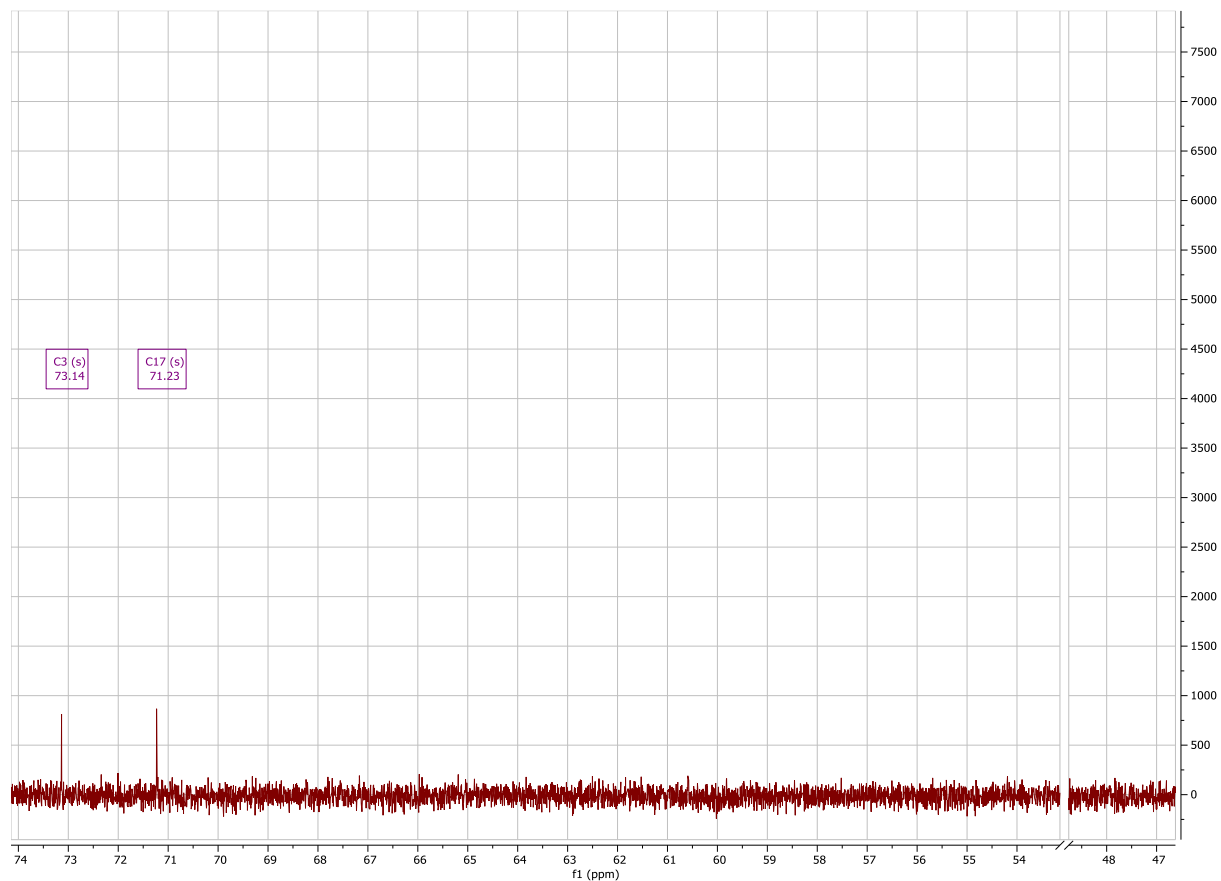
Figure 3.42C ^{13}C Spectrum of DHEA C_{17}-(S)-N$_3$ PG (7)

The loss of δ_C 48.12 (C_{17}, **6**) and gain of δ_C 71.23 (C_{17}, **7**) indicates the substitution of the iodide group through an S_N2 reaction to an azide group based on DHEA C_{17} Iodide PG (**6**) (see Figure 3.42C). δ_C 73.14 was identified as C_3 based on chemical shift and previous characterization of C_3 for DHEA C_{17} Iodide PG (**6**) (see Figure 3.42C).
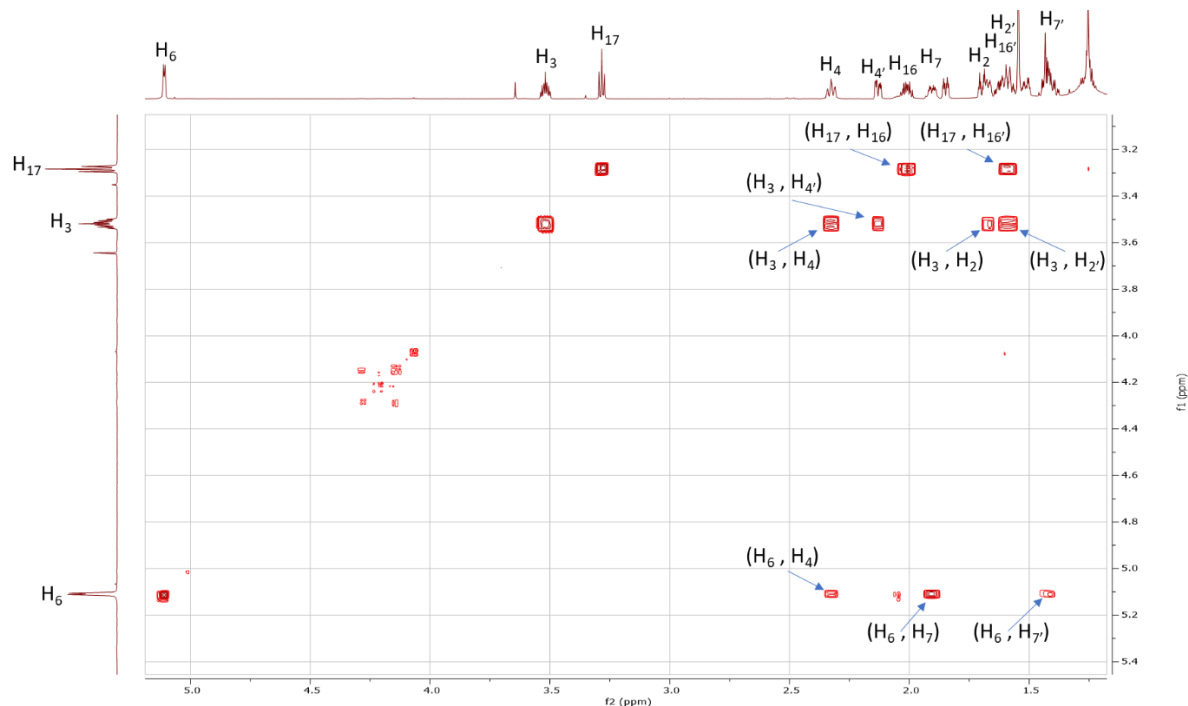
Figure 3.43 Initial ^{1}H-^{1}H COSY Correlations for DHEA C$_{17}$-(S)-N$_3$ PG (7)

Diastereotopic proton, δ_H 2.33 (H$_4$), from the A ring was identified from COSY correlations with H$_3$ (δ_H 3.52) and H$_6$ (δ_H 5.11) (see Figure 3.43). H$_{4'}$ (δ_H 2.13) was identified by COSY correlation to H$_3$ (δ_H 3.52) and chemical shift (see Figure 3.43). Methylene protons, δ_H 1.68 (H$_2$) and δ_H 1.60 (H$_{2'}$), were discerned from COSY correlations with H$_3$ (δ_H 3.52) (see Figure 3.43). In addition, diastereotopic protons δ_H 1.90 (H$_7$) and δ_H 1.42 (H$_{7'}$) in the B ring were identified from COSY correlations with H$_6$ (δ_H 5.11) (see Figure 3.43). In the D ring, diastereotopic protons, δ_H 2.01 (H$_{16}$) and δ_H 1.60 (H$_{16'}$) were discerned from COSY correlations with H$_{17}$ (δ_H 3.28) (see Figure 3.43).
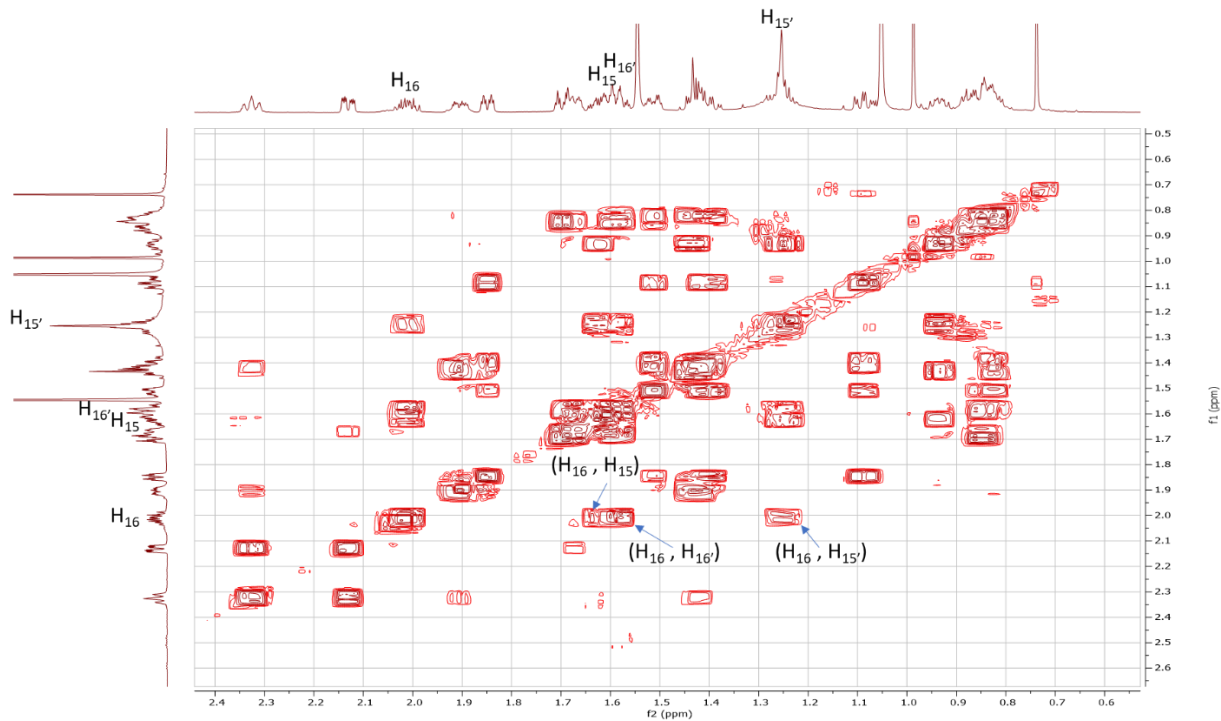
Figure 3.44A ^{1}H-^{1}H COSY Correlations in D ring for DHEA C$_{17}$-(S)-N$_3$ PG (7)
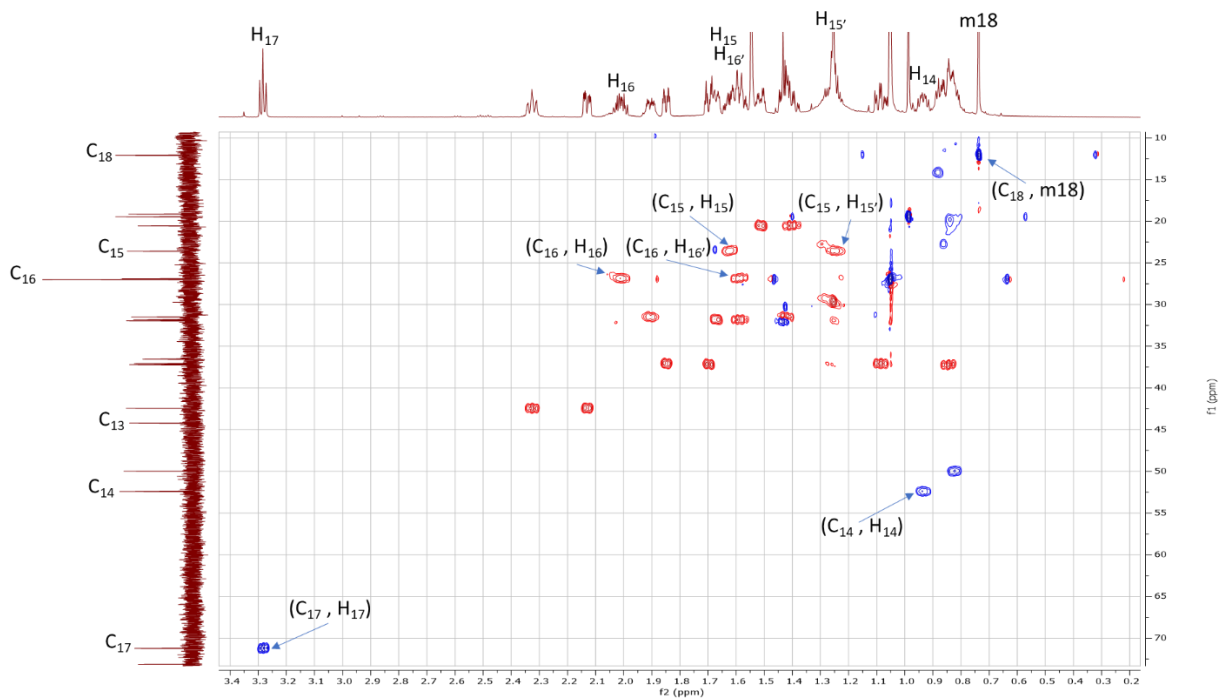
Figure 3.44B ^{1}H-^{13}C HSQC Correlations in D ring for DHEA C$_{17}$-(S)-N$_3$ PG (7)
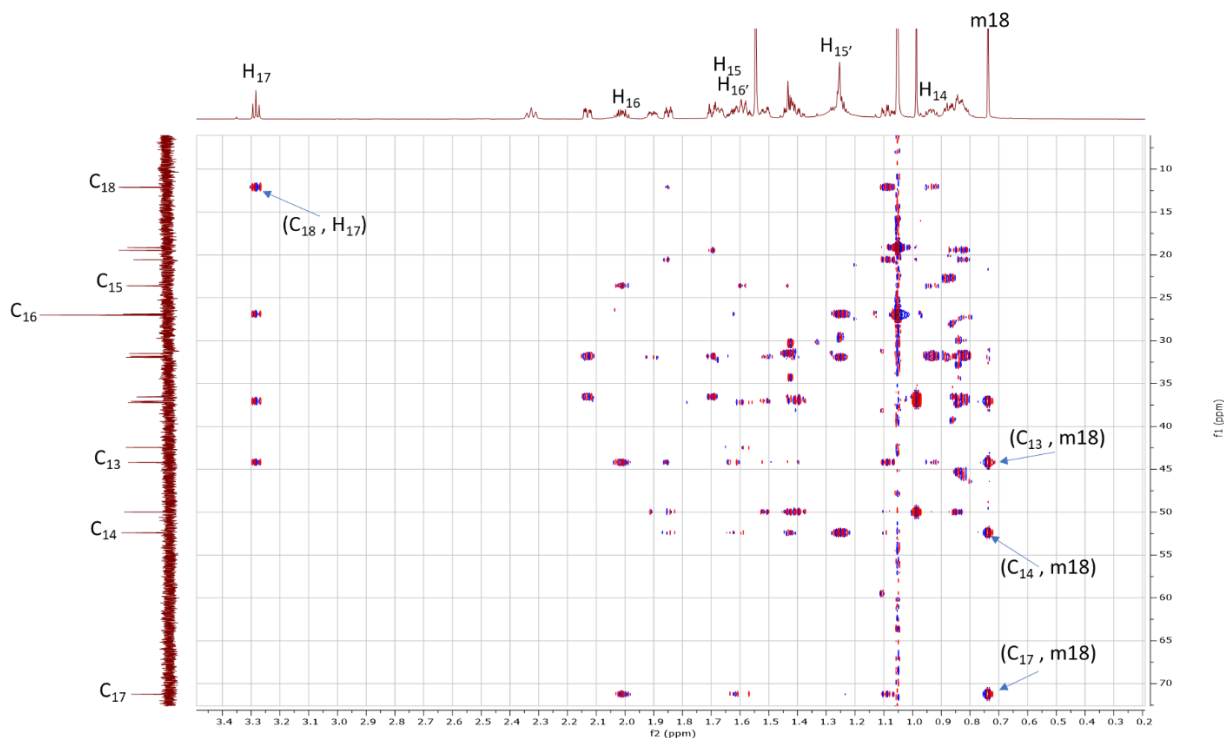
Figure 3.44C ^{1}H-^{13}C HMBC Correlations in D ring for DHEA C$_{17}$-(S)-N$_3$ PG (7)

Starting with the D ring, δ_C 71.23 was identified as C$_{17}$ from the HSQC correlation with δ_H 3.28 (H$_{17}$) and HMBC correlations to m18 (δ_H 0.74), the methyl protons on C$_{18}$ (see Figure 3.44B and 3.44C). Methylene protons, δ_H 2.01 (H$_{16}$) and δ_H 1.60 (H$_{16'}$), were correlated by HSQC to δ_C 26.91 (C$_{16}$) (see Figure 3.44B). Next, diastereotopic proton, δ_H 1.26 (H$_{15'}$), was discerned from COSY correlation to H$_{16}$ (δ_H 2.01) (see Figure 3.44A). From HSQC correlation, δ_H 1.26 (H$_{15'}$) showed HSQC correlation to δ_C 23.61 (C$_{15}$) and H$_{15}$ (δ_H 1.60) was identified by HSQC correlation to C$_{15}$ (δ_C 23.61) in addition to COSY correlation to δ_H 2.01 (H$_{16}$) (see Figure 3.44A and 3.44B). C$_{14}$ (δ_C 52.41) was identified by HMBC correlation to m18 (δ_H 0.74) (see Figure 3.44C). H$_{14}$ (δ_H 0.94) was distinguished based on HSQC correlation to C$_{14}$ (δ_C 52.41) (see Figure 3.44B). Continuing with m18, δ_C 12.11 (C$_{18}$) was identified from HSQC correlation to m18 (δ_H 0.74) and HMBC correlation to δ_H 3.28 (H$_{17}$) (see Figure 3.44B and 3.44C). Therefore, the methyl protons on C$_{19}$, m19, could be identified at δ_H 0.99 based on integration and splitting (see Figure 3.42B).

Quaternary carbon, δ_C 44.21 (C_{13}), was discerned from HMBC correlation to m18 (δ_H 0.74) and no observable HSQC correlation (see Figure 3.44B and 3.44C).

Figure 3.45A ^{1}H-^{13}C HSQC Correlations in B ring for DHEA C_{17}-(S)-N$_3$ PG (7)
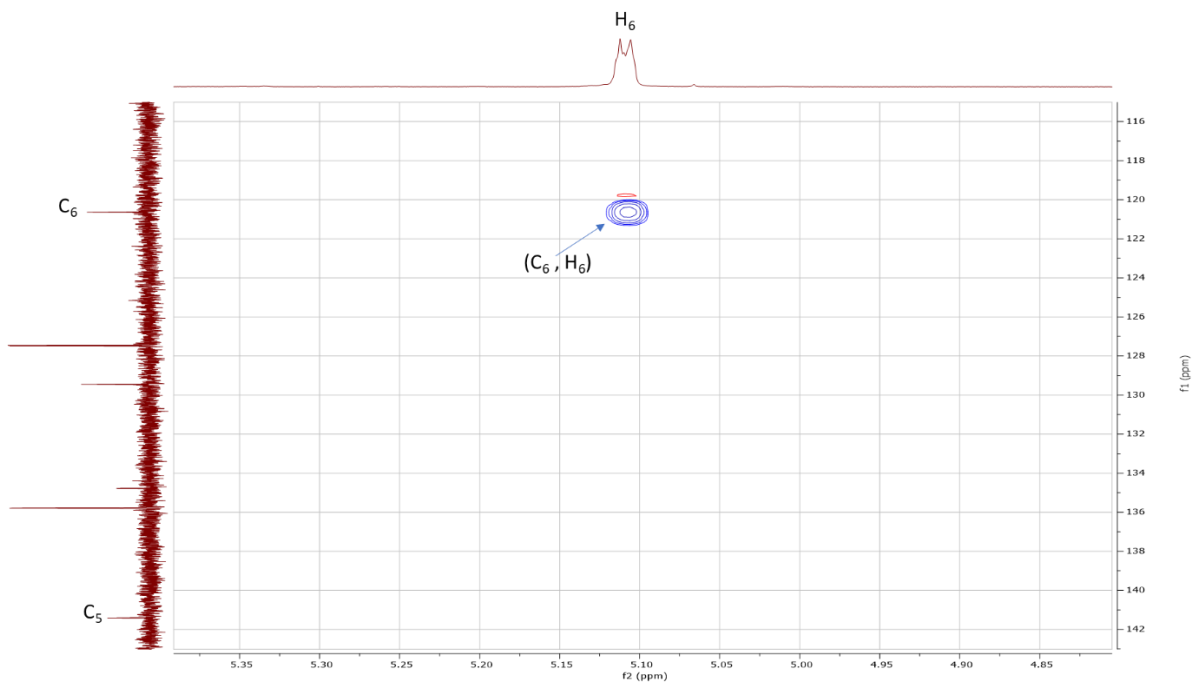
Figure 3.45B ^{1}H-^{13}C HSQC Correlations in B ring for DHEA C_{17}-(S)-N$_3$ PG (7) (C_5-C_6)
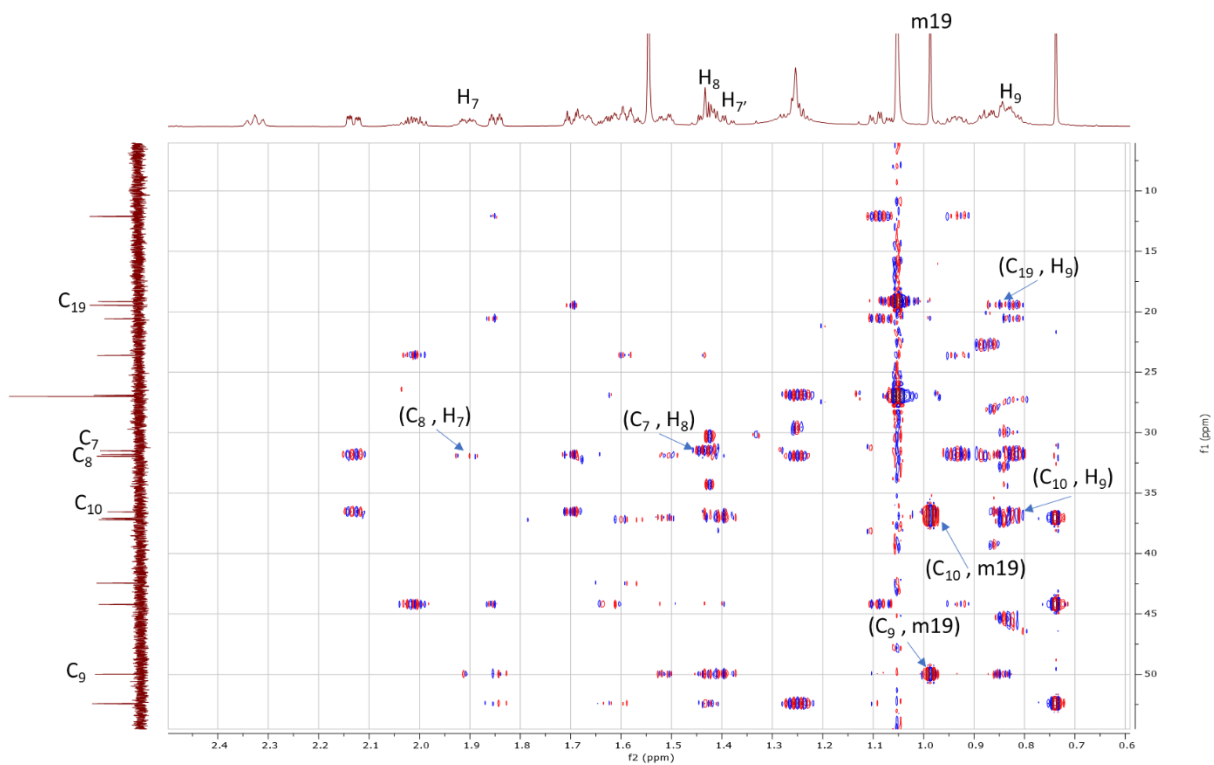
Figure 3.45C ^{1}H-^{13}C HMBC Correlations in B ring for DHEA C$_{17}$-(S)-N$_3$ PG (7)
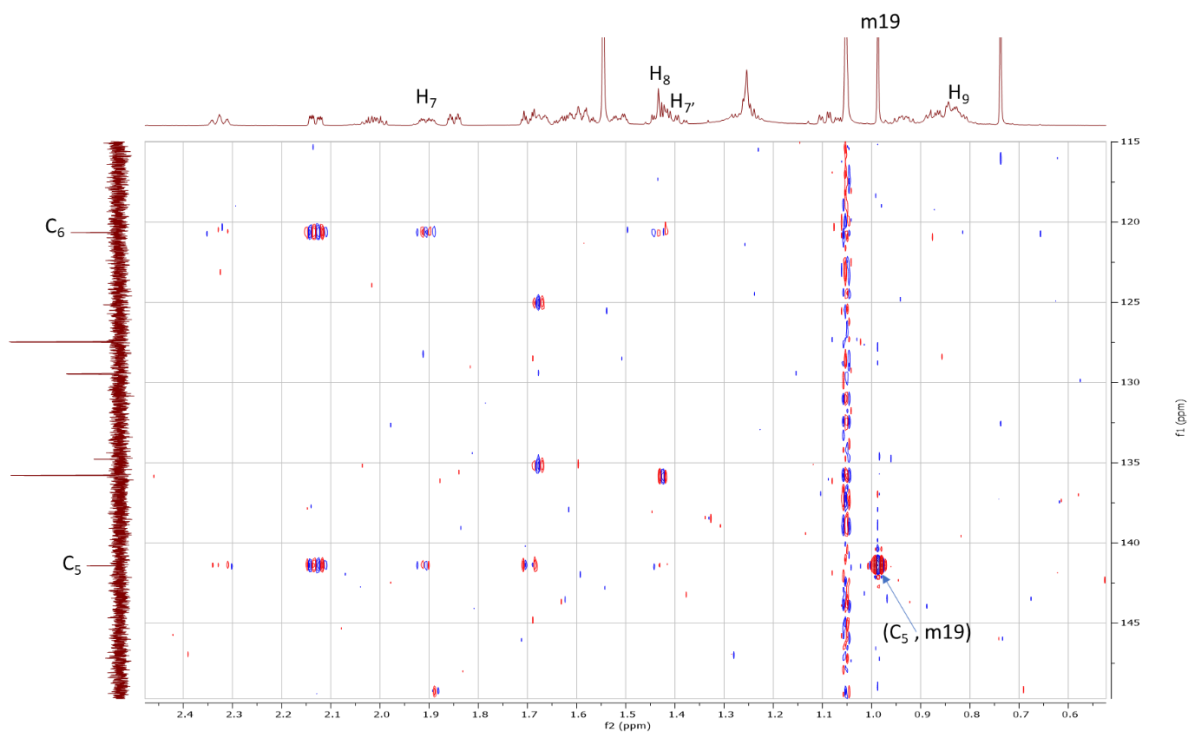
Figure 3.45D ^{1}H-^{13}C HMBC Correlations in B ring for DHEA C$_{17}$-(S)-N$_3$ PG (7) (C$_5$-C$_6$)

Next with the B ring, methyl protons, m19 (δ_H 0.99) exhibited HSQC correlation to δ_C 19.45 (C_{19}) (see Figure 3.45A). δ_C 141.41 (C_5) was determined on the basis of no HSQC correlation, chemical shift, and HMBC correlation to m19 (δ_H 0.99) (see Figure 3.45B and 3.45D). Vinyl carbon, C_6 (δ_C 120.64) was correlated by HSQC to δ_H 5.11 (H_6) (see Figure 3.45B). Methylene protons, δ_H 1.90 (H_7) and δ_H 1.42 ($H_{7'}$), exhibited HSQC correlation to δ_C 31.50 (C_7) (see Figure 3.45A). C_8 (δ_C 31.95) was correlated by HMBC to δ_H 1.90 (H_7) (see Figure 3.45C). Methine proton, H_8, was discerned at δ_H 1.42 based on HMBC correlation to C_7 (δ_C 31.50) and HSQC correlation to C_8 (δ_C 31.95) (see Figure 3.45A and 3.45C). The remaining methine proton, H_9 (δ_H 0.85), displayed correlation by HSQC to δ_C 49.99 (C_9) and by HMBC to δ_C 19.45 (C_{19}) (see Figure 3.45A and 3.45C). The remaining quaternary carbon, C_{10} (δ_C 36.55), was assigned based on HMBC correlation to m19 (δ_H 0.99) along with H_9 (δ_H 0.85) and no HSQC correlation (see Figure 3.45A and 3.45C).
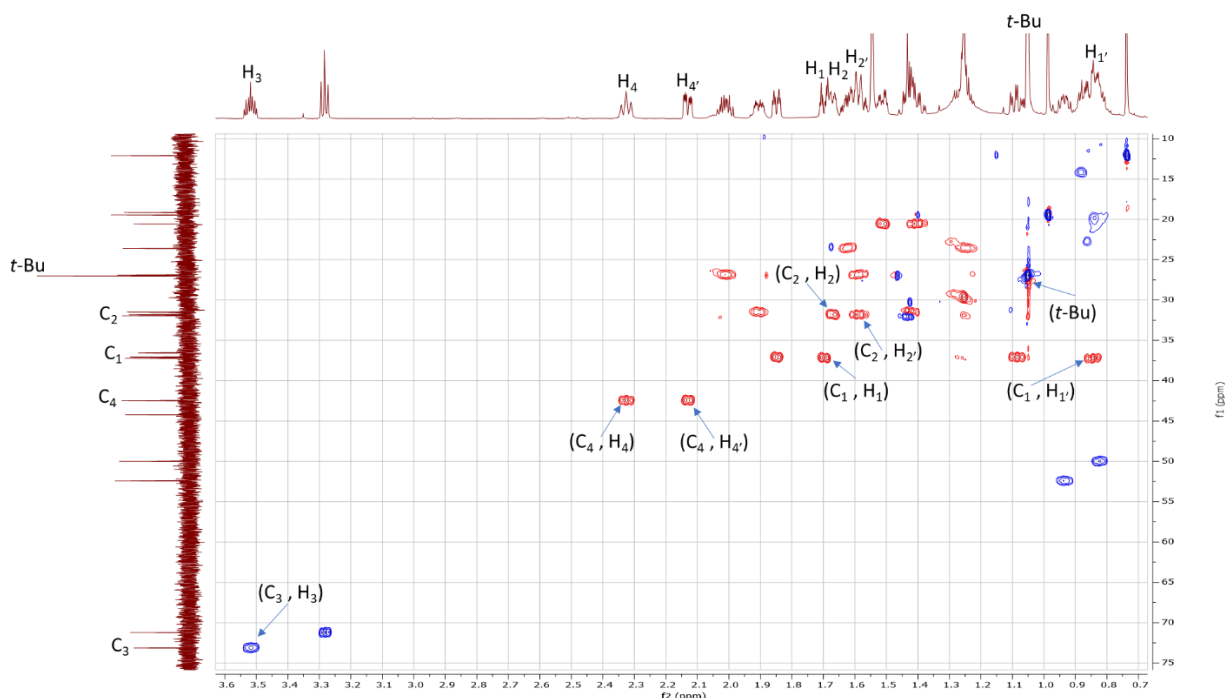
Figure 3.46A ^{1}H-^{13}C HSQC Correlations in A ring for DHEA C_{17}-(S)-N_3 PG (7)
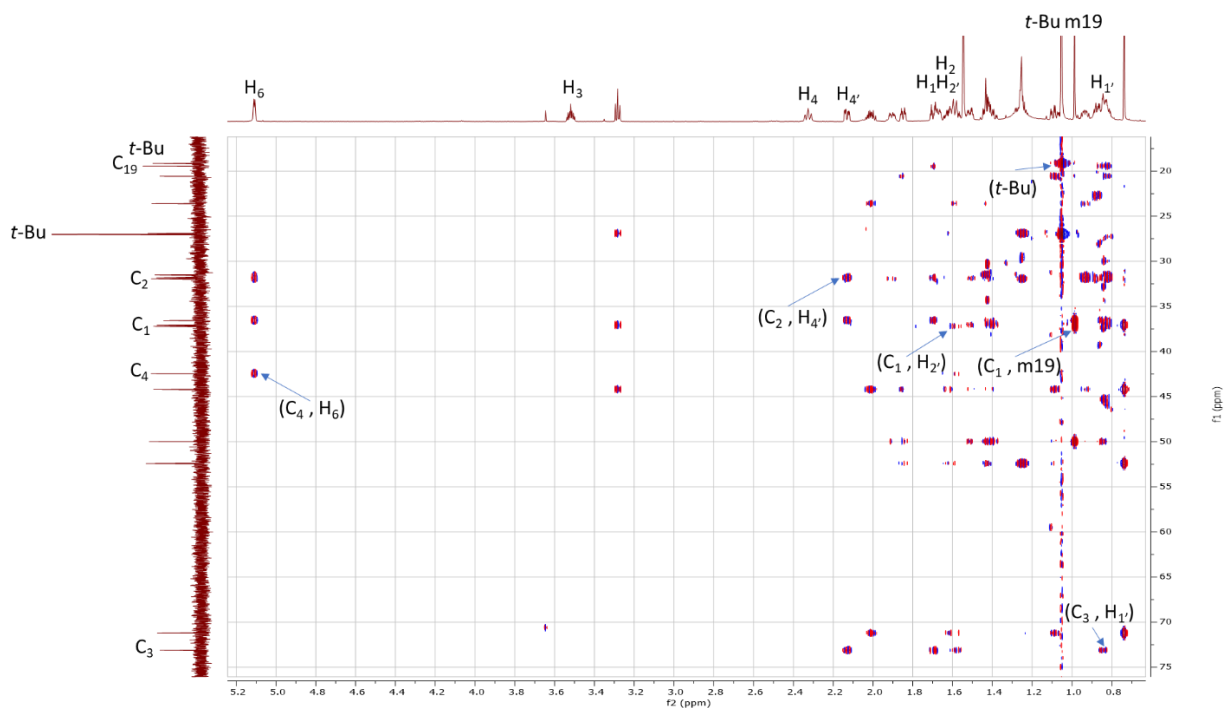
Figure 3.46B ^{1}H-^{13}C HMBC Correlations in A ring for DHEA C$_{17}$-(S)-N$_3$ PG (7)

Continuing with the A ring, δ_H 3.52 (H$_3$) exhibited HSQC correlation to δ_C 73.14 (C$_3$) (see

Figure 3.46A). Methylene protons, δ_H 2.33 (H$_4$) and δ_H 2.13 (H$_{4'}$), displayed HSQC correlation to

δ_C 42.45 (C$_4$), which shows HMBC correlation to H$_6$ (δ_H 5.11) (see Figure 3.46A and 3.46B).

Diastereotopic protons, δ_H 1.68 (H$_2$) and δ_H 1.60 (H$_{2'}$), displayed HSQC correlation to δ_C 31.82

(C$_2$), which showed HMBC correlation to H$_{4'}$ (δ_H 2.13) (see Figure 3.46A and 3.46B). δ_C 37.21 (C$_1$)

was discerned from HMBC correlation to m19 (δ_H 0.99) and H$_{2'}$ (δ_H 1.60) (see Figure 3.46A and

3.46B). From there, methylene protons, δ_H 1.68 (H$_1$) and δ_H 0.85 (H$_{1'}$) displayed HSQC correlation

to δ_C 37.21 (C$_1$) and HMBC correlation to δ_C 73.14 (C$_3$) (see Figure 3.46A and 3.46B). The *tert*-

butyl (*t*-Bu) protons of TBDPS were recognized based as the δ_H 1.05 singlet, which integrated to

nine (see Figure 3.42B). In addition, δ_C 27.00 (*t*-Bu) displayed HSQC correlation to δ_H 1.05 (*t*-Bu)

(see Figure 3.46A). δ_C 19.15 (*t*-Bu) displayed HMBC correlation to δ_H 1.05 (*t*-Bu) (see Figure

3.46B).
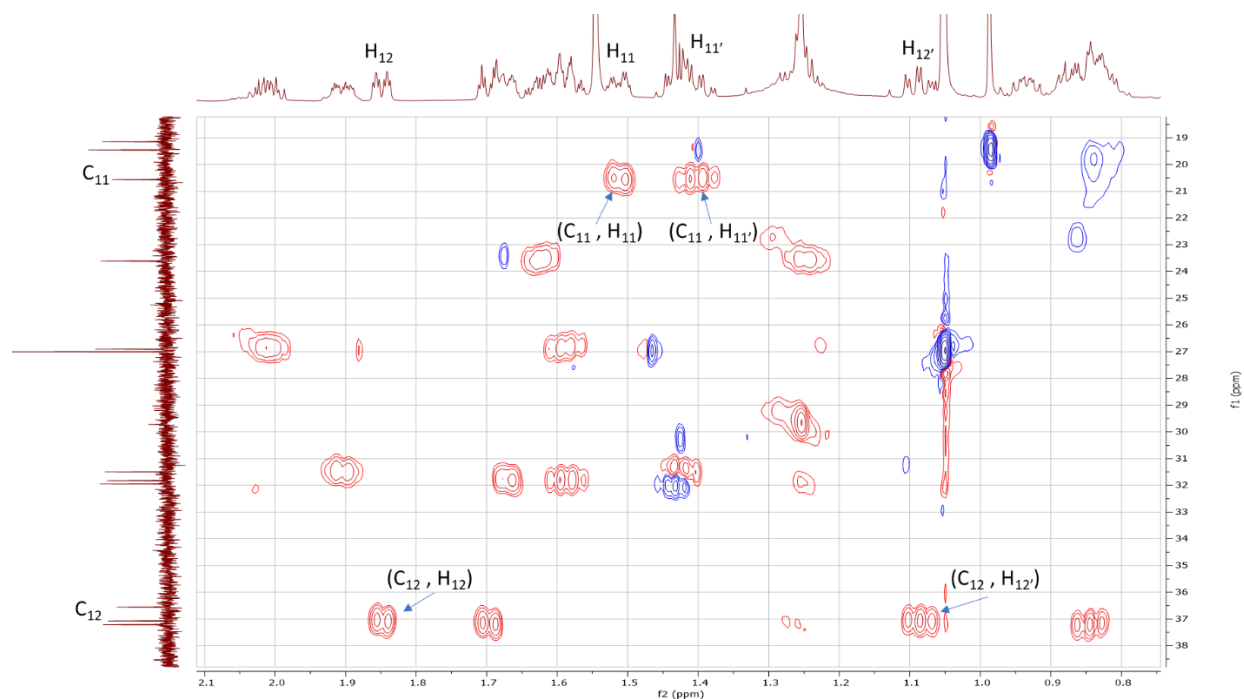
Figure 3.47A ^1H-^{13}C HSQC Correlations in C ring for DHEA C_{17}-(S)-N_3 PG (7)
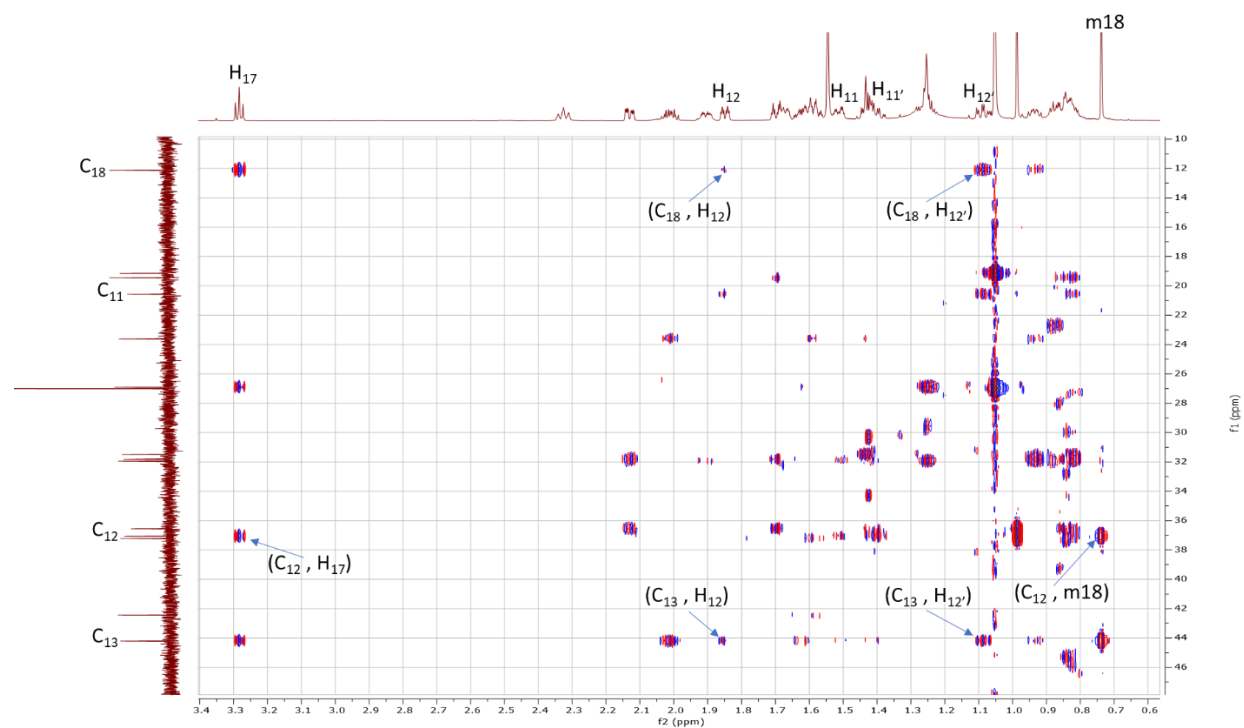
Figure 3.47B ^1H-^{13}C HMBC Correlations in C ring for DHEA C_{17}-(S)-N_3 PG (7)

Concluding with the C ring, δ_C 37.07 (C_{12}) displayed HMBC correlations to m18 (δ_H 0.74)

and H_{17} (δ_H 3.28) (see Figure S3.21). δ_H 1.85 (H_{12}) and δ_H 1.09 ($H_{12'}$) were discerned from HSQC

correlations to δ_C 37.07 (C_{12}) and HMBC correlations to C_{13} (δ_C 44.21) and C_{18} (δ_C 12.11). The remaining δ_C 20.57 (C_{11}) displayed HSQC correlation to δ_H 1.51 (H_{11}) and δ_H 1.42 ($H_{11'}$), thus completing full assignment of DHEA C_{17}-(S)-N_3 PG (**7**).
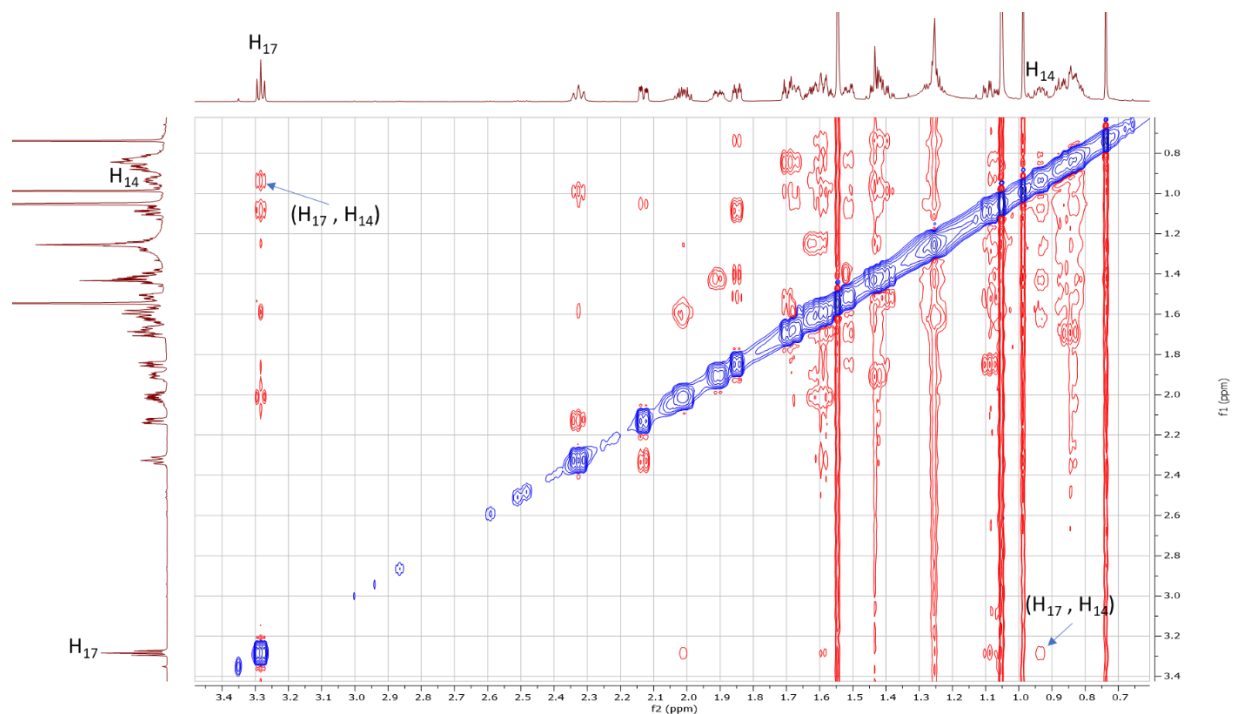
Figure 3.48 ^{1}H-^{1}H NOESY Correlations for DHEA C_{17}-(S)-N_3 PG (7)

The stereochemistry of the azide group at C_{17} is "S" based on NOESY correlation between δ_H 3.28 (H_{17}) and δ_H 0.94 (H_{14}) (see Figure 3.48).
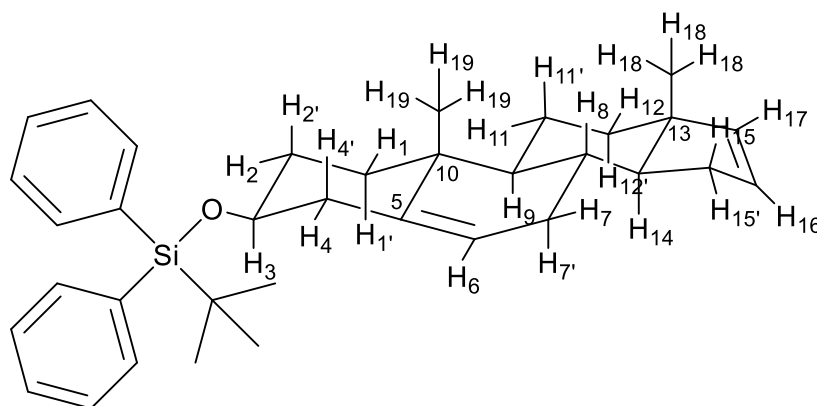
Figure 3.49A Chair Conformation of 7a

Figure 3.49B ^{1}H Spectrum of DHEA C$_{17-16}$ Alkene PG (7a)

Aromatic protons of the TBDPS group were identified at δ_H 7.36, δ_H 7.41, and δ_H 7.68 based upon chemical shift (see Figure 3.49B). δ_H 5.14 and δ_H 3.53 were identified as H$_6$ and H$_3$ respectively based upon chemical shift, splitting, and previous characterization of **1** to **7** (see

150

Figure 3.49B). δ_H 5.82 and δ_H 5.69 were identified as H_{17} and H_{16}, respectively based upon chemical shift and splitting (see Figure 3.49B). The methyl protons on C_{18} and C_{19} could be identified at either δ_H 1.02 or δ_H 0.76 (see Figure 3.49B). The latter assignments for H_3, H_6, H_{16}, H_{17}, H_{18}, and H_{19} matched previous ^{1}H assignments (Blanco et al., 2014), (Kiss et al., 2018).
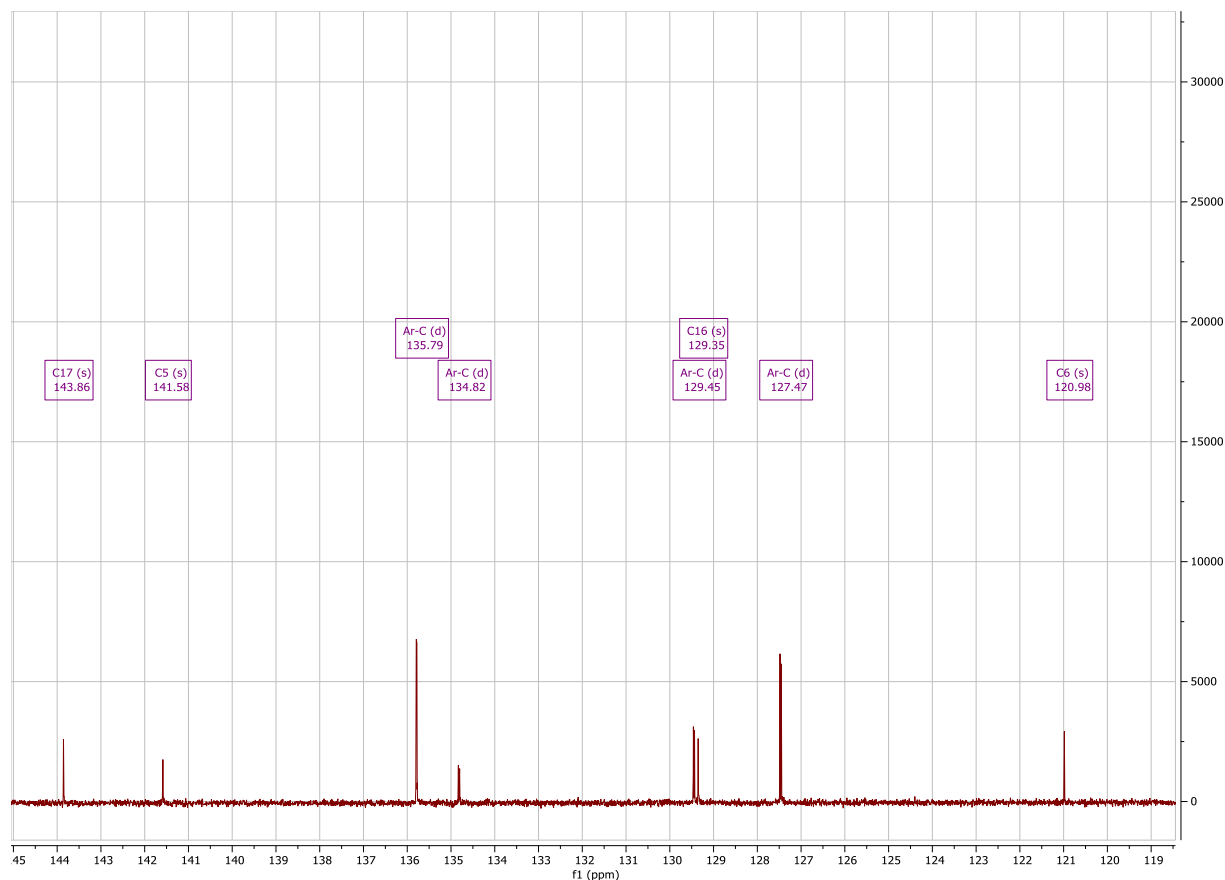
Figure 3.49C [13]C Spectrum of DHEA C_{17-16} Alkene PG (7a)

The appearance of two additional vinyl peaks at δ_C 143.86 and δ_C 129.35 indicates a double bond may be present between C_{17} and C_{16} (see Figure 3.49C). δ_C 141.58 and δ_C 120.98 were identified as C_5 and C_6 respectively based on chemical shift and previous characterization of C_6/C_5 for DHEA C_{17} Iodide PG (**6**) (see Figure 3.49C). In addition, the presence of the aromatic carbons of the TBDPS group were detected based on the appearance of previously observed carbon peaks between δ_C 120-140 (see Figure 3.49C).
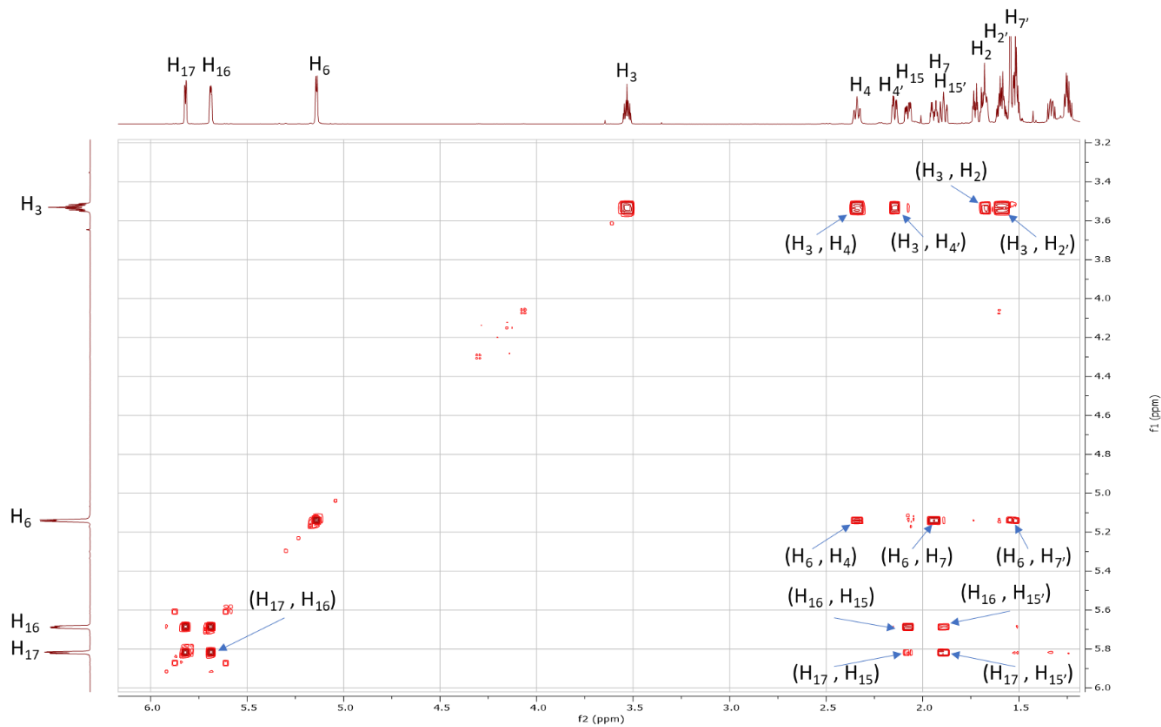
Figure 3.50 Initial ^{1}H-^{1}H COSY Correlations for DHEA C$_{17\text{-}16}$ Alkene PG (7a)

Diastereotopic proton, δ_H 2.34 (H$_4$), from the A ring was identified from COSY correlations with H$_3$ (δ_H 3.53) and H$_6$ (δ_H 5.14) (see Figure 3.50). δ_H 2.14 (H$_{4'}$) was identified by COSY correlation to H$_3$ (δ_H 3.53) and chemical shift (see Figure 3.50). Methylene protons, δ_H 1.68 (H$_2$) and δ_H 1.59 (H$_{2'}$), were discerned from COSY correlations with H$_3$ (δ_H 3.53) (see Figure 3.50). In addition, diastereotopic protons δ_H 1.94 (H$_7$) and δ_H 1.51 (H$_{7'}$) in the B ring were identified from COSY correlations with H$_6$ (δ_H 5.14) (see Figure 3.50). In the D ring, diastereotopic protons, δ_H 2.08 (H$_{15}$) and δ_H 1.89 (H$_{15'}$) were discerned from COSY correlations with δ_H 5.82 (H$_{17}$) and δ_H 5.69 (H$_{16}$) (see Figure 3.50).
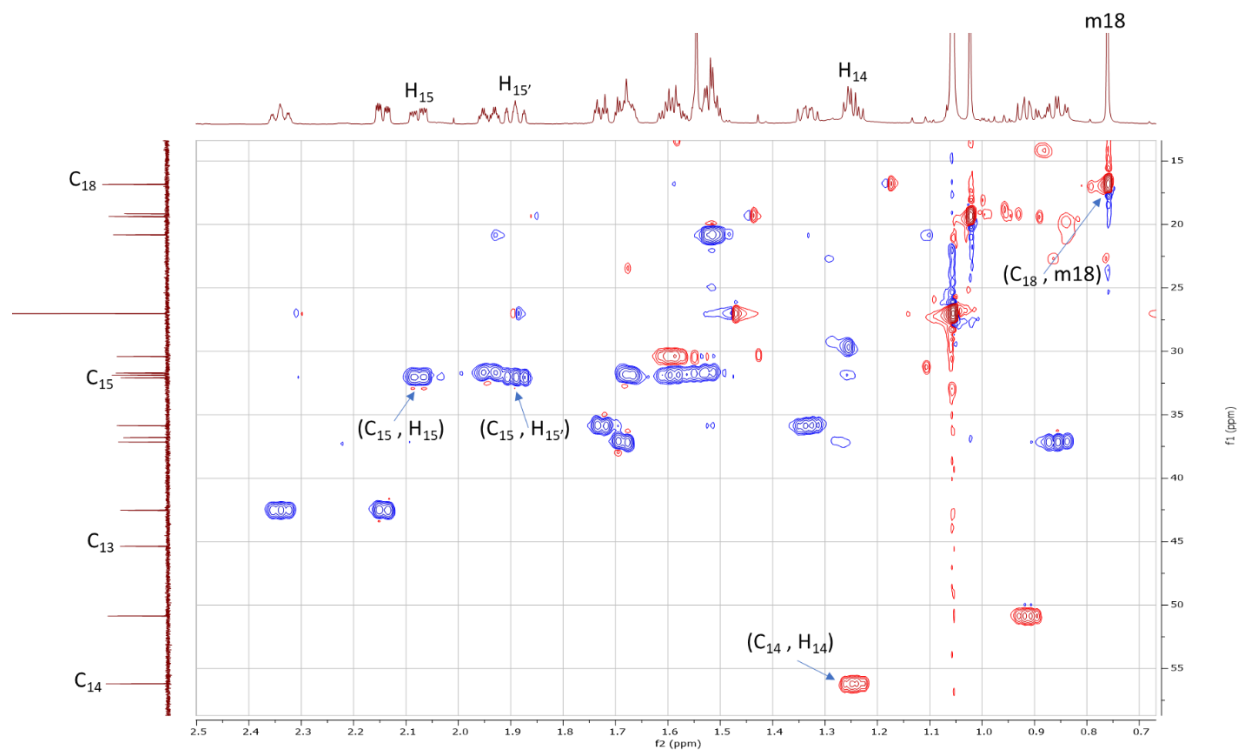
Figure 3.51A ^{1}H-^{13}C HSQC Correlations in D ring for DHEA C$_{17-16}$ Alkene PG (7a)
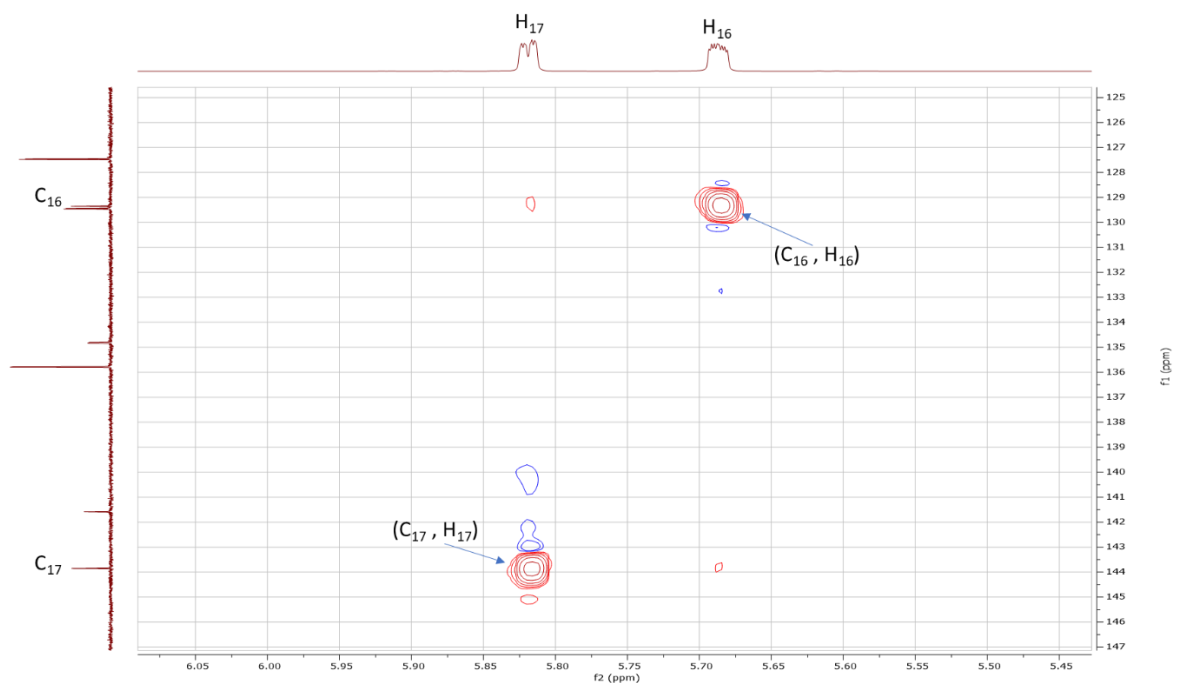
Figure 3.51B ^{1}H-^{13}C HSQC Correlations in D ring for DHEA C$_{17-16}$ Alkene PG (7a) (C$_{16}$-C$_{17}$)
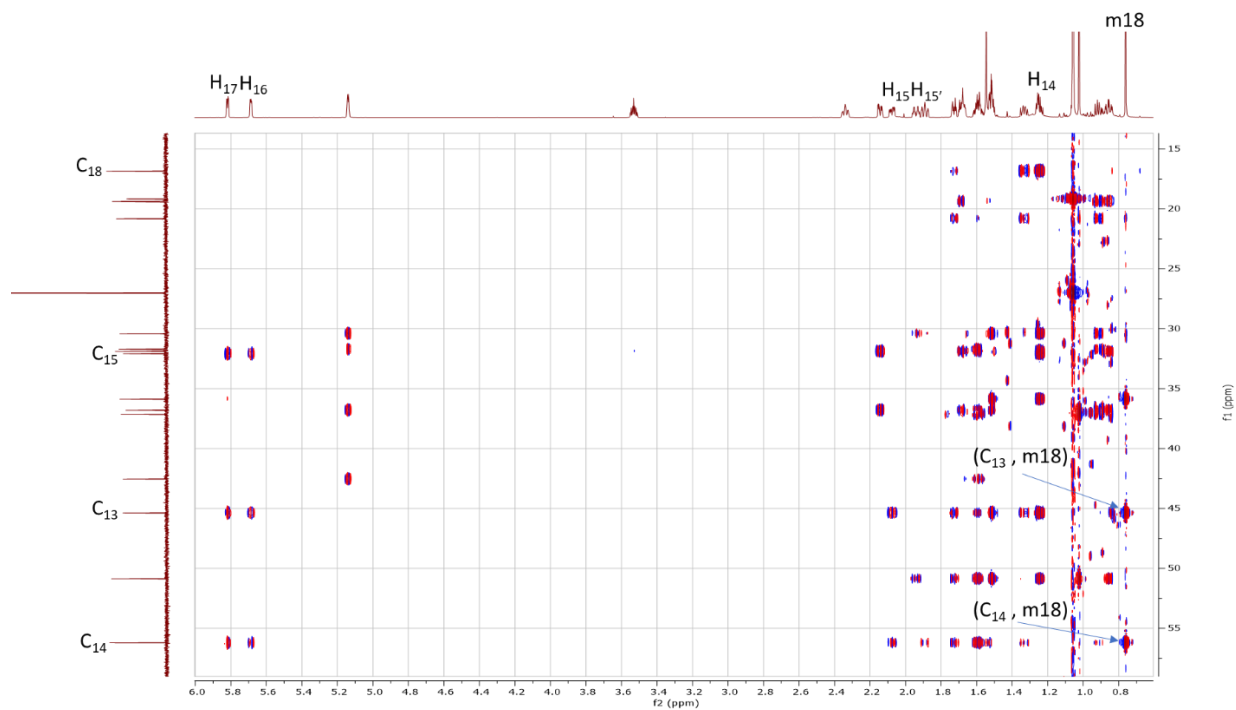
Figure 3.51C ^{1}H-^{13}C HMBC Correlations in D ring for DHEA C$_{17\text{-}16}$ Alkene PG (7a)

Figure 3.51D ^{1}H-^{13}C HMBC Correlations in D ring for DHEA C$_{17\text{-}16}$ Alkene PG (7a) (C$_{16}$-C$_{17}$)
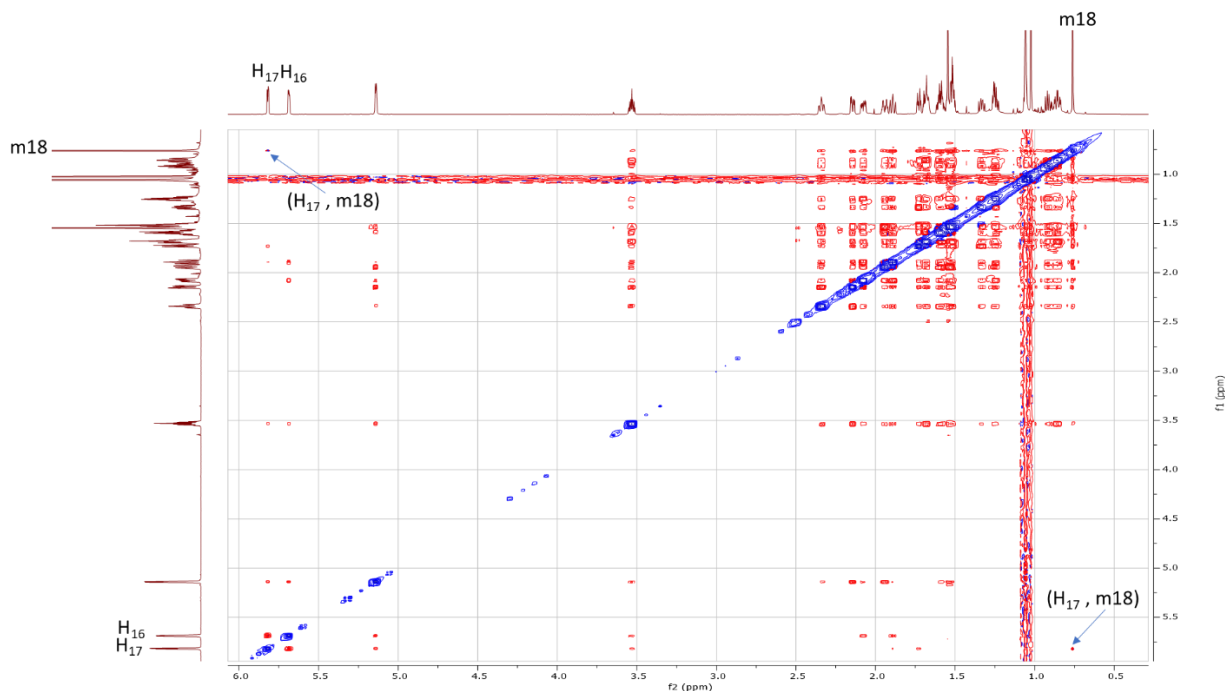
Figure 3.51E ^{1}H-^{1}H NOESY Correlations in D ring for DHEA C$_{17\text{-}16}$ Alkene PG (7a)

Starting with the D ring, δ_H 5.82 (H$_{17}$) displayed moderate NOESY correlation to m18 (δ_H 0.76), the methyl protons on C$_{18}$ (see Figure 3.51E). δ_C 143.86 was identified as C$_{17}$ from HSQC correlation with δ_H 5.82 (H$_{17}$) and strong HMBC correlations to m18 (δ_H 0.76) (see Figure 3.51B and 3.51D). Next, δ_H 5.69 (H$_{16}$) exhibited HMBC correlation to C$_{17}$ (δ_C 143.86) (see Figure 3.51D). Vinyl proton, δ_H 5.69 (H$_{16}$) was correlated by HSQC to δ_C 129.35 (C$_{16}$) (see Figure 3.51B). δ_H 2.08 (H$_{15}$) and δ_H 1.89 (H$_{15'}$) showed HSQC correlation to δ_C 32.08 (C$_{15}$) (see Figure 3.51A). C$_{14}$ (δ_C 56.21) was identified by HMBC correlation to m18 (δ_H 0.76) (see Figure 3.51C). H$_{14}$ (δ_H 1.25) was distinguished based on HSQC correlation to C$_{14}$ (δ_C 56.21) (see Figure 3.51A). Continuing with m18, δ_C 16.84 (C$_{18}$) was identified from HSQC correlation to m18 (δ_H 0.76) (see Figure 3.51A). Therefore, the methyl protons on C$_{19}$, m19, could be identified at δ_H 1.02 based on integration and splitting (see Figure 3.49B). Quaternary carbon, δ_C 45.37 (C$_{13}$), was discerned from HMBC correlation to m18 (δ_H 0.76) and no observable HSQC correlation (see Figure 3.51A and 3.51C).
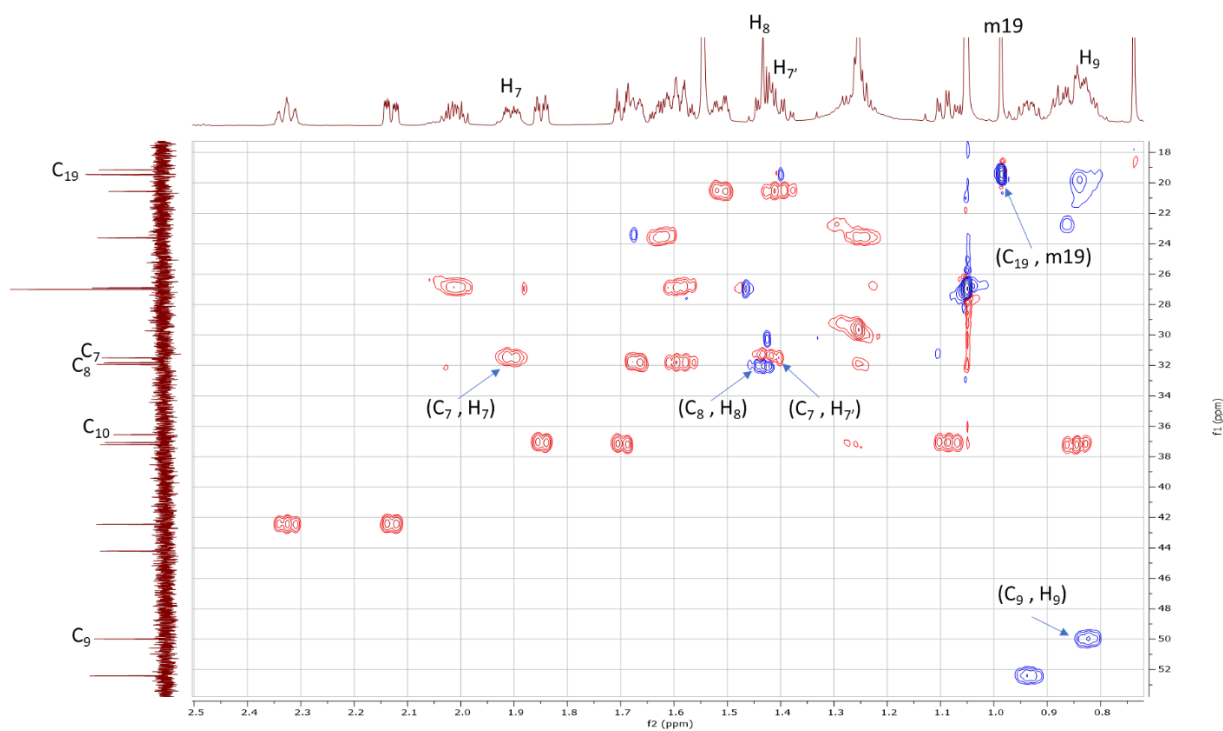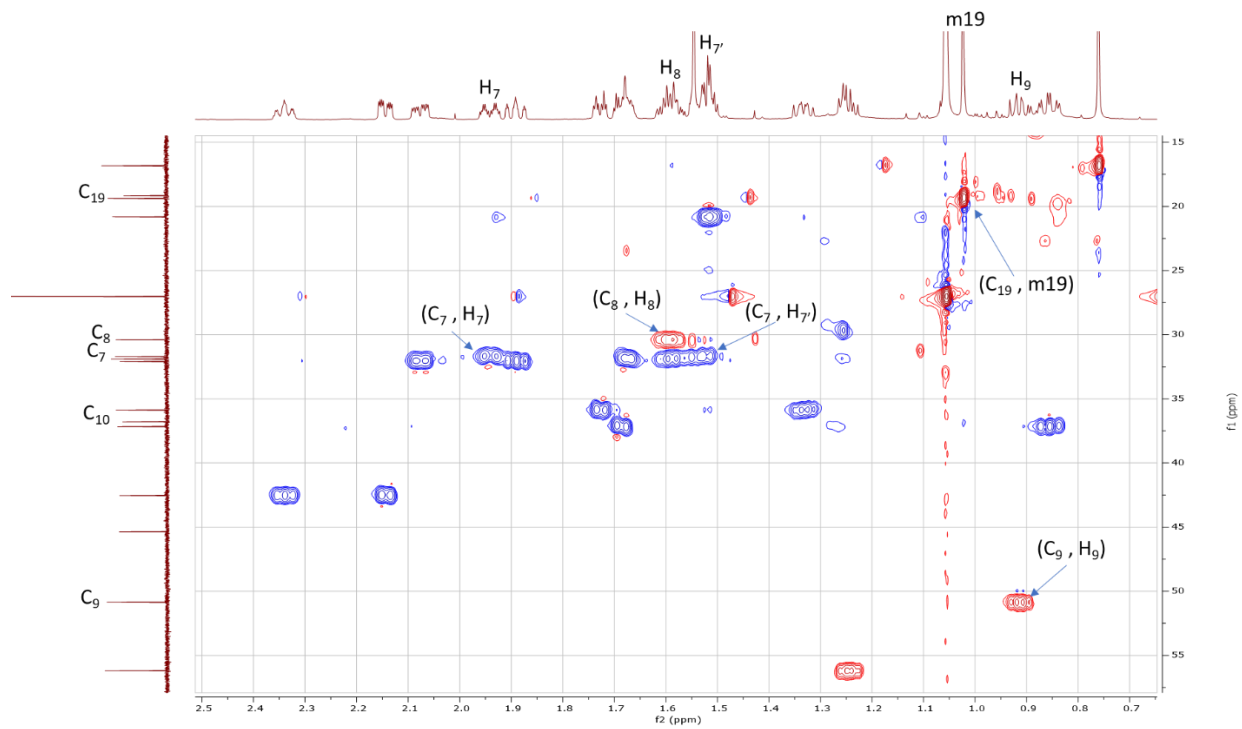
Figure 3.52A ^{1}H-^{13}C HSQC Correlations in B ring for DHEA C_{17-16} Alkene PG (7a)
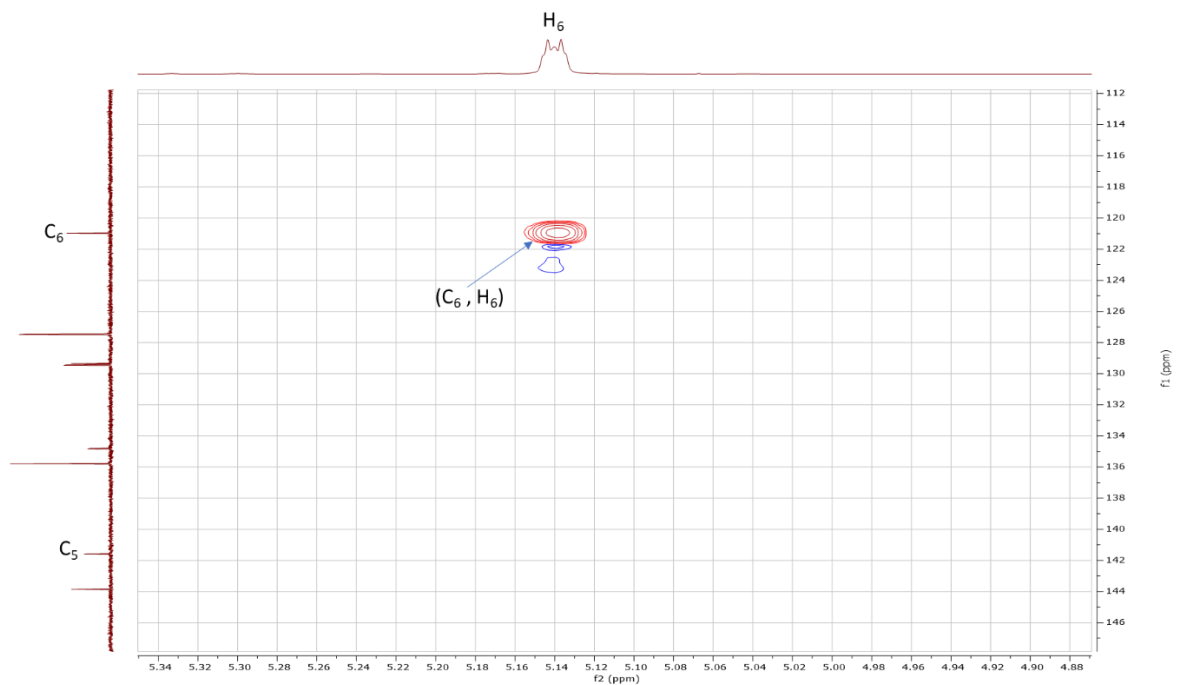
Figure 3.52B ^{1}H-^{13}C HSQC Correlations in B ring for DHEA C_{17-16} Alkene PG (7a) (C_5-C_6)
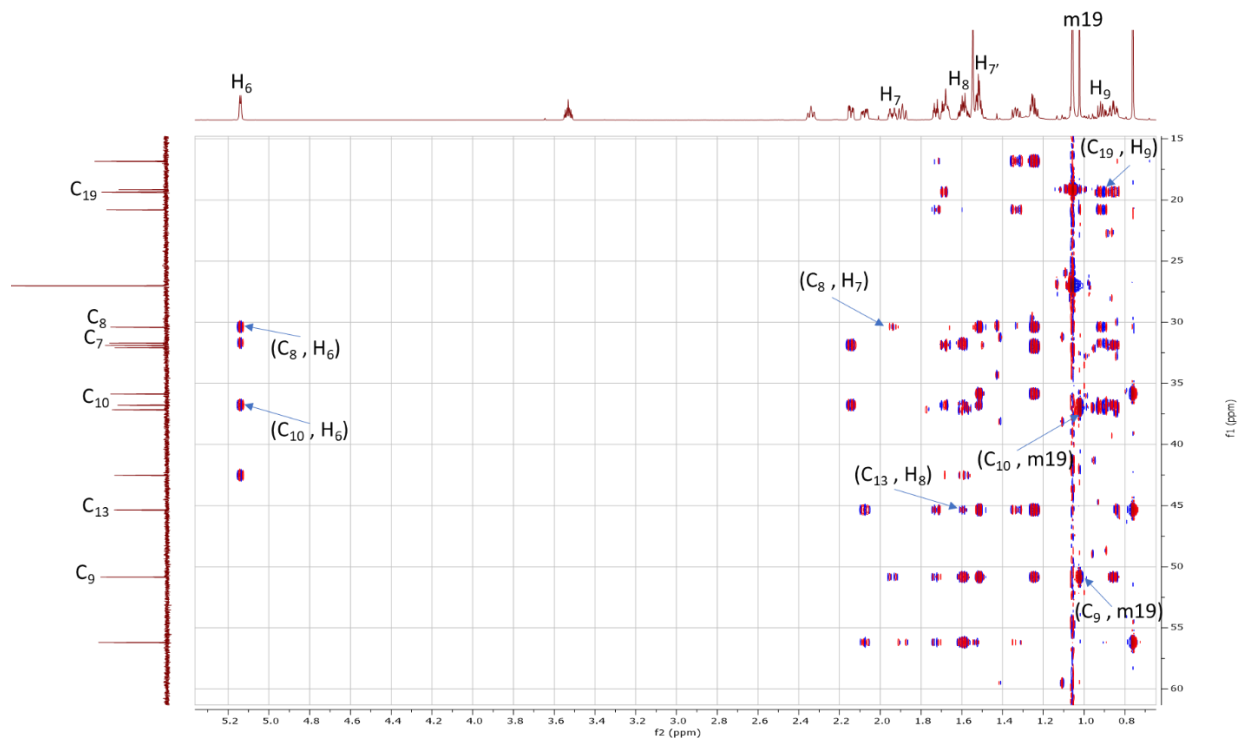
Figure 3.52C ^{1}H-^{13}C HMBC Correlations in B ring for DHEA C$_{17\text{-}16}$ Alkene PG (7a)
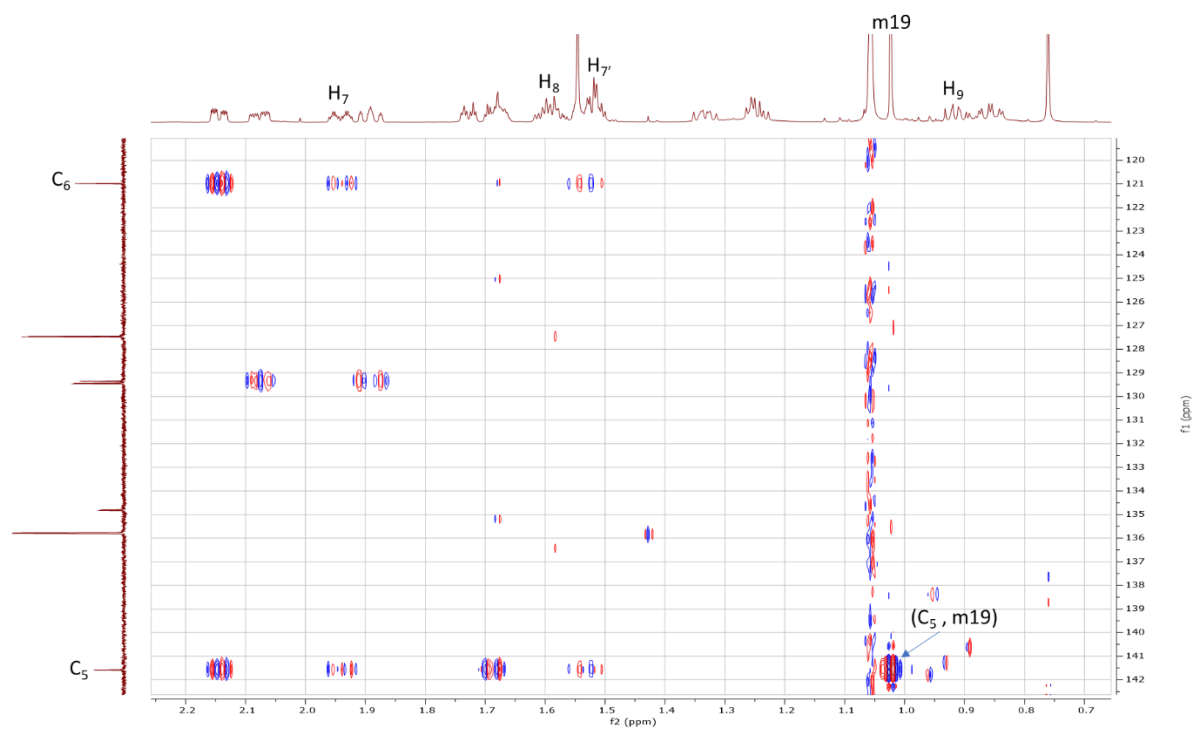
Figure 3.52D ^{1}H-^{13}C HMBC Correlations in B ring for DHEA C$_{17\text{-}16}$ Alkene PG (7a) (C$_5$-C$_6$)

Next with the B ring, methyl protons, m19 (δ_H 1.02) exhibited HSQC correlation to δ_C 19.37 (C_{19}) (see Figure 3.51A). δ_C 141.58 (C_5) was determined on the basis of no HSQC correlation, chemical shift, and HMBC correlation to m19 (δ_H 1.02) (see Figure 3.52B and 3.52D). Vinyl carbon, C_6 (δ_C 120.98) was correlated by HSQC to δ_H 5.14 (H_6) (see Figure 3.52B). Methylene protons, δ_H 1.94 (H_7) and δ_H 1.51 ($H_{7'}$), exhibited HSQC correlation to δ_C 31.72 (C_7) (see Figure 3.52A). C_8 (δ_C 30.41) was correlated by HMBC to δ_H 1.94 (H_7) and H_6 (δ_H 5.14) (see Figure 3.52C). Methine proton, H_8, was discerned at δ_H 1.59 based on HMBC correlation to C_{13} (δ_H 45.37) and HSQC correlation to C_8 (δ_C 30.41) (see Figure 3.52A and 3.52C). The remaining methine proton, H_9 (δ_H 0.91), displayed correlation by HSQC to δ_C 50.86 (C_9) and by HMBC to δ_C 19.37 (C_{19}) (see Figure 3.52A and 3.52C). Quaternary carbon, C_{10} (δ_C 36.80), was assigned based on HMBC correlation to H_6 (δ_H 5.14) and m19 (δ_H 1.02) and no HSQC correlation (see Figure 3.52A and 3.52C).
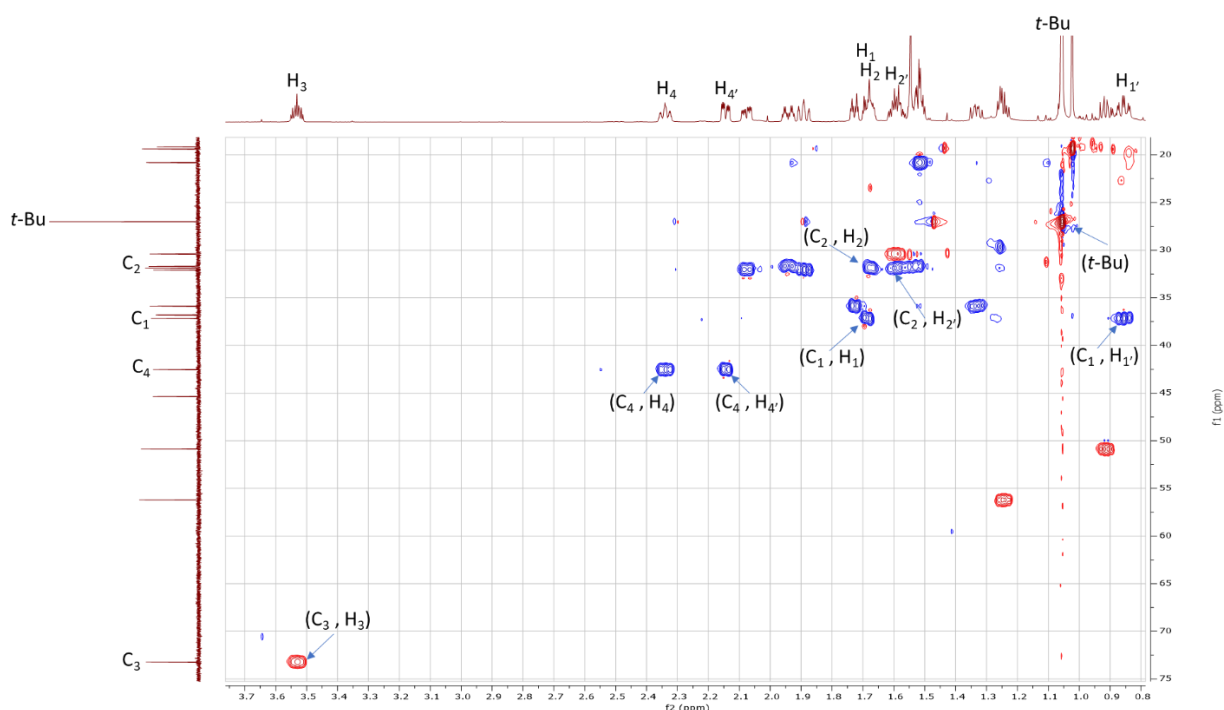
Figure 3.53A ^{1}H-^{13}C HSQC Correlations in A ring for DHEA C_{17-16} Alkene PG (7a)
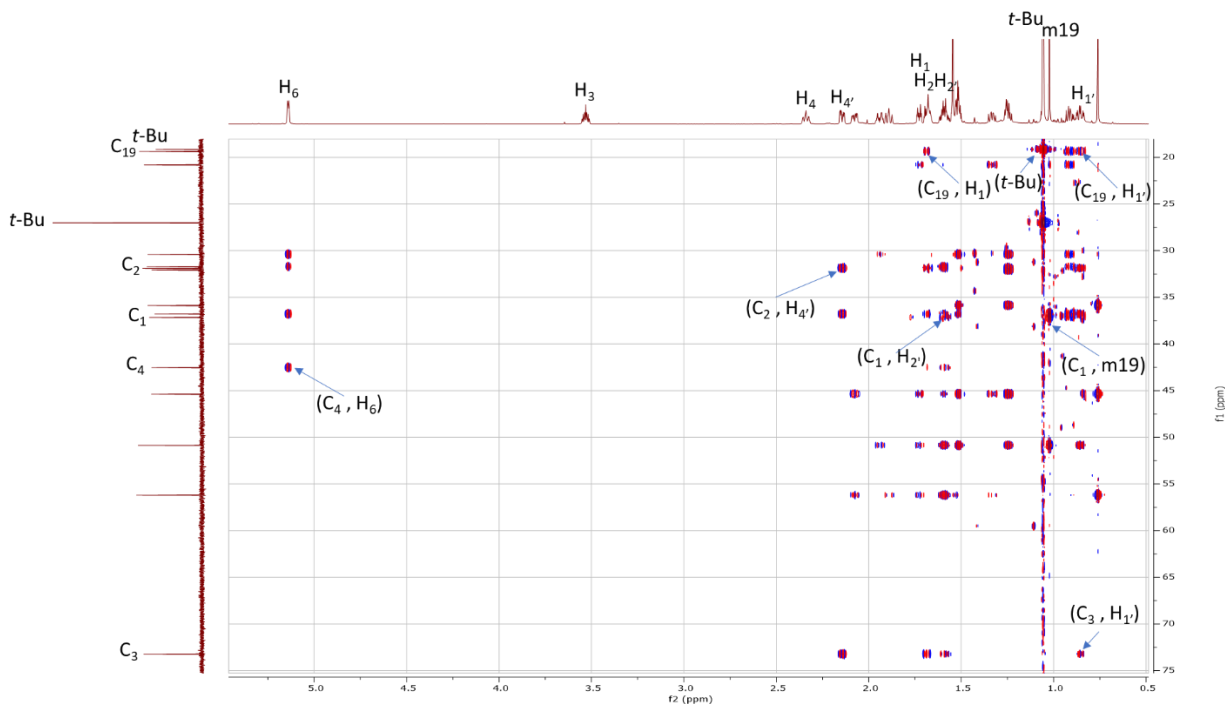
Figure 3.53B ^{1}H-^{13}C HMBC Correlations in A ring for DHEA C$_{17\text{-}16}$ Alkene PG (7a)

Continuing with the A ring, δ_H 3.53 (H$_3$) exhibited HSQC correlation to δ_C 73.23 (C$_3$) (see Figure 3.53A). Methylene protons, δ_H 2.34 (H$_4$) and δ_H 2.14 (H$_{4'}$), displayed HSQC correlation to δ_C 42.54 (C$_4$), which showed HMBC correlation to H$_6$ (δ_H 5.14) (see Figure 3.53A and 3.53B). Diastereotopic protons, δ_H 1.68 (H$_2$) and δ_H 1.59 (H$_{2'}$), displayed HSQC correlation to δ_C 31.89 (C$_2$), which showed HMBC correlation to H$_{4'}$ (δ_H 2.14) (see Figure 3.53A and 3.53B). δ_C 37.16 (C$_1$) was discerned from HMBC correlation to m19 (δ_H 1.02) and H$_{2'}$ (δ_H 1.59) (see Figure 3.53B). From there, methylene protons, δ_H 1.68 (H$_1$) and δ_H 0.86 (H$_{1'}$) displayed HSQC correlation to δ_C 37.16 (C$_1$) and HMBC correlation to C$_3$ (δ_C 73.23) along with C$_{19}$ (δ_C 19.37) (see Figure 3.53A and 3.53B). The *tert*-butyl (*t*-Bu) protons of TBDPS were recognized based as the δ_H 1.06 singlet, which integrated to nine (see Figure 3.49B). In addition, δ_C 27.02 (*t*-Bu) displayed HSQC correlation to δ_H 1.06 (*t*-Bu) (see Figure 3.49A). δ_C 19.16 (*t*-Bu) displayed HMBC correlation to δ_H 1.06 (*t*-Bu) (see Figure 3.53B).
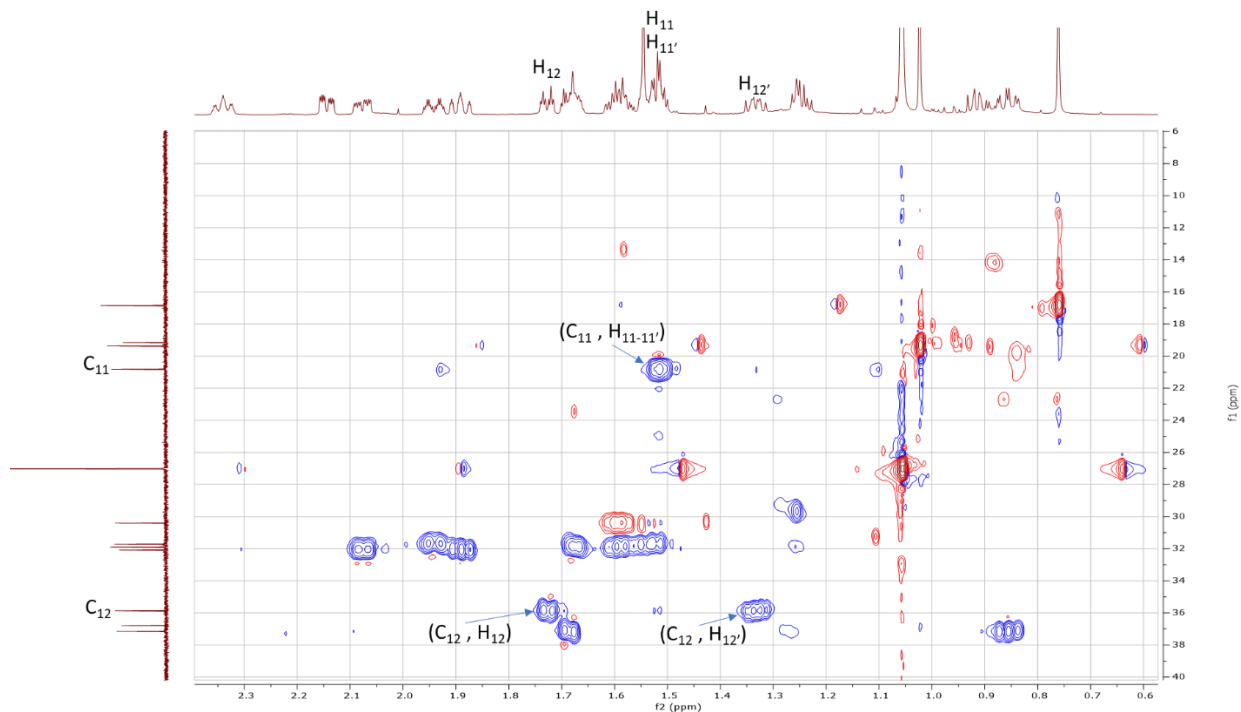
**Figure 3.54A ^{1}H-^{13}C HSQC Correlations in C ring for DHEA $C_{17\text{-}16}$ Alkene PG (7a)**
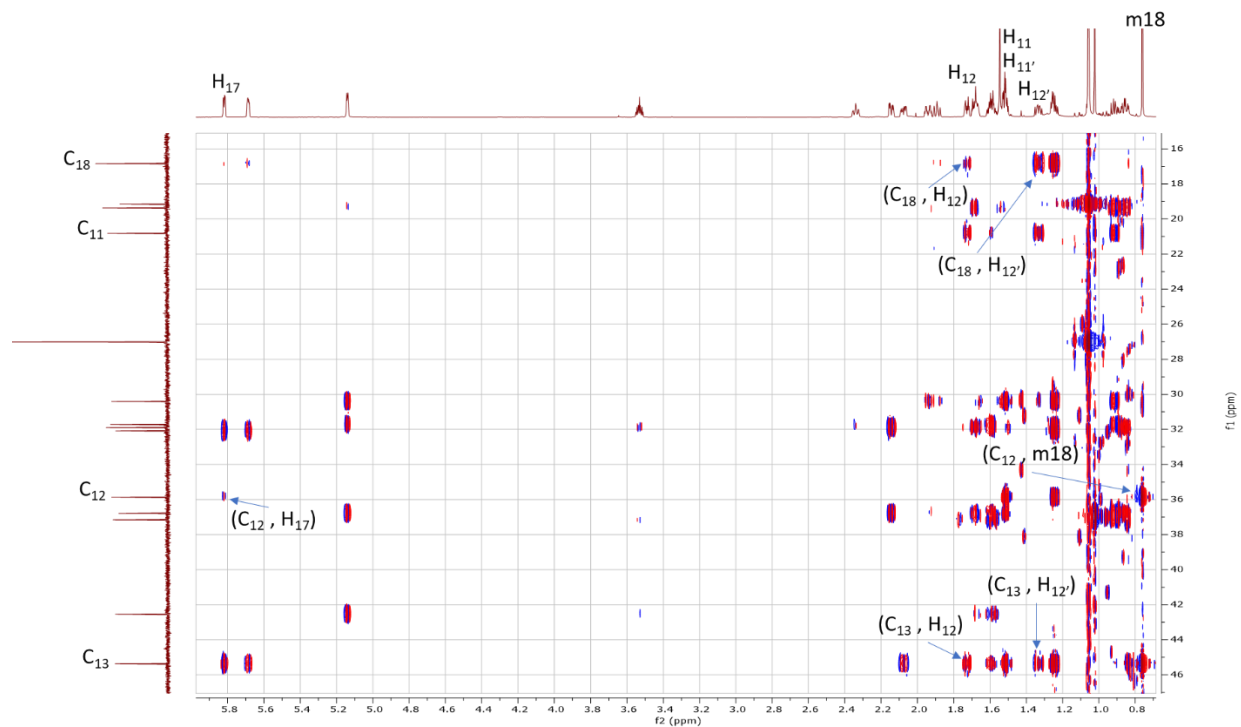
Figure 3.54B ^{1}H-^{13}C HMBC Correlations in C ring for DHEA $C_{17\text{-}16}$ Alkene PG (7a)

Concluding with the C ring, δ_C 35.86 (C_{12}) displayed HMBC correlations to m18 (δ_H 0.76) and H_{17} (δ_H 5.82) (see Figure 3.54B). δ_H 1.73 (H_{12}) and δ_H 1.33 ($H_{12'}$) were discerned from HSQC

correlations to δ_C 35.86 (C_{12}) and strong HMBC correlations to C_{13} (δ_C 45.37) and C_{18} (δ_C 16.84) (see Figure 3.54A and 3.54B). The remaining δ_C 20.81 (C_{11}) displayed HSQC correlation to δ_H 1.51 (H_{11}) and δ_H 1.48 ($H_{11'}$) (see Figure 3.54A), thus completing full assignment of DHEA C_{17-16} Alkene PG (**7a**).
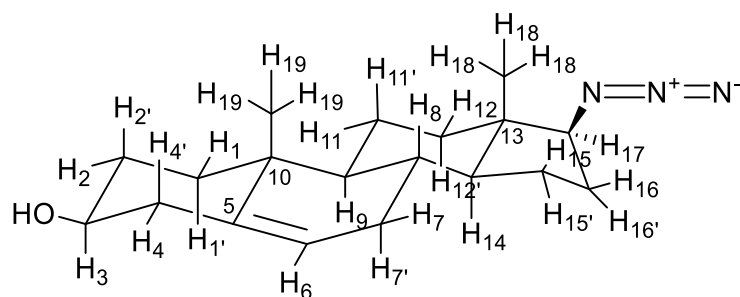
Figure 3.55A Chair Conformation of 8
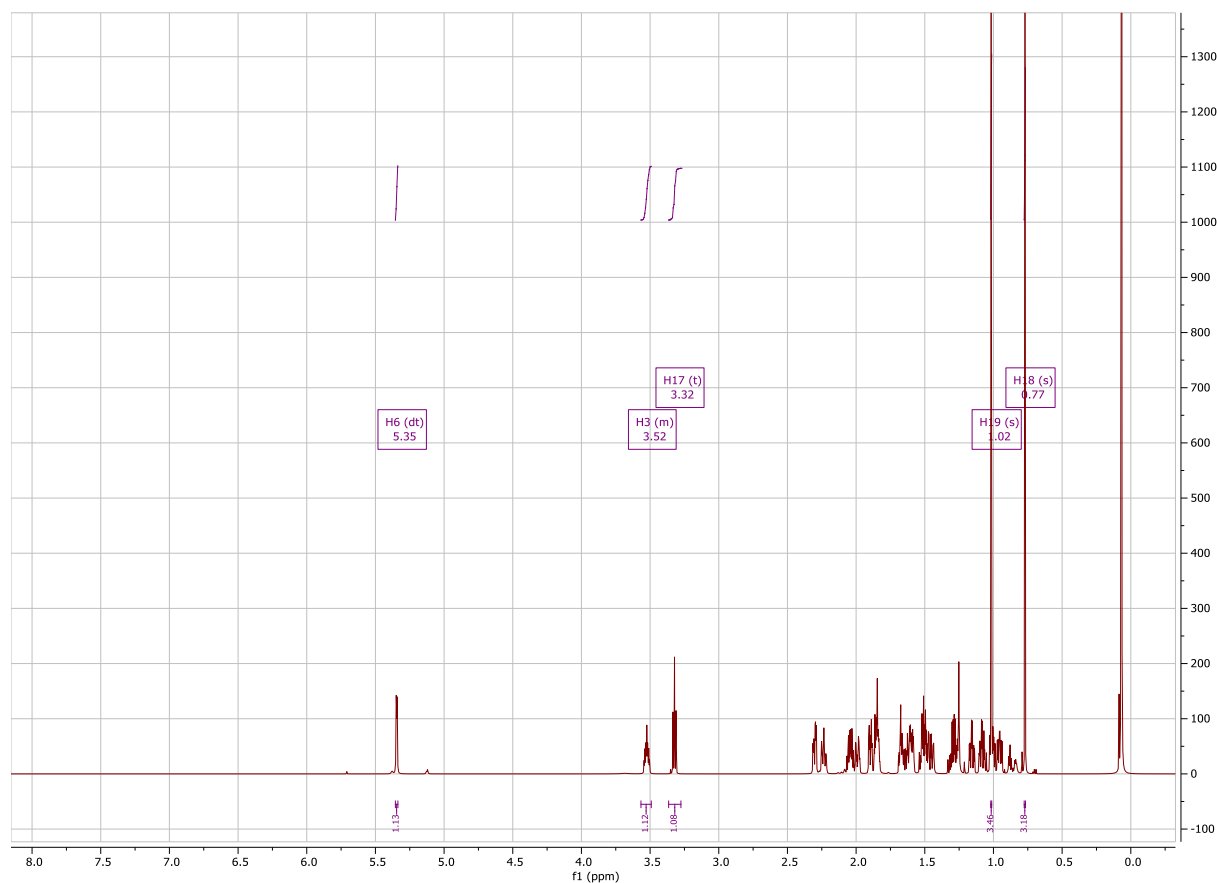
Figure 3.55B ^{1}H Spectrum of DHEA C$_{17}$-(S)-N$_3$ probe (8)

There is no presence of the TBDPS protecting group as nothing appeared from δ_H 6.5-8 (see Figure 3.55B). δ_H 5.35, δ_H 3.32, and δ_H 3.52 were identified as H$_6$, H$_{17}$, and H$_3$ respectively based upon chemical shift and splitting (see Figure 3.55B). The methyl protons on C$_{18}$ and C$_{19}$

could be identified at either δ_H 1.02 or δ_H 0.77 (see Figure 3.55B). The latter assignments for H_3, H_6, H_{17}, H_{18}, and H_{19} matched previous ^1H assignments (Blanco et al., 2014), (Kiss et al., 2018).

Figure 3.55C ^{13}C Spectrum of DHEA C$_{17}$-(S)-N$_3$ probe (8)

The loss of the TBDPS protecting group was shown by the reduction of peaks between δ_C 120-140 (see Figure 3.55C). δ_C 140.89 and δ_C 121.23 were identified as C_5 and C_6 respectively based on chemical shift and peak height (see Figure 3.55C).
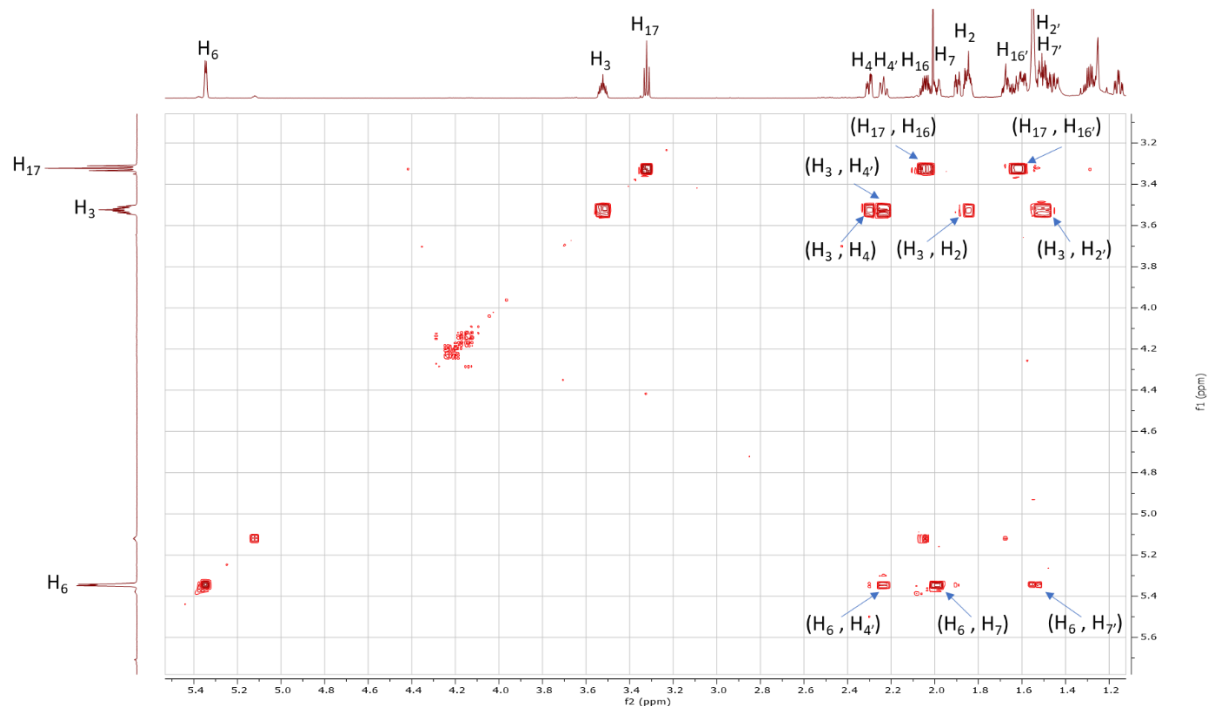
Figure 3.56 Initial ^{1}H-^{1}H COSY Correlations for DHEA C$_{17}$-(S)-N$_3$ probe (8)

Diastereotopic proton, δ_H 2.24 (H$_{4'}$), from the A ring was identified from COSY correlations with H$_3$ (δ_H 3.52) and H$_6$ (δ_H 5.35) (see Figure 3.56). δ_H 2.30 (H$_4$) was identified by COSY correlation to H$_3$ (δ_H 3.52) and chemical shift (see Figure 3.56). Methylene protons, δ_H 1.85 (H$_2$) and δ_H 1.49 (H$_{2'}$), were discerned from COSY correlations with H$_3$ (δ_H 3.52) (see Figure 3.56). In addition, diastereotopic protons δ_H 1.99 (H$_7$) and δ_H 1.49 (H$_{7'}$) in the B ring were identified from COSY correlations with H$_6$ (δ_H 5.35) (see Figure 3.56). In the D ring, diastereotopic protons δ_H 2.04 (H$_{16}$) and δ_H 1.61 (H$_{16'}$) were discerned from COSY correlations with H$_{17}$ (δ_H 3.32) (see Figure 3.56).
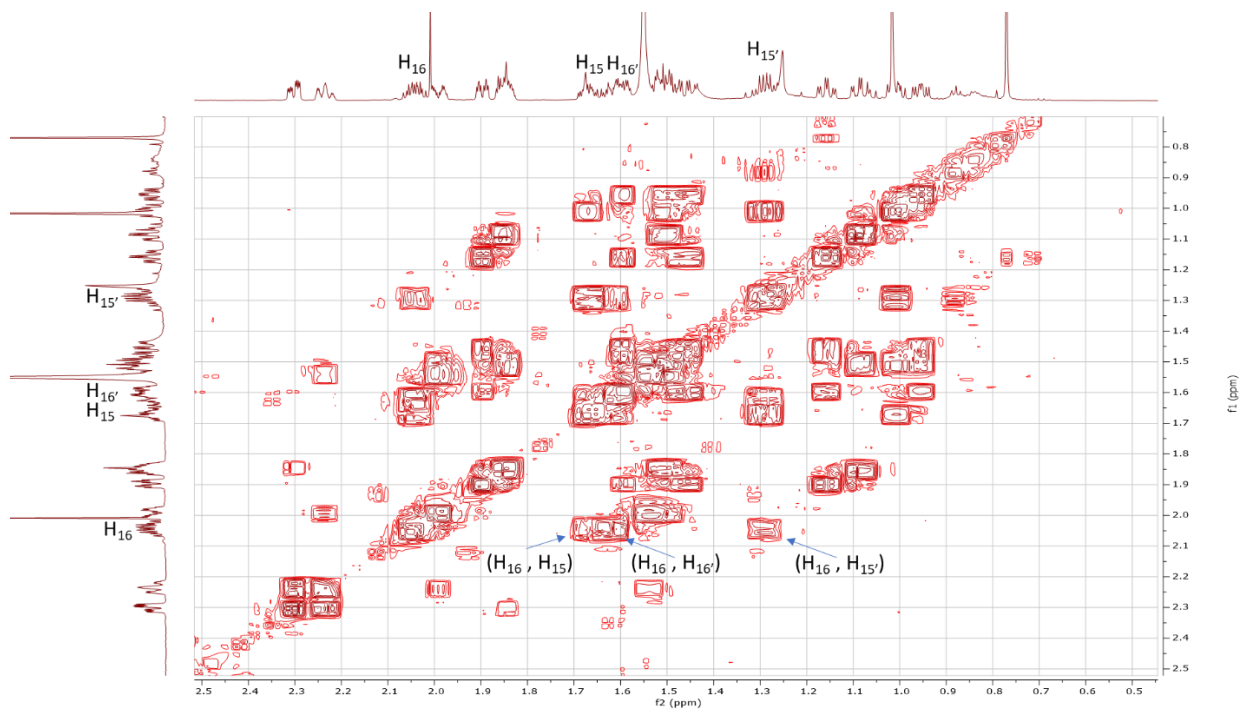
Figure 3.57A ^1H-^1H COSY Correlations in D ring for DHEA C_{17}-(S)-N_3 probe (8)
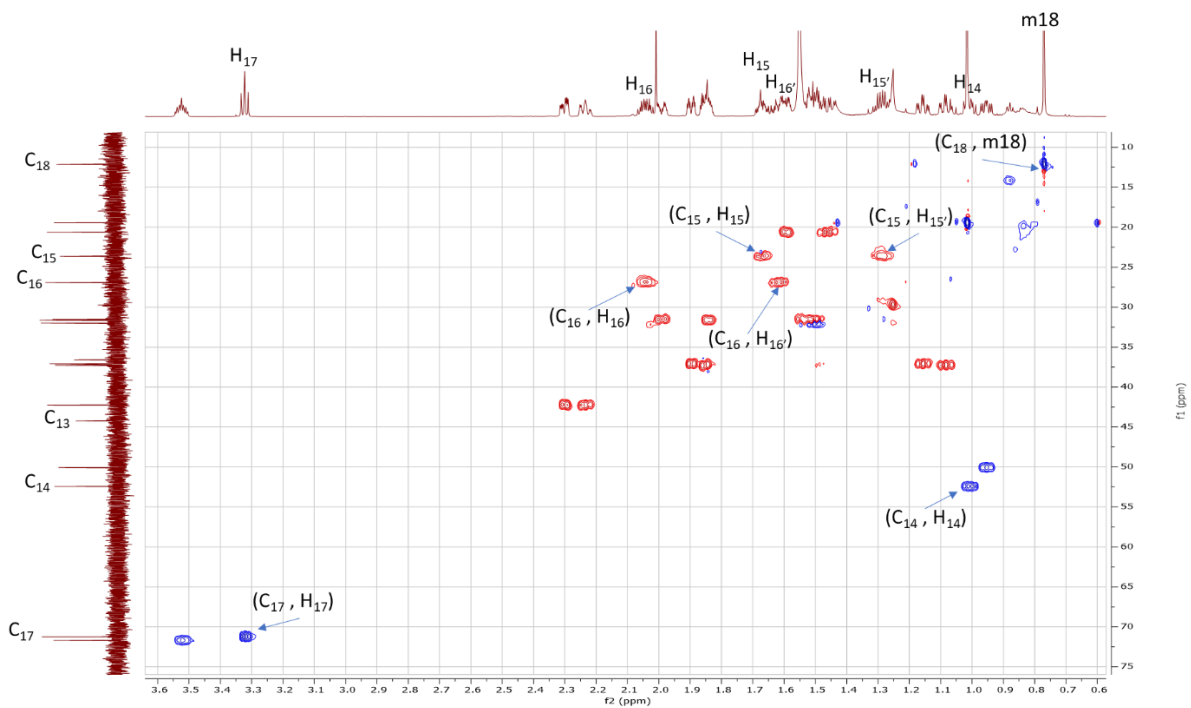
Figure 3.57B ^1H-^{13}C HSQC Correlations in D ring for DHEA C_{17}-(S)-N_3 probe (8)
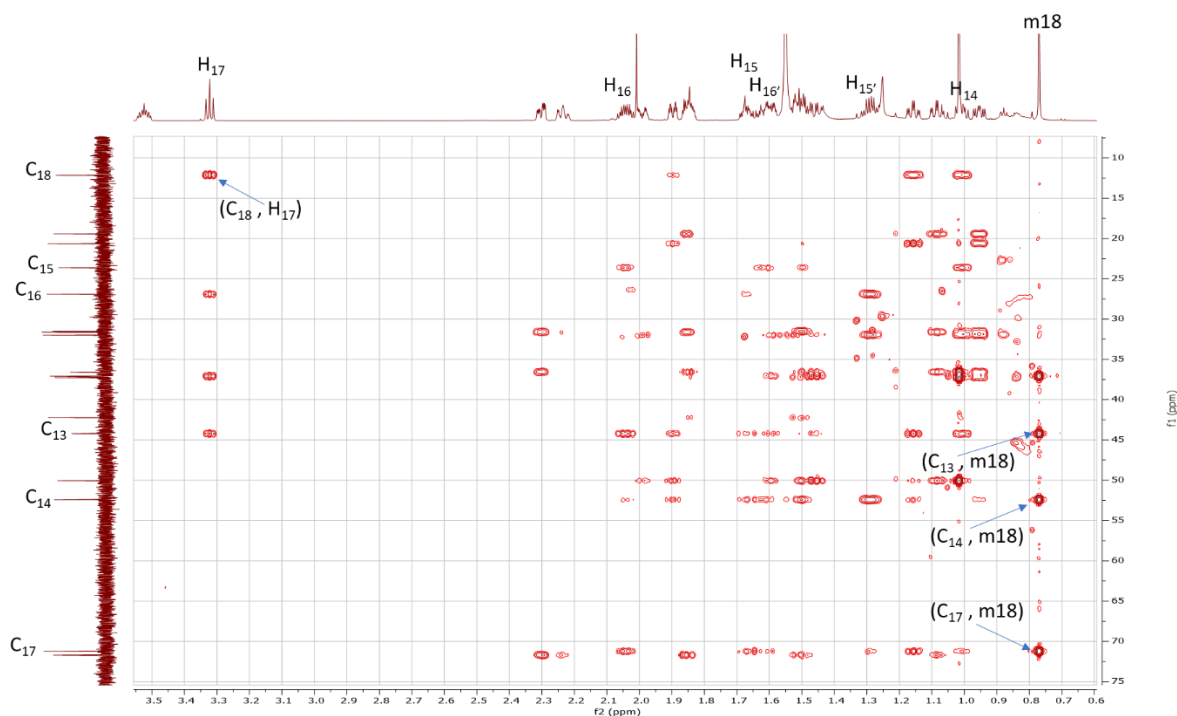
Figure 3.57C ^{1}H-^{13}C HMBC Correlations in D ring for DHEA C$_{17}$-(S)-N$_3$ probe (8)

Starting with the D ring, δ_C 71.24 was identified as C$_{17}$ from the HSQC correlation with δ_H 3.32 (H$_{17}$) and HMBC correlations to m18 (δ_H 0.77), the methyl protons on C$_{18}$ (see Figure 3.57B and 3.57C). Methylene protons, δ_H 2.04 (H$_{16}$) and δ_H 1.61 (H$_{16'}$), was correlated by HSQC to δ_C 26.93 (C$_{16}$) (see Figure 3.57B). Next, diastereotopic protons, δ_H 1.29 (H$_{15'}$) and δ_H 1.67 (H$_{15}$), was discerned from COSY correlation to H$_{16}$ (δ_H 2.04) (see Figure 3.57A). From HSQC correlation, δ_H 1.29 (H$_{15'}$) and δ_H 1.67 (H$_{15}$), showed HSQC correlation to δ_C 23.64 (C$_{15}$) (see Figure 3.57B). C$_{14}$ (δ_C 52.43) was identified by HMBC correlation to m18 (δ_H 0.77) (see Figure 3.57C). H$_{14}$ (δ_H 1.00) was distinguished based from HSQC correlation to C$_{14}$ (δ_C 52.43) (see Figure 3.57B). Continuing with m18, δ_C 12.15 (C$_{18}$) was identified from HSQC correlation to m18 and HMBC correlation to δ_H 3.32 (H$_{17}$) (see Figure 3.57B and 3.57C). Therefore, the methyl protons on C$_{19}$, m19, could be identified at δ_H 1.02 based on integration and splitting (see Figure 3.55B). Quaternary carbon, δ_C 44.23 (C$_{13}$), was discerned from HMBC correlation to m18 (δ_H 0.77) and no observable HSQC correlation (see Figure 3.57B and 3.57C).
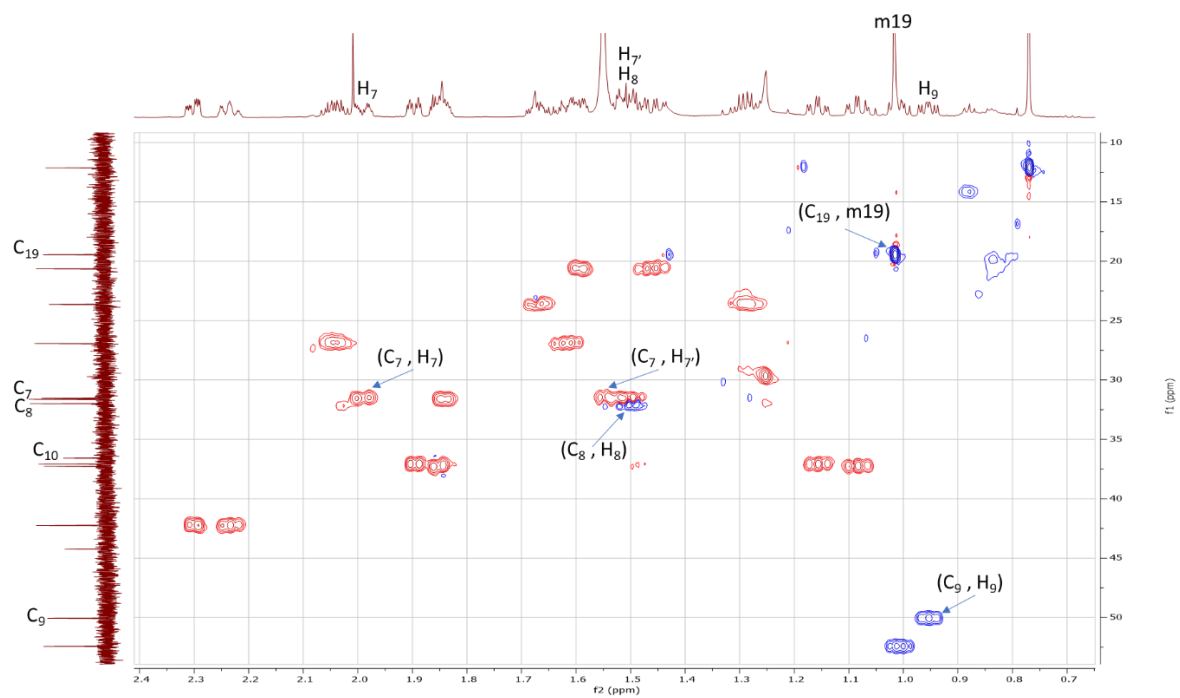
Figure 3.58A ^{1}H-^{13}C HSQC Correlations in B ring for DHEA C_{17}-(S)-N_3 probe (8)
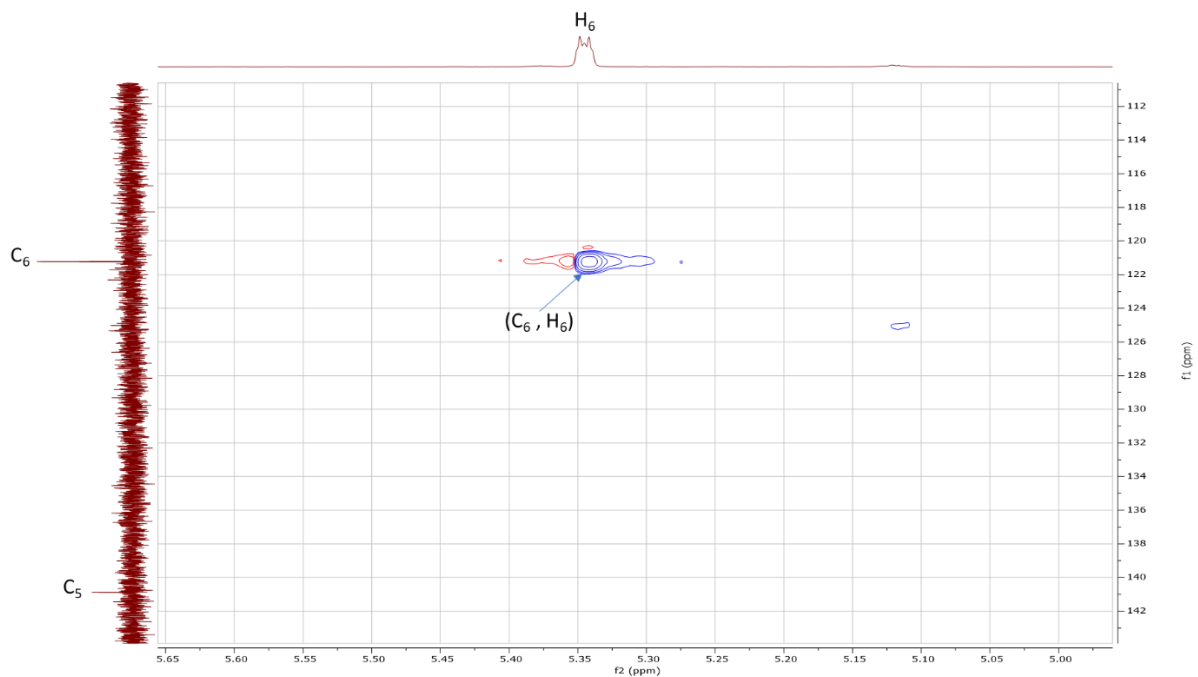
Figure 3.58B ^{1}H-^{13}C HSQC Correlations in B ring for DHEA C_{17}-(S)-N_3 probe (8) (C_5-C_6)
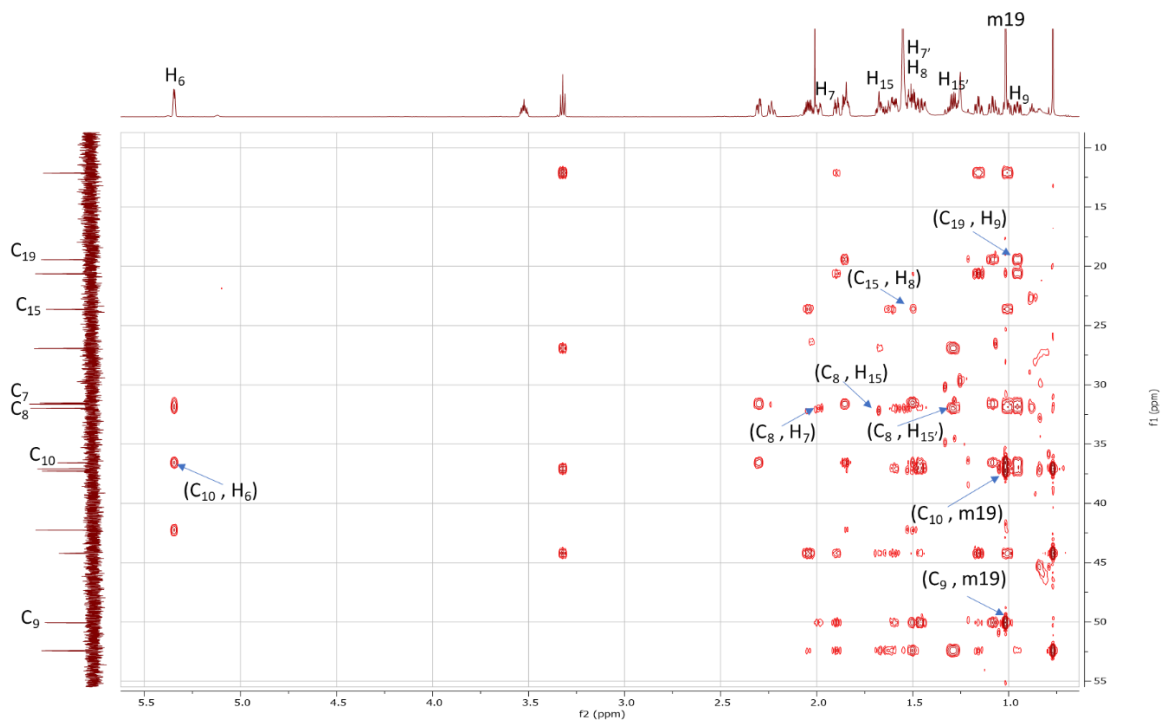
Figure 3.58C ^{1}H-^{13}C HMBC Correlations in B ring for DHEA C$_{17}$-(S)-N$_3$ probe (8)
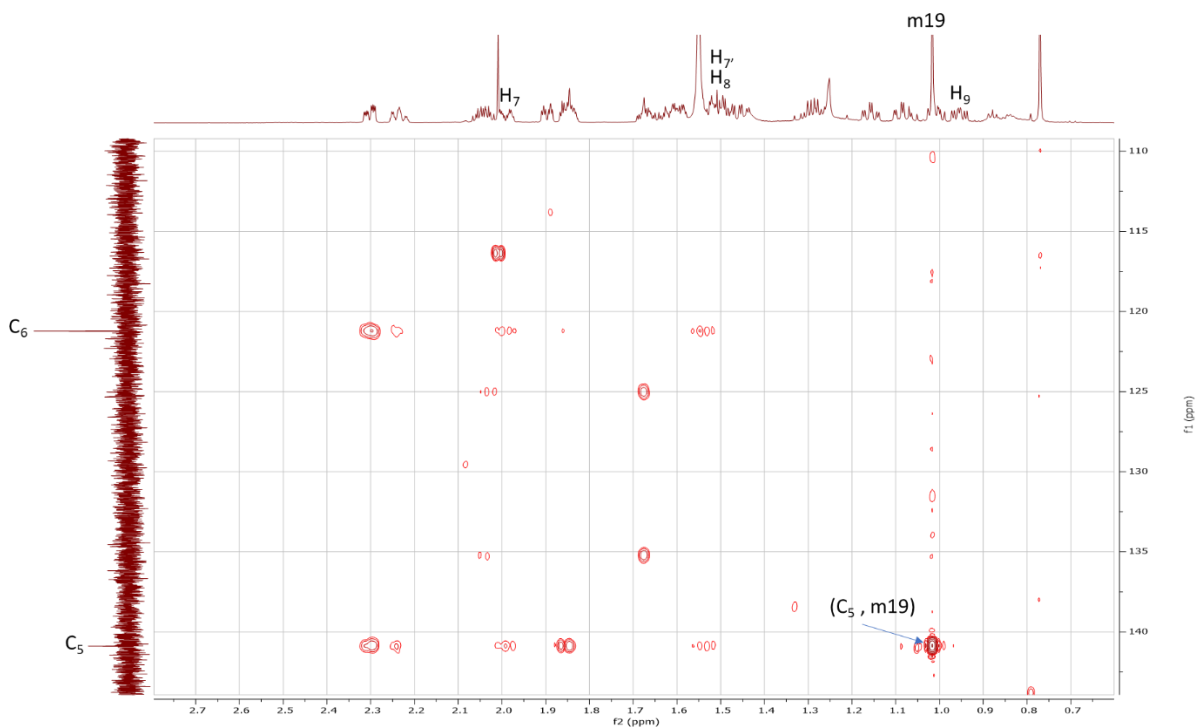
Figure 3.58D ^{1}H-^{13}C HMBC Correlations in B ring for DHEA C$_{17}$-(S)-N$_3$ probe (8) (C$_5$-C$_6$)

Next with the B ring, methyl protons, m19 (δ_H 1.02) exhibited HSQC correlation to δ_C 19.44 (C$_{19}$) (see Figure 3.58A). δ_C 140.89 (C$_5$) was determined on the basis of no HSQC correlation,

chemical shift, and HMBC correlation to m19 (δ_H 1.02) (see Figure 3.58B and 3.58D). Vinyl carbon, C_6 (δ_C 121.23) was correlated by HSQC to δ_H 5.35 (H_6) (see Figure 3.58B). Methylene protons, δ_H 1.99 (H_7) and δ_H 1.49 ($H_{7'}$), exhibited HSQC correlation to δ_C 31.53 (C_7) (see Figure 3.58A). C_8 (δ_C 32.00) was correlated by HMBC to δ_H 1.99 (H_7), δ_H 1.29 ($H_{15'}$) and δ_H 1.67 (H_{15}) (see Figure 3.58C). Methine proton, H_8, was discerned at δ_H 1.49 based on HMBC correlation to C_{15} (δ_C 23.64) and HSQC correlation to C_8 (δ_C 32.00) (see Figure 3.58A and 3.58C). The remaining methine proton, H_9 (δ_H 0.95), displayed correlation by HSQC to δ_C 50.07 (C_9) and by HMBC to δ_C 19.44 (C_{19}) (see Figure 3.58A and 3.58C). Quaternary carbon, C_{10} (δ_C 36.58), was assigned based on HMBC correlation to H_6 (δ_H 5.35), m19 (δ_H 1.02), and no observable HSQC correlation (see Figure 3.58A and 3.58C).
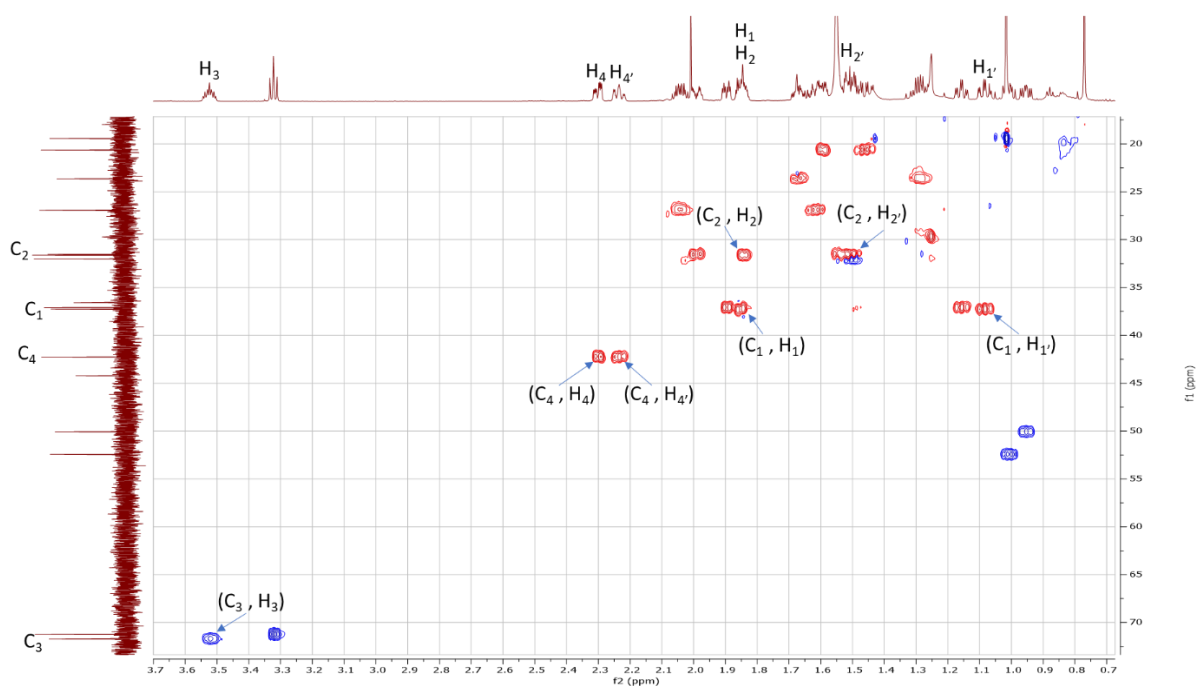
Figure 3.59A ^{1}H-^{13}C HSQC Correlations in A ring for DHEA C_{17}-(S)-N$_3$ probe (8)
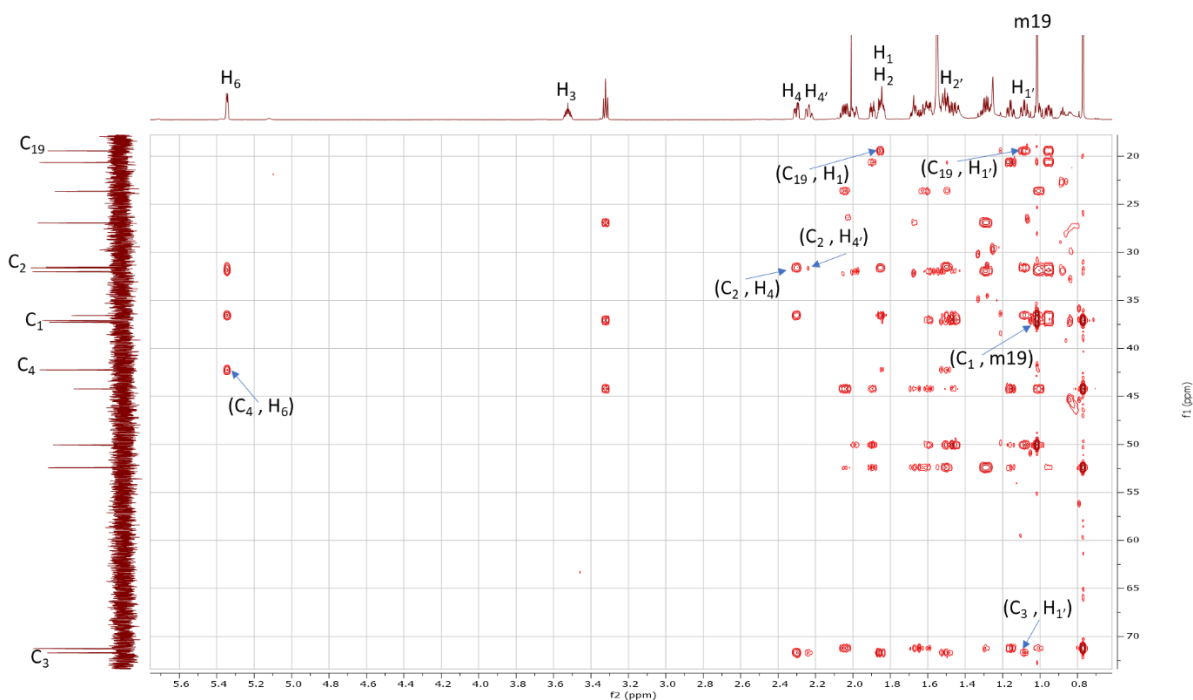
Figure 3.59B ^{1}H-^{13}C HMBC Correlations in A ring for DHEA C_{17}-(S)-N_3 probe (8)

Continuing with the A ring, δ_H 3.52 (H$_3$) exhibited HSQC correlation to δ_C 71.71 (C$_3$) (see Figure 3.59A). Methylene protons, δ_H 2.30 (H$_4$) and δ_H 2.24 (H$_{4'}$), displayed HSQC correlation to δ_C 42.25 (C$_4$), which shows HMBC correlation to H$_6$ (δ_H 5.35) (see Figure 3.59A and 3.59B). Diastereotopic protons, δ_H 1.85 (H$_2$) and δ_H 1.49 (H$_{2'}$), displayed HSQC correlation to δ_C 31.63 (C$_2$), which showed HMBC correlation to H$_{4'}$ (δ_H 2.24) and H$_4$ (δ_H 2.30) (see Figure 3.59A and 3.59B). δ_C 37.27 (C$_1$) was discerned from HMBC correlation to m19 (δ_H 1.02) (see Figure 3.59B). From there, methylene protons, δ_H 1.85 (H$_1$) and δ_H 1.08 (H$_{1'}$) displayed HSQC correlation to δ_C 37.27 (C$_1$) and HMBC correlation to δ_C 19.44 (C$_{19}$) along with δ_C 71.71 (C$_3$) (see Figure 3.59A and 3.59B).
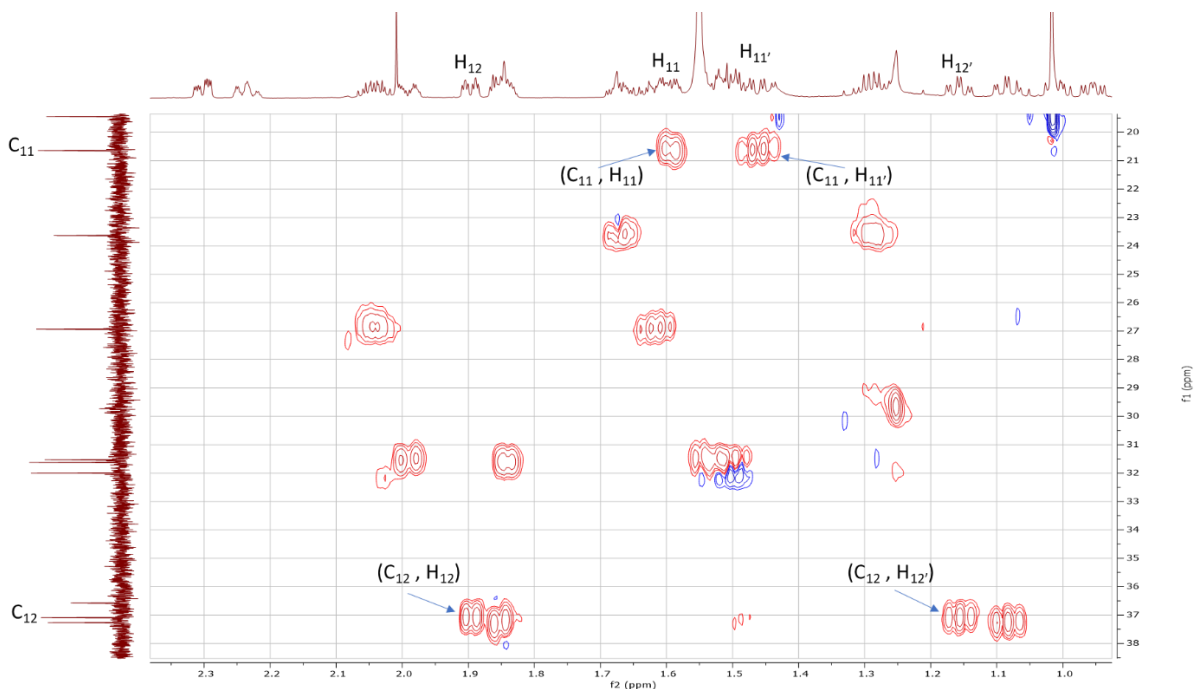
Figure 3.60A ^{1}H-^{13}C HSQC Correlations in C ring for DHEA C_{17}-(S)-N_3 probe (8)
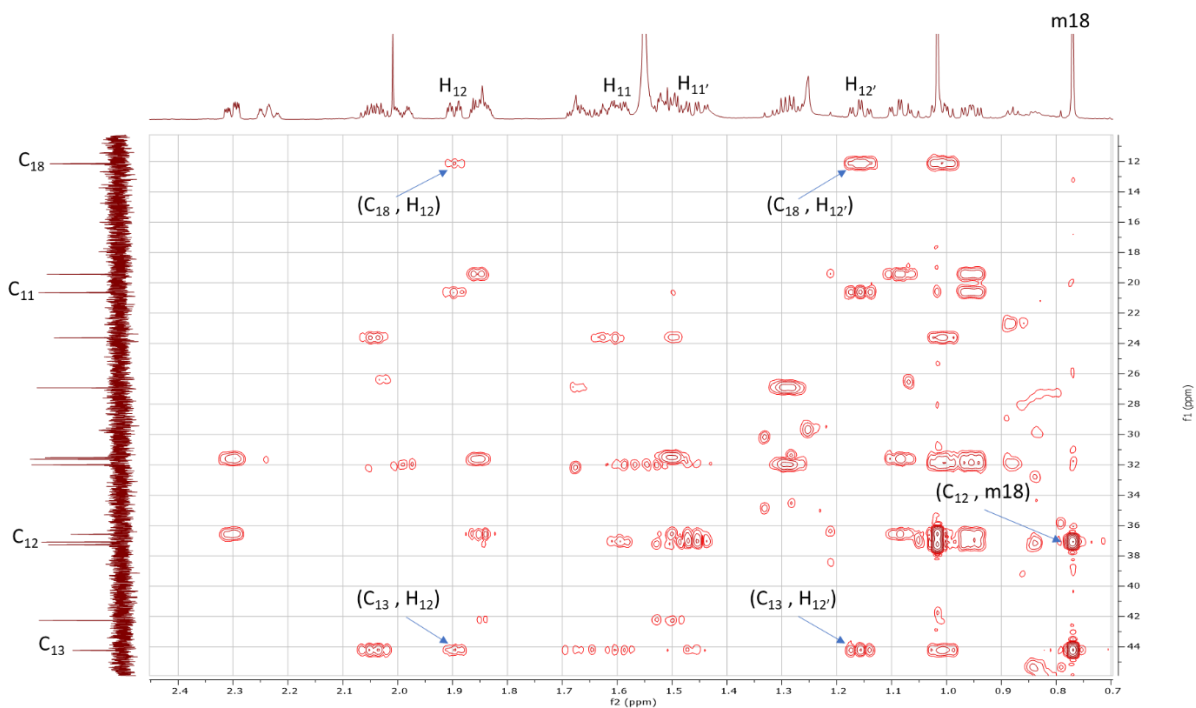
Figure 3.60B ^{1}H-^{13}C HMBC Correlations in C ring for DHEA C_{17}-(S)-N_3 probe (8)

Concluding with the C ring, δ_C 37.09 (C_{12}) displayed HMBC correlations to m18 (δ_H 0.77) (see Figure 3.60B). δ_H 1.90 (H_{12}) and δ_H 1.16 ($H_{12'}$) were discerned from HSQC correlations to δ_C

37.09 (C_{12}) and strong HMBC correlations to C_{13} (δ_C 44.23) and C_{18} (δ_C 12.15) (see Figure 3.60A and 3.60B). The remaining δ_C 20.64 (C_{11}) displayed HSQC correlation to δ_H 1.61 (H_{11}) and δ_H 1.49 ($H_{11'}$) (see Figure 3.60A), thus completing full assignment of DHEA C_{17}-(S)-N_3 probe (**8**).
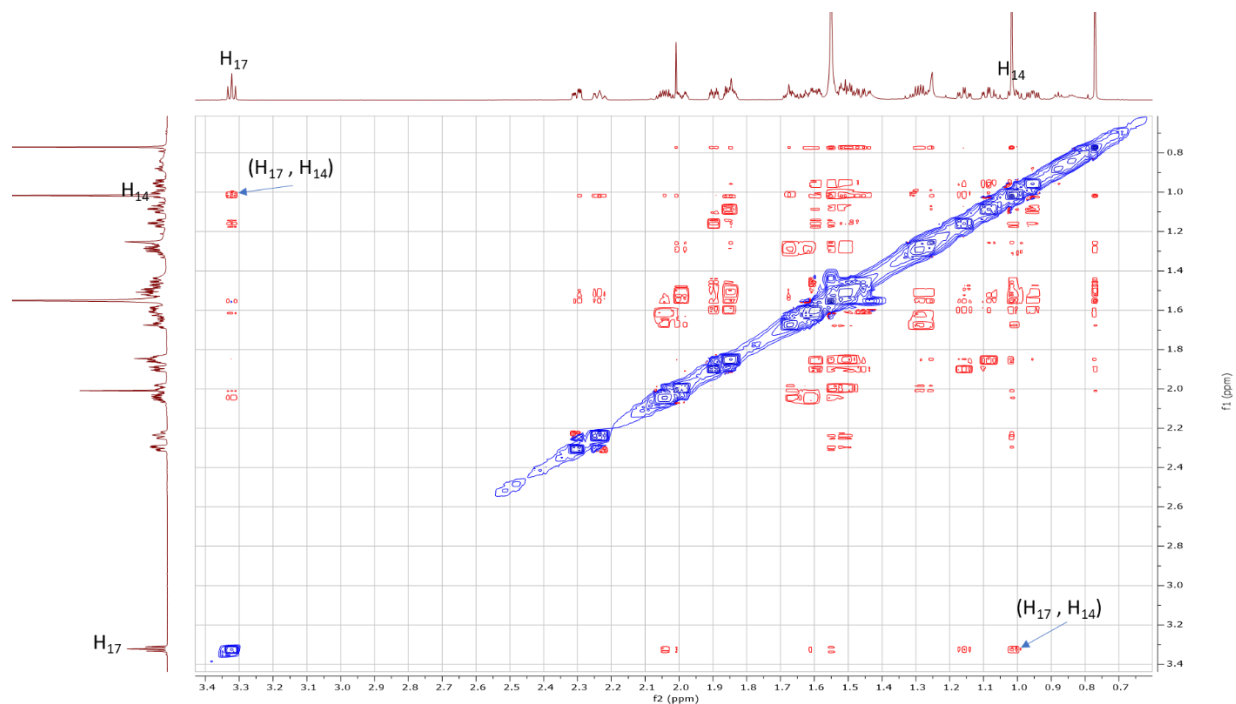
Figure 3.61 ^{1}H-^{1}H NOESY Correlations for DHEA C_{17}-(S)-N_3 probe (8)

The stereochemistry of the azide group at C_{17} is "S" based on NOESY correlation between δ_H 3.32 (H_{17}) and δ_H 1.00 (H_{14}) (see Figure 3.61).
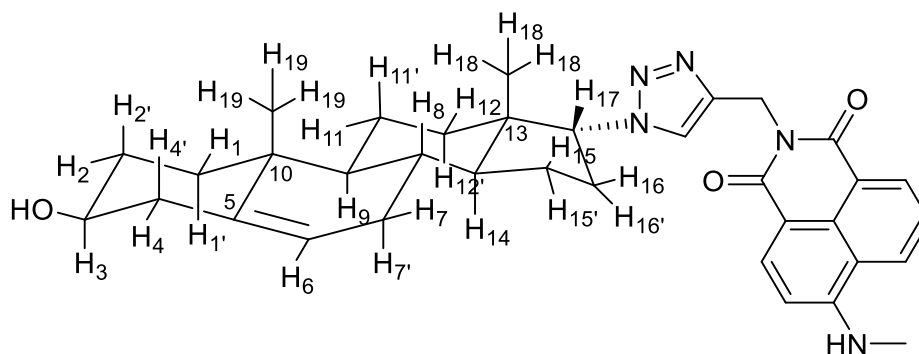
Figure 3.62A Chair Conformation of 29
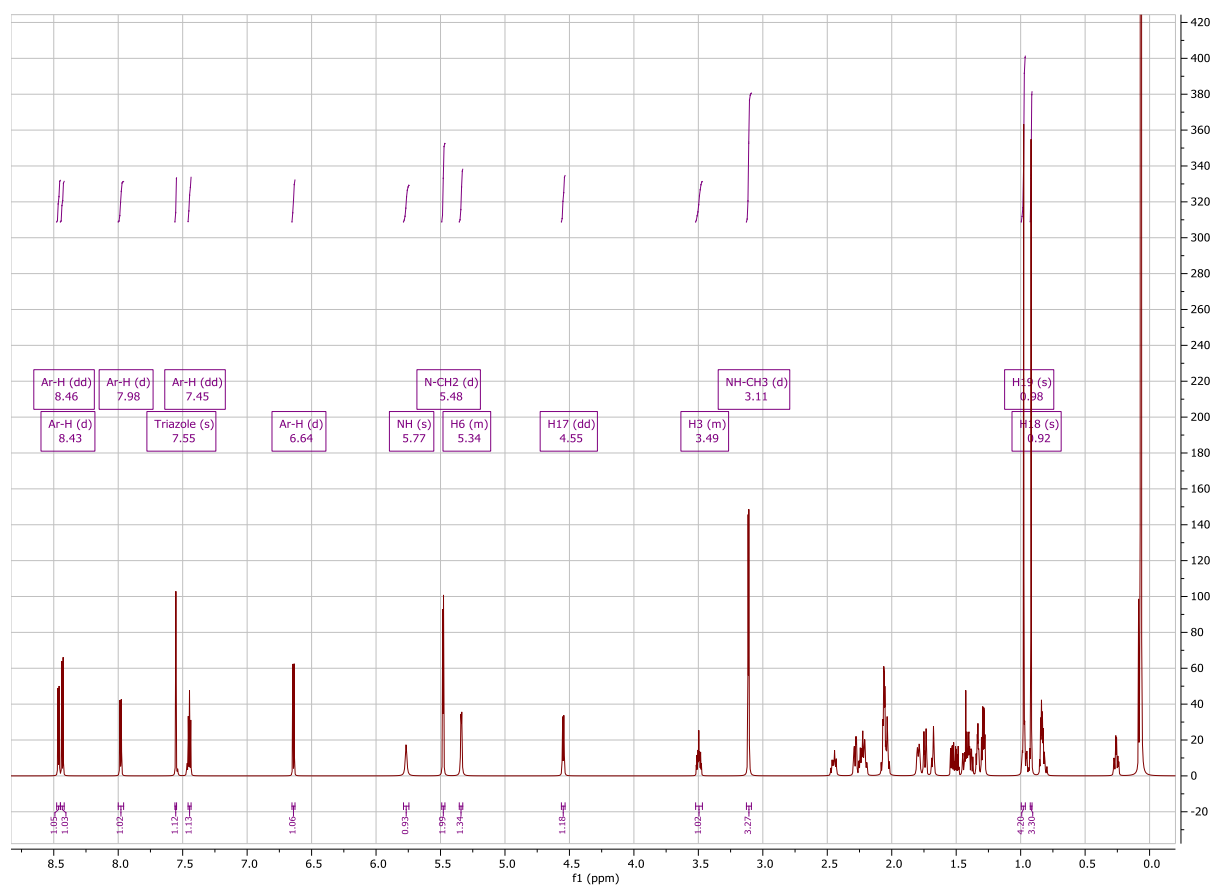
Figure 3.62B ^{1}H Spectrum of DHEA C$_{17}$-(R)-N$_3$-MAN Product (29)

δ_H 5.34, δ_H 4.55, and δ_H 3.49 were identified as H$_6$, H$_{17}$, and H$_3$ respectively based upon chemical shift, splitting, integration, and previous characterization of **5** (see Figure 3.62B). The methyl protons on C$_{18}$ and C$_{19}$ could be identified at either δ_H 0.98 or δ_H 0.92 (see Figure 3.62B). In addition, the triazole proton, N*H*-CH$_3$, N-C*H*$_2$, and NH-C*H*$_3$ could be identified at δ_H 7.55, δ_H

5.77, δ_H 5.48, and δ_H 3.11, respectively based on chemical shift, integration, and splitting (see Figure 3.62B). The aromatic protons on **MAN** could be identified at δ_H 8.46, δ_H 8.43, δ_H 7.98, δ_H 7.45, and δ_H 6.64 based on chemical shift and splitting (see Figure 3.62B).
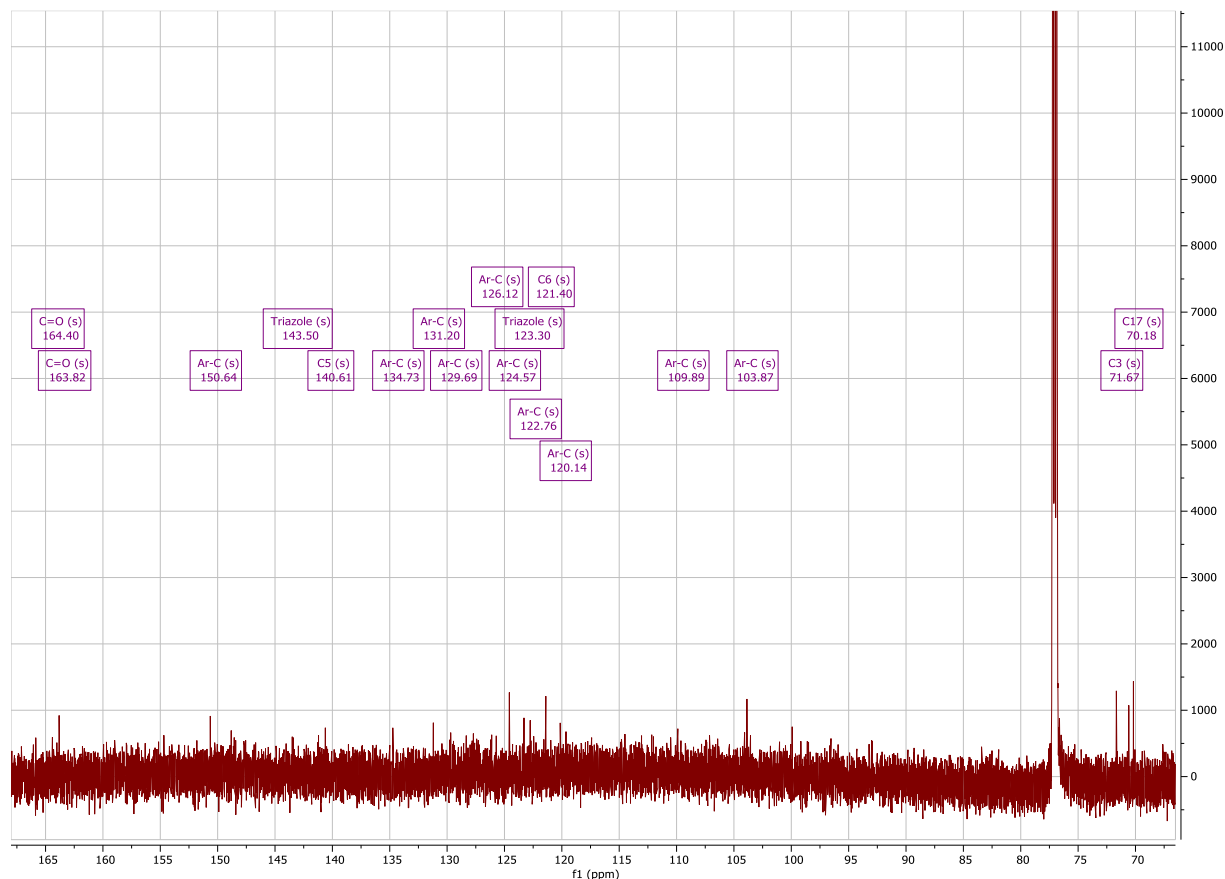
Figure 3.62C ^{13}C Spectrum of DHEA C_{17}-(R)-N_3-MAN Product (29)

The formation of the triazole moiety could be observed by the loss of δ_C 71.45 (C_{17}, **5**) and gain of δ_C 70.18 (C_{17}, **29**) (see Figure 3.62C). δ_C 71.67 was identified as C_3 based on chemical shift and previous characterization of C_3 for DHEA C_{17}-(R)-N_3 probe (**5**) (see Figure 3.62C). δ_C 140.61 and δ_C 121.40 were identified as C_5 and C_6 respectively based on chemical shift and previous characterization of C_5/C_6 for DHEA C_{17}-(R)-N_3 probe (**5**) (see Figure 3.62C). In addition, the appearance of several peaks between δ_C 100-165 may signify the presence of **MAN** and the triazole moiety (see Figure 3.62C).

174
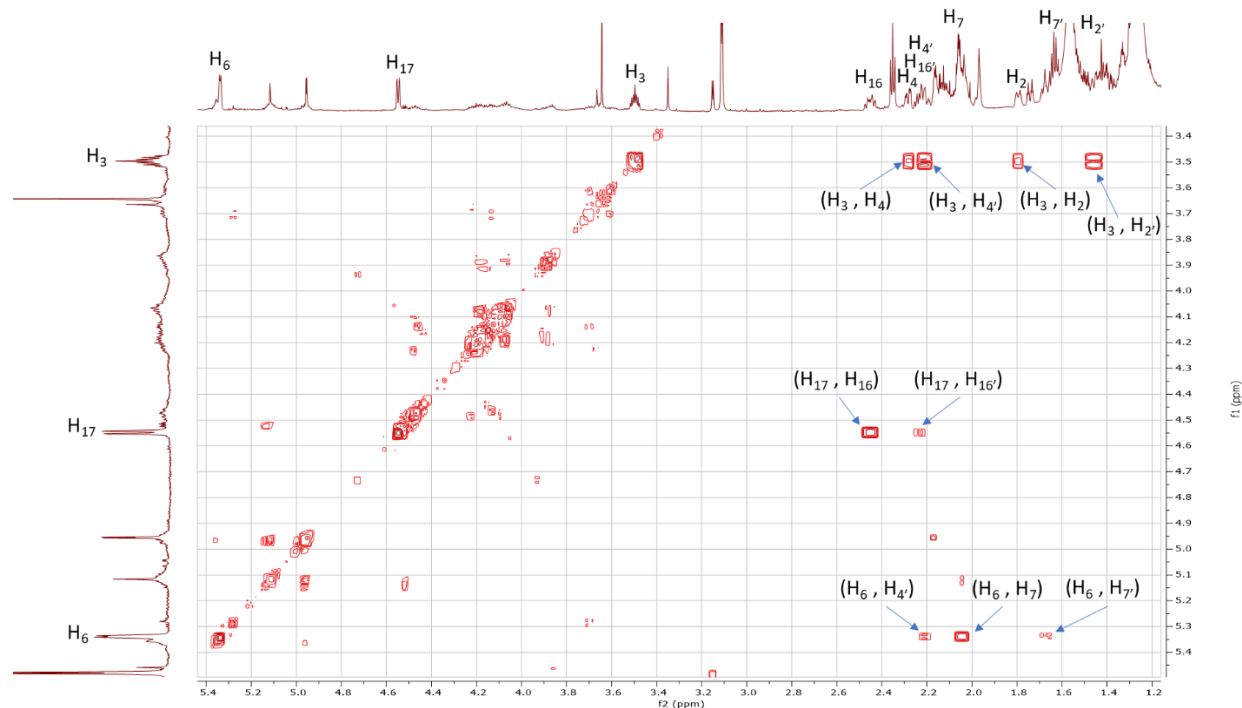
Figure 3.63 Initial ^{1}H-^{1}H COSY Correlations for DHEA C_{17}-(R)-N_3-MAN Product (29)

Diastereotopic proton, δ_H 2.23 ($H_{4'}$), from the A ring were identified from COSY correlations with H_3 (δ_H 3.49) and H_6 (δ_H 5.34) (see Figure 3.63). δ_H 2.28 (H_4) was identified by COSY correlation to H_3 (δ_H 3.49) and chemical shift (see Figure 3.63). Methylene protons, δ_H 1.79 (H_2) and δ_H 1.37 ($H_{2'}$), were discerned from COSY correlations with H_3 (δ_H 3.49) (see Figure 3.63). In addition, diastereotopic protons δ_H 2.05 (H_7) and δ_H 1.68 ($H_{7'}$) in the B ring were identified from COSY correlations with H_6 (δ_H 5.34) (see Figure 3.63). In the D ring, diastereotopic protons δ_H 2.45 (H_{16}) and δ_H 2.23 ($H_{16'}$) were discerned from COSY correlations with H_{17} (δ_H 4.55) (see Figure 3.63).
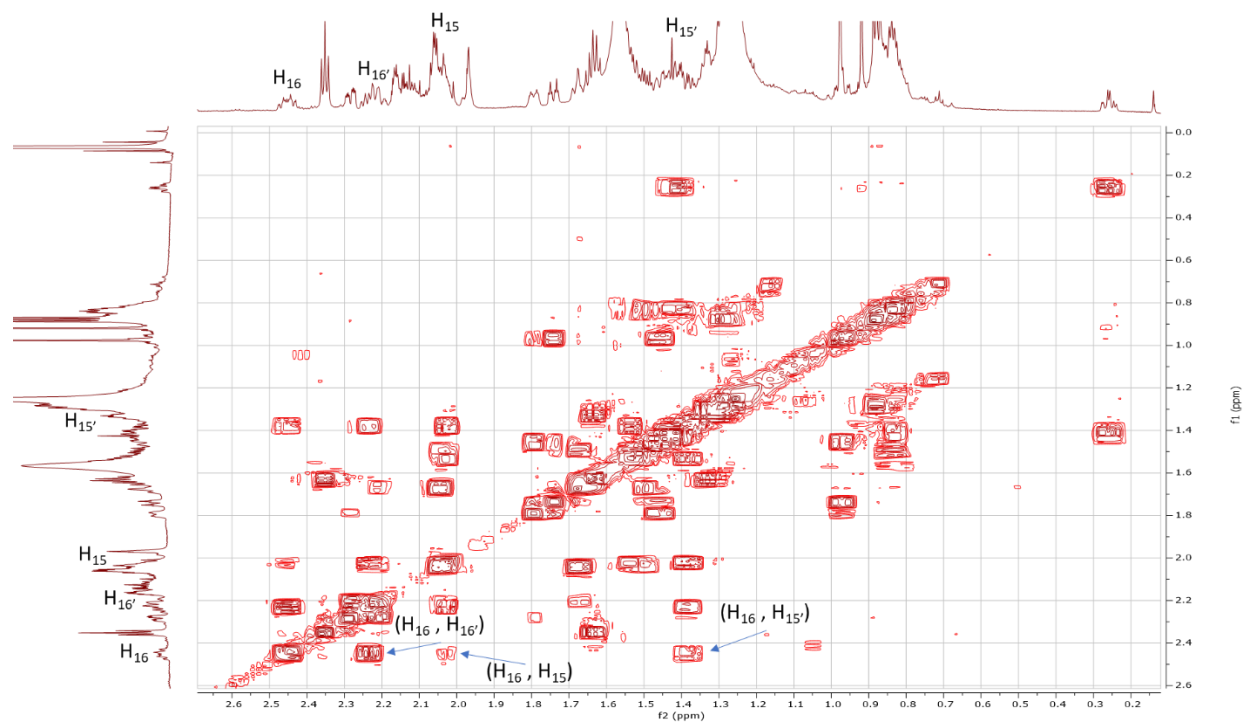
Figure 3.64A ^{1}H-^{1}H COSY Correlations in D ring for DHEA C$_{17}$-(R)-N$_3$-MAN Product (29)
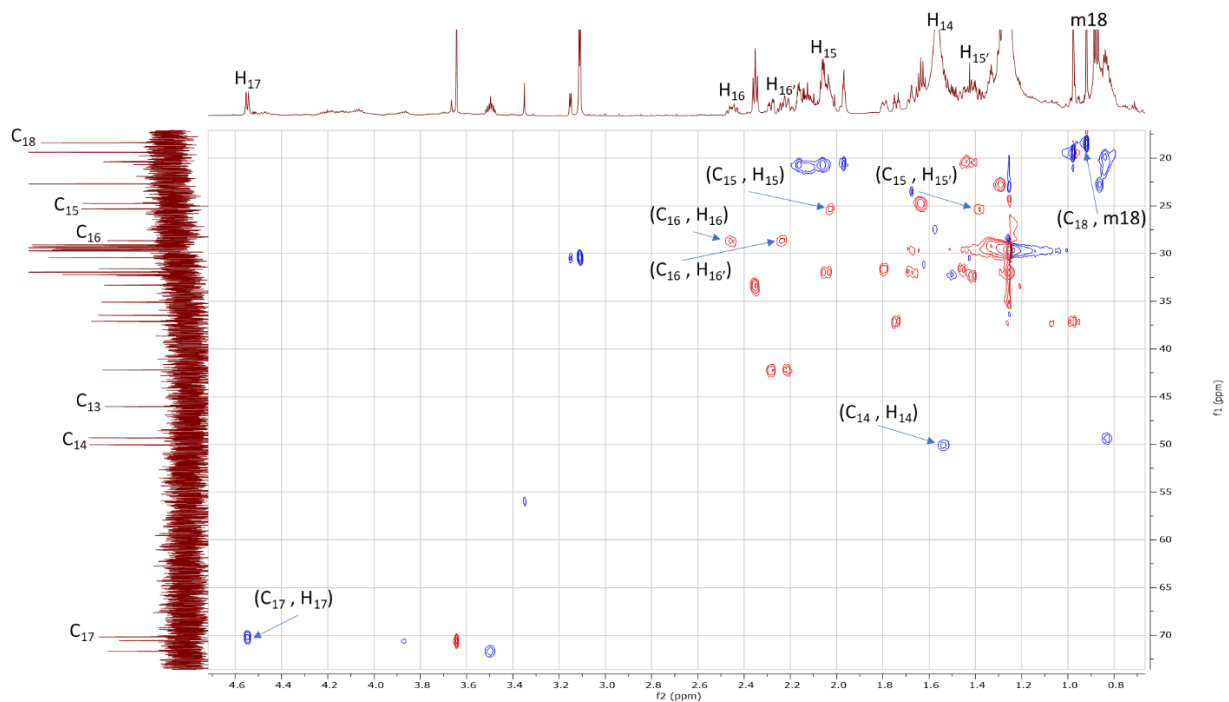
Figure 3.64B ^{1}H-^{13}C HSQC Correlations in D ring for DHEA C$_{17}$-(R)-N$_3$-MAN Product (29)
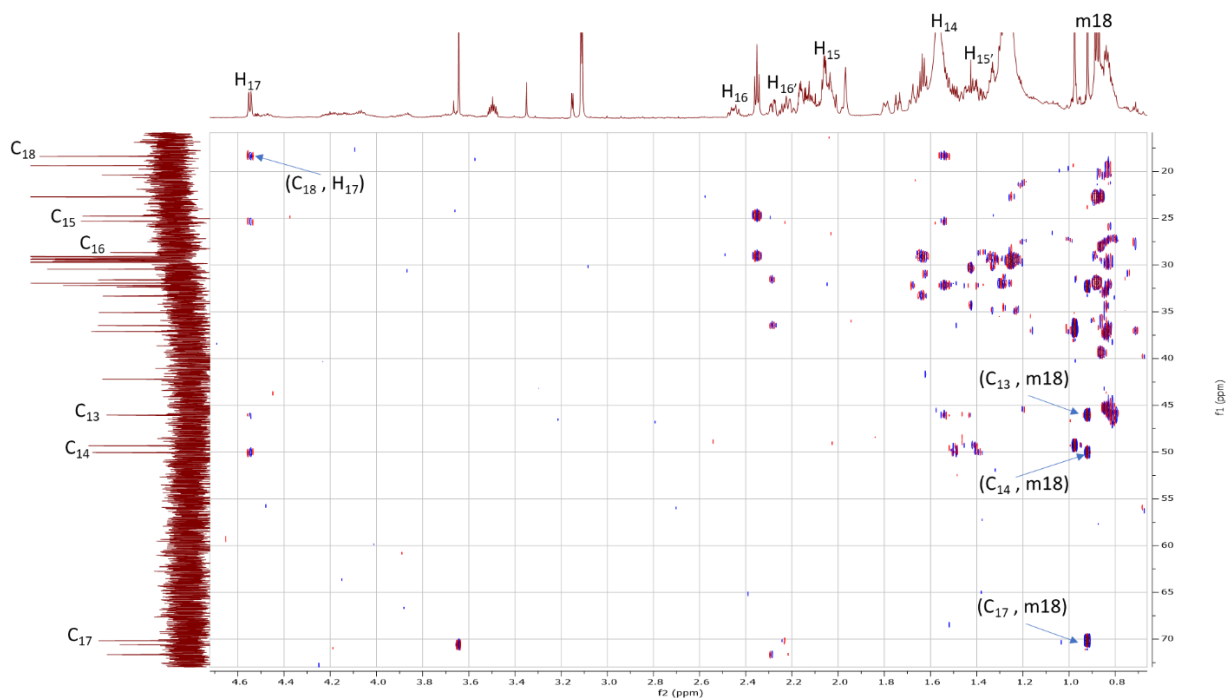
Figure 3.64C ^{1}H-^{13}C HMBC Correlations in D ring for DHEA C$_{17}$-(R)-N$_3$-MAN Product (29)

Starting with the D ring, δ_C 70.18 was identified as C$_{17}$ from the HSQC correlation with δ_H 4.55 (H$_{17}$) and HMBC correlations to m18 (δ_H 0.92), the methyl protons on C$_{18}$ (see Figure 3.64B and 3.64C). Methylene protons, δ_H 2.45 (H$_{16}$) and δ_H 2.23 (H$_{16'}$), was correlated by HSQC to δ_C 28.66 (C$_{16}$) (see Figure 3.64B). Next, diastereotopic protons, δ_H 1.37 (H$_{15'}$) and δ_H 2.05 (H$_{15}$), was discerned from COSY correlation to H$_{16}$ (δ_H 2.45) (see Figure 3.64A). From HSQC correlation, δ_H 1.37 (H$_{15'}$) and δ_H 2.05 (H$_{15}$), showed HSQC correlation to δ_C 25.33 (C$_{15}$) (see Figure 3.64B). C$_{14}$ (δ_C 50.04) was identified by HMBC correlation to m18 (δ_H 0.92) (see Figure 3.64C). H$_{14}$ (δ_H 1.51) was distinguished based from HSQC correlation to C$_{14}$ (δ_C 50.04) (see Figure 3.64B). Continuing with m18, δ_C 18.39 (C$_{18}$) was identified from HSQC correlation to m18 (δ_H 0.92) and HMBC correlation to δ_H 4.55 (H$_{17}$) (see Figure 3.64B and 3.64C). Therefore, the methyl protons on C$_{19}$, m19, could be identified at δ_H 0.98 based on integration and splitting (see Figure 3.62B). Quaternary carbon, δ_C 46.04 (C$_{13}$), was discerned from HMBC correlation to m18 (δ_H 0.92) and no observable HSQC correlation (see Figure 3.64B and 3.64C).
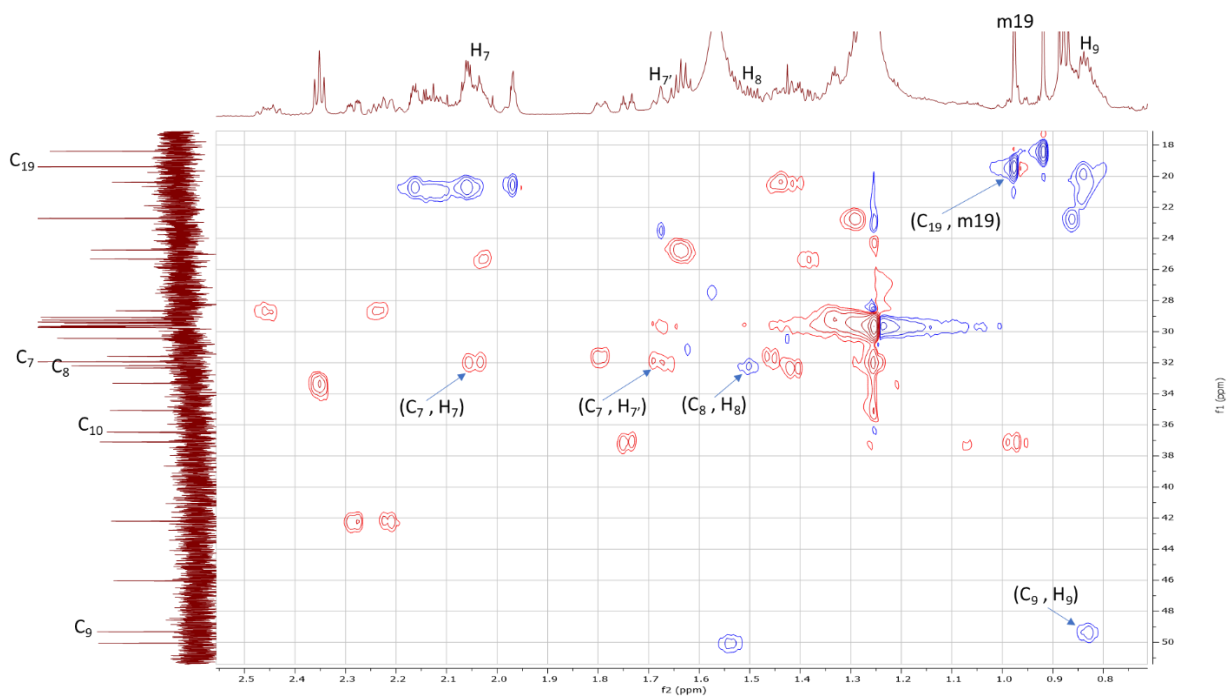
Figure 3.65A ^1H-^{13}C HSQC Correlations in B ring for DHEA C_{17}-(R)-N_3-MAN Product (29)
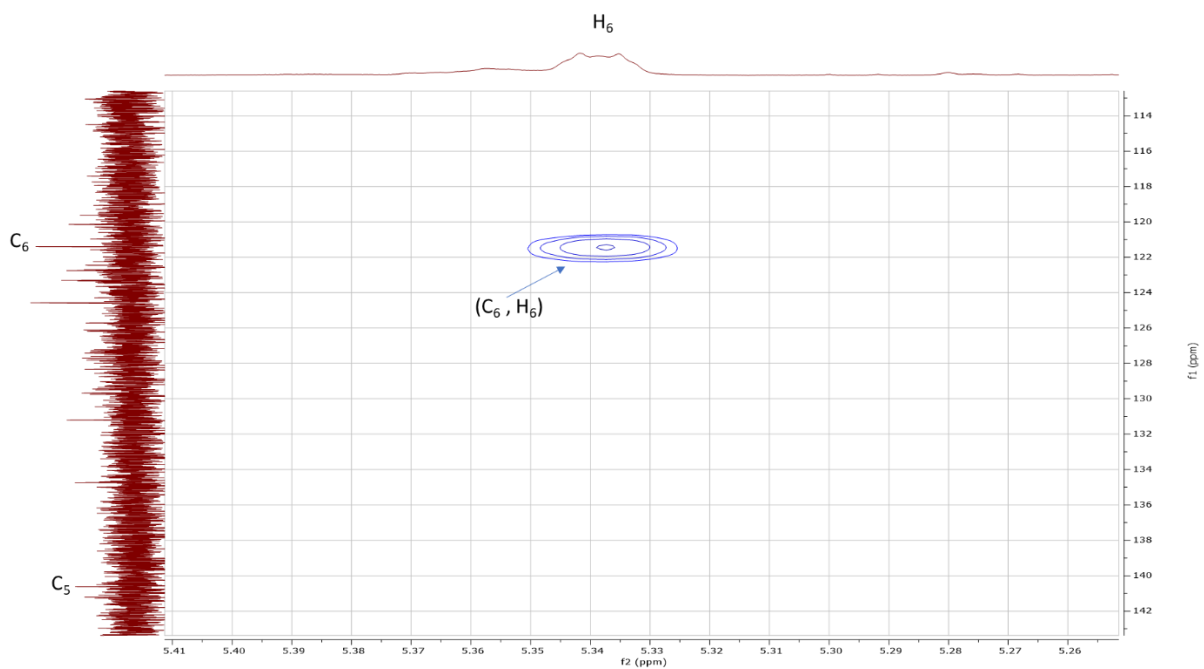
Figure 3.65B ^1H-^{13}C HSQC Correlations in B ring for DHEA C_{17}-(R)-N_3-MAN Product (29) (C_5-C_6)
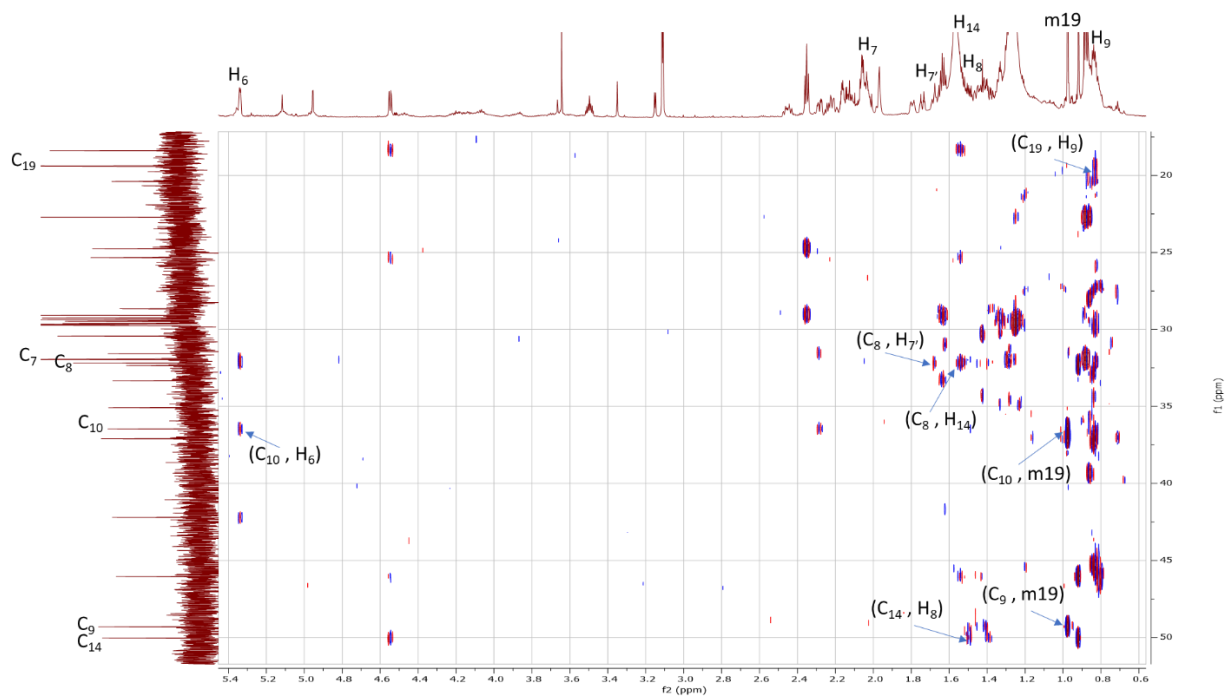
Figure 3.65C ^{1}H-^{13}C HMBC Correlations in B ring for DHEA C$_{17}$-(R)-N$_3$-MAN Product (29)

Figure 3.65D ^{1}H-^{13}C HMBC Correlations in B ring for DHEA C$_{17}$-(R)-N$_3$-MAN Product (29) (C$_5$-C$_6$)

Next with the B ring, methyl protons, m19 (δ_H 0.98) exhibited HSQC correlation to δ_C 19.39 (C$_{19}$) (see Figure 3.65A). δ_C 140.61 (C$_5$) was determined on the basis of no HSQC correlation,

chemical shift, and HMBC correlation to m19 (δ_H 0.98) (see Figure 3.65B and 3.65D). Vinyl carbon, C_6 (δ_C 121.40) was correlated by HSQC to δ_H 5.34 (H_6) (see Figure 3.65B). Methylene protons, δ_H 2.05 (H_7) and δ_H 1.68 ($H_{7'}$), exhibited HSQC correlation to δ_C 31.95 (C_7) (see Figure 3.65A). C_8 (δ_C 32.19) was correlated by HMBC to δ_H 1.68 ($H_{7'}$) and H_{14} (δ_H 1.51) (see Figure 3.65C). Methine proton, H_8, was discerned at δ_H 1.51 based on HMBC correlation to C_{14} (δ_C 50.04) and HSQC correlation to δ_C 32.19 (C_8) (see Figure 3.65A and 3.65C). The remaining methine proton, H_9 (δ_H 0.82), displayed correlation by HSQC to δ_C 49.32 (C_9) and by HMBC to δ_C 19.39 (C_{19}) (see Figure 3.65A and 3.65C). Quaternary carbon, C_{10} (δ_C 36.47), was assigned based on HMBC correlation to H_6 (δ_H 5.34) and m19 (δ_H 0.98) and no HSQC correlation (see Figure 3.65A and 3.65C).
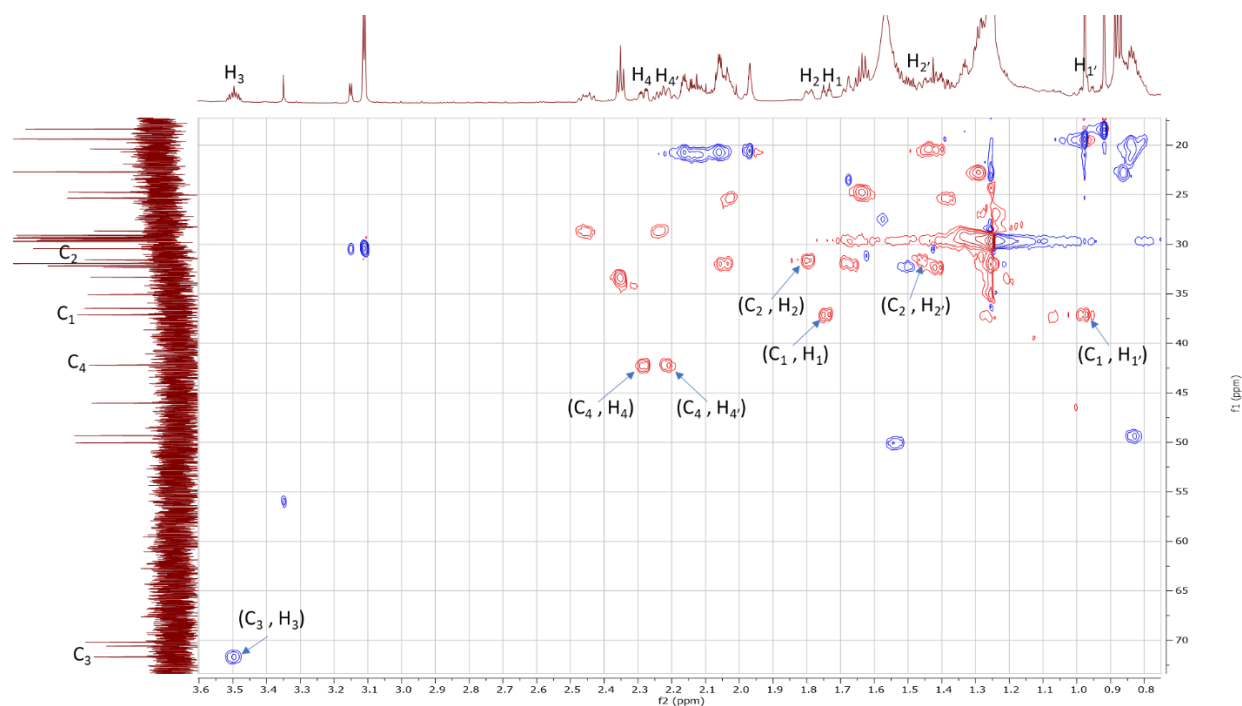
Figure 3.66A ^{1}H-^{13}C HSQC Correlations in A ring for DHEA C_{17}-(R)-N_3-MAN Product (29)
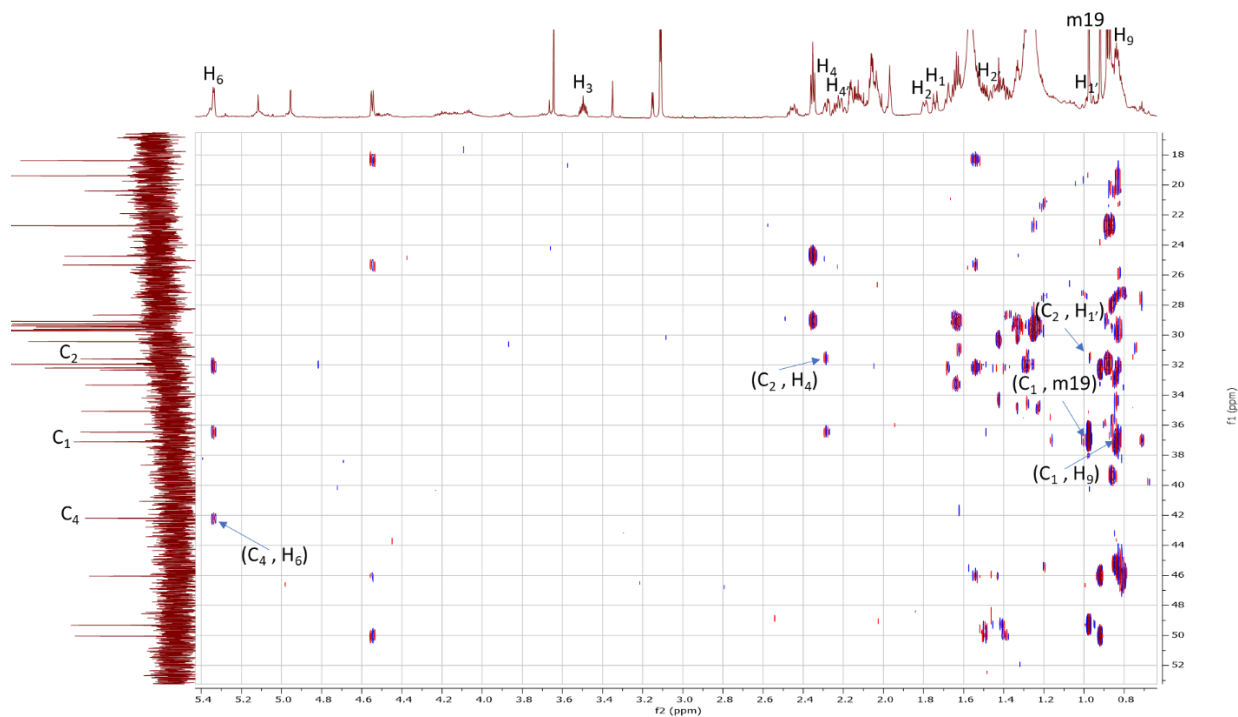
Figure 3.66B ^{1}H-^{13}C HMBC Correlations in A ring for DHEA C$_{17}$-(R)-N$_3$-MAN Product (29)

Continuing with the A ring, δ_H 3.49 (H$_3$) exhibited HSQC correlation to δ_C 71.67 (C$_3$) (see Figure 3.66A). Methylene protons, δ_H 2.28 (H$_4$) and δ_H 2.23 (H$_{4'}$), displayed HSQC correlation to δ_C 42.20 (C$_4$), which shows HMBC correlation to H$_6$ (δ_H 5.34) (see Figure 3.66A and 3.66B). Diastereotopic protons, δ_H 1.79 (H$_2$) and δ_H 1.37 (H$_{2'}$), displayed HSQC correlation to δ_C 31.58 (C$_2$), which showed HMBC correlation to H$_4$ (δ_H 2.28) (see Figure 3.66A and 3.66B). δ_C 37.10 (C$_1$) was discerned from HMBC correlation to m19 (δ_H 0.98) and H$_9$ (δ_H 0.83) (see Figure 3.66B). From there, methylene protons, δ_H 1.74 (H$_1$) and δ_H 0.98 (H$_{1'}$) displayed HSQC correlation to δ_C 37.10 (C$_1$) and HMBC correlation to δ_C 31.61 (C$_2$) (see Figure 3.66A and 3.66B).

181
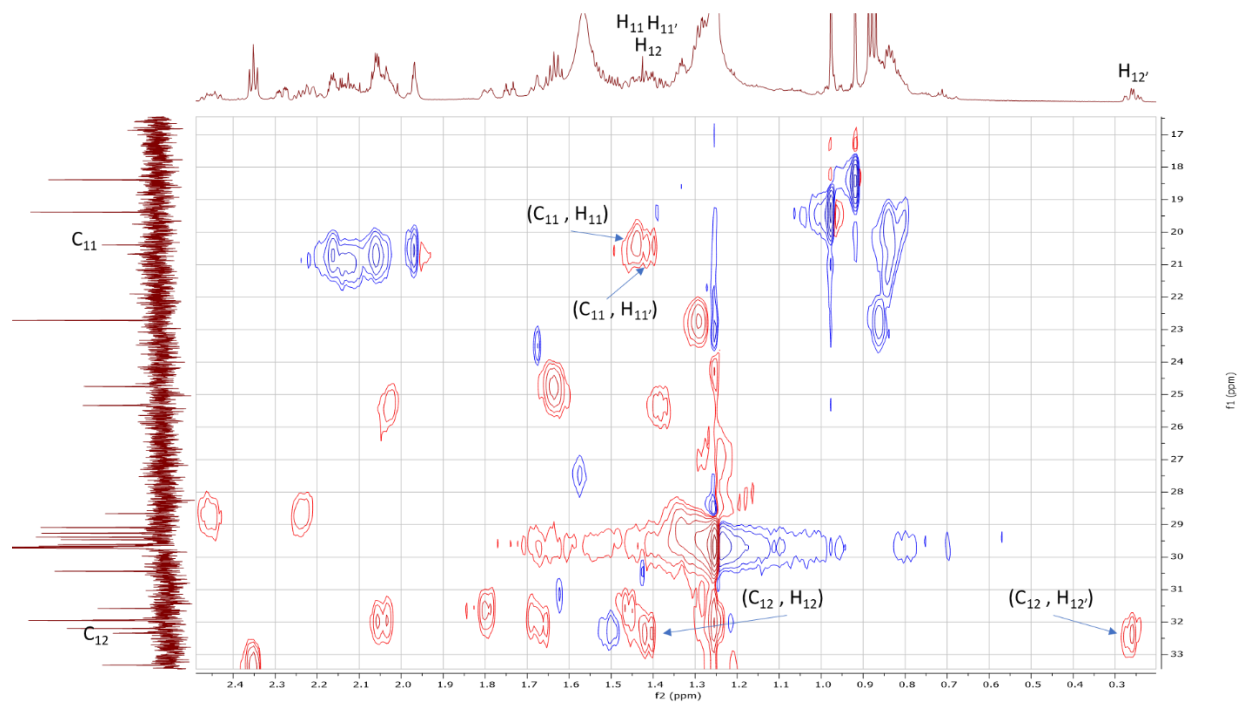
Figure 3.67A ^{1}H-^{13}C HSQC Correlations in C ring for DHEA C$_{17}$-(R)-N$_3$-MAN Product (29)
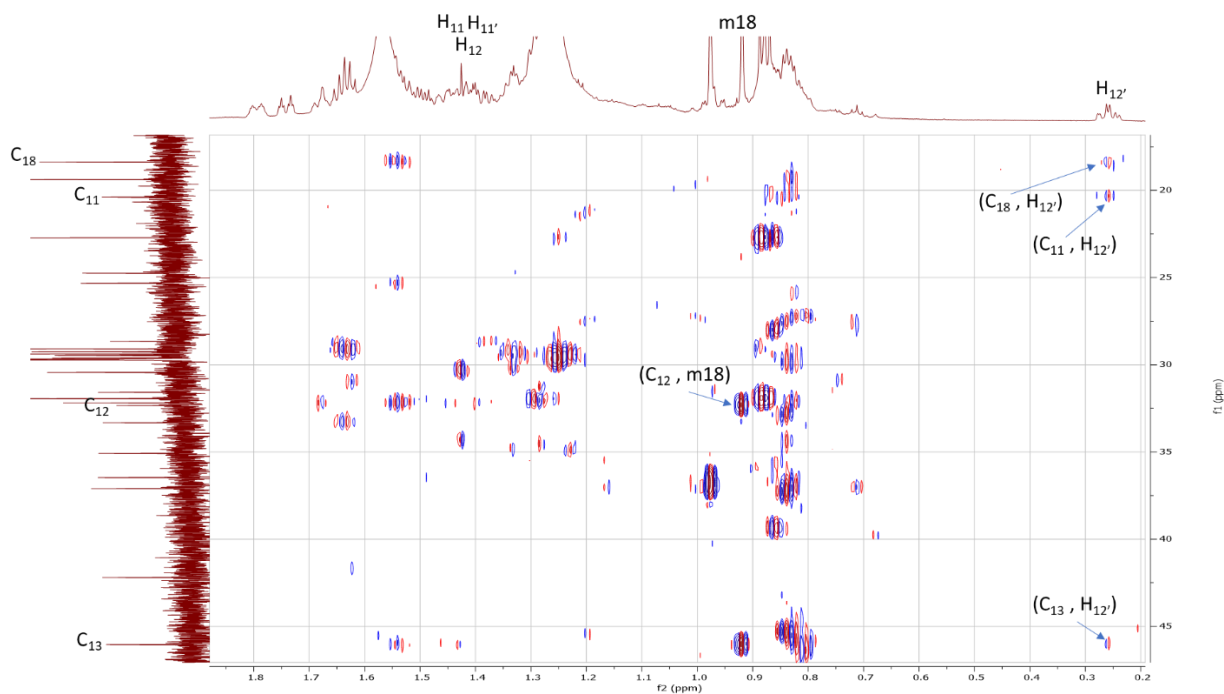
Figure 3.67B ^{1}H-^{13}C HMBC Correlations in C ring for DHEA C$_{17}$-(R)-N$_3$-MAN Product (29)

Concluding with the C ring, δ_C 32.34 (C$_{12}$) displayed strong HMBC correlations to m18 (δ_H 0.92) (see Figure 3.67B). δ_H 1.37 (H$_{12}$) and δ_H 0.26 (H$_{12'}$) were discerned from HSQC correlations

to δ_C 32.34 (C_{12}) and HMBC correlations to C_{13} (δ_C 46.04) and C_{18} (δ_C 18.39) (see Figure 3.67A and 3.67B). The remaining δ_C 20.39 (C_{11}) displayed HSQC correlation to δ_H 1.37 (H_{11}) and δ_H 1.37 ($H_{11'}$) along with HMBC correlation to $H_{12'}$ (δ_H 0.26) (see Figure 3.67A and 3.67B), thus completing full assignment of DHEA C_{17}-(R)-N_3-MAN product (**29**).
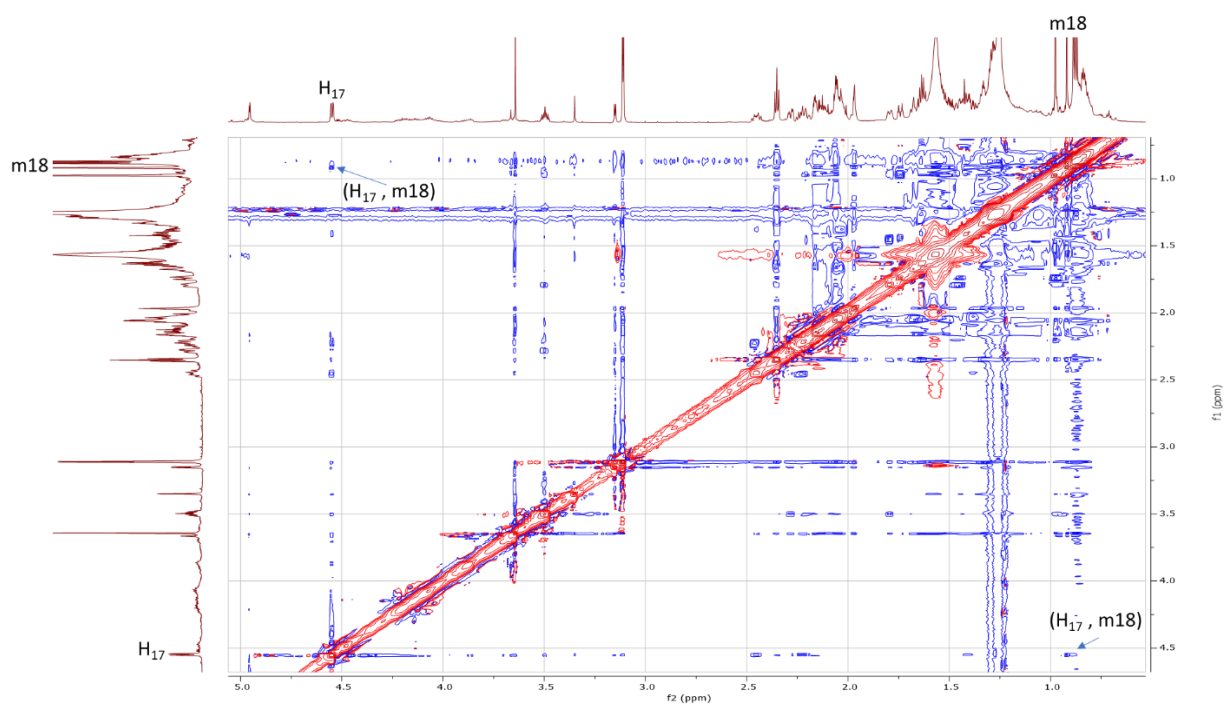
Figure 3.68 ^{1}H-^{1}H NOESY Correlations for DHEA C_{17}-(R)-N_3-MAN Product (29)

The stereochemistry of the triazole group at C_{17} is "R" based on NOESY correlation between δ_H 4.55 (H_{17}) and δ_H 0.92 (m18) (see Figure 3.68).

Table 3.1 ¹H NMR Shifts 1-8

Proton #	DHEA (1)	DHEA-PG (2)	DHEA C_{17} OH-PG (3)	DHEA C_{17} (R)-N_3 PG (4)	DHEA C_{17} (R)-N_3 probe (5)	DHEA C_{17} I-PG (6)	DHEA C_{17} (S)-N_3 PG (7)	DHEA $C_{17\text{-}16}$ Alkene PG (7a)	DHEA C_{17} (S)-N_3 probe (8)
1	1.86[a]	1.71	1.73	1.7	1.86	1.73	1.7	1.69	1.85
1'	1.11[a]	0.88	0.88	0.87	1.1	0.91	0.84	0.85	1.08
2	1.86[a]	1.69	1.71	1.67	1.84	1.7	1.67	1.67	1.84
2'	1.52[a]	1.58	1.56	1.59	1.51	1.6	1.59	1.59	1.51
3	3.53[a]	3.53[b,c]	3.53[b,c]	3.55[c]	3.53[c,d]	3.54[b,c]	3.52[c]	3.53[c]	3.52[c,d]
4	2.31[a]	2.35	2.37	2.32	2.3	2.35	2.33	2.34	2.3
4'	2.24[a]	2.16	2.16	2.14	2.24	2.16	2.13	2.14	2.24
5	N/A	N/A	N/A	N/A	N/A	N/A	N/A	N/A	N/A
6	5.37[a]	5.15[b,c]	5.13[b,c]	5.13[c]	5.34[c,d]	5.13[b,c]	5.11[c]	5.14[c]	5.35[c,d]
7	2.11[a]	2.04	1.95	1.92	2.01	1.97	1.91	1.94	1.99
7'	1.66[a]	1.54	1.4	1.51	1.61	1.54	1.42	1.53	1.54
8	1.66[a]	1.63	1.47	1.38	1.43	1.41	1.43	1.59	1.5
9	0.99[a]	0.88	0.84	0.86	0.98	0.91	0.82	0.91	0.95
10	N/A	N/A	N/A	N/A	N/A	N/A	N/A	N/A	N/A
11	1.66[a]	1.61	1.57	1.56	1.64	1.54	1.51	1.52	1.6
11'	1.5[a]	1.44	1.45	1.42	1.47	1.37	1.4	1.48	1.46
12	1.83[a]	1.8	1.8	1.57	1.64	1.49	1.85	1.72	1.9
12'	1.28[a]	1.21	1.03	1.55	1.6	1.42	1.09	1.33	1.16
13	N/A	N/A	N/A	N/A	N/A	N/A	N/A	N/A	N/A
14	1.28[a]	1.21	0.94	1.18	1.25	1.51	0.93	1.24	1.01
15	1.96[a]	1.9	1.6	1.73	1.78	1.88	1.62	2.08	1.67
15'	1.55[a]	1.5	1.29	1.18	1.21	1.3	1.25	1.89	1.29
16	2.45[a]	2.44	2.07	2.13	2.16	2.77	2.01	5.69	2.04
16'	2.09[a]	2.06	1.45	1.66	1.69	2.43	1.59	N/A	1.62
17	N/A	N/A	3.61[b,c]	3.5[c,d]	3.53[c,d]	4.34[d]	3.28[c,d]	5.82[c,d]	3.32[c,d]
18	0.88[a]	0.86[b,c]	0.73[b,c]	0.73[c,d]	0.76[c,d]	0.82[d]	0.74[c,d]	0.76[c,d]	0.77[c,d]
19	1.03[a]	1.01[b,c]	1[b,c]	1[c,d]	1.01[c,d]	1.01[d]	0.99[c,d]	1.02[c,d]	1.02[c,d]
t-Bu	N/A	1.06	1.06	1.06	N/A	1.07	1.05	1.06	N/A

Reference key [a: (Wishart et al., 2009), b: (Jan et al., 2016), c: (Blanco et al., 2014), d: (Kiss et al., 2018)]

The ¹H NMR shifts for **1** through **8** are shown above (see Table 3.1). The assignments highlighted in yellow have been previously reported in the literature. From looking at the table, there are a few key protons that can be used to track the progression from **1** to **8**: $H_{4\text{-}4'}$, H_6, H_{14}, $H_{16\text{-}16'}$, and H_{17}.

Beginning with $H_{4-4'}$, δ_H 2.31 (H_4) and δ_H 2.24 ($H_{4'}$) were identified for DHEA (**1**). As the TBDPS protecting group was attached to the hydroxyl group on C_3, δ_H 2.35 (H_4) and δ_H 2.16 ($H_{4'}$) were identified for DHEA-PG (**2**), which indicates a slight downfield shift for H_4 and an upfield shift for $H_{4'}$. The latter trend regarding ^1H NMR shifts for H_4 and $H_{4'}$ of **2** can also be observed for **3**, **4**, **6**, **7**, and **7a** as the TBDPS group is attached to C_3 of all five compounds. As the TBDPS group is removed, which is the case for **5** and **8**, ^1H NMR shifts of H_4 and $H_{4'}$ are reverted back to δ_H 2.30 (H_4) and δ_H 2.24 ($H_{4'}$) just like previously observed for **1**. Therefore, the ^1H NMR shifts for H_4 and $H_{4'}$ can be used to monitor the protection/deprotection and stability of the TBDPS group. As the TBDPS group is attached to C_3, it was expected that H_3 would show a dramatic change in its ^1H NMR shift. However, that was not the case as δ_H 3.52-3.55 was identified as H_3 from **1-8** and little to no change was observed.

Next with H_6, δ_H 5.37 (H_6) was identified for **1**. As the TBDPS protecting group was attached to the hydroxyl group on C_3, δ_H 5.15 (H_6) was identified for DHEA-PG (**2**), which indicates an upfield shift for H_6. The latter trend regarding ^1H NMR shifts for H_6 for **2** can also be observed for **3**, **4**, **6**, **7**, and **7a** as the TBDPS group is attached to C_3 of all five compounds. As the TBDPS group is removed, which is the case for **5** and **8**, ^1H NMR shifts H_6 are reverted back to δ_H 5.34-5.35 (H_6) just like previously observed for **1**. Therefore, the ^1H NMR shift for H_6 can be used to monitor the protection and deprotection and stability of the TBDPS group in addition to H_4 and $H_{4'}$.

Continuing with H_{14}, δ_H 1.21-1.28 (H_{14}) was identified for **1** and **2** as both groups contained a ketone group at C_{17}. For **3**, **7**, and **8** which have a heteroatom (O or N) group in the S configuration at C_{17}, δ_H 0.93-1.01 (H_{14}) was identified. For **4**, **5**, **6**, and **7a** which have a heteroatom (O or N) group in the R configuration at C_{17} or a π bond between C_{16-17}, δ_H 1.18-1.51 (H_{14}) was identified. Therefore, the ^1H NMR shift for H_{14} can be used to monitor the configuration of the heteroatom group from modification of the ketone moiety at C_{17} in which groups in the R

185

configuration at C_{17} or a π bond between C_{16-17} (**4**, **5**, **6**, and **7a**) exhibit no change or a downfield shift from δ_H 1.20 (**1** and **2**) while groups in the S configuration at C_{17} (**3**, **7**, and **8**) exhibit an upfield shift from δ_H 1.20 (**1** and **2**).

Following with $H_{16-16'}$, δ_H 2.44-2.45 (H_{16}) and δ_H 2.06-2.09 ($H_{16'}$) were identified for **1** and **2.** Starting with the ketone group being modified into a hydroxyl group, δ_H 2.07 (H_{16}) and δ_H 1.45 ($H_{16'}$) were identified for **3**. With the ketone group is modified into an azido group regardless of configuration, δ_H 2.01-2.16 (H_{16}) and δ_H 1.59-1.69 ($H_{16'}$) were identified for **4**, **5**, **7**, and **8**. If the ketone group is modified into an iodo group, δ_H 2.77 (H_{16}) and δ_H 2.43 ($H_{16'}$) was identified for **6**. Rather than modifying the ketone group with a heteroatom group but instead an alkene moiety, δ_H 5.69 (H_{16}) was observed for **7a**. In summary, H_{16} and $H_{16'}$ can be used to monitor the functionality at C_{17} from a ketone to hydroxyl to azido to iodo and to alkene group.

While H_{14} and $H_{16-16'}$ can be used together to discover the identity and configuration of the heteroatom group attached at C_{17} after modification of the ketone moiety, H_{17} can singlehandedly be used to discern the latter information with ease. Beginning with **3** in which the hydroxyl group is in the S configuration, H_{17} was identified at δ_H 3.61 with an apparent triplet splitting. Next with **4** and **5** in which the azido group is in the R configuration, H_{17} was identified at δ_H 3.50-3.52 with an apparent doublet splitting. Continuing with **6** in which the iodo group is in the R configuration, H_{17} was identified at δ_H 4.34 with an apparent doublet splitting. Following with **7a** in which the alkene group is attached between C_{16-17}, H_{17} was identified at δ_H 5.82 with a doublet of doublet or doublet splitting. Concluding with **7** and **8** in which the azido group is in the S configuration, H_{17} was identified at δ_H 3.28-3.32 with an apparent triplet splitting. In summary, the ^{1}H NMR shift and splitting pattern of H_{17} can discern the functionality and configuration of the heteroatom group attached at C_{17} after modification of the ketone moiety.
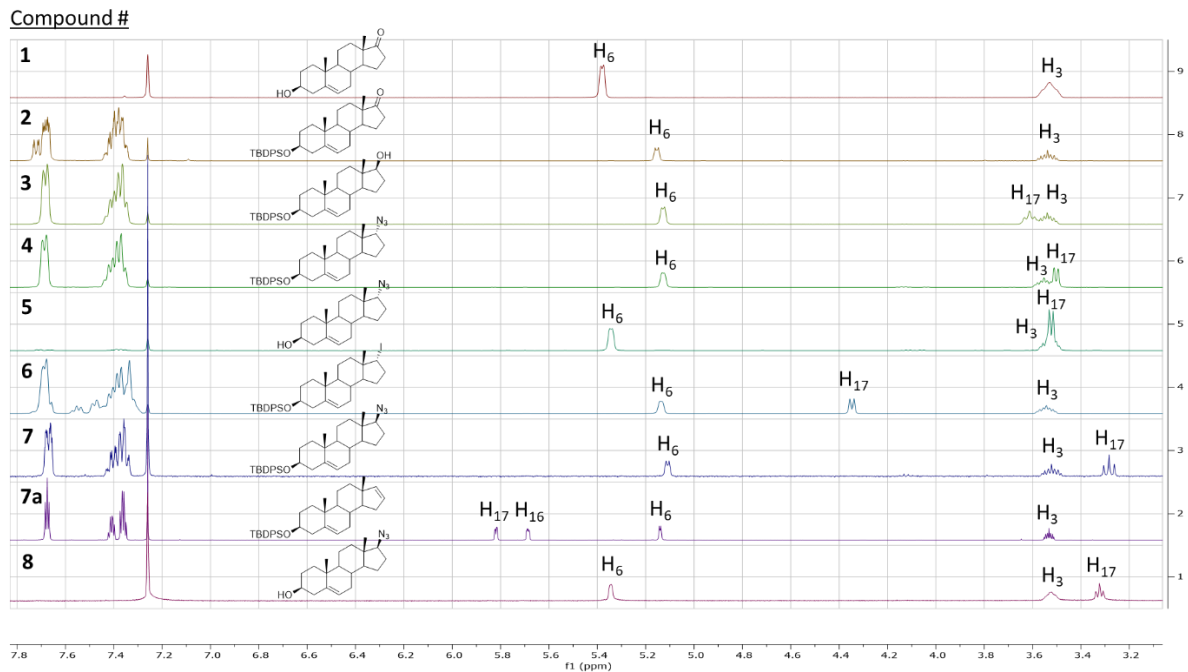
Figure 3.69 ¹H Stacked Spectrum of 1-8

In conclusion, H_6 and H_{17} at a quick glance can be used to track the progression from **1** to **8** by means of chemical shift and/or splitting pattern (see Figure 3.69). However, $H_{4-4'}$, H_{14}, and $H_{16-16'}$ when looked deeply can also be used to track the progression from **1** to **8**.

Table 3.2 ^{13}C NMR Shifts 1-8

Carbon #	DHEA (1)	DHEA-PG (2)	DHEA C$_{17}$ OH-PG (3)	DHEA C$_{17}$ (R)-N$_3$ PG (4)	DHEA C$_{17}$ (R)-N$_3$ probe (5)	DHEA C$_{17}$ I-PG (6)	DHEA C$_{17}$ (S)-N$_3$ PG (7)	DHEA C$_{17\text{-}16}$ Alkene PG (7a)	DHEA C$_{17}$ (S)-N$_3$ probe (8)
1	37.17	37.16	37.25	37.24	37.26	37.22	37.21	37.16	37.27
2	31.48	31.82	31.87	31.87	31.61	31.87	31.82	31.89	31.63
3	71.53	73.09[b]	73.19	73.17	71.69[a]	73.19	73.14	73.23	71.71[a]
4	42.17	42.46	42.49	42.47	42.23	42.46	42.45	42.54	42.25
5	141.04	141.55	141.4	141.22	140.69[a]	141.18	141.41	141.58	140.89[a]
6	120.88	120.4	120.82	120.88	121.45[a]	120.89	120.64	120.98	121.23[a]
7	30.77	30.78	31.48	32.14	32.14	31.95	31.5	31.72	31.53
8	31.54	31.44	31.93	32.05	32.06	32.54	31.95	30.41	32
9	50.21	50.18	50.18	49.71	49.76	49.43	49.99	50.86	50.07
10	36.62	36.64	36.58	36.56	36.55	36.49	36.55	36.8	36.58
11	20.35	20.32	20.62	20.57	20.62	21.79	20.57	20.81	20.64
12	31.41	31.48	36.58	32.47	32.47	40.66	37.07	35.86	37.09
13	47.54	47.55	42.71	45.71	45.72	45.18	44.21	45.37	44.23
14	51.74	51.78	51.34	49.85	49.86	49.43	52.41	56.21	52.43
15	21.87	21.88	23.43	24.81	24.81	25.18	23.61	32.08	23.64
16	35.84	35.85	30.52	28.7	28.71	36.82	26.91	129.35	26.93
17	221.27	221.23[b]	81.91	71.48	71.45[a]	48.12	71.23	143.86	71.24[a]
18	13.54	13.54	10.94	17.43	17.44[a]	15.47	12.11	16.84	12.15[a]
19	19.42	19.46	19.47	19.46	19.46[a]	19.57	19.45	19.37	19.44[a]
t-Bu	N/A	19.15	19.15	19.16	N/A	19.18	19.15	19.16	N/A
t-Bu	N/A	27.02	27.01	27.03	N/A	27.04	27	27.02	N/A

Reference Key [a: (Kiss et al., 2018), b: (Jan et al., 2016)]

The ^{13}C NMR shifts for **1** through **8** are shown above (see Table 3.2). The assignments highlighted in yellow have been previously reported. From looking at the table, there are a few key carbons that can be used to track the progression from **1** to **8**: C$_3$, C$_{12}$, C$_{16}$, C$_{17}$, and C$_{18}$.

Beginning with C$_3$, δ_C 71.53 (C$_3$) was identified for DHEA (**1**). As the TBDPS protecting group was attached to the hydroxyl group on C$_3$, δ_C 73.09 (C$_3$) was identified for DHEA-PG (**2**), indicating a slight downfield shift. δ_C 73.14-73.23 (C$_3$) was also observed for **3**, **4**, **6**, **7**, and **7a** as the TBDPS group is attached to C$_3$ of all five compounds. As the TBDPS group is removed, which is the case for **5** and **8**, ^{13}C NMR shift C$_3$ are reverted back to δ_C 71.69-71.71 (C$_3$) just like previously observed for **1**. Therefore, the ^{13}C NMR shifts for C$_3$ can be used to monitor the protection/deprotection and stability of the TBDPS group.

Continuing with C_{12}, δ_C 31.41-31.48 (C_{12}) was identified for **1** and **2.** Starting with the ketone group being modified into a hydroxyl group, δ_C 36.58 (C_{12}) was identified for **3**. With the ketone group is modified into an azido group in the R configuration, δ_C 32.47 (C_{12}) was identified for **4** and **5** while modification into an azido group in the S configuration identified C_{12} at δ_C 37.07-37.09 for **7** and **8**. If the ketone group is modified into an iodo group, δ_C 40.66 (C_{12}) was identified for **6**. Rather than modifying the ketone group with a heteroatom group but instead an alkene moiety, δ_C 35.86 (C_{12}) was observed for **7a**. In summary, C_{12} can be used to monitor the functionality and configuration at C_{17} from a ketone to hydroxyl to azido to iodo and to alkene group.

Next with C_{16}, δ_C 35.84-35.85 (C_{16}) was identified for **1** and **2.** Starting with the ketone group being modified into a hydroxyl group, δ_C 30.52 (C_{16}) was identified for **3**. With the ketone group is modified into an azido group in the R configuration, δ_C 28.70-28.71 (C_{16}) was identified for **4** and **5** while modification into an azido group in the S configuration identified C_{16} at δ_C 26.91-26.93 for **7** and **8**. If the ketone group is modified into an iodo group, δ_C 36.82 (C_{16}) was identified for **6**. Rather than modifying the ketone group with a heteroatom group but instead an alkene moiety, δ_C 129.35 (C_{16}) was observed for **7a**. In summary, C_{16} can be used to monitor the functionality and configuration at C_{17} just like C_{12}.

Following with C_{17}, δ_C 221.23-221.27 (C_{17}) was identified for **1** and **2.** Starting with the ketone group being modified into a hydroxyl group, δ_C 81.91 (C_{17}) was identified for **3**. With the ketone group is modified into an azido group in the R configuration, δ_C 71.45-71.48 (C_{17}) was identified for **4** and **5** while modification into an azido group in the S configuration identified C_{17} at δ_C 71.23-71.24 for **7** and **8**. If the ketone group is modified into an iodo group, δ_C 48.12 (C_{17}) was identified for **6**. Rather than modifying the ketone group with a heteroatom group but instead an alkene moiety, δ_C 143.86 (C_{17}) was observed for **7a**. In summary, C_{17} can be used to monitor the functionality and configuration at C_{17} just like C_{12} and C_{16}.

Finishing with C_{18}, δ_C 13.54 (C_{18}) was identified for **1** and **2.** Starting with the ketone group being modified into a hydroxyl group, δ_C 10.94 (C_{18}) was identified for **3**. With the ketone group is modified into an azido group in the R configuration, δ_C 17.43-17.44 (C_{18}) was identified for **4** and **5** while modification into an azido group in the S configuration identified C_{18} at δ_C 12.11-12.15 for **7** and **8**. If the ketone group is modified into an iodo group, δ_C 15.47 (C_{18}) was identified for **6**. Rather than modifying the ketone group with a heteroatom group but instead an alkene moiety, δ_C 16.84 (C_{18}) was observed for **7a**. In summary, C_{18} can be used to monitor the functionality and configuration at C_{17} just like C_{12}, C_{16}, and C_{17}.
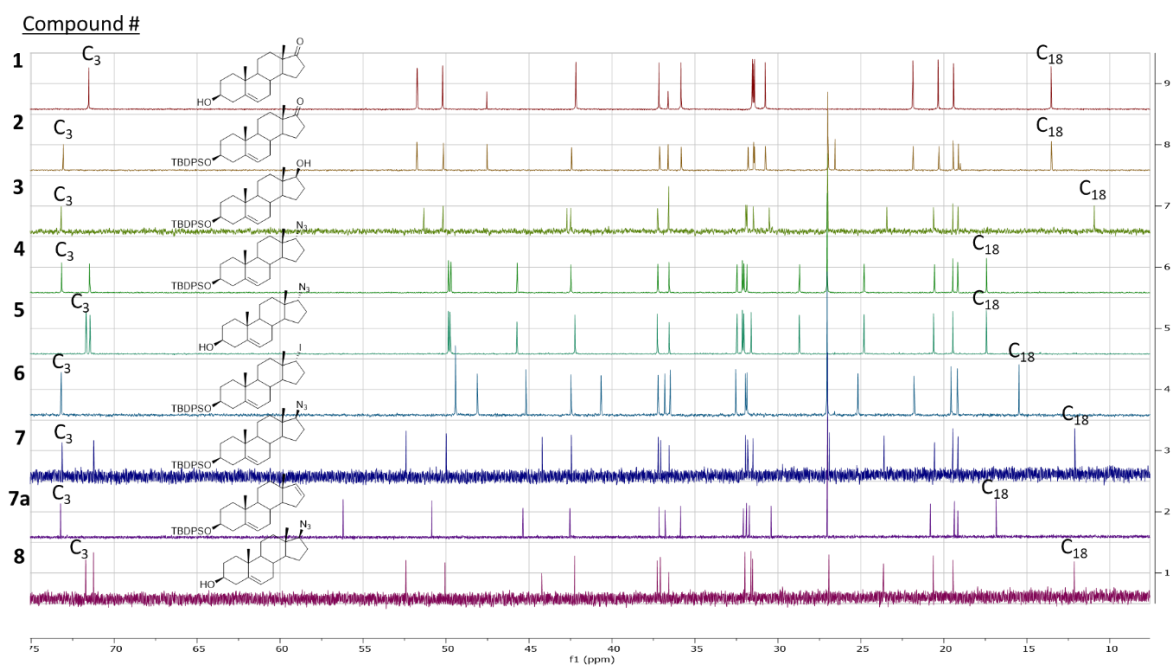
Figure 3.70 ^{13}C Stacked Spectrum of 1-8

In conclusion, C_3 and C_{18} at a quick glance can be used to track the progression from **1** to **8** by means of chemical shift (see Figure 3.70). However, C_{12}, C_{16}, and C_{17} when looked closely can be used to track the progression from **1** to **8** by means of chemical shift.

In addition to following the synthesis of **5** and **8** from DHEA (**1**), full characterization of every proton (H$_{1-1'}$-H$_{19}$) and carbon (C$_1$-C$_{19}$) could be used to track the formation of the "clicked" product (**29**) via upfield or downfield trends of the ^{1}H and ^{13}C chemical shift values in the C and D rings from **5** to **29**.

Table 3.3 ^{1}H NMR Shifts 29

Proton #	DHEA-R-N$_3$ Click MAN (29)		
1	1.74	10	N/A
1'	0.98	11	1.44
2	1.8	11'	1.41
2'	1.46	12	1.42
3	3.49	12'	0.26
4	2.28	13	N/A
4'	2.22	14	1.54
5	N/A	15	2.03
6	5.34	15'	1.38
7	2.05	16	2.45
7'	1.67	16'	2.24
8	1.5	17	4.55
9	0.83	18	0.92
		19	0.98

The ^{1}H NMR shifts for **29** are shown above (see Table 3.3). From comparing the ^{1}H shifts of **5** to the ^{1}H shifts of **29**, there are a few key protons that show significant change: H$_9$, H$_{11-11'}$, H$_{12-12'}$, H$_{14}$, H$_{15-15'}$, H$_{16-16'}$, H$_{17}$, and m18. Starting with the protons in the C ring, H$_9$ shifted upfield from δ$_H$ 0.98 (**5**) to δ$_H$ 0.83 (**29**). For the methylene protons, H$_{11-11'}$ shifted upfield from δ$_H$ 1.64 (H$_{11}$, **5**) and δ$_H$ 1.47 (H$_{11'}$, **5**) to δ$_H$ 1.44 (H$_{11}$, **29**) and δ$_H$ 1.41 (H$_{11'}$, **29**), respectively. In addition, H$_{12-12'}$ also shifted upfield from δ$_H$ 1.64 (H$_{12}$, **5**) and δ$_H$ 1.60 (H$_{12'}$, **5**) to δ$_H$ 1.42 (H$_{12}$, **29**) and δ$_H$ 0.26 (H$_{12'}$, **29**), respectively. Next with the protons in the D ring, H$_{14}$ shifted downfield from δ$_H$ 1.25 (**5**) to δ$_H$ 1.54 (**29**). For the methylene protons, H$_{15-15'}$ shifted downfield from δ$_H$ 1.78 (H$_{15}$, **5**) and δ$_H$ 1.21 (H$_{15'}$, **5**) to δ$_H$ 2.03 (H$_{15}$, **29**) and δ$_H$ 1.38 (H$_{15'}$, **29**), respectively. Also, H$_{16-16'}$ shifted downfield from δ$_H$ 2.16 (H$_{16}$, **5**) and δ$_H$ 1.69 (H$_{16'}$, **5**) to δ$_H$ 2.45 (H$_{16}$, **29**) and δ$_H$ 2.24 (H$_{16'}$, **29**), respectively. With

H$_{17}$, the proton shifted downfield from δ$_H$ 3.53 (**5**) to δ$_H$ 4.55 (**29**). Finishing with m18, these methyl protons shifted downfield from δ$_H$ 0.76 (**5**) to δ$_H$ 0.92 (**29**). In conclusion, the protons in the C ring observed an upfield trend in chemical shift while the protons in the D ring observed a downfield trend in chemical shift from the CuAAC reaction between **5** and **MAN**.

Table 3.4 ^{13}C NMR Shifts 29

Carbon #	DHEA-R-N$_3$ Click MAN (29)	10	36.47
1	37.1	11	20.39
2	31.58	12	32.34
3	71.67	13	46.04
4	42.2	14	50.04
5	140.61	15	25.33
6	121.4	16	28.66
7	31.95	17	70.18
8	32.19	18	18.39
9	49.32	19	19.39

The ^{13}C NMR shifts for **29** are shown above (see Table 3.4). From comparing the ^{13}C shifts of **5** to the ^{13}C shifts of **29**, there are a few key carbons that show significant change: C$_{17}$ and C$_{18}$. Starting with C$_{17}$, it shifted upfield from δ$_C$ 71.45 (**5**) to δ$_C$ 70.18 (**29**). With C$_{18}$, it shifted downfield from δ$_C$ 17.44 (**5**) to δ$_C$ 18.39 (**29**). In conclusion, it seems there are no observable ^{13}C trends in chemical shift for the CuAAC reaction between **5** and **MAN**.

In summary, assignment of every ^{1}H and ^{13}C NMR shift of **1-8** and **29** helped track the progression of synthesizing **5**, **8**, and **29** from **1** in addition to unforeseen trends in chemical shifts.

Figure S3.1 ^{1}H Spectrum of (1) (400 MHz, chloroform-*d*) δ 5.41 – 5.37 (m, 1H, H$_6$), 3.61 – 3.46 (m, 1H, H$_3$), 2.46 (dd, *J* = 19.2, 8.9 Hz, 1H, H$_{16}$), 2.36 – 2.20 (m, 2H, H$_4$, H$_4$), 2.17 – 2.03 (m, 2H, H$_7$, H$_{16}$), 1.99 – 1.90 (m, 1H, H$_{15}$), 1.88 – 1.81 (m, 3H, H$_1$, H$_2$, H$_{12}$), 1.73 – 1.57 (m, 3H, H$_7$, H$_{11}$, H$_8$), 1.58 – 1.42 (m, 3H, H$_2$' , H$_{11'}$, H$_{15'}$), 1.33 – 1.23 (m, 2H, H$_{12}$, H$_{14}$), 1.15 – 1.06 (m, 1H, H$_{1'}$), 1.03 (s, 3H, H$_{19}$), 1.02 – 0.96 (m, 1H, H$_9$), 0.88 (s, 3H, H$_{18}$).

193
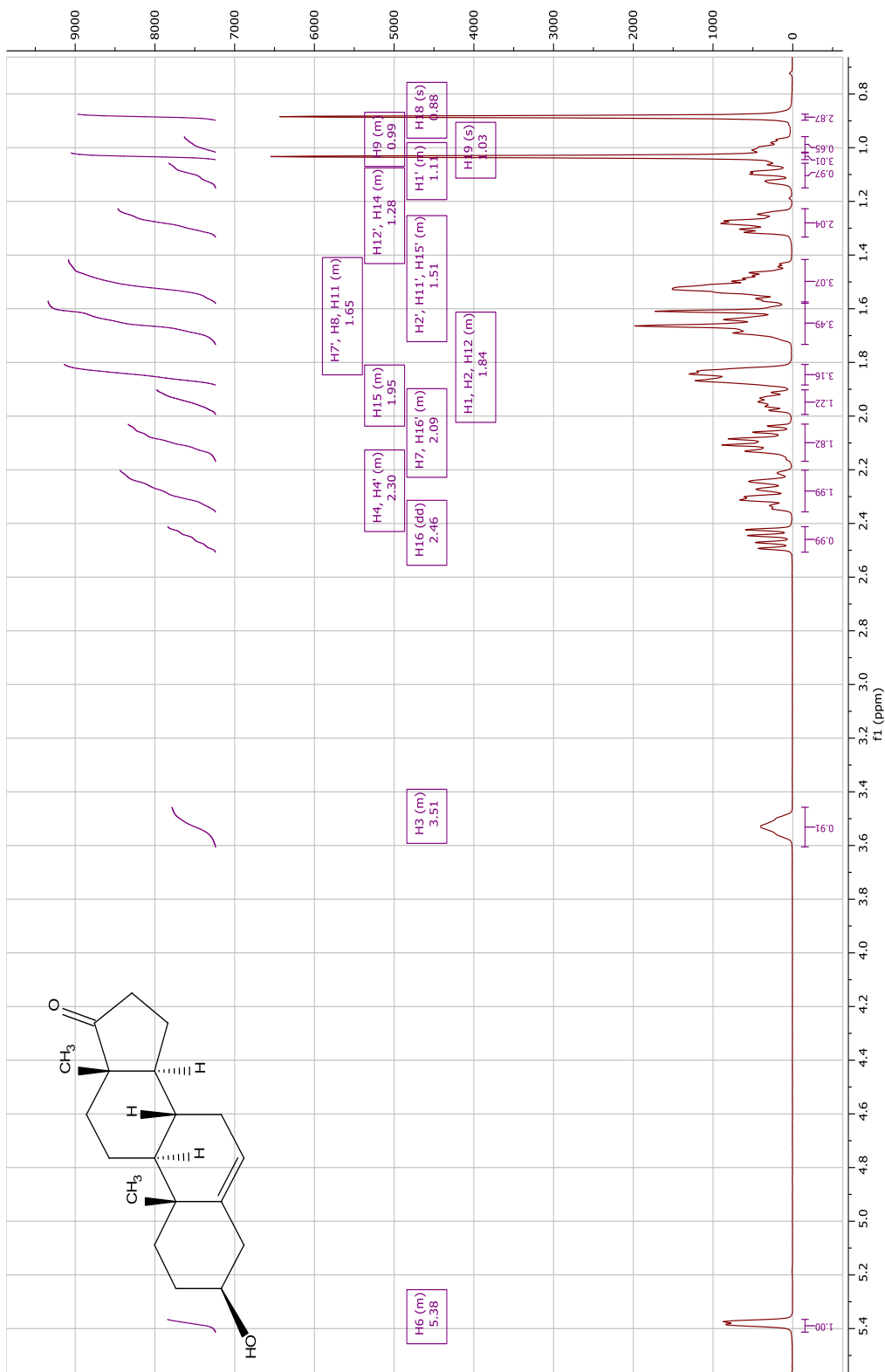
Figure S3.2 ^{13}C Spectrum of (1) (151 MHz, chloroform-*d*) δ 221.27 (C$_{17}$), 141.04 (C$_{5}$), 120.88 (C$_{6}$), 71.53 (C$_{3}$), 51.74 (C$_{14}$), 50.21 (C$_{9}$), 47.54 (C$_{13}$), 42.17 (C$_{4}$), 37.17 (C$_{1}$), 36.62 (C$_{10}$), 35.84 (C$_{16}$), 31.54 (C$_{8}$), 31.48 (C$_{2}$), 31.41 (C$_{12}$), 30.77 (C$_{7}$), 21.87 (C$_{15}$), 20.35 (C$_{11}$), 19.42 (C$_{19}$), 13.54 (C$_{18}$).
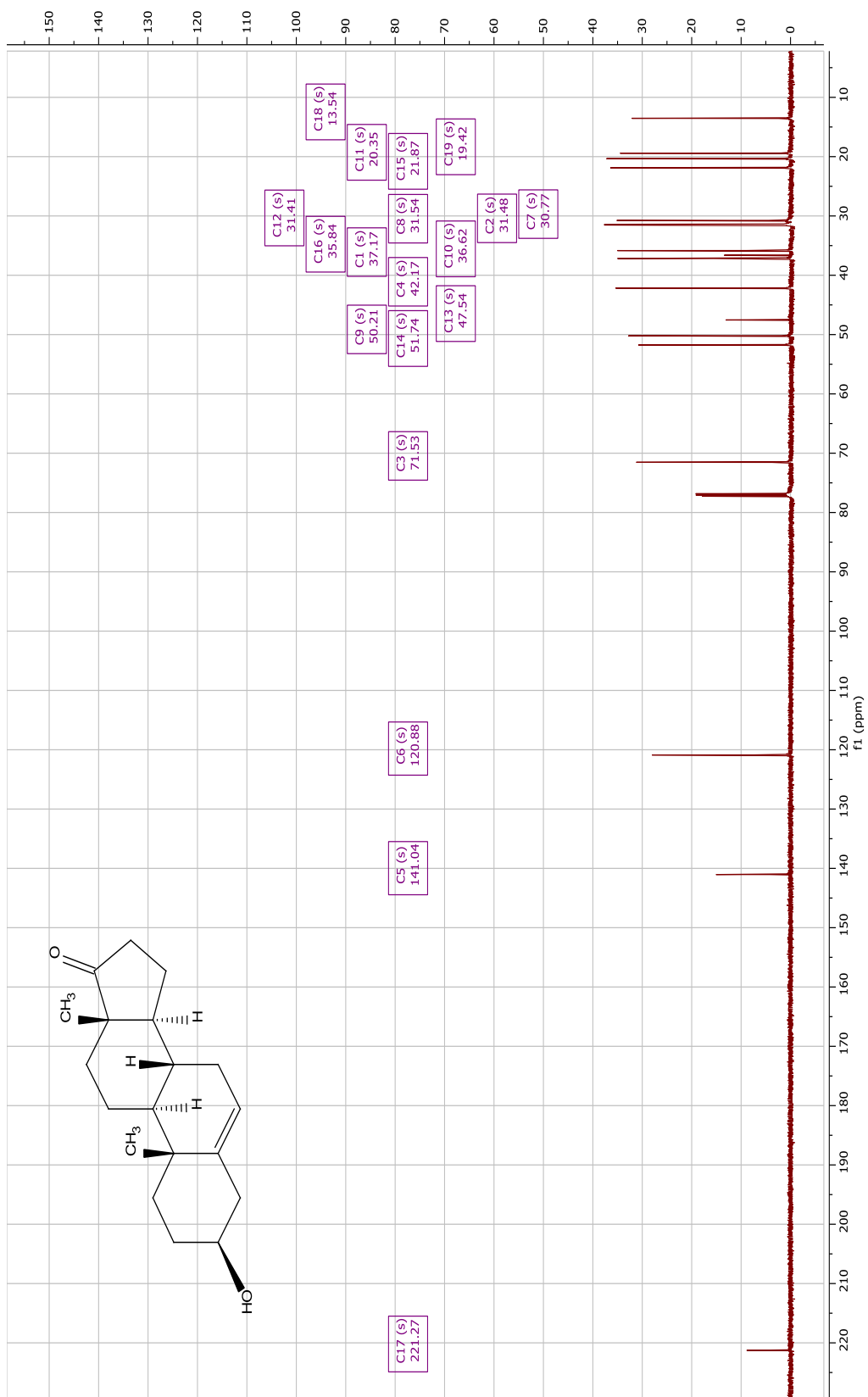
Figure S3.3 ^{1}H-^{1}H COSY Spectrum of (1)
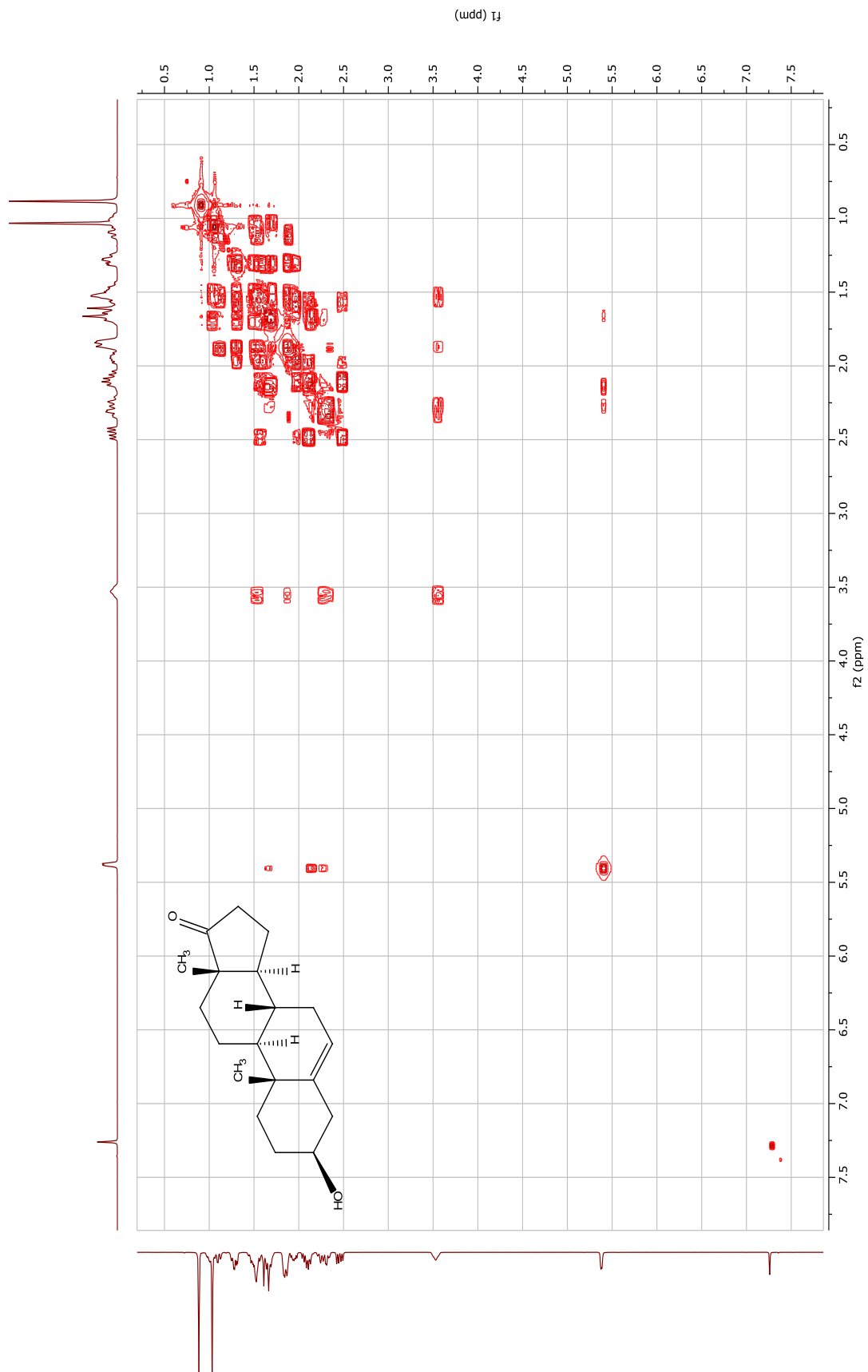
Figure S3.4 ^{1}H-^{13}C HSQC Spectrum of (1)

196
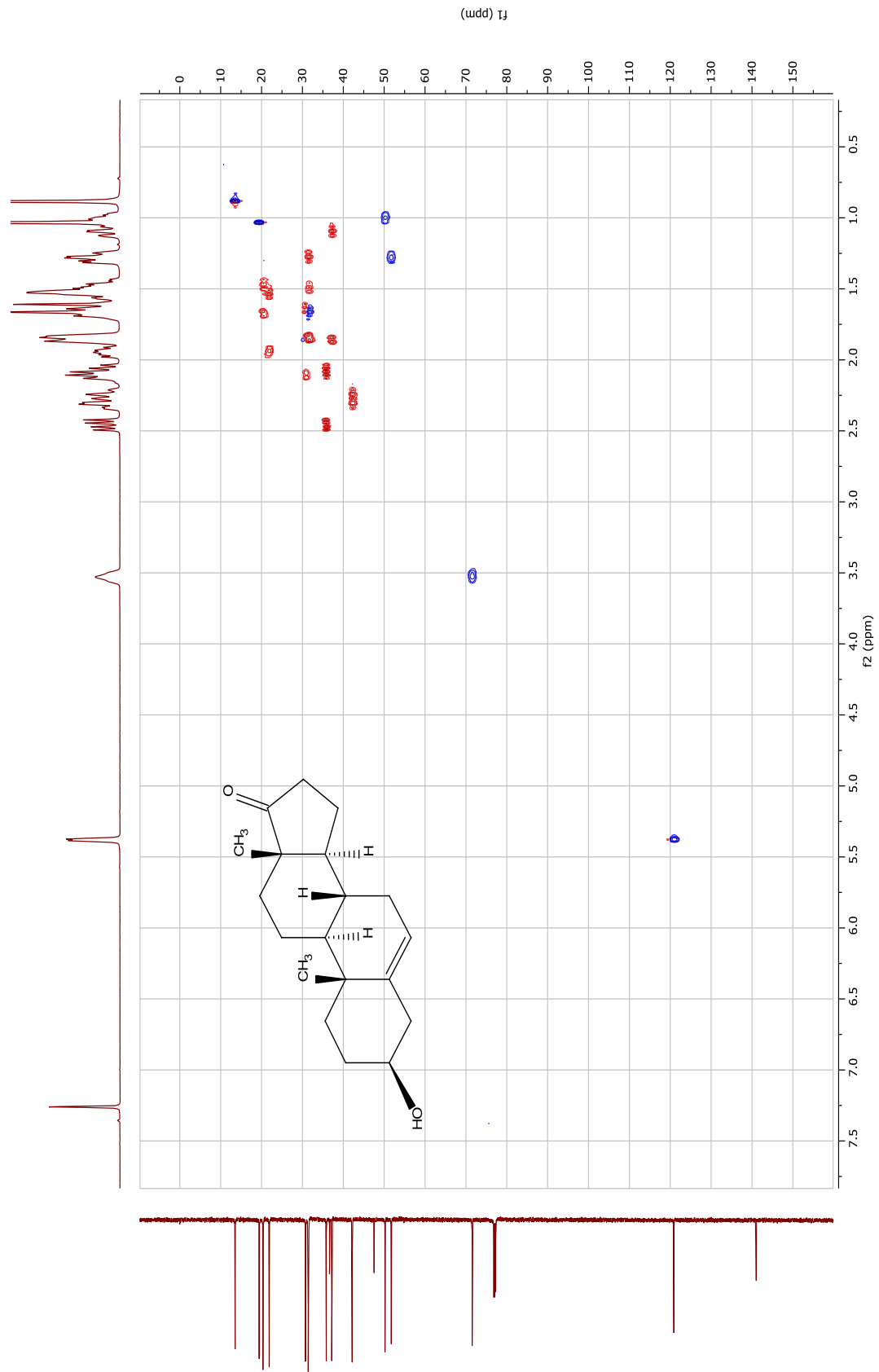
Figure S3.5 ^{1}H-^{13}C HMBC Spectrum of (1)
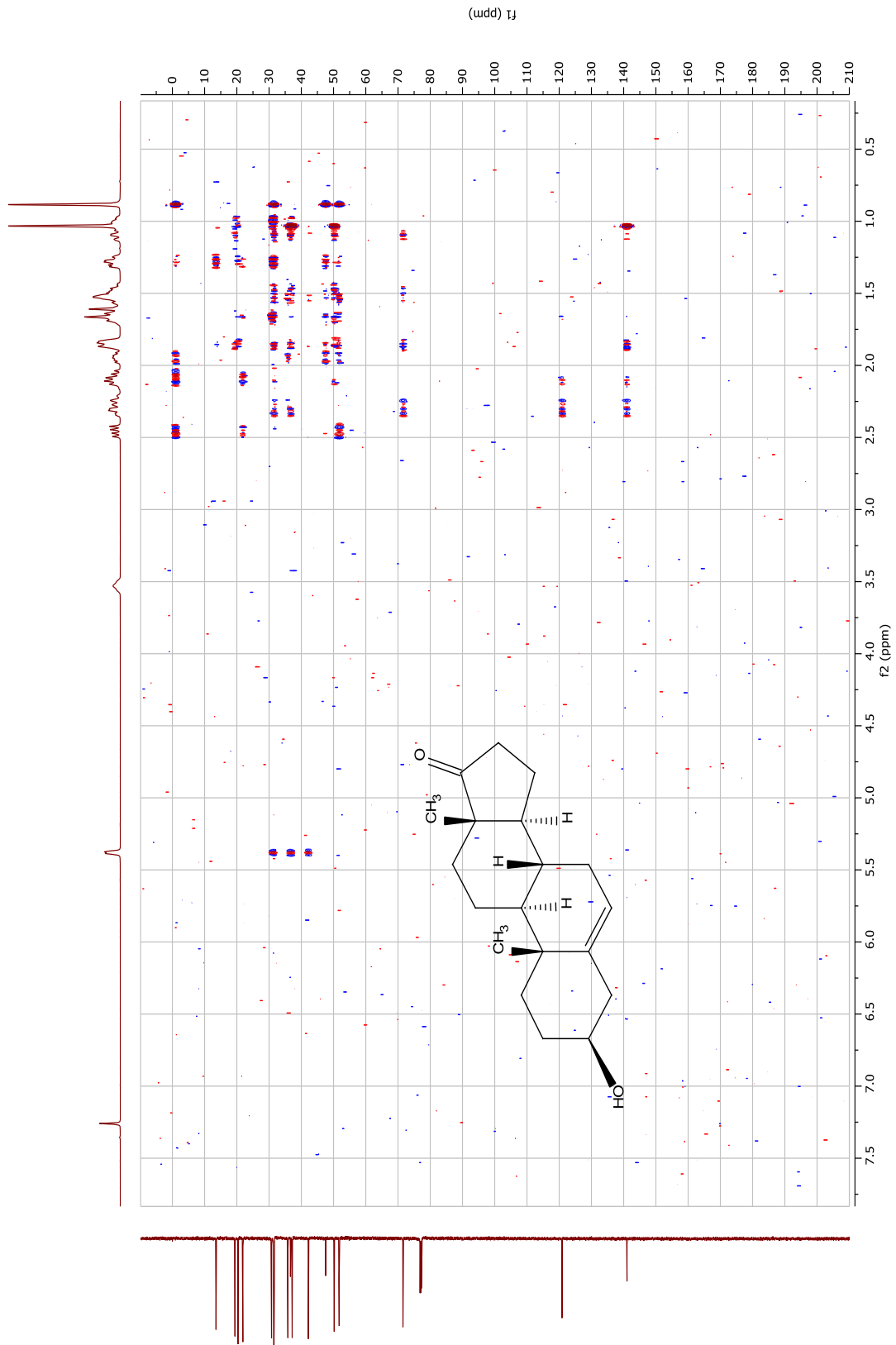
Figure S3.6 ^{1}H Spectrum of (2)
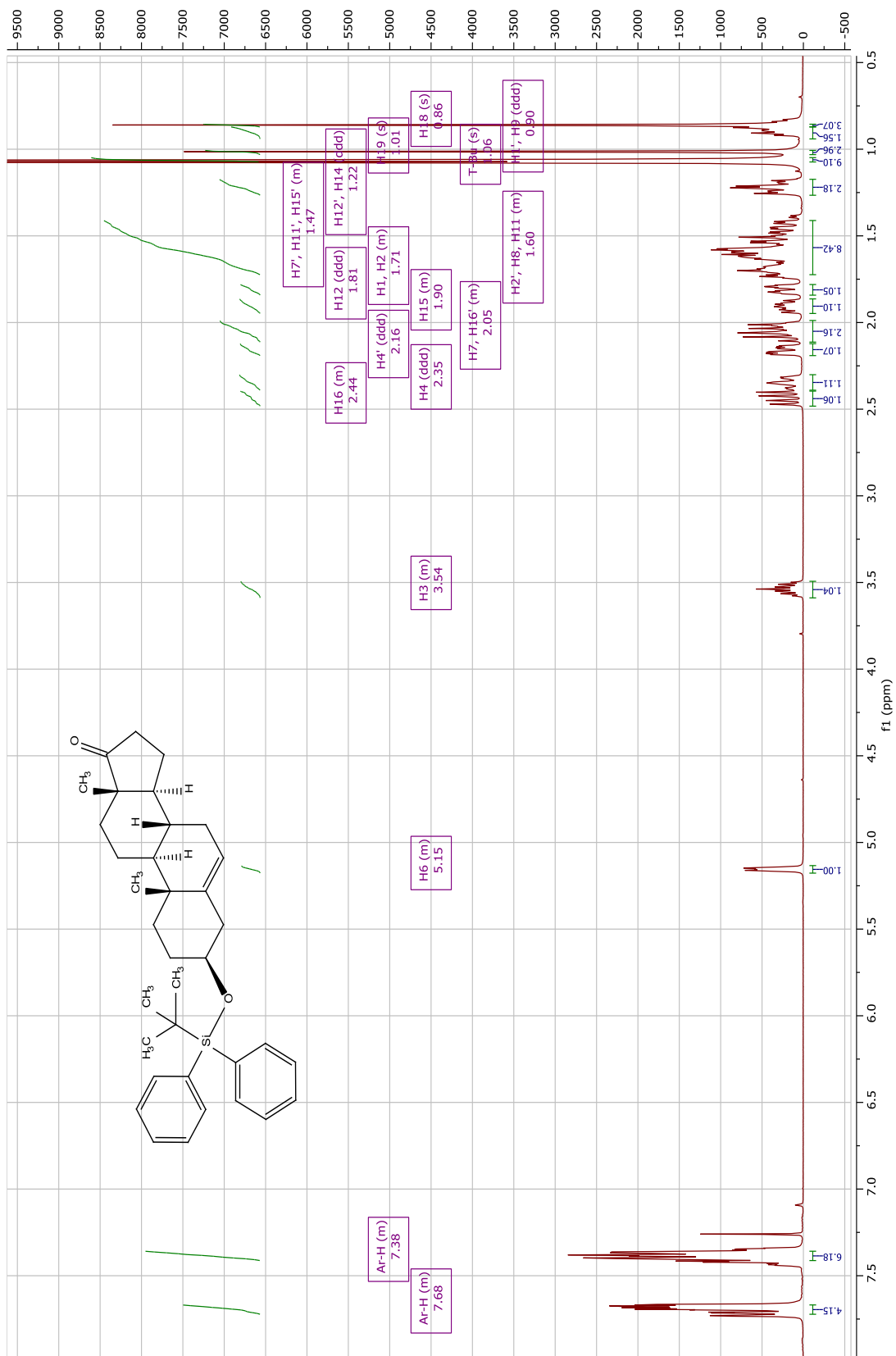
Figure S3.7 ^{13}C Spectrum of (2)

199
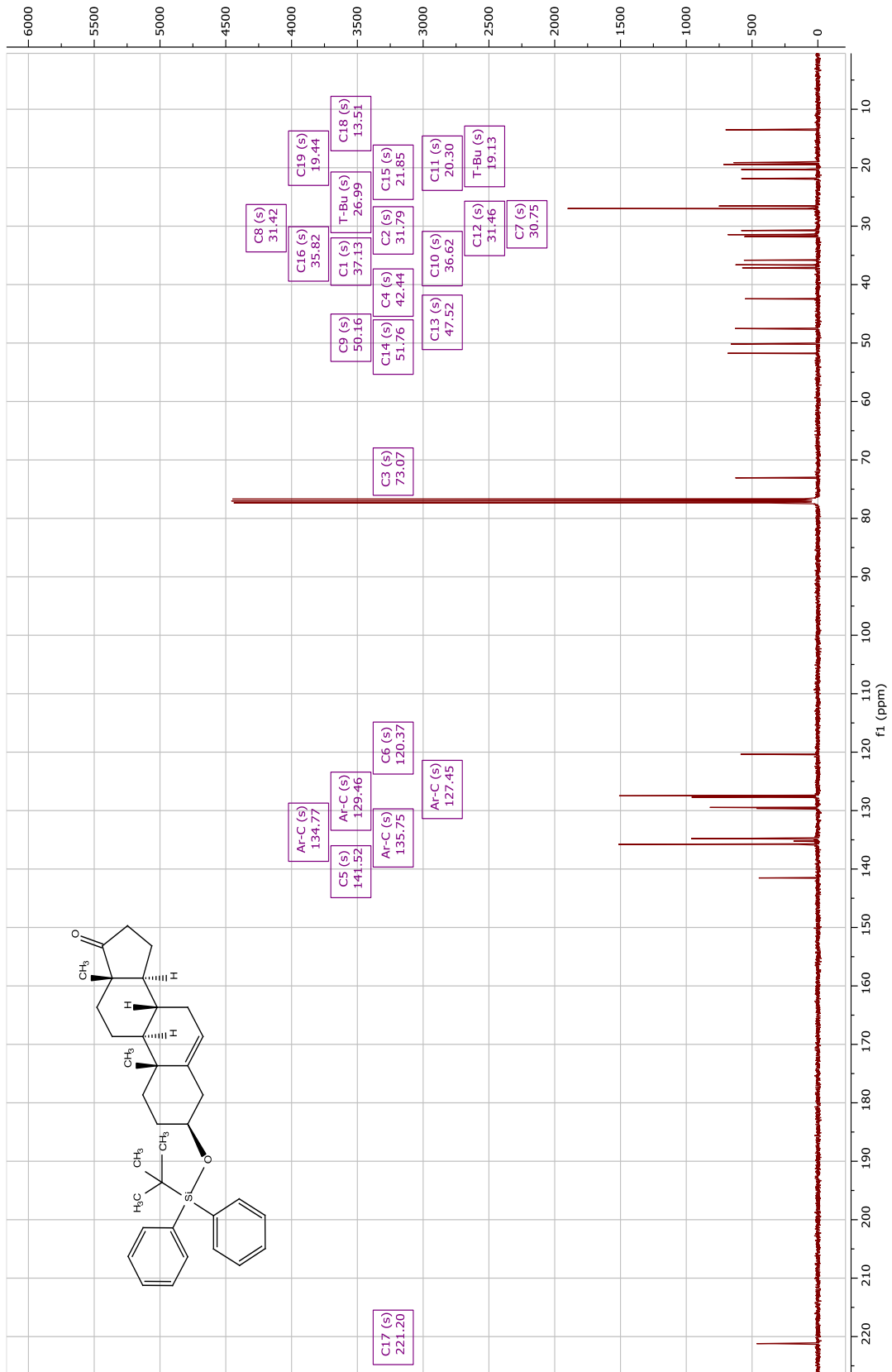
Figure S3.8 ^{1}H-^{1}H COSY Spectrum of (2)
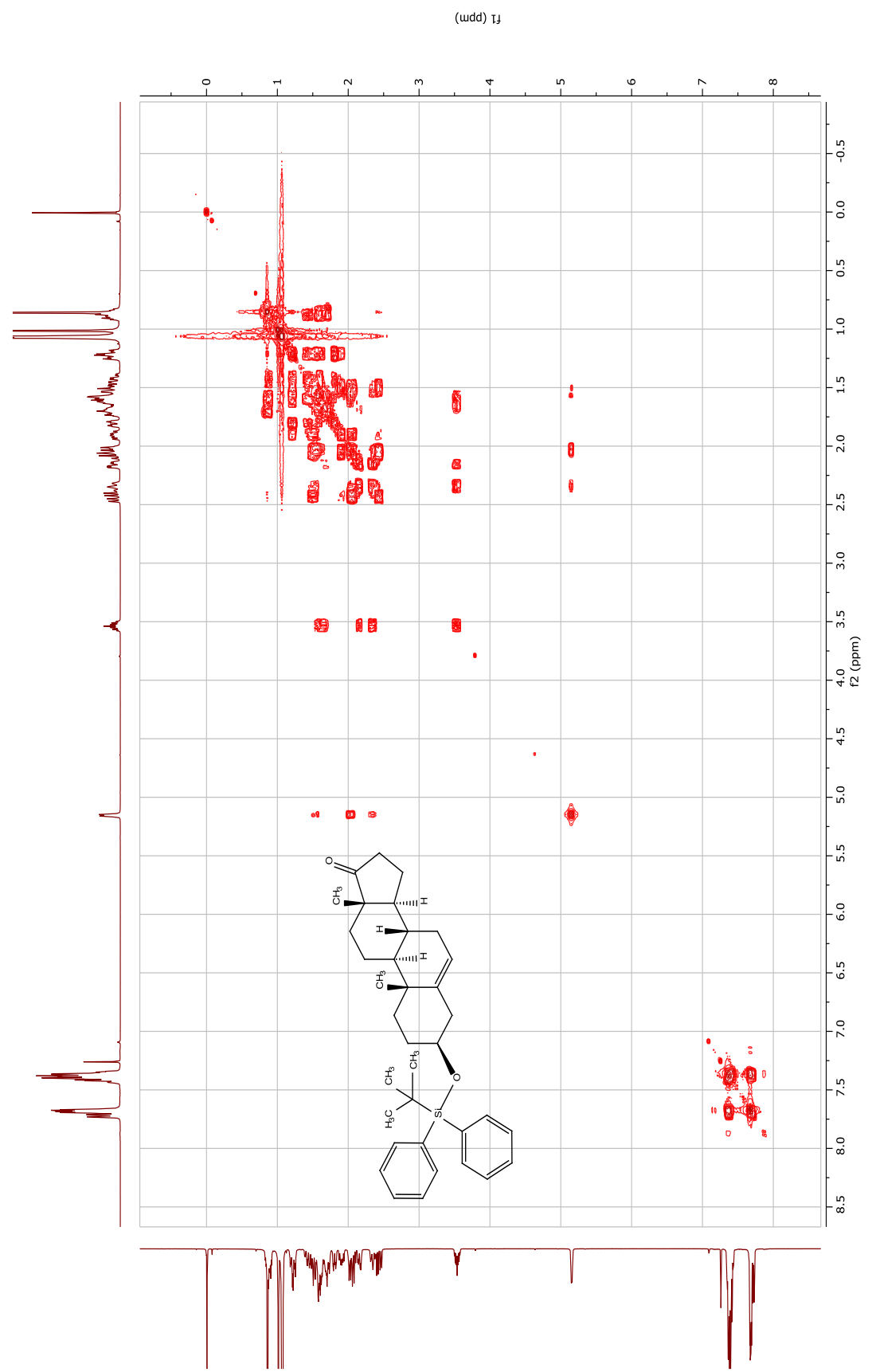
Figure S3.9 ^{1}H-^{13}C HSQC Spectrum of (2)

201
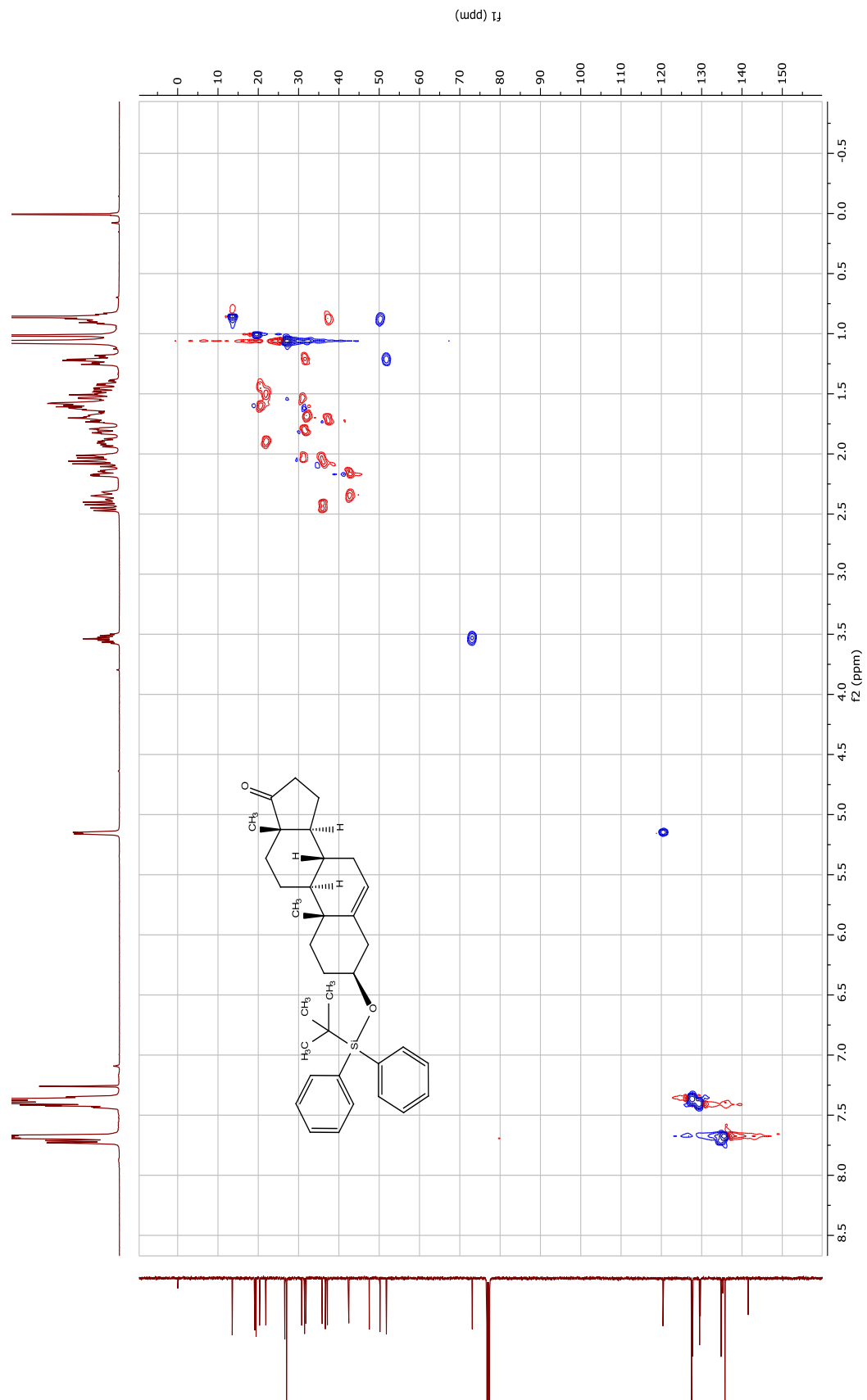
Figure S3.10 ^{1}H-^{13}C HMBC Spectrum of (2)
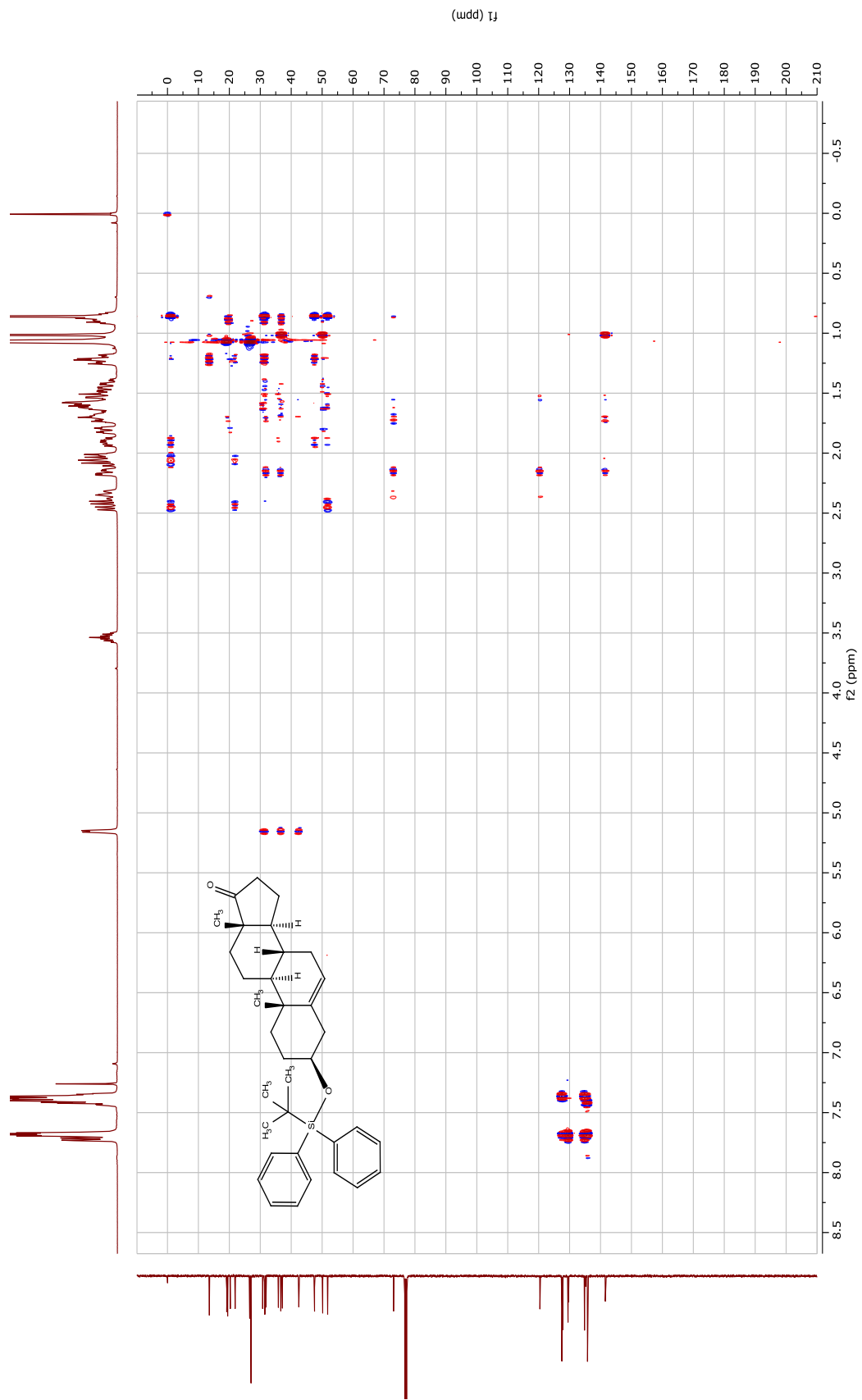
Figure S3.11 ^{1}H Spectrum of (3)
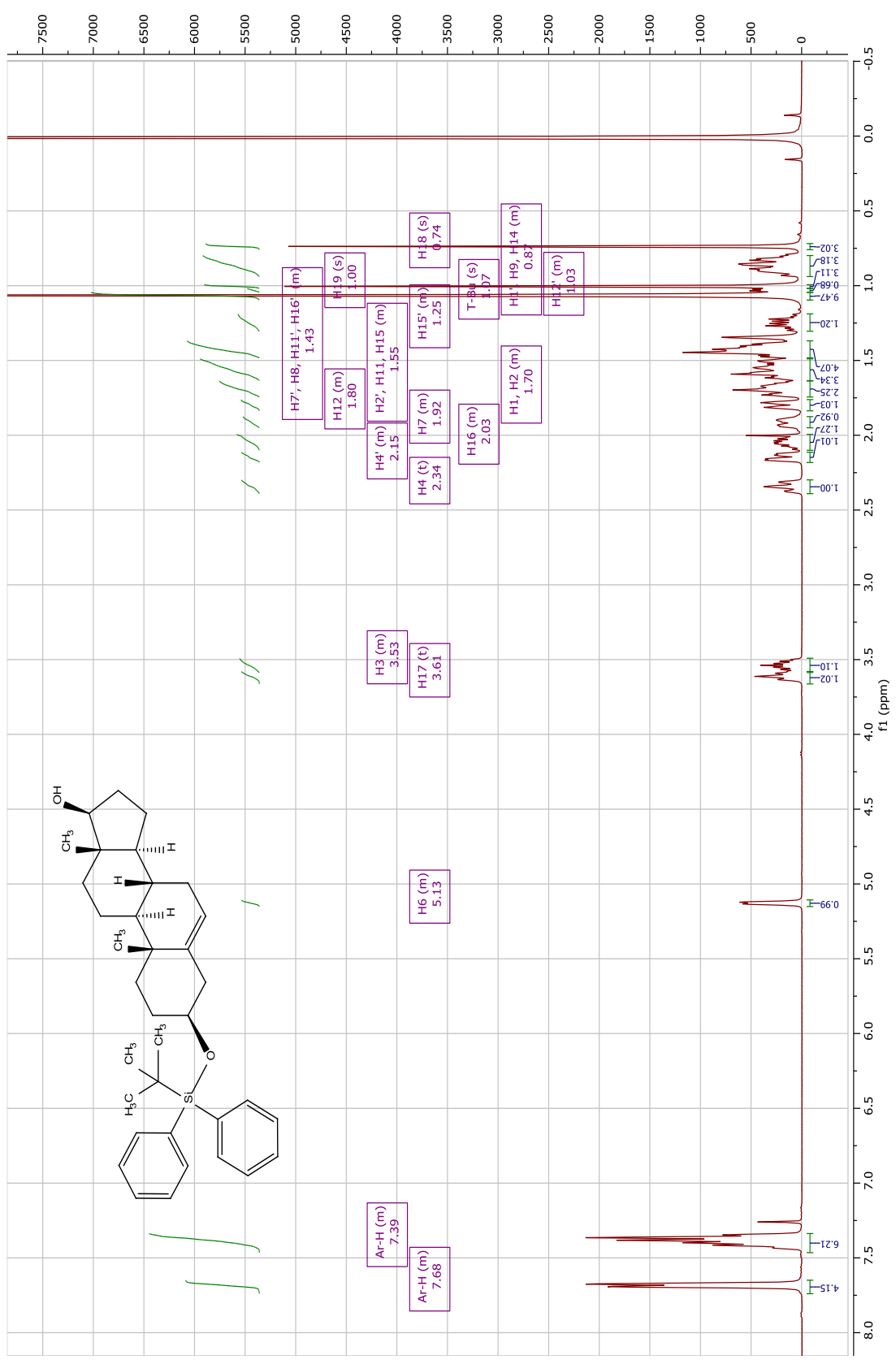
Figure S3.12 ¹³C Spectrum of (3)
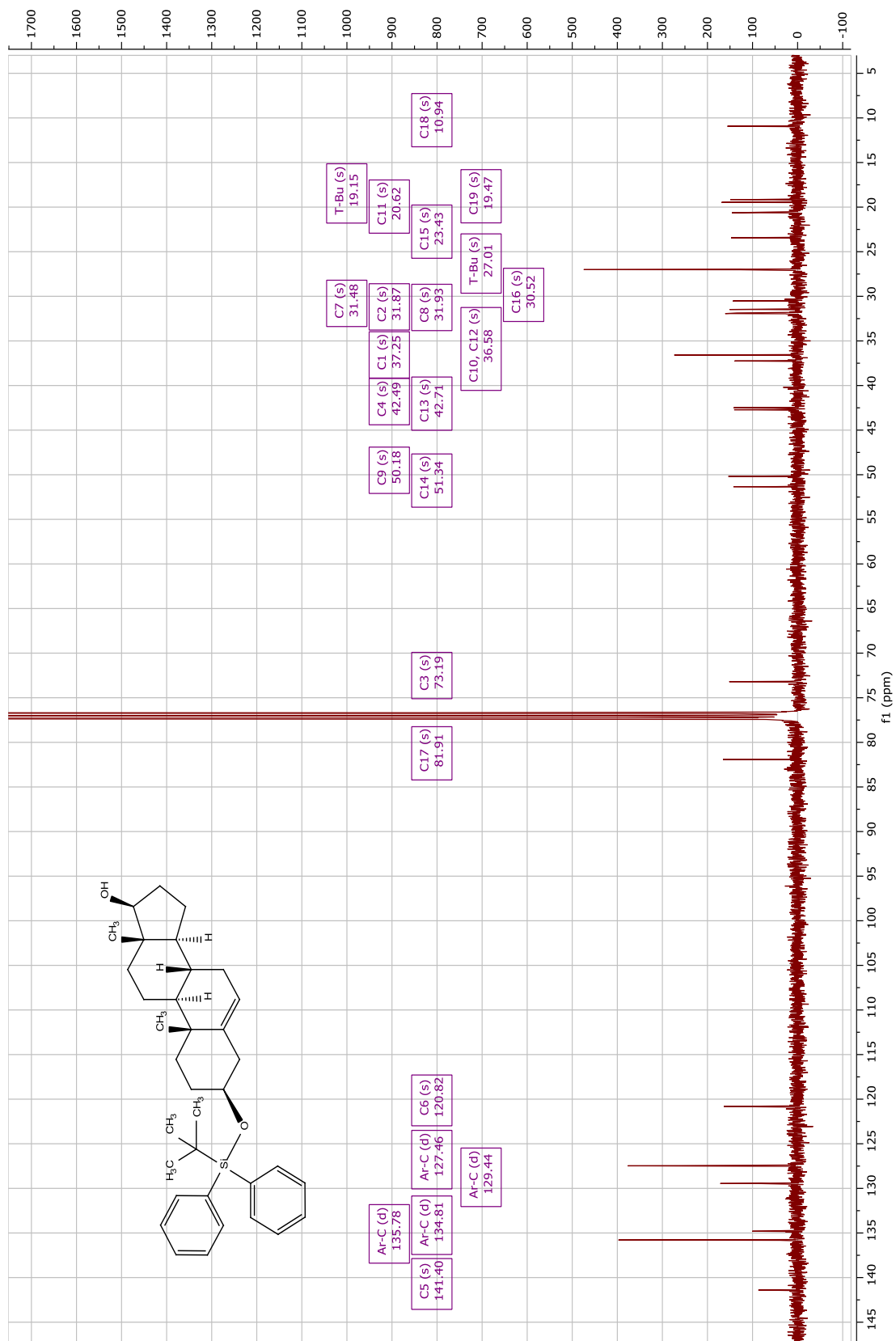
Figure S3.13 ^{1}H-^{1}H COSY Spectrum of (3)
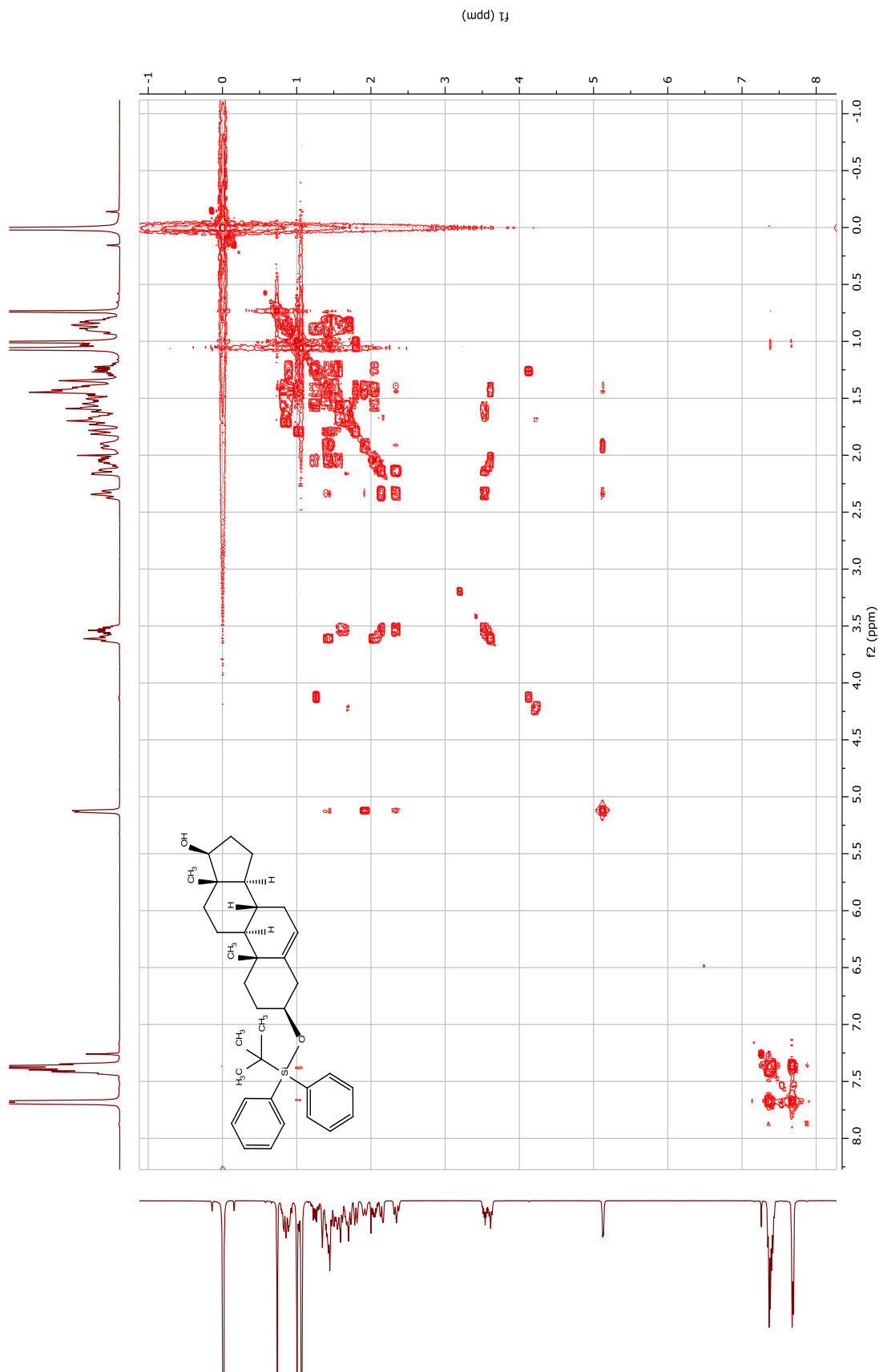
Figure S3.14 ^{1}H-^{13}C HSQC Spectrum of (3)
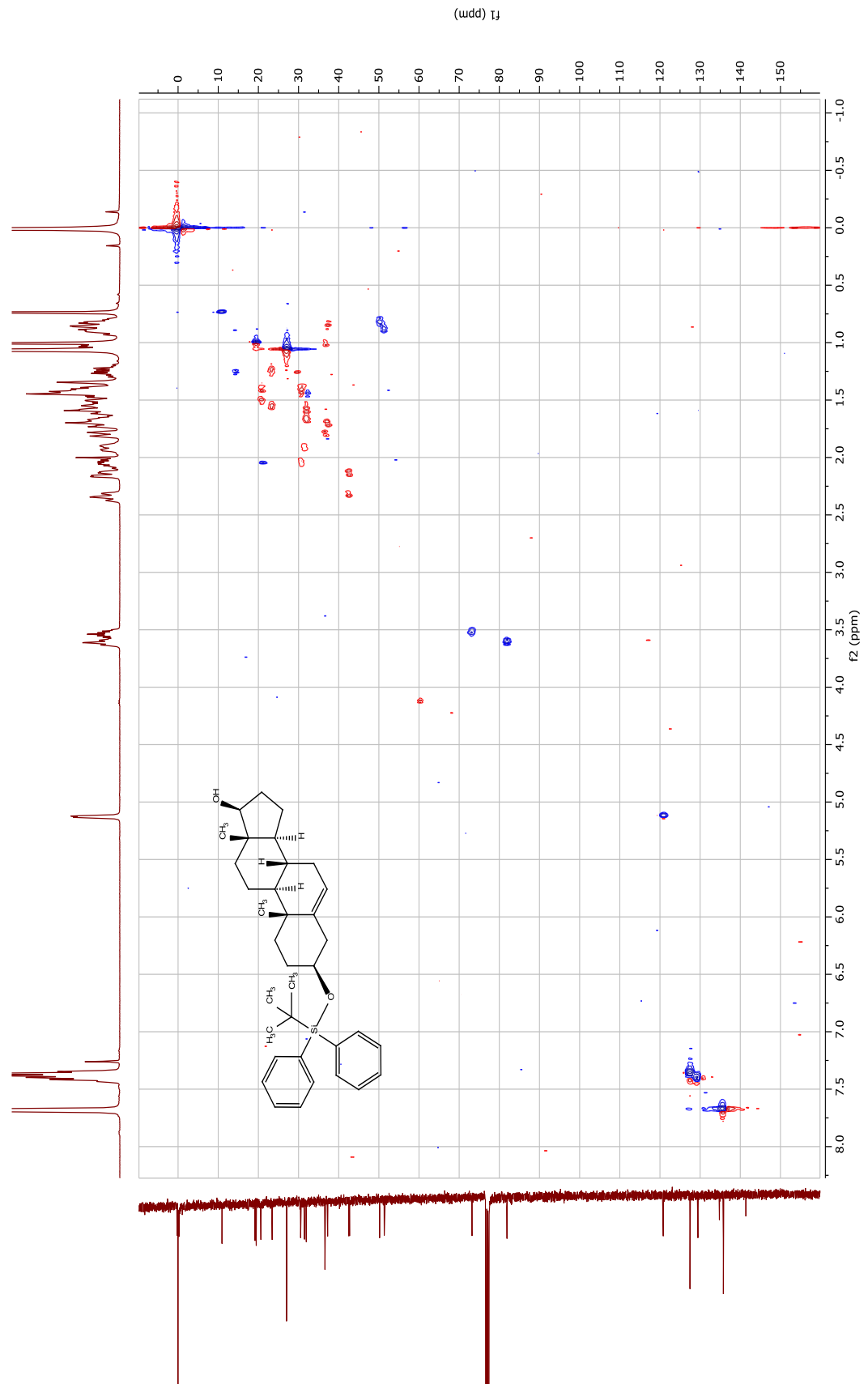
Figure S3.15 ^{1}H-^{13}C HMBC Spectrum of (3)
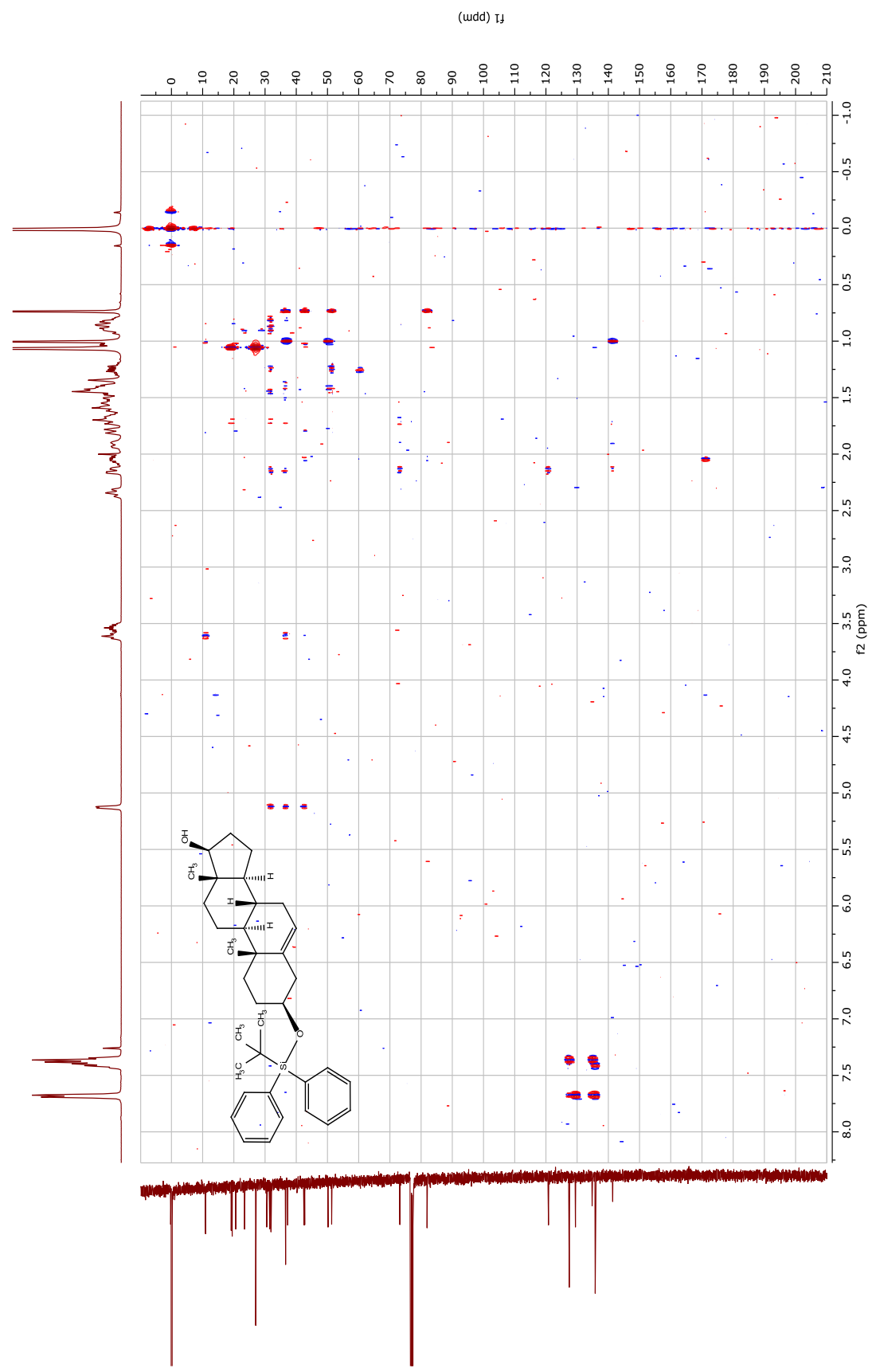
Figure S3.16 ^{1}H-^{1}H NOESY Spectrum of (3)

208
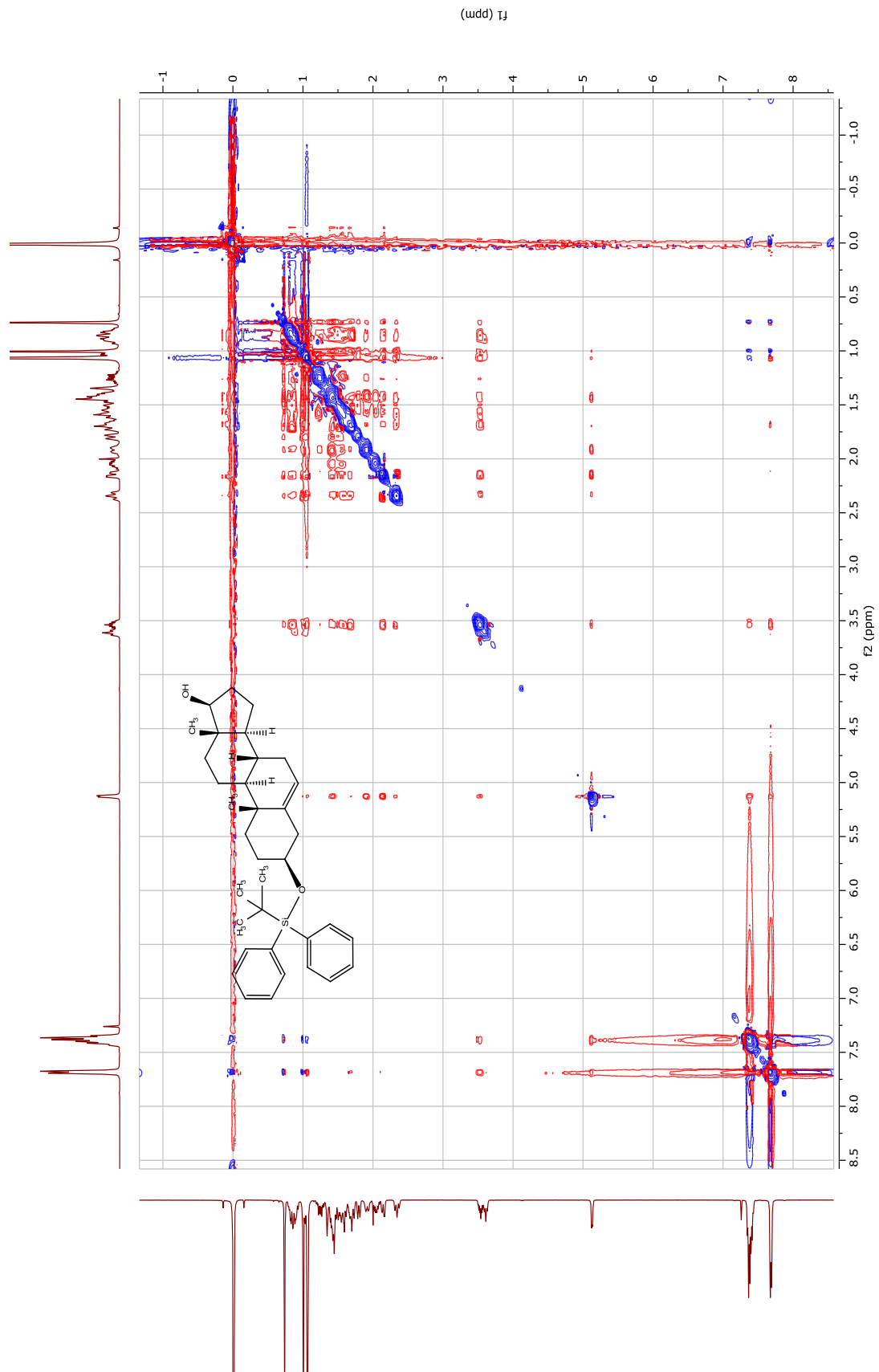
Figure S3.17 ¹H Spectrum of (4)
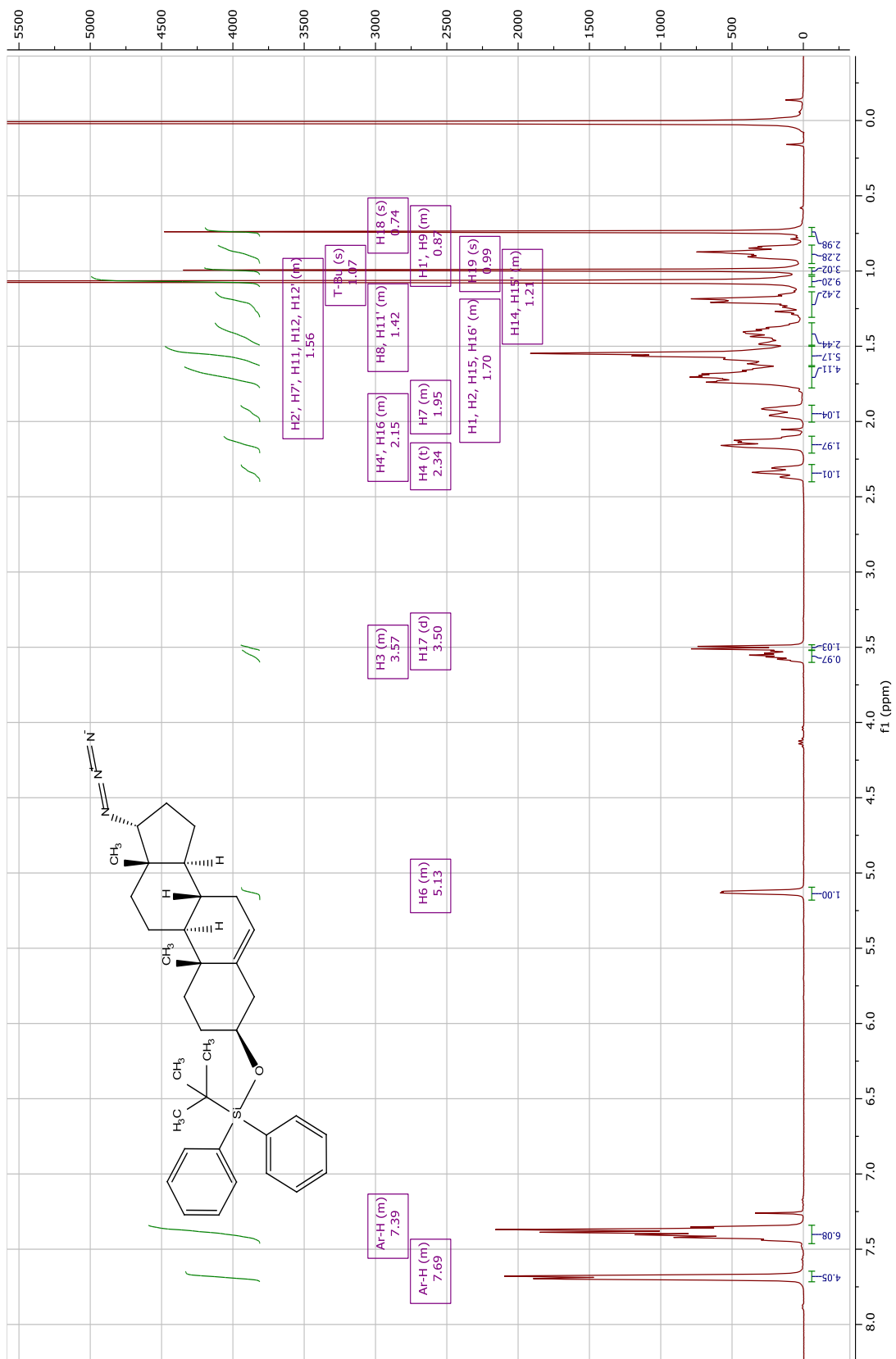
Figure S3.18 ^{13}C Spectrum of (4)
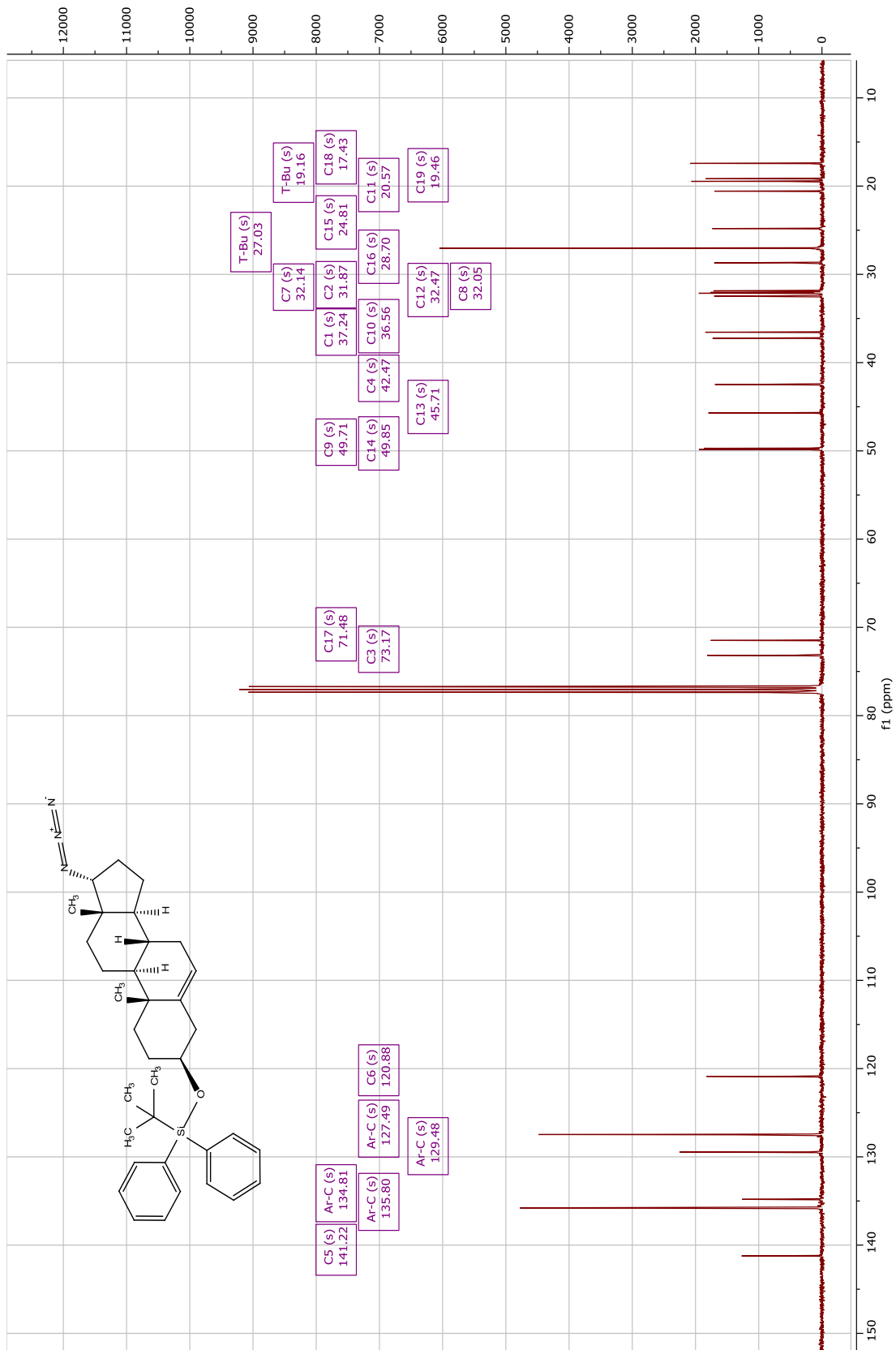
Figure S3.19 ^{1}H-^{1}H COSY Spectrum of (4)
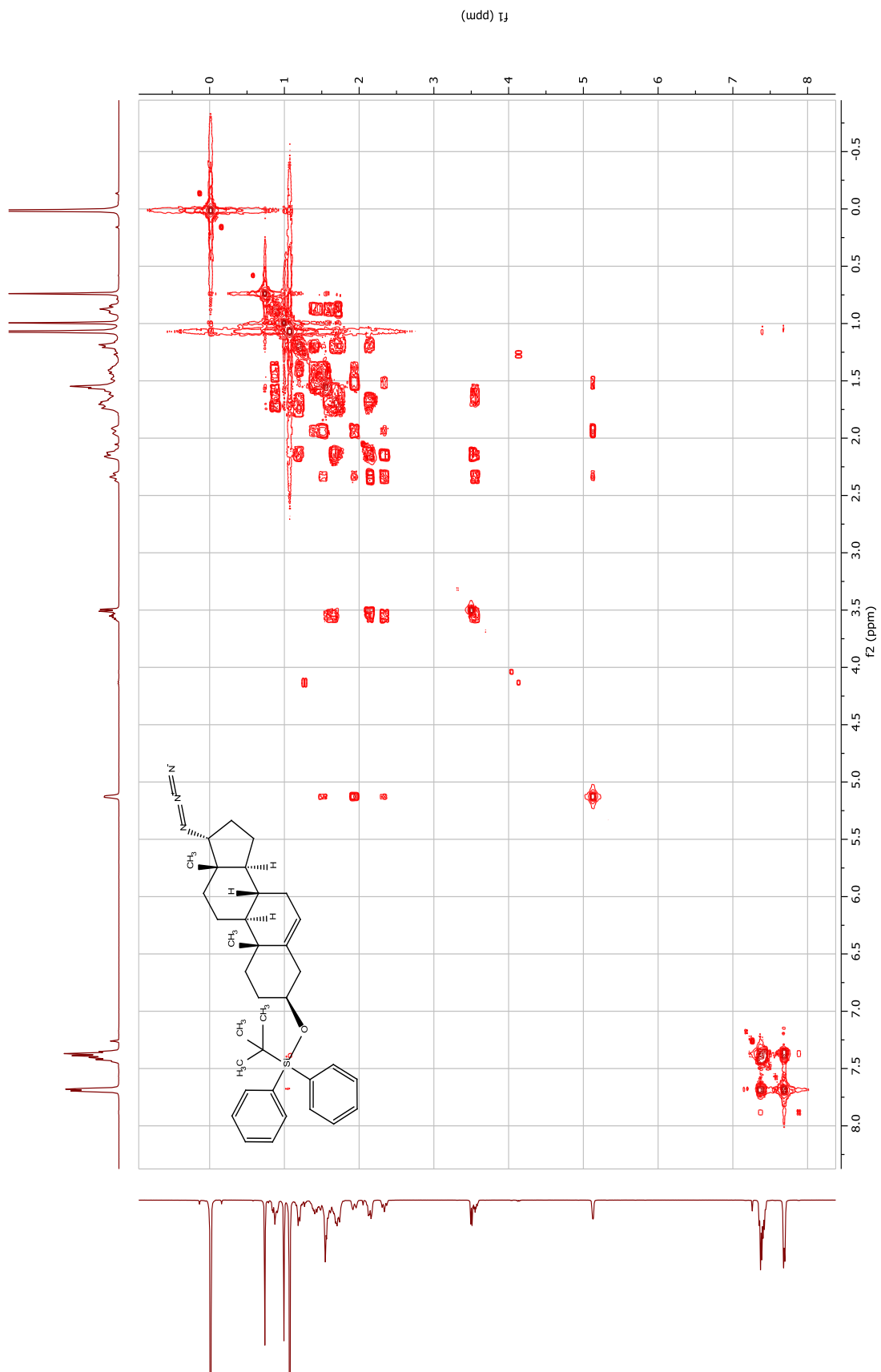
Figure S3.20 ^{1}H-^{13}C HSQC Spectrum of (4)
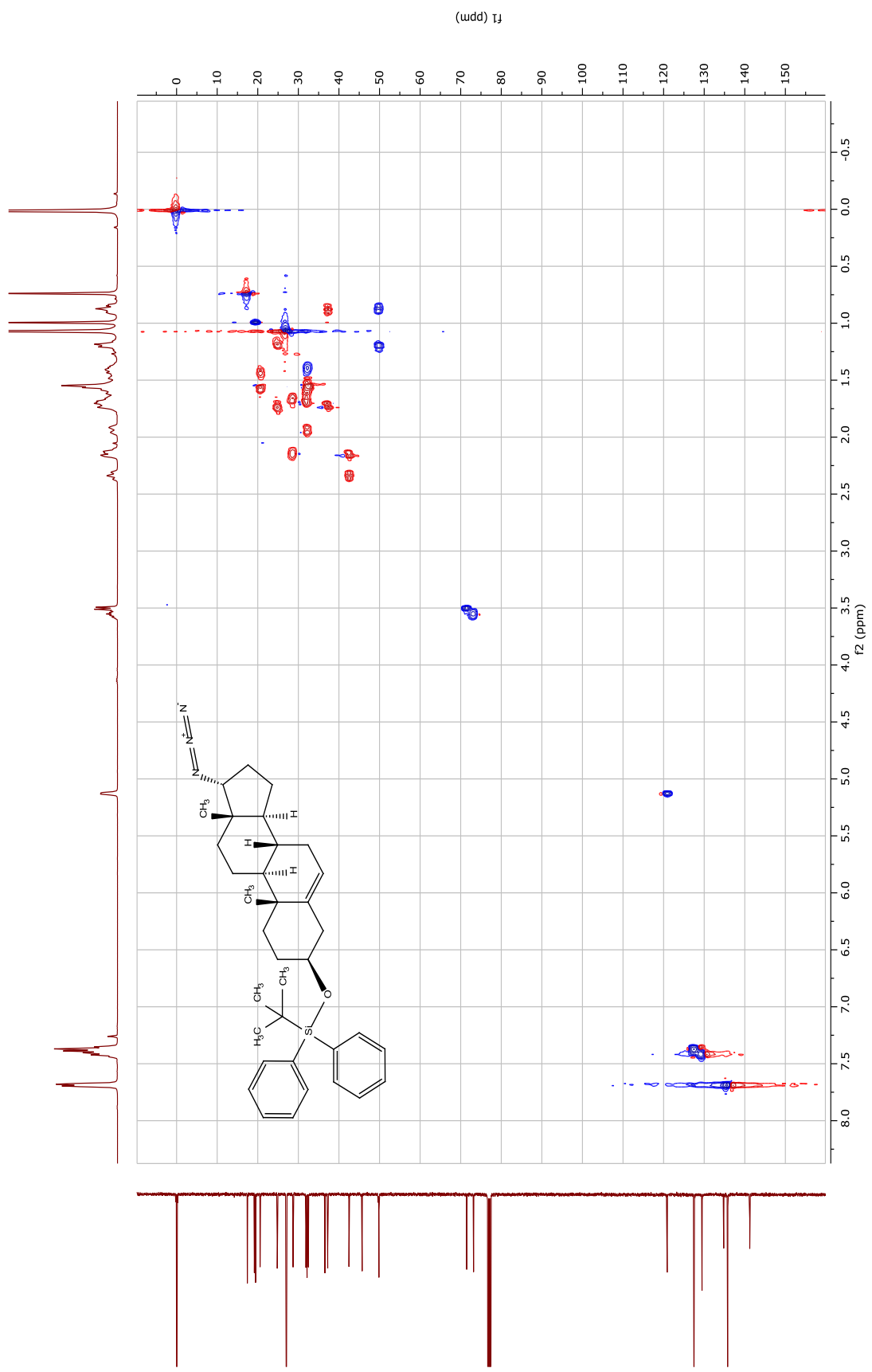
Figure S3.21 ^{1}H-^{13}C HMBC Spectrum of (4)

213
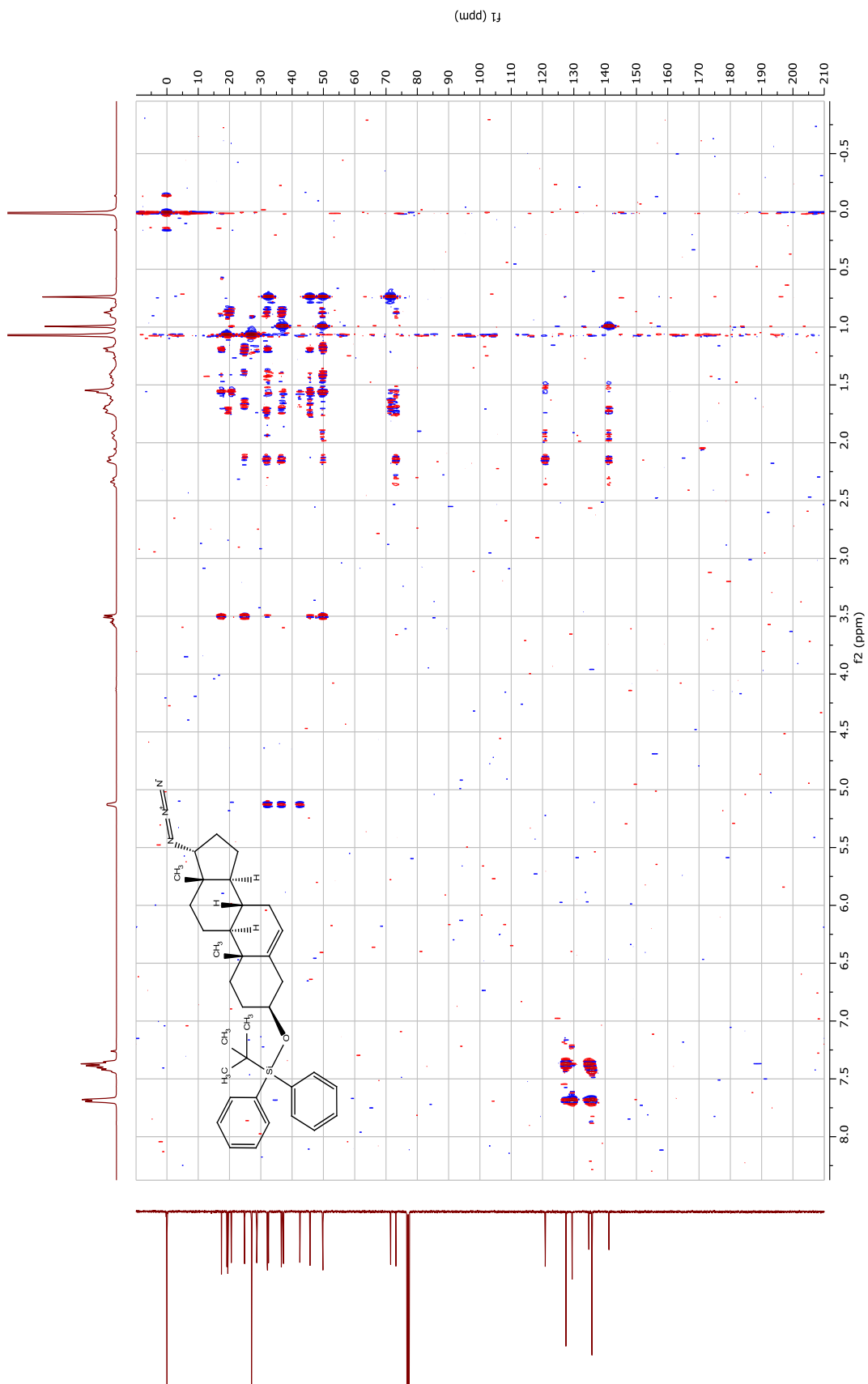
Figure S3.22 ¹H-¹H NOESY Spectrum of (4)

Figure S3.23 ¹H Spectrum of (5)
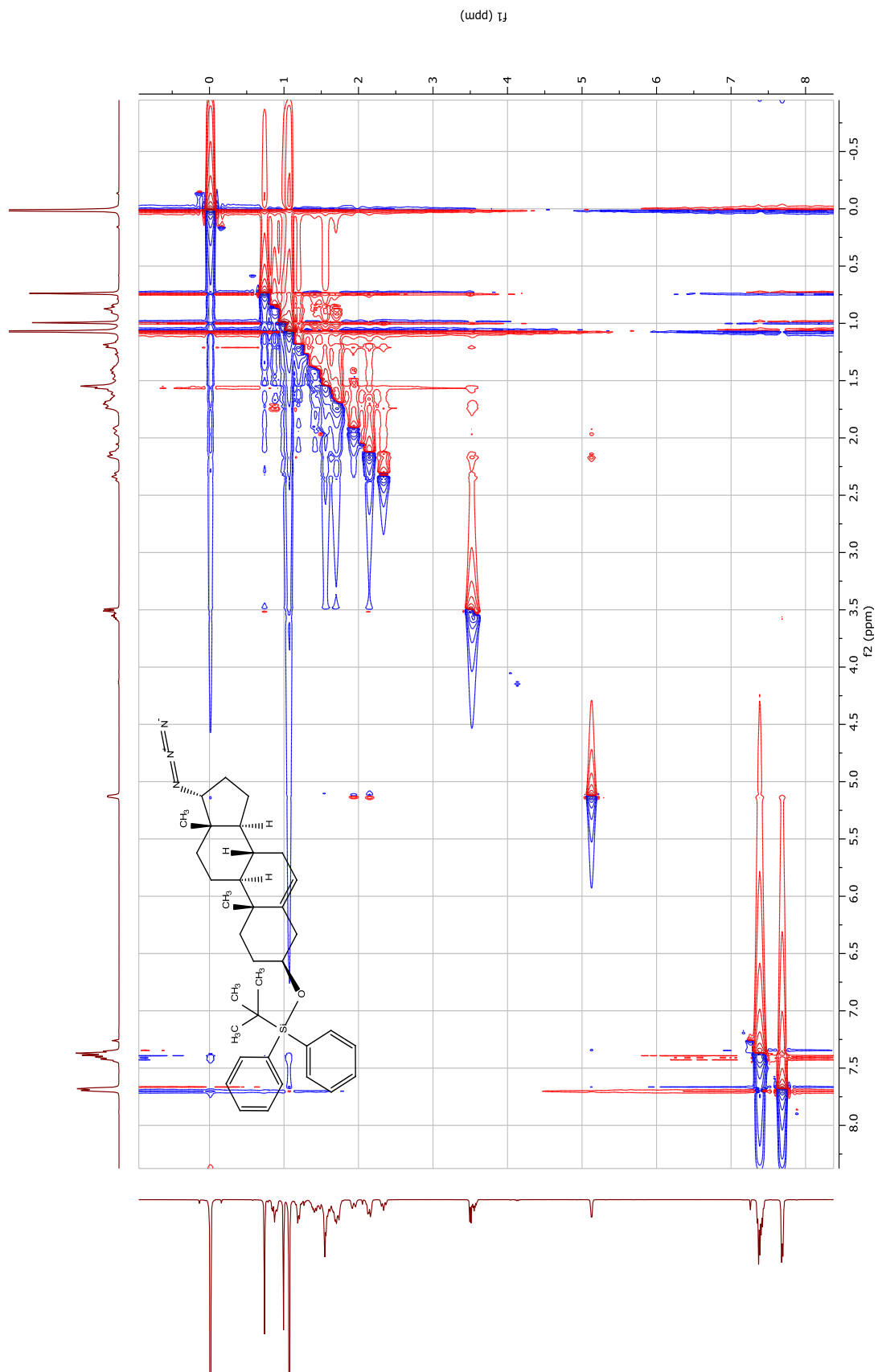
Figure S3.24 ^{13}C Spectrum of (5)
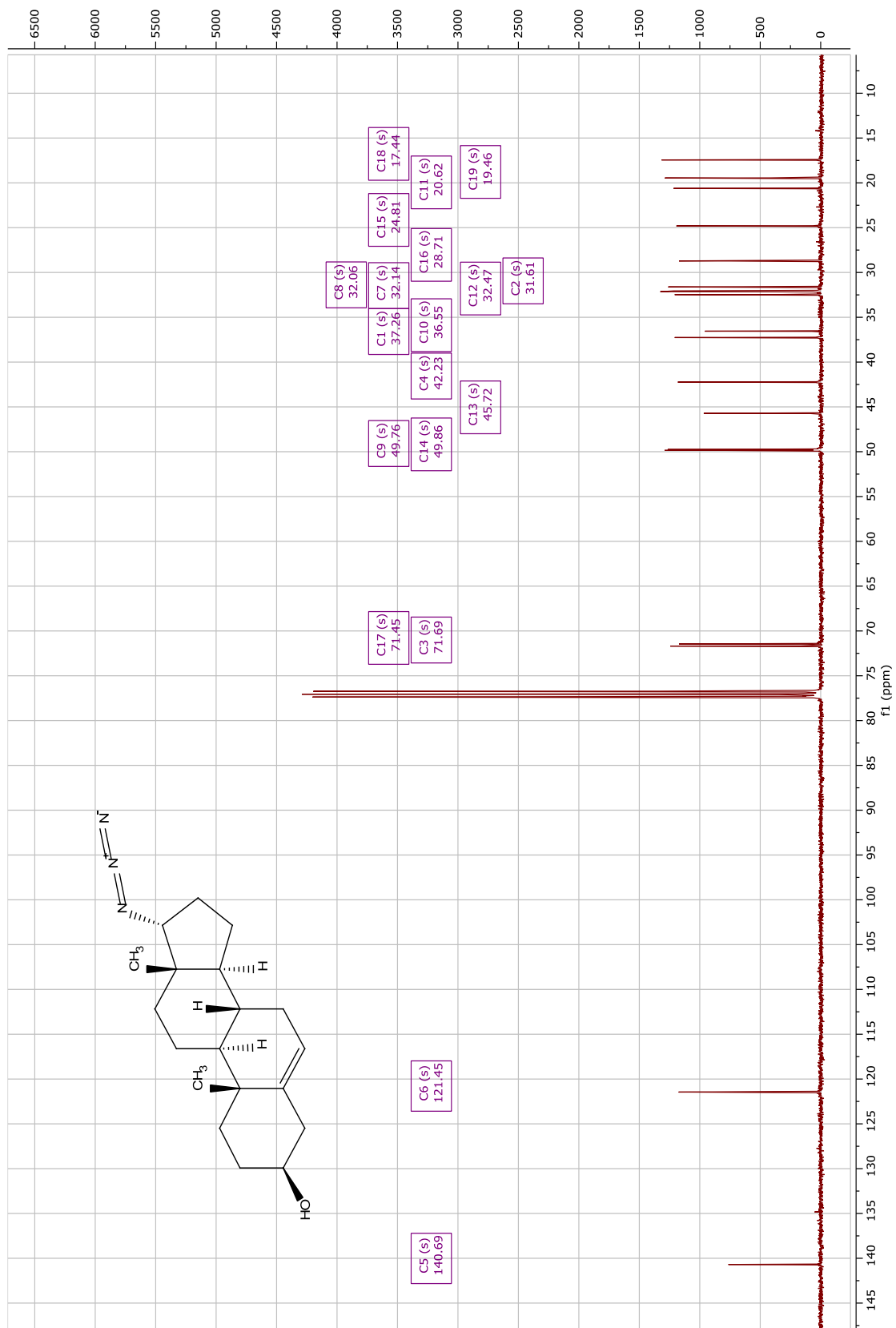
Figure S3.25 ^{1}H-^{1}H COSY Spectrum of (5)

217

Figure S3.26 ^{1}H-^{13}C HSQC Spectrum of (5)
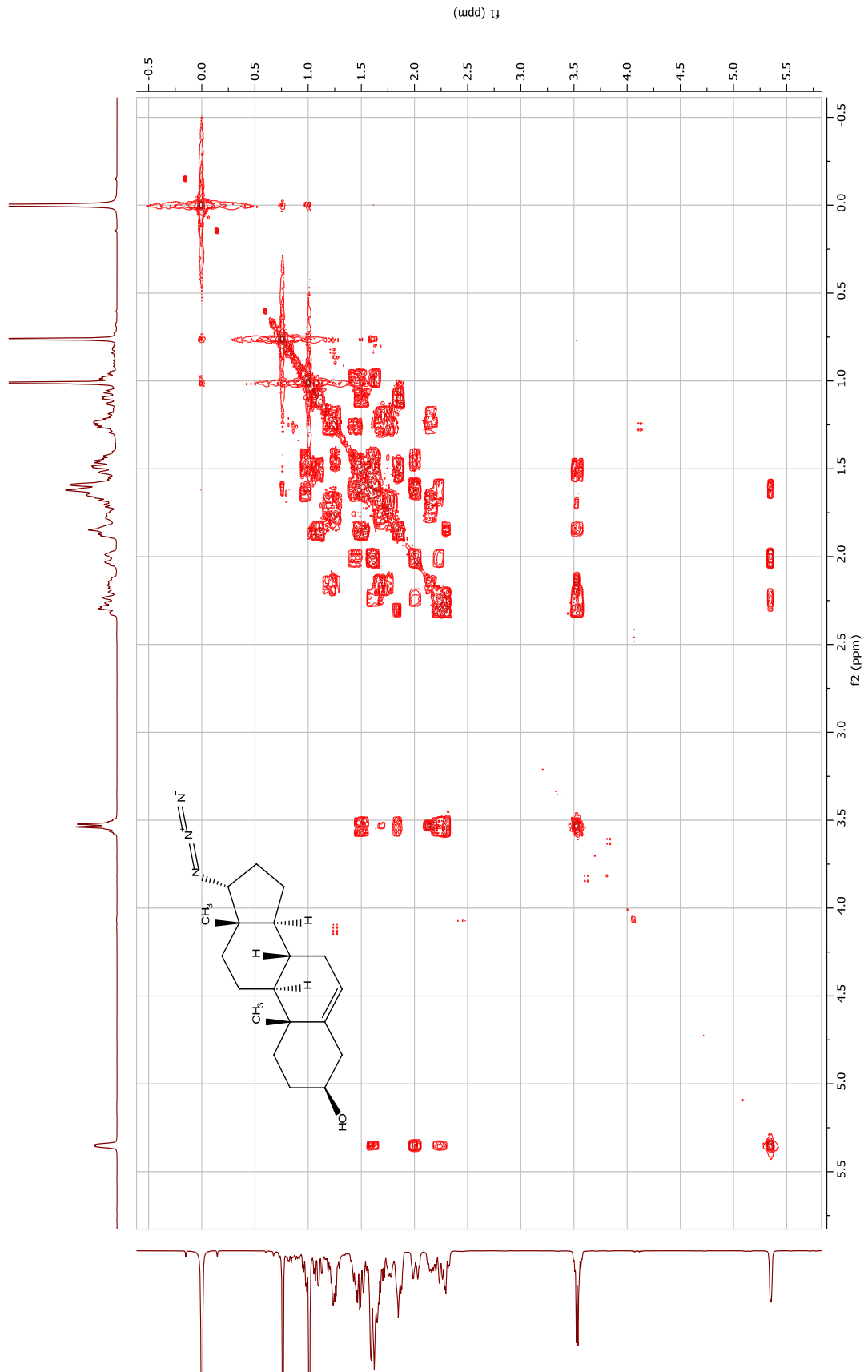
Figure S3.27 ^{1}H-^{13}C HMBC Spectrum of (5)

219
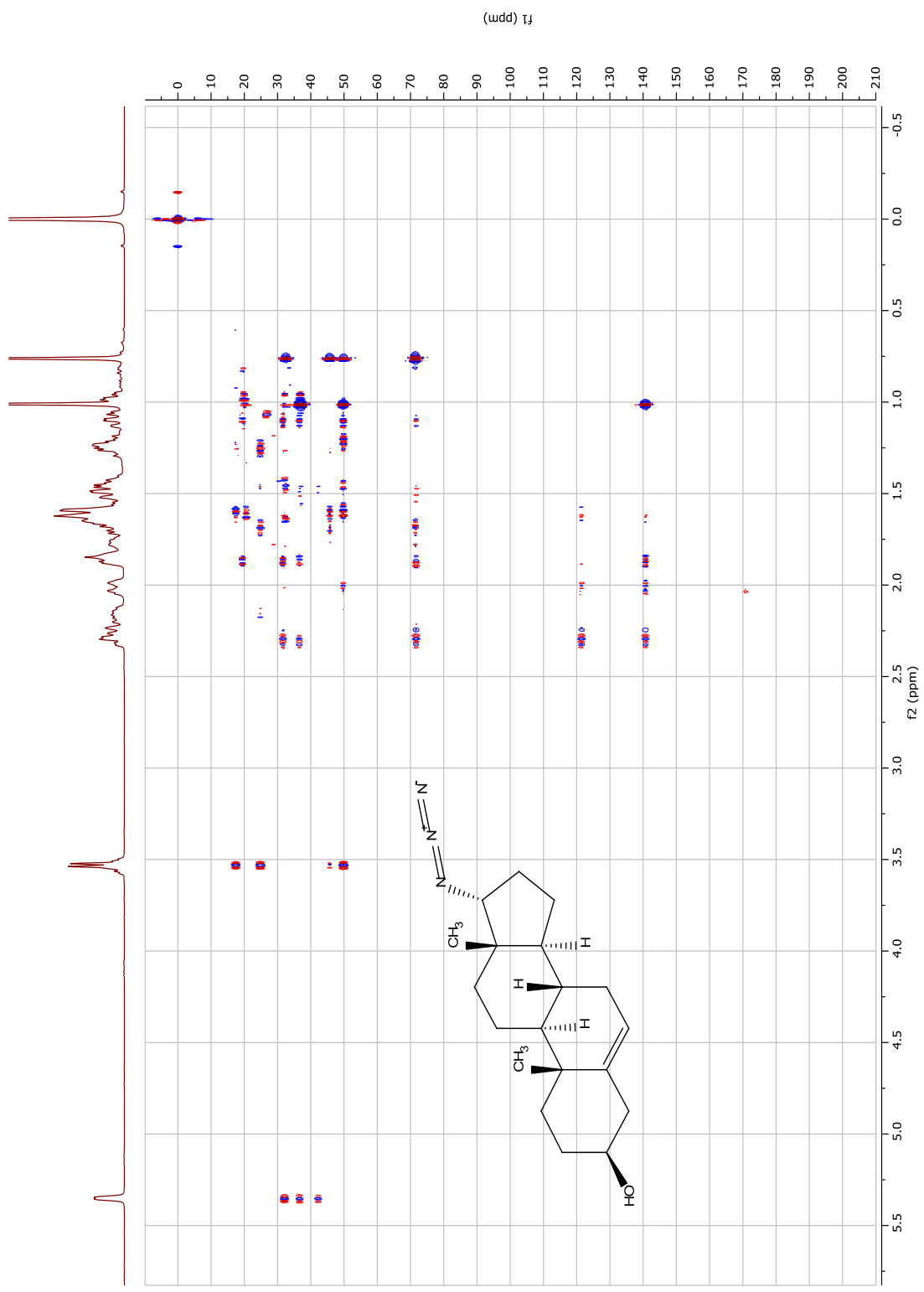
Figure S3.28 ^{1}H-^{1}H NOESY Spectrum of (5)

220
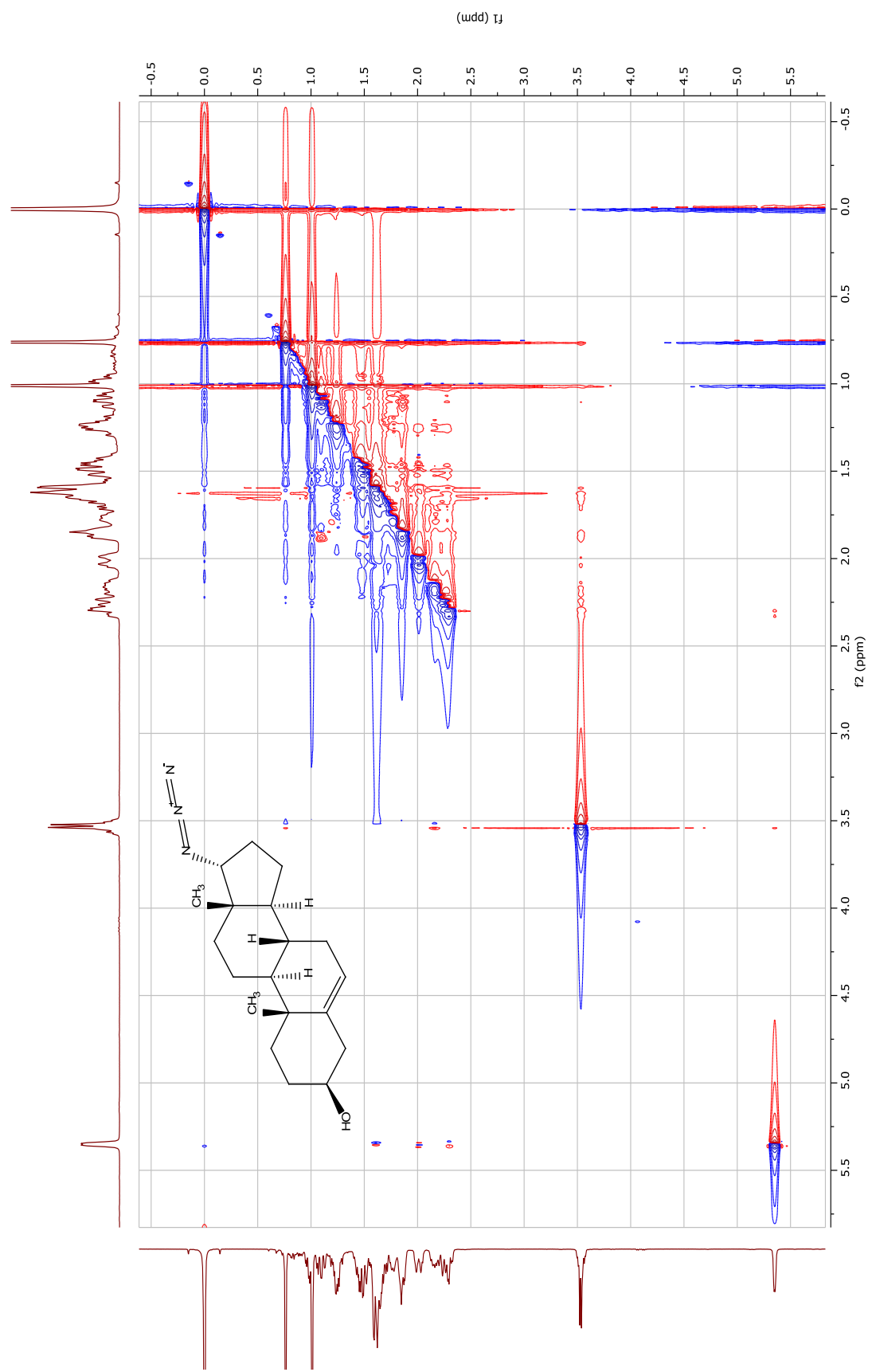
Figure S3.29 ^{1}H Spectrum of (6)
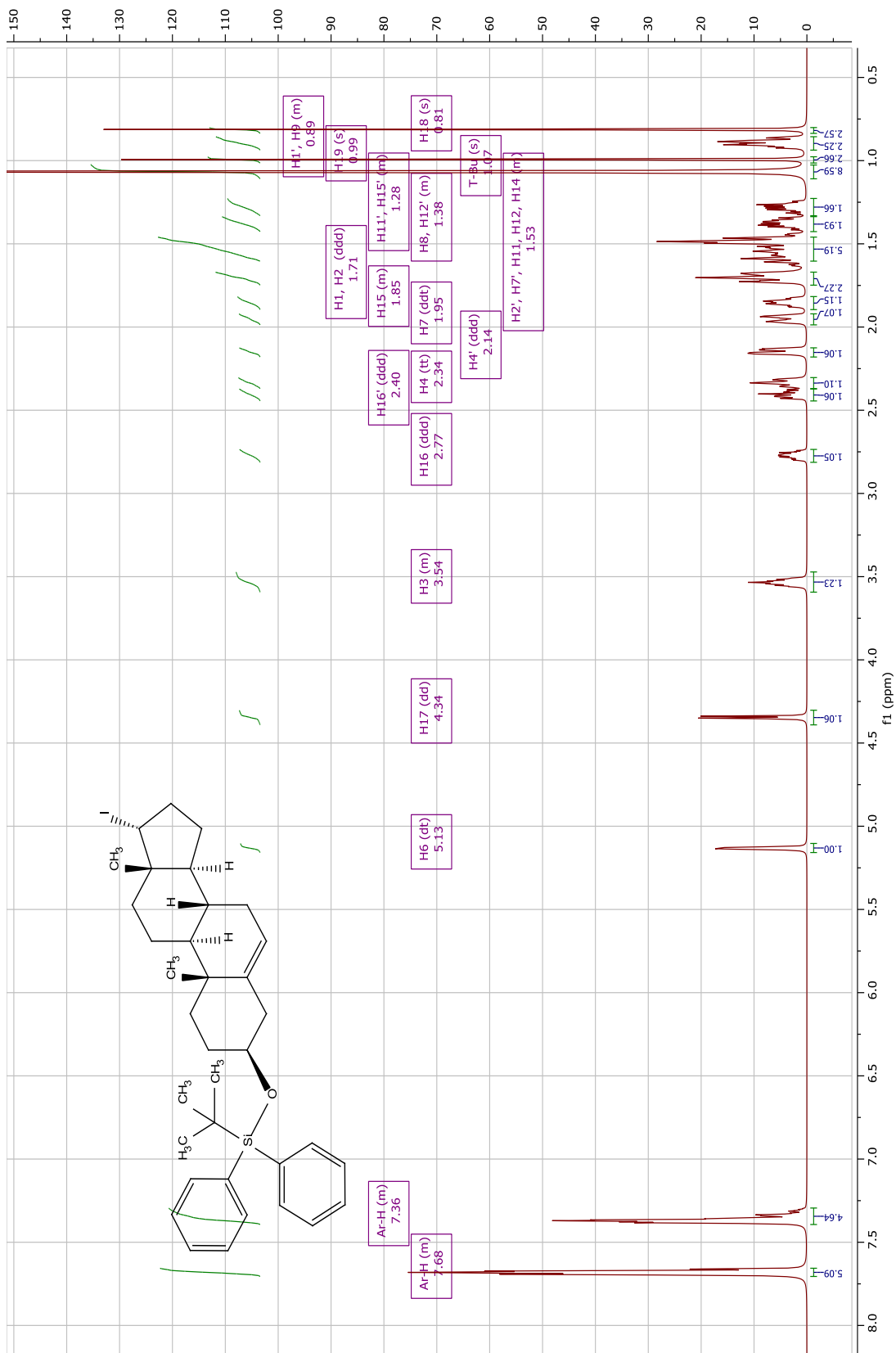
Figure S3.30 ^{13}C Spectrum of (6)
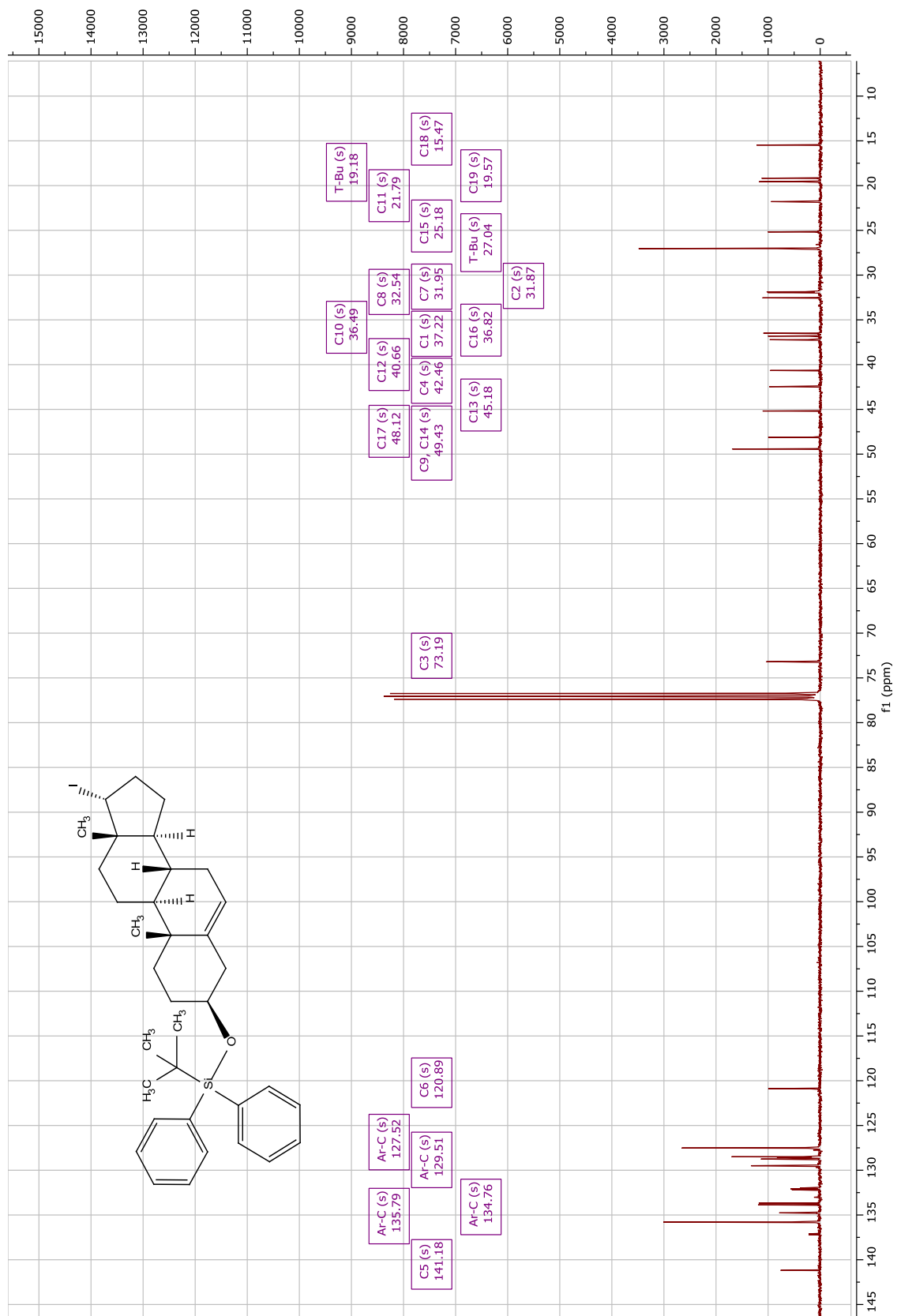
Figure S3.31 DEPT-135 Spectrum of (6)
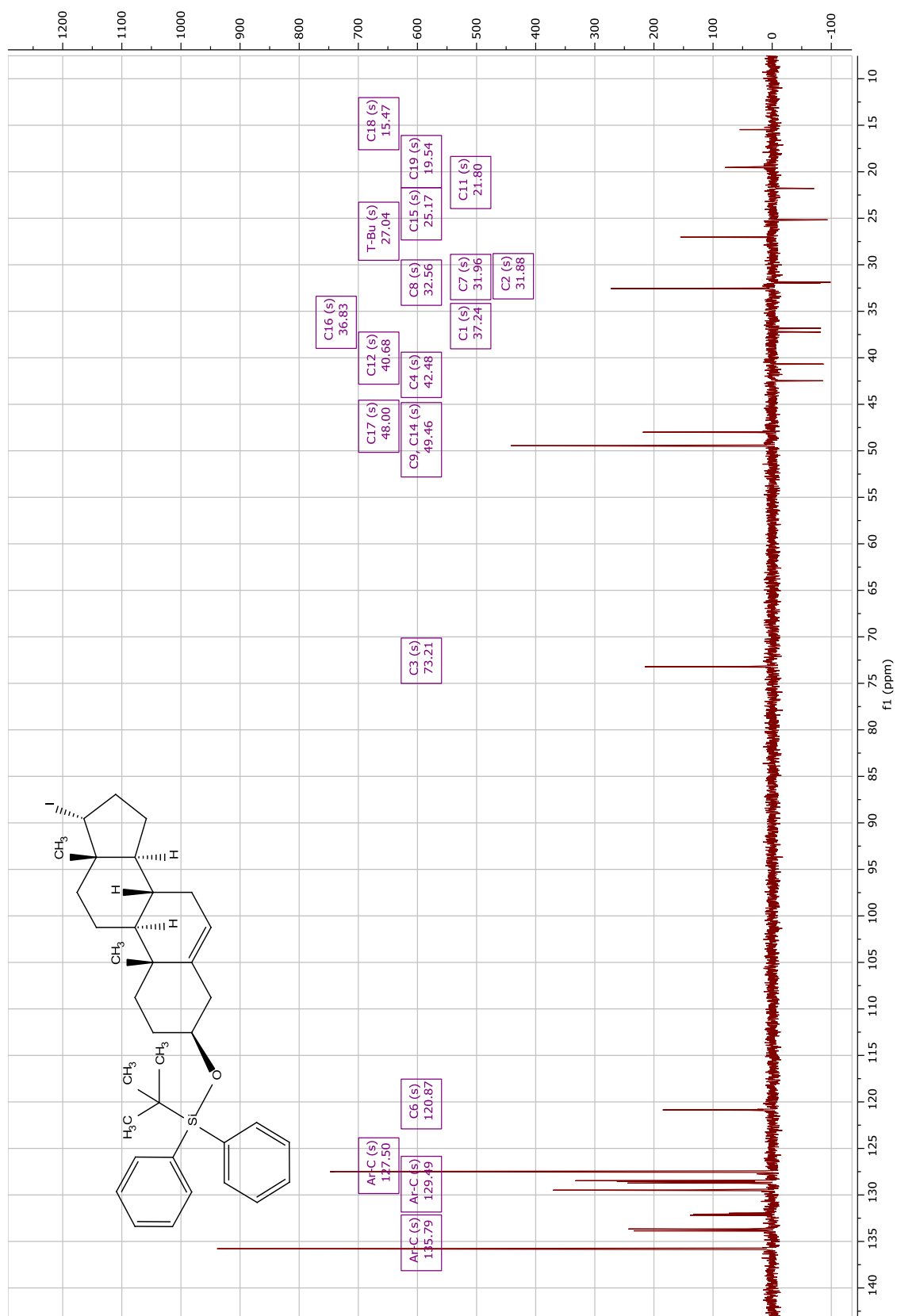
Figure S3.32 ^{1}H-^{1}H COSY Spectrum of (6)

224
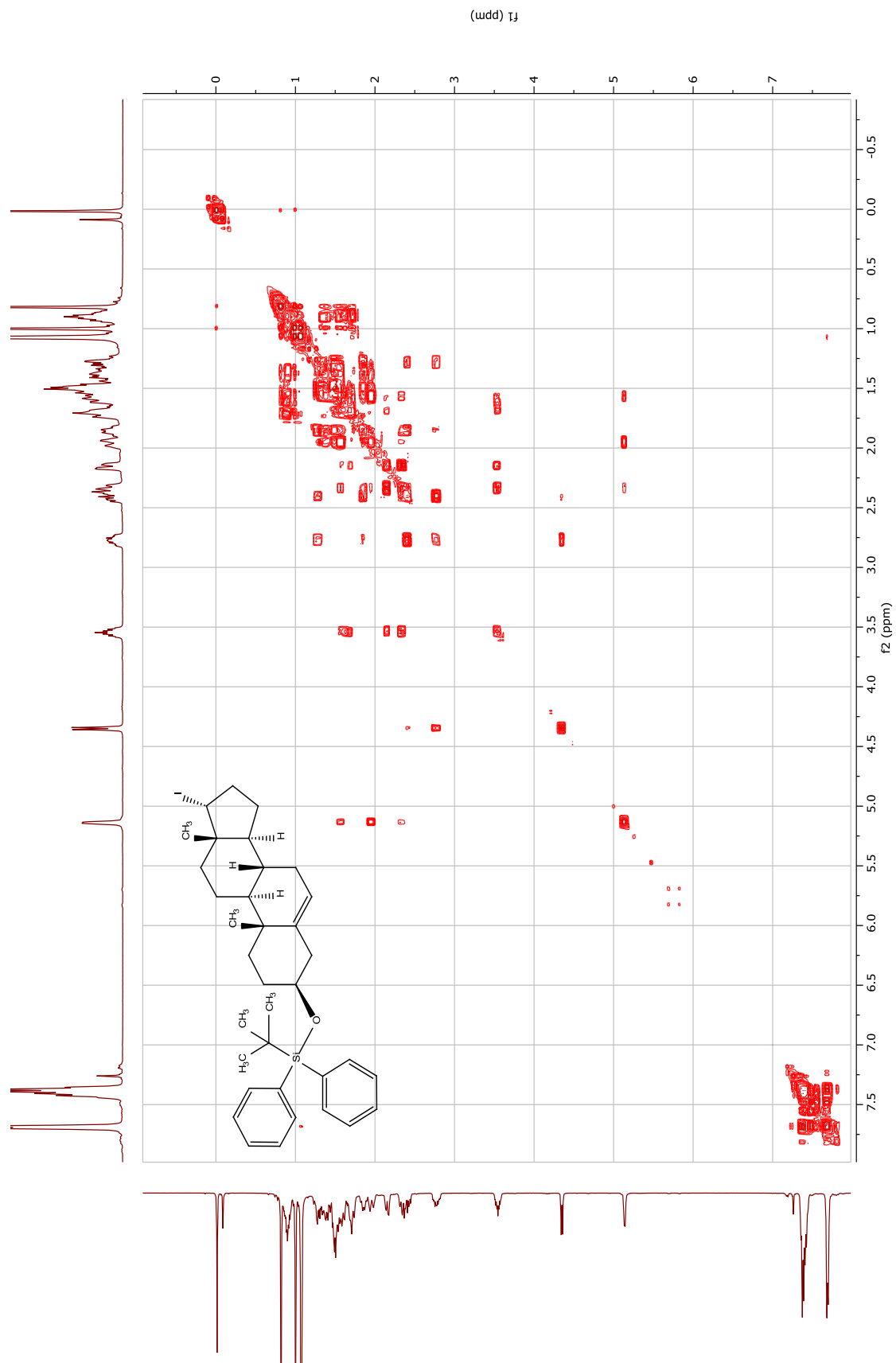
Figure S3.33 ^{1}H-^{13}C HSQC Spectrum of (6)

225
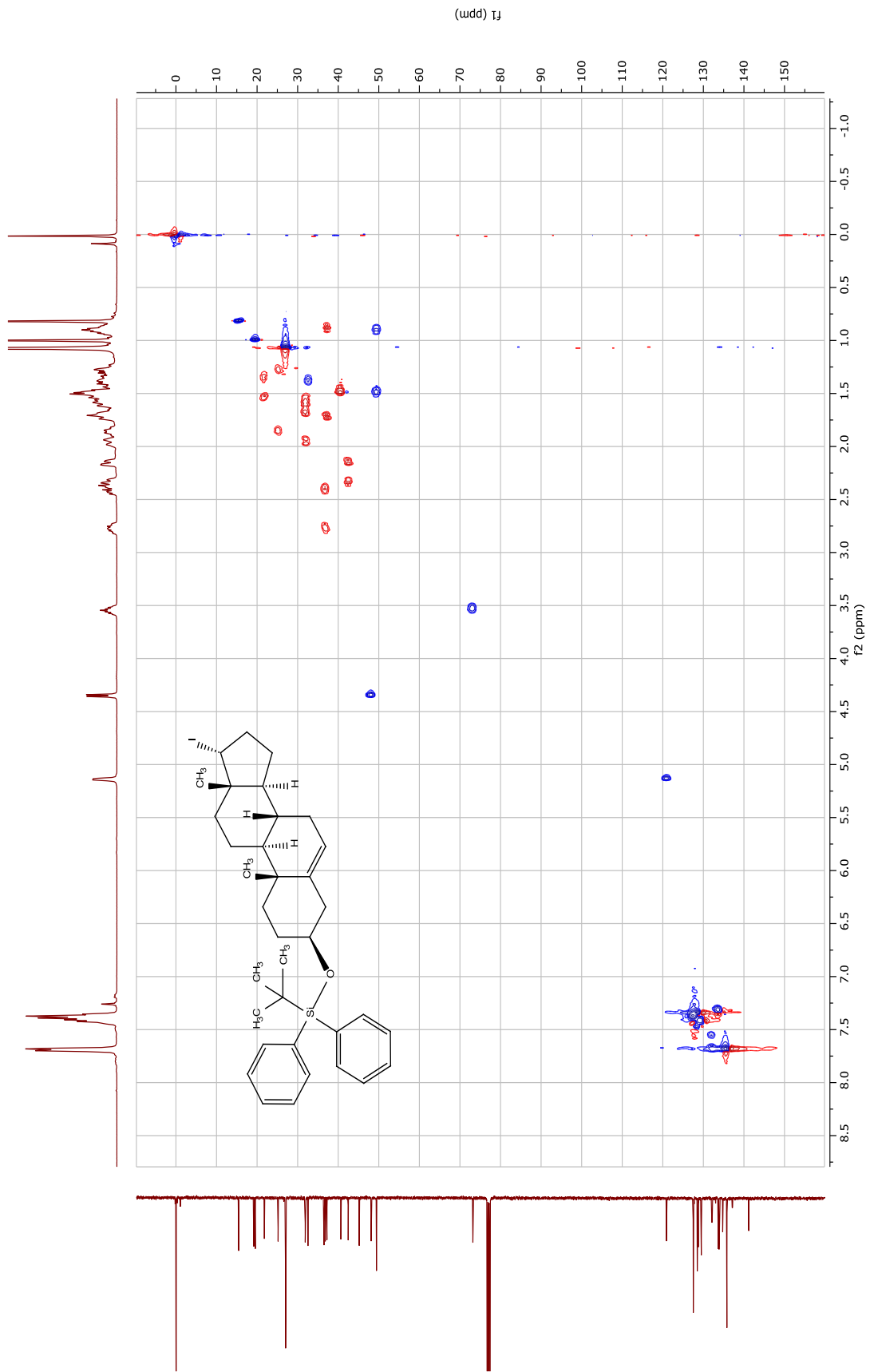
Figure S3.34 ^{1}H-^{13}C HMBC Spectrum of (6)

226
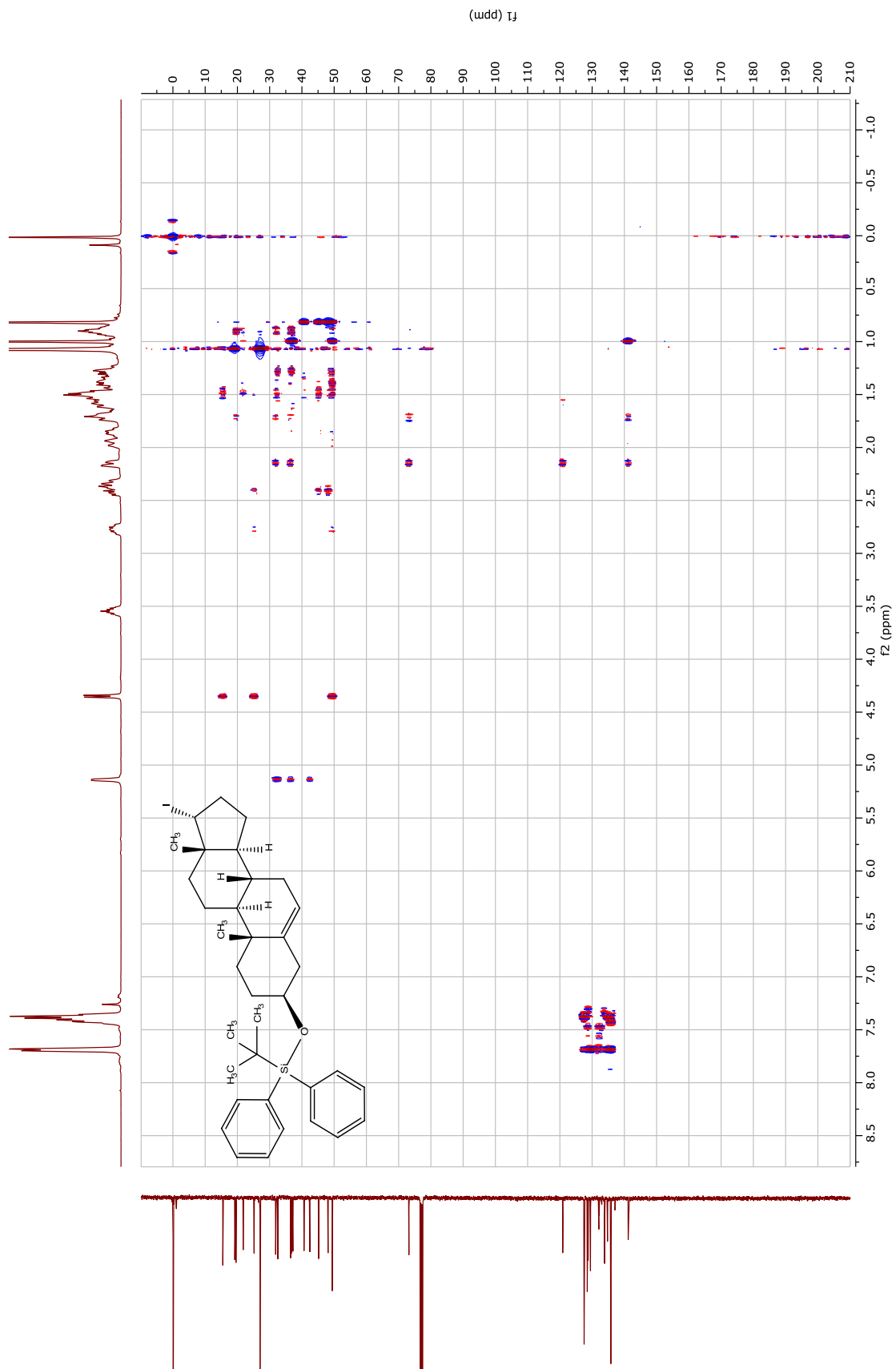
Figure S3.35 ^{1}H-^{1}H NOESY Spectrum of (6)

227
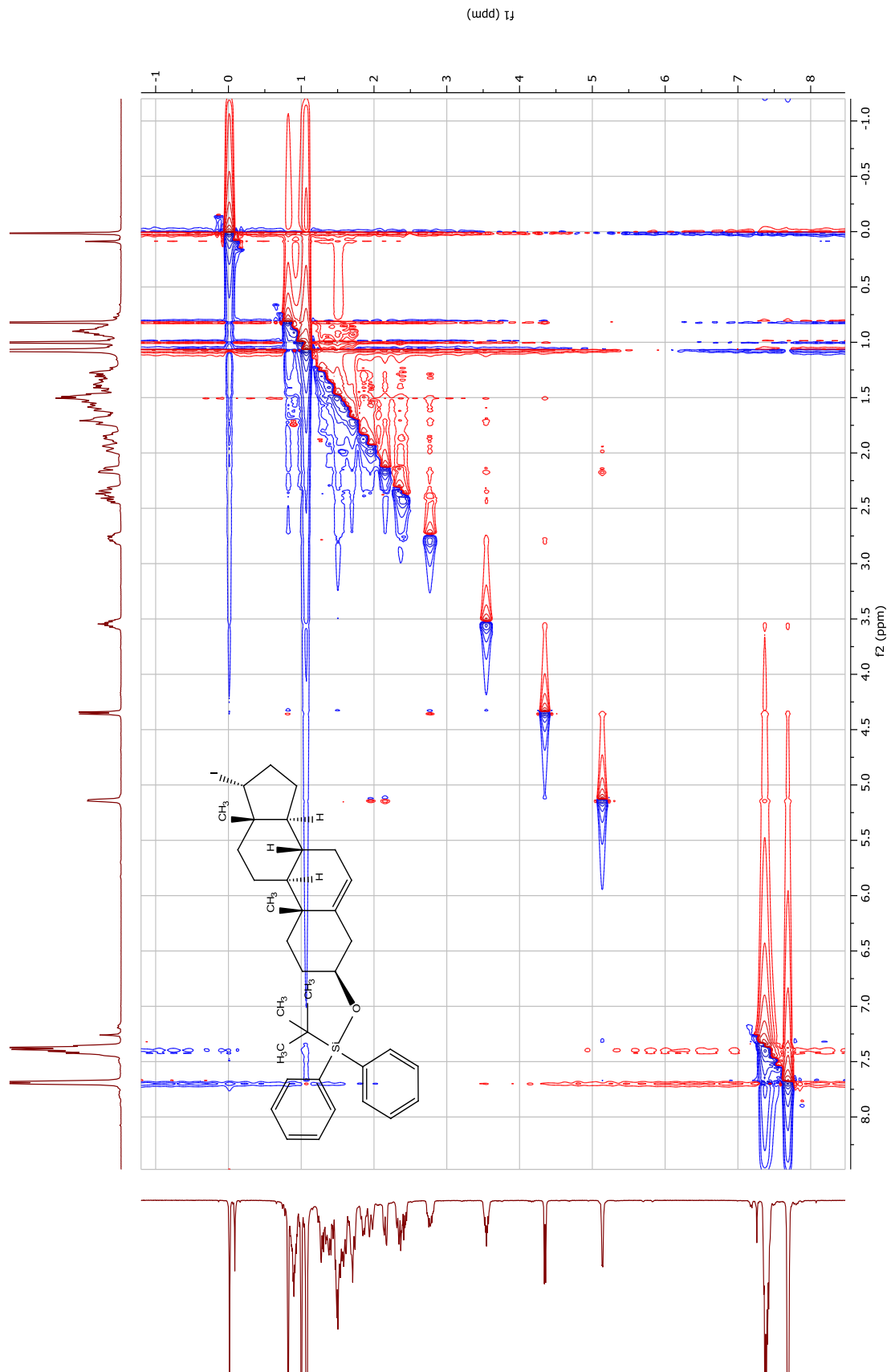
Figure S3.36 ^{1}H Spectrum of (7)

228

Figure S3.37 ^{13}C Spectrum of (7)
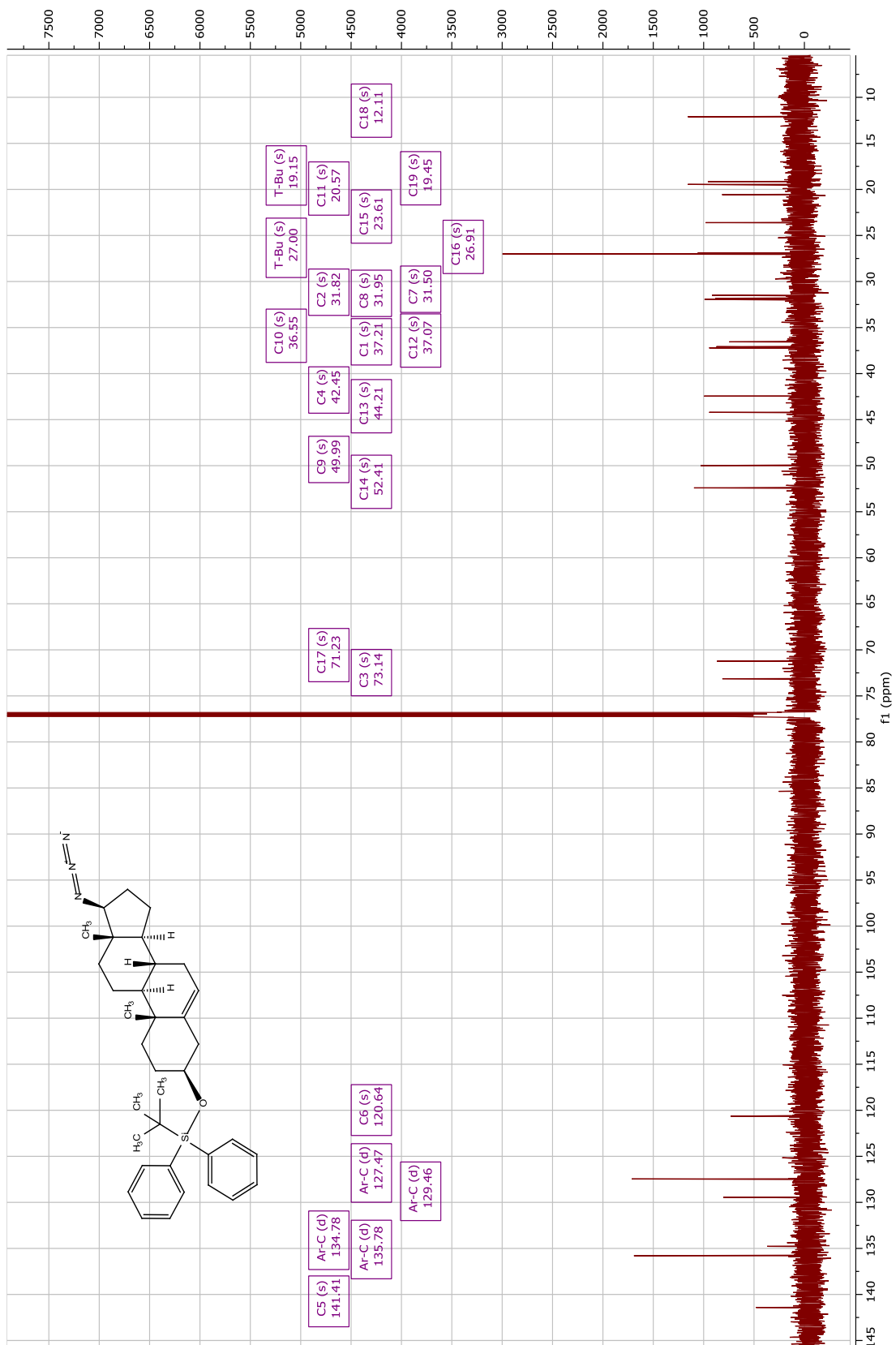
Figure S3.38 ^{1}H-^{1}H COSY Spectrum of (7)

230

Figure S3.39 ^{1}H-^{13}C HSQC Spectrum of (7)

Figure S3.40 ^{1}H-^{13}C HMBC Spectrum of (7)
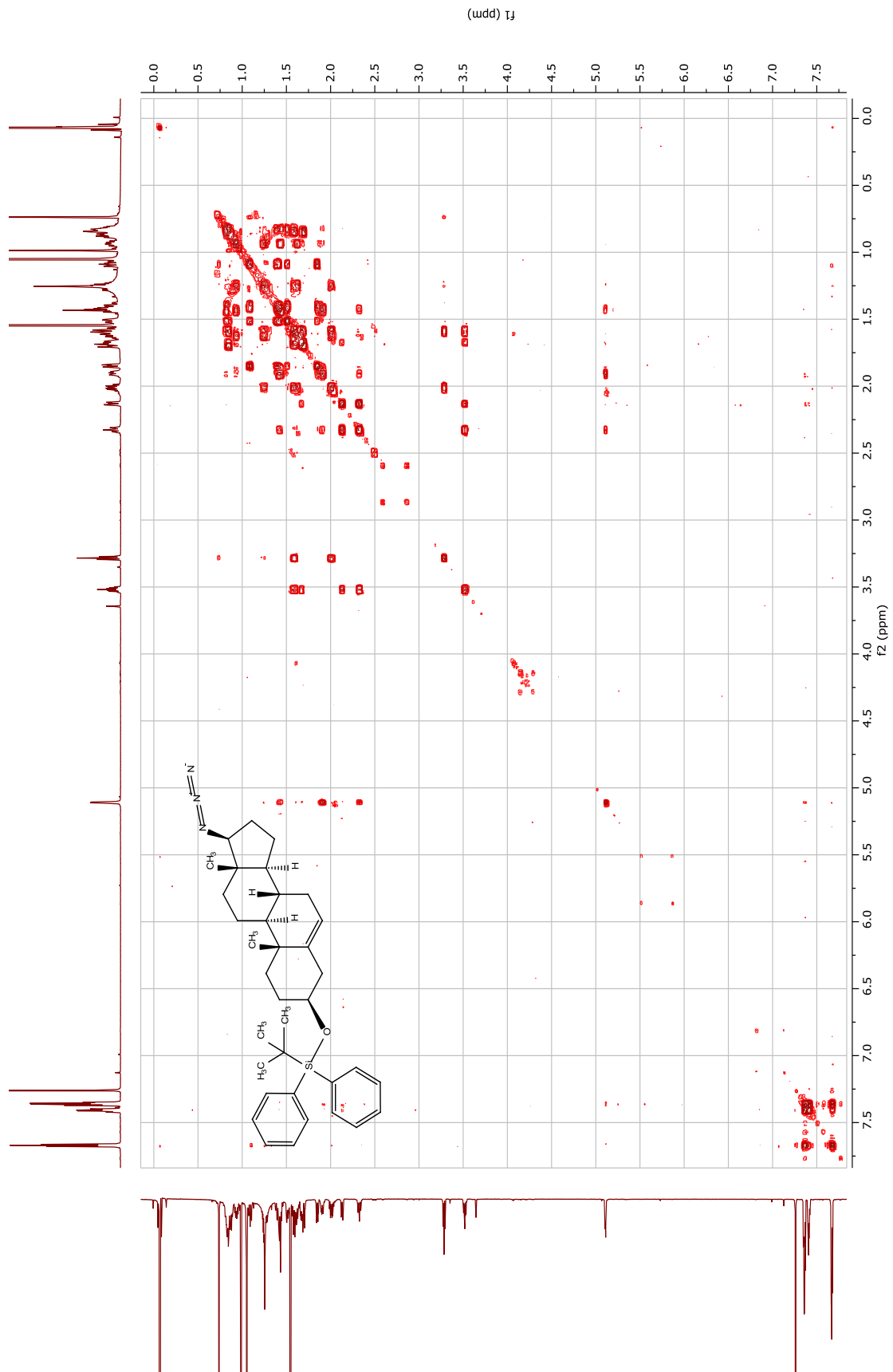
Figure S3.41 ^{1}H-^{1}H NOESY Spectrum of (7)
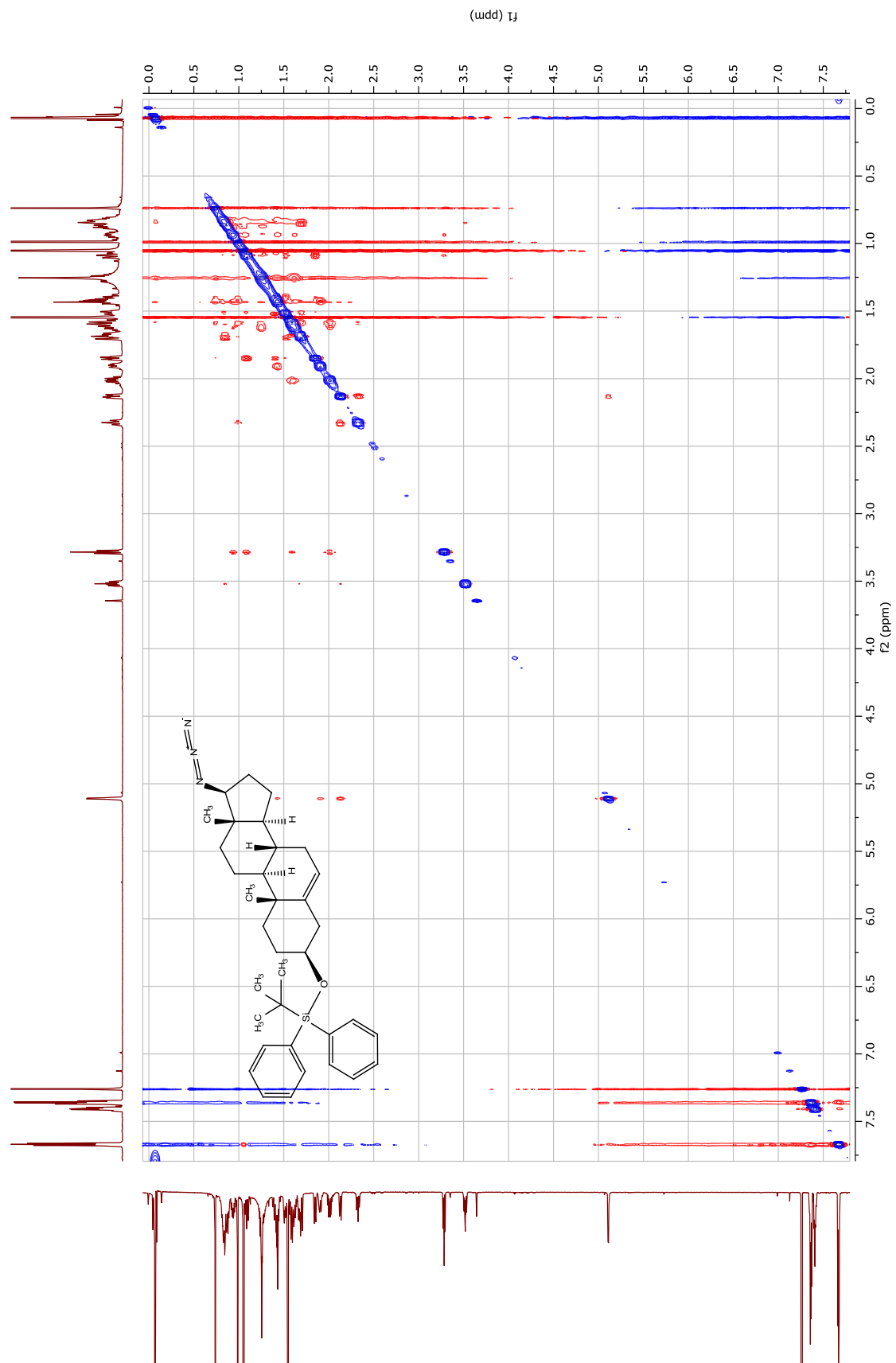
Figure S3.42 ^{1}H Spectrum of (7a)
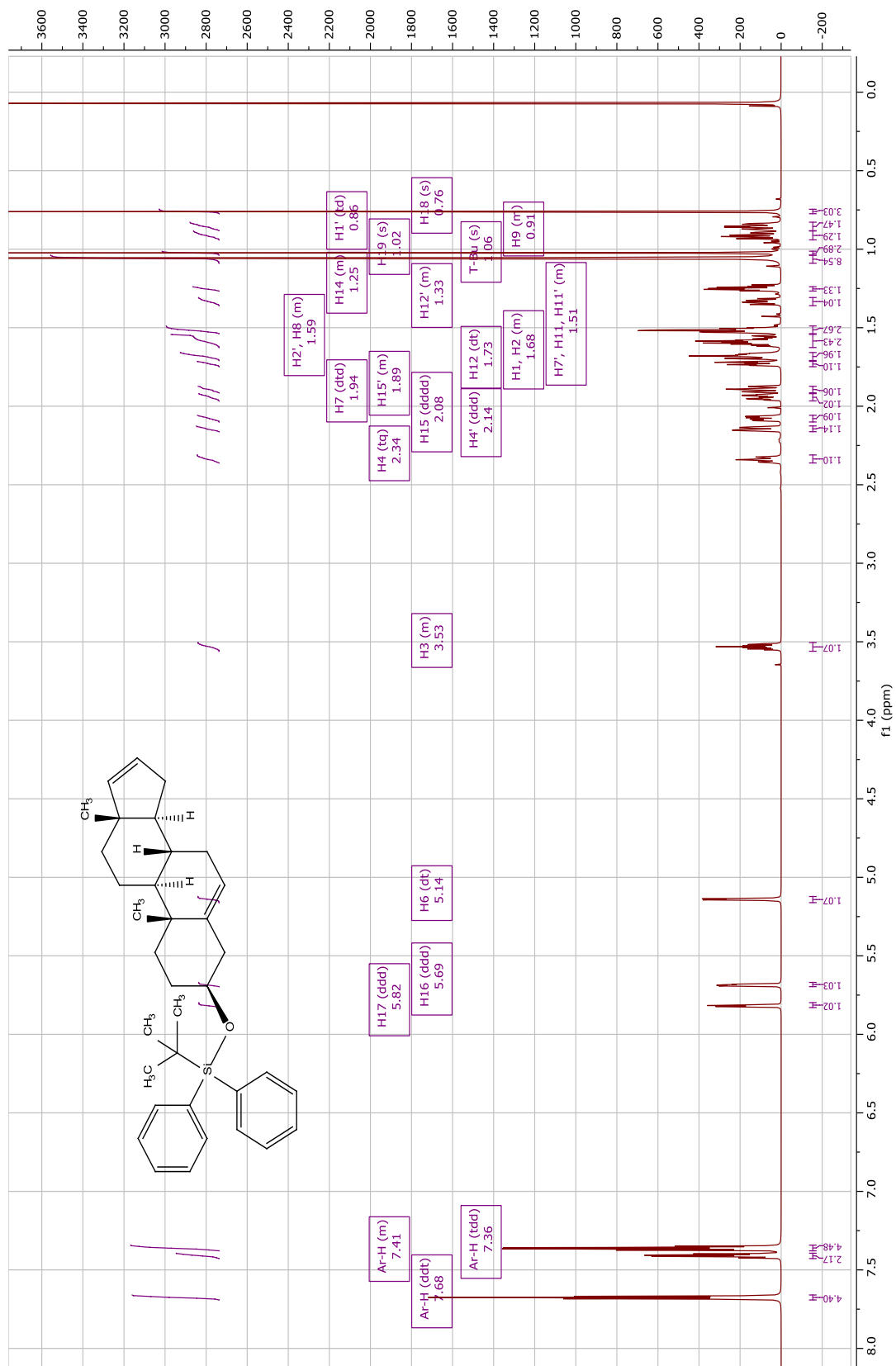
Figure S3.43 ^{13}C Spectrum of (7a)
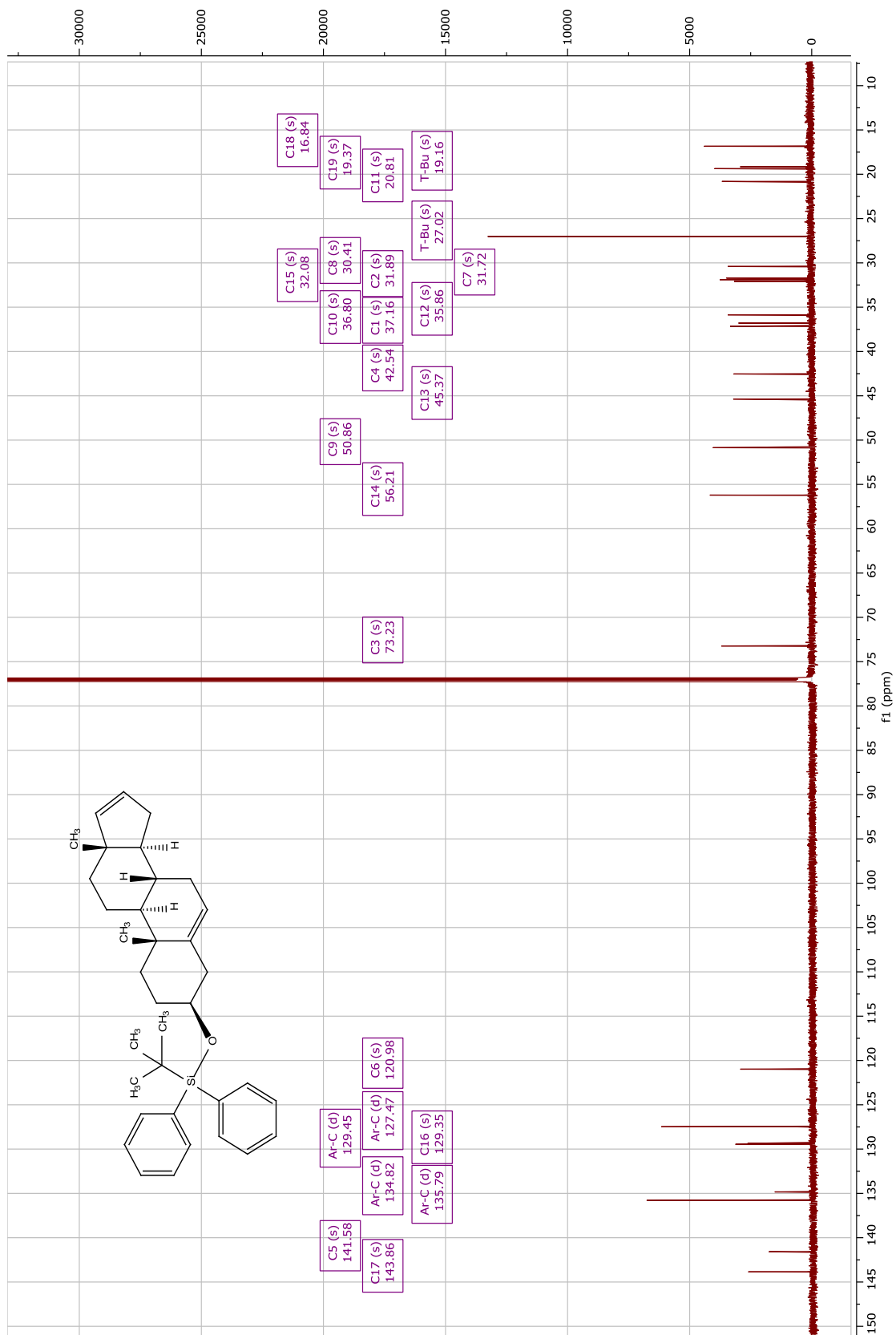
Figure S3.44 ^{1}H-^{1}H COSY Spectrum of (7a)
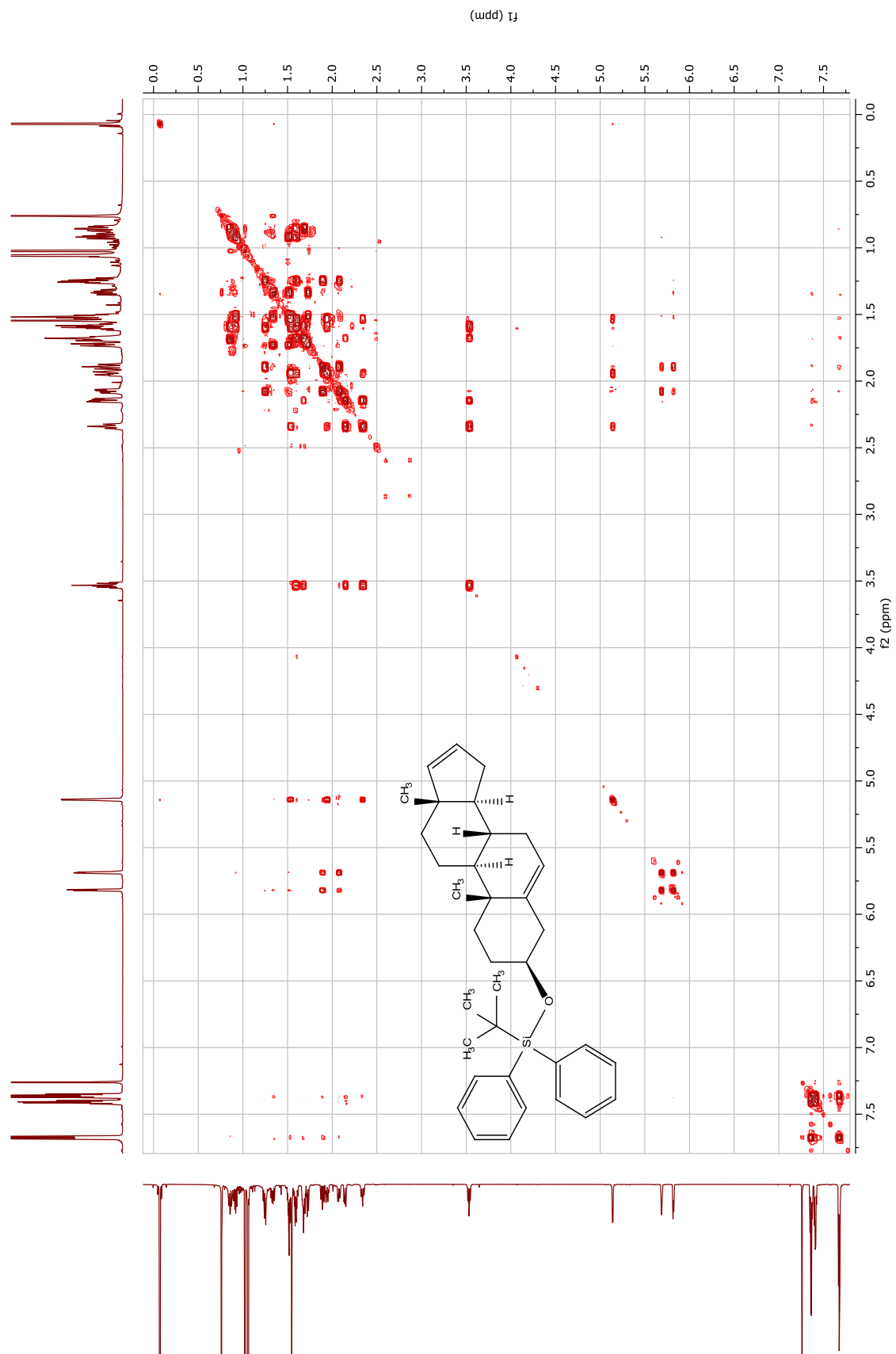
Figure S3.45 ^{1}H-^{13}C HSQC Spectrum of (7a)
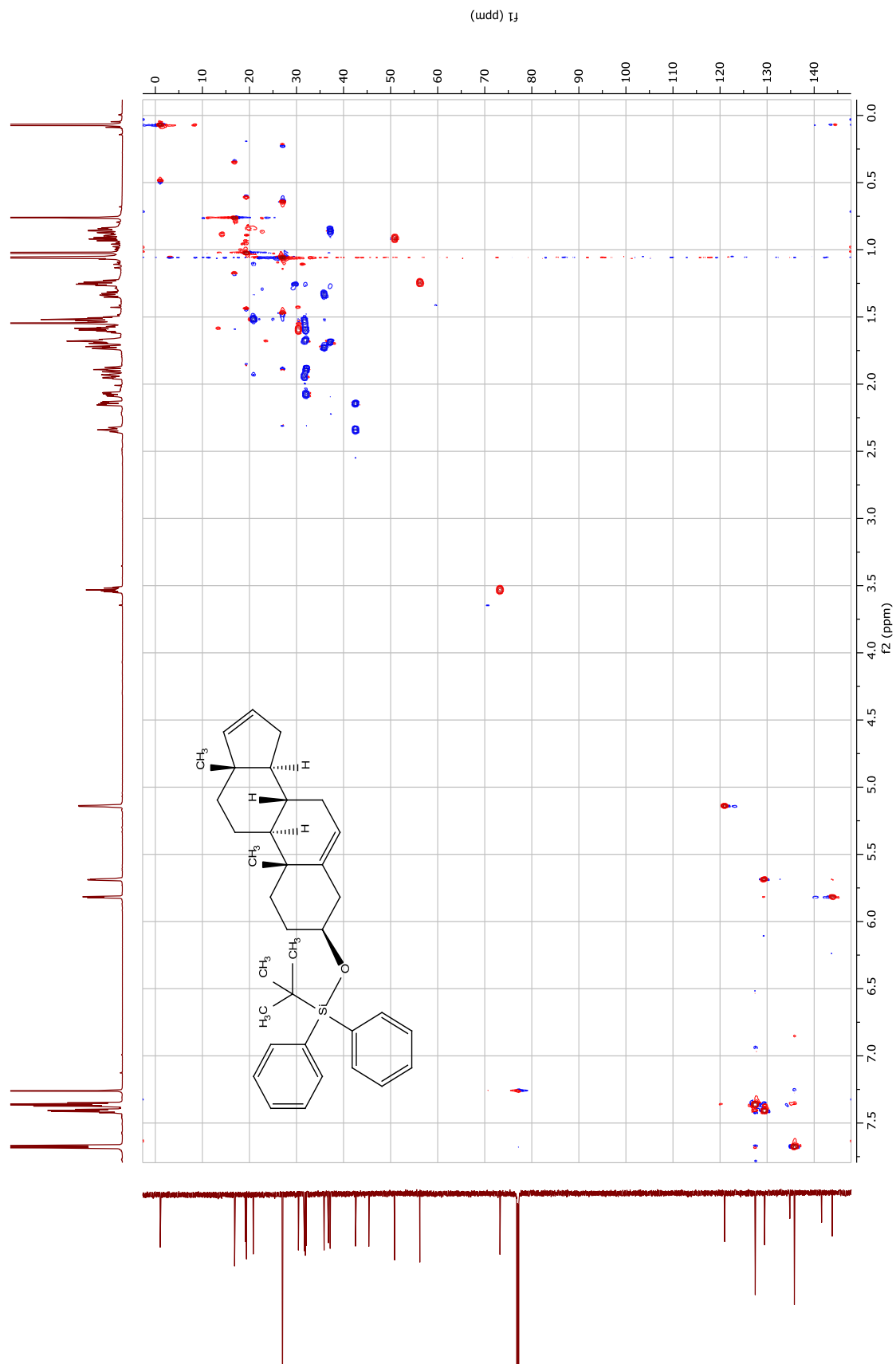
Figure S3.46 ^{1}H-^{13}C HMBC Spectrum of (7a)

238
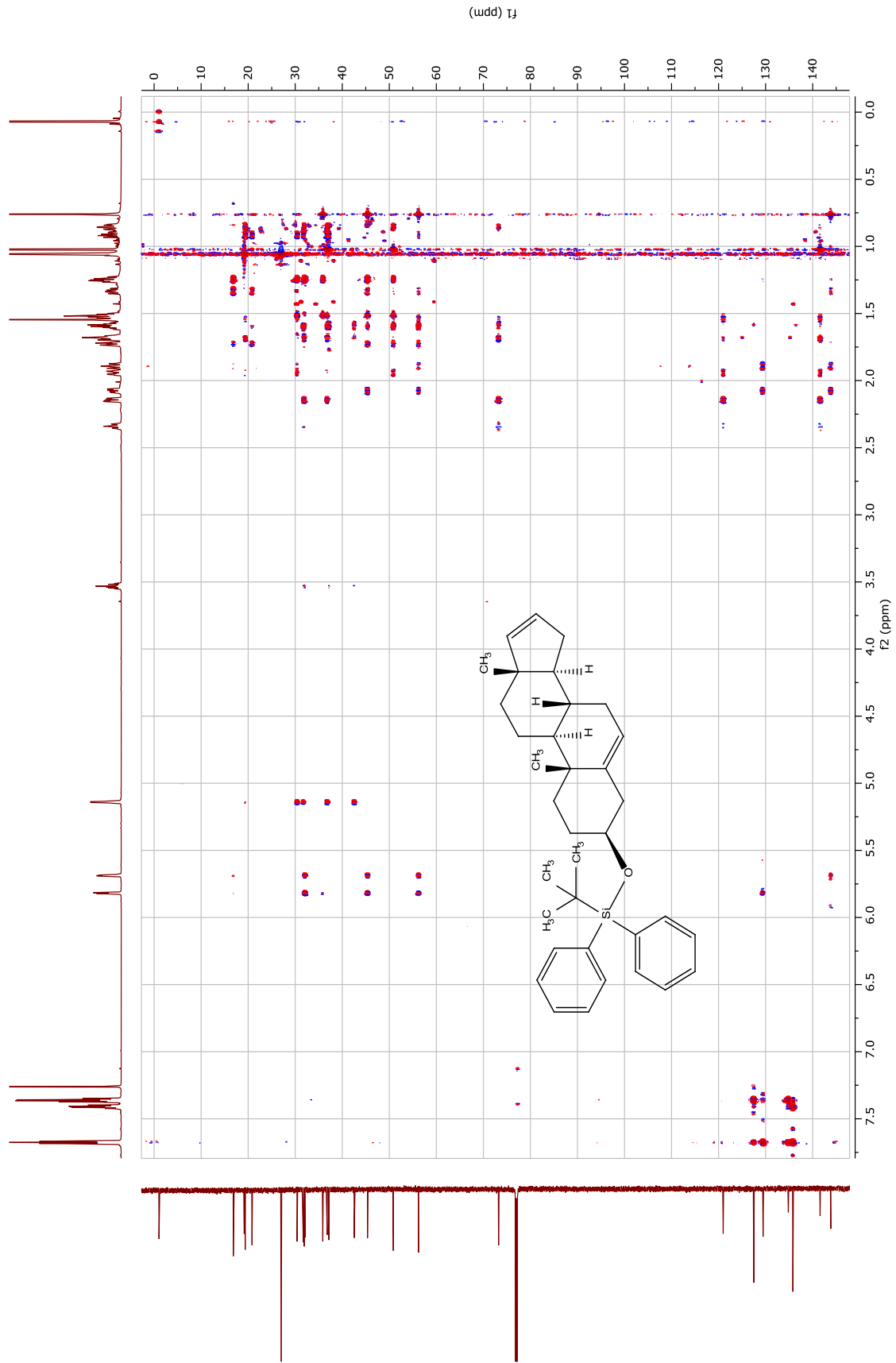
Figure S3.47 ^{1}H-^{1}H NOESY Spectrum of (7a)

239
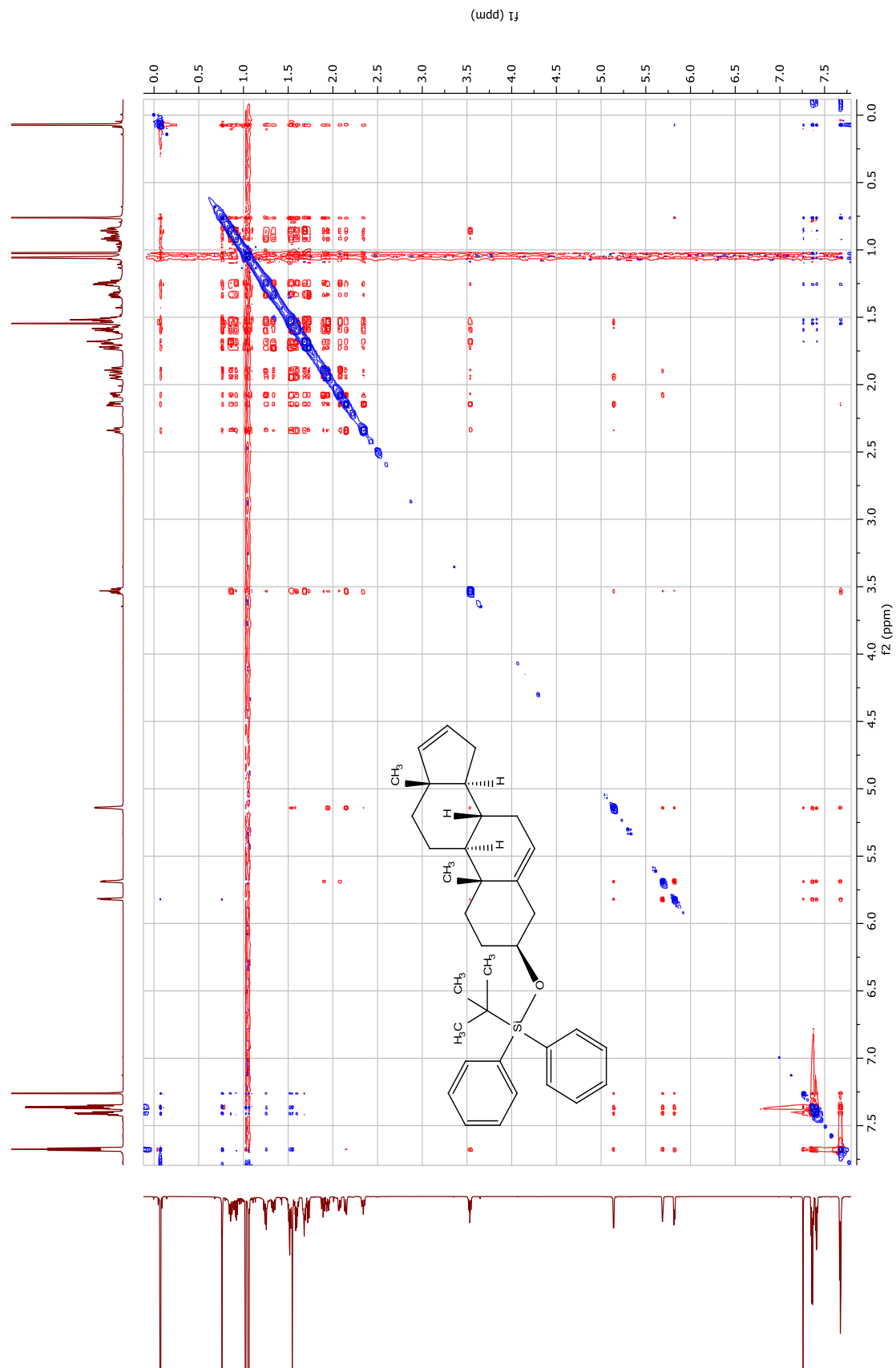
Figure S3.48 ^{1}H Spectrum of (8)
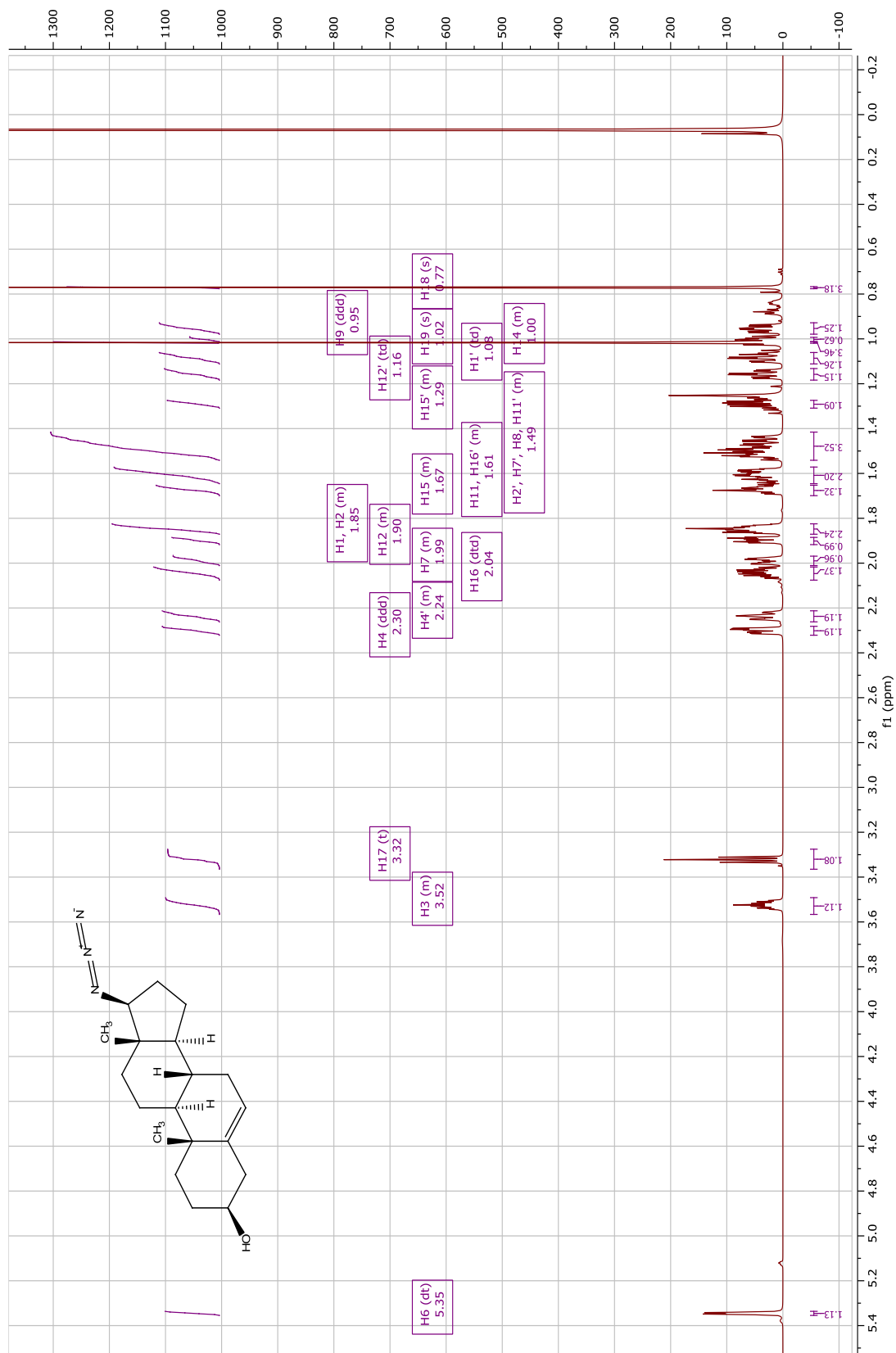
Figure 3.49 ^{13}C Spectrum of (8)

C18 (s) 12.15

C19 (s) 19.44
C11 (s) 20.64
C15 (s) 23.64

C16 (s) 26.93
C2 (s) 31.63
C8 (s) 32.00
C7 (s) 31.53

C10 (s) 36.58
C1 (s) 37.27
C12 (s) 37.09

C4 (s) 42.25
C13 (s) 44.23

C9 (s) 50.07
C14 (s) 52.43

C3 (s) 71.71
C17 (s) 71.24

C6 (s) 121.23

C5 (s) 140.89

f1 (ppm)
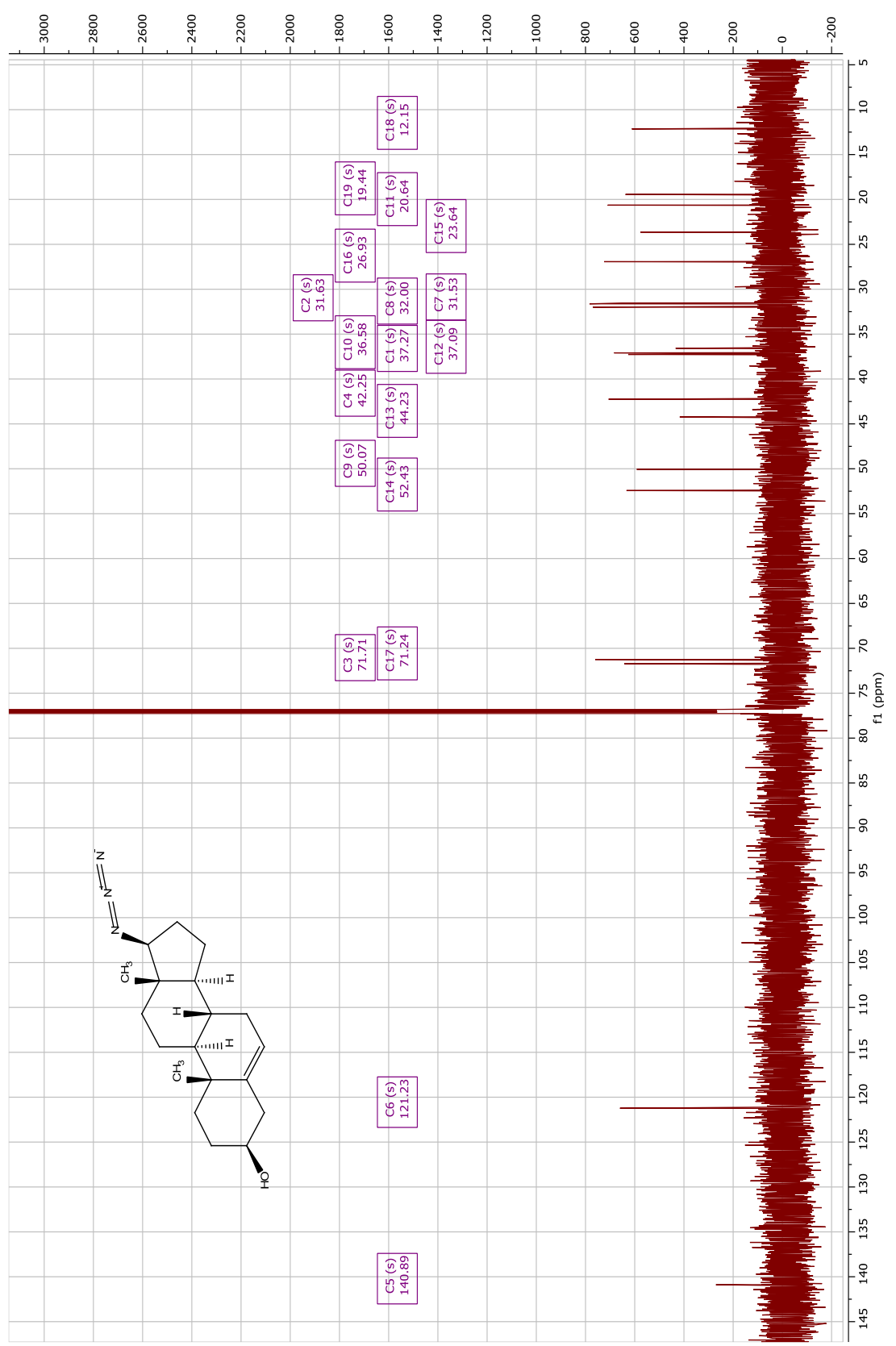
Figure S3.50 ^{1}H-^{1}H COSY Spectrum of (8)

242
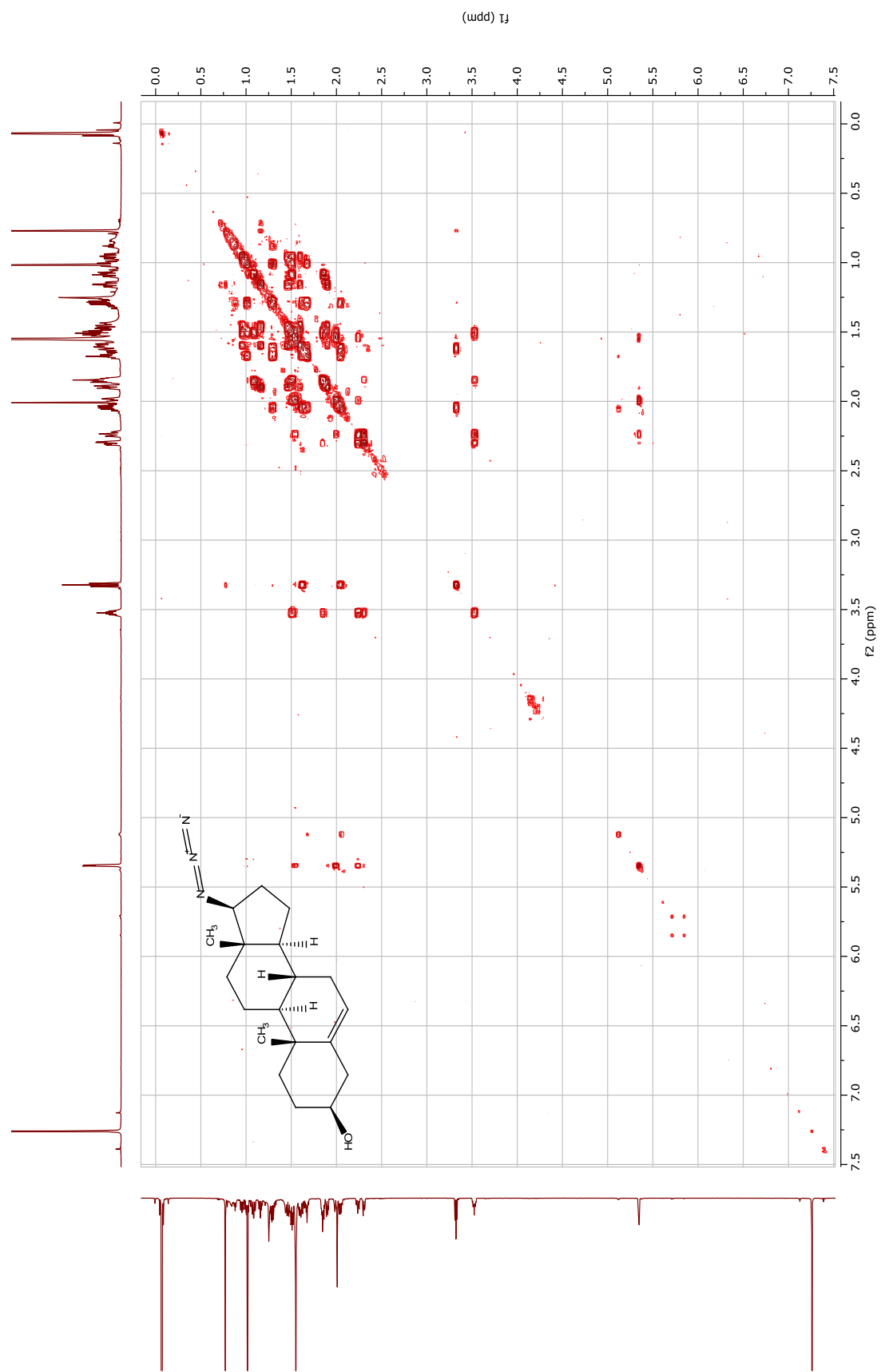
Figure S3.51 ^{1}H-^{13}C HSQC Spectrum of (8)
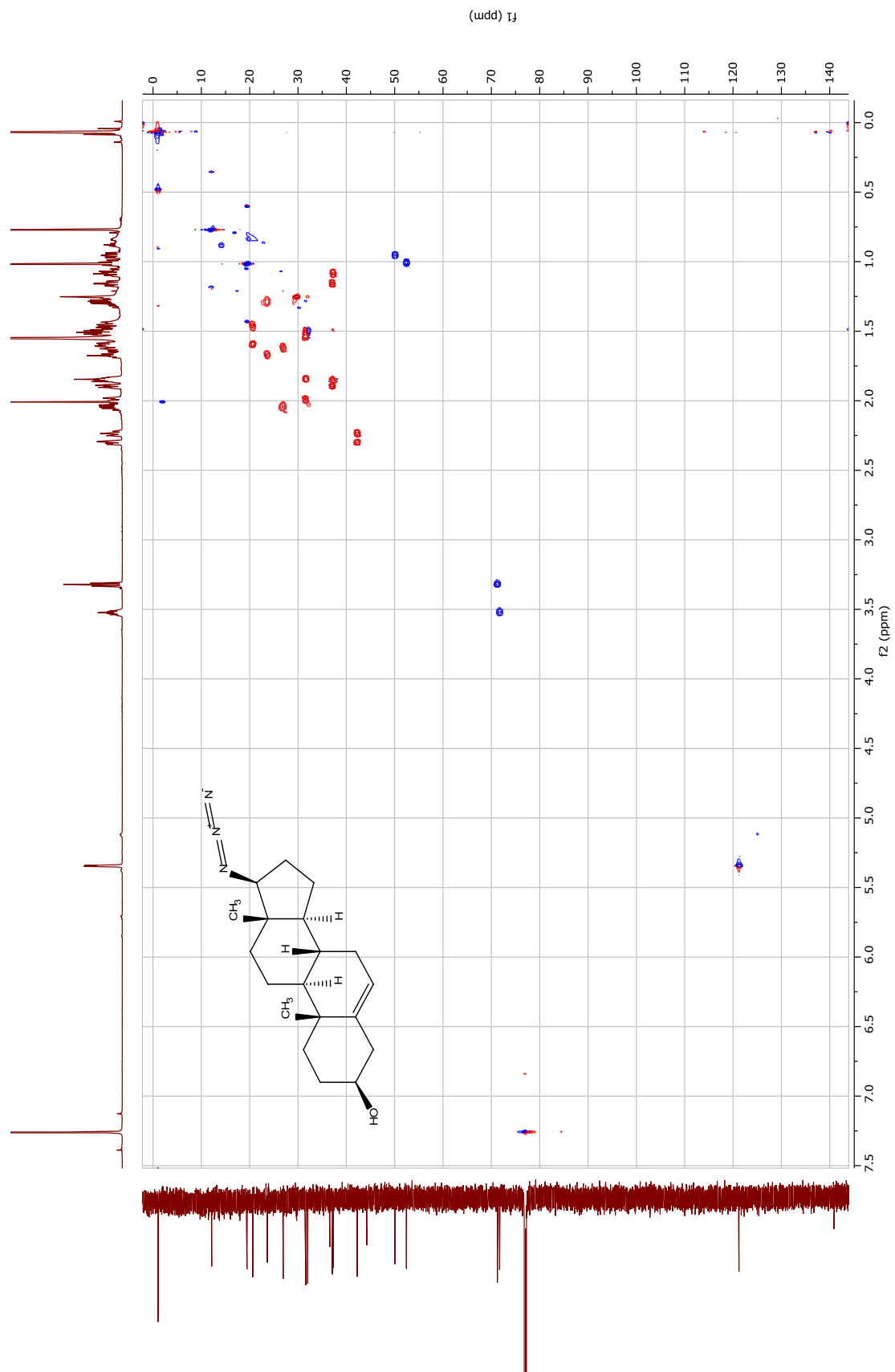
Figure S3.52 ^{1}H-^{13}C HMBC Spectrum of (8)

244
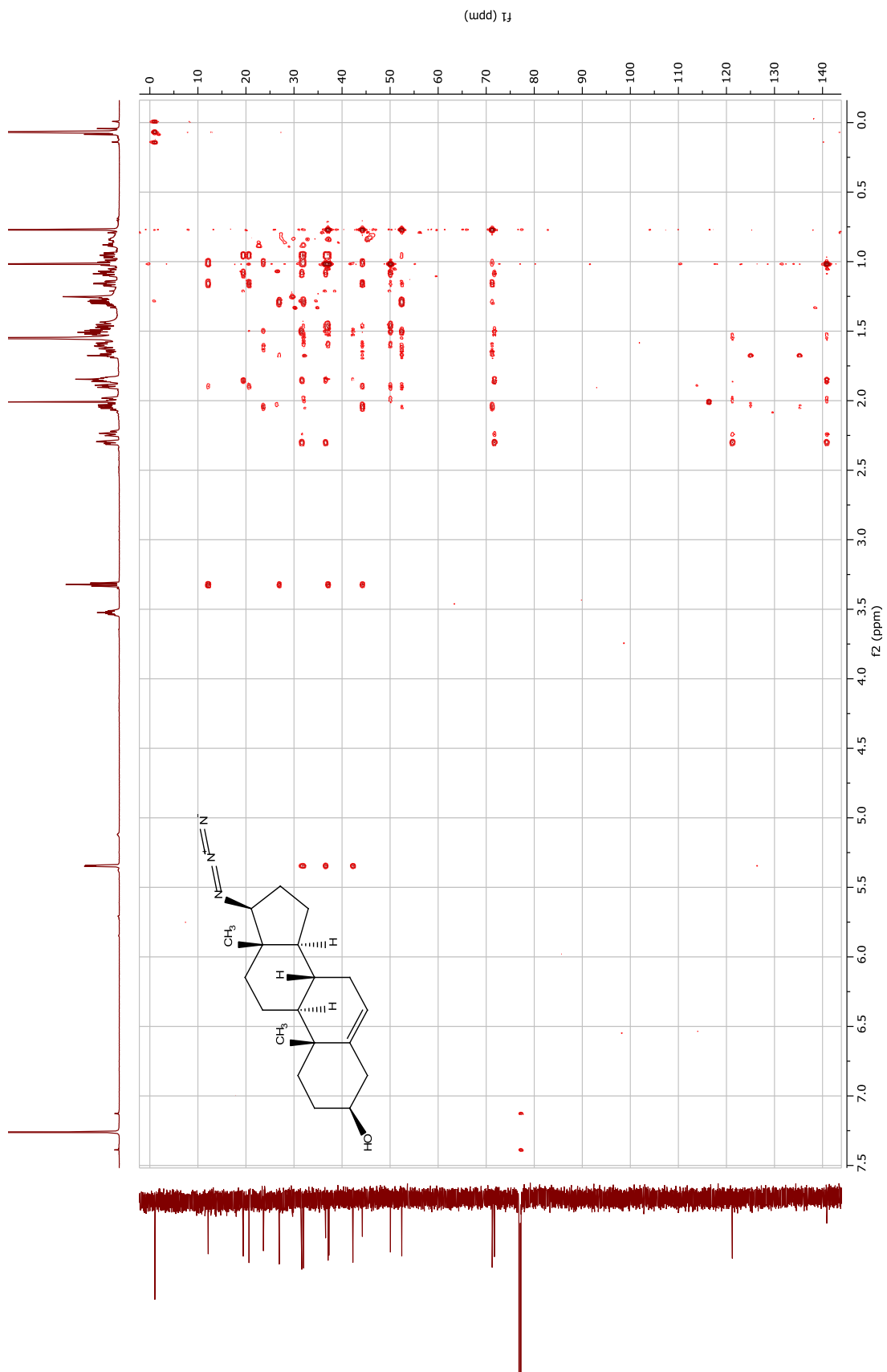
Figure S3.53 ^{1}H-^{1}H NOESY Spectrum of (8)
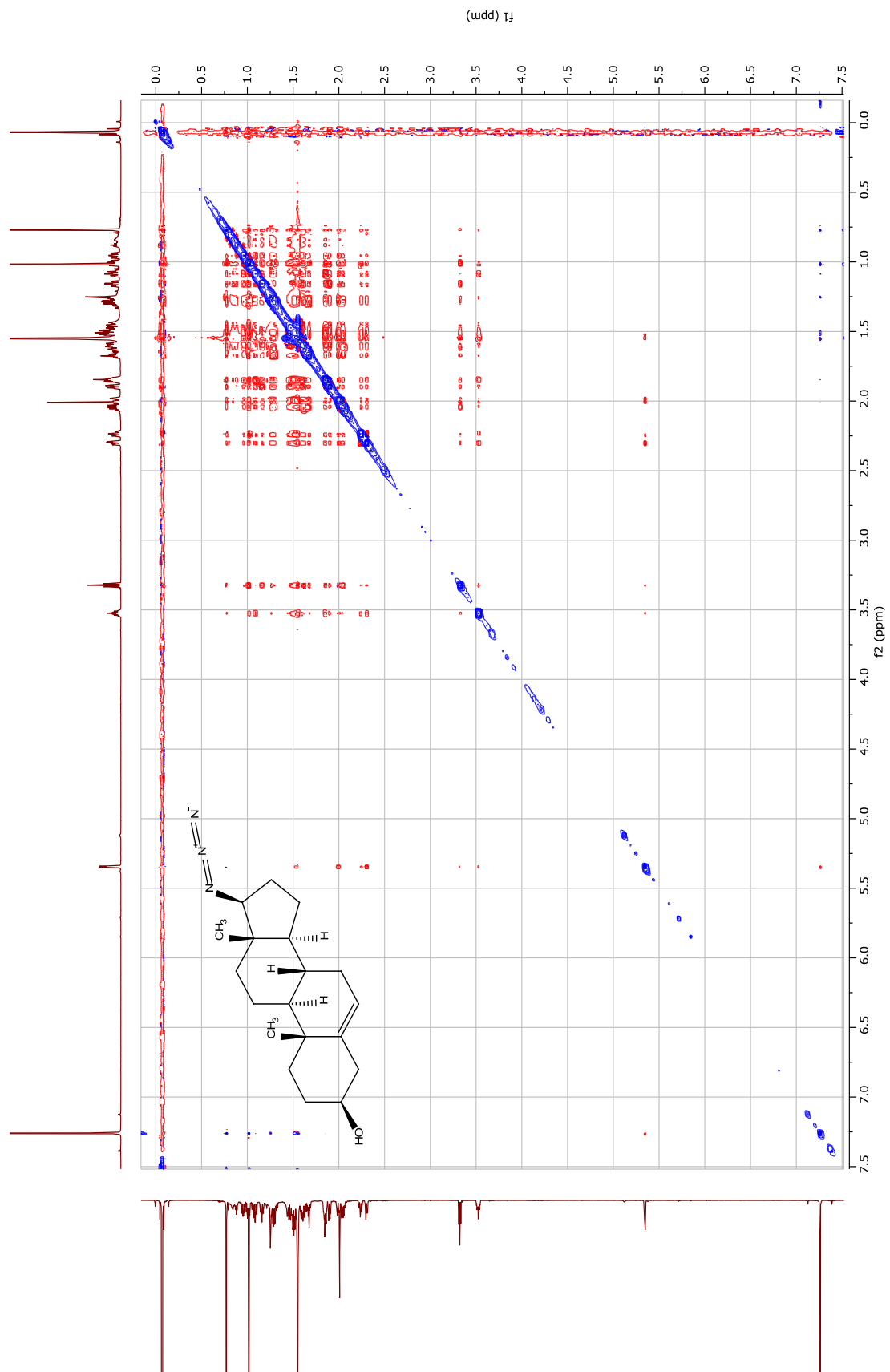
Figure S3.54 ¹H Spectrum of (29)
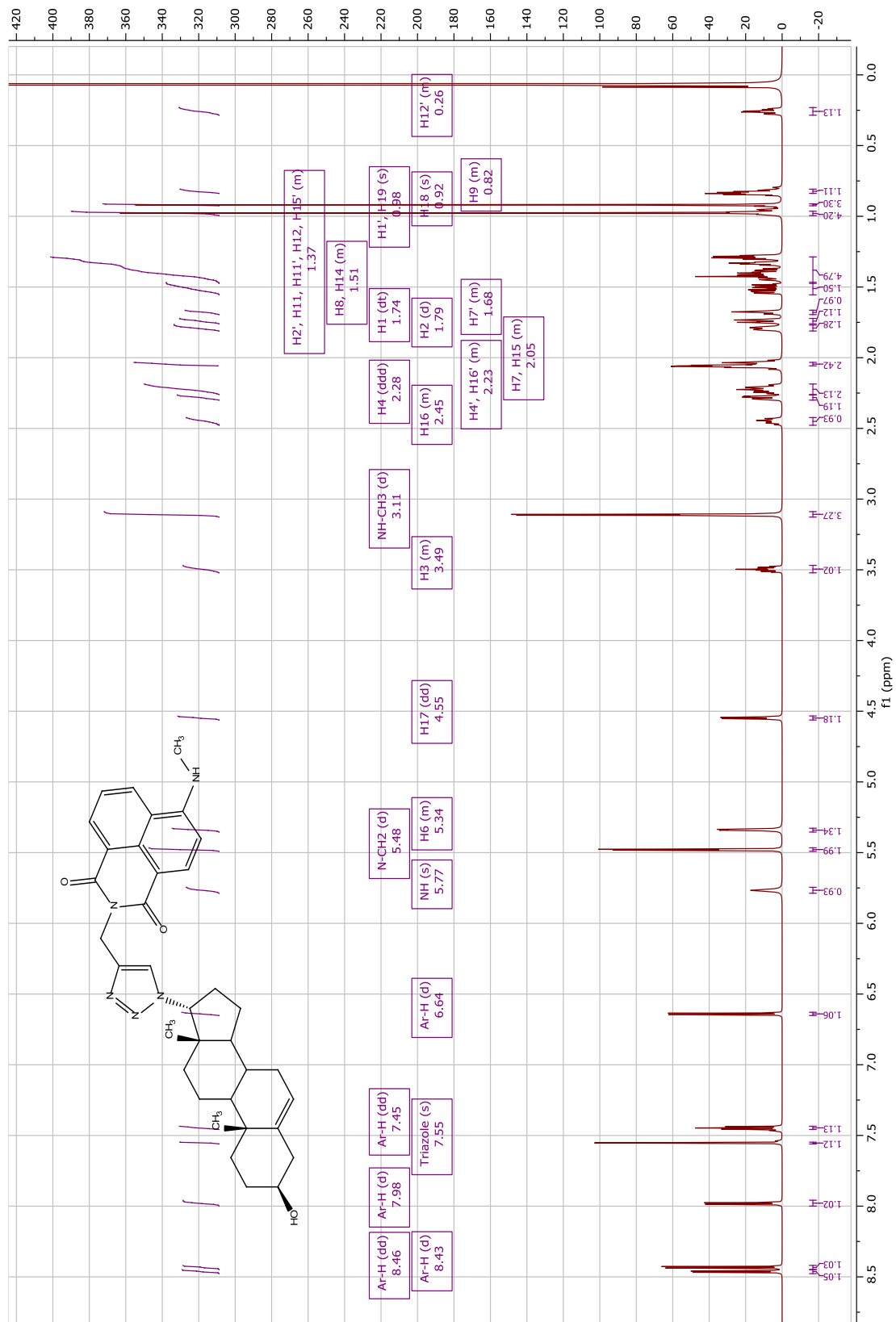
Figure S3.55 13C Spectrum of (29)
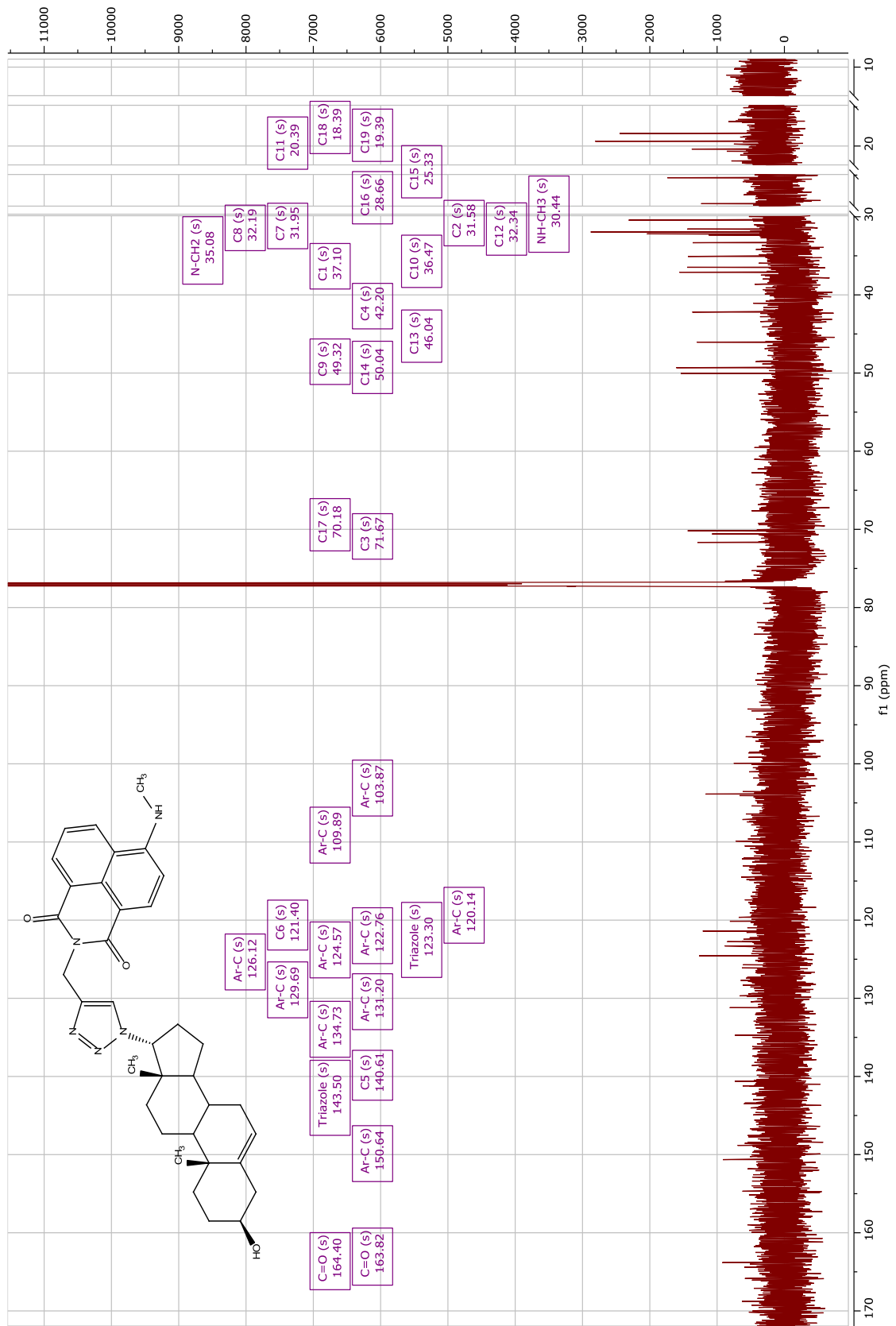
Figure S3.56 ^{1}H-^{1}H COSY Spectrum of (29)
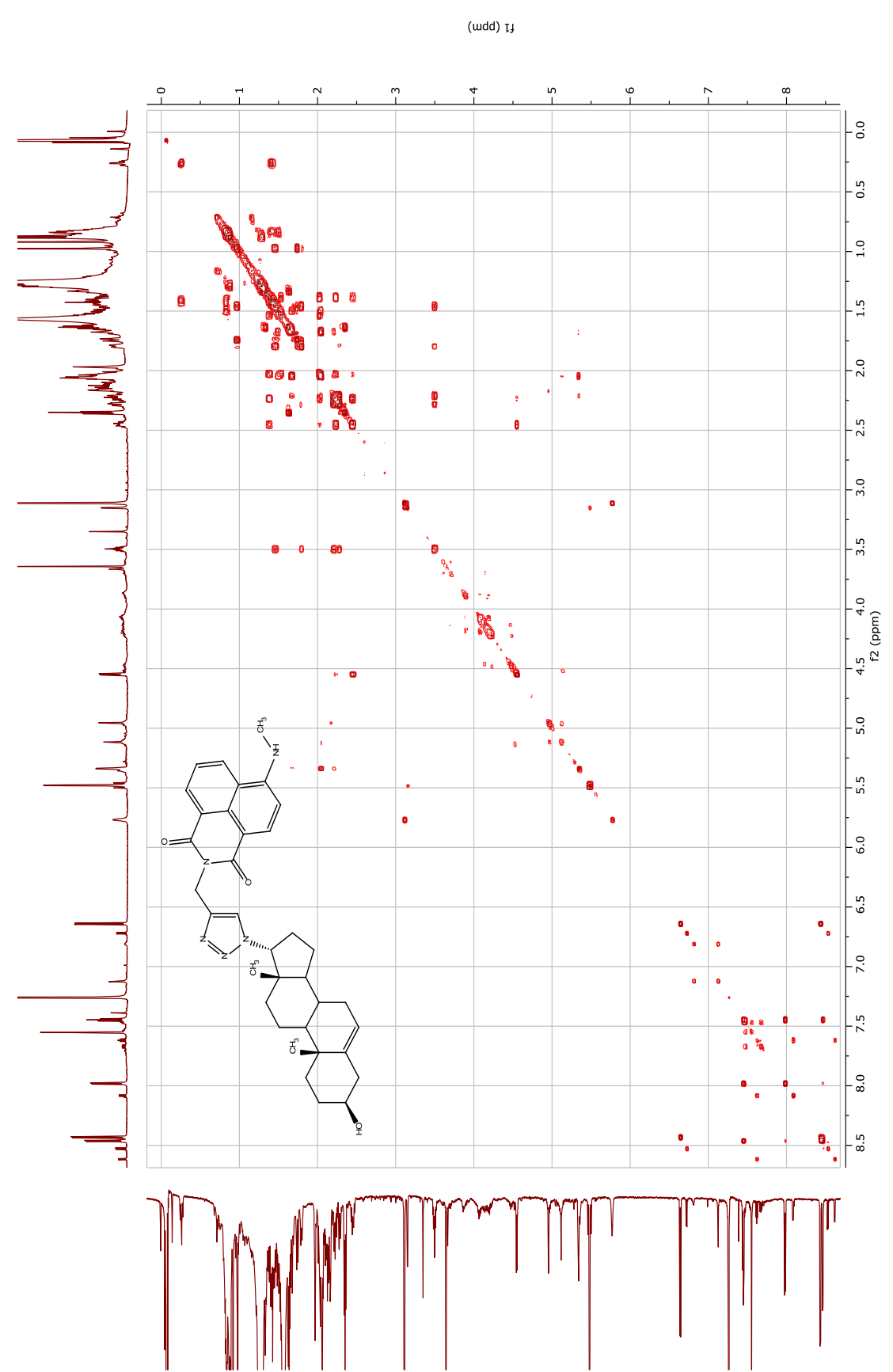
Figure S3.57 ^{1}H-^{13}C HSQC Spectrum of **(29)**
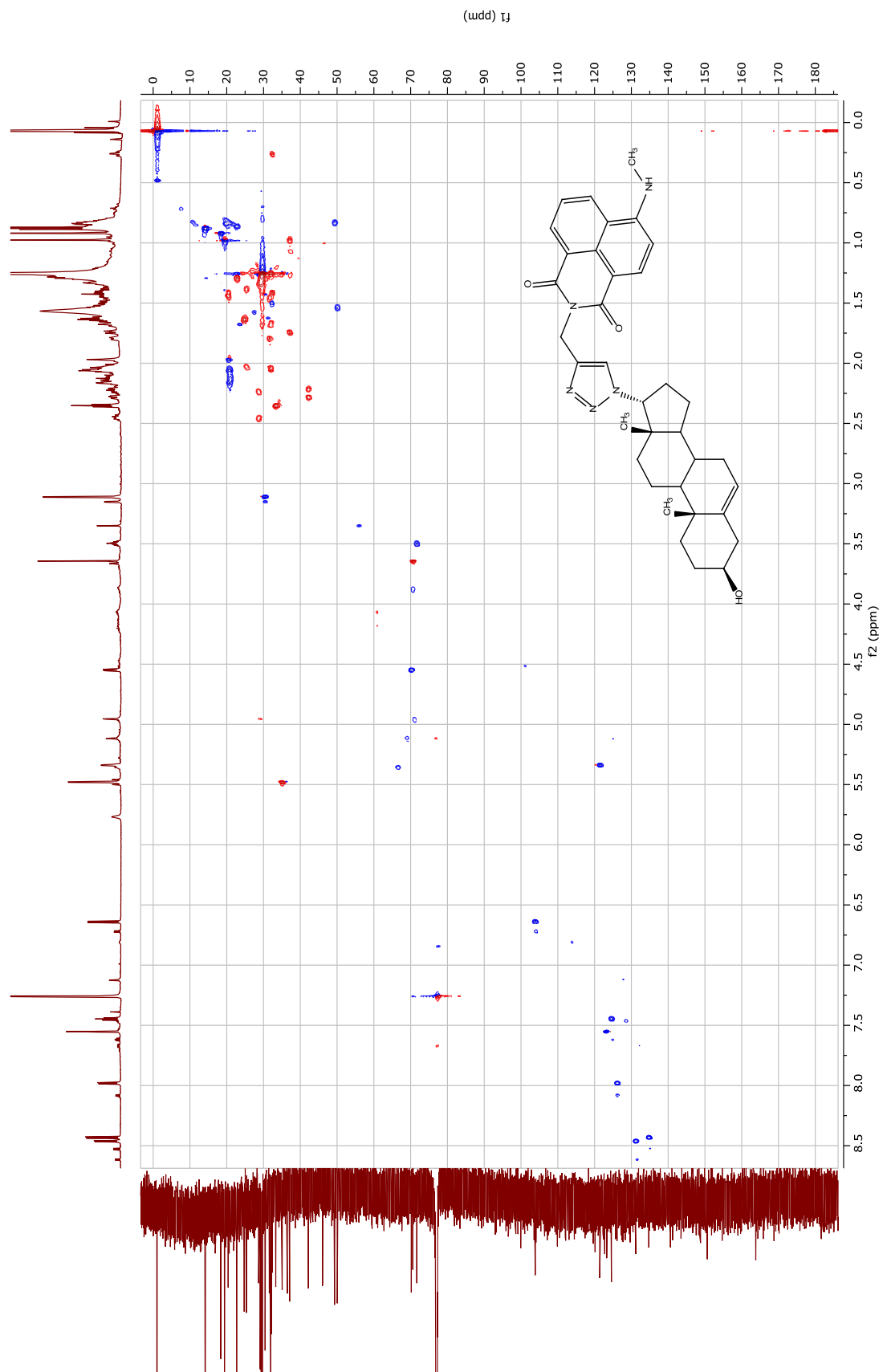
Figure S3.58 ^{1}H-^{13}C HMBC Spectrum of (29)
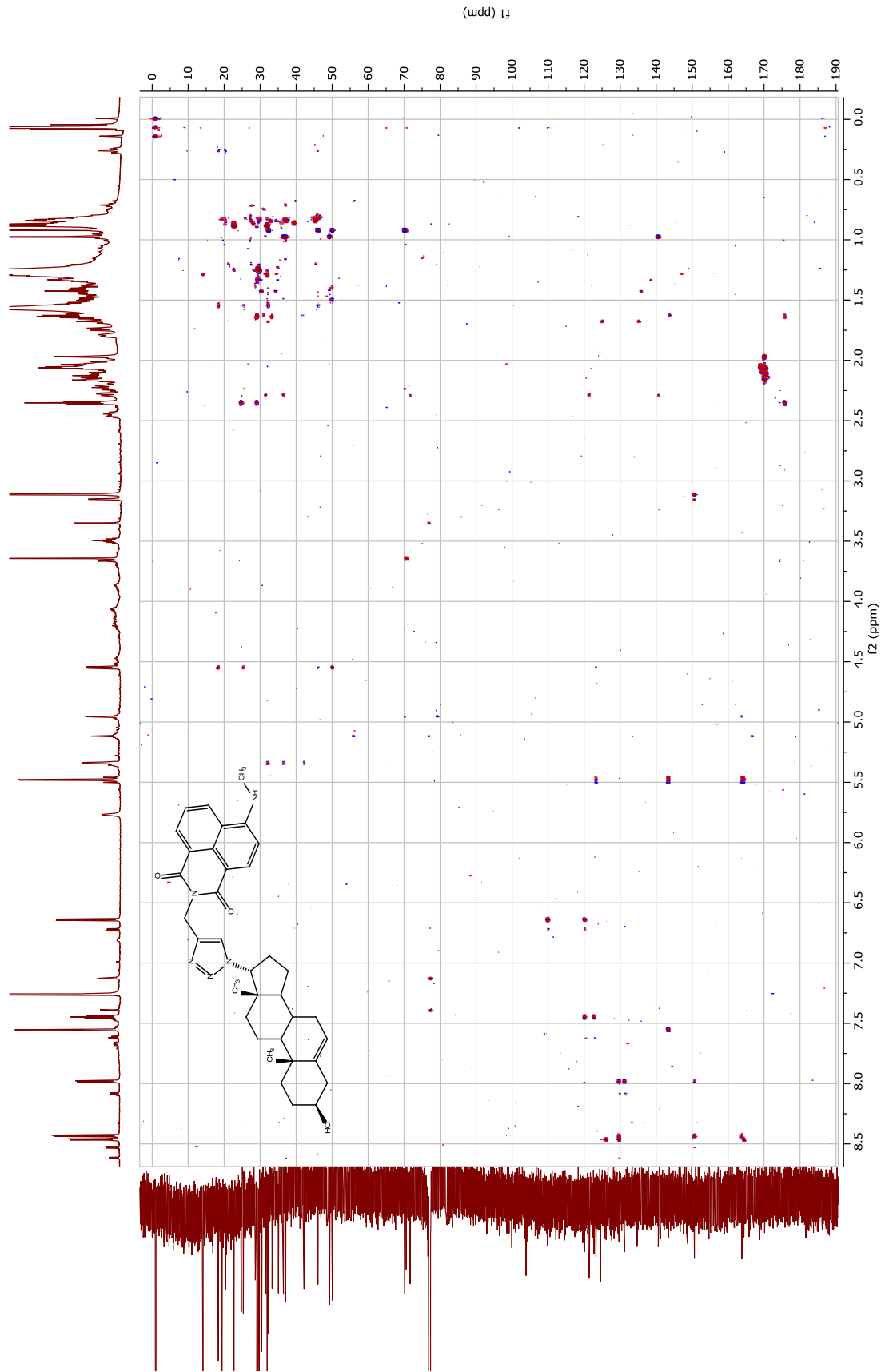
Figure S3.59 ¹H-¹H NOESY Spectrum of (29)

251
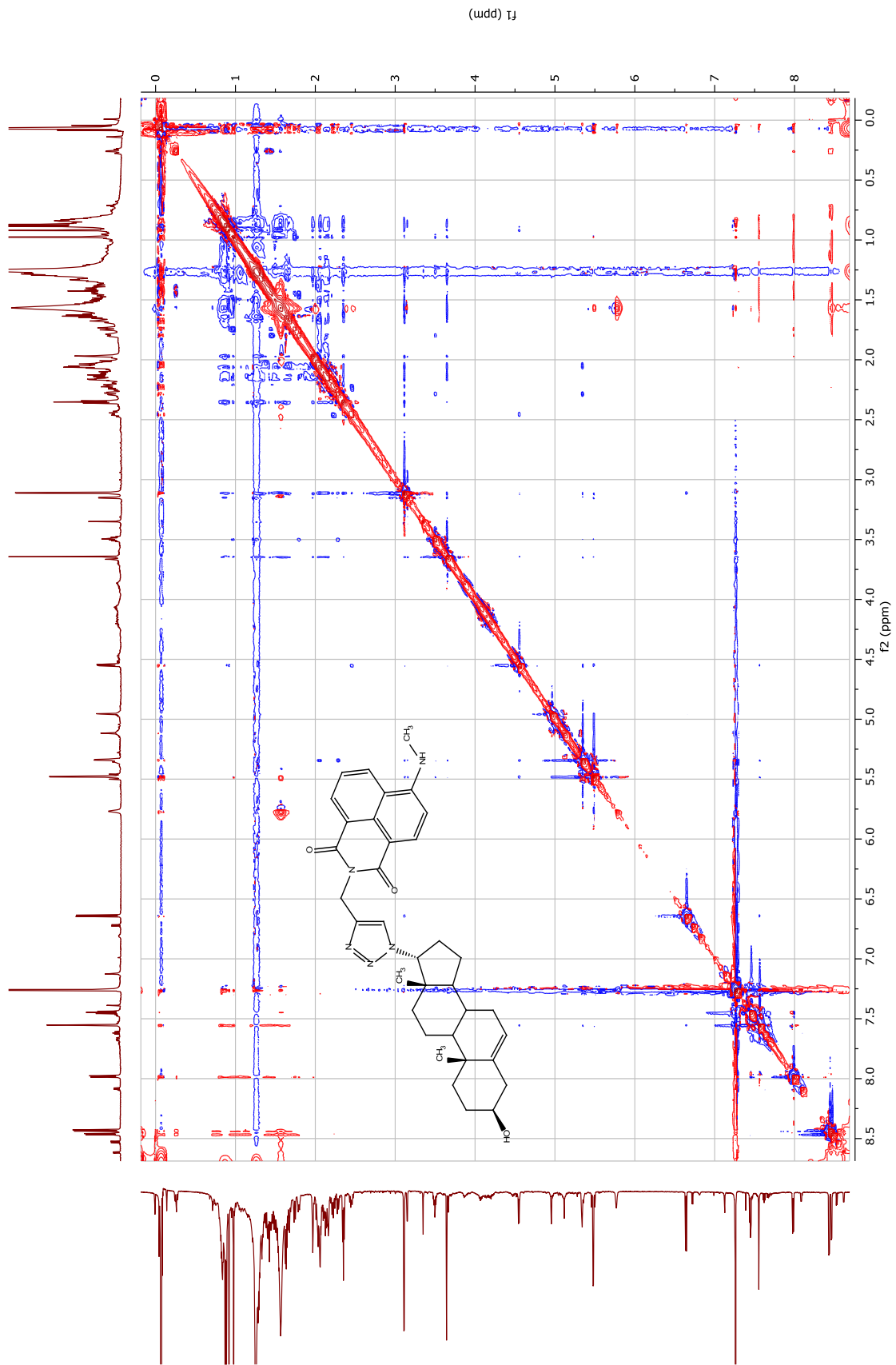
Figure S3.60 ^{1}H Stacked Spectrum of 1-8
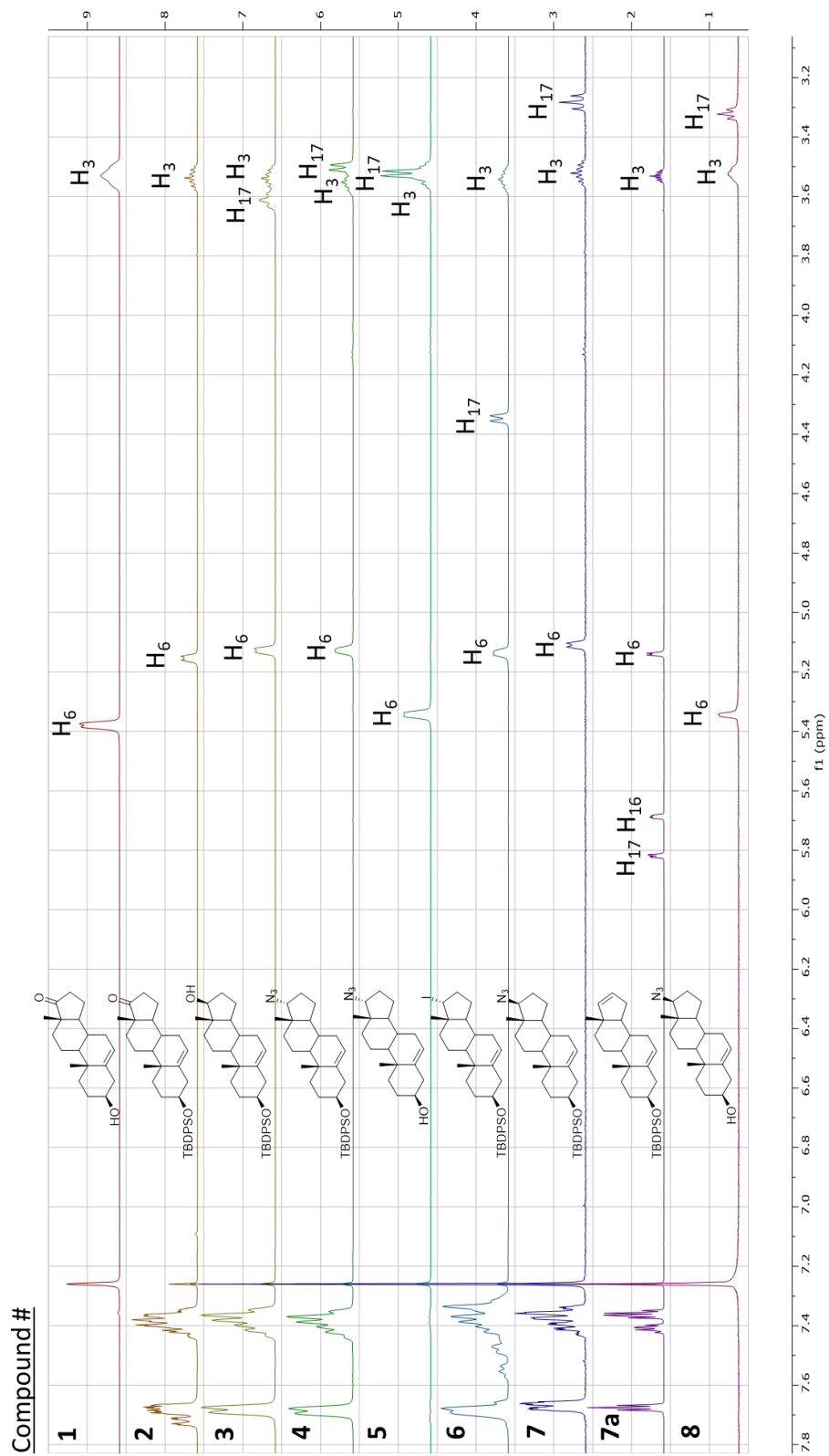
Section 3.15: References

Blanco G., Georg G. I., Syeda S. S., inventors. Regents of the University of Minnesota, The University of Kansas, assignees. Contraceptive Agents. US 2014/0005132. 2014 January 02

Jan, H. M., Chen, Y. C., Shih, Y. Y., Huang, Y. C., Tu, Z., Ingle, A. B., Liu, S. W., Wu, M. S., Gervay-Hague, J., Mong, K. K. T., Chen, Y. R., & Lin, C. H. (2016). Metabolic labelling of cholesteryl glucosides in: *Helicobacter pylori* reveals how the uptake of human lipids enhances bacterial virulence. *Chemical Science*, *7*(9), 6208–6216. https://doi.org/10.1039/c6sc00889e

Kiss, A., Herman, B. E., Görbe, T., Mernyák, E., Molnár, B., Wölfling, J., Szécsi, M., & Schneider, G. (2018). Synthesis of novel 17-triazolyl-androst-5-en-3-ol epimers via Cu(I)-catalyzed azide-alkyne cycloaddition and their inhibitory effect on 17α-hydroxylase/C17,20-lyase. *Steroids*, *135*(February), 79–91. https://doi.org/10.1016/j.steroids.2018.03.006

Wishart DS, Knox C, Guo AC, Eisner R, Young N, Gautam B, Hau DD, Psychogios N, Dong E, Bouatra S, Mandal R, Sinelnikov I, Xia J, Jia L, Cruz JA, Lim E, Sobsey CA, Shrivastava S, Huang P, Liu P, Fang L, Peng J, Fradette R, Cheng D, Tzur D, Clements M, Lewis A, De Souza A, Zuniga A, Dawe M, Xiong Y, Clive D, Greiner R, Nazyrova A, Shaykhutdinov R, Li L, Vogel HJ, Forsythe I: HMDB: a knowledgebase for the human metabolome. Nucleic Acids Res. 2009 Jan;37(Database issue):D603-10. doi: 10.1093/nar/gkn810. Epub 2008 Oct 25. Human Metabolome Database: 1H NMR Spectrum () (hmdb.ca)

Chapter 4

Glycosylceramide bioactivity and probe synthesis

As previously described in the literature, CD1d is a protein that binds to glycosylceramides, like α-GalCer, and this coupled complex is then presented to iNKT cells to produce signaling molecules called T_H1/T_H2 cytokines (Zhang et al., 2008). However, the role and metabolism of sterol glycosides during CD1d binding and T_H1/T_H2 cytokine release is unclear. In addition, the sugar exchange between sterol lactosides and ceramides is uncertain. Therefore, the synthesis of sterol glycoside probes is being pursued to study the latter phenomenon, which leads to DHEA C_{17} N_3 lactosyl probes (**14**, **15**, **16**, **17**). The purpose of the DHEA C_{17} N_3 lactosyl probes (**14**, **15**, **16**, **17**) is to study the role and metabolism of sterol glycosides during T_H1/T_H2 cytokine release and the sugar exchange with ceramides while providing efficient non-disruptive extraction via CuAAC. The design and synthesis of the azido-sterol component (**5** and **8**) is briefly described in Section 2.1. The α/β attachment of the lactose group to the sterol component will utilize the synthetic procedure from Davis et al. (Davis et al., 2015).
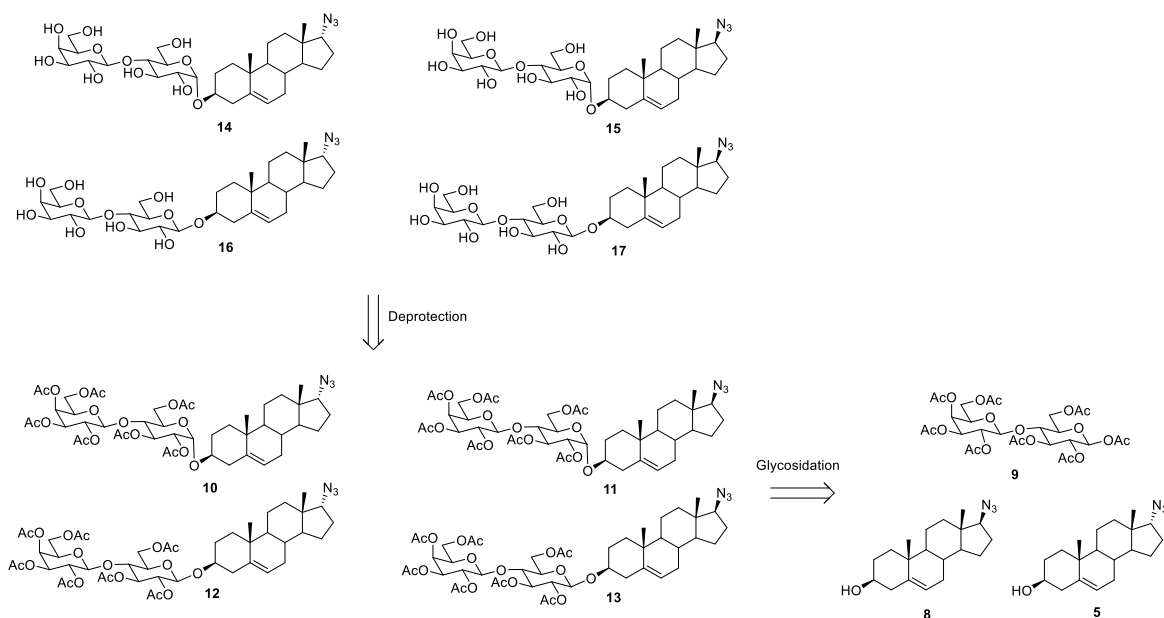
Scheme 4.1 Retrosynthesis of DHEA C_{17} N_3 Lactosyl Probes

From the retrosynthesis (see Scheme 4.1), acetate groups are attached to the free hydroxyl groups on lactose from **14-17** to make **10-13**, respectively. Next, the lactose group in

either an α or β configuration is removed via hydrolysis at C_3 of **10-13** to form two separate starting

components: an azido sterol component (**5** and **8**) and a sugar component (Lactose Octaacetate,

9).
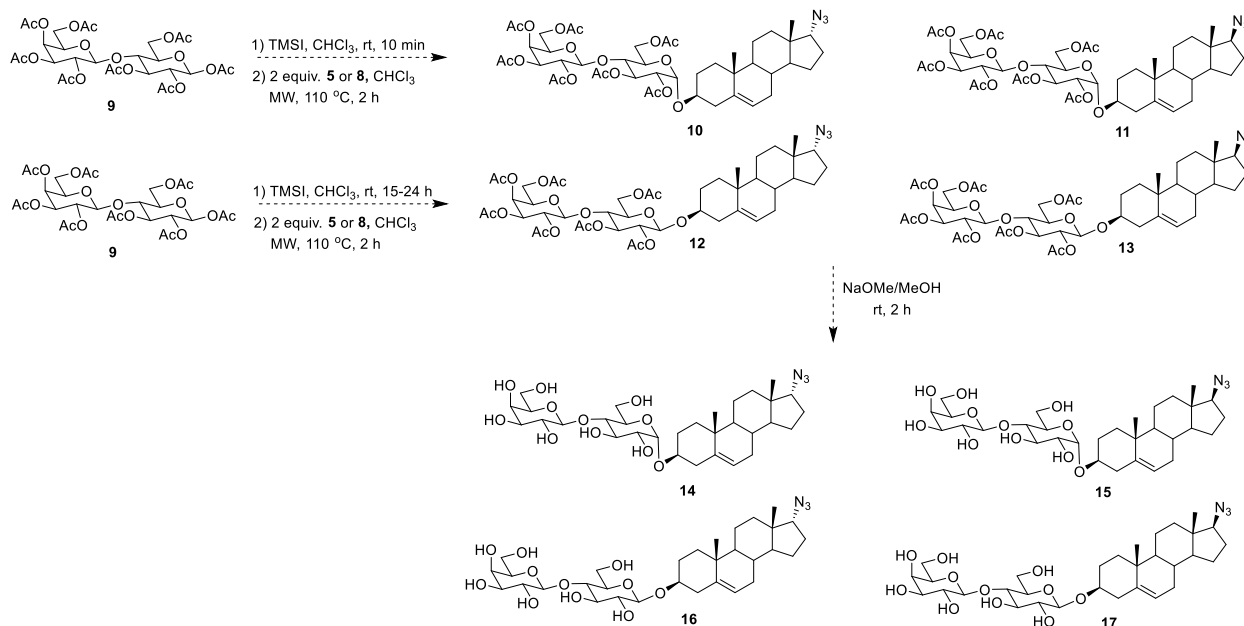
Scheme 4.2 DHEA C_{17} N_3 Lactosyl Probes Synthetic Scheme

      The scheme begins with **9** in which the anomeric acetate group of Per-*O*-acetylated

lactose is substituted with an iodide group. Next, **5** and **8** will undergo microwave radiation with

the α/β-lactosyl iodide synthesized above (**25** or **26**) to form **10**, **11**, **12**, and **13** (see Scheme 4.2).

The α/β configuration of the iodide group is important as the α-lactosyl iodide (**26**) will lead to

primary formation of **16/17** while the β-lactosyl iodide (**25**) will lead to primary formation of **14/15**.

It is proposed that the formation of **10**, **11**, **12**, and **13** will arise from analogous methods previously

developed in the Gervay-Hague lab (Davis et al., 2015).

256
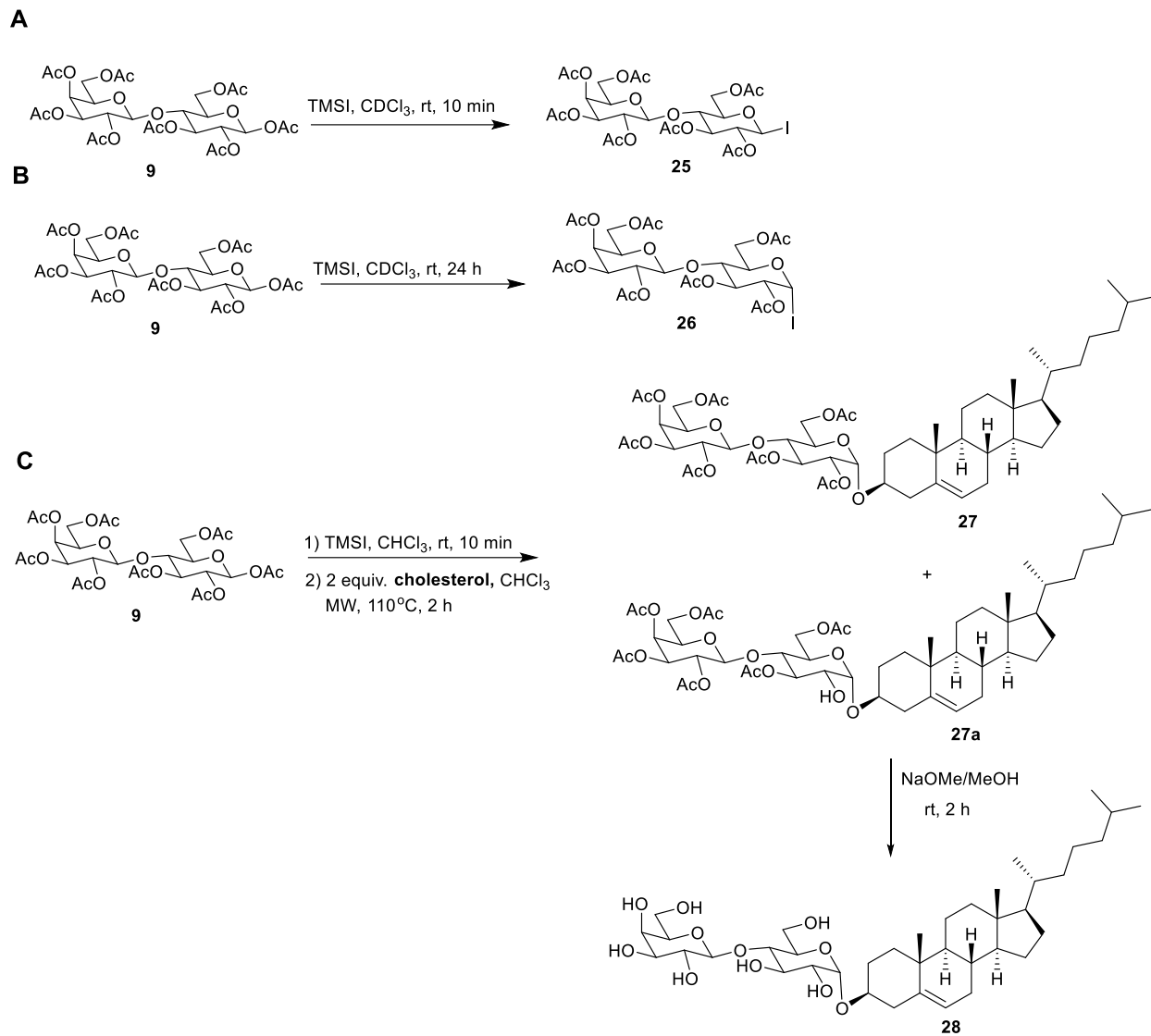
Scheme 4.3 Davis et al. 2015 Procedure. (A) Synthetic Scheme for β-Lactosyl Iodide (25), (B) Synthetic Scheme for α-Lactosyl Iodide (26), (C) Synthetic Scheme for α-Cholesterol Lactoside (28)

As shown in Scheme 4.3(A), **9** was reacted with 1.1 eq. of TMSI in deuterated chloroform (0.15 M). Deuterated chloroform was chosen over regular chloroform, so the formation of **25** and **26** can be monitored real-time via NMR. The reaction was conducted at rt in 10 min which afforded **25** in situ and quantitively (Davis et al., 2015). The formation of **25** was confirmed by NMR by the appearance of a doublet peak at 5.78 ppm with a *J* coupling value of 9.0 Hz, identified as H_1. As shown in Scheme 4.3(B), **9** was reacted with 1.1 eq. of TMSI in deuterated chloroform (0.15 M). The reaction was conducted at rt in 15 h which afforded **26** in situ and quantitively (Davis et al.,

2015). The formation of **26** was confirmed by NMR by the appearance of a doublet peak at 6.89 ppm with a J coupling value of 4.3 Hz, identified as H_1. However, when repeating the procedure shown in Figure 4.3(B) to generate **26**, another compound (**26a**) was identified by NMR.

The 600 MHz ^{1}H NMR spectrum showed a doublet peak at 6.89 ppm with a J coupling value of 4.3 Hz which was previously identified to be H_1 α-lactosyl iodide (**26**) (see Figure S4.1) (Davis et al., 2015). However, another doublet peak at 6.82 ppm with a J coupling value of 4.1 Hz was also evident and identified to be H_1 of **26a** (see Figure S4.1). The 600 MHz COSY NMR spectrum showed that doublet peak at 6.89 ppm is coupled to a multiplet peak at 4.12 ppm via a COSY correlation, which agrees with the previous literature's assignment of H_2 of **26** (see Figure S4.2) (Davis et al., 2015). However, the doublet at 6.82 ppm showed COSY coupling to a doublet of doublet of doublet peak at 2.81 ppm which is identified as H_2 of **26a** which is a significant upfield shift compared to H_2 of **26** (see Figure S4.2). These separately identified H_1 and H_2 for **26** and **26a** were interpreted as two different compounds as the doublet of doublet of doublet peak at 2.81 ppm (H_2 of **26a**) showed no COSY and TOCSY correlation to the doublet peak at 6.89 ppm (H_1 of **26**) (see Figure S4.2 and S4.3). Therefore, **26** contains all the acetate groups while the **26a** has lost the acetate group at C_2. In the ^{29}Si DEPT-20 NMR spectrum, three singlet peaks at 7.33, 0, and -20.77 ppm were identified as a trimethylsilyl group, tetramethylsilane, and excess trimethylsilyl iodide, respectively (see Figure S4.4). It was later identified that the acetate group at C_2 for **26a** was converted to a hydroxyl group as indicated by the lack of correlation between the ^{1}H doublet of doublet of doublet peak at 2.81 ppm (H_2 of **26a**) and the ^{29}Si singlet peak at 7.33 ppm (trimethylsilyl) in the ^{29}Si HMBC NMR spectrum (see Figure S4.5).

With the formation of **25** in chloroform (0.15M), 2 eq. of cholesterol (**33**) were added under Ar and immediately microwaved in a Biotage microwave reactor. The reaction took place for 2 h at 110 °C, resulting in a yield of 12% of **27** (see Scheme 4.3C) (Davis et al., 2015). In addition, a

59% yield was observed for **27a** in which the acetate group is lost at C_2 (Davis et al., 2015)**.** However, the β-anomer (**31**) was also formed in a yield of 10% from **25** as previously reported**.**
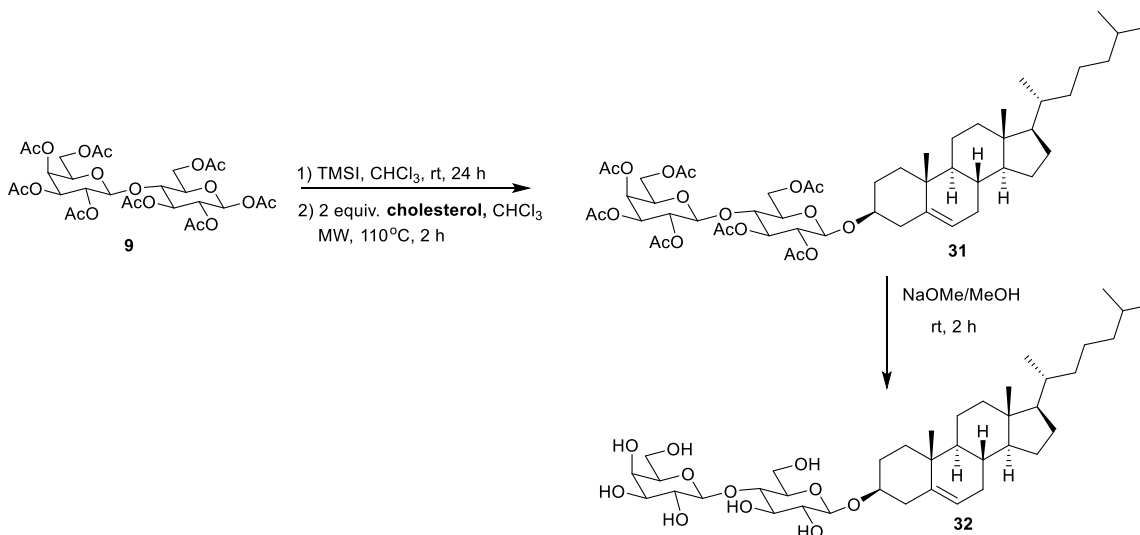
Scheme 4.4 Synthetic Scheme for β-Cholesterol Lactoside (32)

The Davis et al. 2015 procedure was repeated with **26** to determine if primary formation of **32** would occur (see Scheme 4.4). By TLC, it seems **27a** was the major glycosylation product while **31** was the minor glycosylation product based on the intensive R_f spot at 0.40 from the 2 h TLC plate (see Figure 4.1B). From the glycosylation reactions between cholesterol (**33**) and **26/27** (see Schemes 4.3C and 4.4), it seems a mixture of desired and undesired cholesterol lactoside anomers appeared from repeating the Davis et al. procedure (Davis et al., 2015)**.** Therefore, a new method was proposed to minimize the formation of undesired cholesterol lactoside anomers.
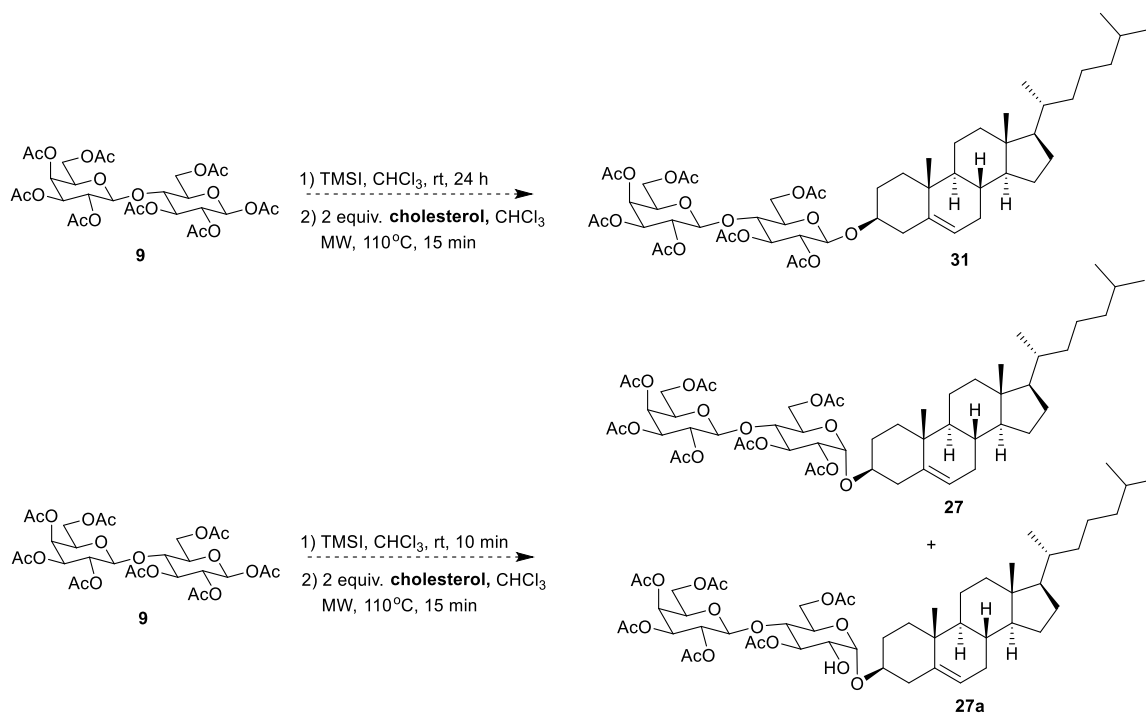
Scheme 4.5 Proposed Microwave Reaction Scheme for 27/27a and 31

In the proposed microwave scheme, instead of reacting **25** or **26** with cholesterol (**33**) for 2 h in the microwave, they will be allowed to react for 15 min in three "5 min" intervals (see Scheme 4.5). Having a shorter interval of microwave radiation would hopefully prevent any excess I⁻ ions from TMSI to undergo nucleophilic attack of preformed **25** or **26** which would lead to an undesired cholesterol lactoside anomer.
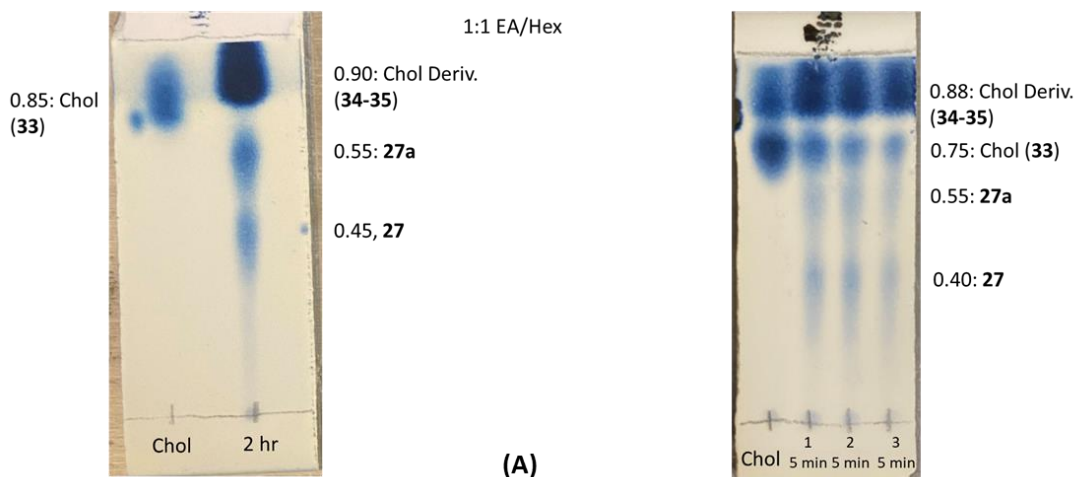
Figure 4.1A 2 hr vs. 15 min TLC Plates between 25 and Chol.

In Figure 4.1A, 15 min of microwave radiation rather than 2 h was enough for glycosylation between **25** and cholesterol (**33**) as seen by the appearance of R_f spots at 0.55 and 0.40 which were previously reported as **27** and **27a** in which the acetate group at C_2 on lactose was lost, respectively (Davis et al., 2015). However, it was observed by ^{1}H NMR that undesired **31** was present based on the appearance of a doublet peak at 4.55 ppm with a *J* coupling value of 8.0 Hz, identified as H_1.

1:1 EA/Hex

0.81: Chol (**33**)

0.90: Chol Deriv. (**34-35**)

0.40: **27**

Chol   2 hr

0.91: Chol Deriv. (**34-35**)

0.75: Chol (**33**)

0.50: **31**

Chol   1 5 min   2 5 min   3 5 min

(B)
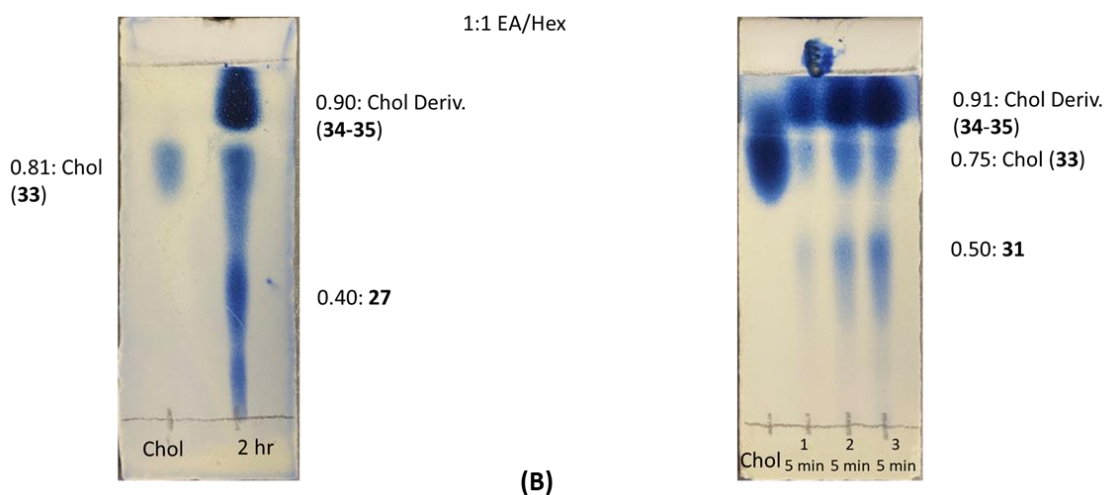
Figure 4.1B 2 hr vs. 15 min TLC Plates between 26 and Chol.

In Figure 4.1B, 15 min rather than 2 h of microwave radiation was also enough for glycosylation between **26** and cholesterol (**33**) as seen by the appearance of the R_f spot at 0.50 which was previously reported as **31** (Davis et al., 2015). However, it seemed that a small amount of undesired **27** and **27a** was present via ^{1}H NMR based on the appearance of a doublet peak at 5.13 ppm with a *J* coupling value of 3.8 Hz and a doublet peak at 4.98 ppm with a *J* coupling value of 3.6 Hz which were previously identified as H_1 of **27** and H_1 of **27a**, respectively (Davis et al., 2015).

α   1:1 EA/Hex   β

0.88: Chol Deriv.   0.91: Chol Deriv.
(34-35)   (34-35)
0.75: Chol (33)   0.75: Chol (33)

0.55: 27a   0.50: 31

0.40: 27

Chol 1 2 3 5 min 5 min 5 min   Chol 1 2 3 5 min 5 min 5 min

(C)
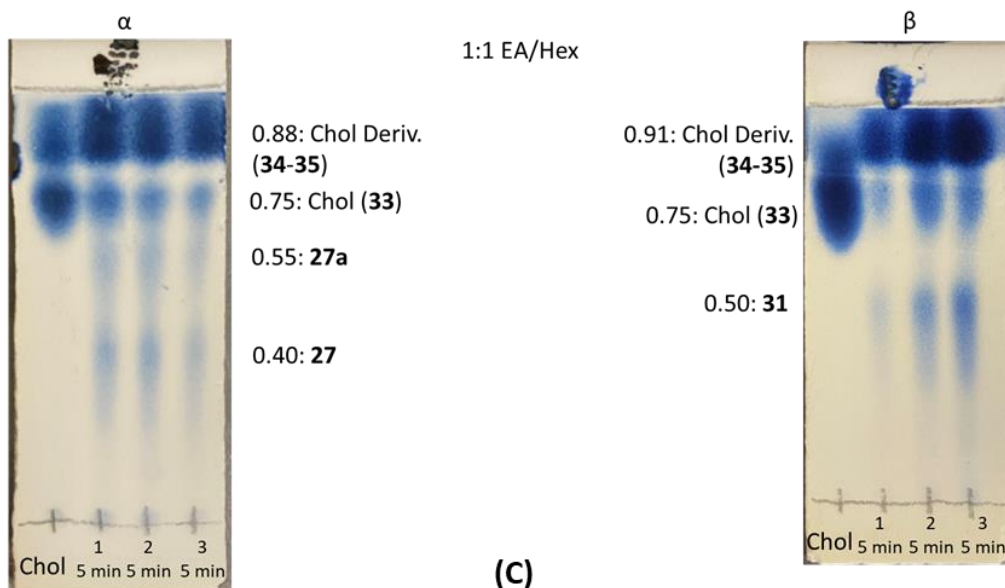
Figure 4.1C Side by Side 15 min TLC Plates between (A) and (B)

Comparing the 15 min TLC plates in Figures 4.1A and 4.1B, it seems 15 min of microwave radiation between **25** and cholesterol (**33**) leads to primary formation of **27** and **27a** based on the R_f spots at 0.55 and 0.40, while 15 min of microwave radiation between **26** and cholesterol (**33**) seems to lead to primary formation of **31** based on the R_f spot at 0.50 thus indicating possible selective glycosylation (see Figure 4.1C). However, 15 min of microwave radiation between **25/26** and cholesterol (**33**) (see Scheme 4.5) led to primary formation of cholesterol analogues (**34-35**) (R_f spot at 0.90-0.91) and excess cholesterol (**33**) (R_f spot at 0.75-0.81) (see Figures 4.1C). In addition, undesired cholesterol lactoside anomers (**27/27a** for reaction between **26** and cholesterol (**33**) or **31** for reaction between **25** and cholesterol (**33**)) still appeared via ^{1}H NMR. The structures of all the products formed from the 15 min microwave experiments are shown in Figure 4.1D. Therefore, future work will be directed to developing a method to limit the formation of cholesterol iodides/acetates (**34-35**) and prevent unwanted glycosylation products by consuming excess acetic and hydroiodic acid.

262
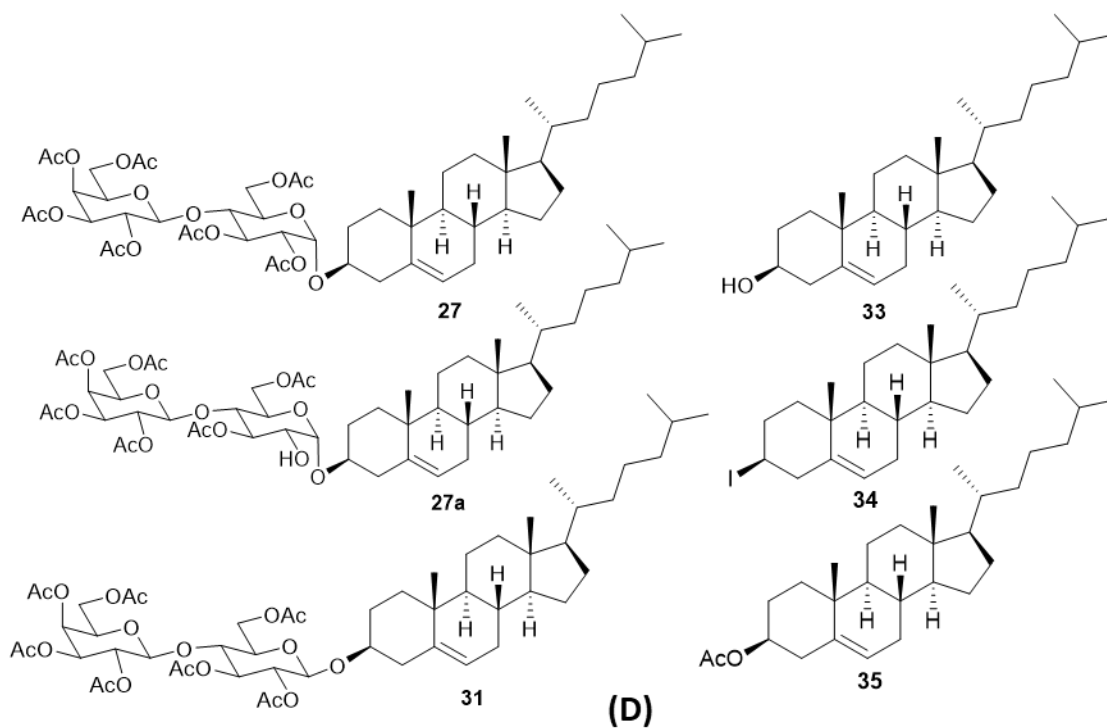
Figure 4.1D 15 min Microwave Reaction Products

Once achieving selective glycosylation in future studies, the acetate groups of **27/27a** and **31** will be deprotected with sodium methoxide in methanol under rt for 2 h (Davis et al., 2015). Next, a modified Davis et al. 2015 procedure will be utilized to synthesize the DHEA C_{17} N_3 Lactosyl Probes (**14**, **15**, **16**, and **17**) to study the metabolism of sterol glycosides in T_H1 and T_H2 cytokine response and sugar exchange with glycosylceramides. In addition, full characterization of **10**, **11**, **12**, **13**, **14**, **15**, **16**, and **17** will be achieved via ^1H, ^{13}C, COSY, HSQC, HMBC, and NOESY NMR experiments. After full characterization via NMR, **14-17** will undergo a CuAAC reaction with **MAN** using the optimized Blanco et al. procedure developed for **5** and **8** to determine how well they "click" together before subjection to biological studies. Upon *in vitro* subjection, **14-17** will be extracted with **MAN** and characterized via NMR and mass spectrometry for metabolites.

Section 4.2: Glycosylceramides

A

71

n= 16,24

B

72
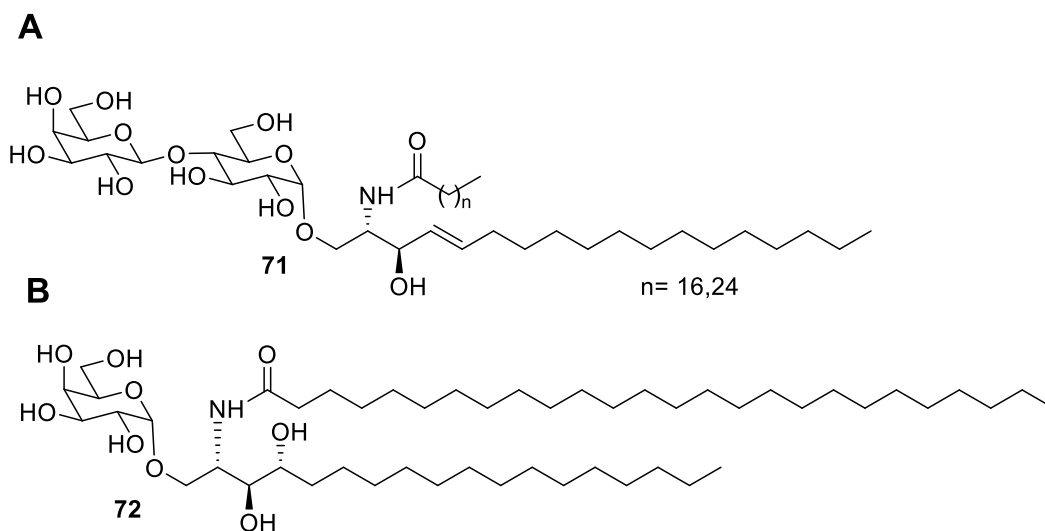
Figure 4.2 Glycosylceramides (A) α-lactosylceramide (α-LacCer, 71), (B) α-galactosylceramide (α-GalCer, 72)

In addition to cholesterol glycosides, there is another class of glycolipids called glycosylceramides. As seen by the name, glycosylceramides are made up of two main components, a sugar and lipid component. The sugar component can range from monosaccharides (glucose and galactose) to disaccharides (lactose) to trisaccharides (globotriaose and isoglobotriaose) (Zhang et al., 2008; Lai et al., 2019; Hsieh et al., 2014). As for the lipid component, ceramides are composed of an acyl chain and sphingosine-like base. A sphingosine is a mono-unsaturated 18-carbon amino alcohol (Lai et al., 2019). The two main glycosylceramides discussed are α-lactosylceramide (α-LacCer, **71**) and α-galactosylceramide (α-GalCer, **72**) (see Figure 4.2A-B). In comparison to CG (**51**) and CAG (**52**), all four of these glycolipids share an α-linkage between the lipid and sugar component. Between the two glycosylceramides, the sphingosine-like backbones can differ. In Figure 4.2, α-GalCer (**72**) contains a phytosphingosine base while α-LacCer (**71**) has a sphingosine base. It should be noted that for α-GalCer (**72**) and α-LacCer (**71**), either one can contain a phytosphingosine or sphingosine base. A phytosphingosine is a fully saturated18-carbon amino-hydroxy alcohol showing close resemblance to sphingosine.
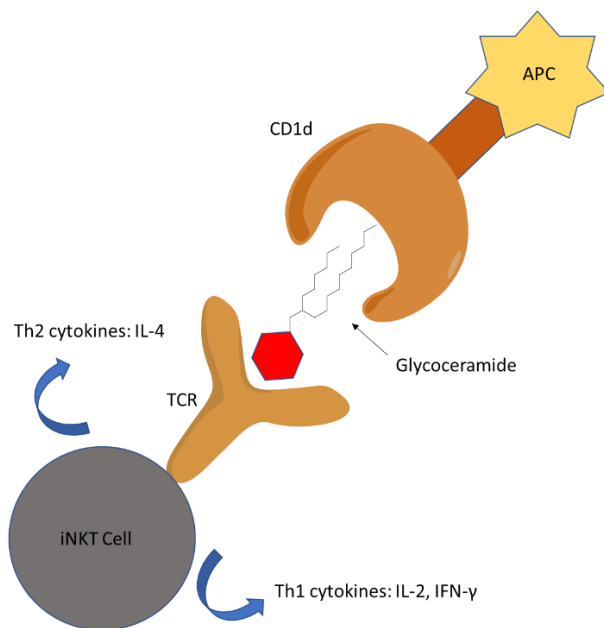
Figure 4.3 CD1d interaction with iNKT cells

α-GalCer (**72**) is a close analogue of various agelasphins, metabolites isolated from the *Agelas* genus of marine sponges (Kinjo et al., 2009). Within the marine sponge's mass (35-60%), a microbial community exists which includes cyanobacteria, heterotrophic bacteria, fungi, etc. (Brinkmann et al., 2017). These microbes could potentially be the source of α-GalCer (**72**) isolated from the *Agelas* genus of marine sponges. A unique feature of α-GalCer (**72**) is the α-linkage between galactose and phytosphingosine, while most other GSLs in nature were known to have a β-linkage between the sugar and lipid component (Kinjo et al., 2009). In terms of bioactivity, α-GalCer (**72**) has been shown to increase the lifespan of B16 mice when introduced intraperitoneally (Zhang et al., 2008). Chemically, the ceramide component of α-GalCer (**72**) interacts specifically with CD1d of MHC-1-like CD1 molecules found on antigen presenting cells (APC) (see Figure 4.3) (Zhang et al., 2008; Lai et al., 2019; Guillaume et al., 2017). CD1d is the protein that presents the glycoceramide to invariant natural killer T cells (iNKT cells) (Zhang et al., 2008). The CD1d-glycolipid complex is recognized by invariant T-cell receptors (TCR) on iNKT cells (see Figure 4.3) (Zhang et al., 2008). This interaction with iNKT cells results in the release of T-helper 1 (T_H1) and T-helper 2 (T_H2) cytokine in contrast to sitosteryl β-glucoside's biased T_H1

response (see Figure 4.3) (Lee et al., 2007; Zhang et al., 2008; Lai et al., 2019). T_H1 and T_H2 cytokines are small proteins released from iNKT cells as signaling molecules that help initiate cellular communication (Kim et al., 2013). Examples for T_H1 and T_H2 cytokines include (IFN-γ, IL-2) and (IL-4), respectively (Zhang et al., 2008; Lai et al., 2019; Kim et al., 2012; Kim et al., 2013). T_H1 cytokines are considered pro-inflammatory cytokines while T_H2 cytokines are considered anti-inflammatory cytokines (Kim et al., 2013). The release of T_H1 and T_H2 cytokines can lead to activation of natural killer (NK), B, and T cells (Lai et al., 2019). Secretion of IFN-γ from iNKT cells activate NK cells which has been correlated to anti-tumor activity (Zhang et al., 2008). Various other conditions are regulated by the latter T_H1 and T_H2 cytokines including malignancy, infection, and autoimmune diseases. However, activation of iNKT cells by α-GalCer (**72**) have been shown to induce airway hyperactivity (AHR) and concavalin A (ConA)-induced liver injury (Lai et al., 2019). Also, co-secretion of T_H1 and T_H2 cytokines has been shown to prolong certain diseases, like atherosclerosis, due to reciprocal inhibition which results in no overall change in immunity (Zhang et al., 2008; Kim et al., 2012).

α-LacCer (**71**) was also shown to activate iNKT cells and induce the release of T_H1 and T_H2 cytokines IFN-γ and IL-4, respectively. It was reported from an *in vitro* murine cytokine assay that α-LacCer (**71**) induced a dominant release of IL-4 as effectively as α-GalCer but not IFN-γ, thus indicating α-LacCer's (**71**) bias for secretion of T_H2 cytokines in contrast to sitosteryl β-glucoside's biased T_H1 response (Bouic et al., 1996; Lee et al., 2007; Zhang et al., 2008). It was also shown that the cleavage of the terminal galactose unit for lactose was necessary for α-LacCer's (**71**) T_H1 and T_H2 cytokine release (Zhang et al., 2008). Continuing on, Lai et al. reported α-LacCer (**71**) secreting IFN-γ and IL-4 at far lower concentrations compared to α-GalCer (**72**). The difference in efficacy of α-LacCer (**71**) between the two studies was correlated to the shorter acyl chain length (C18 vs C26) (Lai et al., 2019). From there, it was shown α-LacCer (**71**) could act as a competitive antagonist for CD1d receptors with α-GalCer (**72**) (Lai et al., 2019). ConA-

induced liver damage and AHR were attenuated in the presence of both α-GalCer (**72**) and α-LacCer (**71**). Conclusively, α-LacCer's (**71**) biased release of T_H2 cytokines could potentially be used as a starting point for the development of anti-inflammatory therapeutics.

Section 4.3: Previously Reported Glycosylceramide Derivatives and Probes
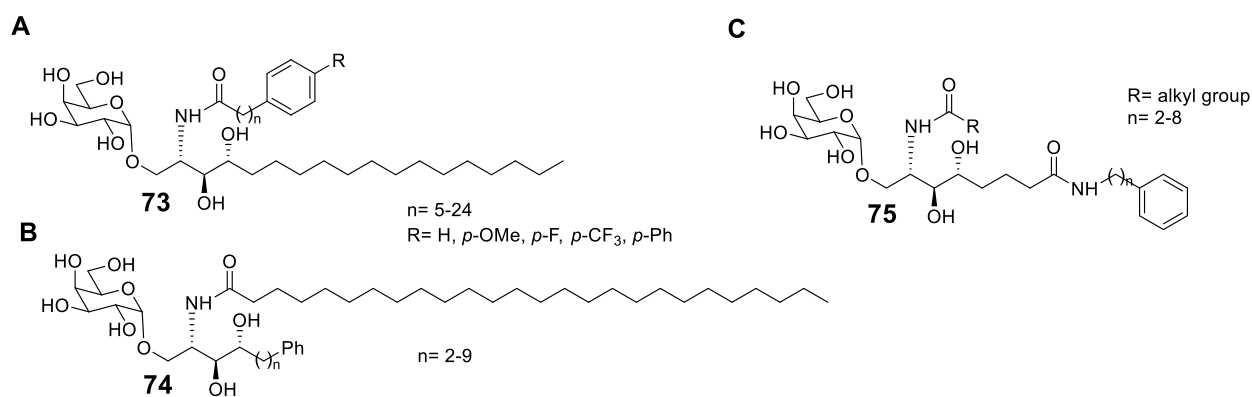
Figure 4.4 α-GalCer Derivatives. (A) Scaffold 1 (73), (B) Scaffold 2 (74), (C) Scaffold 3 (75)

Various derivatives of α-GalCer (**72**) were synthesized to monitor changes in T_H1 and T_H2 cytokine release compared to α-GalCer (**72**). The discussion below will focus on α-GalCer derivatives in which a heterocyclic and/or phenyl group is added to the phytosphingosine base. Li et al. utilized two scaffolds, one with a phenyl group in the amide chain (**73**) (see Figure 4.4A) and the other with a phenyl group in a truncated phytosphingosine backbone (**74**) (see Figure 4.4B). Guillaume et al. utilized a scaffold in which a terminal phenyl group is attached to a sphingamide backbone (**75**) (see Figure 4.4C). For α-GalCer derivatives utilizing scaffold 2 (**74**), all analogues produced low to moderate amounts of IFN-γ and IL-4 compared to α-GalCer (Li et al., 2010). For α-GalCer probes utilizing scaffold 3 (**75**), there was significantly low secretion of IFN-γ and IL-4 (Guillaume et al., 2017). There was no reported bias for T_H1 or T_H2 cytokine release among probes utilizing scaffold 2 (**74**) or 3 (**75**) (Li et al., 2010; Guillaume et al., 2017). For α-GalCer derivatives utilizing scaffold 1 (**73**), analogues with an acyl chain spacer length of 6-11 were able to induce iNKT cells to release significant amounts IFN-γ, while analogues with an acyl

chain spacer length of ≥ 15 displayed low secretion of IFN-γ (Li et al., 2010). In regard to IL-4 release, there was no significant difference amongst the α-GalCer derivatives utilizing scaffolds 1 compared to α-GalCer (Li et al., 2010). Overall, α-GalCer derivatives utilizing scaffold 1 (**73**) instigated a biased T_H1 response.

R= **1** $-CH_2-$⟨benzene⟩$-CH_2CH_2CH_2CH_2CH_2CH_3$

5 $-CH_2CH_2CH_2CH_2CH_2-$⟨benzene⟩$-CH_2CH_3$

2 $-CH_2CH_2-$⟨benzene⟩$-CH_2CH_2CH_2CH_2CH_3$

6 $-CH_2CH_2CH_2CH_2CH_2CH_2-$⟨benzene⟩$-CH_3$

3 $-CH_2CH_2CH_2-$⟨benzene⟩$-CH_2CH_2CH_2CH_3$

7 $-CH_2CH_2CH_2CH_2CH_2CH_2CH_2-$⟨benzene⟩

4 $-CH_2CH_2CH_2CH_2-$⟨benzene⟩$-CH_2CH_2CH_3$
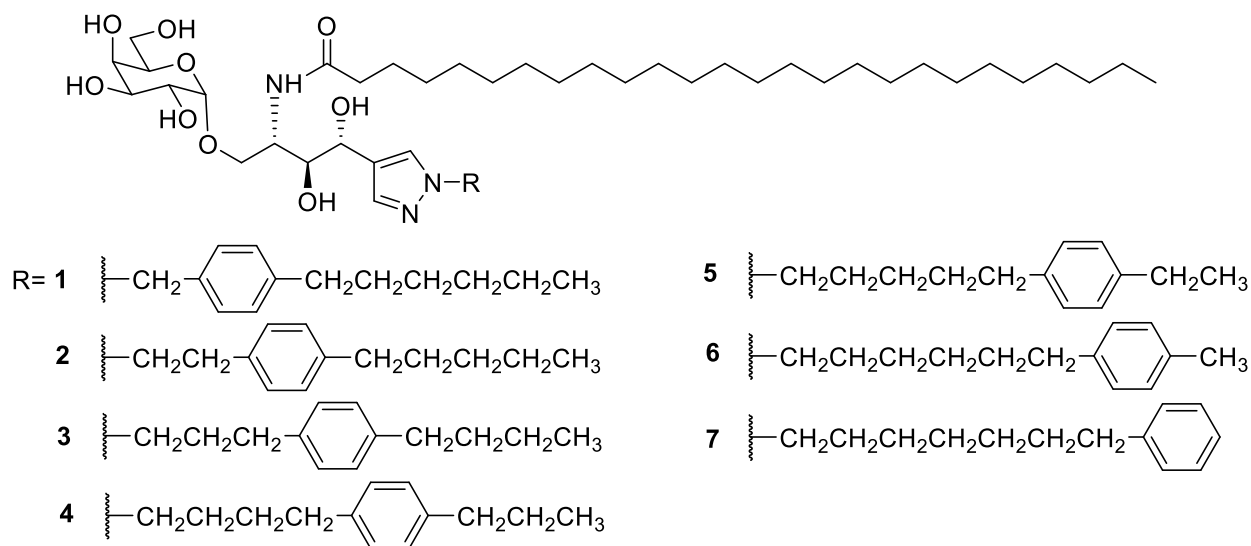
Figure 4.5 Heterocyclic α-GalCer Derivatives

As seen with the α-GalCer derivatives above, modifications were made at the phytosphingosine backbone or acyl chain. Kim et al. reported the synthesis and biological evaluation of heterocyclic α-GalCer derivatives, with a pyrazole moiety and phenyl group introduced to the phytosphingosine backbone (see Figure 4.5) (Kim et al., 2012; Kim et al., 2013). The introduction of the pyrazole and phenyl group were based from key interactions between the phytosphingosine backbone and three essential amino acids located in the CD1d protein: Tyr[73], Phe[77], and Trp[133], through docking investigations (Kim et al., 2012). In their first study, Kim et al. reported **1**, (see Figure 4.5), as the analogue with the highest cytokine release. In particular, **1** showed a biased T_H2 response as opposed to the α-GalCer derivatives utilizing scaffold 1 (**73**) (see Figure 4.5) (Li et al., 2010; Kim et al., 2012).

Continuing, Kim et al. reported on the optimal position of the phenyl group within the phytosphingosine backbone to induce a strong T_H2 response. Among analogues **1**-**7**, **3** produced the highest amount of IL-4, similar to that of α-GalCer (**72**) (see Figure 4.5) (Kim et al., 2013). Simultaneously, **3** also showed significant reduction of IFN-γ and IL-17 (see Figure 4.5) (Kim et al., 2013). Therefore, **3** is the best analogue to induce a dominant T_H2 response (see Figure 4.5). In addition to measuring cytokine secretion levels, **3** attenuated the pathogenicity of an inflammatory demyelinating disease of the central nervous system (CNS) (see Figure 4.5) (Kim et al., 2013). All in all, **3** shows high potential as an anti-inflammatory therapeutic (see Figure 4.5).
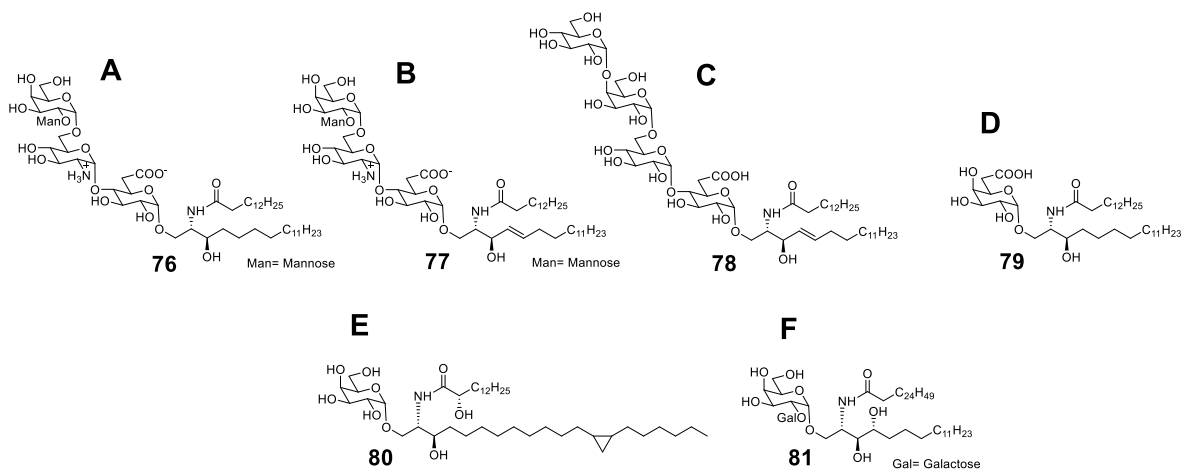
Figure 4.6 *Sphingomonas spp.* GSL Antigens. (A) GSL-4A (76), (B) GSL-4Au (77), (C) GSL-4Bu (78), (D) GSL-1 (79), (E) GalGSL-C21cycl (C21, 80), (F) αGal(1-2)αGalCer (GGC, 81)

In addition to the α-GalCer derivatives shown above, glycosphingolipids (GSLs) from *Sphingomonas spp.* bacteria were shown to induce cytokine response (see Figure 4.6). In comparison to α-GalCer (**72**), *Sphingomonas spp.* GSLs share the α-linkage between the sugar and lipid component like α-GalCer (**72**). Also, both glycolipids seem to be derived from microbial sources thereby presenting a correlation between microbes and α-linked GSLs. Sphingolipids are a class of eukaryotic lipids that include ceramides (*N*-acyl-sphingosine) and sphingomyelin (MacEyka & Spiegel, 2014). Thus, adding the prefix "glyco" indicates the attachment of a sugar moiety to the sphingolipid i.e., ceramide. In particular, the cytokine response of *Sphingomonas spp.* GSLs with tetrasaccharides: GSL-4A (**76**), GSL-4Au (**77**), and GSL-4Bu (**78**) (see Figure

4.6A-C) were compared to GSL-1 (**79**) (see Figure 4.6D), which had the highest stimulation of IL-2 (Kinjo et al., 2009). GSL-4A (**76**) and GSL-4Au (**77**) both contain a *N*-glucosamine unit while GSL-4Bu (**78**) does not. Both GSL-4A (**76**) and GSL-4Au (**77**) were are to stimulate the secretion of IL-2 (T$_H$1 cytokine) from Vα14i NKT cell hybridomas at lower levels compared to GSL-1 (**79**) (Kinjo et al., 2009). Moreover, the addition of a double bond in the sphingosine-like backbone had little effect on IL-2 production. However, GSL-4Bu (**78**) was observed to have no secretion of IL-2 from Vα14i NKT cell hybridomas (Kinjo et al., 2009). Therefore, the presence of an *N*-glucosamine seems to have played a role in IL-2 release.

In previous studies, αGal(1-2)αGalCer (GGC, **81**) (see Figure 4.6F) was required to participate in lysosomal processing to remove of the terminal galactose and become αGalCer (**72**) in order to be recognized by Vα14i NKT cells (Kinjo et al., 2009). Therefore, GSL-4A (**76**), GSL-4Au (**77**), and GSL-4Bu (**78**) were assayed to determine if lysosomal cleavage of the tetrasaccharide was responsible for the low IL-2 production (Kinjo et al., 2009). Overall, lysosomal processing was not required for the low secretion of IL-2 for GSL-4A (**76**) and GSL-4Au (**77**) as GSL-4Bu (**78**) showed no IL-2 production.

In regard to *Sphingomonas spp.* GSLs with tetrasaccharides, a *Sphingomonas spp.* GSL with a cyclopropyl-C21:0 chain, GalGSL-C21cycl (C21, **80**) (see Figure 4.6E), was analyzed to determine its antigenic properties. C21 (**80**) was able to induce moderate amounts of IL-2 from Vα14i NKT cell hybridomas (Kinjo et al., 2009). The amount secreted was lower than that of αGalCer (**72**), but higher than GSL-1 (**79**) (Kinjo et al., 2009). It was also determined that lysosomal processing was not required for C21 (**80**) as predicted, analogous to αGalCer (**72**) and GSL-1 (**79**) (Kinjo et al., 2009). C21 (**80**) was also able to stimulate Vα14i NKT cells *in vivo* as seen by moderate secretion of IFN-γ and IL-4 with no bias, albeit lower than that of αGalCer (**72**) (Kinjo et al., 2009). It was noted that various GSLs, including GSL-4A (**76**), lacked stimulation of cytokine production *in vivo* (Kinjo et al., 2009). In comparison to α-GalCer (**72**), most of the

Sphingomonas spp. GSLs induced a biased T_H1 response while α-GalCer (**72**) displayed no bias which could be attributed to the sugar component. Given the limitations of these *Sphingomonas spp.* GSLs, these antigens could potentially serve as pro-inflammatory therapeutics.

In summary, the α-GalCer derivatives described above with variations in the sphingosine backbone displayed various levels of T_H1 and T_H2 secretion compared to αGalCer (**72**). In addition, *Sphingomonas spp.* GSLs with tetrasaccharides displayed lower secretion of IL-2 compared to GSL-1 (**79**). Therefore, it can be observed that the ceramide and sugar components of glycosylated sphingolipids are critical for the control of T_H1 and T_H2 secretion in the hopes of designing potent therapeutics.
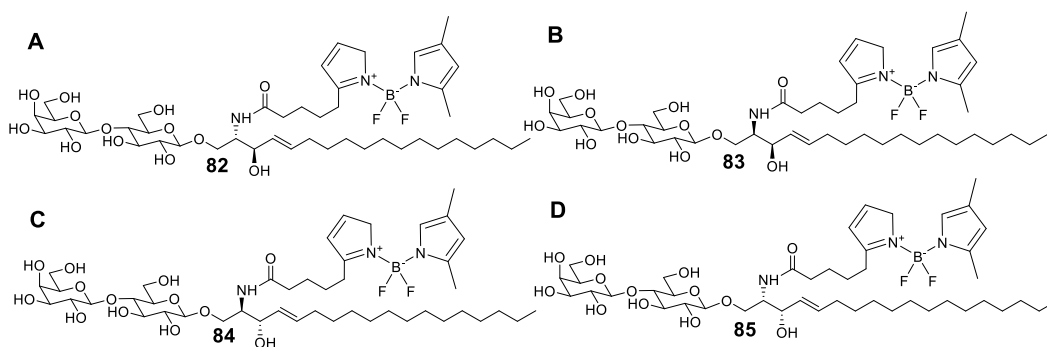
Figure 4.7 C_5-BODIPY-β-LacCer Probes. (A) (2S,3R) (82), (B) (2R,3R) (83), (C) (2R,3S) (84), (D) (2S,3S) (85)

As seen with α-GalCer probes' role in assaying cytokine release, β-LacCer probes were identified as a potential tool in assaying various biological events and imaging. For example, a BODIPY fluorophore attached to C_5 of a five-carbon fatty acid was added to four different β-LacCer backbones, synthesizing fluorescent LacCer probes: (2S,3R)-C_5-BODIPY-β-LacCer (**82**), (2R,3R)-C_5-BODIPY-β-LacCer (**83**), (2R,3S)-C_5-BODIPY-β-LacCer (**84**), and (2S,3S)-C_5-BODIPY-β-LacCer (**85**) (see Figure 4.7A-D). Having the BODIPY group terminally attached to the five-carbon acyl chain was reported to be ideally suited for biological applications (Pagano et al., 2000). In regard to the four C_5-BODIPY-LacCer probes synthesized by Liu et al., they were used to study intracellular trafficking of various GSLs in normal and diseased cells, in particular the role

of stereochemistry of the sphingosine backbone in uptake through endocytosis (Liu & Bittman, 2006; (Pagano et al., 2000). The mechanism for endocytosis is dependent on how well the sphingosine backbone interacts with other lipids in the membrane microdomains (Adar & Ilan, 2008). Among the four analogues, it was reported that only (2S,3R)-C_5-BODIPY-β-LacCer (**82**) displayed interactions with the microdomains (Adar & Ilan, 2008). In previous studies, it was reported that (2S,3R)-C_5-BODIPY-β-LacCer (**82**) was primarily located in lysosomes of diseased cells but localized at the Golgi apparatus in normal fibroblasts (Liu & Bittman, 2006). Additionally, engulfed C_5-BODIPY-LacCer were observed to transport to endosomes and lysosomes in cells at moderate temperatures (37°C) (Pagano et al., 2000).
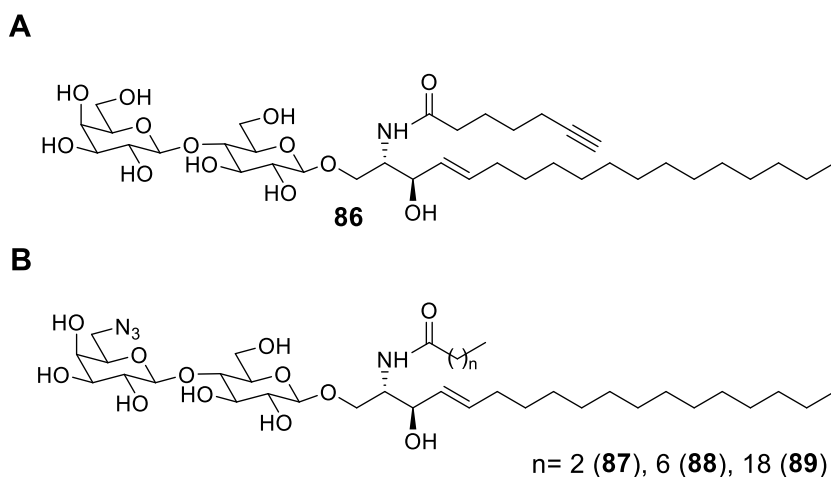
Figure 4.8 β-lactosyl ceramide click probes. (A) [2S,3R]-Alkyne-β-lactosyl ceramide (86), (B) [2S,3R]-N₃-β-lactosyl ceramide (87-89)

Dauner et al. reported the synthesis of four β-LacCer probes able to utilize click chemistry to study trafficking of glycosphingolipids. One included the addition of an alkyne moiety to the ω-carbon of an acyl chain (**86**) and the remaining three with various acyl chain lengths had an azide group substituting the 6'-OH of lactose (**87-89**) (see Figure 4.8A-B). For [2S,3R]-alkyne-β-lactosyl ceramide (**86**), only plasma membrane staining was observed, but at low fluorescence intensity (Dauner et al., 2016). It was hypothesized that the alkyne probe became very hydrophilic after the click reaction and was washed away, thus resulting in low fluorescence (Dauner et al., 2016).

For [2S,3R]-N$_3$-β-lactosyl ceramide probes, the two derivatives with an acyl chain of four (**87**) or eight (**88**) carbons showed bright staining in plasma membranes of HEK 293T cells while the derivative with an acyl chain of 20 (**89**) carbons showed no staining in plasma membranes of HEK 293T cells (Dauner et al., 2016).

Currently, there are very few studies utilizing LacCer derivatives to observe whether there is a change in cytokine release and CD1d binding. As seen with the LacCer probes described above, they were primarily used to monitor trafficking and uptake of GSLs *in vivo*, but not for changes in immune response. In addition, they are all in the β-configuration, thus highlighting the need to develop synthetic schemes for α-LacCer derivatives. Next, there are few methods for determining any structural changes for glycosylceramide antigens that may occur after administration of the compound. Therefore, future studies are needed to observe the effect of α/β-LacCer derivatives on T$_H$1 and T$_H$2 cytokine secretion and also identify metabolic changes to the antigens, which inspired the current project.

Section 4.4: Current Project Glycosylceramide Probes
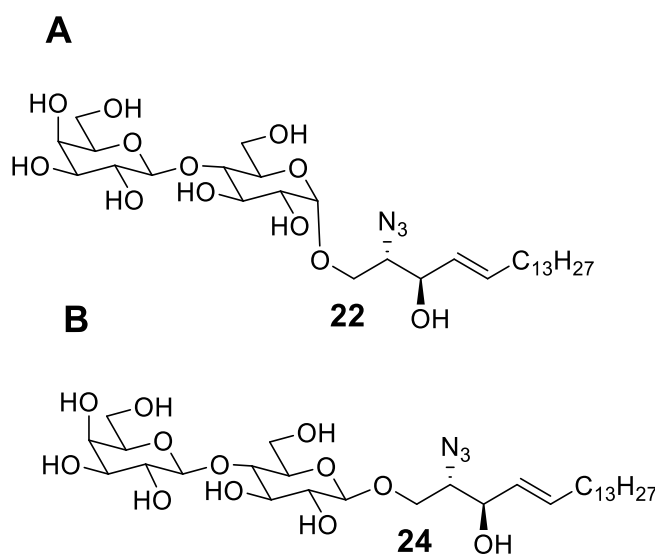
Figure 4.9 Lactosyl-N$_3$-sphingosine Probes. (A) [2S,3R]-α-lactosyl-N$_3$-sphingosine (22), (B) [2S,3R]-β-lactosyl-N$_3$-sphingosine (24)

In order to study the immunological effect of LacCer derivatives on cytokine release, two LacCer probes were proposed. The purpose of the lactosyl-N_3-sphingosine probes: [2S,3R]-α-lactosyl-N_3-Sphingosine (**22**) and [2S,3R]-β-lactosyl-N_3-Sphingosine (**24**), is to observe the effect of LacCers on CD1d binding and T_H1/T_H2 cytokine release (see Figure 4.9A-B). Previously reported by Li et al., α-GalCer derivatives were synthesized to monitor changes in T_H1/T_H2 cytokine release, CD1d binding, and TCR affinity compared to α-GalCer (**72**). However, there seems to be a lack of studies discussing the use of LacCer derivatives in measuring T_H1/T_H2 cytokine release and CD1d binding. It was shown that α-LacCer (**71**) had stronger affinity for CD1d molecules than α-GalCer (**72**) (Lai et al., 2019). In addition, the α-GalCer derivatives utilized by Li et al. (**73-74**) were not screened for structural changes as there was no extraction method to isolate the derivative. Therefore, the lactosyl-N_3-sphingosine probes (**22** and **24**) will be used to monitor changes in T_H1/T_H2 cytokine release and CD1d binding. These changes will be compared to α-LacCer (**71**) and α-GalCer (**72**). Specifically, the effect of α/β linkage between lactose and N_3-sphingosine in addition to the loss of an acyl chain on will be monitored for the latter bioactive responses. These lactosyl-N_3-sphingosine probes (**22** and **24**) could potentially be extracted using CuAAC and monitored for metabolic changes. In particular, the lactosyl-N_3-sphingosine probes (**22** and **24**) will be observed to see how lactose is exchanged with DHEA C_{17} N_3 probes (**5** and **8**) as seen previously between cholesterol and ceramides (see Figure 1.5). Specifically, the lactosyl-N_3-sphingosine probes (**22** and **24**) will be examined to see if the lactose group is cleaved of its terminal galactose subunit or substituted entirely with a glucose group as this change was crucial for cytokine release (Zhang et al., 2008). The synthesis of the lactosyl-N_3-sphingosine probes (**22** and **24**) will utilize methods previously reported (Du & Gervay-Hague, 2005; Davis et al., 2015; Hsieh et al., 2014). A sphingosine was chosen to be the base of the ceramide based on its synthetic efficiency (less protecting groups required), simpler NMR characterization, and its minimal effect on T_H1/T_H2 cytokine release compared to α-GalCer (**72**)

in murine iNKT cells (Dangerfield et al., 2012). Details regarding the synthesis will be described thoroughly below in Section 4.5.

Section 4.5: Lactosyl C$_{17}$ azido-sphingosine probes (**22** and **24**)
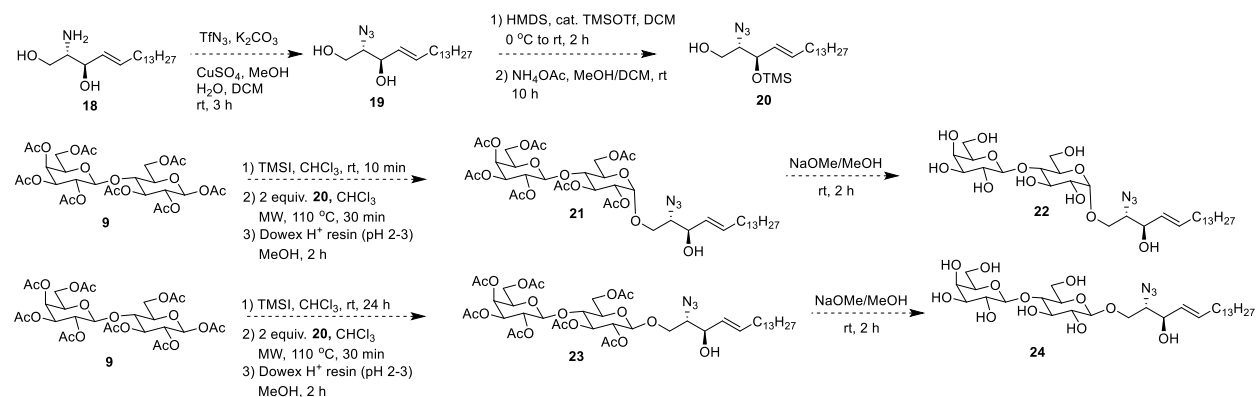
Scheme 4.6 Synthetic scheme of lactosyl C$_{17}$ azido-sphingosine probes (22 and 24)

They synthesis of **22** and **24** will utilize previous synthetic methods developed in the Gervay-Hague research group to study the metabolism of glycosylceramides in T$_H$1 and T$_H$2 cytokine response in addition to sugar exchange with sterols (Hsieh et al., 2014), (Davis et al., 2015), (Du & Gervay-Hague, 2005) (see Scheme 4.6). In addition, full characterization of **18**, **19**, **20**, **21**, **22**, **23**, and **24** will be achieved via ^{1}H, ^{13}C, COSY, HSQC, HMBC, and NOESY NMR experiments. After full characterization via NMR, **22** and **24** will undergo a CuAAC reaction with **MAN** using the optimized Blanco et al. procedure developed for **5** and **8** to determine how well they "click" together before subjection to biological studies. Upon *in vitro* subjection, **22** and **24** will be extracted with **MAN** and characterized via NMR and mass spectrometry for metabolites.

Figure S4.1 ^{1}H Spectrum of α-Lactosyl Iodide (26). ^{1}H NMR (600 MHz, chloroform-*d*) δ 6.89 (d, *J* = 4.3 Hz, 1H), 6.82 (d, *J* = 4.1 Hz, 1H), 5.46 – 5.40 (m, 1H), 5.33 (dt, *J* = 6.6, 3.0 Hz, 3H), 5.18 (t, *J* = 9.2 Hz, 1H), 5.14 – 5.05 (m, 3H), 4.95 (ddt, *J* = 10.9, 6.2, 3.0 Hz, 3H), 4.55 – 4.40 (m, 6H), 4.21 – 4.01 (m, 9H), 3.97 – 3.82 (m, 7H), 3.81 – 3.72 (m, 1H), 2.81 (ddd, *J* = 9.6, 4.1, 1.1 Hz, 1H), 2.22 – 1.81 (m, 94H).
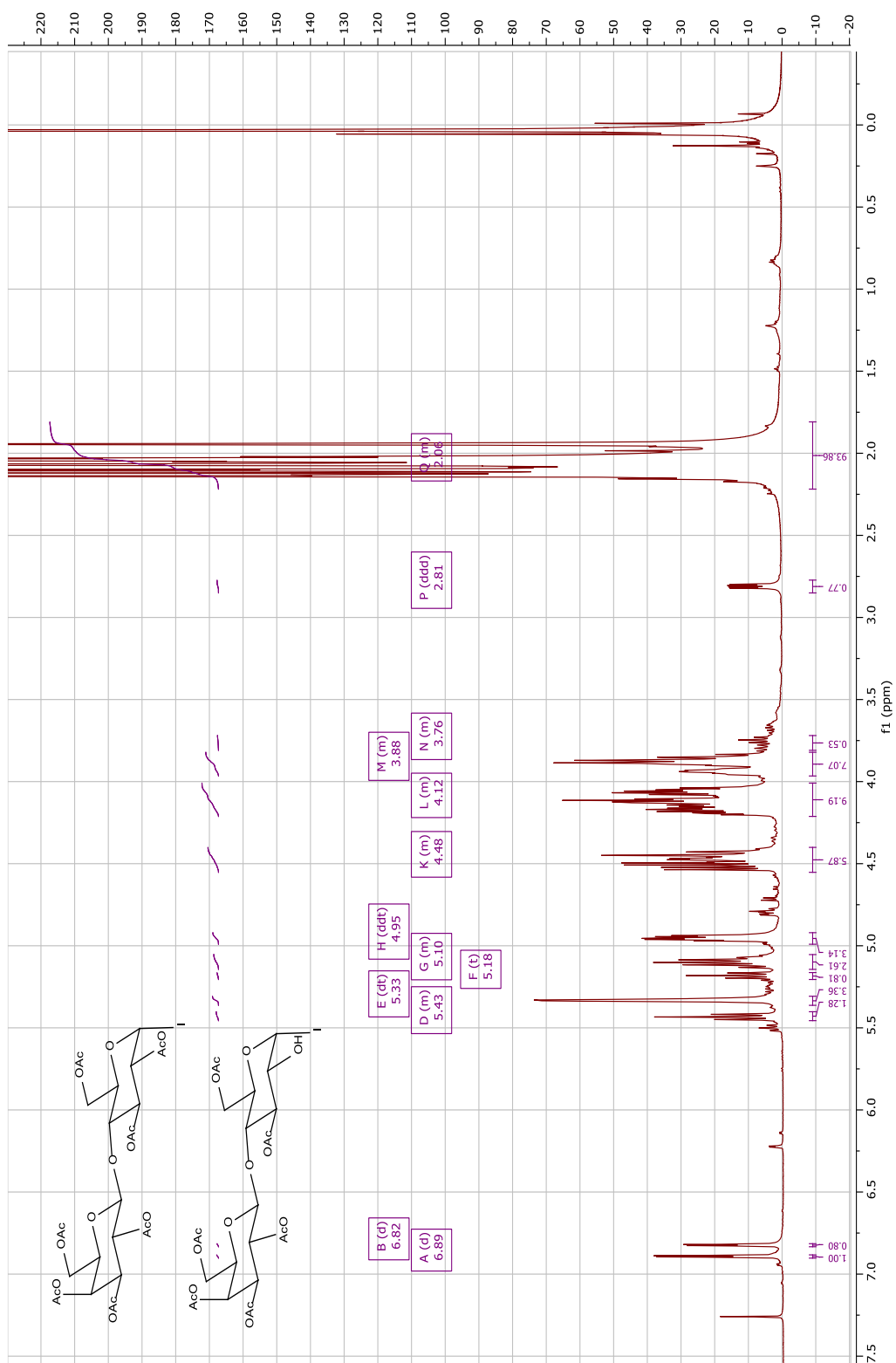
Figure S4.2 ^{1}H-^{1}H COSY Spectrum of α-Lactosyl Iodide (26)

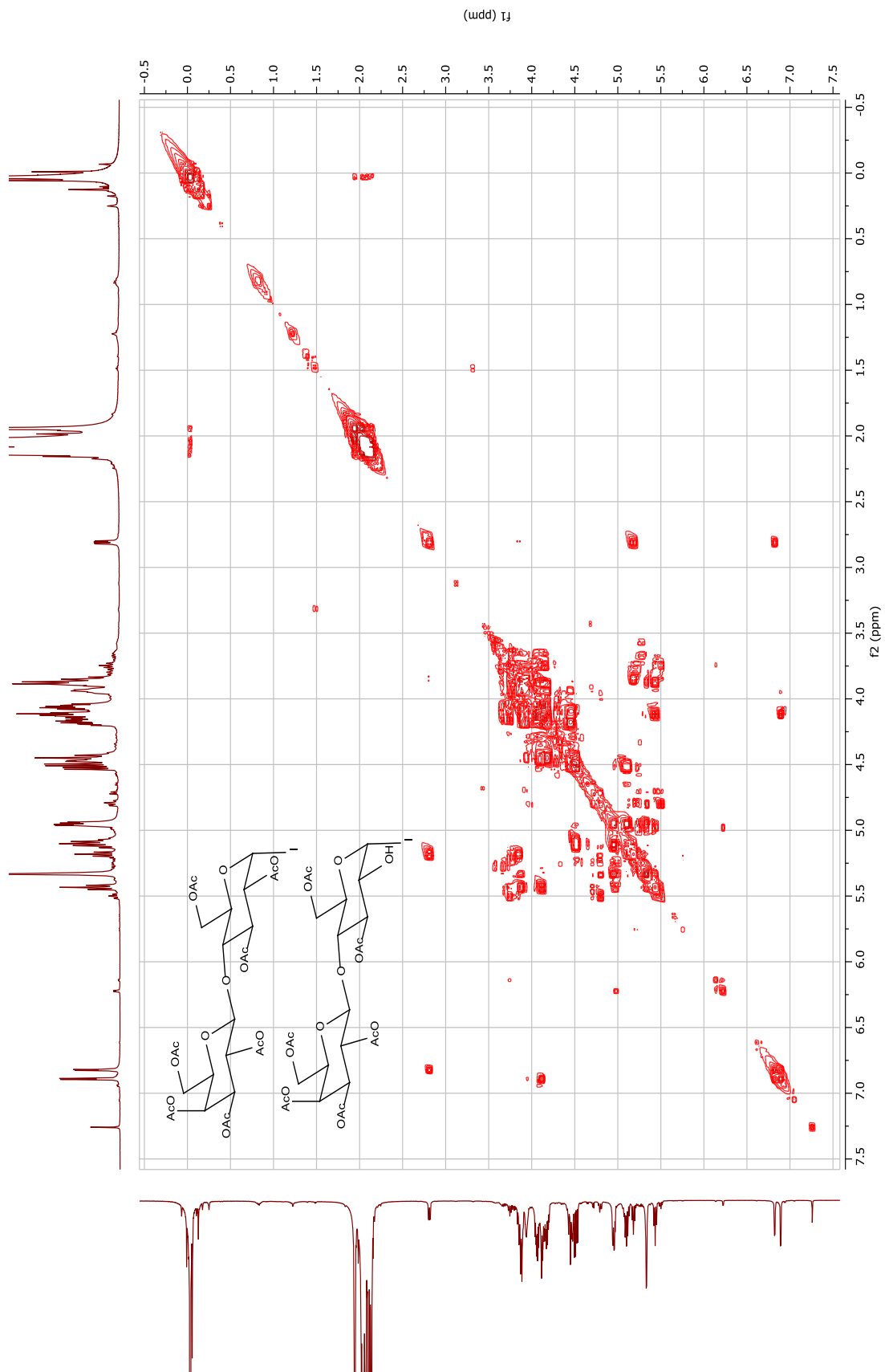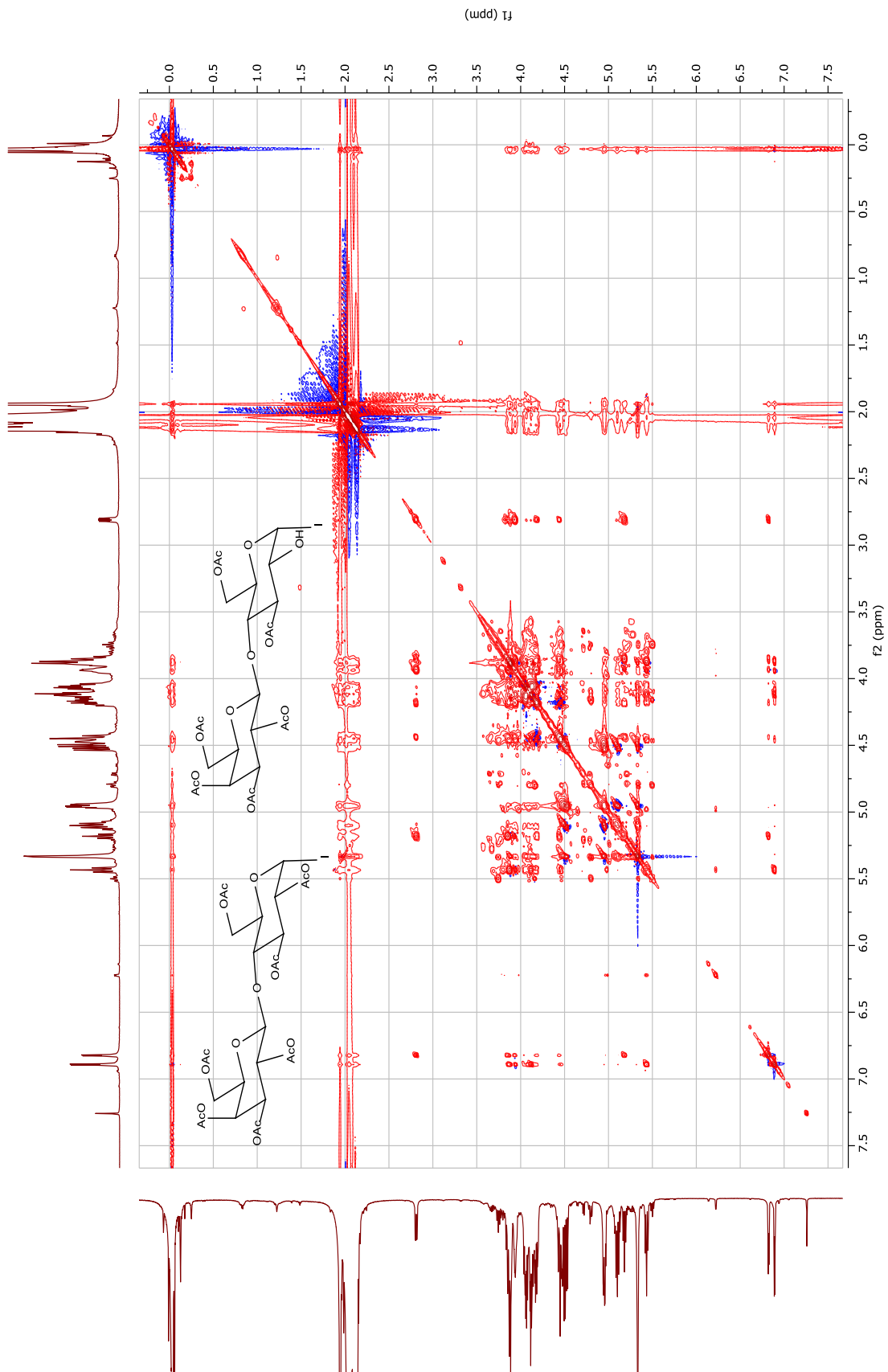**Figure S4.3 ^{1}H-^{1}H TOCSY Spectrum of α-Lactosyl Iodide (26)**

Figure S4.4 ^{29}Si DEPT-20 Spectrum of α-Lactosyl Iodide (26). ^{29}Si NMR (79 MHz, chloroform-*d*) δ 7.33, 0.00, -20.77.

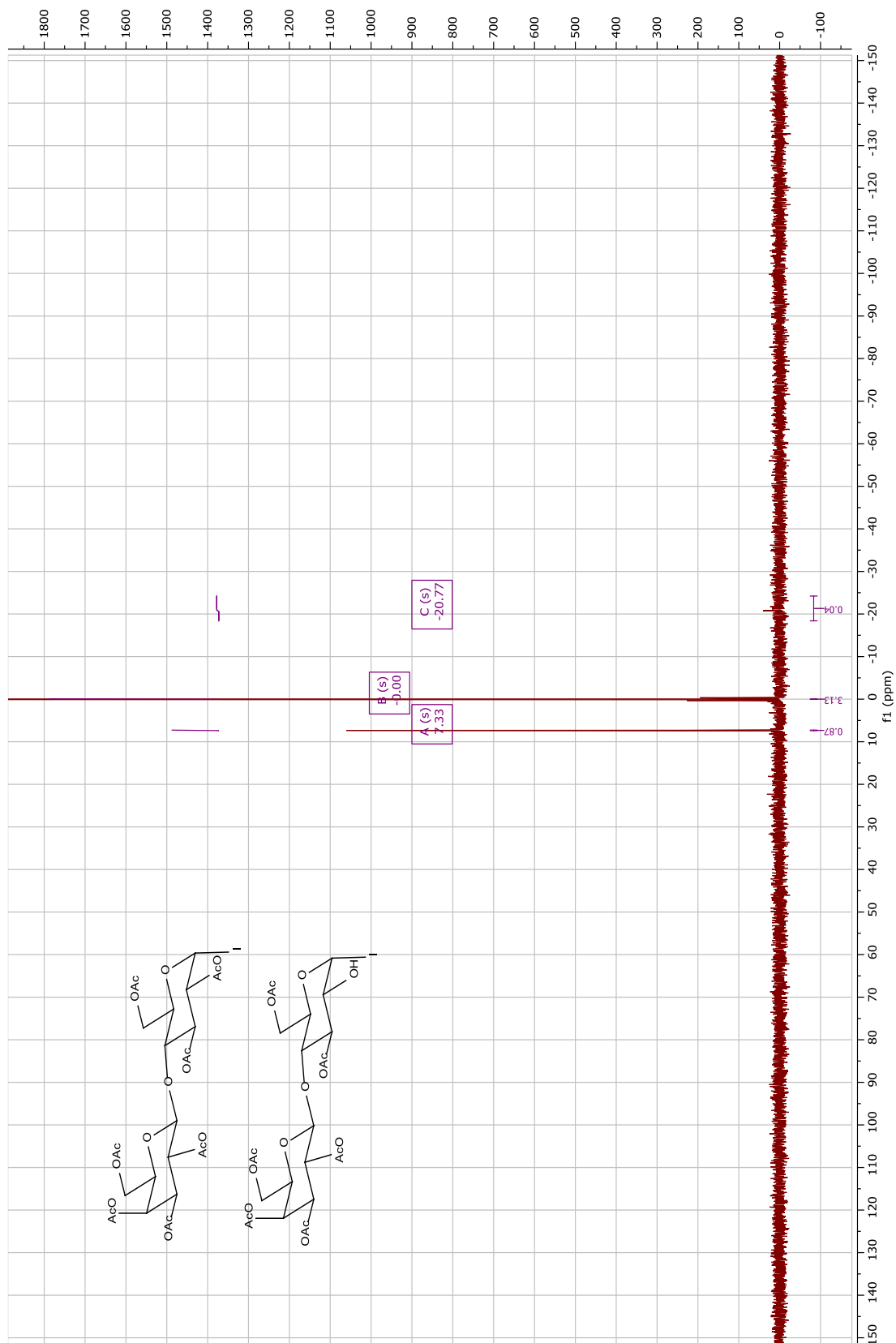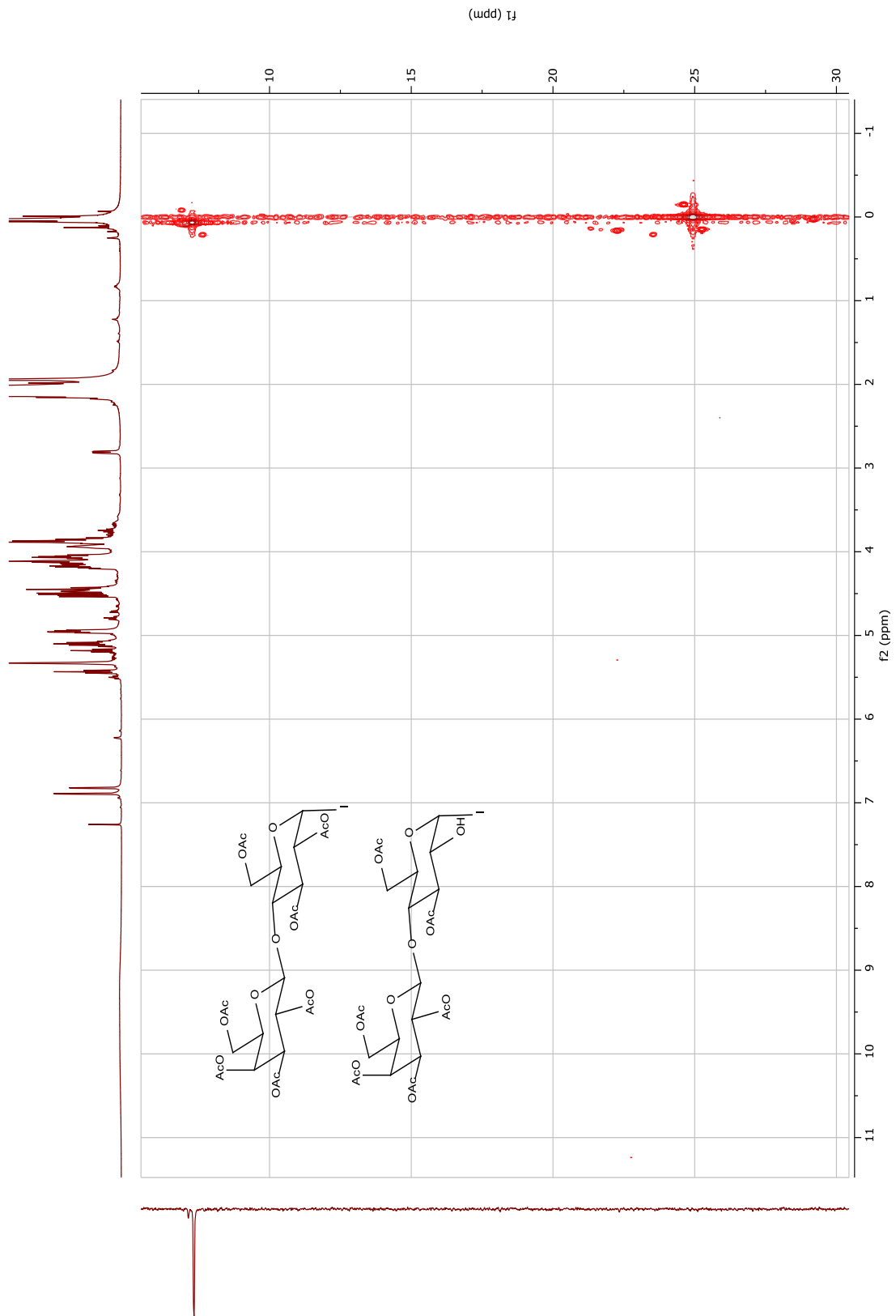**Figure S4.5 ^{29}Si HMBC Spectrum of α-Lactosyl Iodide (26)**

Section 4.7: References

Adar, T., & Ilan, Y. (2008). B-Glycosphingolipids As Immune Modulators. *Journal of Immunotoxicology*, *5*(2), 209–220. https://doi.org/10.1080/15476910802129620

Bouic, P. J. D., Etsebeth, S., Liebenberg, R. W., Albrecht, C. F., Pegel, K., & Van Jaarsveld, P. P. (1996). Beta-sitosterol and beta-sitosterol glucoside stimulate human peripheral blood lymphocyte proliferation: Implications for their use as an immunomodulatory vitamin combination. *International Journal of Immunopharmacology*, *18*(12), 693–700. https://doi.org/10.1016/S0192-0561(97)85551-8

Brinkmann, C. M., Marker, A., & Kurtböke, D. I. (2017). An overview on marine sponge-symbiotic bacteria as unexhausted sources for natural product discovery. *Diversity*, *9*(4). https://doi.org/10.3390/d9040040

Dangerfield, E. M., Cheng, J. M. H., Knight, D. A., Weinkove, R., Dunbar, P. R., Hermans, I. F., Timmer, M. S. M., & Stocker, B. L. (2012). Species-Specific Activity of Glycolipid Ligands for Invariant NKT Cells. *ChemBioChem*, *13*(9), 1349–1356. https://doi.org/10.1002/cbic.201200095

Dauner, M., Batroff, E., Bachmann, V., Hauck, C. R., & Wittmann, V. (2016). Synthetic Glycosphingolipids for Live-Cell Labeling Supporting. *Bioconjugate Chemistry*, *27*(7), 1624–1637. https://doi.org/10.1021/acs.bioconjchem.6b00177

Davis, R. A., Fettinger, J. C., & Gervay-Hague, J. (2015). Synthesis of cholesteryl-α-d-lactoside via generation and trapping of a stable β-lactosyl iodide. *Tetrahedron Letters*, *56*(23), 3690–3694. https://doi.org/10.1016/j.tetlet.2015.05.012

Du, W., & Gervay-Hague, J. (2005). Efficient synthesis of α-galactosyl ceramide analogues using glycosyl iodide donors. *Organic Letters*, *7*(10), 2063–2065.

https://doi.org/10.1021/ol050659f

Guillaume, J., Wang, J., Janssens, J., Remesh, S. G., Risseeuw, M. D. P., Decruy, T., Froeyen, M., Elewaut, Di., Zajonc, Di. M., & Calenbergh, S. Van. (2017). Galactosylsphingamides: New α-GalCer analogues to probe the F'-pocket of CD1d. *Scientific Reports*, *7*(1), 1–18. https://doi.org/10.1038/s41598-017-04461-7

Hsieh, H. W., Schombs, M. W., & Gervay-Hague, J. (2014). Integrating ReSET with glycosyl iodide glycosylation in step-economy syntheses of tumor-associated carbohydrate antigens and immunogenic glycolipids. *Journal of Organic Chemistry*, *79*(4), 1736–1748. https://doi.org/10.1021/jo402736g

Kim, Y., Kim, J., Oh, K., Lee, D. S., & Park, S. B. (2012). Heteroaromatic moieties in the sphingosine backbone of α- Galactosylceramides for noncovalent interactions with CD1d. *ACS Medicinal Chemistry Letters*, *3*(2), 151–154. https://doi.org/10.1021/ml200278u

Kim, Y., Oh, K., Song, H., Lee, D. S., & Park, S. B. (2013). Synthesis and biological evaluation of α-galactosylceramide analogues with heteroaromatic rings and varying positions of a phenyl group in the sphingosine backbone. *Journal of Medicinal Chemistry*, *56*(17), 7100–7109. https://doi.org/10.1021/jm400949h

Kinjo, Y., Pei, B., Bufali, S., Raju, R., Richardson, S. K., Imamura, M., Fujio, M., Wu, D., Khurana, A., Wong, C., Howell, A. R., & Seeberger, P. H. (2009). Natural Sphingomonas Glycolipids Vary Greatly in their Ability to Activate Natural Killer T Cells. *Chemical Biology*, *15*(7), 654–664.

Lai, A. C. Y., Chi, P. Y., Thio, C. L. P., Han, Y. C., Kao, H. N., Hsieh, H. W., Gervay-Hague, J., & Chang, Y. J. (2019). α-Lactosylceramide Protects Against iNKT-Mediated Murine Airway Hyperreactivity and Liver Injury Through Competitive Inhibition of Cd1d Binding. *Frontiers in*

Chemistry, *7*(November), 1–12. https://doi.org/10.3389/fchem.2019.00811

Lee, J. H., Lee, J. Y., Park, J. H., Jung, H. S., Kim, J. S., Kang, S. S., Kim, Y. S., & Han, Y. (2007). Immunoregulatory activity by daucosterol, a β-sitosterol glycoside, induces protective Th1 immune response against disseminated Candidiasis in mice. *Vaccine*, *25*(19), 3834–3840. https://doi.org/10.1016/j.vaccine.2007.01.108

Li, X., Fujio, M., Imamura, M., Wu, D., Vasan, S., Wong, C. H., Ho, D. D., & Tsuji, M. (2010). Design of a potent CD1d-binding NKT cell ligand as a vaccine adjuvant. *Proceedings of the National Academy of Sciences of the United States of America*, *107*(29), 13010–13015. https://doi.org/10.1073/pnas.1006662107

Liu, Y., & Bittman, R. (2006). Synthesis of fluorescent lactosylceramide stereoisomers. *Chemistry and Physics of Lipids*, *142*(1–2), 58–69. https://doi.org/10.1016/j.chemphyslip.2006.03.001

MacEyka, M., & Spiegel, S. (2014). Sphingolipid metabolites in inflammatory disease. *Nature*, *510*(7503), 58–67. https://doi.org/10.1038/nature13475

Pagano, R. E., Watanabe, R., Wheatley, C., & Dominguez, M. (2000). Applications of BIODIPY-sphingolipid analogs to study lipid traffic and metabolism in cells. In *Methods in Enzymology* (Vol. 312, Issue 1994). Elsevier Masson SAS. https://doi.org/10.1016/s0076-6879(00)12937-4

Zhang, W., Zheng, X., Xia, C., Perali, R. S., Yao, Q., Liu, Y., Zheng, P., & Wang, P. G. (2008). α-lactosylceramide as a novel "sugar-capped" CD1d ligand for natural killer T cells: Biased cytokine profile and therapeutic activities. *ChemBioChem*, *9*(9), 1423–1430. https://doi.org/10.1002/cbic.200700625